

AD-A236 219

(2)



PIEZOELECTRIC AND ELECTROSTRRICTIVE MATERIALS
FOR TRANSDUCER APPLICATIONS

DTIC

2025 RELEASE UNDER E.O. 14176

31.07.1991 D C

Period February 1, 1990 to January 31, 1991

Annual Report

VOLUME I

OFFICE OF NAVAL RESEARCH
Contract No. N00014-89-J-1689

APPROVED FOR PUBLIC RELEASE -- DISTRIBUTION UNLIMITED

Reproduction in whole or in part is permitted for any purpose
of the United States Government

L. E. Cross
R. E. Newnham
A. S. Bhalla
J. P. Dougherty
J. H. Adair
V. K. Varadan
V. V. Varadan

PENNSTATE



THE MATERIALS RESEARCH LABORATORY
UNIVERSITY PARK, PA

91-01137



91 6 4 022

REPORT DOCUMENTATION PAGE

Form Approved
OMB No. 0704-0189

1. REPORT SECURITY CLASSIFICATION			12. RESTRICTIVE MARKINGS	
2A. SECURITY CLASSIFICATION AUTHORITY			3. DISTRIBUTION/AVAILABILITY OF REPORT Reproduction in whole or in part is permitted for any purpose of the United States Government	
2B. DECLASSIFICATION/DOWNGRADING SCHEDULE				
4. PERFORMING ORGANIZATION REPORT NUMBER(S) N00014-89-J-1689			5. MONITORING ORGANIZATION REPORT NUMBER(S)	
6A. NAME OF PERFORMING ORGANIZATION Materials Research Laboratory		6B. OFFICE SYMBOL (If applicable)	7A. NAME OF MONITORING ORGANIZATION	
8C. ADDRESS (City, State, and ZIP Code) The Pennsylvania State University University Park, PA 16802			7B. ADDRESS (City, State, and ZIP Code)	
8A. NAME OF FUNDING/SPONSORING ORGANIZATION		8B. OFFICE SYMBOL (If applicable)	9. PROCUREMENT INSTRUMENT IDENTIFICATION NUMBER	
8C. ADDRESS (City, State, and ZIP Code)			10. SOURCE OF FUNDING NUMBERS	
			PROGRAM ELEMENT NO.	PROJECT NO.
			TASK NO.	WORK UNIT ACCESSION NO.
11. TITLE (Include Security Classification) Piezoelectric and Electrostrictive Materials for Transducer Applications				
12. PERSONAL AUTHOR(S) L.E. Cross, R.E. Newnham, A.S. Bhalla, J.P. Dougherty, J.H. Adair, V.K. Varadan, V.V. Varadarajan				
13a. TYPE OF REPORT ANNUAL		13b. TIME COVERED FROM 2/1/90 TO 1/31/91	14. DATE OF REPORT (Year, Month, Day)	
15. SUPPLEMENTARY NOTATION				
17. COSATI CODES			18. SUBJECT TERMS (Concurse on reverse if necessary and identify by block number)	
FIELD	GROUP	SUB-GROUP		
19. ABSTRACT (Concurse on reverse if necessary and identify by block number)				
SEE REVERSE SIDE OF PAGE.				
20. DISTRIBUTION/AVAILABILITY OF ABSTRACT <input type="checkbox"/> UNCLASSIFIED/UNLIMITED <input type="checkbox"/> SAME AS RPT. <input type="checkbox"/> OTHER USERS			21. ABSTRACT SECURITY CLASSIFICATION	
22A. NAME OF RESPONSIBLE INDIVIDUAL			22B. TELEPHONE (Include Area Code)	22C. OFFICE SYMBOL

ABSTRACT

This report documents work carried out in the Materials Research Laboratory of the Pennsylvania State University over the second year of a three year program on "Piezoelectric and Electrostrictive Materials for Transducer Applications" sponsored under grant No. N00014-89-J-1689 from the Office of Naval Research.

Highlights of the year's activity include: Participation of a number of senior faculty in program to better define the role of ferroelectrics in "smart materials" and the manner in which these developing interests will impact the needs for transducers as both actuators and sensors. New progress has been made with the flexensional (moonie) type structures and with the evolution of the 1 : 3 composites towards commercial development as large area actuators.

The year has seen major advance in the understanding of the relaxor type ferroelectrics which are most useful as dielectrics and electrostrictors. It has become clear that the original superparaelectric model is only a first approximation valid for the very high temperature behaviour and that in fact both the Lead magnesium niobate and the PZT materials are close analogues of the magnetic spin glasses. Interaction between the polar micro-regions leads to a Vogel-Fulcher like slowing down and freezing, and provides understanding of the micros to macrodomain transitions, the hysteretic behaviour and the coupled elastic responses.

An essential component of the program is the excellent capability in synthesis and processing which has been developed to provide the many new compositions and controlled microstructures which are essential for the proper understanding of the properties.

The report gives a brief narrative description of the researches which are more fully documented in the published papers of the technical appendices.

**PIEZOELECTRIC AND ELECTROSTRRICTIVE MATERIALS
FOR TRANSDUCER APPLICATIONS**

Period February 1, 1990 to January 31, 1991

Annual Report

VOLUME I

**OFFICE OF NAVAL RESEARCH
Contract No. N00014-89-J-1689**

APPROVED FOR PUBLIC RELEASE -- DISTRIBUTION UNLIMITED

**Reproduction in whole or in part is permitted for any purpose
of the United States Government**

L. E. Cross
R. E. Newnham
A. S. Bhalla
J. P. Dougherty
J. H. Adair
V. K. Varadan
V. V. Varadan



Accession For	WILL CRAZI	<input checked="" type="checkbox"/>
By	DILC 148	<input type="checkbox"/>
Classification	<input type="checkbox"/>	
By	<input type="checkbox"/>	
Classification	<input type="checkbox"/>	
Available for	<input type="checkbox"/>	
Dist. by Special	<input type="checkbox"/>	
A-1		

TABLE OF CONTENTS

ABSTRACT	1
INTRODUCTION	2
1.0 GENERAL SUMMARY PAPERS	3
2.0 SMART MATERIALS	4
3.0 COMPOSITE MATERIALS	4
4.0 THEORETICAL STUDIES	5
5.0 ELECTROSTRICKTION/RELAXOR FERROELECTRICS	6
6.0 OPTICAL STUDIES	8
7.0 PREPARATIVE STUDIES	9
8.0 MISCELLANEOUS PAPERS	10
9.0 APPRENTICE PROGRAM	11
10.0 PAPERS PUBLISHED IN REFEREEED JOURNALS	15
11.0 INVITED LECTURES	17
12.0 CONTRIBUTED PAPERS	18
13.0 HONORS TO MRL FACULTY & STUDENTS	22

APPENDICES

Volume I

General Summary Papers

1. R.E. Newnham and W. Huebner, "Electroceramics," Science of Advanced Materials, Chapter 9 (1990).
2. L. Eric Cross, "Polarization Controlled Ferroelectric High Strain Actuators (1990).
3. R.E. Newnham and S. Trolier-McKinstry, "Crystals and Composites," J. Appl. Cryst. 23, 447-457 (1990).

TABLE OF CONTENTS (continued)

Smart Materials

4. R.E. Newnham and G.R. Ruschau, "Smart Electroceramics," *J. Am. Ceram. Soc.* 74 (3), 463-480 (1991).
5. R.E. Newnham, "Tunable Transducers: Nonlinear Phenomena in Electroceramics," *National Institute of Standards and Technology Special Publication 804, Chemistry of Electronic Ceramic Materials, Proceedings of the International Conference held in Jackson, WY, August 17-22, 1990*, issued January 1991.
6. D. Damjanovic and R.E. Newnham, "Electrostrictive and Piezoelectric Materials for Actuator Applications," A Section in Chapter 5 - Intelligent Materials Systems, ASME/NASA Monograph on Flight-Vehicle Materials, Structures and Dynamics Technologies - Assessment and Future Directions. Edited by Ahmed K. Noor and Samuel L. Venneri.
7. W.Y. Pan, C.Q. Dam, Q.M. Zhang and L.E. Cross, "Large Displacement Transducers Based on Electric Field Forced Phase Transitions in the Tetragonal ($Pb_{0.97}La_{0.02}$)(Ti,Zr,Sn)O₃ Family of Ceramics," *J. Appl. Phys.* 66 (12), 6014-6023 (1989).

Composite Materials

8. Q.C. Xu, J.R. Belsick, S. Yoshikawa and R.E. Newnham, "Piezoelectric Composites with High Sensitivity and High Capacitance for Use at High Pressures," *Materials Research Laboratory, The Pennsylvania State University, University Park, PA 16802*.
9. A.S. Bhalla and R.Y. Ting, "Hydrophone Figure of Merit," *Sensors and Materials* 4, 181-185 (1989).
10. K.A. Hanner, A. Safari, R.E. Newnham and J. Runt, "Thin Film 0-3 Polymer/Piezoelectric Ceramic Composites : Piezoelectric Paints," *Ferroelectrics* 100, 255-260 (1989).
11. G.S. Lee, S. Kim and T.R. Shrout, "Fabrication of 0-3 Piezoelectric-Glass Composites," *Sensors and Materials* 2 (1), 7-15 (1990).
12. M.G. Grewe, T.R. Gururaja, T.R. Shrout and R.E. Newnham, "Acoustic Properties of Particle/Polymer Composites for Ultrasonic Transducer Backing Applications," *IEEE Transactions on Ultrasonics, Ferroelectrics, and Frequency Control* 37 (6), 506-514 (1990).
13. A.R. Ramachandran, Q.C. Xu, L.E. Cross and R.E. Newnham, "Passive Piezoelectric Damping," Presented at *IEEE Ultrasonics Symposium (UFFC)*, Honolulu, Hawaii (December 1-7, 1990).

TABLE OF CONTENTS (continued)

Theoretical Studies

14. B.N. Narahari Achair and G.R. Barsch, "Anharmonic Perturbation Theory of Electrostriction in a Perovskite Oxide at Finite Temperature," Solid State Communication 74 (5), 323-325 (1990).
15. L.E. Cross and G.A. Rossetti, Jr., "Origin of the First-Order Phase Change at the Curie Temperature in KNbO₃," J. Appl. Phys. 62 (2), 896-898 (1991).
16. G.A. Rossetti, Jr., K.R. Udayakumar, M.J. Haun and L.E. Cross, "Thermodynamic Theory of Single-Crystal Lead Titanate with Consideration of Elastic Boundary Conditions," J. Am. Ceram. Soc. 73 (11), 3334-38 (1990).
17. G.A. Rossetti, Jr., T. Nishimura and L.E. Cross, "X-Ray and Phenomenological Study of Lanthanum Modified Lead Zirconate - Titanate Compositions Incipient to the Relaxor Ferroelectric Phase Transition Region." (Submitted to J. of Appl. Phys.)

Electrostriction/Relaxor Ferroelectrics

18. T.R. Shrout and J. Fielding, Jr., "Relaxor Ferroelectric Materials," Materials Research Laboratory, The Pennsylvania State University, University Park, PA 16802.
19. A.D. Hilton, D.J. Barber, C.A. Randall and T.R. Shrout, "On Short Range Ordering in the Perovskite Lead Magnesium Niobate." (1989)
20. C.A. Randall and A.S. Bhalla, "Nanostructural-Property Relations in Complex Lead Perovskites," Japanese J. Appl. Phys. 29 (2), 327-333 (1990).
21. C.A. Randall, A.S. Bhalla, T.R. Shrout and L.E. Cross, "Classification and Consequences of Complex Lead Perovskite Ferroelectrics with Regard to B-Site Cation Order," J. Mater. Res. 5 (4), 829-834 (1990).
22. D.C. Dube, S.C. Mathur, S.J. Jang and A.S. Bhalla, "Electrical Behaviour of Diffused Phase Ferroelectrics in the Microwave Region," Ferroelectrics 102, 151-154 (1990).
23. D. Viehland, S.J. Jang, L.E. Cross and M. Wuttig, "Freezing of the Polarization Fluctuations in Lead Magnesium Niobate Relaxors," J. Appl. Phys. 68 (6), 2916-2921 (1990).
24. D. Viehland, S.J. Jang, L.E. Cross and M. Wuttig, "Local Polar Configurations in Lead Magnesium Niobate Relaxors," J. Appl. Phys. 69 (1), 414-419 (1991).
25. D. Viehland, S. Jang, L.E. Cross and M. Wuttig, "The Dielectric Relaxation of Lead Magnesium Niobate Relaxor Ferroelectrics." (Accepted Phil. Mag. B)
26. D. Viehland, J.F. Li, S. Jang, L.E. Cross and M. Wuttig, "The Glassy Polarization Behaviour of Relaxor Ferroelectrics." (Accepted Phys. Rev. B)

TABLE OF CONTENTS (continued)

APPENDICES

Volume II

Electrostriction/Relaxor Ferroelectrics (continued)

27. D. Viehland, J.F. Li, S.J. Jang, L.E. Cross and M. Wuttig, "A Dipolar Glass Model for Lead Magnesium Niobate." (Accepted Phys. Rev. B)
28. D. Viehland, J.S. Jang, L.E. Cross and M. Wuttig, "Anelastic Relaxation and Internal Strain in Lead Magnesium Niobate Relaxors." (Accepted Phil. Mag. B)
29. D. Viehland, S.J. Jang, L.E. Cross and M. Wuttig, "Internal Stain Relaxation Due to the Tilting of the Oxygen Octahedra and the Glassy Behaviour of LA Modified Lead Zirconate Titanate Relaxors." (Accepted J. Appl. Phys.)
30. D. Viehland, S.J. Jang, L.E. Cross and M. Wuttig, "The Dependence of the Glassy Polar Behaviour on Chemical Ordering in Relaxor Ferroelectrics."
31. J.R. Giniewicz, A.S. Bhalla and L.E. Cross, "An Investigation of the Structural and Dielectric Properties of the Solid Solution System $(1-x)Pb(Sc_{1/2}Ta_{1/2})O_3 - (x)PbTiO_3$," *Ferroelectrics Letters* 12, 35-42 (1990).
32. T.R. Shrout, Z.P. Chang, N. Kim and S. Markgraf, "Dielectric Behaviour of Single Crystals Near the $(1-x)Pb(Mg_{1/3}Nb_{2/3})O_3 - (x)PbTiO_3$ Morphotropic Phase Boundary," *Ferroelectrics Letters* 12, 63-69 (1990).
33. J.R. Giniewicz, D.A. McHenry, T.R. Shrout, S.J. Jang and A.S. Bhalla, "Characterization of $(1-x)Pb(Mg_{1/3}Nb_{2/3})O_3 - (x)PbTiO_3$ and $Pb(Sc_{1/2}Ta_{1/2})O_3$ Transparent Ceramics Prepared by Uniaxial Hot-Pressing," *Ferroelectrics* 109, 167-172 (1990).
34. D.A. McHenry, J.R. Giniewicz, T.R. Shrout, S.J. Jang and A.S. Bhalla, "Electrical and Optical Properties of Relaxor Ferroelectrics," *Ferroelectrics* 102, 161-171 (1990).
35. D.J. Taylor, D. Damjanovic, A.S. Bhalla and L.E. Cross, "Large Hydrostatic Piezoelectric Coefficient in Lead Magnesium Niobate: Lead Titanate Ceramics," Materials Research laboratory, The Pennsylvania State University, University Park, PA 16802.

Optical Studies

36. D.A. McHenry, J.R. Giniewicz, S.J. Jang, T.R. Shrout and A.S. Bhalla, "Optical and Electro-Optical Properties of Lead Magnesium Niobate-Lead Titanate," *Ferroelectrics* 107, 45-46 (1990).

TABLE OF CONTENTS (continued)

Optical Studies (continued)

37. D.A. McHenry, J. Giniewicz, S.J. Jang A. Bhalla and T.R. Shrout, "Optical Properties of Hot Pressed Relaxor Ferroelectrics," *Ferroelectrics* **23**, 351-359 (1989).
38. G.R. Fox, J.K. Yamamoto, D.V. Miller, L.E. Cross and S.K. Kurtz, "Thermal Hysteresis of Optical Second Harmonic in Paraelectric BaTiO₃," *Materials Letters* **2** (7, 8), 284-288 (1990).

Preparative Studies

39. A.D. Hilton[†], C.A. Randall*, D.J. Barber[†] and T.R. Shrout*, "The Influence of Processing on Dielectric Properties of PMN:PT Based Ceramics." [†]Department of Physics, University of Essex, Colchester, United Kingdom; *Materials Research Laboratory, The Pennsylvania State University, University Park, PA 16802.
40. W.R. Xue, W.A. Schulze and R.E. Newnham, "Effects of Sm₂O₃ and Gd₂O₃ + Nd₂O₃ on Electromechanical Properties of PbTiO₃ Ceramics," *J. Am. Ceram. Soc.* **73** (6) 1783-84 (1990).
41. P. Ravindranathan, S. Komaraneni, A.S. Bhalla, L.E. Cross and R. Roy, "Solution-Sol-Gel Processing of Lead Magnesium Niobate Thin Films," *Ferroelectrics Letters* **12**, 29-34 (1990).
42. P. Papet, J. P. Dougherty and T.R. Shrout, "Particle and Grain Size Effects on the Dielectric Behaviour of the Relaxor Ferroelectric Pb(Mg_{1/3}Nb_{2/3})O₃," *J. Mater. Res.* **5** (12), 2902-2909 (1990).
43. J.T. Fielding, Jr., S.J. Jang and T.R. Shrout, "Thermal Degradation of Relaxor-Based Piezoelectric Ceramics," Materials Research Laboratory, The Pennsylvania State University, University Park, PA 16802.
44. N. Kim, S.J. Jang and T.R. Shrout, "Relaxor Based Fine Grain Piezoelectric Materials," Materials Research Laboratory, The Pennsylvania State University, University Park, PA 16802.
45. F.G. Jones, C.A. Randall, S.J. Jang and T.R. Shrout, "Preparation in Characterization of Indium Based Complex Perovskites - Pb(In_{1/2}Nb_{1/2})O₃ (PIN), Ba(In_{1/2}Nb_{1/2})O₃ (BIN), and Ba(In_{1/2}Ta_{1/2})O₃ (BIT)," *Ferroelectrics Letters* **12**, 55-62 (1990).
46. T.R. Shrout, "Conventionally Prepared Submicron Electro-Ceramic Powders by Reactive Calcination," National Institute of Standards and Technology Special Publication 804, Chemistry of Electronic Ceramic Materials, Proceedings of the International Conference held in Jackson, WY, August 17-22, 1990, issued January 1991.

TABLE OF CONTENTS (continued)

Preparative Studies (continued)

47. S. Kim*, G.S. Lee* and T.R. Shrout* and S. Venkataramani+, "Fabrication of Fine Grain Piezoelectric Ceramics Using Reactive Calcination," *Materials Research Laboratory, The Pennsylvania State University, University Park, PA 16802; +General Electric Co., Schenectady, NY 12301.
48. T.R. Shrout, P. Papet, S. Kim and G.S. Lee, "Conventionally Prepared Submicron Lead-Based Perovskite Powders by Reactive Calcination," Materials Research Laboratory, The Pennsylvania State University, University Park, PA 16802.
49. T.R. Shrout*, Y.S. Kim*, J. Fielding, Jr.* and S. Venkataramani+, "Fabrication of Porous Electroceramics Structures by Reactive Calcination," *Materials Research Laboratory, The Pennsylvania State University, University Park, PA 16802; +General Electric Co., Schenectady, NY 12301.

Miscellaneous Papers

50. J.K. Yamamoto, C.A. Randall, S.A. Markgraf, A.S. Bhalla and M.A. Saifi, "Growth and Characterization of Ferroelectric/Polar Single Crystal Fibers," Ferroelectrics 107, 191-193 (1990).
51. S.A. Markgraf, C.A. Randall and A.S. Bhalla, "Incommensurate Phase In Ba₂TiSi₂O₈," Solid State Communications 75 (10), 821-824 (1990).
52. S.A. Markgraf and A.S. Bhalla, "Low-Temperature Phase Transition in Ba₂TiGe₂O₈," Phase Transitions 18, 55-76 (1989).
53. Z.P. Chang and A.S. Bhalla, "Elastic Anomaly In Fresnoite (Ba₂TiSi₂O₈) Single Crystal," Materials Letters 8 (10), 418-420 (1989).
54. S.A. Markgraf and A.S. Bhalla, "Pyroelectric and Dielectric Properties of Hemimorphite, Zn₂Si₂O₇(OH)₂ · H₂O" Materials Letters 8 (5), 179-181 (1989).

ABSTRACT

This report documents work carried out in the Materials Research Laboratory of the Pennsylvania State University over the second year of a three year program on "Piezoelectric and Electrostrictive Materials for Transducer Applications" sponsored under grant No. N00014-89-J-1689 from the Office of Naval Research.

Highlights of the year's activity include: Participation of a number of senior faculty in program to better define the role of ferroelectrics in "smart materials" and the manner in which these developing interests will impact the needs for transducers as both actuators and sensors. New progress has been made with the flextensional (moonie) type structures and with the evolution of the 1 : 3 composites towards commercial development as large area actuators.

The year has seen major advance in the understanding of the relaxor type ferroelectrics which are most useful as dielectrics and electrostrictors. It has become clear that the original superparaelectric model is only a first approximation valid for the very high temperature behaviour and that in fact both the Lead magnesium niobate and the PZT materials are close analogues of the magnetic spin glasses. Interaction between the polar micro-regions leads to a Vogel-Fulcher like slowing down and freezing, and provides understanding of the micros to macrodomain transitions, the hysteretic behaviour and the coupled elastic responses.

An essential component of the program is the excellent capability in synthesis and processing which has been developed to provide the many new compositions and controlled microstructures which are essential for the proper understanding of the properties.

The report gives a brief narrative description of the researches which are more fully documented in the published papers of the technical appendices.

INTRODUCTION

This report documents work carried out in the Materials Research Laboratory of The Pennsylvania State University over the second year of a three year program on "Piezoelectric and Electrostrictive Materials for Transducer Applications" sponsored under grant No. N00014-89-J-1689 from the Office of Naval Research. The topics under study build on and expand work carried on over the first year of the contract. In general the emphasis is being moved slowly from our earlier concern with large area sensors towards problems associated with materials for the actuator components, a response to the developing Navy interest in 'smart' materials and systems which is currently most limited by the actuator component.

For reporting purposes, the activities are grouped under the following major headings.

1. GENERAL SUMMARY PAPERS
2. SMART MATERIALS
3. COMPOSITE MATERIALS
4. THEORETICAL STUDIES
5. ELECTROSTRICTION/RELAXOR FERROELECTRICS
6. OPTICAL STUDIES
7. PREPARATIVE STUDIES
8. MISCELLANEOUS PAPERS

Highlights of the years activities include the participation of a number of the faculty in attempts to better define the role of ferroelectrics in 'smart' materials and structures and the manner in which these developments will impact the needs for sensors and actuators for both military and civilian systems. For the composite piezoelectrics, further development of the stress transferring "moonie" structures has induced three companies to begin commercial development. The 1:3 composites are now being produced in larger area sections through a cooperative program with Fiber Materials Inc. who have the ultraloom equipment for automated assembly. As expected, the large area 1:3 polymer: PZT composites show excellent properties for large area actuators with coupling coefficients $K_T \sim 70\%$ giving $\sim 50\%$ electrical to mechanical energy conversion.

The year has seen a major burst of activity on the Electrostrictive/Relaxor ferroelectric systems with new work on preparation and fabrication microstructure and nanostructure. A

crucial advance in understanding has come from the application of the magnetic spin glass formalism to the relaxors both in PMN:PT and in the PLZT families of compositions.

Optical studies which further help to define the polarization mechanisms in the relaxor ferroelectrics have been included for completeness.

In this program, as we have often reiterated, an essential component which undergirds all of the property studies is the fine work on preparation of both existing and new electroceramic compositions. This year the group has been making excellent use of reactive calcination as a technique for the economical development of ultrafine powders in both PZT and PMN families.

Following well established precedent this report summarizes in a brief narrative form the most important developments during the year connecting this narrative to an extensive set of appendices which document the work more fully in the form of papers published throughout the year.

1.0 GENERAL SUMMARY PAPERS

Professors R.E. Newnham and W. Huebner provided an excellent review article for the Journal of the American Ceramic Society (Appendix 1) summarizing the current status across the whole family of Electroceramic materials and devices. The article reviews capacitors, thermistors, varistors and other ceramic components, stressing the trend towards integrated systems. Sensors, actuators and smart systems are discussed and the trends towards miniaturization considered.

In a review article presented at the Joint US:JAPAN meeting on Adaptive Structures L.E. Cross (Appendix 2) discussed the status of high strain polarization controlled actuators. The paper summarizes the driving need to consider phase and domain change systems and discusses polarization control, switching speed and fatigue effects in these very high strain systems.

Exciting analogies between Composites and Crystal structures are drawn in a review for the Journal of Applied Crystallography (Appendix 3) by R.E.Newnham and S. Trolier-McKinstry. It is fascinating to see how some behaviours transpose almost exactly whilst in others, such as the ability to control scale in the composite there are no direct crystallographic equivalences through of course the symmetry properties are retained.

2.0 SMART MATERIALS

A theme which is certain to be recurring in this program on transducer materials is the developing need for electrically controllable shape and compliance for the actuator functions in smart elastic systems. In appendix 4, R.E. Newnham and G. R. Ruschau discuss smart electroceramics underscoring the new possibilities which sensor, control and actuation provide when incorporated in a smart material or system. The paper ranges over a very wide spectrum of applications and forms a very useful introduction to the concepts.

A more specialized family of 'smart' materials are discussed in appendix 5, namely those in which non linearity can be used to tune the response. Examples are taken in the PZT:Soft rubber 2:2 composites where the non linear elasticity of the rubber is used to tune the piezoelectric resonance frequency and in the PMN:PT family where electric field control of the nano-to-macrodomain transition can be used to control both magnitude and sign of the piezoelectric response. Appendix 6 discusses in some detail the complex panoply of polarization processes which contribute to the piezoelectric properties of the PZTs and the electrostrictive properties in the PMN family.

The important characteristics of the PL_xSn_yZT family of high strain polarization controlled actuators are summarized appendix 7.

3.0 COMPOSITE MATERIALS

A summary of the current status of the "moonie" flexensional type transducer is given in appendix 8. The finite element code ANSYS version 4.3 has been used to model the stress distribution in both metal and ceramic for the device under hydrostatic pressure. The model highlights the efficacy of the stress transfer and shows clearly the importance of the DC stress bias which is induced by the simple method of fabrication. The results show that $\Delta h_{gh} \sim 50,000 \text{ M}^2/\text{N}$ is achievable with a permittivity still in the range of 1,500.

A most useful discussion of the hydrophone figure of merit for a range of single phase and composite materials is given in Appendix 9. The conclusions come down heavily in favour of the composite systems which provide large g_h thickness product, and the possibility to tailor out pyroelectric noise. The fabrication of 0:3 type composites using paint technology is discussed in appendix 10, and an unusual type of 0:3 composite PbTiO_3 : glass ceramic is described in appendix 11.

The possibility of using particle:polymer composites in a completely different way to control acoustic impedance and attenuation for the backing layers of transducers is considered in appendix 12. The paper makes a systematic analysis of the factors which affect acoustic characteristics and makes recommendations for the phases and configurations required.

Another different type of use for the PZT:polymer composites is discussed in appendix 13 which examines the possibility for passive damping by resistive dissipation of the electric signal of the vibrating system. The discussion highlights the importance of high piezoelectric coupling for effective attenuation.

4.0 THEORETICAL STUDIES

In appendix 14, earlier work which calculated the temperature dependence of electrostriction in the perovskite SrTiO_3 using anharmonic perturbation theory has been finalized. The calculations based on an anharmonic shell model which was used earlier to calculate the coefficients of the static crystal in shown to give good agreement with the observed temperature characteristics.

In simple Devonshire phenomenological theory, the weak first order phase change in BaTiO_3 is shown to arise through electrostrictive coupling Appendix 15 musters the appropriate experimental information from the literature to demonstrate that the much stronger first order phase change at T_c in KNbO_3 also occurs through the same coupling.

A second application of the Devonshire phenomenology is made to lead titanate in appendix 16 which demonstrates good agreement with the observed shift of T_c with pressure, and explores the effects of pressure on polarization, dielectric and piezoelectric constants.

During a leave of absence taken at Mitsubishi Kasei Corporation, G.A. Rossetti carried out an interesting study extending the PZT phenomenology developed by Haun et al (see ONR

annual report for 1989) along the $Pb_{1-x}La_x(Zr_{0.65}Ti_{0.35})_{1-x/4}-O_3$ line into the PLZT phase diagram. In appendix 17 it is shown that in the $X = 0$ to 0.04 region the results are consistent with the existence of a local RMS polarization which persists up to $360^\circ C$ independent of the composition (x). Polarization and relative phase stabilities were in good agreement with experiment at low temperature, but at higher temperature relaxor character becomes important suggesting that polar regions below 5-15nm in diameter became unstable against thermal motion.

5.0 ELECTROSTRICTION/RELAXOR FERROELECTRICS

A general review of the properties of relaxor ferroelectrics has been given in appendix 18 which highlights their exceptionally large dielectric response that makes them particularly useful for MLC capacitors, electrostrictive actuators, agile transducers and electro-optic light valves. Discussions of the underlying "fossil" chemistry which gives rise to the dispersive relaxor behaviour is summarized in three papers, appendices 19, 20, 21. It is demonstrated in appendix 19 that in PMN and a range of PMN:PT solid solutions ordering of the Mg:Nb cations on the B site of the ABO_3 structure occurs but that the ordered regions are strictly limited in extent. In appendix 20 it is suggested that this local non stoichiometric ordering gives rise to very local polar regions which are unstable against thermal disordering at higher temperatures, and a number of relaxor compositions are analyzed to highlight the correlation between local ordering and the dispersive dielectric behaviour. Normal ferroelectric or antiferroelectric behaviour is shown to occur in either totally disordered or in fully long range ordered systems. This argument is further developed in the paper presented in appendix 21 which gives more detail of the arguments and the TEM studies upon which they are based.

Important additional experimental information for the dielectric response of the PMN:PT family is given in appendix 22 which delineates new microwave measurements on these ceramics. The extreme shifting of the dielectric maximum under 10 GHZ excitation is startling but most important for later predictive studies.

Perhaps the most important progress to date in the understanding of relaxor behaviour is given in the sequence of papers presented in appendices 23-30. These studies show step by step in a systematic manner that both the PMN and the PLZT based relaxor compositions have all the expected characteristics of a dielectric spin glass. In appendix 23 the polar glassy model is applied to analyze the frequency dependence of the dielectric maximum which is shown to follow the Vogel Fulcher relation well known in magnetic spin glasses. The freezing of the

fluctuation component of polarization is attributed to a coupling between the nano scale polar regions.

The electric field behaviour of the response is analyzed in appendix 24. Small electric fields were found to destabilize the local cluster formation in the glassy state enhancing the kinetics of polarization fluctuation . Larger biases appear to destroy the local fields forming clusters, destroying the dipole glass character and leading to long range order. Weak field dielectric response is analyzed in more detail in appendix 25 which explores the distribution of relaxation times and the marked broadening of this distribution near the freezing temperature of the glass. To explore the relaxor behaviour in the PLZTs at the 65:35 Zr:Ti ratio the build up of macroscopic polarization on warming the glassy state from low temperature under DC bias was explored (appendix 26). As expected the temperature of the maximum pyroelectric charging current decreases with increasing bias and can be modelled using the de Almeida Thouless relation to predict an average local moment of $3 \cdot 10^{-27} \text{ cm}$. For PMN, the quasi static hysteresis and the characteristic change from square loop to slim loop behaviour have been modeled using a modified Neel equation for the magnetization of a superparamagnet (appendix 28). A temperature dependent internal dipole field was introduced to approximate the cluster interactions.

Finally the anelastic relaxation and its correlation with the internal strain behaviour has been explored in both PMN (appendix 29) and in PLZT (appendix 30). Both internal and macro-strain in the PMN can be explained through the electrostrictive strains associated with local and global polarizations. In the PLZTs, the effects are a little more complicated due to a ferroelastic contribution from the oxygen octahedron tilts which occur in addition to the electrostrictive deformations.

We believe that the overwhelming balance of evidence now confirms that the relaxor ferroelectrics are the dielectric analogue of the magnetic spin glasses. In some senses however the properties are much more interesting, because of the strong electrostrictive couplings in all dielectric systems.

The phenomenological description of these properties is now almost complete, what remains is the correlation of the local polarizations with the fossil chemistry and their relation to local and more global chemical ordering (Appendix 30).

Experimental studies of the interesting solid solution system between lead scandium tantalate and lead titanate are discussed in appendix 31. The occurrence of a near morphotropic phase boundary between rhombohedral and tetragonal ferroelectric forms is shown to occur at between 60 and 55 Vol % PST. In the rhombohedral phase a wide range of dielectric responses between diffuse relaxor and sharp ferroelectric response is observed with increasing PT content with very large $K_{max} \sim 33,000$.

In the PMN:PT family, single crystals have been grown using flux methods (appendix 32). Compositions between 0.7PMN:0.3PT and 0.6PMN:0.4PT exhibit a phase change from rhombohedral to tetragonal symmetry. Relaxation behaviour again decreases with increasing PT content and dielectric maxima up to 60,000 are evident for fields in both 100 and 111 directions. Poled crystals show very high piezoelectric constants with d_{33} values up to 1,500 pC/N.

Hot pressing was used to prepare transparent samples in the composition fields PMN:PT and PST (appendix 33). The objective of these studies was to produce transparent samples of high density and to explore the effects of a range of preparative conditions and heat treatments on dielectric and optical properties. Optical properties of the 0.9PMN:0.1PT composition are presented in appendix 34. The optical dispersion is well described by a single term Sellmeier equation, and the onset of micro-polar regions at 390°C is evidenced in the temperature dependence of the refractive index.

A most useful study of the hydrostatic piezoelectric behaviour in electric field biased PMN:PT is given in appendix 34. It is shown that very large values of d_{33} , d_{31} and d_h occur under quite low driving fields in the 0.9PMN:0.1PT compositions.

It must be noted that the $d_{ij} \neq 2\epsilon_i Q_{ji} P_i$ and that even the qualitative form of d_h is not given by $d_h = 2\epsilon_3 P_3 Q_h$. A clear indication of the relaxation component of the polarizability.

6.0 OPTICAL STUDIES

The optical studies of the relaxor ferroelectrics have been carried out largely on our DARPA funded nanocomposite program and are included here for completeness.

The quadratic electro-optic constants R_{33} and g_{33} have been measured for 0.9PMN:0.1PT and 0.93PMN:0.07PT compositions (appendix 35). Both R and g constants

increase with PT concentration. A more detailed account of the optical behaviour for these hot pressed compositions is give in appendix 36 which delineates index dispersion, temperature dependence of index and the transverse electro-optic data.

In an interesting study of the optical second harmonic behaviour of BaTiO₃ single crystals and powders at temperatures embracing the Curie Point (T_c) appendix 36. It is evident that a small SHG signal persists after heating the samples through T_c. In the Remeika grown crystal the signal above T_c can be reduced below noise by annealing but in high purity fiber crystals and in high purity powders higher temperature (T > 250°C) may be required. In the Remeika crystal it is likely that the defect dipole structure responsible for aging stabilizes the polarization above T_c until the defects are randomized by the thermal treatment. For the higher purity crystals and powders the origin of the acentricity above T_c is not clear.

7.0 PREPARATIVE STUDIES

A careful study of the effects of processing upon the behaviour of relaxor ferroelectric ceramics in the PMN:PT family is discussed in appendix 37. The grain size dependence of the dielectric properties is shown to be dominated by a grain boundary (extrinsic) impedance due to a very thin amorphous layer at the boundary. Evidence is also adduced for an intrinsic grain size dependence which becomes important for fine grain ceramics and may be critical in thin films. Studies on Sm, Gd and Bd doped PbTiO₃ ceramics (appendix 38) have focused on the ionic size effects of the dopants to show that the very large anisotropy in the 10% Sm composition (kp/kt) can not be duplicated in the size equivalent Gd:Nd combination.

Techniques for forming thin PMN:PT films by sol-gel methods are discussed in appendix 39. Highly (III) oriented films with more than 95% perovskite structure have been formed.

A more comprehensive study of grain and particle size effects on the pure PMN relaxor is given in appendix 39.

Reactive calcination was used to prepare ultra fine 70 nanometer particulates which were densified by uniaxial hot pressing to form materials with grain size in the range 0.3 to 6 μ meters.

From dielectric spectroscopy on both ceramics and 0:3 polymer ceramic composites it was concluded that an intrinsic low permittivity surface region ($K \sim 300$) better describes the behaviour than the conventional extrinsic boundary phase model at the smaller grain sizes.

The columbite precursor method was used to produce Lanthanum modified PMN:PT compositions close to the morphotropic phase boundary (appendix 40). The lanthanum addition appears to refine the grain structure ($\leq 1 \mu\text{m}$) giving high dielectric constant $K_s \sim 5,000$ and $d_{33} \sim 500 \text{ pC/N}$.

Attempts to produce highly ordered Lead and Barium Indium Niobates and Tantalates (PIN, BIN and BIT) as low loss antiferroelectrics were frustrated (appendix 41) by the appearance of the pyrochlore phase for all conditions of annealing which were explored.

The concepts associated with the preparation of fine powders of the lead based perovskites by using the very large volumetric expansion which occurs on calcination is explored in appendices 42, 43, 44 and 45. Conditions to achieve the optimum states of soft agglomeration are discussed in appendix 42. The application of the method to forming powders from fine grained ($1 \sim 2 \mu\text{m}$) dense PZT ceramics with properties equivalent to normal large grain materials are discussed in 43. Application to a wider range of PbTiO_3 , PbZrO_3 , PZT and PMN compositions is discussed in 44 and the benefits which can be derived from the low sintering temperatures for these highly reactive powders are explored. In appendix 45, the possible application of the large volumetric expansion to the production of highly porous ceramics which can now be fabricated without a fugitive binder phase are examined.

8.0 MISCELLANEOUS STUDIES

Faculty and Students partially supported on this program have been associated with a number of ferroelectric developments which are reported here.

Exploratory studies have been accomplished to develop a laser heated pedestal growth technique for single crystal fibers (Appendix 46). The original system at Bell Communication Red Bank was improved and an updated system build in MRL. A number of perovskite, pyrochlore tungsten bronze and fresnoite structure ferroelectrics and polar crystal have been grown as single crystal fibers.

Studies of the incommensurate phase in fresnoite ($\text{Ba}_2\text{TiSi}_2\text{O}_8$) are described in appendix 47, and the unusual low temperature phase transition in the germanium analogue $\text{Ba}_2\text{TiGe}_2\text{O}_8$ is suggested to be a lock-in transition (Appendix 48). The elastic anomaly which accompanies the incommensurate change in fresnoite is examined in appendix 49. Pyroelectric and dielectric properties of the crystal hemicmorphite $\text{Zn}_2\text{Si}_2\text{O}_7(\text{OH})_2\text{H}_2\text{O}$ (appendix 50) show that this material is highly pyroelectric ($-45 \mu\text{C/m}^2\text{C}$) at room temperature with low dielectric constant and very weak piezoelectricity, suggesting that it may be a most useful pyroelectric crystal.

9.0 APPRENTICE PROGRAM

1990 ONR APPRENTICE PARTICIPANTS

1. NAME: Randolph D. Lucas
HOME ADDRESS: 5426 Woodrine Ave.
Philadelphia, PA 19181
COLLEGE: Lincoln University (Junior, Physics Major)
Lincoln, PA 19352
2. NAME: Helen Andrews
HOME ADDRESS: 2201 W. Ruffner St.
Philadelphia, PA 19140
HIGH SCHOOL: Simon Gratz
COLLEGE: Shaw University (Freshman)
Raleigh, NC
3. NAME: Rasheed Hassan Lance Bethel
HOME ADDRESS: 2909 Carter Rd.
Trevose, PA 19047
HIGH SCHOOL: Bensalem High School
COLLEGE: Penn State University (Freshman)
University Park, PA 16802
4. NAME: Tasha Blakeley
HOME ADDRESS: 4025 Old York Rd.
Philadelphia, PA 19410
HIGH SCHOOL: Girls High
COLLEGE: University of Maryland (Freshman)
Maryland

Randolph Lucas performed scanning electron microscopic (SEM) characterization of dielectric ceramic: polymer composites as a function of ceramic loading. He evaluated the degree of particle alignment and overall homogeneity.

Helen Andrews performed library research on scientific literature relevant to the Materials Research Laboratory. Her work evaluated classification and format structuring of the pertinent journals.

Rasheed Bethel assisted graduate students in the fabrication of dielectric:polymer composites for microwave absorbers. He also assisted in the fabrication and characterization of low K polyimide silica substrates.

Tasha Blakely assisted in the fabrication and property measurements of silver (Ag)-loaded polymers to be used for flexible conductors. She also performed literature searches in the area of conducting polymers.

Certificates are appended.

PENNSTATE



Materials Research Laboratory

Office of Naval Research
Apprentice Program Certification

for successful completion of the 7 week project/study program in
Electronic Ceramics

Randolph D. Lucas

August 1990
Date

PENNSTATE



Materials Research Laboratory

Office of Naval Research
Apprentice Program Certification

for successful completion of the 7 week project/study program in
Electronic Ceramics

Helen Andrews

August 1990
Date

PENNSTATE



Materials Research Laboratory

Office of Naval Research
Apprentice Program Certification

for successful completion of the 7 week project/study program in
Electronic Ceramics

Rasheed Hassan Lance Bethel

August 1990
Date

PENNSTATE



Materials Research Laboratory

Office of Naval Research
Apprentice Program Certification

for successful completion of the 7 week project/study program in
Electronic Ceramics

Tasha Blakeley

August 1990
Date

10.0 PAPERS PUBLISHED IN REFERRED JOURNALS

1. R.E. Newnham and S. Trolier-McKinstry, "Crystals and Composites," *J. Appl. Cryst.* **23**, 447-457 (1990).
2. R.E. Newnham and G.R. Ruschau, "Smart Electroceramics," *J. Am Ceram. Soc.* **74** (3), 463-480 (1991).
3. W.Y. Pan, C.Q. Dam, Q.M. Zhang and L.E. Cross, "Large Displacement Transducers Based on Electric Field Forced Phase Transitions in the Tetragonal $(\text{Pb}_{0.97}\text{La}_{0.02})(\text{Ti},\text{Zr},\text{Sn})\text{O}_3$ Family of Ceramics," *J. Appl. Phys.* **66** (12), 6014-6023 (1989).
4. A.S. Bhalla and R.Y. Ting, "Hydrophone Figure of Merits," *Sensors and Materials* **4**, 181-185 (1989).
5. K.A. Hanner, A. Safari, R.E. Newnham and J. Runt, "Thin Film 0-3 Polymer/Piezoelectric Ceramic Composites : Piezoelectric Paints," *Ferroelectrics* **100**, 255-260 (1989).
6. G.S. Lee, S. Kim and T.R. Shrout, "Fabrication of 0-3 Piezoelectric-Glass Composites," *Sensors and Materials* **2** (1), 7-15 (1990).
7. B.N. Narahari Achair and G.R. Barsch, "Anharmonic Perturbation Theory of Electrostriction in a Perovskite Oxide at Finite Temperature," *Solid State Communications* **74** (5), 323-325 (1990).
8. L.E. Cross and G.A. Rossetti, Jr., "Origin of the First-Order Phase Change at the Curie Temperature in KNbO_3 ," *J. Appl. Phys.* **69** (2), 896-898 (1991).
9. G.A. Rossetti, Jr., K.R. Udayakumar, M.J. Haun and L.E. Cross, "Thermodynamic Theory of Single-Crystal Lead Titanate with Consideration of Elastic Boundary Conditions," *J. Am. Ceram. Soc.* **73** (11), 3334-38 (1990).
10. C.A. Randall and A.S. Bhalla, "Nanostructural-Property Relations in Complex Lead Perovskites," *Japanese J. Appl. Phys.* **29** (2), 327-333 (1990).
11. C.A. Randall, A.S. Bhalla, T.R. Shrout and L.E. Cross, "Classification and Consequences of Complex Lead Perovskite Ferroelectrics with Regard to B-Site Cation Order," *J. Mater. Res.* **5** (4), 829-834 (1990).
12. D.C. Dube, S.C. Mathur, S.J. Jang and A.S. Bhalla, "Electrical Behaviour of Diffused Phase Ferroelectrics in the Microwave Region," *Ferroelectrics* **102**, 151-154 (1990).
13. D. Viehland, S.J. Jang, L.E. Cross and M. Wuttig, "Freezing of the Polization Fluctuations in Lead Magnesium Niobate Relaxors," *J. Appl. Phys.* **68** (6), 2916-2921 (1990).
14. D. Viehland, S.J. Jang, L.E. Cross and M. Wuttig, "Local Polar Configurations in Lead Magnesium Niobate Relaxors," *J. Appl. Phys.* **69** (1), 414-419 (1991).

10.0 PAPERS PUBLISHED IN REFEREED JOURNALS (continued)

15. J.R. Giniewicz, A.S. Bhalla and L.E. Cross, "An Investigation of the Structural and Dielectric Properties of the Solid Solution System $(1-x)\text{Pb}(\text{Sc}_{1/2}\text{Ta}_{1/2})\text{O}_3 - (x)\text{PbTiO}_3$," *Ferroelectrics Letters* **12**, 35-42 (1990).
16. T.R. Shrout, Z.P. Chang, N. Kim and S. Markgraf, "Dielectric Behaviour of Single Crystals Near the $(1-x)\text{Pb}(\text{Mg}_{1/3}\text{Nb}_{2/3})\text{O}_3 - (x)\text{PbTiO}_3$ Morphotropic Phase Boundary," *Ferroelectrics Letters* **12**, 63-69 (1990).
17. J.R. Giniewicz, D.A. McHenry, T.R. Shrout, S.J. Jang and A.S. Bhalla, "Characterization of $(1-x)\text{Pb}(\text{Mg}_{1/3}\text{Nb}_{2/3})\text{O}_3 - (x)\text{PbTiO}_3$ and $\text{Pb}(\text{Sc}_{1/2}\text{Ta}_{1/2})\text{O}_3$ Transparent Ceramics Prepared by Uniaxial Hot-Pressing," *Ferroelectrics* **109**, 167-172 (1990).
18. D.A. McHenry, J.R. Giniewicz, T.R. Shrout, S.J. Jang and A.S. Bhalla, "Electrical and Optical Properties of Relaxor Ferroelectrics," *Ferroelectrics* **102**, 161-171 (1990).
19. D.A. McHenry, J.R. Giniewicz, S.J. Jang, T.R. Shrout and A.S. Bhalla, "Optical and Electro-Optical Properties of Lead Magnesium Niobate-Lead Titanate," *Ferroelectrics* **107**, 45-46 (1990).
20. D.A. McHenry, J. Giniewicz, S.J. Jang, A. Bhalla and T.R. Shrout, "Optical Properties of Hot Pressed Relaxor Ferroelectrics," *Ferroelectrics* **93**, 351-359 (1989).
21. G.R. Fox, J.K. Yamamoto, D.V. Miller, L.E. Cross and S.K. Kurtz, "Thermal Hysteresis of Optical Second Harmonic in Paraelectric BaTiO_3 ," *Materials Letters* **2** (7, 8), 284-288 (1990).
22. W.R. Xu, W.A. Schulze and R.E. Newnham, "Effects of Sm_2O_3 and $\text{Gd}_2\text{O}_3 + \text{Nd}_2\text{O}_3$ on Electromechanical Properties of PbTiO_3 Ceramics," *J. Am. Ceram. Soc.* **73** (6), 1783-84 (1990).
23. P. Ravindranathan, S. Komaraneni, A.S. Bhalla, L.E. Cross and R. Roy, "Solution-Sol-Gel Processing of Lead Magnesium Niobate Thin Films," *Ferroelectrics Letters* **12**, 29-34 (1990).
24. P. Papet, J.P. Dougherty and T.R. Shrout, "Particle and Grain Size Effects on the Dielectric Behaviour of the Relaxor Ferroelectric $\text{Pb}(\text{Mg}_{1/3}\text{Nb}_{2/3})\text{O}_3$," *J. Mater. Res.* **5** (12), 2902-2909 (1990).
25. F.G. Jones, C.A. Randall, S.J. Jang and T.R. Shrout, "Preparation and Characterization of Indium Based Complex Perovskites - $\text{Pb}(\text{In}_{1/2}\text{Nb}_{1/2})\text{O}_3$ (PIN), $\text{Ba}(\text{In}_{1/2}\text{Nb}_{1/2})\text{O}_3$ (BIN), and $\text{Ba}(\text{In}_{1/2}\text{Ta}_{1/2})\text{O}_3$ (BIT)," *Ferroelectrics Letters* **12**, 55-62 (1990).
26. J.K. Yamamoto, C.A. Randall, S.A. Markgraf, A.S. Bhalla and M.A. Saifi, "Growth and characterization of Ferroelectric/Polar Single Crystal Fibers," *Ferroelectrics* **107**, 191-193 (1990).
27. S.A. Markgraf, C.A. Randall and A.S. Bhalla, "Incommensurate Phase In $\text{Ba}_2\text{TiSi}_2\text{O}_8$," *Solid State Communications* **75** (10), 821-824 (1990).

10.0 PAPERS PUBLISHED IN REFEREED JOURNALS (continued)

28. S.A. Markgraf and A.S. Bhalla, "Low-Temperature Phase Transition in $\text{Ba}_2\text{TiGe}_2\text{O}_8$," *Phase Transitions* **18**, 55-76 (1989).
29. Z.P. Chang and A.S. Bhalla, "Elastic Anomaly in Fresnoite ($\text{Ba}_2\text{TiSi}_2\text{O}_8$) Single Crystal," *Materials Letters* **8** (10), 418-420 (1989).
30. S.A. Markgraf and A.S. Bhalla, "Pyroelectric and Dielectric Properties of Hemimorphite, $\text{Zn}_2\text{Si}_2\text{O}_7(\text{OH})_2 \cdot \text{H}_2\text{O}$," *Materials Letters* **8** (5), 179-181 (1989).

11.0 INVITED LECTURES

1. 92nd Annual Meeting of the American Ceramic Society, Dallas, Texas (April 24, 1990). L.E. Cross, "Agile Piezoelectric Sensors."
2. International Symposium on Application of Ferroelectrics, ISAF 90, Urbana, Illinois, (June 8, 1990). L.E. Cross, "Plenary IV - Review and Future."
3. The Science Behind Materials Synthesis, Materials Research Laboratory, University Park, PA (June 10-13, 1990). L. Eric Cross, "Ferroelectric Materials for Applications in the 1990s."
4. MRS International 1990, Beijing, China (June 18-22, 1990). L.E. Cross, "High Performance Ceramics."
5. First Joint U.S./Japan Conference on Adaptive Structures, Maui, Hawaii (November 13-15, 1990). L. Eric Cross, "Passive Piezoelectric Vibration Damping."
6. First Joint U.S./Japan Conference on Adaptive Structures, Maui, Hawaii (November 13-15, 1990). L. Eric Cross, "Polarization Controlled Ferroelectric High Strain Actuators."
7. The 28th Ceramics Basic Science Conference, Fukuoka, Japan (January 24, 1990). S. Iijima, T.Ota, Iyamai, R. Newnham and S. Yoshikawa, "Electrical Resistivity of Conductive Ceramic-Polymer Composites."
8. The Third International Conference on Ceramic Powder Processing Science, San Diego, CA (February 4-7, 1990). S. Yoshikawa, C.L. Haertling, D. Smith and R.E. Newnham, "Patterned Ceramics Using UV Curable Binders."
9. American Crystallographic Association Annual Meeting, New Orleans, Louisiana (April 8-13, 1990). R.E. Newnham, "Structure-Property Relations in Nanocomposites."
10. Materials Research Society Meeting, San Francisco, CA (April 16-21, 1990). G.R. Ruschau, R.E. Newnham and J. Runt, "Conductive Composites as Chemical Sensors."
11. American Ceramic Society Meeting, Dallas, TX (April 21-24, 1990). D.J. Smith, R.E. Newnham and S. Yoshikawa, "Ultraviolet Curable System for Ceramic Tape Casting."

11.0 INVITED LECTURES (continued)

12. Swedish Royal Academy, Stockholm, Sweden (May 30, 1990). R.E. Newnham, "How Smart is a Ceramic?"
13. International Symposium on Application of Ferroelectrics (ISAF), University of Illinois, Urbana, IL (June 6-8, 1990). R.E. Newnham, "Global Perspectives on the Applications of Ferroelectrics."
14. Conference on the Science Behind Materials Synthesis, University Park, PA (June 10-13, 1990). R.E. Newnham, "Smart Ceramics."
15. Albrecht Rabenau Festsymposium, Schloss Ringberg, Barvarian Mountains, Germany (July 22-28, 1990). R.E. Newnham, "Smart Ceramics."
16. Keynote Speech at the International Symposium on Fine Ceramics, Arita, Japan (November 7, 1990). R.E. Newnham, "Tunable Transducers: Nonlinear Properties of Ceramics."
17. Second International Ceramic Science and Technology Congress, Orlando, Florida (November 12-15, 1990). R.E. Newnham, "Electronic Composites: Sensors, Actuators and Packages."
18. The Fifth US/Japan Seminar on Dielectric and Piezoelectric Ceramics, Kyoto, Japan (December 1990). T.R. Shrout, Y.S. Kim, J. Fielding and S. Venkataramani, "Fabrication of Porous Electroceramic Structures by Reaction Calcination."
19. IEEE Ultrasonics Symposium (December 1990). T.R. Shrout and J. Fielding, Jr., "Relaxor Ferroelectric Materials."
20. 10th Electronic Ceramic Processing Meeting, Shonan Institute of Technology, Japan (December 1990). T.R. Shrout, "Relaxor Processing for Electronic Ceramics."

12.0 CONTRIBUTED PAPERS

The Third International Conference on Ceramic Powder Processing Science, San Diego, CA (February 4-7, 1990).

1. "Patterned Ceramic Green Films Using UV Curable Binders," S. Yoshikawa, C. Haertling, D. Smith and R.E. Newnham (February 1990).

American Ceramic Society Annual Meeting, Dallas, Texas (April 1990).

1. "Fatigure Effect Associated with Ac Electric Field Excitation in Ferroelectric Type Ceramics," W.Y. Pan, K.A. Koshkarian, S. Krupanidhi and L.E. Cross, Pennsylvania State University, University Park, PA; and H.C. Cao, University of California, Santa Barbara, CA (April 1990).
2. "Chemical Etched Surface Layers on Ferroelectrics," Q.Y. Jiang and L.E. Cross, Pennsylvania State University, University Park, PA (April 1990).

12.0 CONTRIBUTED PAPERS (continued)

***American Ceramic Society Annual Meeting, Dallas, Texas (April 1990).
(continued)***

3. "A Study of the Volume Fraction, Temperature, and Pressure Dependence of the Resistivity in a Ceramic-Polymer Composite Using a General Effective Media Theory Equation," M. Blaszkiewicz, D.A. McLachlan and R.E. Newnham (April 1990).
4. "Low Dielectric Planarization Coatings for Electronic Packaging," M.L. Mulvihill, A. Das, P. Fuierer, W.K. Kim and W. Huebner (April 1990).

***Materials Research Society, Spring Meeting Symposium, San Francisco, CA
(April 16-21, 1990).***

1. "A Study of the volume Fraction, Temperature, and Pressure Dependence of the Resistivity in a Ceramic-Polymer Cmposite using a General Effective Media Theory Equation," D.S. McLachlan, M. Blaszkiewicz, S. Yoshikawa and R.E. Newnham (April 1990).

***Electrochemical Society Meeting, Montreal, Quebec, Canada
(May 6-11, 1990).***

1. "High Temperature Electroceramic Sensors and Actuators," R.E. Newnham, A. Ando, P. Fuierer, W.K. Kim and W. Huebner (May 1990).

Seventh International Symposium on the Application of Ferroelectrics (ISAF 1990), University Illinois, Champaign, Illinois (June 6-8, 1990).

1. "Smart Ferroelectric for Acoustic or Vibration Control," S. Kumar, Q.C. Xu, D. Damjanovic, A. Bhalla, R.E. Newnhma and L.E. Cross, Materials Research Laboratory, Pennsylvania State University, University Park, PA (June 1990).
2. "Local Interactions in Relaxor Ferroelectrics," D. Viehland, S. Jang and L.E. Cross, Materials Research Laboratory, Pennsylvania State University, University Park, PA; and M. Wuttig, University of Maryland, College Park, MD (June 1990).
3. "Fabrication and Characterization of Morphotropic Phase Boundary PMN-PT Sol-Gel Thin Films," K.R. Udayakumar, J. Chen, S.B. Krupanidhi and L.E. Cross, Materials Research Laboratory, Pennsylvania State University, University Park, PA (June 1990).
4. "Sol-Gel Derived PZT Thin Films for Switching Applications," K.R. Udayakumar, J. Chen, S.B. Krupanidhi and L.E. Cross, Materials Research Laboratory, Pennsylvania State University, University Park, PA (June 1990).
5. "Electromechanical Nonlinearity of PZT Ceramics and Related Domain Wall Excitation in Tetragonally Distored Ferroelectric Ceramics," L.E. Cross, Shaoping Li, U. Kumar and K.R. Udayakumar, Materials Research Laboratory, Pennsylvania State University, University Park, PA (June 1990).

12.0 CONTRIBUTED PAPERS (continued)

Seventh International Symposium on the Application of Ferroelectrics (ISAF 1990), University Illinois, Champaign, Illinois (June 6-8, 1990). (continued)

6. "Passive Piezoelectric Damping," A.R. Ramachandran, Q.C. Xu, R.E. Newnham and L.E. Cross, Materials Research Laboratory, Pennsylvania State University, University Park, PA (June 1990).
7. "Ion Bombardment Modification of the Surface of PLZT Type Electro-Optical Ceramics," Q. Jiang, S.B. Krupanidhi and L.E. Cross, Materials Research Laboratory, Pennsylvania State University, University Park, PA (June 1990).
8. "Multilayer Composite Tunable Transducer," Q.C. Xu, M. Blaszkiewicz, T.T. Fang, T.T. Srinivasan, S. Yoshikawa and R.E. Newnham, Materials Research Laboratory, Pennsylvania State University, University Park, PA (June 1990).
9. "Piezoelectric Composites with High Sensitivity for Use at High Pressure," Q.C. Xu, J. Belsick, S. Yoshikawa and R.E. Newnham, Materials Research Laboratory, Pennsylvania State University, University Park, PA (June 1990).
10. "Ultraviolet Curable System for Ceramic Tape Casting," D.J. Smith, R.E. Newnham and S. Yoshikawa, Materials Research Laboratory, Pennsylvania State University, University Park, PA (June 1990).
11. "Nonlinear Multilayer Composite Transducers," Q.C. Xu, J. Belsick, S. Yoshikawa, T.T. Srinivasan and R.E. Newnham, Materials Research Laboratory, Pennsylvania State University, University Park, PA (June 1990).
12. "Effect of Particle Size on Dielectric and Piezoelectric Properties in Various Volume Percent Loaded Sm and Mn Doped Polymer - PbTiO₃ Composites, D.M. Reed, T.T. Srinivasan, Q.C. Xu and R.E. Newnham, Materials Research Laboratory, Pennsylvania State University, University Park, PA (June 1990).
13. "Aging of Ferroelectric Ceramic/Polymer 0-3 Composites," Q.C. Xu, R. Flannigan, T.T. Srinivasan and R.E. Newnham (June 1990).
14. "Electrical Properties of Co-Fired High and Low Dielectric Constant Multilayer Package Materials," M.H. Meghiri, J.P. Doughery, G.O. Dayton and R.E. Newnham (June 1990).
15. "Nonlinear Ceramic-Polymer 2-2 Piezoelectric Composites," R.E. Newnham, M. Blaszkiewicz, Q.C. Xu, T.T. Fang, T.T. Srinivasan and S. Yoshikawa (June 1990).
16. "High Temperature Ferroelectric Ceramics," P.A. Fuierer, A. Ando and R.E. Newnham (June 1990).
17. "Piezoelectric Composites with High Sensitivity and High Capacitance for Use at High Pressures," Q.C. Xu, J. Belsick, S. Yoshikawa, T.T. Srinivasan and R.E. Newnham (June 1990).

12.0 CONTRIBUTED PAPERS (continued)

18. "Magnetolectric Multilayer Composites," G. Harshe, T.T. Srinivasan, J.P. Dougherty and R.E. Newnham (June 1990).
19. "Spectroscopic Ellipsometry Study of Ferroelectric Surfaces," S. Trolier-McKinstry and R.E. Newnham (June 1990).
20. "Electric Field Dependence of d_3 in Lead Magnesium Niobate Lead Titanate Ceramics," D.J. Taylor, D. Damjanovic, A.S. Bhalla and L.E. Cross (June 1990).
21. "Thermal Degradation of Relaxor Based Piezoelectrics," J.F. Fielding, Jr., S.J. Jang and T.R. Shroud (June 1990).
22. "Microwave Properties of Ferroelectric/Polymer Composites," F. Jones, T.R. Shroud, S.J. Jang and J. Lanagon (June 1990).
23. "Relaxor Based Fine Grain Piezoelectric Materials," N.C. Kim, S.J. Jang and T.R. Shroud (June 1990).
24. "The role of Particle Size or Reaction Calcination of PZT Ceramics," G.S. Lee, P. Papet and T.R. Shroud (June 1990).

Second International Ceramic Science and Technology Congress, Orlando, Florida (November 12-15, 1990).

1. "Conductor-Polymer Composite for Electronic Connectors," S. Yoshikawa, G.R. Ruschau and R.E. Newnham (November 1990).
2. "Low Dielectric Constant Planarization Coating for Electronic Packaging," M.L. Mulvihill, A. Das, J.P. Dougherty and R.E. Newnham (November 1990).
3. "Effects of Filler Particle Size on the Electrical Resistance of Conductor-Polymer Composites," T. Ota, I. Yamai, J. Takahashi, R.E. Newnham and S. Yoshikawa (November 1990).
4. "Ferroelasticity Studies of $\text{YBa}_2\text{Cu}_3\text{O}_7\text{-}8$ High Temperature Superconductor Single Crystals," R.P. Brodeur, C.A. Randall, A.S. Bhalla and R.E. Newnham (November 1990).
5. "Chemical Interactions at Interfaces in Novel Cofired Structures," C.W. Nies, C.A. Randall and R.E. Newnham (November 1990).
6. "Thermal Expansion Study of Perovskite Relaxor Ferroelectrics," H. Takahara, L. Kamdar, A.S. Bhalla and R.E. Newnham (November 1990).
7. "The Electric Field Dependence of Piezoelectric and Pyroelectric Properties of $0.9\text{PbMg}_{1/3}\text{Nb}_{2/3}\text{O}_3 - 0.1\text{PbTiO}_3$," D.J. Taylor, D. Damjanovic, A. Bhalla and L.E. Cross (November 1990).

13.0 HONORS TO MRL FACULTY AND STUDENTS

<u>Name of Person Receiving Award</u>	<u>Name of Award</u>	<u>Sponsor</u>
G. Barsch	Fellow	American Physics Society
A.S. Bhalla	Fellow	American Ceramic Society
L.E. Cross	Chairman	IEEE Ferroelectrics section of UFFC
L.E. Cross	National Representative	IUPAP International Committee on Ferroelectrics
R.E. Newnham	Educator of the Year	Ceramic Education Council
R.E. Newnham	John Jeppson Medal	American Ceramic Society

GENERAL SUMMARY PAPERS

APPENDIX 1

9

ELECTROCERAMICS

R.E. NEWNHAM

W. HUEBNER

Materials Research Laboratory
The Pennsylvania State University
University Park, Pennsylvania

Abstract

Structure-property relationships in electronic ceramic materials are reviewed to provide insight into the behavior of capacitors, thermistors, varistors, and other electroceramic components. Rapid progress in the integration and miniaturization of ceramic components has led to the development of multi-purpose electronic packages containing complex three-dimensional circuitry. At the same time, a wide variety of smart sensors, transducers, and actuators are being constructed using composite materials to concentrate fields and forces. At present, the processing methods make use of tape casting and thick film techniques, but several upset technologies loom on the horizon. During the years ahead, electroceramic devices can be expected to follow in the footsteps of semiconductor technology as the component sizes drop below 1 μm , and nanocomposite devices become a reality.

1 ELECTROCERAMICS MARKET

The multibillion dollar electroceramics market (Fig. 1) includes Mn-Zn ferrites, PZT transducers, BaTiO₃ multilayer capacitors, ZnO varistors, Al₂O₃ packages, and SiO₂ optical fibers. Roughly speaking, the market is divided into six equal parts (Japan Electronics Almanac, 1986). Rapidly developing technologies can be identified within each market segment: tellurium oxide coatings for video disks, barium hexaferrites for perpendicular recording silver and cooper electrode systems for multilayer capacitors, buried resistors and capacitors in ceramic packages, catalytic coatings for chemical sensors, and PZT piezoelectric motors. As in all

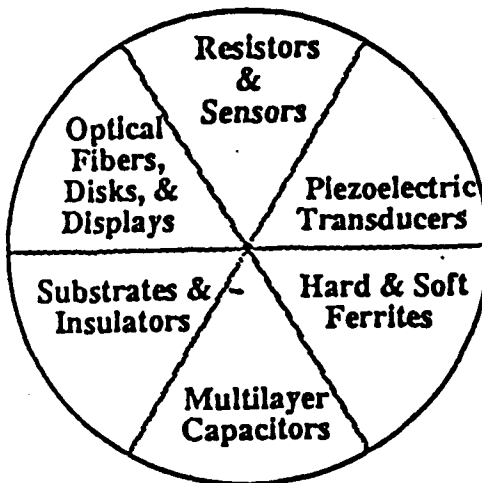


Fig. 1 Electroceramics market.

rapidly evolving fields of science and engineering, there is a sense of excitement as a number of different technologies come together in a synergistic manner.

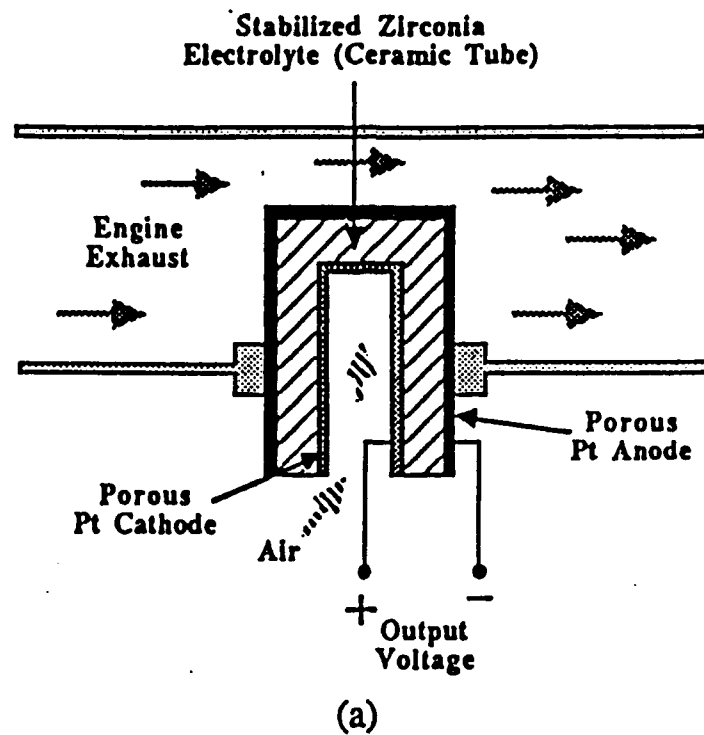
2 CERAMIC SENSORS

The most economical and most widely used sensors are ceramic bodies.¹ To illustrate structure-property relationships in ceramic sensors, six types of sensors will be described—three chemical sensors and three thermistors. The sensors make use of a variety of electrical phenomena sensitive to small changes in chemical composition or temperature.

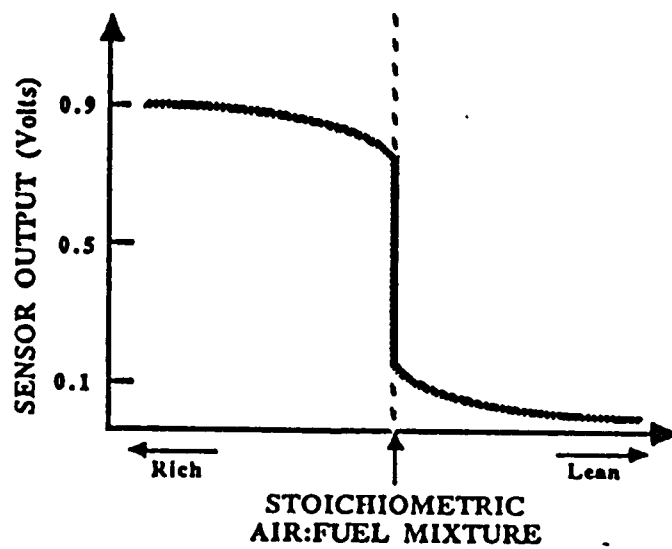
2.1 Oxygen Sensors

Superionic conductors are used to determine the air/fuel mixture in automobile engines.² One surface of the conductor is in contact with exhaust gas through a porous electrode (Fig. 2), while the opposite surface is in contact with air. The diffusion of oxygen ions through the solid electrolyte causes a voltage to appear between the electrodes. Heating the sensor raises the conductivity level. Monitoring the composition of the air/fuel mixture results in greater fuel efficiency and reduced air pollution.

Stabilized zirconia is the most widely used ionic conductor for oxygen sensors. Partial substitution of Mg^{2+} , Ca^{2+} , or Y^{3+} for zirconium stabilizes the cubic fluorite structure with a sizable concentration of oxygen vacancies. An oxygen vacancy is created for every zirconium replaced by magnesium, as indicated by the structural formula $(Zr_{1-x}Mg_x)(O_{2-x}\square_x)$.



(a)



(b)

Fig. 2 (a) Automotive exhaust sensor using stabilized ZrO_2 as an ionic conductor. (b) Improved fuel efficiency is obtained by monitoring the sensor voltage and adjusting the air/fuel mixture.

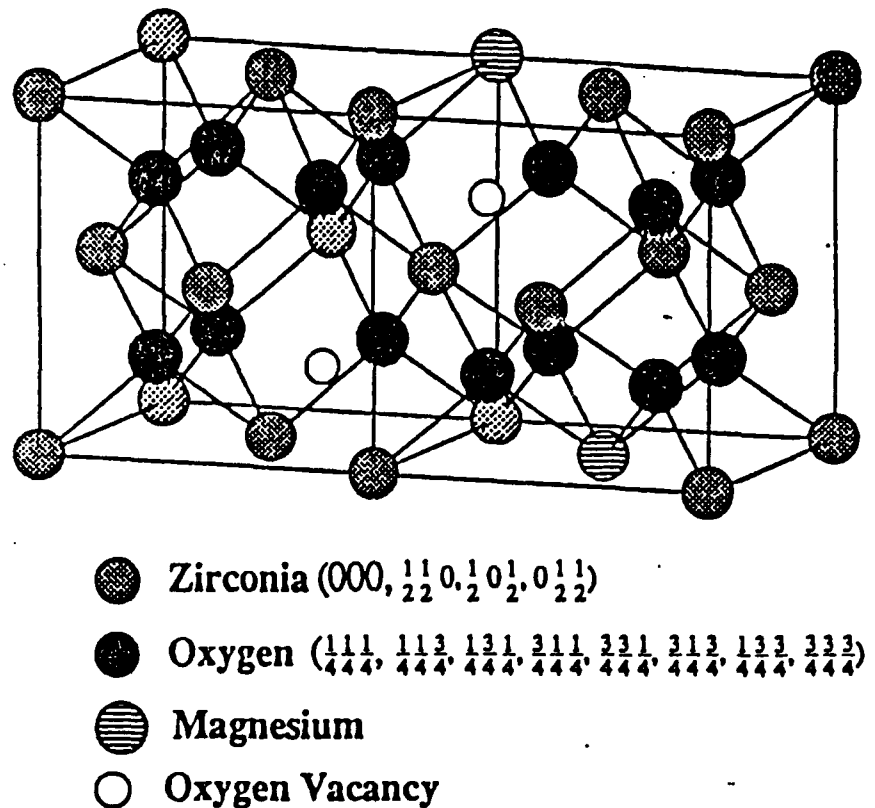


Fig. 3 Stabilized zirconia is an excellent ionic conductor because of a high concentration of oxygen vacancies and the close proximity of anion sites.

Magnesium replaces zirconium in the cubic cation sites of the fluorite structure (Fig. 3), with oxygen vacancies compensating for the lower cation charge. In the fluorite structure, the cations form a face-centered cubic lattice, and the anions have a simple cubic arrangement. The anion sites are very close to one another (~ 2.5 Å) making it easy for oxygens to jump to an adjacent empty site. This promotes ionic conductivity in fluorite-family oxides with defect structures, making them useful as oxygen sensors.³

2.2 Humidity Sensors

Humidity sensors are used in microwave ovens and for electronic spark timing in automobile engines. The surface resistance changes by several orders of magnitude with humidity (Fig. 4). Metal oxide substrates of $\text{MgCr}_2\text{O}_4\cdot\text{TiO}_2$ with high surface area and salt-impregnated coatings are especially sensitive to small changes in humidity.⁴ The physical mechanism

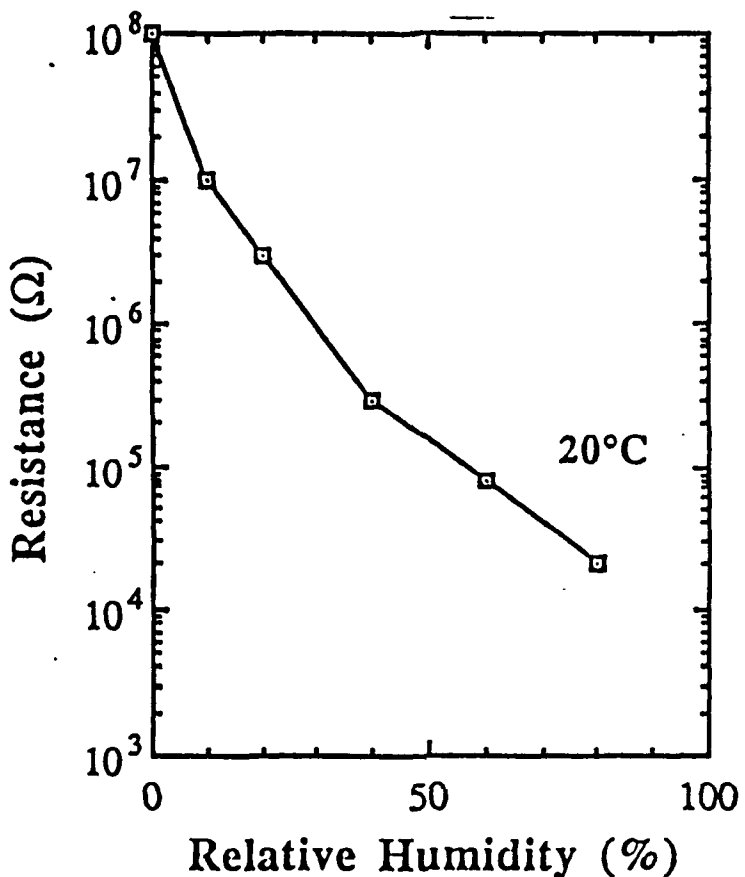


Fig. 4 Electrical resistance of an oxide humidity sensor.⁴

of surface conduction involves the adsorption of water vapor followed by dissociation into hydronium and hydroxyl ions:



Conduction takes place by means of the Grotthuss chain reaction, in which protons are transferred from one water molecule to the next in the physisorbed water layer on the surface of the oxide, effectively passing along a hydronium ion in the direction of the current.

The process is illustrated in Fig. 5. As reported recently, hydroxyapatite ceramics make particularly effective humidity sensors because of the attractive forces between surface hydroxyl groups and adjacent water molecules. The chemisorbed layer is surmounted by a physisorbed layer in which conduction takes place. At high humidity levels, a deeper, more fluid-like surface layer is formed and the conduction mechanism changes.

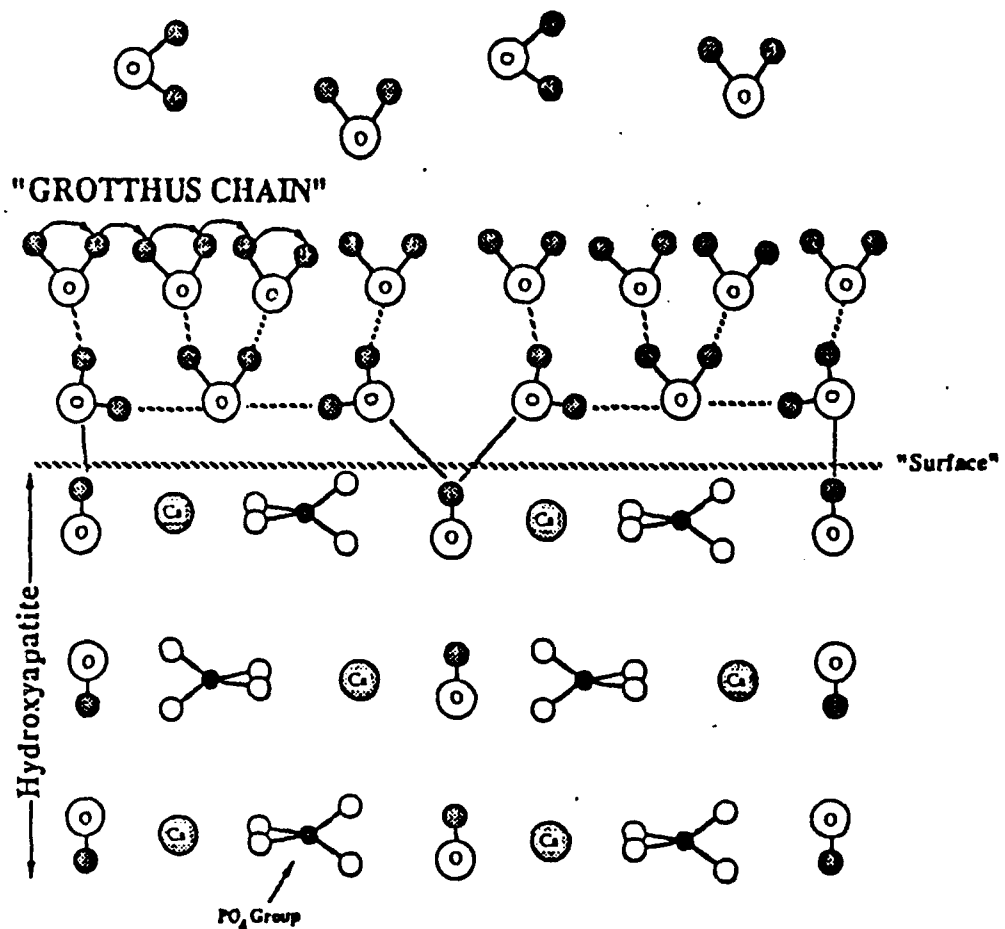


Fig. 5 Pictorial view of the surface structure of a hydroxyapatite humidity sensor. Conduction takes place via a Grotthuss chain reaction in the adsorbed water layers.

2.3 pH Sensors

Oxide pH sensors are made from semiconducting transition-metal oxides such as RuO_2 and IrO_2 .⁵ Both compounds are isostructural with rutile (Fig. 6a). When protons approach the surface of the oxide, a chemical reaction takes place. Two protons combine with a surface oxygen to form a water molecule. The reaction is accompanied by valence changes of the ruthenium ions to maintain charge neutrality. Electrons liberated from the metal ions complete the reaction and cause a current to flow in the solid. The resulting voltage depends on the hydrogen ion concentration (Fig. 6b).

The three chemical sensors described above all involve ion motion, but in a different way. Bulk ionic conduction occurs in the zirconia oxygen sensor,

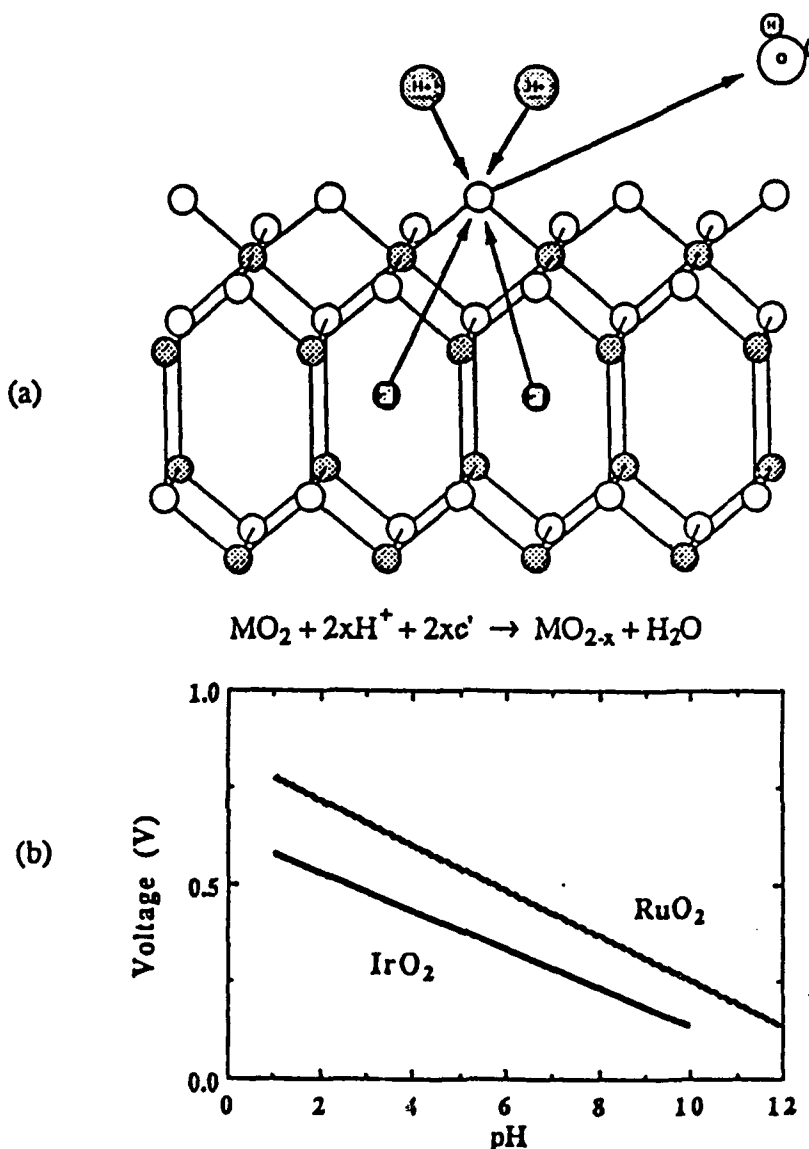


Fig. 6 (a) Transition metal oxides are used as pH sensors in which protons react with surface oxygens to form water molecules. The reaction is accompanied by valence changes and current flow in the solid. (b) The resulting electric voltage is proportional to pH.⁵

whereas surface ionic conduction takes place in a humidity sensor. In the pH sensor, a chemical reaction takes place at the surface between protons and oxygen ions.

In the next section, three temperature sensors are discussed, again with three different structure-property relationships, but this time the sensing involves electron motion rather than ion motion.

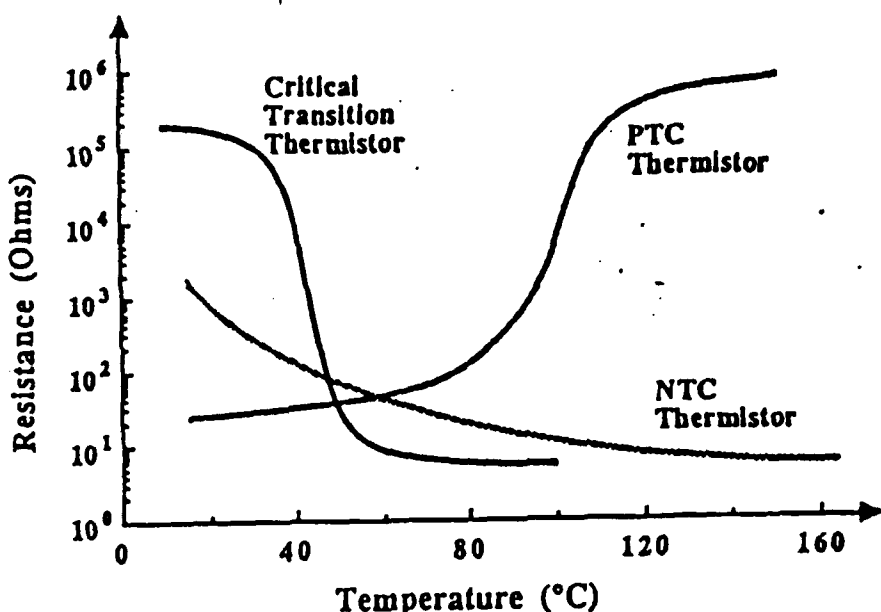


Fig. 7 Typically, the electrical resistance of thermistors change by several orders of magnitude with temperature. In negative temperature coefficient thermistors, the resistance decreases steadily with increasing temperature, but sudden changes at phase transitions are involved in positive temperature coefficient and critical temperature thermistors.

3 THERMISTORS

Three types of ceramic thermistors are in widespread use—critical temperature thermistors, negative temperature coefficient (NTC) thermistors, and positive temperature coefficient (PTC) thermistors. Typical resistance changes with temperature are illustrated in Fig. 7.

3.1 Critical Temperature Thermistors

Vanadium dioxide is often used in critical temperature thermistors. Below 80 °C, VO₂ is a semiconductor with a negative temperature coefficient of resistance. Above 80 °C, it exhibits metallic behavior with a great increase in conductivity (typically two orders of magnitude) and very little change with temperature. The critical temperature of 80 °C can be modified somewhat by changes in chemical composition.

The V⁴⁺ ion in VO₂ has a peculiar electron configuration with one 3d electron outside a closed shell. In the low-temperature state, adjacent V⁴⁺ ions form electron pair bonds, giving rise to a band gap and semiconductor

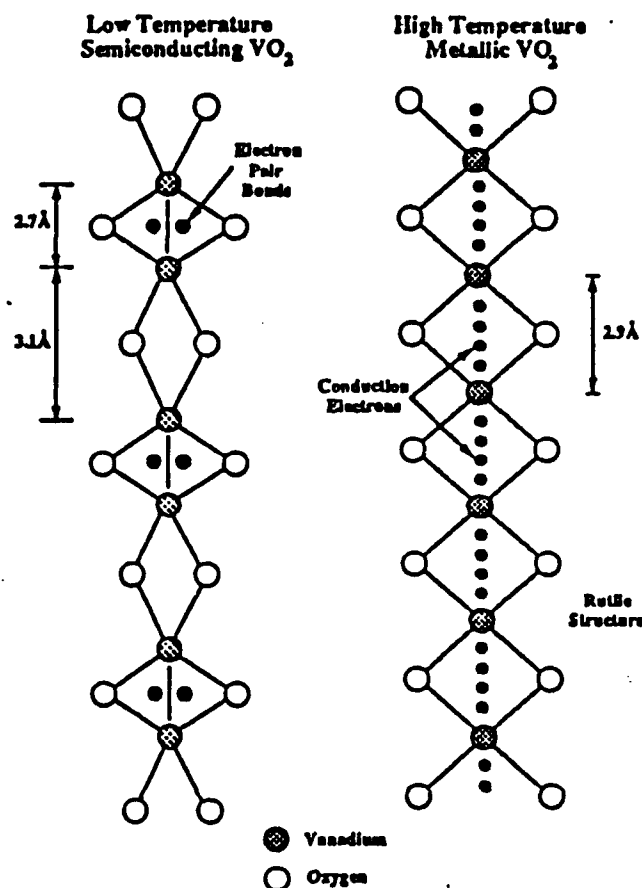
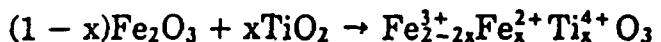


Fig. 8 Structural changes take place in the VO_2 ceramics used as critical temperature thermistors. At the metal semiconductor transition, the resistance changes by several orders of magnitude and the bond lengths change. At high temperature, the metal-like structure is isomorphous with tetragonal rutile, but changes to the semiconducting monoclinic state below 80 °C.

behavior. A phase transition takes place at 80 °C, in which the 3d electrons are liberated from the pair bonds and are free to conduct electricity. Changes in the crystal structure (Fig. 8) accompany the phase transformation. The rutile-like structure found at high temperatures transforms to a distorted monoclinic form below 80 °C. The formation of electron pair bonds is reflected in the interatomic distances. In the rutile structure, the $\text{V}^{4+} - \text{V}^{4+}$ distance across shared octahedral edges is 2.9 Å. Below the transition, half are 2.7 Å and half are 3.1 Å. This distortion in structures locks the electrons into localized states, creating a band gap and semiconducting behavior.

3.2 Negative Temperature Coefficient Thermistors

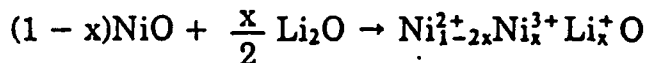
Electrical resistance decreases exponentially with increasing temperature in an negative temperature coefficient thermistor. Unlike critical temperature thermistors, there is no phase transition involved. Most negative temperature coefficient thermistors are composed of doped transition-metal oxides.⁶ Typical of these controlled valency semiconductors are $\text{Fe}_2\text{O}_3:\text{Ti}$ and $\text{NiO}:\text{Li}$. Reacting Fe_2O_3 with TiO_2 in air yields:



This is an n-type semiconductor in which electrons are transferred between iron atoms of different valence.



The electron concentration and electrical resistivity are controlled by the titanium content; p-type negative temperature coefficient thermistors are made from nickel oxide doped with lithium.



The hole conduction process involves charge transfer between divalent and trivalent nickel ions:



Doped nickel oxide has the rocksalt structure (Fig. 9a), with lithium partially replacing nickel in the cation sites. Ionic radii for Ni^{2+} (0.84 Å), Ni^{3+} (0.74 Å), and Li^+ (0.88 Å) all favor octahedral coordination with oxygen. As shown in Fig. 9b, resistivity decreases with increasing lithium content. Color is another indication of increased conductivity. The green color of pure nickel oxide deepens to black with increased doping.

For semiconducting compositions near $\text{Ni}_{0.95}\text{Li}_{0.05}\text{O}$, the band gap is about 0.15 eV. The physical origin of this band gap is attributed to the attractive forces between Li^+ dopant ions and the compensating Ni^{3+} ions. Charge is neutralized best when these ions are next nearest neighbors (Fig. 9a). Polarization of the surrounding structure also contributes to the band gap energy.

Electrical conductivity is proportional to the charge carrier concentration n , the charge of each carrier q , and the mobility μ :

$$\sigma = nq\mu$$

In thermistor materials, the temperature dependence of the conductivity

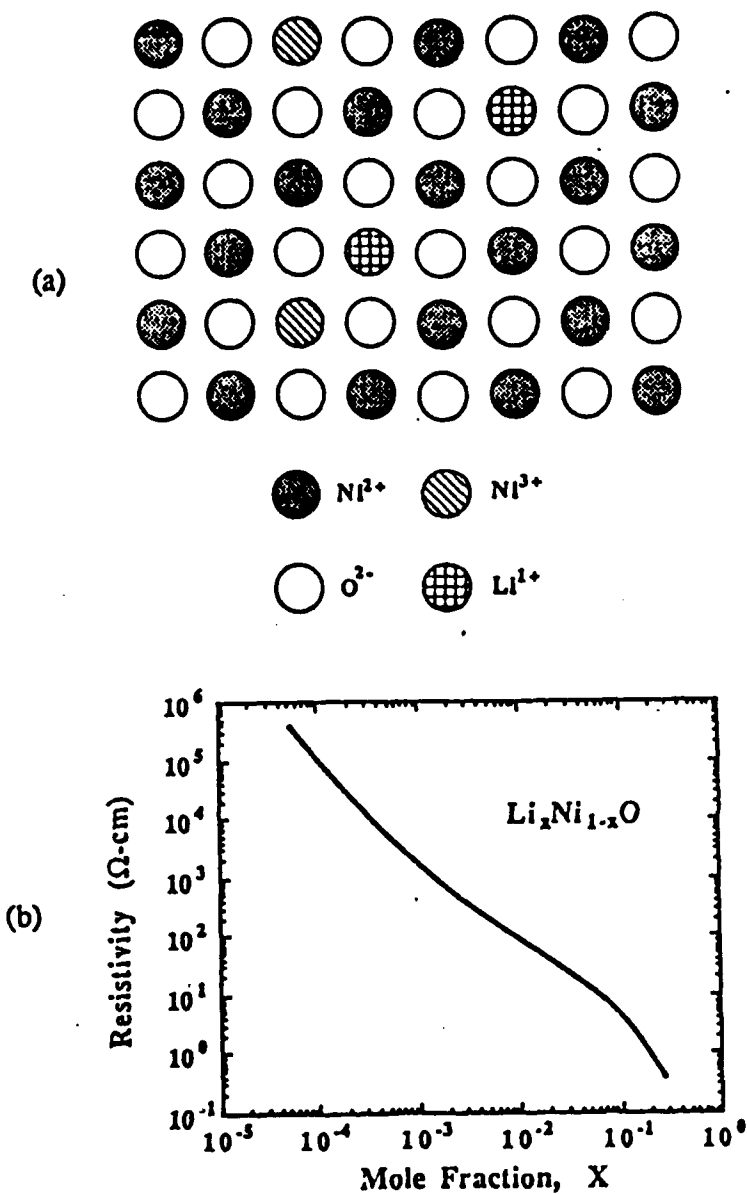


Fig. 9 Nickel-doped oxide thermistor. (a) The crystal consists of Ni^{2+} , Ni^{3+} , and Li^+ ions in a rocksalt-like solid solution. (b) Room-temperature electrical resistivity decreases with increasing lithium content.

is of great importance. Both n and μ depend on temperature. For a semiconductor, the carrier concentration varies exponentially with temperature, $n \approx \exp(-E/kT)$, where E is the energy required to liberate charge carriers. The temperature dependence of the mobility depends on its physical origin. For most scattering processes, mobility follows an inverse

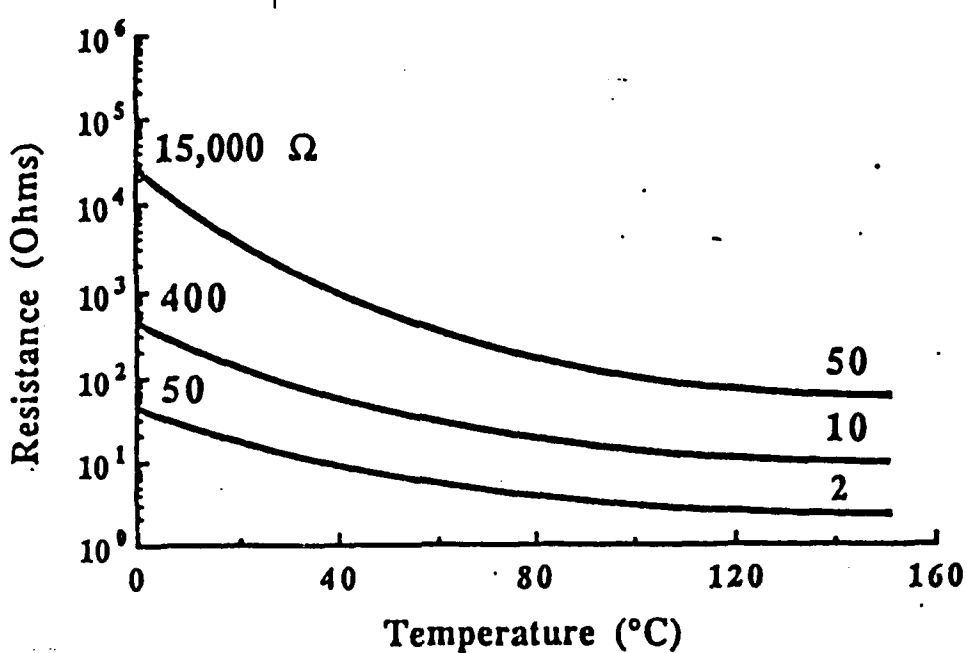


Fig. 10 Dependence of resistance on temperature for typical negative temperature coefficient thermistors. R decreases by about 4% for each degree increase in temperature.

power law ($\mu = T^{-b}$), in which mobility decreases with increasing temperature because of atomic thermal vibration. A different temperature dependence is found for hopping processes. Here the mobility depends on thermal excitation and increases exponentially with temperature, $\mu = \exp(E'/kT)$. Summing up, the temperature dependence of the electrical conductivity is:

$$\sigma(T) \approx T^{-b} e^{-(E+E')/kT} = T^{-b} e^{-E'/kT}$$

Because exponentials tend to dominate, the electrical resistance of a negative temperature coefficient thermistor can be described by:

$$R = Ae^{\beta/T}$$

For typical thermistors (Fig. 10), R lies in the range 1 to 10^4 Ω, and B is 2000 to 6000 K. The temperature coefficient α describes the percentage change in resistance with increasing temperature:

$$\alpha = \frac{1}{R} \frac{dR}{dT} = \frac{1}{R} \frac{d}{dT}(Ae^{\beta/T}) = \frac{-\beta}{T^2}$$

If $\beta = 3600$ K and $T = 273$ K, α is approximately 4%/°C.

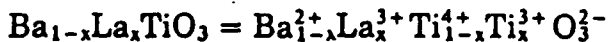
Negative temperature coefficient thermistors are used in flow meters, in which the velocity is measured by monitoring the temperature difference between two thermistors. A heater positioned between the two thermistors provides the temperature difference. Thermistors are also used as inrush limiters to protect diodes, fuses, switches, and light bulbs. The sudden surge of current that occurs when a light bulb is turned on often ruptures the bulb filament. With an negative temperature coefficient thermistor in series with the bulb, the energy of the initial surge is dissipated as heat in the thermistor.

3.3 Positive Temperature Coefficient Thermistors

Positive temperature coefficient thermistors differ from negative temperature coefficient thermistors in several important respects. The resistance of a positive temperature coefficient thermistor increases with temperature, but only over a limited temperature range near a phase transition. The resistance change is very large at this temperature because of grain boundary effects.⁷

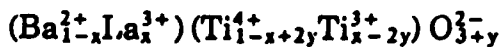
Barium titanate ceramics are widely used in positive temperature coefficient thermistors. When doped with donor ions such as La^{3+} or Ce^{3+} (for Ba^{2+}) or Nb^{5+} (for Ti^{4+}), the resistivity material shows a pronounced positive temperature coefficient effect (Fig. 11a). This low-resistivity material shows a pronounced positive temperature coefficient effect (Fig. 11b) if fired in air. Only normal negative temperature coefficient behavior is observed in ceramics prepared in a reducing atmosphere.

Explanation of the positive temperature coefficient effect rests upon understanding the defect structure. When sintered at high temperature, lanthanum-doped BaTiO_3 becomes an n-type semiconductor:



with conduction taking place via transfer of electrons between titanium ions as $\text{Ti}^{4+} + e^- \rightarrow \text{Ti}^{3+}$. Thus, the barium titanate grains in the ceramic are conducting and remain conducting on cooling to room temperature.

However, the grain boundary region changes during cooling. Oxygen is adsorbed on the surface of the ceramic and diffuses to grain boundary sites, altering the defect structure along the grain boundaries. The added oxygen ions attract electrons from nearby Ti^{3+} ions, thereby creating an insulating barrier between grains. If y excess oxygen ions are added per formula unit, the grain boundary region can be described as follows:



A schematic illustration of the defect perovskite structure is shown in Fig. 12.

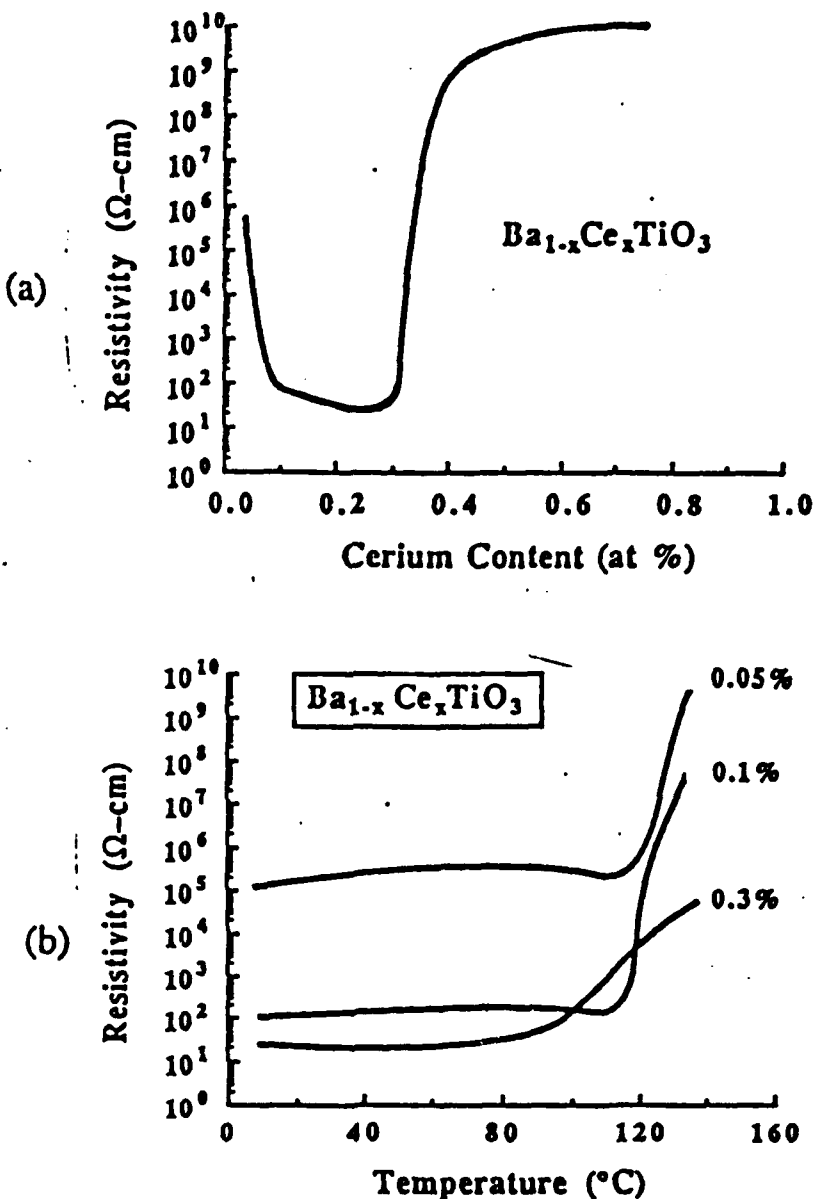


Fig. 11 (a) Resistivity of cerium-doped barium titanate, $\text{Ba}_{1-x}\text{Ce}_x\text{TiO}_3$, plotted as a function of composition. (b) Resistivity of three cerium-doped barium titanate ceramics measured as a function of temperature. A large positive temperature control anomaly occurs near the Curie temperature.

The net result of this process is that the ceramic consists of semiconducting grains separated by thin insulating grain boundaries. The electrical resistance of the ceramic is inversely proportional to grain size because smaller grains mean more insulating grain boundaries and therefore higher resistance.

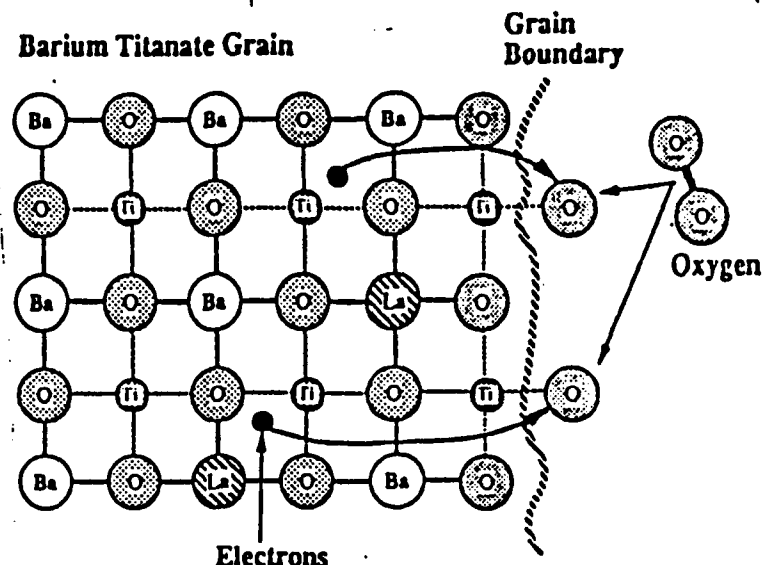


Fig. 12 Schematic view of the $\text{Ba}_{1-x}\text{La}_x\text{TiO}_3$ structure near the surface of a grain boundary. Atmospheric oxygen dissociates and diffuses rapidly along a grain boundary where the atoms attract electrons and form insulating barriers.

To explain the positive temperature coefficient effect, it is necessary to consider the ferroelectric phase transition in BaTiO_3 and its effect on the insulating barriers between grains.⁸ Barium titanate is cubic and paraelectric above 130 °C, its Curie temperature. Below this temperature, the perovskite structure distorts to a tetragonal ferroelectric state in which a large spontaneous polarization P_s develops on the (001) faces. The dielectric constant reaches a maximum at T_c and then falls off in the high-temperature paraelectric state following a Curie-Weiss law:

$$K = \frac{C}{T - T_c} \text{ for } T > T_c$$

The Curie constant, C, is about 10^5 °C.

The positive temperature coefficient anomaly in doped BaTiO_3 occurs at temperatures near T_c and is strongly affected by the appearance of ferroelectricity. Both the spontaneous polarization and the Curie-Weiss law play an important role in the positive temperature coefficient effect.

At room temperature, the resistance of a positive temperature coefficient thermistor is low, because the electron charge trapped in grain boundary regions is partially neutralized by spontaneous polarization. Wherever the domain structure is advantageously positioned, positive polarization charge will cancel the negatively charged barriers between conductive grains, thereby establishing low resistance paths across the ceramic (Fig. 13a).

000 / Science of Advanced Materials

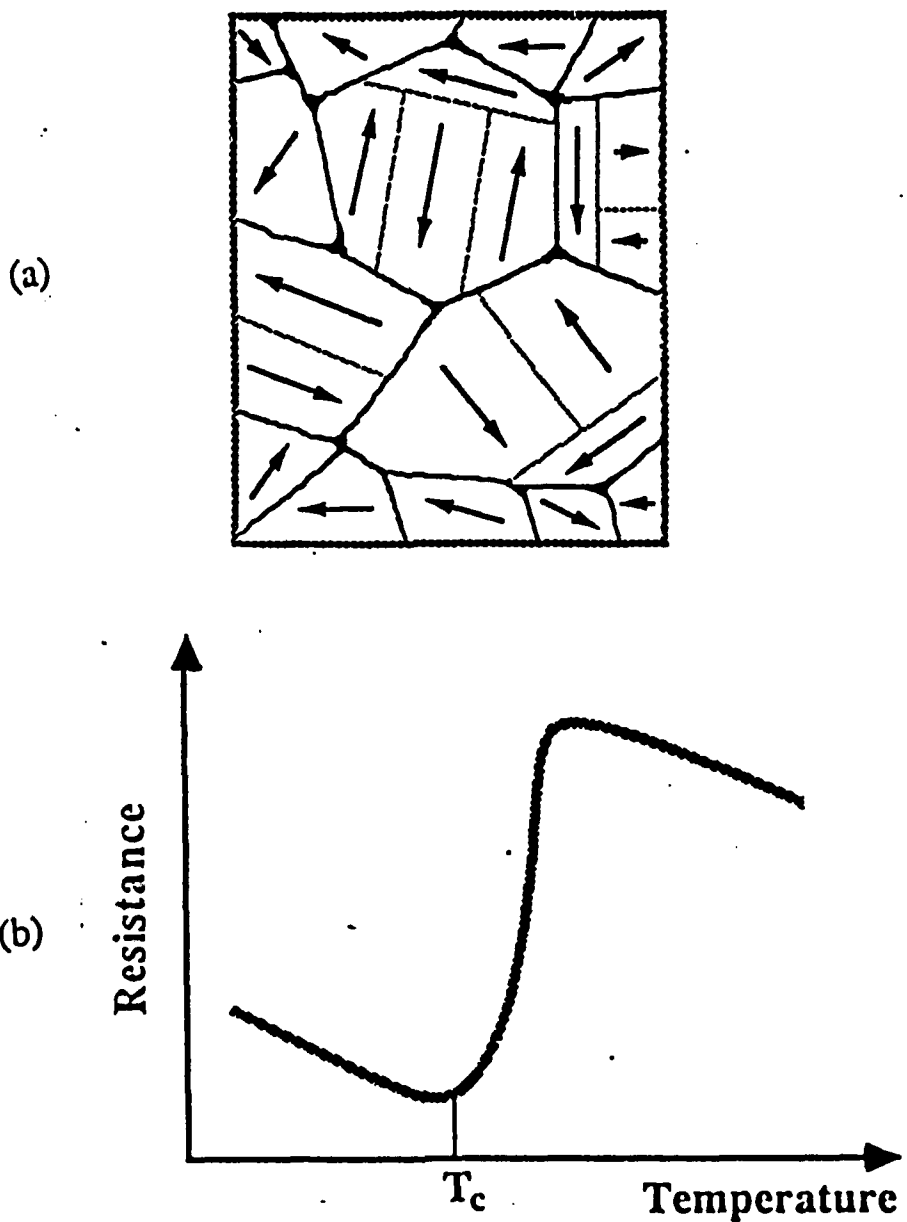


Fig. 13 (a) At temperatures below T_c , spontaneous polarization charges neutralize the potential energy barriers, creating low resistance paths through the ceramic. (b) Above T_c , the dielectric constant decreases causing the electrical resistance to increase.

Above T_c , the spontaneous polarization disappears and the resistivity increases, giving rise to the positive temperature coefficient effect. At first, the increase is very slow because of the high dielectric constant at the Curie point. The barrier height is inversely proportional to the dielectric constant of the surrounding medium; a highly polarizable medium shields the

charges trapped at the grain boundary, reducing the height of the barrier and the electrical resistance. As the temperature increases further above T_c , the dielectric constant K decreases rapidly in accordance with the Curie-Weiss law. Decreases in K cause rapid increases in the barrier between grains and an increase in the electric resistance. Eventually, the resistance increase levels off as the decrease in dielectric constant slows and the normal negative temperature coefficient effect of the semiconducting grains takes over (Fig. 13b).

Positive temperature coefficient thermistors are used as protection against overvoltage and short circuits. When connected in series with the load, a positive temperature coefficient thermistor limits the current to safe levels. Large currents cause the temperature of the thermistor to rise into the positive temperature coefficient range, thereby raising the resistance and lowering the current. Additional applications include liquid level indicators and thermostat control elements.

To summarize, the ceramic sensors described above make use of six different structure-property relations. The humidity sensor involves ionic conduction on surfaces with proton hopping between absorbed water molecules, whereas the zirconia oxygen sensor involves bulk ionic conduction through grains. In metal-oxide pH sensors, a chemical reaction takes place at the surface with protons reacting with surface oxygen atoms.

The three types of temperature sensors discussed in the last section make use of electronic phenomena in ceramics. Critical temperature thermistors employ a structural phase transformation in which the bulk electronic condition changes from metallic to semiconducting. A phase transformation is also involved in positive temperature coefficient thermistors, but grain boundaries are important here. Schottky barriers between the conducting ceramic grains are neutralized by the spontaneous polarization associated with the ferroelectric phase transition in BaTiO_3 . This is a much more complicated conduction phenomenon than that in a negative temperature coefficient thermistor. Bulk electronic conduction controls the resistivity of the transition metal oxides used in negative temperature coefficient thermistors.

4 METAL OXIDE VARISTORS

Varistors are ceramic semiconductors with a nonlinear current-voltage relationship (Fig. 14). At low voltages, the varistor behaves like a negative temperature coefficient thermistor with small temperature-dependent currents. At a certain critical breakdown voltage V_B , however, the resistance suddenly diminishes and currents increase dramatically. The phenomenon differs from normal electric breakdown in that the I-V characteristic is

000 / Science of Advanced Materials

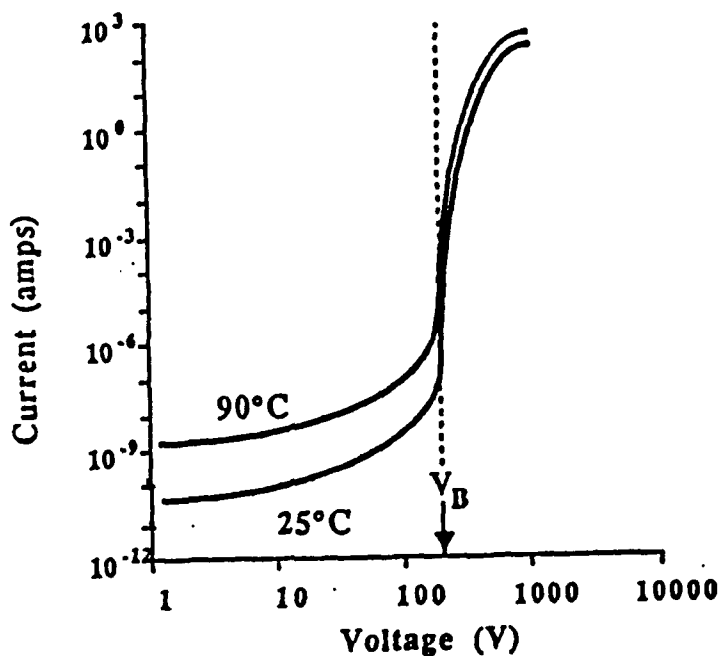


Fig. 14 Typical I-V relation for a ZnO varistor. The current increases very rapidly at the breakdown voltage V_B .

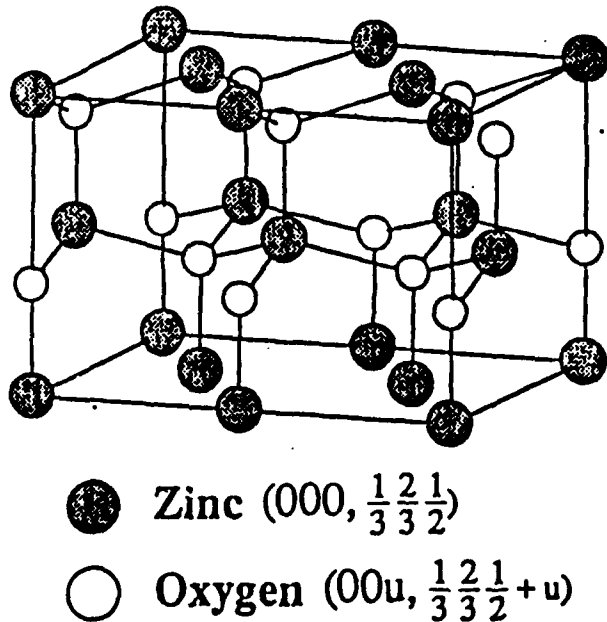


Fig. 15 Unit cell of the hexagonal ZnO structure used in varistors. Lattice parameters are $a \times 3.24$, $c = 5.19$ Å.

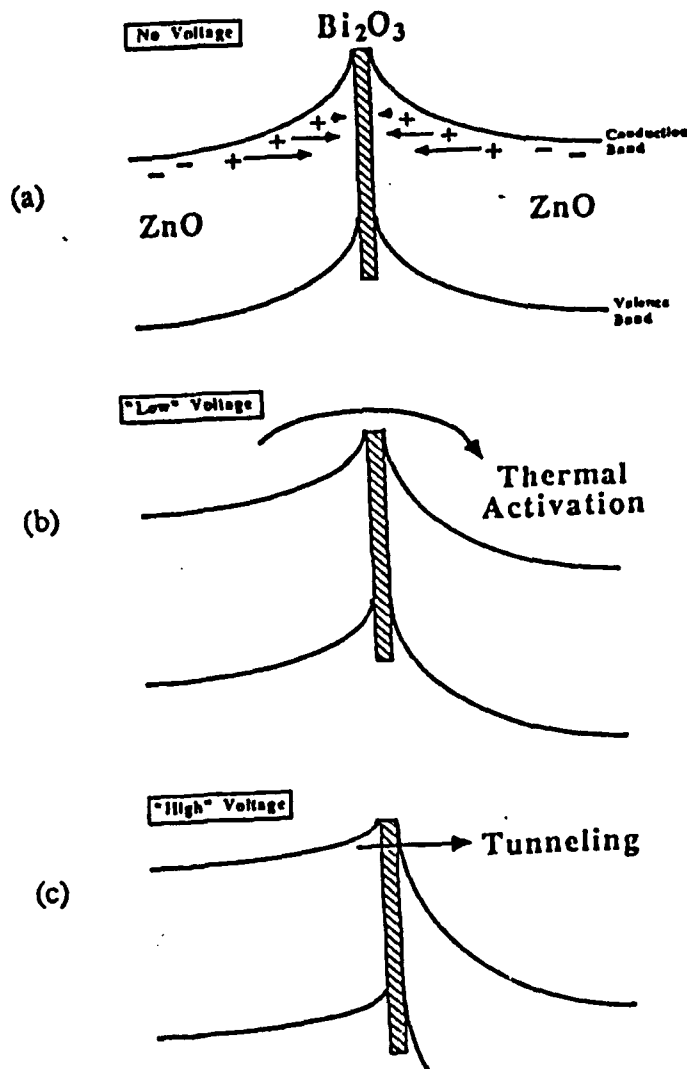


Fig.16 (a) Schottky barrier caused by a double depletion layer in a ZnO varistor. Band bending is caused by donor electrons from the zinc oxide grains filling traps in the thin bismuth oxide-rich layer between grains. (b) At low voltages, conduction takes place by thermal activation, but at (c) the breakdown voltage tunneling begins, causing a very large increase in current.

reversible and controllable by the ceramic microstructure. Like the positive temperature coefficient thermistor, the electrical properties are governed primarily by thin insulating barriers at the grain boundaries. In the case of varistors, however, electron tunneling is involved.⁹

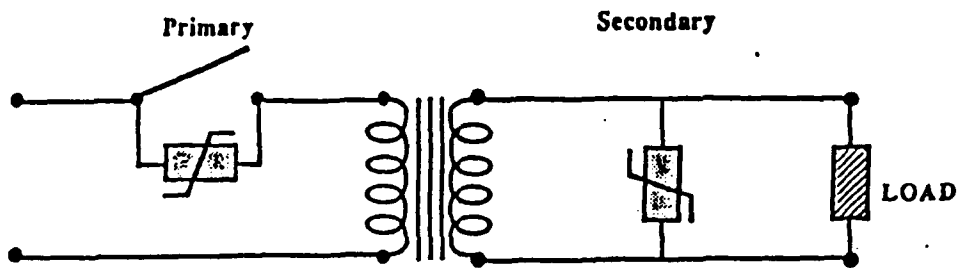


Fig. 17 Varistors are used to protect electrical contacts and loads against inductive surges.

Most varistors are made from zinc oxide with additives of several percent. ZnO has the hexagonal wurtzite structure (Fig. 15) with tetrahedral Zn - O bonds of 1.97 Å. A typical commercial composition for varistors is:

$$(100 - x) \text{ZnO} + \frac{x}{6} (\text{Bi}_2\text{O}_3 + 2\text{Sb}_2\text{O}_3 + \text{Co}_2\text{O}_3 + \text{MnO}_2 + \text{Cr}_2\text{O}_3)$$

where x is the mole percent additives. Excellent varistor action is obtained for compositions with the range of 3 to 10%. The phase relations are rather complex, but when fired at 1350 °C, there are only two important phases. The varistor microstructure consists of doped ZnO grains separated by doped Bi₂O₃ grain boundary regions. TEM micrographs show that the bismuth oxide layer is extremely thin (<30 Å) in many places. This plays an important role in the conduction process.

Electrically, the ceramic varistor consists of conducting ZnO grains with resistivities near 1 Ω·cm, separated by insulating Bi₂O₃-rich grain boundaries. The grains are n-type and the boundaries p-type. Electrons near the boundaries are trapped in the intergranular Bi₂O₃-rich regions leaving ionized donors on both sides of the boundary. The result is a symmetric Schottky barrier about 0.8 eV in height (Fig. 16a).

The nonlinear I-V characteristic (Fig. 14) of a varistor can be explained in terms of the Schottky barrier model. At low voltages, in the prebreakdown region, charge carriers surmount the Schottky barrier by thermal activation (Fig. 16b), giving rise to small temperature-dependent currents. As the applied voltage approaches V_B, the breakdown voltage, tunneling from the filled states in the intergranular region begins (Fig. 16c). Further increases in voltage result in very large current flows through tunneling.

Metal oxide ceramic varistors are used to protect circuit elements against inductive surges, which often damage contacts, relays, and rectifiers. By connecting the varistor in parallel with the circuit element (Fig. 17), any voltage spikes greater than V_B cause currents to flow through the varistor rather than the circuit element. Zinc oxide varistors have proved especially useful as lightning arrestors.¹⁰

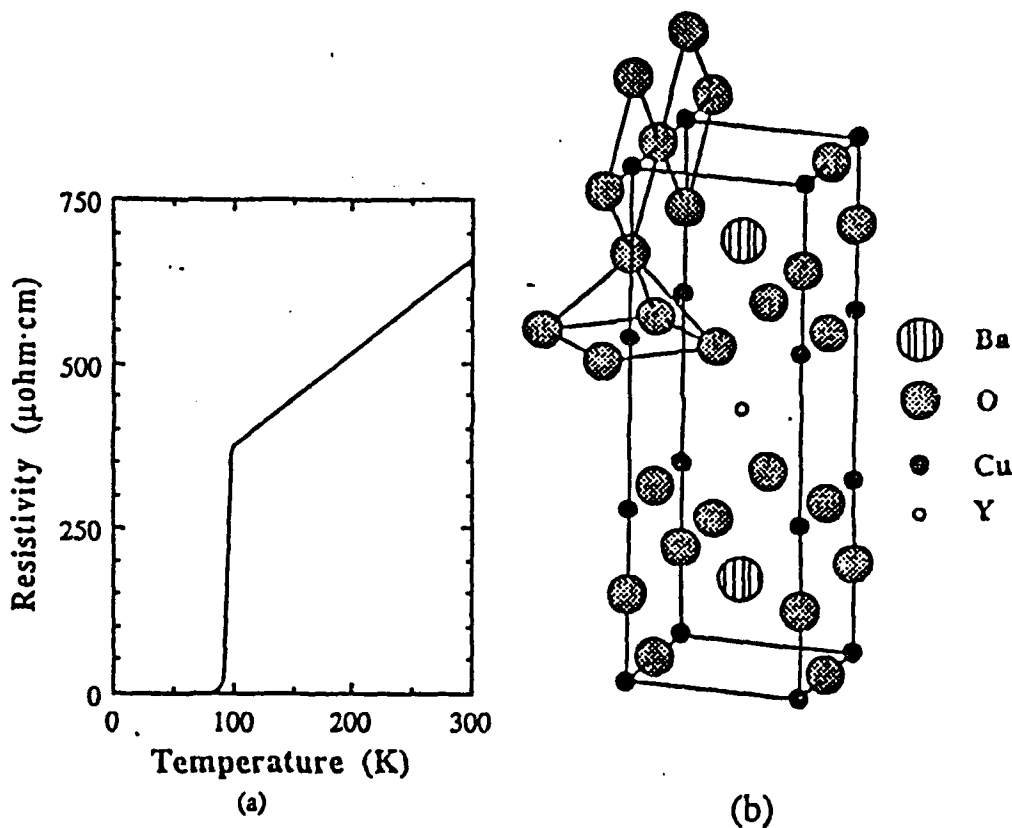


Fig. 18 (a) Resistivity of the newly discovered 1-2-3 cuprate ceramics. (b) The structure contains many missing oxygen atoms in the Cu-O-Cu chains along the top edge of the unit cell.¹³

5 SUPERCONDUCTING CERAMICS

Until 3 years ago, it was taken for granted that superconducting transition temperatures were limited to 25 K. However, with the discovery of lanthanum strontium cuprate,¹¹ the temperature doubled, and doubled again with $\text{YBa}_2\text{Cu}_3\text{O}_7$, the so-called 1-2-3 compound.¹² The triple perovskite unit cell (Fig. 18) contains seven oxygen and two empty oxygen sites.¹³

The mechanism of superconductivity in the copper oxide family is not well understood. In the theory put forward for metallic superconductors, an electron moving through the lattice attracts or repels ions, causing them to vibrate. This quantum of vibrational energy (phonon) represents an attractive force to another electron with opposite magnetic spin and momentum in such a way that the two move in synchronized motion. The paired electrons may be far apart and separated by other particles, but they are indirectly linked, as if by a spring. Each and every motion, even a collision with the lattice, is cancelled by the partner's movement. Moreover, such

000 / Science of Advanced Materials

Cooper pairs travel in concert with other pairs so that conduction electrons move together with remarkable orderliness.

The phonon links between electrons are so tenuous that they remain intact only at very low temperatures. Even a little heat is sufficient to overcome the phonon attraction and destabilize the superconducting state. The Bardeen-Cooper-Schrieffer (BCS) theory predicts an upper limit to the strength of the interaction with a T_c of 30 to 40 K. This suggests that there must be another coupling mechanism in the high T_c copper oxides. Attention is presently focused on the copper-oxygen planes and chains found in all high T_c ceramics. Most of the theories formulated during the past year involve the peculiar bonding between copper and oxygen atoms. Normally, copper has a valence of +1 or +2 in minerals and oxide ceramics, but in the superconductors its valence exceeds two. Alternatively, an unusual valence of -1 can be assigned to some of the oxygen ions. The presence of "excess" oxygen is crucial to the existence of superconductivity.

Three alternative mechanisms have been propounded to explain the coupling of Cooper pairs in superconducting cuprates. Closely related to the BCS theory is an excitonic model in which electron-hole pairs (excitons) perform the same function as phonons in superconducting metals. Another BCS-like model involves magnetic interactions as a coupling mechanism. Ferromagnetic regions with an antiferromagnetic matrix are responsible for the attractive forces between electrons. A third theory postulates the importance of resonating domain walls, which are common in high T_c ceramics. At the present time, theory seems to be of little value in guiding experimentalists.

Ceramic and thin-film specimens both exhibit superconductivity above liquid air temperatures, opening up a large number of possible applications—frictionless generators, motors and high-speed trains, levitating toys and gimmicks, electronic Josephson junctions and resistanceless interconnects, large magnetic fields for NMR medical diagnosis, nuclear accelerators and hydrogen fusion, power transmission lines and closed loop energy storage for load leveling, and radiation detectors for astronomy, oil exploration, and brain wave research. The feasibility of many applications rests upon improvements in the critical current density. Ways must be found for stabilizing the superconducting phase under high magnetic fields and electric currents. Several interesting composite structures are under investigation.

Although ceramic superconductors have captured the imagination of thousands of scientists, this work is outside the mainstream of electroceramics. Until a major market is demonstrated, it will remain a curiosity. The main thrust in electroceramics research is not in the discovery of new materials, but in the miniaturization and integration of existing components.

6 FERROELECTRIC CERAMICS

Multilayer capacitors make use of ferroelectric oxides such as barium titanate.¹⁴ Ferroelectric oxides with the perovskite, tungsten bronze, pyrochlore, and bismuth titanate layer structures all have high dielectric constants and high refractive indices, and all contain corner-linked octahedral networks of Ti^{4+} , Nb^{5+} , or other d^o ions. These transition metal elements are the highly polarizable "active" ions promoting ferroelectricity and the high permittivities required for capacitors.

With reference to the periodic system of elements, there are two major groups of active ions, and both are near electronic "crossover" points where different types of atomic orbitals are comparable in energy and where hybrid bond formation is prevalent. The first group typified by Ti^{4+} , Nb^{5+} , and W^{6+} are d^o ions octahedrally coordinated to oxygen. For Ti^{4+} , the electronic crossover involves the 3d, 4s, and 4p orbitals, which combine with the σ - and π -orbitals of its six O²⁻ neighbors to form a number of molecular orbitals for the $(TiO_6)^{8-}$ complex. The bond energy of the complex can be lowered by distorting the octahedron to a lower symmetry. This leads to dipole moments, ferroelectricity, and large dielectric constants.

A second group of active elements contributing to polar distortions in ceramic dielectrics is the lone-pair ions having two electrons outside a closed shell in an asymmetric hybrid orbital. Among oxides, the most important of these lone-pair ions are Pb²⁺ and Bi³⁺, which are involved in a number of ferroelectrics ($PbTiO_3$, $Bi_4Ti_3O_{12}$, $PbNb_2O_6$) with high Curie temperatures. In many of these compounds, Pb²⁺ and Bi³⁺ are in pyramidal coordination with oxygen and therefore contribute to the spontaneous polarization.

6.1 BaTiO₃ Capacitors

Many capacitor formulations are based on BaTiO₃, one of a number of ferroelectric substances crystallizing with the perovskite structure. Barium atoms are located at the corners of the unit cell and oxygens at the face centers (Fig. 19). Both barium and oxygen ions have radii of about 1.4 Å, and together they make up a face-centered cubic array having a lattice parameter near 4 Å. Octahedrally coordinated titanium ions located at the center of the cubic perovskite cell are the active ions in promoting ferroelectricity. The low-lying d-orbitals of titanium lead to accentric atomic arrangements and large electric polarizability.

On cooling from high temperature, the crystal structure of BaTiO₃ undergoes three ferroelectric phase transitions. All three are displacive in nature with atomic movements of 0.1 Å or less. The point symmetry changes from cubic m3m to tetragonal 4mm at the Curie temperature of

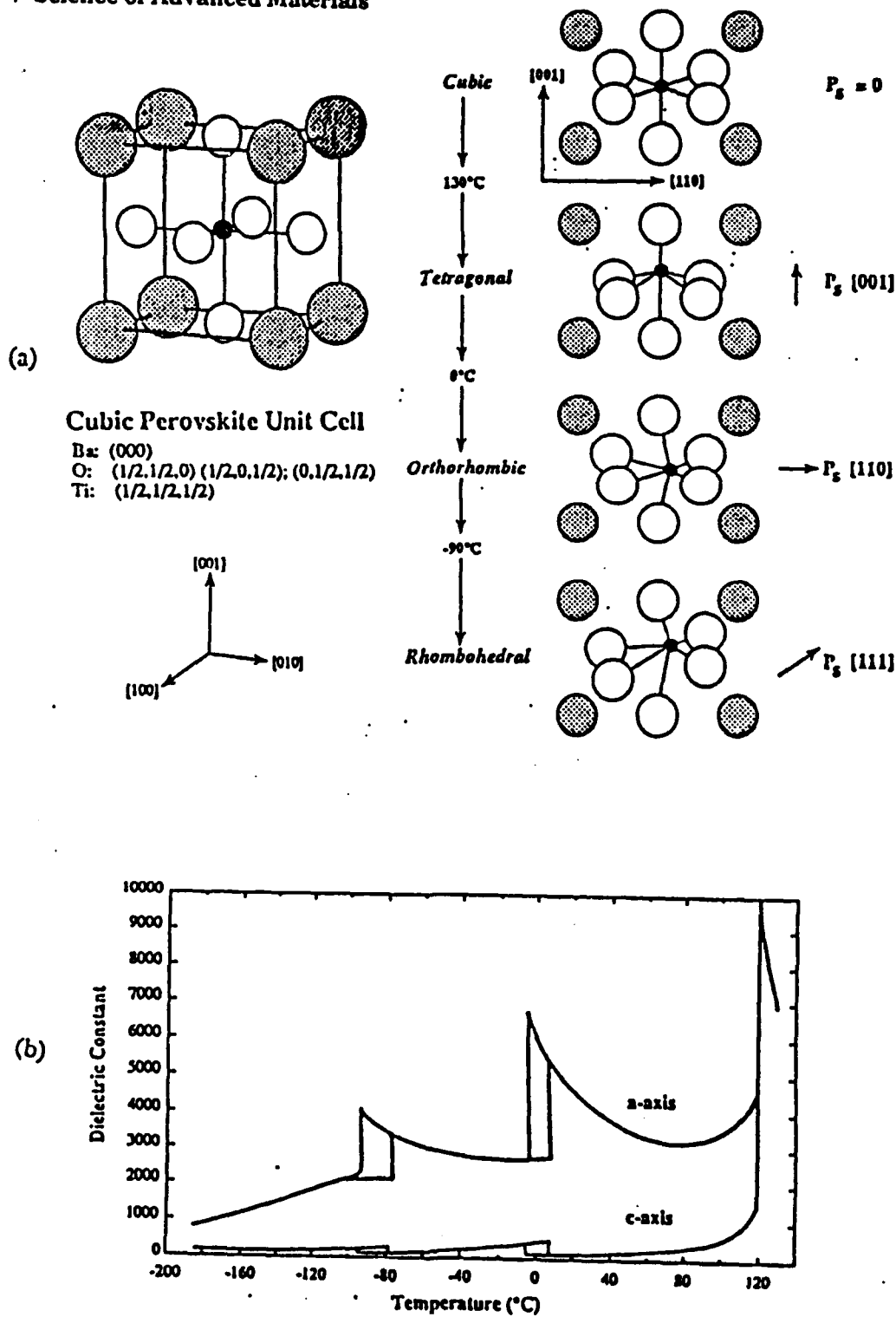


Fig. 19 Structural changes occurring at the three ferroelectric phase transformations in BaTiO_3 result in large values of the dielectric constant over a wide temperature change.

130 °C. The tetragonal state with its spontaneous polarization along [001] persists down to 0 °C, where it transforms to orthorhombic ($mm2$ symmetry) as P_z shifts to a [110] direction. On further cooling, the orthorhombic state transforms to rhombohedral ($3m$) near -90 °C. The structural changes are illustrated in Fig. 19. A peak in the dielectric constant occurs at each of the phase transitions (Fig. 19). In regard to capacitors, it is extremely important that the dielectric constant be high over a wide temperature range. The presence of the two lower ferroelectric transformations ensures that the dielectric constant remains high below the Curie temperature. Note in Fig. 19 that the dielectric constant along the a -axis is larger than that along the polar c -axis. The instability of the structure makes it easy to tilt the spontaneous polarization vector with a transverse electric field.

Because barium titanate is by far the most popular compound for multilayer ceramic capacitors, there have been many studies of its solid solutions. Substitutions for Ba^{2+} or Ti^{4+} are used to raise the permittivity, flatten its temperature dependence, and lower the losses. Substituting a divalent cation for barium in $BaTiO_3$ modifies the transition temperatures. The three most commonly used "Curie Point Shifters" are Pb^{2+} , Sr^{2+} , and Ca^{2+} . Modest amounts of Pb^{2+} raise T_c , Sr^{2+} lowers T_c , and Ca^{2+} has little effect. Divalent Pb is one of the very few additions that increases the transition temperature; the tetragonal pyramidal coordination favored by Pb^{2+} stabilizes the tetragonal phase with respect to the adjacent cubic and orthorhombic phases. All three Curie point shifters destabilize the orthorhombic and rhombohedral phases of $BaTiO_3$ as the lower two transition temperatures drop when increasing amounts of Pb^{2+} , Sr^{2+} , or Ca^{2+} are added. The opposite effect is achieved by replacing titanium with larger tetravalent ions.

A pinching together of the phase transitions occurs when titanium is replaced with larger tetravalent ions. Typical of this type of behavior are the $BaTi_{1-x}Zr_xO_3$ solid solutions. With increasing zirconium content, the Curie temperature drops while the lower two transition temperatures are raised, thus causing the three transition temperatures to converge near $x = 0.1$ and $T_c = 50$ °C. As a consequence, the three peaks in the dielectric constant merge to give an immense peak of about $K = 8000$.

6.2 Domain Walls and Dielectric Loss

Domain walls are an important source of dielectric loss for temperatures below T_c .¹⁵ Under applied electric fields, domain wall motion takes place, dissipating energy. A number of different types of walls are found in $BaTiO_3$, with varying wall mobilities. Tetragonal $BaTiO_3$ has 180° walls, and both charged and uncharged 90° walls. Charged walls are important only in

000 / Science of Advanced Materials

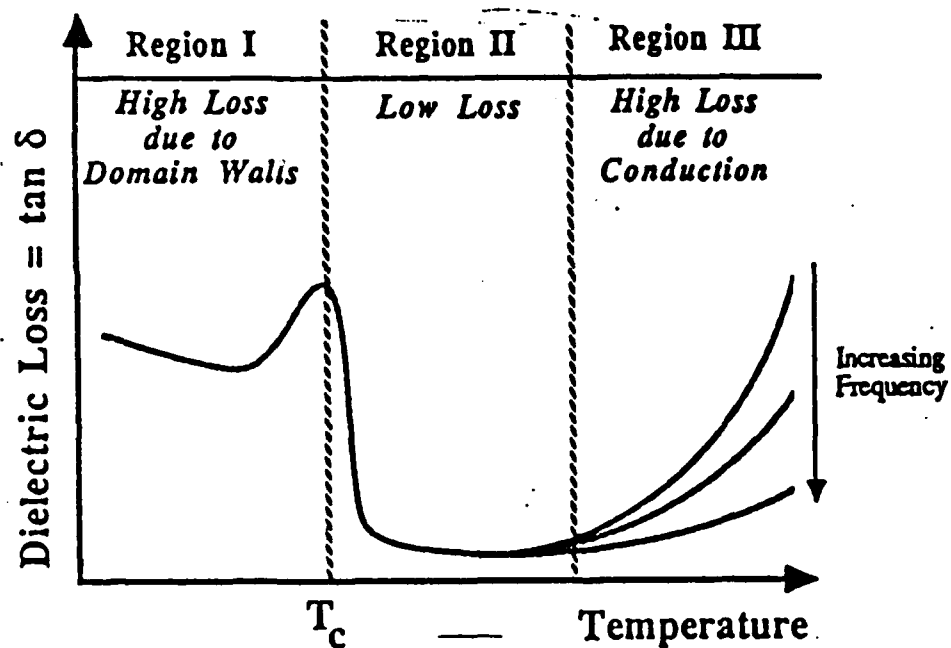


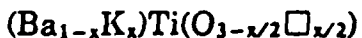
Fig. 20 Temperature dependence of the electrical loss, $\tan \delta$. At high temperatures, the losses are caused by conduction, whereas domain walls are responsible at low temperatures.

conducting BaTiO_3 where currents can flow, neutralizing the charge. The 180° walls are generally more mobile than 90° walls because of the mechanical strain associated with 90° walls.

In general, the electrical loss of ferroelectric ceramics displays three identifiable temperature ranges (Fig. 20). Below T_c , the losses are moderately high and are caused by domain walls. The magnitude of $\tan \delta$ increases rapidly with the applied field, but does not depend strongly on frequency.

The second temperature range—typically extending 100 to 200° C above the Curie temperature—has very low dielectric loss. Above T_c , there are no domains to cause dielectric loss, and the temperature is too low for appreciable conductivity loss. At high temperatures, the loss due to conductivity becomes important, causing $\tan \delta$ to increase rapidly with temperature. Conduction losses are inversely proportional to the measurement frequency.

Acceptor dopants such as K^+ or Fe^{3+} create oxygen vacancies in BaTiO_3 :



and



Oxygen vacancies exert a much greater influence on the dielectric loss than barium or titanium vacancies. The way in which oxygen vacancies affect $\tan\delta$ depends on temperature and the dominant loss mechanism. Below T_c , where domain wall losses predominate, oxygen vacancies lower $\tan\delta$. The explanation of why donors and acceptors affect the dissipation factor differently involves the pinning of domain walls. Donor-doped perovskite ferroelectrics have lossy hysteresis loops and considerable domain wall motion, whereas acceptor-doped perovskites do not.

The reason domain walls are pinned more effectively in acceptor-doped perovskites is illustrated by the crystal structure. Oxygen vacancies diffuse much faster than cation vacancies because of the proximity of oxygen-sites. The distance between nearest neighbor oxygens is only 2.8 Å compared to 4 Å for the shortest Ti-Ti or Ba-Ba interatomic distance.

Defect dipoles in acceptor-doped BaTiO_3 consisting of paired iron atoms and oxygen vacancies realign more easily than the corresponding dipoles in donor-doped material. Thus, the defect dipoles in acceptor-doped BaTiO_3 align with the spontaneous polarization of the domain structure to pin domain walls, thereby lowering the dissipation factor in the low-temperature region below T_c .

6.3 Conduction Losses and Degradation

Oxygen vacancies are also important in the high-temperature region. The rapid increase of dissipation factor is caused by free carrier conductivity, and the concentration of free carriers depends on doping and temperature. The loss factor ($\tan\delta$) is inversely proportional to frequency in this temperature range.

Based on a number of experiments, the following picture has been developed for the DC degradation process in barium titanate ceramics. Polycrystalline titanates are appreciably reduced at the temperatures used in firing ceramic capacitors. On cooling, rapid reoxidation occurs above 1100 °C, but effectively stops at some temperature between 600 and 900 °C. As a consequence, the outside of the sample and, to some extent, the outside of each grain is well oxidized, but the interior of the grains remains oxygen deficient. Oxygen vacancies carry an effective charge of +2e, which is neutralized by 3d electrons on the titanium atoms, forming two Ti^{3+} ions for every oxygen vacancy. At low temperatures, the oxygen vacancies and Ti^{3+} ions are bound by a small energy of 0.1 to 0.2 eV, sufficiently large that only a few of the defects are separated. Electrons associated with the unattached Ti^{3+} ions are responsible for conduction, making use of the narrow 3d conduction band. Alternatively, the conduction process can be described as electron hopping via $\text{Ti}^{3+} \rightarrow \text{Ti}^{4+} + e^-$ transfer. Unattached

000 / Science of Advanced Materials

oxygen vacancies also contribute to the conductivity, but their mobility is much smaller than that of electrons. Neutralized bound defects do not participate directly in the conduction process, but experience a torque tending to align the dipole moment with the applied field. This in turn creates dielectric polarization and dielectric loss. Oxygen vacancies are also important in the AC degradation of BaTiO₃ ceramics. Electrostrictive pumping of the oxygen vacancies to the grain boundary has been proposed as a mechanism.

Trivalent manganese plays an important role in a number of capacitor compositions by lowering conduction losses. Mn³⁺ has the 3d⁴ electron configuration and is widely known as a Jahn-Teller ion. It seems likely that the large tetragonal distortions associated with Jahn-Teller ions are effective in anchoring oxygen vacancies.

6.4 Relaxor Ferroelectrics

Ordered perovskites generally have low dielectric constants because the linkage between "active" ions is severed. In disordered structures such as the relaxor ferroelectrics, the dielectric constant can be extremely large, making them useful as capacitor dielectrics. The monolithic Pb-based compositions under development in Japan¹⁶ are excellent examples. Not only do the Pb(Fe_{0.5}Nb_{0.5})O₃-Pb(Fe_{0.67}W_{0.33})O₃ ceramics have dielectric constants in excess of 15,000, but they can be sintered in air at 850 °C with silver electrodes.

Relaxor ferroelectrics are characterized by temperature-sensitive micro-domains resulting from the many different "active" ion linkages in the disordered octahedral framework. Each (NbO₆)-octahedron may be bonded to anywhere from zero to six other (NbO₆)-octahedra. Connections between these octahedra are assumed to be essential to ferroelectricity and high K values. As temperature decreases from the high-temperature paraelectric state, these microdomains gradually coalesce to macrodomains giving rise to a diffuse phase transformation. These polarization fluctuations are also dependent on bias field and measurement frequency. The dielectric constant drops rapidly with frequency (hence the name "relaxor"), because it takes time for the polarization fluctuations to respond. Direct current bias fields favor coalescence, having the same effect as lowering the temperature.

Relaxor behavior is very common among Pb-based perovskites, suggesting that Pb²⁺ and its "lone-pair" electrons play a role in the microdomain process, possibly by adjusting the orientation of the lone-pair. Multilayer relaxor ferroelectrics are used as micropositioners as well as capacitors. The electrostrictive distortions are highly reproducible and have found widespread use in active optic systems.¹⁷

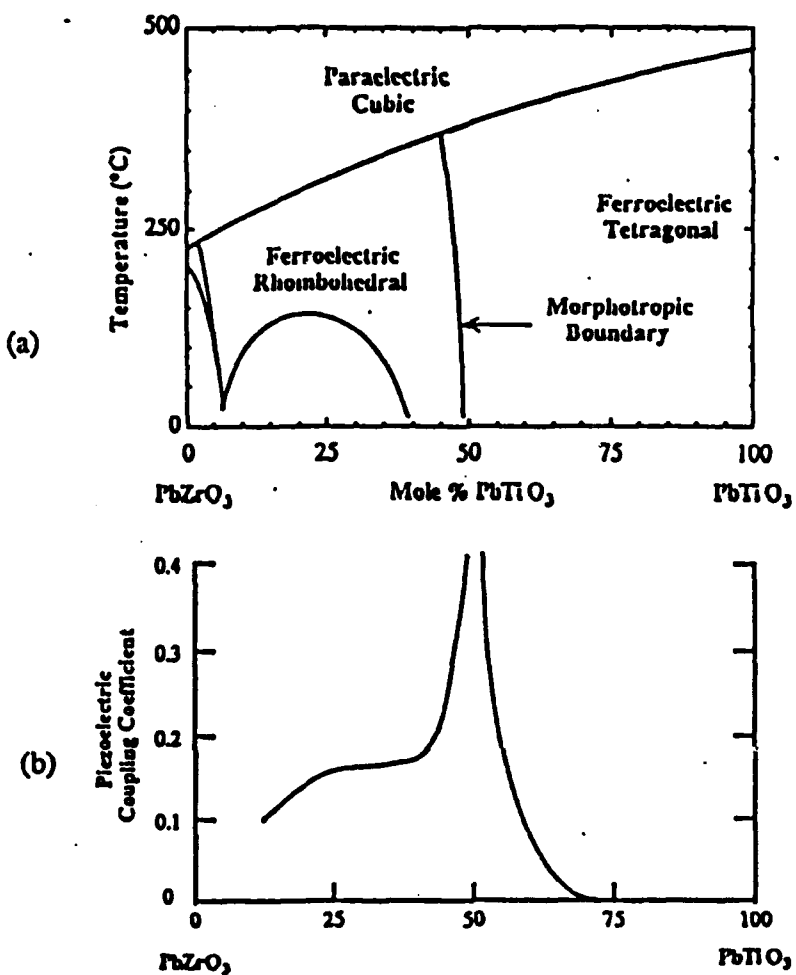


Fig. 21 (a) Binary phase diagram of the lead zirconate-lead titanate ceramics used in transducers. (b) Large piezoelectric coefficients are obtained for poled ceramics with compositions near the morphotropic phase boundary.

6.5 Piezoelectric Transducers

Piezoelectric transducers convert mechanical energy to electrical energy (the direct piezoelectric effect), or electrical energy to mechanical energy (the converse piezoelectric effect). ¹⁸ Ferroelectric ceramics such as lead zirconate titanate become piezoelectric when electrically poled. Poling is carried out under intense electric fields at temperatures just below the ferroelectric Curie point where the domains are most easily aligned.

The phase diagram of the $\text{PbZrO}_3\text{-PbTiO}$ (PZT) system is shown in Fig. 21(a). A complete solid solution forms at high temperature, with Zr and Ti randomly distributed over the octahedral sites of the cubic perovskite structure. On cooling, the structure undergoes a displacive phase

000 / Science of Advanced Materials

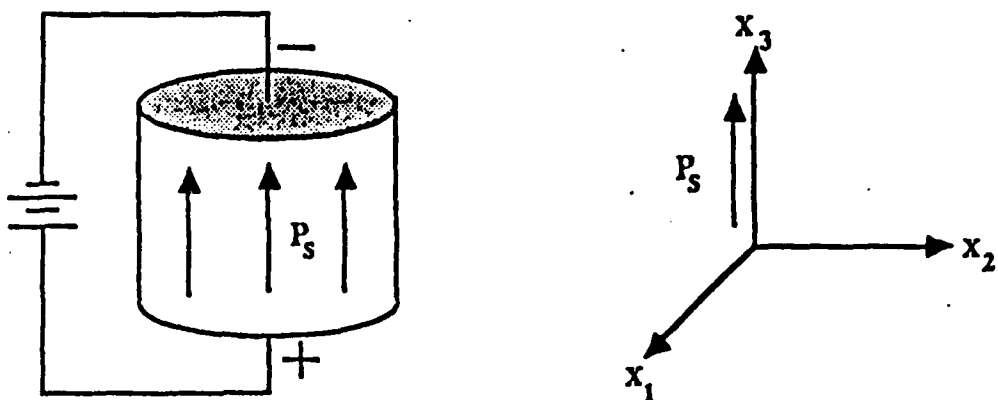


Fig. 22 (a) Poled piezoelectric ceramics have a symmetry imposed by the electric field vector. This symmetry determines the form of the piezoelectric tensor, which is referred to the axial system shown in (b).

transformation into a distorted perovskite structure. Titanium-rich compositions favor a tetragonal modification with sizable elongation along [001] and a large spontaneous polarization in the same direction. There are six equivalent polar axes in the tetragonal state corresponding to the [100], $[\bar{1}00]$, [010], $[0\bar{1}0]$, [001], and $[0\bar{0}1]$ directions of the cubic paraelectric state. A rhombohedral ferroelectric state is favored for zirconium-rich compositions. Here, the distortion and polarization are along [111] directions, giving rise to eight possible domain states: [111], $[\bar{1}\bar{1}1]$, $[1\bar{\bar}{1}]$, $[11\bar{\bar}{1}]$, $[\bar{1}\bar{1}\bar{1}]$, $[1\bar{\bar}{\bar}{1}]$, $[\bar{1}\bar{\bar}{\bar}{1}]$, and $[1\bar{\bar}{\bar}{\bar}{1}]$.

The compositions that pole best lie near the morphotropic boundary between the rhombohedral and tetragonal ferroelectric phases. For these compositions, there are fourteen possible poling directions over a very wide temperature range. This explains why the piezoelectric coefficients are largest near the morphotropic boundary (Fig. 21b).

Morphotropic boundaries are relatively common in Pb-based perovskites, more so than in other perovskite phase diagrams. In solid solutions based on BaTiO_3 , a different sequence of phase transformations appears. On cooling from high temperatures, the cubic phase undergoes transformations to tetragonal, orthorhombic, and rhombohedral. The intervening orthorhombic phase makes it impossible for the tetragonal phase to transform to rhombohedral. Thus, there is no morphotropic phase boundary in BaTiO_3 -based ceramics.

It appears that morphotropic boundaries occur in PbTiO_3 -based systems because of the suppression of the orthorhombic phase. The Pb^{2+} ion plays a major role in the suppression. Because of its lone-pair $6s^2$ electron configuration, Pb^{2+} favors pyramidal bonding. In the tetragonal and rhombohedral

perovskites, such bonding occurs, but not in the orthorhombic ferroelectric form. Here, Pb^{2+} is forced to move directly toward a neighboring oxygen ion, an extremely unfavorable coordination.¹⁹

Poled ceramic transducers have conical symmetry (point group ∞m), the symmetry of a polar vector. By convention, the x_3 axis is chosen along the polar axis with the orthogonal x_1 and x_2 axes perpendicular to x_3 (Fig. 22). The piezoelectric coefficients relate polarization to mechanical stress. P_1 , P_2 , and P_3 are the components of the stress-induced polarization along axes x_1 , x_2 , and x_3 . In matrix notation, stress components σ_1 , σ_2 , and σ_3 are the applied tensile stresses parallel to x_1 , x_2 , and x_3 . Shear stresses about x_1 , x_2 , and x_3 are designated σ_4 , σ_5 , and σ_6 , respectively.

For poled ferroelectric ceramics, conical symmetry dictates that all piezoelectric coefficients are zero except $d_{31} = d_{32}$, d_{33} , and $d_{15} = d_{24}$. The direct piezoelectric effect can therefore be described by the following matrix expression:

$$\begin{pmatrix} P_1 \\ P_2 \\ P_3 \end{pmatrix} = \begin{pmatrix} 0 & 0 & 0 & 0 & d_{15} & 0 \\ 0 & 0 & 0 & d_{15} & 0 & 0 \\ d_{31} & d_{31} & d_{33} & 0 & 0 & 0 \end{pmatrix} \begin{pmatrix} \sigma_1 \\ \sigma_2 \\ \sigma_3 \\ \sigma_4 \\ \sigma_5 \\ \sigma_6 \end{pmatrix}$$

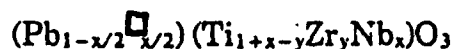
multiplying out:

$$\begin{aligned} P_1 &= d_{15}\sigma_5 \\ P_2 &= d_{15}\sigma_4 \\ P_3 &= d_{31}(\sigma_1 + \sigma_2) + d_{33}\sigma_3 \end{aligned}$$

Thus, polarization along x_1 can only be generated by shear stresses about x_2 . For hydrostatic pressure p , $\sigma_1 = \sigma_2 = \sigma_3 = -p$, and $\sigma_4 = \sigma_5 = \sigma_6 = 0$. The resulting polarization appears along x_3 : $P_3 = (2d_{31} + d_{33})(-p)$.

Molecular mechanisms for piezoelectric coefficients d_{33} , d_{31} , and d_{15} are illustrated and explained in Fig. 23. For PZT compositions near the morphotropic boundary, $d_{33} \approx 400$ pC/N, $d_{31} \approx -170$, and $d_{15} \approx 500$. The magnitudes depend markedly on dopants and defect structure because of their influence on domain wall motion.

Donor ions create Pb vacancies in the PZT structure. As an example, when Nb^{5+} is substituted for Ti^{4+} , vacancies in the lead-site results:



Donor doping is not effective in pinning domain walls. Pinning is believed to result from the alignment of defect dipoles with the spontaneous polarization within a domain. The defect dipoles come from the negatively charged Pb-vacancies paired with dopant Nb^{5+} ions. Because the defect dipoles are

000 / Science of Advanced Materials

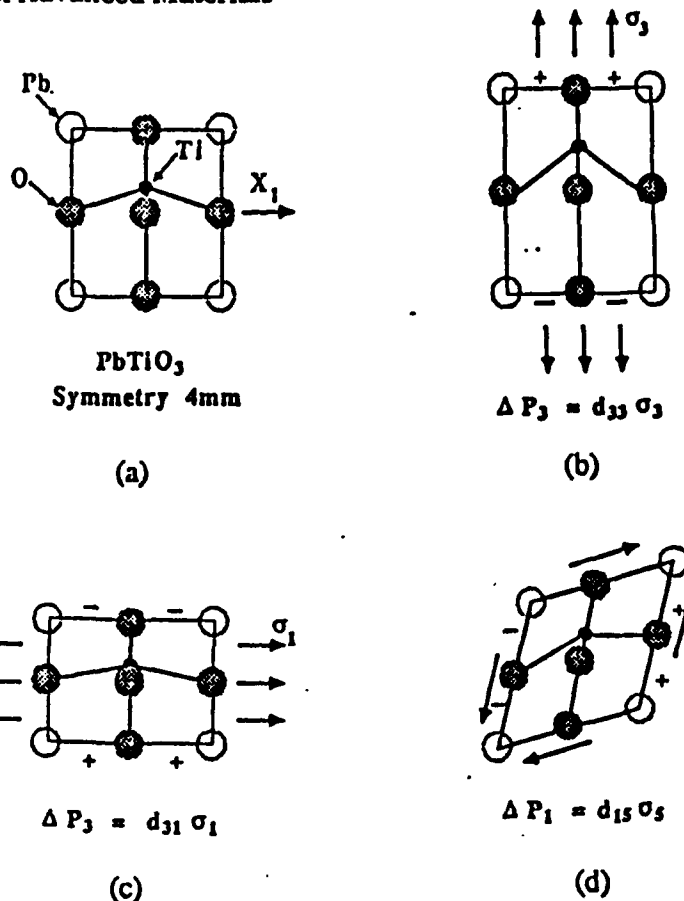


Fig. 23 (a) Tetragonal PbTiO_3 is noncentrosymmetric with the titanium ion displaced from the center of the unit cell. (b) When a tensile stress is applied parallel to x_3 , the Ti^{4+} ion displaces further in its off-center position, creating a positive polarization in this direction: $P_3 = d_{33}\sigma_3$. (c) If the stress is applied along x_1 , the dipole moment of the unit cell is diminished, and a negative polarization appears. Hence, d_{31} is negative, whereas d_{13} is positive. (d) For a shear stress about x_2 , the dipole moment is tipped, producing polarization in the x_1 direction, $P_1 = d_{15}\sigma_5$.

formed at high temperature, the dipoles are not aligned with P , initially because the spontaneous polarization is zero in the cubic paraelectric state. Alignment can only take place below the Curie temperature (~ 350 °C for PZT) where diffusion rates are low. Such is the case for donor-doped PZT, a so-called “soft” PZT. In a soft PZT, domain wall motion contributes to the size of the dielectric and piezoelectric coefficients. Hence, soft PZT transducers are used as hydrophones and ultrasonic detectors where high sensitivity to weak signals is needed. Conversely, however, soft PZT ceramics

are easily depoled because the domain walls are not pinned. For this reason, soft PZT ceramics are not used for sonar transmitters or spark generators.²⁰

Acceptor doping with lower valent ions such as K⁺ (for Ba²⁺) or Fe³⁺ (for Ti⁴⁺) is employed to produce "hard" PZT. Oxygen vacancies are generated by acceptor doping:



Domain walls are pinned in a hard PZT because the defect dipoles are able to align in accordance with the domain structure. Dipoles consisting of oxygen vacancies and associated dopant ions are able to re-orient easier in a hard PZT. The explanation lies in the ease with which oxygen vacancies diffuse at temperatures below T_c.

Examination of the perovskite structure makes it clear why oxygen vacancies diffuse faster than cation vacancies. Cations are completely surrounded by oxygens and are separated from the nearest cation site by an entire unit cell (~4 Å), making diffusion very difficult. Oxygen sites, on the other hand, are adjacent to one another, only 2.8 Å apart. Hence, oxygens can easily move into nearby oxygen vacancies, realigning defect dipoles and pinning domain walls.

7 MAGNETISM IN OXIDES

Magnetic ordering occurs when the transition-metal atoms are nearest neighbors (metals) or next-nearest neighbors (simple compounds).²¹ Among oxides and fluorides, antiferromagnetism is much more common than ferromagnetism or ferrimagnetism due to the superexchange interaction. Direct exchange seldom occurs in such materials, because the transition-metal ions are not in direct contact, but interact via an intermediate anion. Superexchange is a strong interaction, leading to magnetic transition temperatures comparable to that of metals. Ferromagnetic ordering in Fe occurs at 1040 K, antiferromagnetism in α-Fe₂O₃ at 950 K, and ferrimagnetism in magnetite at 860 K.

In the superexchange interaction, two metal atoms M₁ and M₂ on opposite sides of an oxygen ion interact through a p-orbital of oxygen (Fig. 24). Transition-metal ions with less than half full d-shells will be considered first. Because the oxygen ion is not fully ionized, its outer electrons spend time on the neighboring transition-metal ions. When it enters the d-shell of a transition-ion whose d-orbitals are less than half full, the oxygen electron spin is parallel to those of the metal ion, in accordance with Hund's rule. Meanwhile, the other electron in the same oxygen p-orbital is on the opposite

000 / Science of Advanced Materials

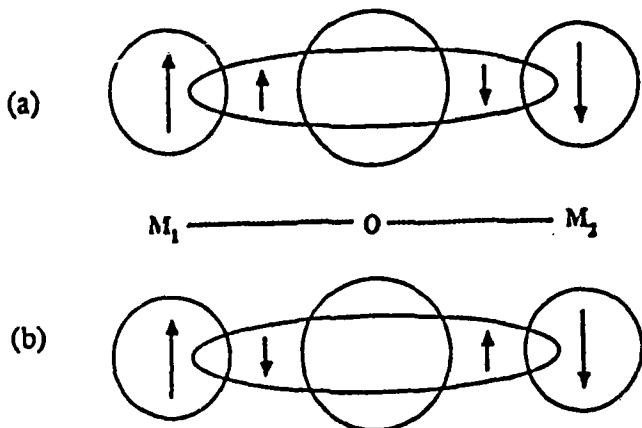


Fig. 24 The 180° superexchange interaction when the transition metal 3d shell is (a) less than half full and (b) half or more than half full.

side of the oxygen ion because of the coulomb repulsion between two electrons in the same p-orbital. While there, the second electron (whose spin is antiparallel to the first electron because of the Pauli exclusion principle) also interacts with transition metal ions, and its spin will again be parallel to that of the metal ion if its d-shell is less than half full. The antiferromagnetic superexchange thus arises from the alignment as shown in Fig. 24: the first metal atom accepts an electron with parallel spin from an oxygen neighbor; the spins of the two electrons in the same oxygen p-orbital are antiparallel; and the second electron spends part of its time in parallel alignment with the d-electrons of the second metal ion.

A similar situation occurs when the d-electron shell of the transition metal ion is more than half full, again resulting in antiferromagnetic superexchange (Fig. 24). The oxygen electrons enter the metal atom d-shell antiparallel to the net spin, but because the same thing happens to the other electron, the interaction remains antiferromagnetic. Superexchange is strongest when the angle M_1-O-M_2 is 180° , allowing maximum overlap of the p-orbital with the two metal ions. The interaction weakens as the angle approaches 90° , even though the metal-metal distance may be shorter.

Long-range magnetic order disappears at high temperatures because of thermal disorder. The transition temperature is called the Curie point (T_c) in a ferromagnet or ferrimagnet, and the Neel point (T_N) in an antiferromagnet. T_c and T_N depend strongly on transition-metal concentration, as expected. The general trend is indicated by the transition temperatures for the following Fe^{3+} compounds, which are arranged in order of decreasing iron content: $(\alpha\text{-})\text{Fe}_2\text{O}_3$ (958 K), $\gamma\text{-Fe}_2\text{O}_3$ (743 K), Fe_2MgO_4

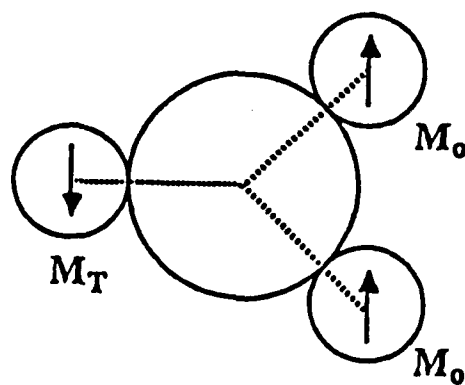


Fig. 25 Oxygen nearest neighbors in the spinel structure. Superexchange coupling between the tetrahedral and octahedral sites is especially strong.

(653 K), $\text{Y}_3\text{Fe}_5\text{O}_{12}$ (563 K), FeF_3 (394 K), FeCl_3 (10 K), Fe_2TeO_6 (219 K), YFeO_3 (643 K), FePO_4 (25 K), $\text{Fe}_3(\text{PO}_4)_2 \cdot 4\text{H}_2\text{O}$ (15 K), $\text{FeNH}_4(\text{SO}_4)_2 \cdot 12\text{H}_2\text{O}$ (< 1 K). Magnetic interactions weaken with increasing dilution, although some noticeable irregularities occur in the list. The transition temperature of FeCl_3 is surprisingly low, whereas that of YFeO_3 is rather high. These exceptions illustrate the influence of crystal structure on the exchange interactions. Ferric chloride has a layer structure with the sequence $-\text{Cl}-\text{Fe}-\text{Cl}-\text{Cl}-\text{Fe}-\text{Cl}-$. Neither direct nor superexchange interactions are possible between layers, hence T_N is very low. In YFeO_3 , the arrangement of iron and oxygen are nearly ideal for 180° superexchange. The compound crystallizes in the perovskite structure with interconnected $-\text{O}-\text{Fe}-\text{O}-\text{Fe}-\text{O}-$ chains in all three directions.

7.1 Spinel Ferrites

Most magnetic ceramics make use of trivalent iron, Fe^{3+} , with its five unpaired electrons. To take advantage of the large magnetic moment, it is necessary to couple the spins through superexchange. In ferrites with the spinel structure, there is a strong antiferromagnetic superexchange coupling between the tetrahedral and octahedral sites. Each oxygen in the spinel structure is bonded to one tetrahedral cation and three octahedral cations (Fig. 25). The tetrahedral ion-oxygen-octahedral cation linkage subtends an angle of 125° at the oxygen ion, which is large enough to make use of a $2p$ orbital in a strong superexchange interaction.

The complexity of the spinel structure is also important; there are twice as many octahedral as tetrahedral metal ions in spinel, and this leads to magnetic imbalance and a net magnetization. This is why magnetite (Fe_3O_4 ,

000 / Science of Advanced Materials

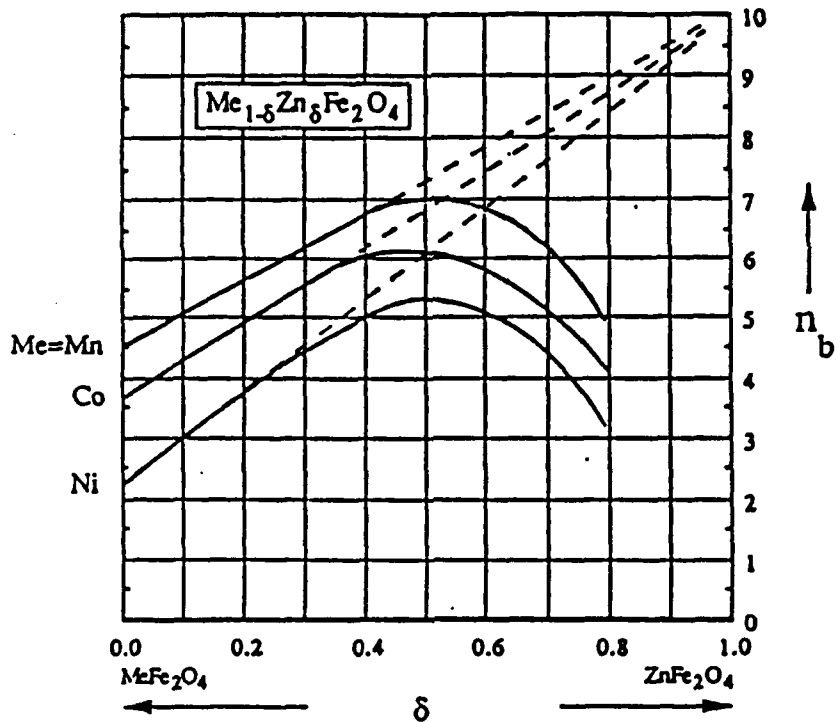


Fig. 26 Addition of zinc raises the magnetization of ferrites.

spinel structure) is ferrimagnetic, whereas hematite ($\alpha\text{Fe}_2\text{O}_3$, corundum structure) and wustite (FeO , rocksalt structure) are antiferromagnetic.

7.2 Magnetization

In the spinel ferrites, the spontaneous magnetization is equal to the difference between the sublattice magnetizations associated with the octahedral and tetrahedral sites. By judicious choice of ions, the difference can be made quite large and leads to an unusual situation in which adding a nonmagnetic ion increases the magnetization. This type of substitution is used to maximize the remanent magnetization of ferrites.

Zinc ferrite (ZnFe_2O_4) is a normal spinel, whereas most other spinel ferrites have the inverse structure. In a normal spinel, divalent cations occupy the tetrahedral sites, in contrast to inverse spinels where the tetrahedral sites are filled with trivalent cations. NiFe_2O_4 is an inverse spinel. In the nickel zinc ferrite solid solution ($\text{Ni}_{1-x}\text{Zn}_x\text{Fe}_2\text{O}_4$) as x is increased, Zn^{2+} replaces Fe^{3+} in the tetrahedral sites, and Fe^{3+} fills the octahedral sites emptied by Ni^{2+} . Divalent zinc has no unpaired electrons, divalent nickel has two, and trivalent iron five. The net magnetization of nickel zinc ferrite is proportional to $5(1+x) + 2(1-x) - 0(x) - 5(1-x) = 2 + 8x$.

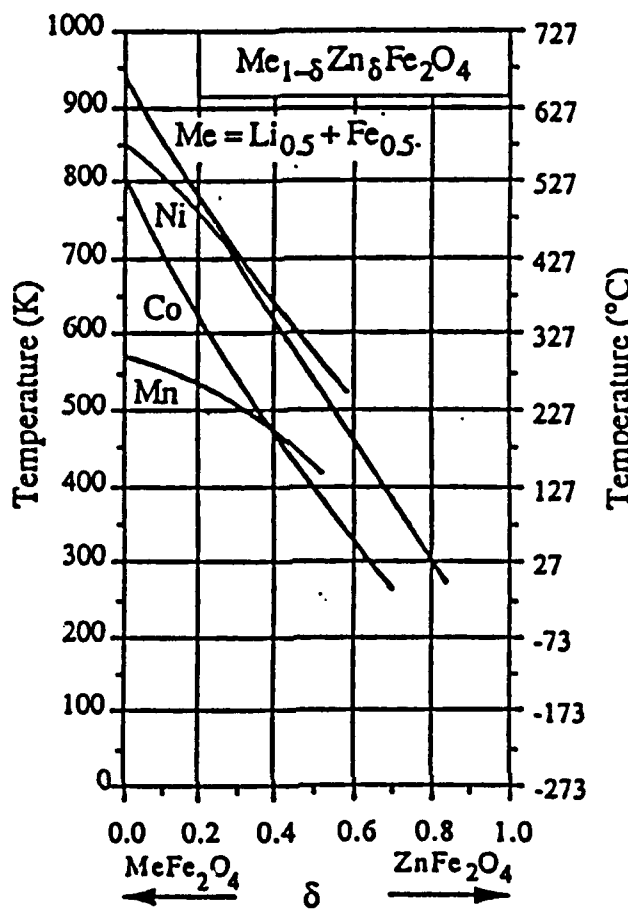


Fig. 27 Addition of zinc lowers the Curie point of magnetic ferrites.

Calculated magnetic moments for several of the zinc ferrite solid solutions are compared with experimental in Fig. 26. As predicted, the magnetizations rise with increasing zinc content until there are so few Fe^{3+} ions remaining in tetrahedral sites that the superexchange coupling between tetrahedral and octahedral sites breaks down. As a result, the Curie temperatures decline rapidly with increasing zinc content, eventually dropping below room temperature (Fig. 27). The ferrite changes from ferrimagnetic to paramagnetic as the composition nears pure zinc ferrite. The most useful compositions are those near $x = 0.5$ where the magnetization is at a maximum.

7.3 Soft Ferrites

Soft ferrites are noted for their high magnetic permeability and high electrical resistivity.²² Eddy current losses are of great importance, and compared to metals, the high resistivity of ferrites greatly reduces loss at

000 / Science of Advanced Materials

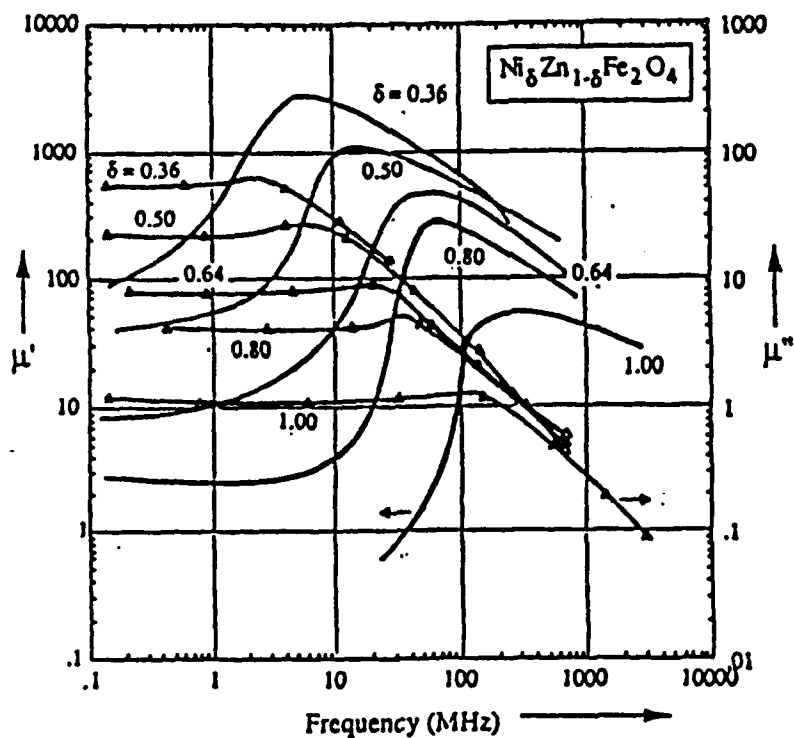


Fig. 28 Permeability spectrum for Ni-Zn ferrites.⁶

high frequencies. Applications for soft ferrites include inductors, transformers, antenna rods, loading coils, deflection yokes, choke coils, recording heads, and magnetic amplifiers.

Manganese zinc ferrite and nickel zinc ferrite are the most widely used of the soft ferrites. Mn-Zn ferrite has the highest saturation magnetization of any ferrite and is a good soft magnetic core material, but Ni-Zn ferrite is superior at high frequencies because of its higher electrical resistivity and lower resonance losses.

The property of greatest interest in soft ferrites is the initial permeability μ_i and its frequency dependence. Permeability is a complex quantity, $\mu = \mu' - i\mu''$, with the magnetic loss factor defined as $\tan\delta = \mu''/\mu'$. Engineers often use $\tan\delta/\mu'$ as a figure of merit in comparing different ferrites at low frequencies. The lowest (best) figures of merit are obtained for Mn-Zn ferrites and for Ni-Zn ferrites at high frequencies. The crossover frequency is approximately 1 MHz.

Figure 28 shows frequency spectrum for several Ni-Zn ferrites. The permeability spectrum is characterized by a broad loss peak at f , associated with domain wall losses. Note that ferrites with the high permeability have the worst frequency dependence; the product $\mu'f$ is approximately constant (Snoek's Law).

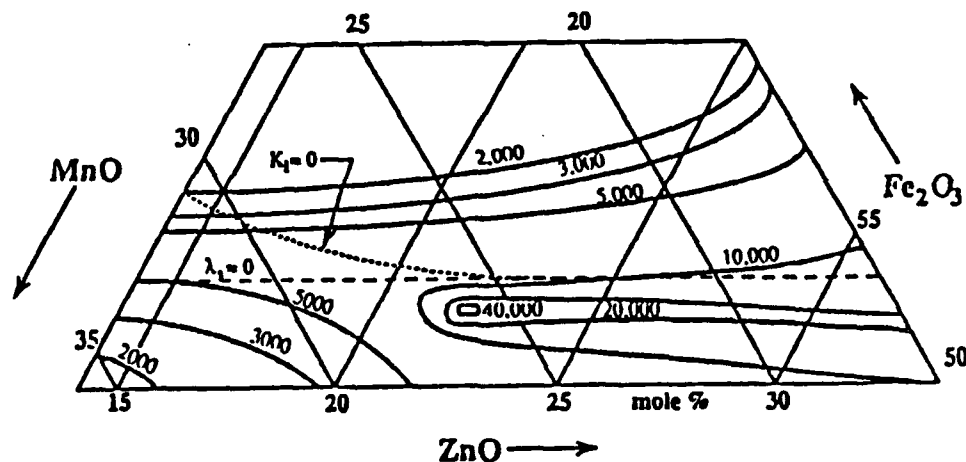


Fig. 29 Constant permeability contours in the Mn-Zn-Fe ferrite system. Maximum permeability occurs near the point of zero magnetostriiction and zero anisotropy.

7.4 Anisotropy, Magnetostriiction, and Mn-Zn Ferrites

To maximize the permeability of a soft ferrite, it is necessary to eliminate restraints on domain wall motion. Crystal anisotropy and magnetostriiction are two restraints that can be greatly reduced through control of chemical composition and microstructure. Mn-Zn ferrites are intrinsically soft because of their low anisotropy fields. Mn^{2+} and Fe^{3+} have half-filled 3d shells and Zn^{2+} has a completely filled shell. All three ions are spherically symmetric with little preference in spin orientation.

The anisotropy field affects both the rotational and domain wall contributions to the permeability. Because the spins in a low anisotropy ceramic are easily deflected by an applied field the rotational permeability is greatly enhanced. Domain wall motion is also enhanced because of the nature of domain walls. Within the walls, spin orientations differ markedly in orientation from the easy axis directions. Thus, wall energy and the ease with which walls can be created or displaced is influenced strongly by the anisotropy field.

Magnetostriiction

The change in shape of a magnetic specimen during the magnetization process is called magnetostriiction. Domain wall motion is responsible for most of the strain. Strain measurements are made on unmagnetized specimens with randomized domain structure. When a field is applied, the specimen changes shape, and eventually both the magnetization and the

000 / Science of Advanced Materials

strain reach saturation values at very large fields. For ferrites, the saturation strain λ ranges from 10^{-6} to 10^{-3} . Small values of λ are essential in a soft ferrite, because strain mismatch impedes domain wall motion and magnetization rotation.

Magnetostrictive coefficients have been measured for a number of ferrites including the manganese zinc ferrites shown in Fig. 29. Adding a few percent Fe^{2+} reduces λ to zero, and it also decreases the anisotropy coefficient K_1 .

Mn-Zn Ferrites

Compositions near the intersection of the $\lambda_s = 0$ and $K_1 = 0$ lines are especially interesting. Magnetic permeabilities as large as 40,000 are measured near the point where magnetostrictive and anisotropy effects are absent. Domain wall and rotational contributions to the permeability are both enhanced at this composition.

In ceramic ferrites, a microstructure consisting of large, defect-free crystallites favors domain wall mobility and high magnetic permeability.²³ Domain wall movements are suppressed in the fine-grained ferrites used in permanent magnets and in high-frequency applications. Small grain microstructures and low porosity are also required for microwave ferrites to eliminate unwanted spin waves.

The distribution of pores in the microstructure is important. Tiny pores distributed uniformly throughout the grains are obtained in ferrites slightly deficient in oxygen. The pores pin domain walls and lower the magnetic permeability. A different pore structure is obtained in ferrites that are deficient in cations. In this case, the pores are swept together at the grain boundaries during sintering, leaving behind relatively perfect crystallites. Very high permeabilities can then be achieved provided the grain size is large.²³

Microstructure also controls magnetic losses. Substituting Fe^{2+} in Mn-Zn ferrites raises the permeability, but it also lowers the electrical resistivity as the extra electron hops easily between iron atoms: $Fe^{2+} \rightarrow Fe^{3+} e^-$. The increased conductivity leads to eddy current losses, which can be controlled by a small amount of silica to the starting material. During the sintering operation, silica forms a grain boundary phase that raises the resistance and eliminates eddy currents. This results in a decrease in the electrical loss $\tan\delta$ and an increase in the figure of merit, $\mu/\tan\delta$.

Eddy currents are the most important source of loss at low frequencies (kHz range), but ferrimagnetic resonance and domain wall damping are the controlling mechanisms in the MHz range. Mn-Zn ferrites are not used at these frequencies because the Larmor precession frequency is too low. Ni-Zn ferrites have stronger internal fields and higher resonant frequencies

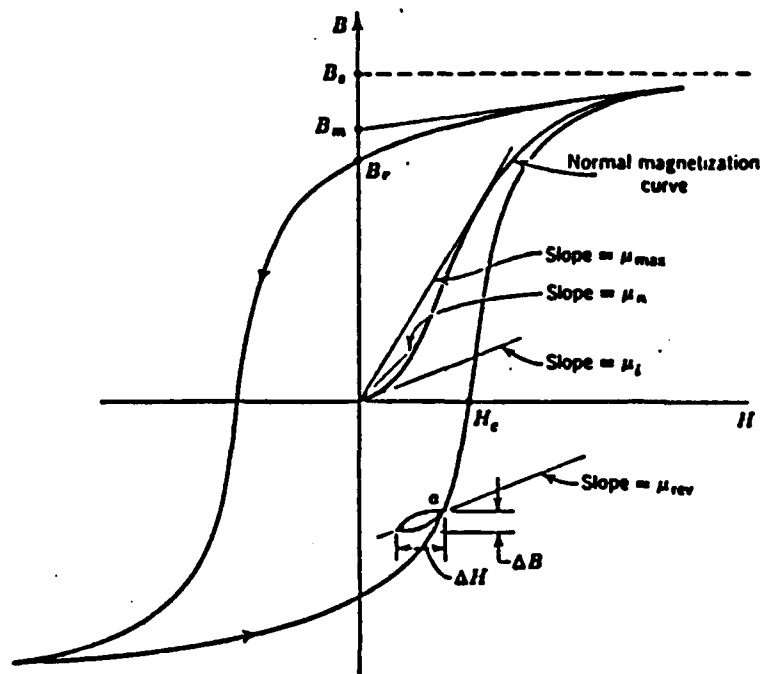


Fig. 30 Hysteresis in magnetic ceramics.

(10 to 1000 MHz). This lowers resonance losses in the 1 to 10 MHz range. Eddy current losses are also small because of the higher resistivity of the Ni-Zn compositions, although the permeability μ' is somewhat smaller.

Domain wall damping contributes to loss at frequencies just below resonance. To limit this factor, it is necessary to minimize wall displacements by making the grain size very small. Hot pressing procedures or the addition of grain-growth inhibitors keep the grain size small and lower losses. Small grain size is also an advantage in microwave ferrites, which operate in the GHz range. When operated at high power levels, parametric excitation of spin waves becomes the dominant loss mechanism. Reductions in grain size to below 2 μm increases the power-handling capability by several orders of magnitude.

7.5 Permanent Magnets

Hard magnets are characterized by high coercive field strength and high remanent magnetization.²⁴ The $(BH)_{\max}$ energy product (Fig. 30) is used as a measure of magnetic "hardness." Processing methods to maximize the BH product are magnetic annealing and the texturing of crystallites by magnetic pressing. Precipitation hardening, superlattice formation, and work hardening also increase the coercive field by restricting domain wall movement.

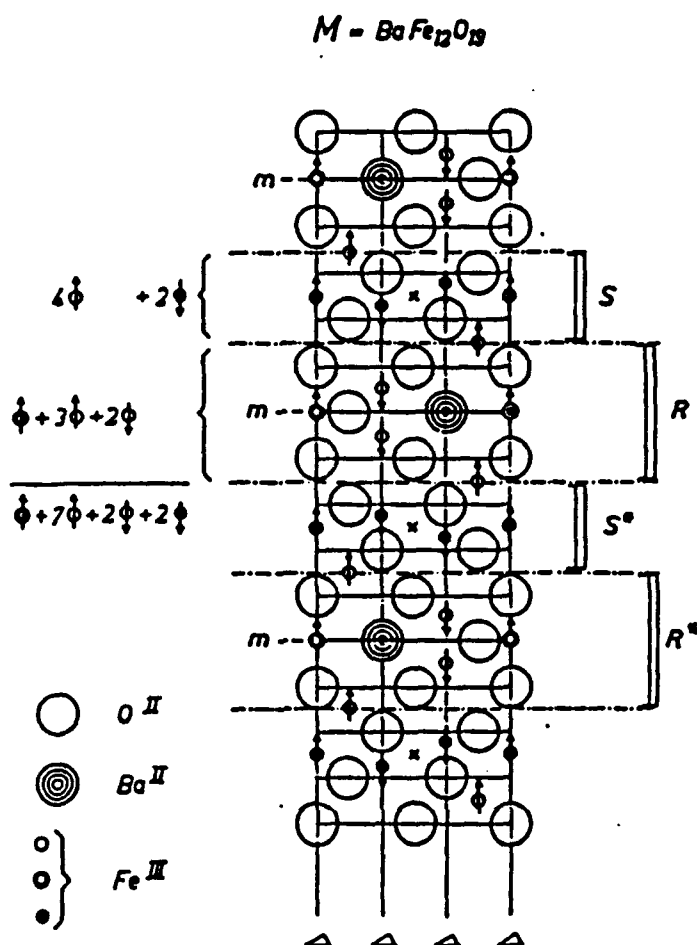


Fig. 31 Cross section of the magnetoplumbite structure M , with the c axis $\downarrow c + \downarrow c \perp$. The arrows indicate the spin orientations. The vertical lines are axes of threefold symmetry and the cross denotes a center of symmetry. All layers containing barium are mirror planes and are denoted by m . This structure consists of spinel-like blocks separated by the layers containing barium. The asterisk indicates a rotation of a block by 180° about the c -axis.⁶

Some oxide magnets utilize particles small enough to have a single domain structure. The OP (oxide powder) magnet with a composition $3CoFe_2O_4 \cdot Fe_3O_4$ invented 50 years ago has large magnetocrystalline anisotropy and large magnetostrictive coefficients as well as small particle size. Oversizing can cause grain growth, resulting in a reduced coercive field.

One of the most widely used permanent magnet materials is barium ferrite, a ferrimagnetic oxide with the magnetoplumbite structure. The large Ba^{2+} ions form a close-packed array with the O^{2-} anions in a mixed sequence of hexagonal and cubic close-packing. Trivalent iron ions occupy

Table 1. Properties of Ferrite Permanent Magnets

Material	B_r , W/m ²	$H_c \cdot 10^4$ A/m	BH_{max} , J/m ³
BaFe₁₂O₁₉			
Isotropic	0.22	0.148	4.0
Oriented (high B_r)	0.384	0.160	14.0
Oriented (high H_c)	0.32	0.204	10.4
Rubber bonded	0.22	0.118	4.4
SrFe₁₂O₁₉			
Oriented (high B_r)	0.40	0.176	14.8
Oriented (high H_c)	0.355	0.252	12.0
OP Magnet			
$\text{Co}_{0.75}\text{Fe}_{0.25}\text{Fe}_2\text{O}_4$	0.25	0.052	4.8
Source: Ref 24			

three types of sites within the magnetoplumbite structure: octahedral, tetrahedral, and an unusual five-coordinated trigonal bipyramidal site.

Magnetic interactions between the iron ions take place via the same $-\text{Fe}-\text{O}-\text{Fe}-$ superexchange mechanism found in spinel ferrites. Four of the twelve irons in $\text{BaFe}_{12}\text{O}_{19}$ align opposite to the other eight, giving a net saturation magnetization of $(8 - 4)5 = 20 \mu_B$ per formula unit. Spin alignments for the various magnetic ions in the unit cell are shown in Fig. 31, illustrating the similarity to the spinel structure. The saturation magnetization is also similar to the spinel ferrites, but the crystalline anisotropy is much larger because of the lower symmetry. In $\text{BaFe}_{12}\text{O}_{19}$, the Fe^{3+} spins are locked tightly to the [001] direction giving a high anisotropy coefficient.

Compared to the best metallic permanent magnets, the ferrite magnets are characterized by a high coercive field (H_c) and low residual magnetic induction (B_r). The origin of the high coercive field is the high magnetocrystalline anisotropy, which locks the spins into the c-axis orientation. Representative properties for the OP magnet, and for barium and strontium hexaferrite, are listed in Table 1. The ferrites are best used in applications that take advantage of the high H_c values, such as DC motors, holding devices, and magnetic separators. Flexible rubber-bonded ferrites are used as stators and as magnetic latching devices.

7.6 Preparation and Applications

Barium ferrites are generally made by calcining BaCO_3 with Fe_2O_3 to form $\text{BaFe}_{12}\text{O}_{19}$. The oxide is then ground to micron-size powder, compacted in a die, and sintered at 1200 to 1300 °C to about 95% theoretical density.

000 / Science of Advanced Materials

To obtain grain alignment with a three-fold improvement in properties, the powder is pressed in the presence of a magnetic field before sintering. Barium ferrite has a plate-like morphology with the easy axis of magnetization perpendicular to the hexagonal plates. The combined action of parallel stress and magnetic field during the forming operation produces a highly oriented grain structure with spins parallel to the magnetic field. To obtain a high remanent magnetization, it is important to avoid grain growth during sintering. Silicate additions are used as grain growth inhibitors.

The uses for permanent magnets are surprisingly numerous and frequently go unnoticed. Among the applications are telephones, electric clocks, televisions, radios, hearing aids, watt-meters, phonographs, and thermostats. Portable appliances such as the electric knife, automobile accessories, and the electric toothbrush use low voltage DC motors with permanent magnets. In industry, they are used in magnetic separators, microwave systems, magnetic chucks, and computers.

The design of a permanent magnet is as important as the choice of materials. Through improved materials and computer-aided design, the performance of permanent magnets has often surpassed electromagnets in lower cost and volumetric efficiency. The performance is governed by the demagnetization curve, the nature of the magnetic circuit, and the dimensions of the magnet.

The basic function of a permanent magnet is to generate a useful magnetic field in an air gap. In a well-designed circuit, the field is concentrated across the gap with the aid of soft magnet pathways for the flux.

The applications for permanent magnets can be subdivided into static and dynamic functions. Static functions include separators, latches, compasses, and chucks where the magnet gives a mechanical force, and magnetrons and beam focussing devices in which the magnet controls an electron beam. Dynamic devices generally involve electric to mechanical energy conversion. Examples are microphones, phonograph pickups, telephone bells, and loudspeakers.

8 SUMMARY

In this brief review, many interesting topics in electroceramics have been omitted or given only cursory attention. More complete discussions can be found in Ref 25 and 26. An overview of structure-property relationships in electroceramics is given in Fig. 32, which illustrates the various atomistic mechanisms utilized in ceramic circuit components. Multilayer capacitors, piezoelectric transducers, and positive temperature coefficient thermistors make use of the properties of ferroelectric perovskites with their high dielectric permittivity, large piezoelectric coefficients, and anomalous

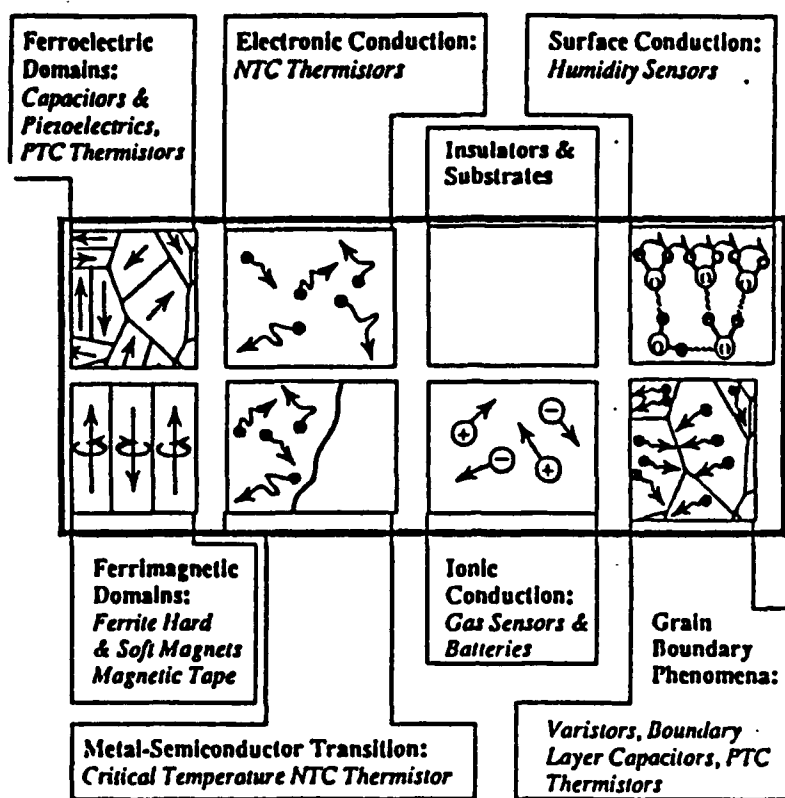


Fig. 32 Overview of the various atomistic mechanisms involved in electroceramic components.

electric conductivity. Similar domain phenomena are observed in ferrimagnetic oxide ceramics such as NiFe_2O_4 . Hard and soft ferrites are analogous to hard and soft PZT and have found substantial markets in magnetic tape and electric motors.

Several kinds of mechanisms are operative in thermistors and other ceramics used as sensors. Most are based on changes in electrical resistivity, but the causes are different. The critical temperature thermistor involves a semiconductor-metal phase transition. Negative temperature coefficient thermistors make use of the semiconducting properties of doped transition-metal oxides. Ionic conductivity is used in oxygen sensors and batteries. Stabilized zirconia is an excellent anion conductor, and β -alumina is one of the best cation conductors.

Humidity sensors make use of surface conduction. Adsorbed water molecules dissociate in hydroxyl in hydronium ions, which alter the electrical resistivity.

Grain boundary phenomena are involved in boundary layer capacitors, varistors, and positive temperature coefficient thermistors. The formation

000 / Science of Advanced Materials

of thin insulating layers between conducting grains is crucial to the operation of all three electroceramic components. Lastly, the importance of electroceramic insulators and substrates should not be overlooked. Here, one strives to eliminate most of the interesting effects described above, but this is not always easy.

REFERENCES

1. B.M. Kulwicki, *J. Phys. Chem. Solids*, **10**, 1971, p 1015-1031.
2. D. Eddy, *IEEE Trans. VT-23*, 1974, p 125-128.
3. P. McGeehin and A. Hooper, *J. Mater. Sci.*, **12**, 1977, p 1-27.
4. T. Nitta, *Ind. Eng. Chem. Prod. Res. Dev.*, **20**, 1981, p 669-674.
5. A. Fog and R.P. Buck, *Sensors and Actuators*, **5**, 1984, p 137-146.
6. J. Smit and H.P.J. Wijn, *Ferrites*, John Wiley & Sons, New York, 1959.
7. O. Saburi, *J. Am. Ceram. Soc.*, **44**, 1964, p 54-63.
8. J. Daniels, K.H. Hardtl and R. Wernicke, *Philips Tech. Rev.*, **38**, 1978, p 73-82.
9. L.M. Levinson and H.R. Philipp, *Ceram. Bull.*, **65**, 1986, p 639-646.
10. R. Einzinger, *Ann. Rev. Mater. Sci.*, **17**, 1987, p 299-321.
11. J.G. Bednorz and K.A. Muller, *Z. Phys. B-Condensed Matter*, **64**, 1986, p 189-193.
12. M.K. Wu, J.R. Ashburn, C.J. Torng, P.H. Hor, R.L. Meng, L. Gao, Z.J. Huang, Y.Q. Wang and C.W. Chu, *Phys. Rev. Lett.*, **58**, 1987, p 908-910.
13. R.J. Cava, B. Batlogg, R.B. VanDonaer, D.W. Murphy, S. Sunshine, T. Siegrist, J.P. Remeika, E.A. Reitman, S. Zahurak and G.P. Espinosa, *Phys. Rev. Lett.*, **58**, 1987, p 1676-1679.
14. J.M. Herbert, *Ceramic Dielectrics and Capacitors*, Gordon and Breach, London, 1985, p 264.
15. K.H. Hardtl, *Ceram. Int.*, **8**, 1981, p 121-127.
16. M. Yonezawa, M. Miyauchi, K. Utsumi and S. Saito, *NEC Res. Dev.*, **85**, 1987, p 1-6.
17. K. Uchino, S. Nomura, L.E. Cross, and, R.E. Newnham, *J. Phys. Soc. Jpn.*, **49B**, 1980, p 45-48.
18. J.M. Herbert, *Ferroelectric Transducers and Sensors*, Gordon and Breach, London, 1982, p 437.
19. W. Heywang and H. Thomann, *Ann. Rev. Mater. Sci.*, **14**, 1984, p 27-47.
20. A.J. Pointon, *IEE Proc.*, **129**, 1982, p 285-307.
21. S. Chikazumi, *Physics of Magnetism*, John Wiley & Sons, New York, 1964, p 554.
22. P.I. Slick, *Ferromagnetic Materials*, **2**, 1980, p 189-241.
23. G.H. Jonker and Stuijts, *Philips Tech. Rev.*, **32**, 1971, p 79-95.
24. J.J. Becker, F.E. Luborsky, and D.L. Martin, *IEEE Trans. Mag.*, **4**, 1968, p 84-98.
25. R.C. Buchanan, *Ceramic Materials for Electronics*, Marcel Dekker, New York, 1986, p 481.
26. L.M. Levinson, *Electronic Ceramics*, Marcel Dekker, New York, 1988, p 553.

APPENDIX 2

TITLE: **POLARIZATION CONTROLLED FERROELECTRIC
HIGH STRAIN ACTUATORS**

AUTHOR: **L. Eric Cross**

AFFILIATION: **Evan Pugh Professor of Electrical Engineering
Materials Research Laboratory
The Pennsylvania State University
University Park, PA 16802 U.S.A.
Tel. (814) 865-1181, FAX (814) 865-2326**

ABSTRACT

The simple phenomenological relation which relates elastic and dielectric properties in an insulating crystalline dielectric takes the form

$$(1) \quad x_{ij} = s_{ijkl}x_{kl} - b_{mij}P_m - Q_{mnij}P_m P_n$$

where x_{ij} is the induced elastic strain
 x_{kl} the imposed elastic stress
 $P_m P_n$ are components of the electric polarization
 s_{ijkl} the elastic compliance tensor
 b_{mij} the piezoelectric tensor in polarization notation
 Q_{mnij} the electrostriction tensor in polarization notation

and the Einstein summation convention is assumed.

Consideration of the values of b and Q for a very wide range of highly polarizable solids shows that for field levels limited by dielectric breakdown in bulk materials, the polarizations which can be induced are such that the strain is limited to the order of 10^{-3} .

On the other hand, in several ferroelectric crystals, values of spontaneous polarization occur which induce strain levels up to 0.13; i.e., 13%. Thus, for the electrical control of large strains ($>10^{-3}$) in bulk materials, it is logical to consider mechanisms which would utilize the very large spontaneous strains. It may be noted that the oxide ferroelectrics in which these large strains often occur are brittle solids so that fracture mechanics would suggest that the solid should

break at these higher strain levels due to stress concentration. It must be remembered however, from equation (1), that the strain can be induced by polarization at zero stress level so that if polarization is homogeneous stress will be all the time zero.

In this talk a number of techniques to exploit spontaneous strain which have been explored in the Materials Research Laboratory (MRL) at Penn State for high strain systems will be discussed.

For the lead lanthanum zirconate titante (PLZT) family of ceramics, compositions can be chosen in which it is possible to switch under electric field from a random nanopolar state of cubic symmetry to a highly strained macropolar state. In these materials strains up to 0.5% can be induced and controlled by the polarization state.

In lead zirconate stannate titanate (PZSnT) ceramics, compositions can be chosen which are poised on the phase boundary between antiferroelectric and ferroelectric states. For a range of compositions and temperatures the ferroelectric state can be induced by electric field resulting in a very large volume expansion. In this system we have demonstrated ceramics which will switch strains up to 0.8%.

Both for the PLZT and the PZSnT systems the phase switching can be very fast in both forward and backward directions so that state change is accomplished in less than 1μ second.

For more specialized applications single crystals of BaTiO₃ can be used at the first order paraelectric ferroelectric phase transition to control strains up to 0.6%. Domain changes in these crystals can be used to generate shape change exceeding 1% and unusual domain controlled bimorph configurations are possible. Large polarization switching in ferroelectric ceramics can often lead to fatigue effects on repeated exercise of the actuator, and techniques to modify and control fatigue will be discussed.

In ferroelectric thin films, electrical breakdown strength is improved over bulk materials by more than an order of magnitude. Piezoelectric and electrostrictive constants however remain comparable to bulk ceramics so that very large strains and high energy densities can now be induced directly. Present results using very thin sol-gel derived lead zirconate titante (PZT) films will be briefly discussed.

INTRODUCTION

To describe the electro-elastic interactions in insulating crystalline dielectric materials it is customary to use the phenomenological equations involving the piezoelectric and electrostrictive deformations induced by electric fields in the form

$$x_{ij} = s_{ijkl}x_{kl} + d_{mij}E_m + g_{mnij}E_m E_n \quad (1)$$

where x_{ij} are components of the induced strain
 X_{ij} components of the applied electric field
 $E_m E_n$ components of the applied electric field
 s_{ijkl} the elastic compliance tensor
 d_{mij} the piezoelectric tensor
 g_{mnij} the electrostriction tensor.

In simple linear dielectrics, alternative forms may be written transposing stress and strain, polarization and field and all constants are related by simple transformations. For the non-linear ferroelectric related dielectrics which are essential for achieving high strain behaviour the relation between E and P is highly nonlinear, often hysteretic and the "constants" d_{mij} and g_{mnij} are strong functions of both field and temperature. In such materials systems it is simpler to describe the elasto-dielectric behaviour using

$$x_{ij} = s_{ijkl}X_{kl} - b_{mij}P_m - Q_{mnij}P_m P_n \quad (2)$$

where P_m, P_n are components of electric polarization
 b_{mij} the piezoelectric tensor now in polarization notation
 Q_{mnij} the electrostriction tensor again in polarization form.

In both equations (1) and (2) the Einstein summation convention is assumed. For (2) however, the coefficients b and Q are now found to be largely independent of temperature and to have similar values in the same structure families.

For bulk samples, the polarization levels which can be induced by realizable electric fields below dielectric breakdown are such that even in very high permittivity ferroelectric or paraelectric dielectrics the constants b and Q do not permit the induction of strains much above $3 \cdot 10^{-4}$. In ferroelectric crystals however, spontaneous polarizations occur which are order of magnitude larger and in some cases induce strains $\sim 1 \cdot 5 \cdot 10^{-1}$.

In looking for new electro-elastic actuators which can control strains much larger than conventional piezoelectric and electrostrictive ceramics it is then natural to look for materials in which P_s the spontaneous polarization can be controlled. Two basically different types have been explored in this study.

1. Systems which may be switched from a macroscopically nonpolar to a macroscopically polar state taking the system from $P = 0$ to $P = P_s$.
2. Systems in which the polarization may be manifest in more than one orientation (ferroelectrics) and where the polar domain structure may be altered by an electric field with corresponding major modification to the strain state.

In both cases it may be noted that enhanced strain is obtained by moving to a highly nonlinear possibly hysteretic behaviour. This paper will however be concerned primarily with the phase change systems.

A third alternative briefly considered here depends upon the fact that recently it has become possible to fabricate perovskite type ferroelectric oxides in thin film form. In these films, as in other organic and inorganic dielectrics, the electric breakdown field is vastly improved over that of the bulk ceramic (~ 1 MV/cm as compared to 100 kV/cm in bulk ceramics) leading to the possibility of very large strains, high energy densities and quasi-linear operation in these thin film systems.

PHASE SWITCHING SYSTEMS

INTRODUCTION

Three types of phase switching systems have been extensively studied. In the PLZT family of relaxor ferroelectrics [1], compositions can be found which switch from a macroscopically cubic nano-polar state into a strongly polar rhombohedral state [2]. The onset of polarization is accompanied by longitudinal strains up to 0.5% with the highest strains occurring for compositions close to the Morphotropic phase boundary between rhombohedral and tetragonal symmetry macro states. Studies in MRL on this system will be briefly summarized and new data presented on the fatigue behaviour under repeated cycling. A more complete account is given in [3].

For certain compositions in the lead lanthanum zirconate stan-nate titanate family of ceramics compositions can be chosen which are in an antiferroelectric state at room temperature but are very close in free energy to a strongly polar ferroelectric state so that antiferroelectric to ferroelectric switching can be achieved under high electric fields. The switching is accompanied by a major volume expansion in the lattice and the resulting strain can be controlled by controlling the volume fraction switched into the polar state by limiting the charge which flows. The work will be briefly summarized here a more detailed account is given in [4].

In highly specialized compact systems such as those used to control the surface profile of infra-red surface deformable mirrors, the high strain actuation which can be achieved in single crystal systems is of interest and data will be presented for phase switching in single crystal BaTiO₃ at temperatures just above T_c.

MICRO-MACRODOMAIN SWITCHING IN LEAD LANTHANUM ZIRCONATE TITANATE (PLZT₀) CERAMMICS

The composition of PLZT explored in this study are identified in the phase diagram of figure 1. Compositions are believed to conform to the formula Pb_{1-3x/2}La_x(Zr_yTi₂)O₃, though they are

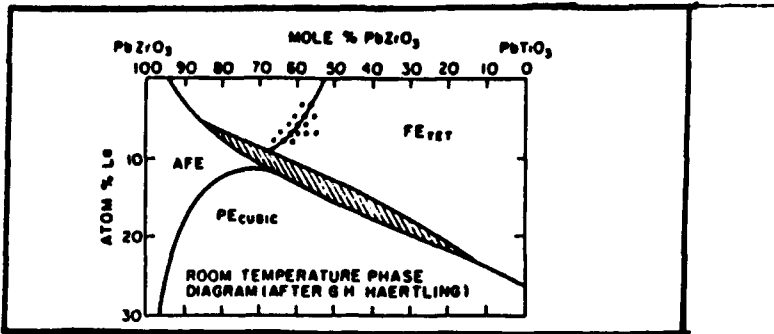


Figure 1 Phase diagram of PLZT system (after Haertling and Land) with the marks of the selected compositions.

batched with excess lead oxide to promote densification. Following convention the description is simplified to the form $100x/100y/100z$ so that for example $Pb_{0.88}La_{0.08}(2r_{0.65}Ti_{0.35})O_3$ is described as an 8/65/35 PLZT. For these studies the La_2O_3 was in the range 4-8 mole% and the Zr/Ti ratio was adjusted to keep the composition close to the morphotropic phase boundary between rhombohedral and tetragonal macro symmetries.

Composition were prepared both by conventional ceramic processing and by uniaxial hot pressing to achieve a range of grain size and of pore structures in the ceramic. For studied of initial dielectric elastic and electrostrive response microstructure and density were not critical. However in fatigue behavior, that is in the loss of properties on repeated cycling these parameters were most important. Typical weak field dielectric response as function of temperature is shown in figure 2, demonstrating the expected increase in dispersion and relaxor ferroelectric behaviour with increasing La content. High field behavior for all compositions is hysteretic, figure 3a and accompanying longitudinal strains are shown in 3b. Parameters of interest for the whole range of compositions are summarized in Table 1. Maximum strain achieved in this family was 0.54% and it may be noted that all members can sustain a remanant strain which is under polarization control. Figure 4 gives typical values of remanence in a 7/65/35 composition.

Switching studies have shown that switching times of under 1μ sec can be achieved at high fields and that aging of the remanent strain is comparable to aging of the fully poled state.

Cyclic switching between states will be essential for practical actuator use so that studies of property degradation as a function of the number of cycles switched (fatigue) are most important. Initial data on fatigue under repeated cycling were very disappointing typical response for a 7/68/32 composition

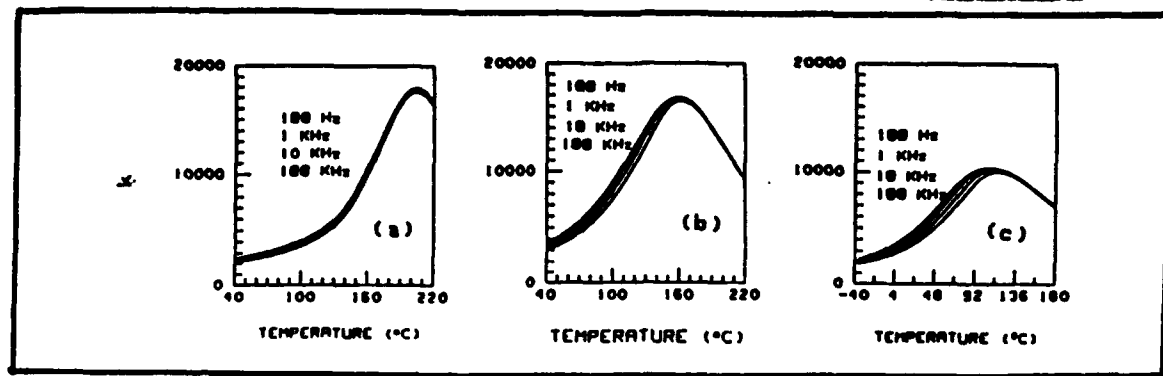


Figure 2 Dielectric constant versus temperature for three MPB ceramic compositions: (a) 6/60/40, (b) 7/62.5/37.5 and (c) 8/65/35.

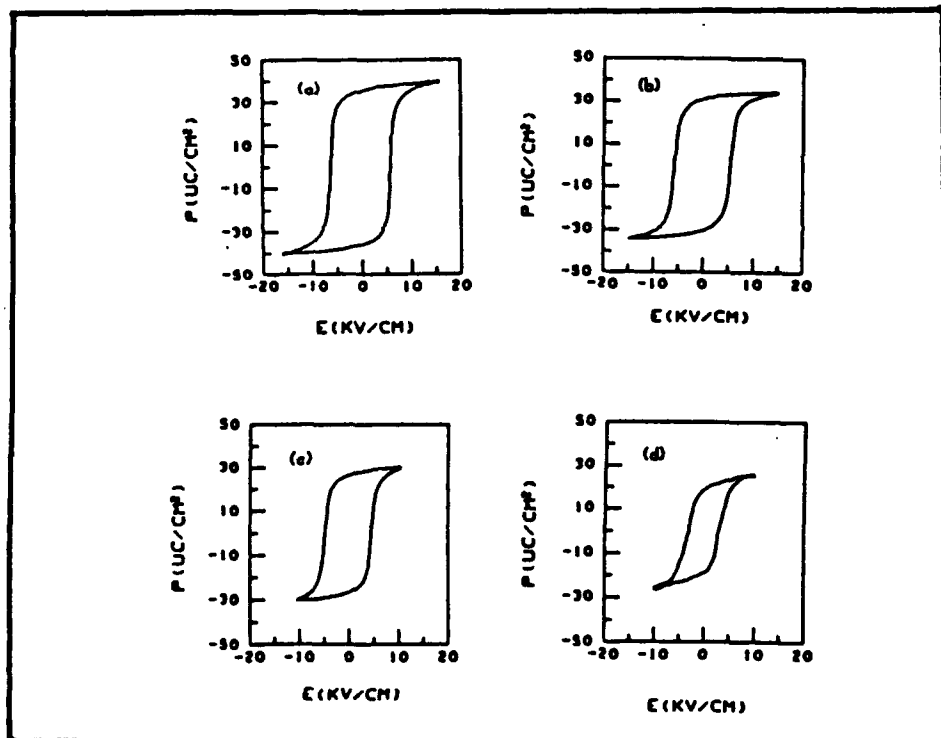


Figure 3 (A): Polarization-electric field hysteresis loops for the MPB compositions: (a) 4/57/43, (b) 6/60/40, (c) 7/62.5/37.5 and (d) 8/65/35.

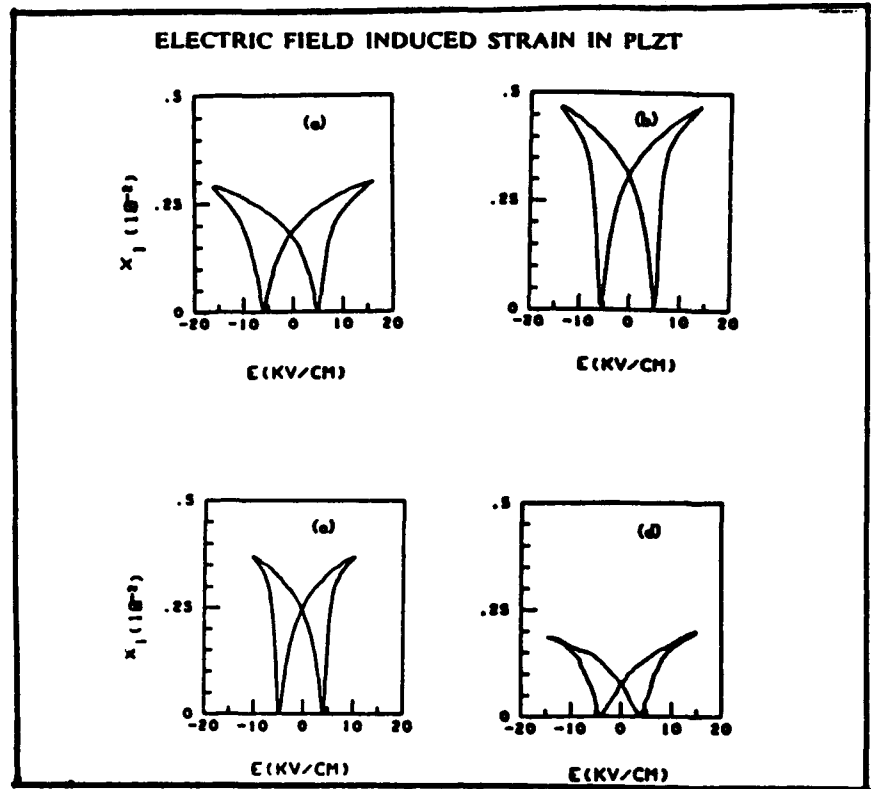


Figure 3 (B): The longitudinal strain-electric field hysteresis loop for the MPB compositions:
 (a) 4/576/43, (b) 6/60/40, (c) 7/62.5/37.5 and
 (d) 8/65/35.

TABLE I
FIELD INDUCED STRAIN AND RELATED DIELECTRIC DATA

Comp.	T _m (°C)	K _m	K ₂₅	E _c (kv/cm)	P _r (uc/cm ²)	x _t (10 ⁻³)	x _l (10 ⁻³)	x _l /x _t
8/67/13	99	12000	5500	2.6	21	0.81	2.5	0.1
8/65/35*	106	11350	4400	3.6	20	0.82	2.3	0.32
8/61/37	114	11300	4500	4.7	21	0.76	1.9	0.32
7/65/35	140	15000	3000	4.5	28.4	1	3.1	0.7
7/62.5/37.5*	160	16000	2900	5	27.2	1.2	3.7	0.64
7/60/40	172	17000	3000	6.3	26.2	1.2	3.8	0.4
7/58/42	180	17300	2600	8	22	1.1	3.2	0.39
7/56/44	190	17200	2200	10	22	0.94	2.3	0.4
6/62/38	196	19000	2100	5	31	1.45	4.1	0.58
6/61/40*	204	18000	2000	5.6	29.5	1.35	4.7	0.57
6/58/42				7.45	29	1.32	3.9	0.53
5/61/40	230	19000	1600	6.52	32	0.79	4.2	0.53
5/58.5/41.5*				6.41	34	1.24	4.5	0.59
5/56/44				8.5	32.1	1.6	5.4	0.56
4/57/43*				7.47	35.2	1.26	3.0	0.6
4/55/45				10	29.5	1.21	2.9	0.55

* MPB compositions: x_t: Transverse strain induced at 15 kv/cm. x_l: Longitudinal strain induced at 15 kv/cm.
 t_m: Transverse remanent strain. T_m: Temp. of dielectric maximum. K_m: Maximum dielectric constant. K₂₅: Dielectric constant at 25°C.

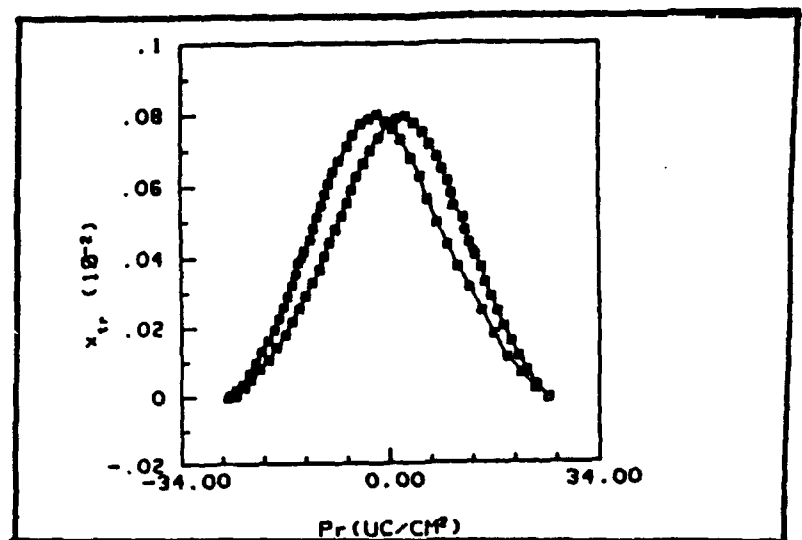


Figure 4 The remanent transverse strain as a function of remanent polarization for PLZT 7.5/65/35 Ceramic.

is given in figure 5 showing severe fatigue starting at $\sim 10^4$ cycles. Several different types of surface treatment modified but did not significantly improve response. Additional experiments (5) have proven however that this premature failure is a surface phenomenon and is traceable to debonding of the gold electrodes used. This field assisted debonding appears associated with traces of organic contamination on the surface and can only be relieved by high temperature annealing immediately before electrode deposition. For a hot pressed 7/65/32 sample subjected to this pre-anneal before electroding, no fatigue at all is evident up to 10^9 cycles with initial and final hysteresis loops superposing exactly and there is no change in strain behavior (figure 6).

In the same composition made by conventional ceramic processing, subjected to the same electrode treatment fatigue is again evident, now however as a volume controlled phenomenon. Other tests in the hot pressed 7/65/35 also show fatigue re-appearing in grain grown material (grain size $\sim 30\mu$ meters).

For the 8·4/65/35 fatigue appears very different. Even in the best hot pressed ceramic fatigue appears associated with internal micro-cracks which are visible in the body of the dielectric and appear to originate at field concentrations near the electroded edges (figure 7).

The reason for this behaviour is not simply the strain level, since 8/65/35 has lower electrostriction than the 7/68/32 composition which shows no evidence of cracking at similar density, grain size and electrode configuration.

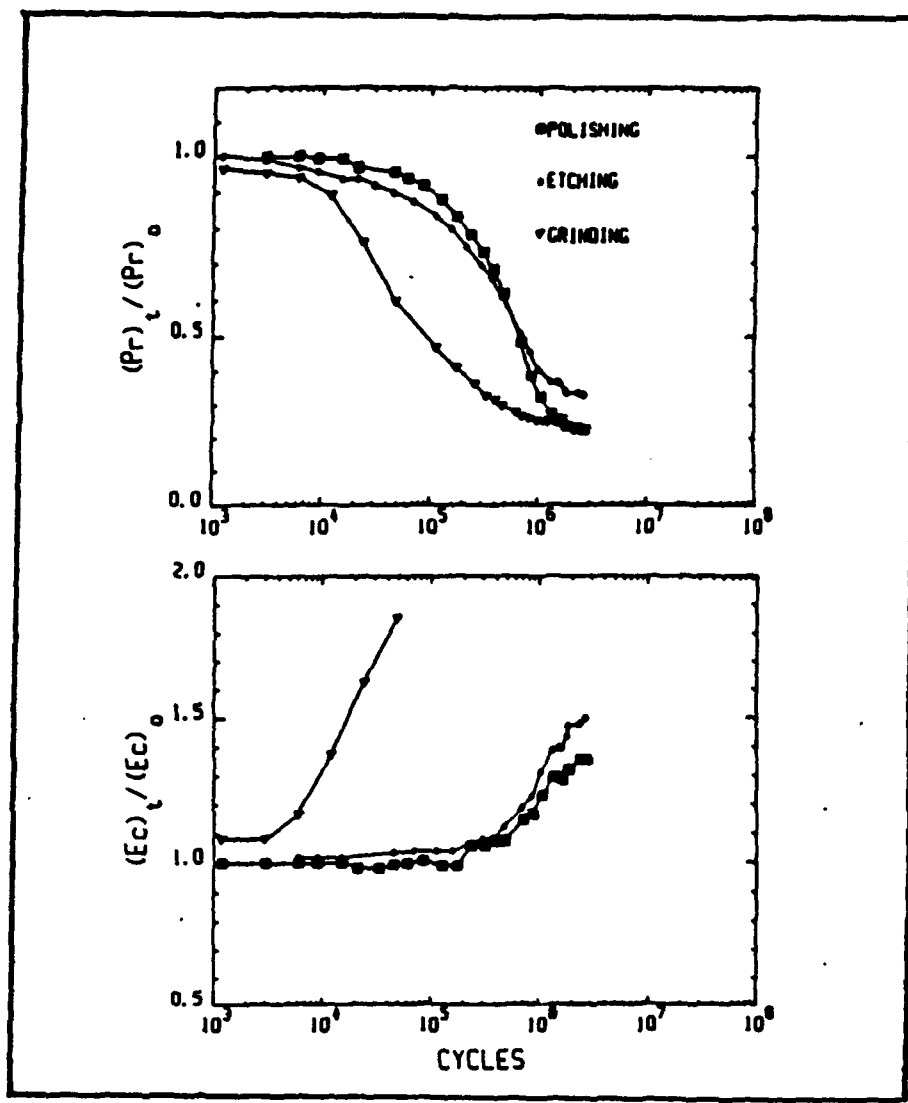
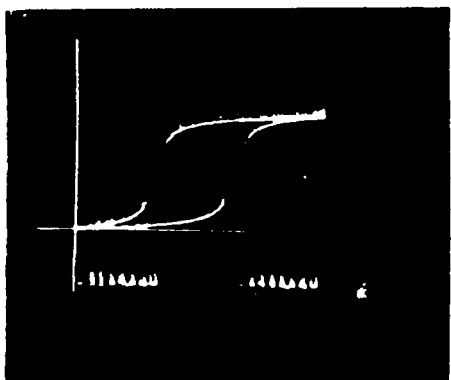
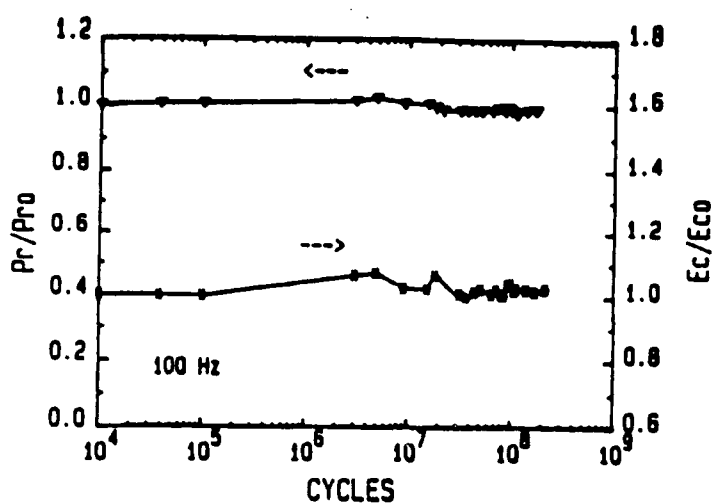
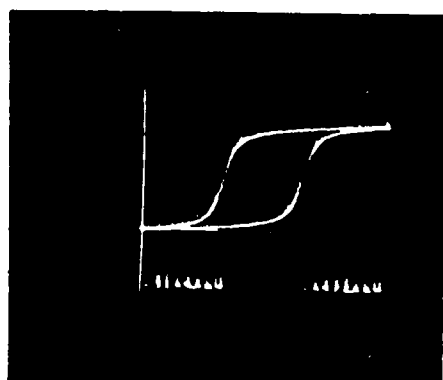


Figure 5 Premature fatigue in a PLZT 7/68/32 showing the effect of different surface treatments, when the gold sputtered electrode is applied after conventional cleaning using organic solvents. The fatigue is associated with field assisted electrode debonding.



No. OF CYCLES: 10^5



No. OF CYCLES: 2×10^8

Figure 6 Absence of fatigue in a 7/68/32 PLZT after high temperature surface cleaning. Sputtered gold electrode.

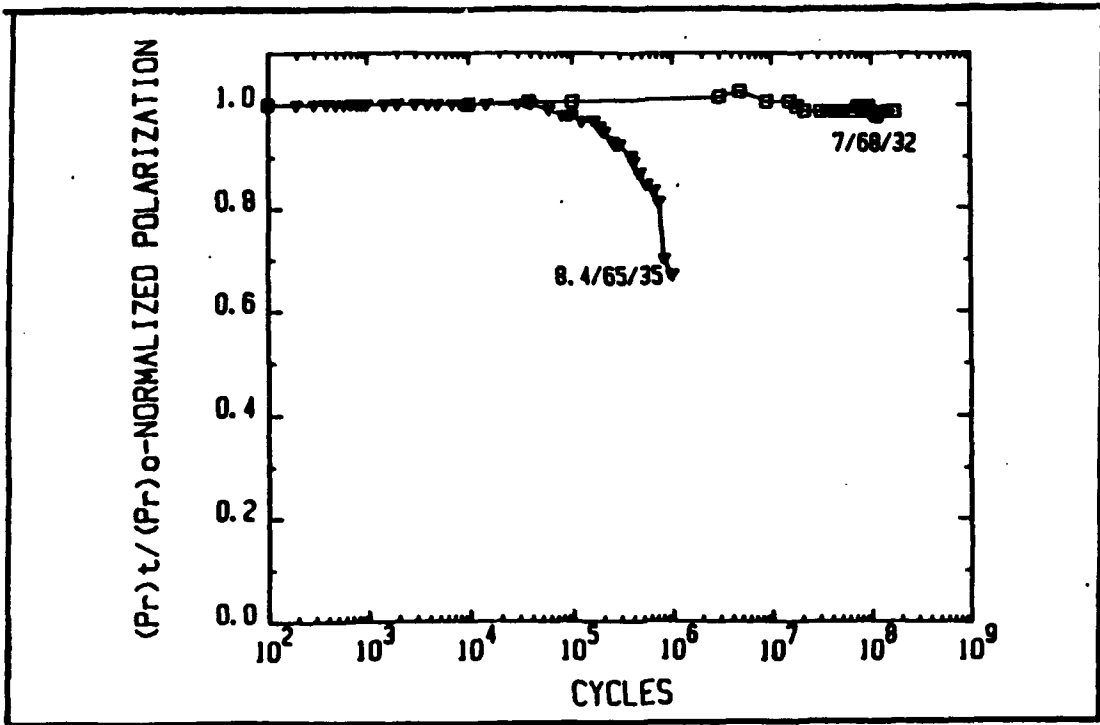


Figure 7 Fatigue to failure in PLZT 8.4/65/35. Mechanism involves the formulation of micro-cracks which lead to macroscopic rupture.

TABLE II
CHEMICAL COMPOSITIONS AND THE REFERENCE NUMBERS

No.	Composition
4	(Pb _{0.9} La _{0.02})(Zr _{0.90} Ti _{0.10} Sn _{0.20})O ₃
5	(Pb _{0.9} La _{0.02})(Zr _{0.93} Ti _{0.07} Sn _{0.20})O ₃
6	(Pb _{0.9} La _{0.02})(Zr _{0.90} Ti _{0.10} Sn _{0.20})O ₃
7	(Pb _{0.9} La _{0.02})(Zr _{0.90} Ti _{0.10} Sn _{0.20})O ₃
8	(Pb _{0.9} La _{0.02})(Zr _{0.90} Ti _{0.10} Sn _{0.20})O ₃
9	(Pb _{0.9} La _{0.02})(Zr _{0.90} Ti _{0.10} Sn _{0.20})O ₃
10	(Pb _{0.9} La _{0.02})(Zr _{0.90} Ti _{0.10} Sn _{0.20})O ₃
11	(Pb _{0.9} La _{0.02})(Zr _{0.90} Ti _{0.10} Sn _{0.20})O ₃
12	(Pb _{0.9} La _{0.02})(Zr _{0.90} Ti _{0.10} Sn _{0.20})O ₃
13	(Pb _{0.9} La _{0.02})(Zr _{0.93} Ti _{0.07} Sn _{0.20})O ₃
14	(Pb _{0.9} La _{0.02})(Zr _{0.90} Ti _{0.10} Sn _{0.20})O ₃

The studies to date on these PLZTs suggest that switching fatigue depends upon the complex interplay of a number of variables including electrode interface properties, microstructure including grain size, density and flaw population and probably also upon the nature of the electro-dielectric interaction in the particular composition. It is however most encouraging to have the demonstration that fatigue can be completely eliminated under certain circumstances.

ANTIFERROELECTRIC: FERROELECTRIC SWITCHING IN MODIFIED LEAD ZIRCONATE STANNATE TITANATE COMPOSITIONS

Studies in the Materials Research Laboratory at Penn State have focused upon antiferroelectric compositions in the family $(\text{Pb}_{0.97}\text{La}_{0.02})(\text{ZrTiSn})\text{O}_3$ in which the Zr:Ti:Sn ratios are adjusted to explore the phase boundary with the ferroelectric rhombohedral form. The compositions studied are tabulated in Table 2 and the position in the phase diagram illustrated in figure 8. Samples were in all cases prepared by conventional ceramic processing from reagent grade oxides.

Typical hysteresis and longitudinal strain curves taken on sample 4 (Table 2) are shown in figure 9 and the parameters for all samples studied are summarized in Table 3. Evidently maximum strains up to 0.87% are possible in the higher zirconia compositions and fortunately this is combined with a lower switching field.

An important consideration for the practical utility of these materials is the speed with which the field forced phase change can be accomplished both in the forward AF \rightarrow F and in the backward F \rightarrow AF transitions. Pulse field studies have shown that forward switching is fast, figure 10 gives data for composition 5 which is quite typical. Clearly switching can be accomplished in times $\sim 1/3\mu$ sec at realizable field. Backward switching when the field is simply reduced to zero is slightly longer, and depends on the degree of original forward poling. But even for very high forward fields (figure 11) the back switching is accomplished in under 2.5μ sec. Thus for most types of AF-F actuators the speed will be set by the propagation of the strain wave and not by the polarization process.

Fatigue in the cyclic switching is illustrated for composition 6, the maximum strain material in figure 12. In spite of the fact that the ceramic is not near theoretical density the polished sample only shows less than 10% change in switched polarization after $5 \cdot 10^7$ cycles a very encouraging result. However much more work is needed to define and control the fatigue processes in these ceramics.

SINGLE CRYSTAL SYSTEMS

Early studies of BaTiO_3 single crystals have shown that the phase change at $T_c(135^\circ\text{C})$ is first order, and that for a range of temperature above T_c , the spontaneous polarization P_s may be

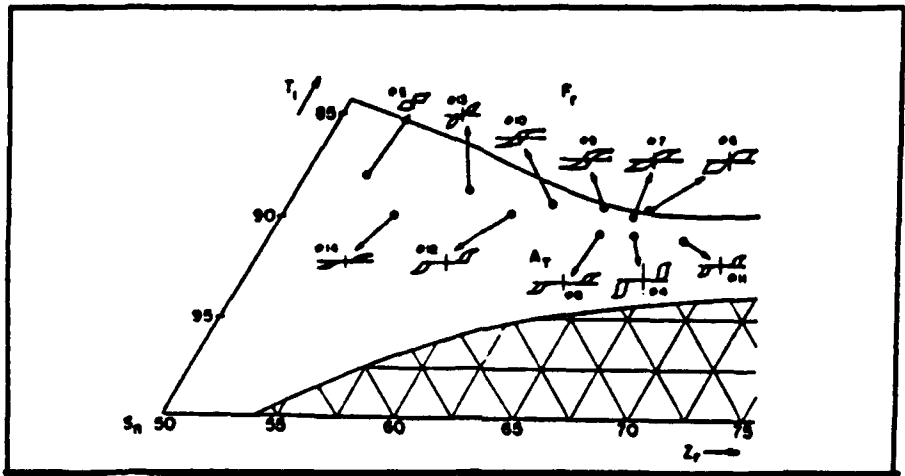


Figure 8 Antiferroelectric tetragonal compositions selected for study and their dielectric hysteresis loops.

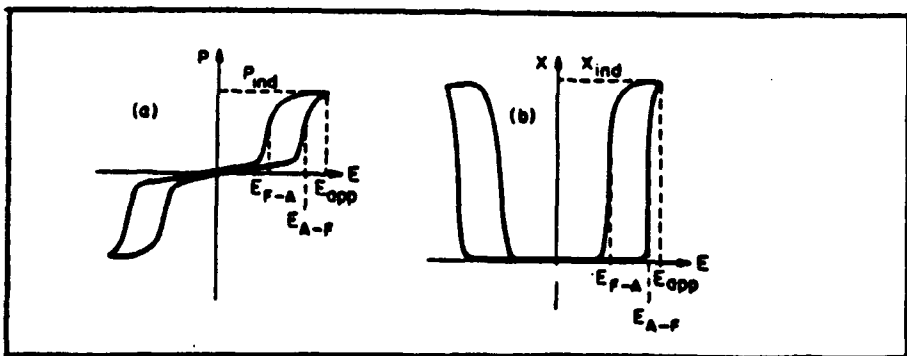


Figure 9 Typical polarization and strain hysteresis loops (composition No. 4) and some illustrated parameters.

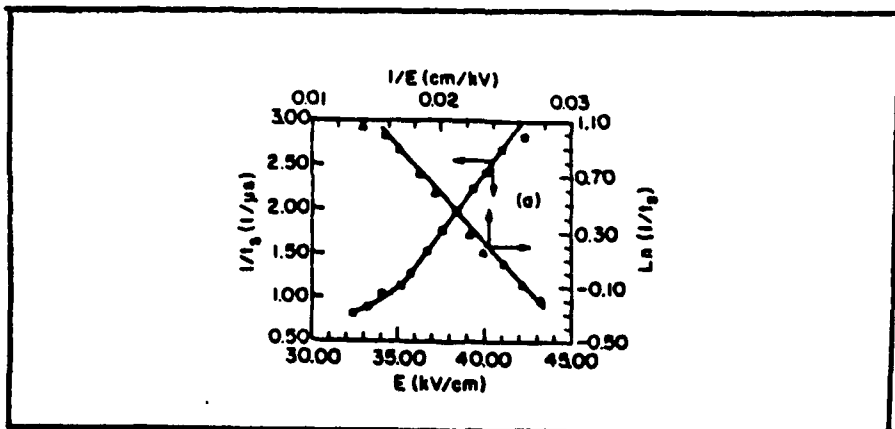


Figure 10 (a) $1/t_s$ (forward switching speed versus E).

TABLE III
SWITCHING DATA FOR DIFFERENT COMPOSITIONS

(a) Group 1 compositions

No.	P (uC/cm ²)	E _{A-F} (kV/cm)	E _{app} (kV/cm)	x ₁ (ind)
5	30	30	35	0.18%
13	28	30	43	0.45%
10	36	28	60	0.5%
9	36	24	60	0.59%
7	36	22	58	0.52%
6	40	21	46	0.87%

(b) Group 2 compositions

14	31	44	56	0.35%
12	32	49	59	0.42%
8	30.5	52	68	0.37%
4	43	50	75	0.55%
11	33	45	60	0.45%

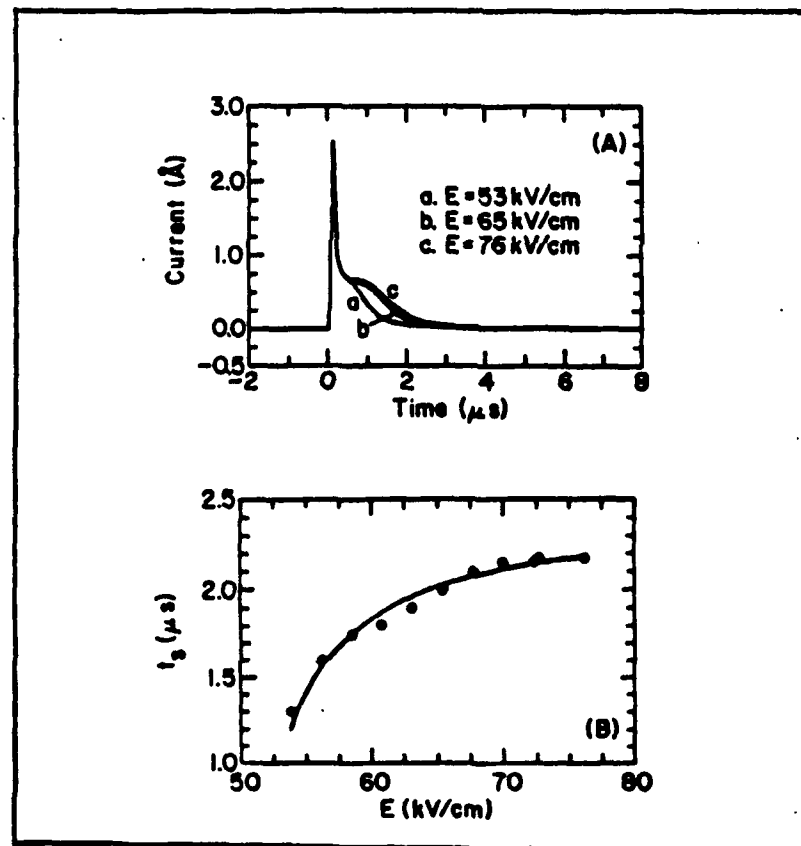


Figure 11 (a) Backward switching current under different dc poling fields and (b) backward switching time as a function of dc poling field for composition No. 4.

AD-A236 219

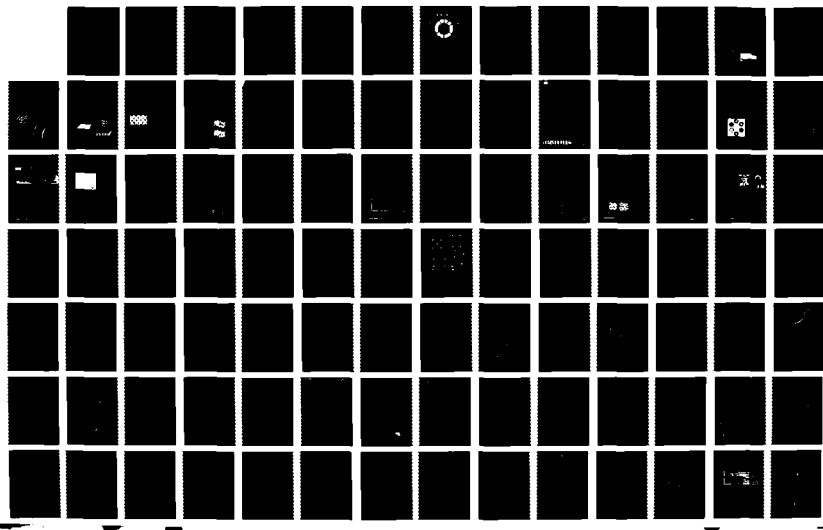
PIEZOELECTRIC AND ELECTROSTRICITIVE MATERIALS FOR
TRANSDUCER APPLICATIONS. (U) PENNSYLVANIA STATE UNIV
UNIVERSITY PARK MATERIALS RESEARCH LAB.

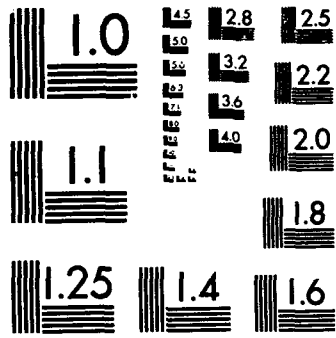
274

UNCLASSIFIED

L E CROSS ET AL. 31 JAN 91 XN-ONR

NL





MICROCOPY RESOLUTION TEST CHART
NATIONAL BUREAU OF STANDARDS-1963-A

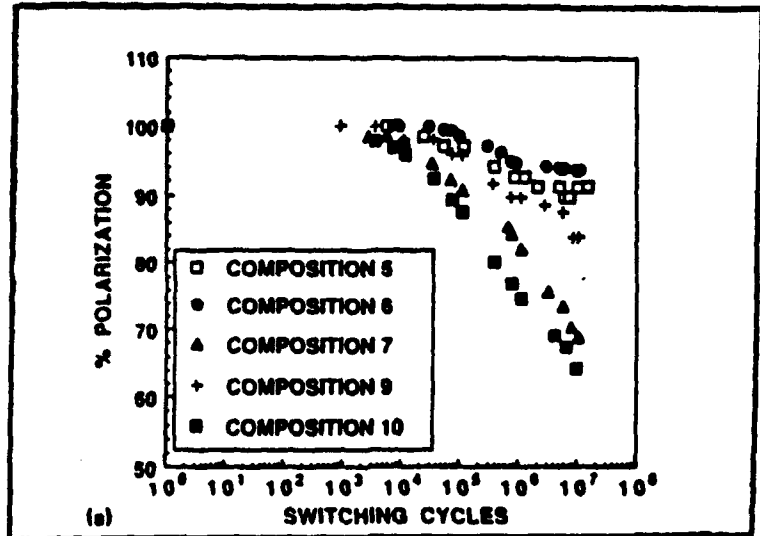


Figure 12 Fatigue in Antiferroelectric Ferroelectric switching for several high strain compositions.

reintroduced by a realizable electric field [6]. The behaviour can be predicted quantitatively on the basis of Devonshire's Phenomenological theory.

For BaTiO₃ the Q matrix is well known and the Q_{ijkl} are only weak functions of temperature, thus it is possible to predict directly the levels of strain which should be achievable as a function of temperature and field above T_c.

Using a Remeika grown crystal the polarization and strain as a function of temperature are shown in figure 13a, b. The maximum strain achievable occurs just above T_c and is of order 0.35%. For crystals with low densities of 90° double twins, there is no evidence of fatigue after many hours of switching at 20 Hz, in crystals electroded with In-Ga electrodes.

Larger strains can be induced below T_c in crystals which contain 90° twins, but for most samples the strain is not completely reproducible. Attempts to measure the strain change associated with the field forced phase change from orthorhombic to tetragonal state at temperatures below 0°C were frustrated by the high density of twins in the low temperature state.

FERROELECTRIC THIN FILMS

Over the last three years, there has been increasing interest in the properties of thin films of PZT and PLZT, deposited on buffered silicon wafers, for use in nonvolatile semiconductor memory [6].

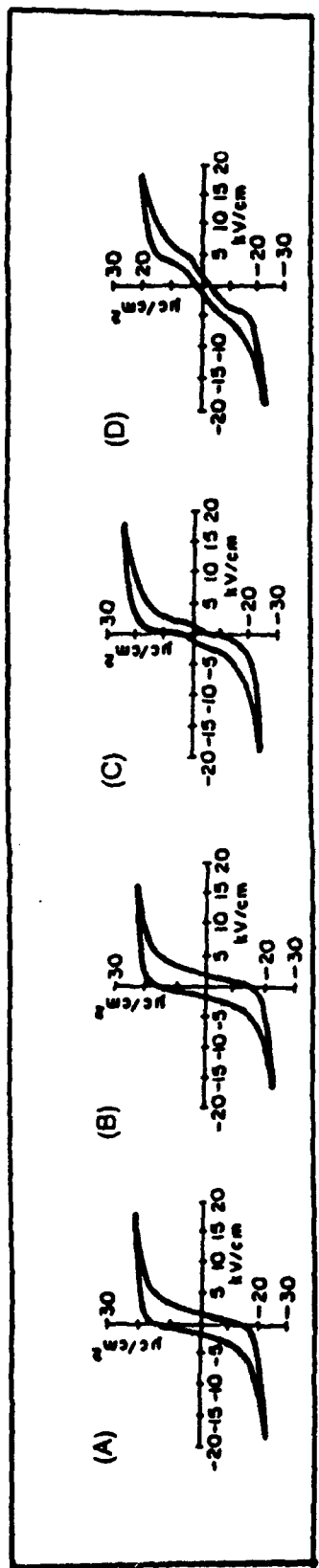


Figure 13a Polarization hysteresis loops for the LT crystal at various temperatures (electric field of 10 kV/cm, 20 Hz) : (A) 25°, (B) 50°, (C) 106.5°, and (D) 115.5°C.

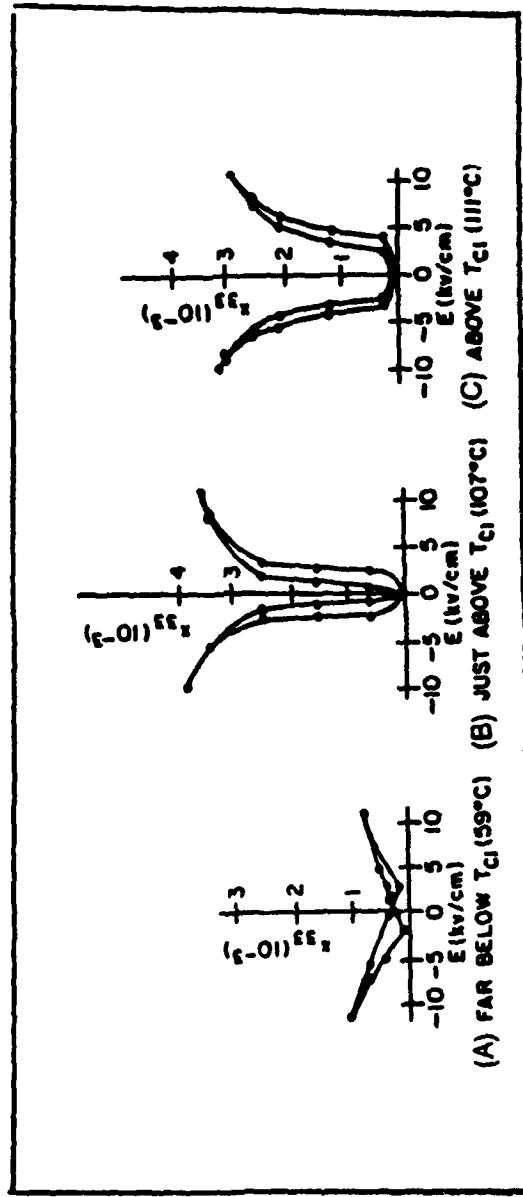


Figure 13b Longitudinal strain hysteresis loops for the LT crystal at various temperatures: (electric field of 10 kV/cm, 20 Hz) : (A) 59°, (B) 107° and (C) 111°C.

The important feature for this work is that it has proven relatively easy to generate fully ferroelectric films which show 'normal' dielectric hysteresis by a range of different low temperature deposition and annealing techniques.

For sol-gel spun on films of PZT 52/48 ranging in thickness from 0.16 to 0.55μ meters, the dielectric response at low fields and the ferroelectric remanent polarization are shown in figure 14a, b. Clearly for such films one must expect that the electrostriction constant Q_{11} will not be strongly perturbed and thus that the films should be strongly piezoelectric. Measurements in our laboratory confirm the linear dependence of film thickness upon applied field figure 15, and show a piezoelectric constant $d_{33} \sim 220$ pC/N almost identical to that of the bulk. Similarly measurements on a monomorph configuration in which the film is deposited on a thin silicon wafer yield values for $d_{31} \sim 89$ pC/N again in good agreement with the bulk.

A fascinating facet of the behaviour of PZT in thin film form is the escalation of the dielectric strength which occurs at these submicron dimensions so that $E_B \sim 1.2$ MV/cm as compared to ~ 80 KV/cm in bulk ceramic. Clearly, if the piezoelectric constant does not decrease dramatically at high field levels above the 10^5 V/cm which has been measured, the direct effect should induce strains of order 10^{-2} at 500 KV/cm.

The high piezoelectric coupling, taken together with the high field capability of the PZT provides very high energy density in the films and the possibility to induce large surface deformations in a monomorph configuration without being in resonance. For such a system then it is possible to develop a traveling surface flexure wave; in a very fine scale structure and thus to generate a micro-minature travelling wave flexure motor. The system which was chosen for initial experimentation is illustrated in figure 16 and has been shown to be capable of spinning a small sub millimeter platter at ~ 120 rpm.

CONCLUSIONS

Phase change systems involving micro to macrodomain switching in PLZT and antiferroelectric to ferroelectric switching in PLSnZT compositions have been shown to give rise to polarization controlled deformations up to 0.85%. Both systems suffer from fatigue effects which reduce polarization and strain levels on repeated switching, but there is strong evidence that the fatigue is not necessarily intrinsic and that at least in the PLZT system switching which is completely free from fatigue can be achieved.

In both ceramic systems, the high strains are accompanied by nonlinear hysteretic behaviour. For certain applications this hysteresis can be beneficial in that it would permit a large bank of actuators to be set up to prescribed strain states using pulses from a single power supply. For both systems

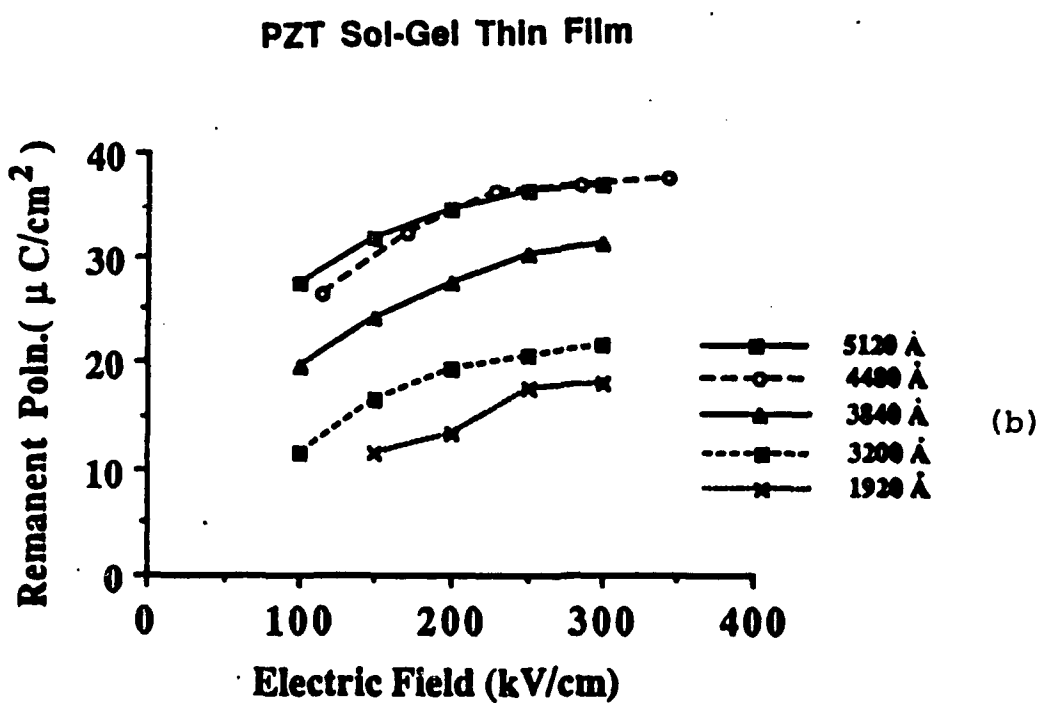
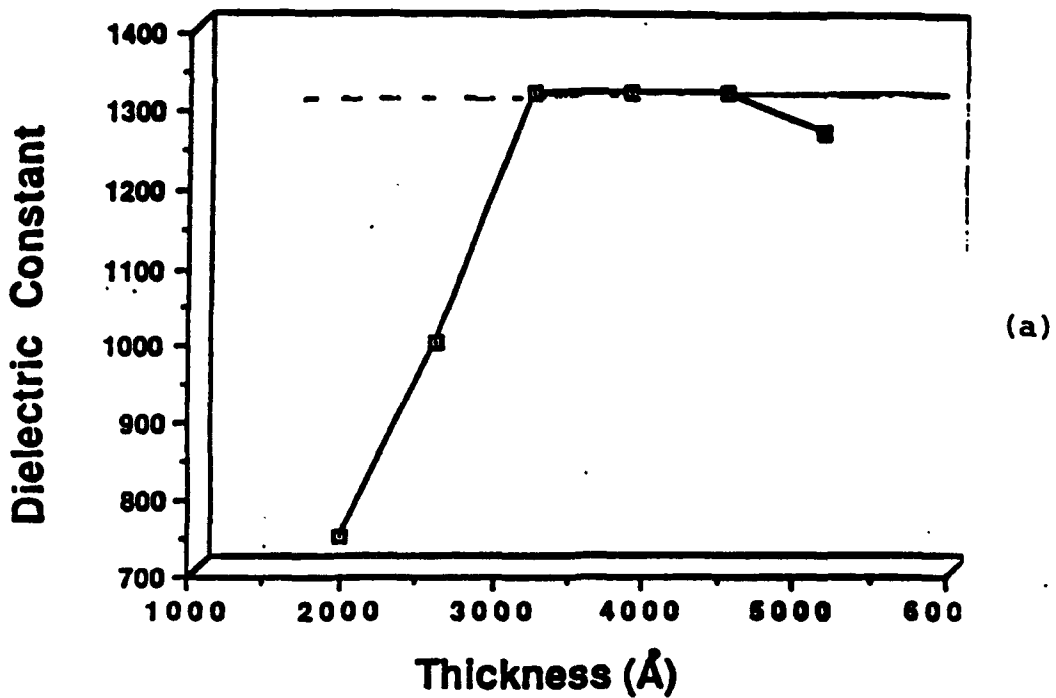


Figure 14 Dielectric properties as function of thickness for PZT 52/48.

- (a) Weak field permittivity.
- (b) Remanent polarization.

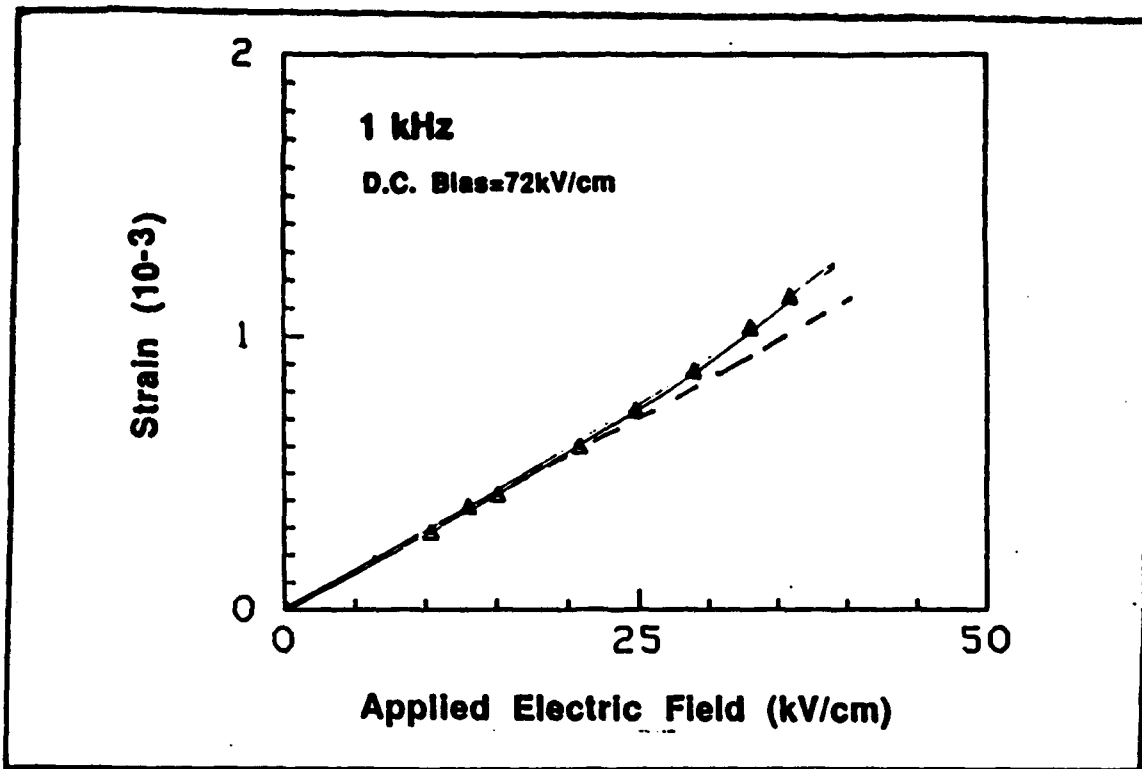


Figure 15 Elastic strain $\times 10^{-3}$ as a function of applied field in PZT 52/42. In a film of 0.5μ meter thickness on silicon.

polarization switching is very fast so that the actuator can be set up in sub microsecond periods.

For special applications it may be advantageous to explore phase switching in single crystal ferroelectrics and the strain effects in BaTiO₃ are used for illustration. Strain levels up to 0.35% are achievable near 135°C in this system and no doubt similar performance near room temperature could be achieved in KTN single crystals of suitable composition.

Ferroelectric films of PZT are shown to have piezoelectric properties close to those of the bulk ceramic, but also to have much higher dielectric strength. The combination suggests the possibility of piezoelectrically controlled strains up to 1% and the high energy densities in the films have already been exploited in an ultra miniature travelling flexure wave piezoelectric motor.

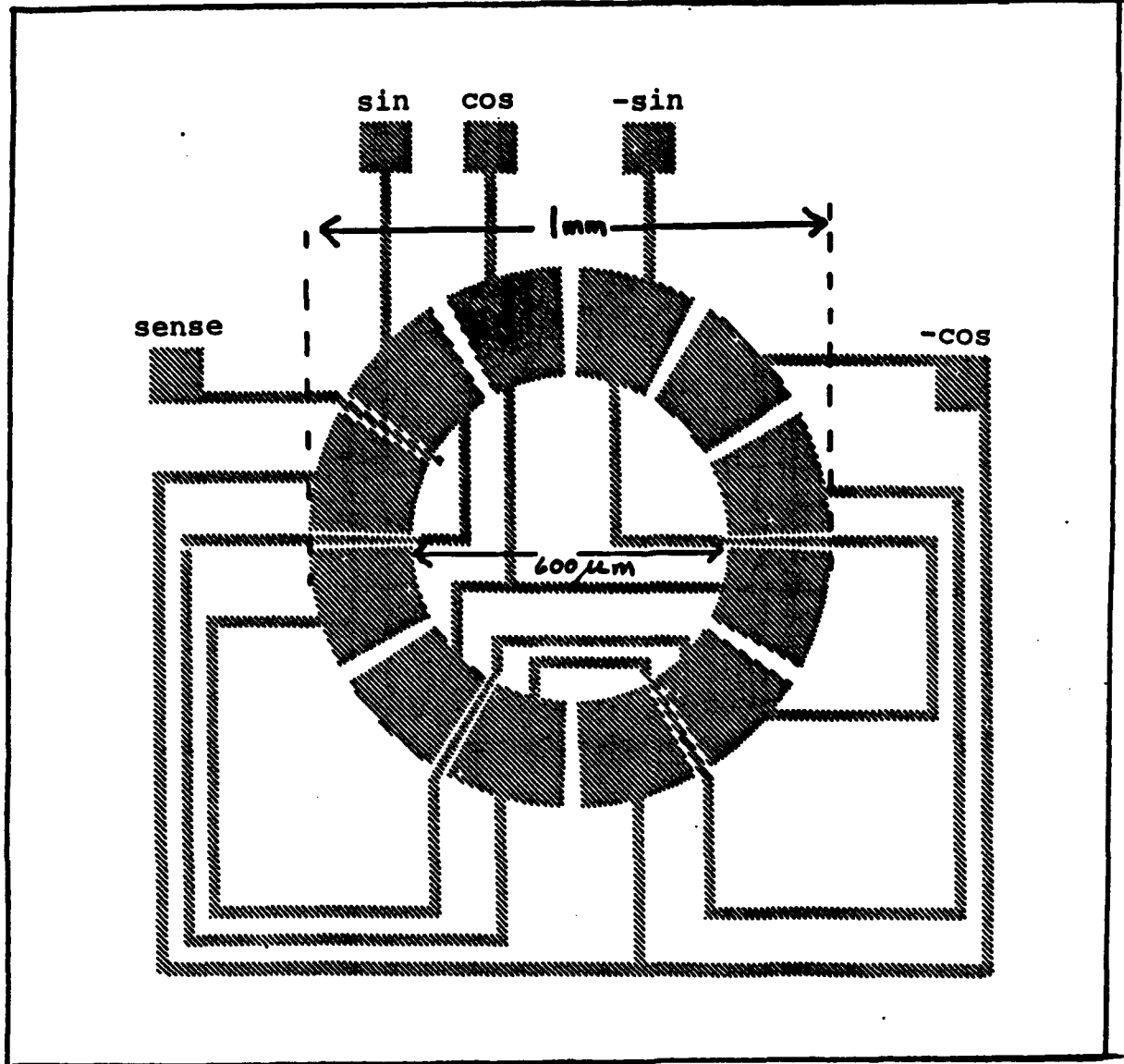


Figure 16 Electrode pattern for a flexure wave motor using PZT
on a silicon nitride diaphragm.

REFERENCES

1. C.H. Haertling, C.E. Land, "Transparent PLZT Ceramics," J. Am Ceram. Soc. 54 (1) (1971).
2. Z.Y. Meng, U.Kumar, L.E. Cross, "Electrostriction in Lead Linthanium Zirconate Titanate Ceramics," J. Am. Ceram. Soc. 68, 459 (1985).
3. W.Y. Pan, Q.M. Zhang, Q.Y. Jiang and L.E. Cross, "Electric Field Induced Strain in (Pb,La)(Ti,Zr)O₃ Ferroelectric Ceramics Near the Tetragonal-Rhombohedral Morphotropic Phase Boundary," Ferroelectrics 88, 1-15 (1988).
4. W.Y. Pan, C.Q. Dam, Q.M. Zhang and L.E.Cross, "Large Displacement Transducers Based on Electric Field Forced Phase Transitions in the Tetragonal (Pb_{0.97}La_{0.02})(Ti,Zr,Sn)O₃ Family of Ceramics," J. Appl. Phys. 66(12), 6014-6023, 1989.
5. W.Y. Pan, K. Koshkarian and L.E. Cross, "Origin of Polarization and Strain Fatigue Effects in Bulk PLZT Ceramics," Applied Physics Letters (in print).
6. W. Pan, Q.Zhang, A.S. Bhalla and L. E. Cross, "Field-Induced Strain in Single-Crystal BaTiO₃," J. Am. Ceram. Soc.71(6), C-302-C-305 (1988).

APPENDIX 3

Lead Article

J. Appl. Cryst. (1990), **23**, 447–457

Crystals and Composites*

BY R. E. NEWNHAM AND S. TROLIER-MCKINSTRY

Materials Research Laboratory, University Park, PA 16802, USA

(Received 9 February 1990; accepted 2 July 1990)

Abstract

This paper is a review of the symmetry and connectivity of composite materials with particular emphasis on the effect that these have on composite properties. Analogies are drawn between composites and crystal structures to demonstrate the similarities between microscopic and macroscopic connectivity. A notation for composite transitions which can be used to describe changes in symmetry and connectivity is also presented.

Introduction

Composite materials are interesting for the wide variety of properties which can be achieved through control of connectivity and symmetry. Most frequently, as engineers design components for new applications, it is these variables, connectivity and symmetry, which are manipulated to optimize behavior. However, with the range of applications for composites expanding from macroscopic electronic or structural components to microwave (Guire, 1987) and optical (Hale, 1976) components, the scale of a composite has also emerged as a critical factor in determining the macroscopic properties. As the natural limit of composite scaling corresponds to unit-cell dimensions, it is interesting to reexamine the symmetry, connectivity and properties of composites as they relate to conventional crystallography.

Sum, product and combination properties

A composite property coefficient can arise in one of three ways: as a *sum* of the corresponding coefficients in the individual phases (properly weighted for volume fraction and orientation), as a *product* of two or more different properties, each of which is present in only one phase, or as a *combination* of two or

more coefficients which are each present in both phases (Newnham, 1985, 1986, 1988). Examples of sum properties include the dielectric constant, thermal expansion coefficient, thermal conductivity and the elastic constants (Hale, 1976). Two extremes for sum properties can be visualized – one in which the phases are aligned parallel to the probing field and the other in which they are perpendicular (see Fig. 1). Mathematically, these limits are described by the series and parallel models familiar from elementary expressions for circuit resistance or capacitance. Although these expressions are useful bounds on sum properties, in general such simplistic mixing rules are poor approximations for experimental data if the two phases have widely different properties. However, if additional information regarding the composite microstructure is available, considerably more-accurate descriptions of the composite property coefficients can be derived (Benveniste & Aboudi, 1982; Ashton, Halpin & Petit, 1969; Milton, 1981, 1982; Veldkamp, 1979).

A product property, however, relies on a reaction to a stimulus in one phase exciting a response in a second phase, and it is this response, rather than the original reaction, which is measured. One of the classic examples of this is the magnetoelectric effect observed in dense mixtures of aligned BaTiO₃ and cobalt titanium ferrite grains (van den Boomgaard, Terrell, Born & Giller, 1974; van Run, Terrell &

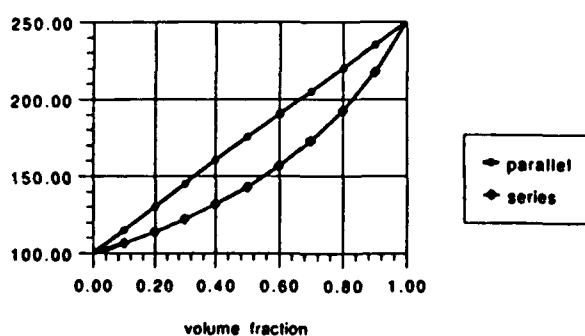


Fig. 1. Series and parallel mixing rules for two-phase composites.

* Editorial note: This invited paper is one of a series of comprehensive Lead Articles which the Editors invite from time to time on subjects considered to be timely for such treatment.

Scholing, 1974). When exposed to a magnetic field, the ferrite grains deform due to magnetostriction. This shape change is passed along to the ferroelectric, which in turn produces a measurable electrical polarization. Here it is easily seen that the combined property, magnetoelectricity, cannot (as would be the case for a sum property) be written as a sum of the magnetoelectric effects of the two phases, as, indeed, neither one of the components is magnetoelectric.

The third type of property, the combination property, can be illustrated by ultrasonic wave velocity. For a long thin rod, the velocity of a wave propagating along the length is $v = (E/\rho)^{0.5}$ where E is Young's modulus and ρ the density. If such a rod is formed from a compliant matrix material reinforced with stiff parallel fibers, the ultrasonic velocity varies widely depending on whether the fibers are oriented parallel or perpendicular to the length of the rod (Ross & Sierakowski, 1975). The distinguishing feature which makes this a combination rather than a sum property is that v_c , the velocity for waves travelling transverse to the fibers, is less than the wave velocity for either of the components. Clearly, such a coefficient could not result from a weighted sum of the two individual wave velocities. Rather, the slowness of this wave is due to the fact that the density and stiffness vary differently with the volume fraction. It is this difference in mixing rules for the two properties which causes the combination property v_c to lie outside the range of the end members. The longitudinal wave, v_L , however, behaves more normally. In this case the stiffness and the density follow the same mixing rule and the values for v_L lie within those of the end members. Another remarkable example of combination properties is found in the thermal and ultrasonic behavior of silica aerogels (Gronauer & Fricke, 1986; Buttner & Fricke, 1985). It has been shown that in a highly porous aerogel (< 10% solid phase) the ultrasonic wave speed can drop as low as $\sim 120 \text{ ms}^{-1}$, considerably below the speed of sound in either air or dense SiO_2 (Gronauer & Fricke, 1986). Moreover, if this material is evacuated, the thermal conductivity falls below that of non-convection air (Buttner & Fricke, 1985). Clearly, combination properties offer tremendous opportunities in the engineering of composites.

Composite symmetry

In attempting to describe the anisotropic properties of a composite, it rapidly becomes apparent that fundamental to any account of composite properties is a description of composite symmetry. Neumann's law states that the symmetry of any physical property of a material must include the symmetry of its point group, so determination of the composite

point group is essential to understanding the property anisotropy.

There are some composites (notably some laminates, cross-plys and perforated or extruded materials) which possess crystallographic symmetry on a macroscopic scale, but for others, one of the Curie limiting groups is more descriptive. The following examples serve to illustrate different types of symmetry and their application to property determination:

Laminated composites made from glass-fiber-reinforced epoxy are good examples of composite materials that conform to crystallographic symmetry. In a unidirectional laminate, glass fibers are aligned parallel to one another, such that the laminate has orthorhombic symmetry (crystallographic point group mmm). Mirror planes are oriented perpendicular to the laminate normal and perpendicular to an axis formed by the intersection of the two other mirrors. Consequently, the physical properties of a unidirectional laminate must include the symmetry elements of the point group mmm . As such a laminate is heated, it will change shape due to thermal expansion. And, since glass has a lower thermal expansion and greater stiffness than the polymer, less expansion will take place parallel to the fiber axis. The laminate will therefore expand anisotropically but it will not change its symmetry, *i.e.* the heated laminate continues to conform to point group mmm .

As a somewhat more complex illustration, consider the case of cross-ply laminates made up of two unidirectional laminates bonded together with the fiber axes at 90° . Such a laminate belongs to the tetragonal point group $42\bar{m}$. Laminated composites with $\pm \theta$ angle-ply alignment exhibit an orthorhombic symmetry which is consistent with point group 222 characteristics. Here again, although considerable deformation takes place on heating, the composite retains a shape compatible with its crystallographic symmetry (see Fig. 2).

Other types of symmetry elements can also be introduced during processing. For example, when a plasticized ceramic slip is extruded [as is the case for the honeycomb ceramics used as catalyst supports (Lachman, Bagley & Lewis 1981)], a large number of different symmetries can be incorporated by suitably altering the die. By filling the extruded form with a second phase, composites with interesting and useful symmetries can be produced. Lead zirconate titanate (PZT) honeycomb ceramics prepared in this way have been transformed into piezoelectric transducers by electroding and poling. The net symmetry of the honeycomb transducers depends on both the symmetry of the honeycomb and on the poling direction. For a square honeycomb pattern, the symmetry of the unpoled ceramic tetragonal ($4/mmm$) with a four-fold axis parallel to the extrusion direction. When poled parallel to the same direction (Shroud, Bowen

& Schulze, 1980) the symmetry decreases to 4 mm . Transversely poled composites filled with epoxy (point group $mm2$) are especially sensitive to hydrostatic pressure waves (Safari, Halliyal, Newnham & Lachman, 1982).

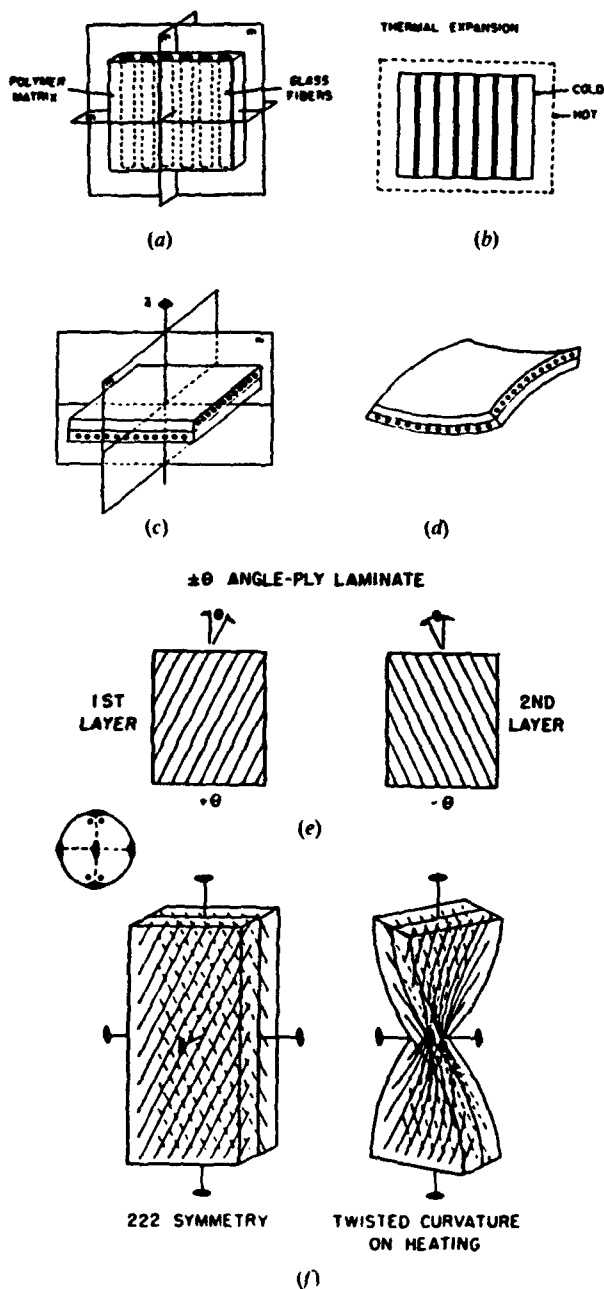


Fig. 2. Changes in laminate shape on heating. (a) Unidirectional laminate consisting of parallel glass fibers in an epoxy material. (b) The orthorhombic $mmmm$ symmetry of the composite is maintained on heating. (c) Cross-ply laminate containing orthogonal fibers in adjacent layers. (d) Double curvature occurs on heating, consistent with $32m$ symmetry. (e) $\pm\theta$ angle-ply laminate with 222 symmetry. (f) Twisted curvature develops when the temperature is raised.

The piezoelectric properties and symmetry of natural composites such as wood and bone, however, conform to texture symmetries. For texture symmetry groups which do not belong to the 32 crystallographic point groups, one of the Curie groups $\infty \infty m$, $\infty \infty$, $\infty/m\bar{m}$, ∞m , ∞/\bar{m} , $\infty 2$ or ∞ is more appropriate. This can be illustrated by considering polar glass ceramics with conical symmetry (Gardopee, Newnham & Bhalla, 1981). A glass can be crystallized under a strong temperature gradient such that polar crystals grow like icicles into the interior from the surface. Certain glass-ceramic systems, such as $\text{Ba}_2\text{TiSi}_2\text{O}_8$ and $\text{Li}_2\text{Si}_2\text{O}_5$, show sizable pyroelectric and piezoelectric effects when prepared in this manner. Polar glass ceramics belong to the Curie point group ∞m , the point group of a polar vector. As the glass is crystallized in a temperature gradient, its symmetry changes from spherical ($\infty \infty m$) to conical (∞m), the same symmetry that is found in a poled ferroelectric ceramic.

Recent work on the patterning of composites by the introduction of a fugitive ink, which is then burned out during firing, leaving controlled voids (Kahn, 1985; Kahn, Rice & Shadwell, 1986; Utsumi, Shimada, Ikeda & Takamizawa, 1986; Utsumi, Tsuzuki, Suga & Takamizawa, 1986) or through chemical etching (Shiosaki & Kawabata, 1986; Shiosaki, Tanizawa, Kamei & Kawabata, 1983; Trolier, Xu & Newnham, 1987, 1988), has greatly increased the possibilities for inducing desired symmetries in composites. The thickness mode transducer shown in Fig. 3, for example, has been etched with a spiral trench to eliminate the appearance of unwanted lateral and coupled modes which would otherwise interfere with the thickness resonance. Unpoled, this device has the symmetry ∞/m , a Curie group which is difficult to induce by conventional processing. With application of a poling field (symmetry ∞m) the correct designation becomes ∞ .

To describe magnetic fields and magnetic properties it is necessary to introduce the black-and-white

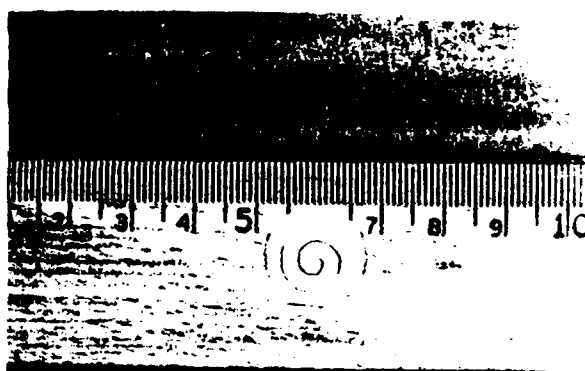


Fig. 3. Spiral etch transducer with symmetry ∞ .

Table 1. Number of independent property coefficients for nonmagnetic and magnetic Curie groups

Curie group (Type of tensor)	Pyroelectricity Polar 1st rank	Permittivity Polar 2nd rank	Piezoelectricity Polar 3rd rank	Elastic compliance Polar 4th rank	Optical activity Axial 2nd rank
$\infty \infty m l'$	0	1	0	2	0
$\infty \infty l'$	0	1	0	2	1
$\infty /mm l'$	0	2	0	5	0
∞ /ml'	0	2	0	5	0
$\infty ml'$	1	2	3	5	0
$\infty 2l'$	0	2	1	5	2
$\infty l'$	1	2	4	5	2
Magnetic Curie group (Type of tensor)	Pyrogmagnetism Axial 1st rank	Magnetic susceptibility Polar 2nd rank	Magnetoelectricity Axial 3rd rank	Piezomagnetism Axial 4th rank	
$\infty \infty m$	0	1	0	0	
$\infty \infty m'$	0	1	0	0	
$\infty \infty$	0	1	0	0	
∞ /mm'	0	2	1	1	
∞ /mm	1	2	0	3	
$\infty /m'm$	0	2	1	0	
$\infty /m'm'$	0	2	2	0	
∞ /m	1	2	1	4	
∞ /m'	0	2	3	0	
∞m	0	2	1	1	
$\infty m'$	1	2	2	3	
$\infty 2$	0	2	2	1	
$\infty 2'$	1	2	1	3	
∞	1	2	3	4	

Curie groups. Magnetic fields are represented by axial vectors with the symmetry ∞/mm' . The symbol m' indicates that the mirror planes parallel to the magnetic field are accompanied by time reversal.

The magnetoelectric composite mentioned earlier is an excellent example of the importance of symmetry in composite materials. In combining a magnetized ceramic (symmetry group ∞/mm) with a polar ceramic (symmetry ∞/ml') the symmetry of the composite is obtained by retaining the symmetry elements common to both groups: $\infty m'$.

An interesting feature of this symmetry description is its effect on physical properties. As stated earlier, the symmetry of any physical property of a material must include the symmetry elements of the point group. A full listing of the independent property coefficients possible for tensors of rank 1–4 is given in Table 1. As can be seen there, although the symmetry of a magnetized ceramic and a poled ferroelectric both forbid the occurrence of magnetoelectricity, their combined symmetry ($\infty m'$) allows it. Thus, by incorporating materials of suitable symmetry into a composite, new and interesting properties can be engineered. Full accounts of symmetry and its effect on properties can be found in books by Shubnikov & Koptsik (1974) and Nye (1985).

Composite connectivity

One classification scheme which has proven instructive in the study of composites has been that of

connectivity. The connectivity of any phase is defined as the number of dimensions in which the component is self-connected. As a matter of convention, active phases are listed first, followed by inactive and then inert phases. Thus a typical polycrystalline material densified by liquid-phase sintering might be designated as a two-phase 0–3 composite to show the grain and grain-boundary connectivities. Similarly, a nearly dense ceramic with isolated trapped pores would be considered a 3–0 composite (Fig. 4). Elaborating the possibilities for two phases leads to sixteen different connectivities: 0–0, 1–0, 2–0, 3–0, 1–1, 2–1, 3–1, 2–2, 3–2, 3–3, 0–1, 0–2, 0–3, 1–2, 1–3, 2–3, the first ten of which are geometrically distinct (Newnham, Skinner & Cross, 1978) (Fig. 5). As the number of phases increases, the following criteria are used to determine the order of components (Pilgrim, Newnham & Rohlfing, 1987):

1. unique desired property (property possessed by only one phase);
2. desired property coefficient in a shared property;
3. tensor order of coefficient or property;
4. volume fraction;
5. weight fraction;
6. formula weight or repeat unit weight.

The connectivity of a composite frequently gives considerable insight into its physical properties. From the natural world, wood is an example of a complex composite composed of a highly polymerized carbohydrate (50–60% of which is cellulose),

lignin, gums, resins and ash. As the tree grows, these materials form a tubular structure (Fig. 6) with the cellulose chains aligned along the tubes. Since the connectivity of the cellulose largely determines the mechanical properties, it is not surprising that the linear thermal expansion coefficient of wood is markedly lower in the longitudinal direction (*i.e.* along the chains) than it is normal to them (Weatherwax & Stamm, 1946).

To capitalize on effects like this, when composites are engineered, the connectivity is often the means through which the property coefficients of the active phase are effectively modified to enhance those of the composite. For example, in hydrophones used as underwater pressure sensors, the hydrostatic piezoelectric strain coefficient, d_h (defined as $d_{33} + 2d_{31}$, where 3 is the polar axis), is related to the overall device sensitivity. For most of the ferroelectrics used in such transducer applications, however, $d_{31} = -\frac{1}{2}d_{33}$, resulting in a very low d_h coefficient. By properly interrupting the continuity of the ferroelectric phase in the transverse direction, changing the ratio of d_{31} to d_{33} , it has been possible to raise the hydrophone figure of merit:

$$g_h d_h = (d_h)^2 / K_{33} \epsilon_0$$

where g_h = hydrostatic piezoelectric voltage coefficient and K_{33} = dielectric constant along the polar

direction, by up to two orders of magnitude (Ganicewicz, 1985).

Connectivity in crystals and composites

One way to emphasize the correlation between a composite's symmetry and connectivity and its properties is to regard macroscopic composites as natural extensions in scale of certain crystal structures. Thus, for example, the highly anisotropic bonding in graphite produces a layer structure (Fig.

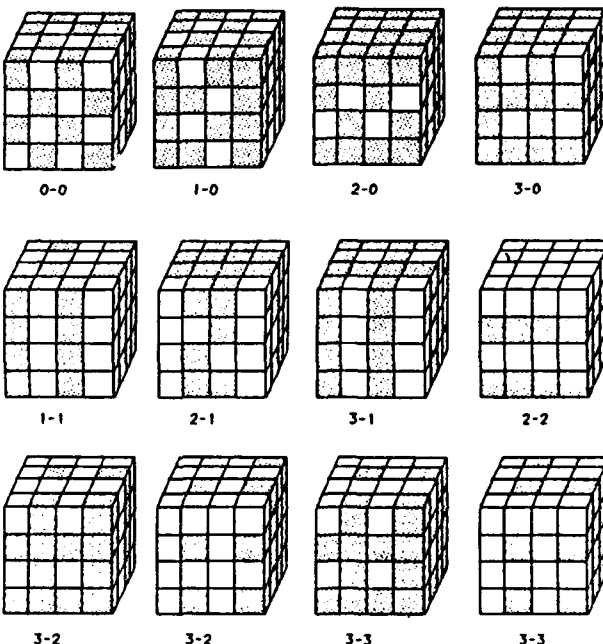
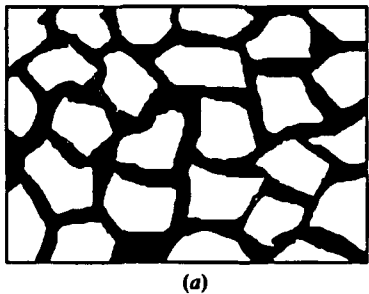
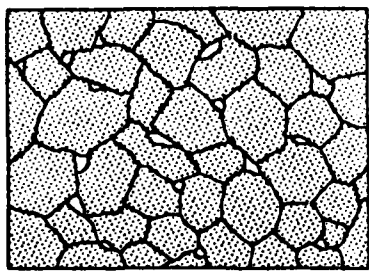


Fig. 5. The ten geometrically distinct connectivity patterns (after Newnham *et al.*, 1978).



(a)



(b)

Fig. 4. Schematic illustrating the difference between 0-3 and 3-0 connectivities. (a) represents a liquid-phase sintered material where the grains have been completely isolated by the grain boundaries giving 0-3 connectivity. In (b) the situation has been reversed so that the active phase is connected in three dimensions while the pores are isolated (3-0 connectivity).

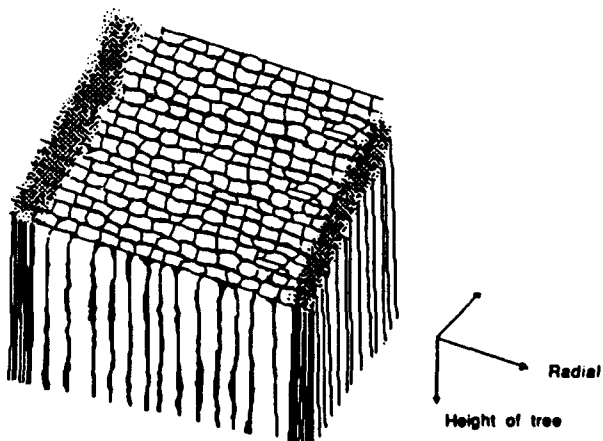


Fig. 6. The microstructure of wood showing the cellulose tubes.

7a) which is a clear prototype for lamellar composites. Hexagonal boron nitride (which crystallizes in a structure similar to graphite) has the same two-dimensional connectivity in the strong bonding. The resulting anisotropy of thermal conductivity makes this material attractive in applications like heat shielding (Newnham, 1975) where it is imperative that any heat generated be conducted rapidly away in two dimensions without penetrating through the third. This is comparable to some of the macroscopic 2-2 composites proposed as multilayer ceramic packages for Si chips (Fig. 7b). Here again it is important that the heat generated by the integrated circuits not be permitted to reach the signal carrying layers where requirements for low dielectric constant mandate the use of porous materials (which are in general poor thermal conductors). If the heat does reach those layers, it dissipates slowly, leading to degradation of the circuit performance as the chips overheat. To prevent these problems, a layer of high thermal conductivity could be incorporated into the design to expedite the transfer of heat to regions where it can be removed more efficiently.

As a second example of this principle, consider the structure of SbSI (shown in Fig. 8a). Here the ferro-

electric chains are clearly separated in the crystal structure itself, leading to a much larger piezoelectric coefficient along the chains than perpendicular to them (Hellwege & Hellwege, 1982). Although SbSI is not a composite, it can be regarded as a prototype for one if the space between the chains is considered a three-dimensionally connected 'phase'. This serves as a good model for the 1-3 biomedical transducers (Gururaja, Schulze, Cross & Newnham, 1985; Gururaja, Schulze, Cross, Newnham, Auld & Wang, 1985; Takeuchi & Nakaya, 1986; Nakaya, Takeuchi & Kataoka, 1987; Takeuchi, Nakaya & Kataoka, 1984; Smith, 1986) in which the ferroelectric active phase is decoupled in the lateral dimensions by dicing a ferroelectric block and backfilling with a polymer (Fig. 8b). By artificially producing an SbSI-like structure in this manner, researchers have been able to reduce coupling to lateral resonances which would otherwise decrease the resolution available from the imaging device (Takeuchi & Nakaya, 1986; Nakaya, Takeuchi & Kataoka, 1987; Takeuchi, Nakaya & Kataoka, 1984; Smith, 1986).

Another elegant example of composite symmetry mimicking crystal symmetry is that of the double diamond phase shown by phase-separating polymers through a narrow range of volume fractions (Thomas, Alward, Kinning, Martin, Handlin & Fetters, 1986; Thomas, Anderson, Henkee & Hoffman, 1988; Hasegawa, Tanaka, Yamasaki & Hashimoto, 1987). Films cast from a mixture of starblock or linear diblock polystyrene-polysisoprene copolymer units dissolved in toluene spontaneously self-

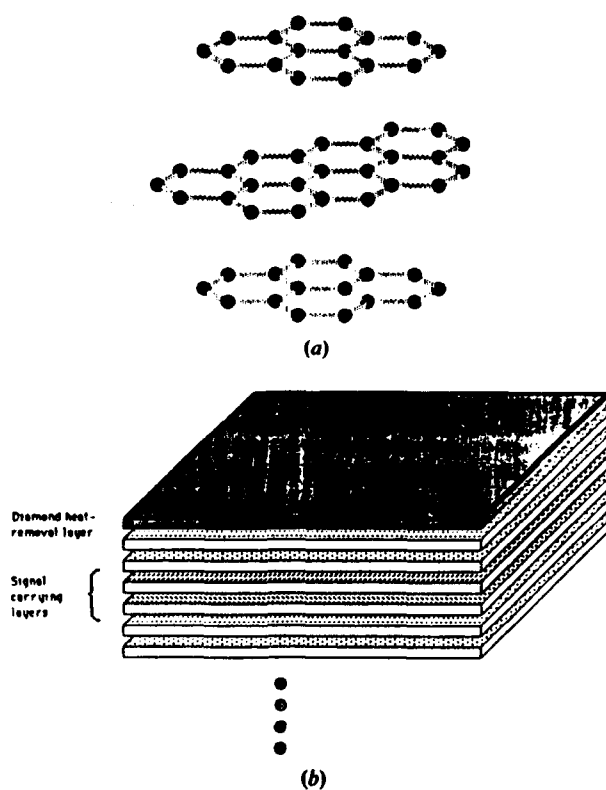


Fig. 7. (a) The crystal structure of graphite showing the layers due to the anisotropy in bonding. (b) A proposed package for Si chips with a diamond layer incorporated to remove heat.

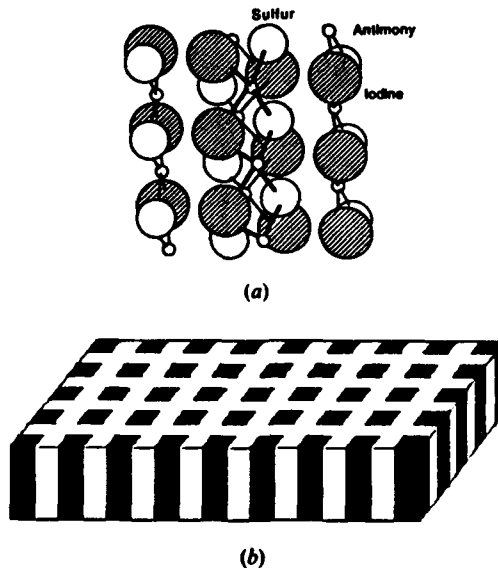


Fig. 8. (a) The crystal structure of SbSI showing the ferroelectric chains. (b) A 1-3 composite transducer used for medical imaging.

assemble into configurations with a minimum of surface separating the two phases. For polystyrene volume fractions between -27 and 38%, the polyisoprene assumes two interpenetrating diamond lattices with the polystyrene serving to fill the space between them. As shown in Fig. 9, this is analogous to the double diamond structure formed by Cu₂O. The properties of the phase-separated polymer reflect the transitions in connectivity as the volume fraction of polystyrene is varied. Thus, as might be expected, the room-temperature storage modulus of the composite jumps by a factor of ten at the transition to the 3-3 connected double diamond structure from the 3-1 cylinder morphology.

Connectivity transitions

One aspect which makes composites interesting to study is that, unlike in a crystal where the connectivity is determined by the structure, in composites the connectivity can be altered continuously through changes in the volume fraction of components, the relative size scale of the phases, and in some cases through applied 'forces' like temperature or pressure. Transitions in connectivity due to any of these factors can cause significant property changes and indeed, in some cases, serve as the basis for composite sensing devices. An example of a composite

showing connectivity transformations as a function of both filler volume fraction and temperature is the family of carbon-black-loaded polyethylene thermistors. As the volume fraction of filler is increased, isolated carbon particles link up and form chains through the matrix, transforming the composite from 0-3 to 3-3 connectivity. The substantial decrease in the resistivity of the composite accompanying the formation of continuous conductor chains can be described by percolation theory (Aharoni, 1972; Bueche, 1978). Use of these composites as thermistors requires that, for a given volume fraction filler, the resistivity change as a function of temperature. In the case of the carbon-loaded polyethylenes, the PTC (positive temperature coefficient of resistance) effect is due to the large volume increase accompanying the crystalline-amorphous transition of polyethylene at ~400 K. This forces the conducting particles apart, leading to a reversion to 0-3 connectivity for the composite and a sudden rise in resistivity.

Composite scaling

A third interesting phenomenon found in composites which lacks an apparent counterpart in crystals arises when another component is added to the above-mentioned thermistor to improve the high-temperature mechanical stability. This second filler [originally mullite or alumina (Rohlfing, 1987)] has a much larger grain size than the carbon particles so that it serves as a framework for the composite at higher temperatures, preventing slumping of the polyethylene. Although it is still acceptable to term this a 0-0-3 composite, a far better description would be 3(0-3)-0 in which the carbon-polyethylene is written as a quasi-composite isotropic on the scale of the mullite (Pilgrim, Newnham & Rohlfing, 1987; Rohlfing, 1987).

Additional protection against the effects of extreme temperature excursions in composite thermistors is possible if the third phase is able to store heat below the slumping temperature of the carbon-polyethylene matrix. Pentaerythritol, C(CH₂OH)₄, for example, has a solid-state phase transition at 453 K. When this material is used as the second filler, heat is absorbed at the transition, and the temperature is stabilized below that where the matrix deforms irreversibly (Brodeur). Moreover, because it is much larger in size than the graphite particles, the pentaerythritol also serves to stabilize mechanically the quasi-composite matrix, as did the mullite in the previous example.

This type of scaling can be especially important when analyzing a composite's properties as a function of the wavelength of an exciting field. Often, the whole point of making a composite is to modify the properties of one phase with that of the other. If the

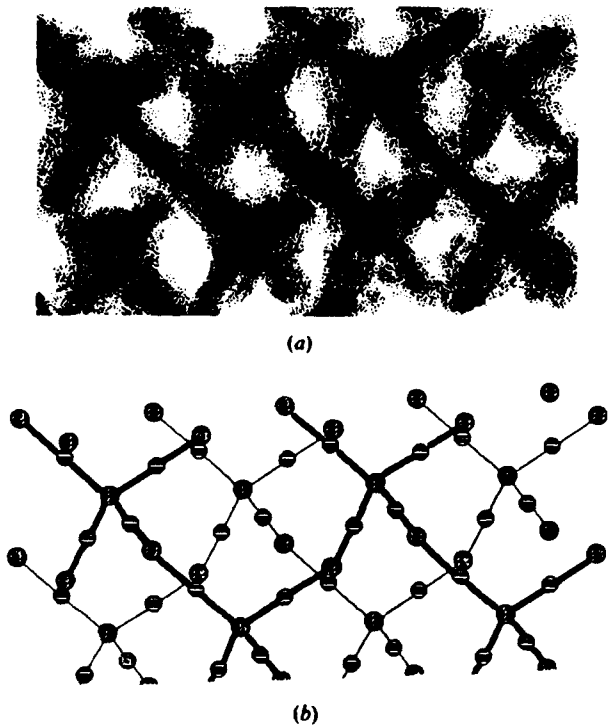


Fig. 9. (a) The double diamond phase shown by phase separating polymers. (b) Cu₂O structure.

wavelength of the interrogating field is too small, however, it encounters only one phase at a time, rather than the desired 'average' of the phases. Scale is critical in the 1-3 composites used to generate and receive ultrasound for biomedical imaging (Fig. 8). In addition to the desired thickness resonance, such systems also undergo lateral running resonances. If the periodicity of the pattern is too coarse, these lateral resonances move to lower frequencies where they may interfere with the purity of the thickness vibration (Smith, 1986). This, in turn, results in spurious signals and a loss in resolution of the diagnostic image. Consequently, to ensure that the composite can be treated as a homogeneous medium vibrating only in the thickness direction, the composite scale must be fine enough to drive the additional modes above the thickness resonance. As a second example, consider the composites used in optical components. Here, the optical properties of the matrix and hence the propagation of an electromagnetic wave can be tailored with a filler that is smaller than the wavelength of light. When, however, the heterogeneities approach the wavelength in size, they begin to scatter light rather than modulate it (Egan & Aspnes, 1982). The whole process is analogous to the scattering of X-rays by crystals.

Similar effects are also noticeable in measuring the fracture toughness of composites (even when the two components are grain and grain boundary in a 'single-phase' material) where, depending on the size of the crack induced, the measured fracture toughness changes (Mussler, Swain & Claussen, 1982). One explanation for this is that large cracks encounter both the matrix and the filler, leading to high fracture toughnesses. Small cracks, on the other hand, might lie entirely within the matrix phase, where there is no mechanism for increasing the toughness, so that the measured fracture toughness is lower even though the material itself is unchanged. For maximum toughness, then, the second phase must be regularly encountered on the scale of the crack. Consequently, in fabricating a composite it is essential to ensure that the scale of the components is acceptable with respect to the probing 'field'.

Transitions in composites

Regarding the connectivity of a composite as linked to the composite's 'state', one can define a notation for connectivity transformations analogous to that developed by Aizu (1965, 1966) for ferroic phase transitions. In Aizu's notation, the transition to a ferroelectric phase caused by any 'force', such as a change in temperature (T) or applied electric field (E), can be described by listing the prototype symmetry and the final symmetry, separating them with an

F to signify the ferroelectric transition. Thus, the cubic-tetragonal phase change in barium titanate would be written as $m\bar{3}m F 4mm$.

It should be noted that Aizu's notation deals with thermodynamically well defined states. Thus, the initial and final states are independent of the path taken to reach them (i.e. whether the material becomes ferroelectric due to a decrease in temperature or under the influence of an applied electric field) and the transitions are reversible. Transitions in composites, however, are often not strictly state changes. Moreover, because composites are not compositionally homogeneous, it is inappropriate to equate transformations in multiphase materials with true phase transitions in single-phase materials. For example, the change from a 3-3 to a 0-3 composite (Fig. 10) in the case of a metal-loaded polymer could be caused by an increase in temperature, a decrease in pressure (P), or the presence of some chemical (C) which swells the matrix phase. Although the net result in each case is a 0-3 insulating phase, there are some fundamental differences between the final 'states' in each case. For this reason, rather than separating the initial and final symmetries with an indication of a 'state' change like Aizu's F , it is better to delineate the transition by the force which is responsible for it. The advantage of a nomenclature of this type is its broad applicability; transitions caused by processing can be described in the same manner as true state changes. Thus, in a single-phase material like a random array of ferroelectric grains, the transition caused by poling would be written as

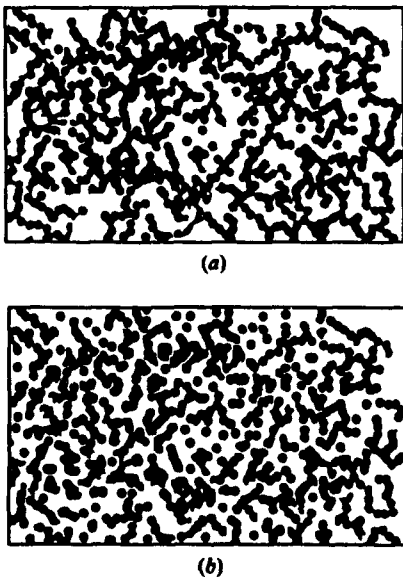


Fig. 10. A schematic of percolation in a two phase composite showing the transition from 3-3 to 0-3 connectivity.

$\infty \infty m E^s \infty m$, where the superscript *s* denotes a symmetry change. Similarly, heating α -quartz above 846 K leads to a displacive phase transition to the β form which can be described as $32 T^s 622$. In a composite, however, both the symmetry and the connectivity should be defined, so the poling of a 0-3 composite of ferroelectric gains in a polymer matrix would be written $\infty \infty m 0-3 E^s \infty m 0-3$.

In general, it can be seen that there are several types of transitions which can take place in composites: transitions in the properties of a single phase, transitions which involve changes in connectivity only, those which involve only a symmetry change (*i.e.* an alignment of symmetry elements already present in one of the phases as shown above for the poling example), and those which involve a simultaneous change of two or more of these. As it is unlikely that one variable alone could force concurrent changes in the symmetry and connectivity, it is important to distinguish between the forces responsible for the different changes. This can be done by denoting F^p as the force responsible for changes in a phase's properties, F^c as the force causing composite symmetry transitions and F^e as the connectivity-changing force. This is similar to the notation proposed by Pilgrim, Newnham & Rohlfing (1987) except that forces changing composite symmetry are also included here.

As an example of the application of this notation to connectivity changes, consider the 0-3 material used as a piezoresistive pressure sensor. Here an epoxy is used as a matrix for powders of Sb-doped SnO_2 or graphite. When pressure is applied, the conducting particles are forced into electrical contact, causing a sharp drop in resistivity. This transition would be written by $\infty \infty m 0-3 P^c \infty \infty m 3-3$. A somewhat more complex example of connectivity change is given by a system composed of an organic solvent, a surfactant (didodecyldimethylammonium bromide) and water (Hofmann & Ebert, 1988). In the diphasic system formed without water, the surfactant appears in rodlike micelles which can link up into a three-dimensional network through the organic solvent. As water is added, it is solubilized in the micelle interiors, resulting in a 1-3 water-surfactant connectivity. (Water is regarded as an active phase here because it conducts electrically.) When the water concentration is raised beyond a certain limit, the rods break down into globules, imprisoning the H_2O at globule centers. As a consequence, the conductor networks are destroyed, and the resistivity rises. The overall conductivity transition would then be written as $\infty \infty m 3(1-3)-3 C^s \infty \infty m 0(0-3)-3$ where *C* denotes the compositional change.

Alignable polycrystalline ceramics provide excellent examples of transitions in symmetry alone. Hence, magnetization of a porous $\gamma\text{-Fe}_2\text{O}_3$ film

would be described by $\infty \infty m 3-0 H^s \infty /mm' 3-0$, and poling of a liquid-phase sintered ferroelectric would be $\infty \infty m 0-3 E^s \infty m 0-3$.

Finally, V_2O_5 -loaded thermistors (Moffatt, Runt, Safari & Newnham, 1986) demonstrate the notation for phase-property changes alone. In this material, the phase transition at 150 K from monoclinic to rhombohedral of the filler is accompanied by a change from semiconducting to metallic conduction. Although this entails changes in the symmetry of the filler phase and the properties of the composite, the overall composite symmetry remains unaltered. Consequently, this transition is written as $\infty \infty m 3-3 T^p \infty \infty m 3-3$. The difference between the high- and low-temperature states is that at lower temperatures both phases are inert so that the higher-volume-fraction polyethylene matrix is written first and at higher temperatures the filler is written first as it has become an active phase (Pilgrim, Newnham & Rohlfing, 1987).

The notation is equally applicable to more complex or to sequential transitions. To return to the case of conductor-loaded insulators, changes in the connectivity due to different forces would be notated as $\infty \infty m 3-3 T^c \infty \infty m 0-3$ for thermistors (Aharoni, 1972; Bueche, 1978; Rohlfing, 1987; Moffatt *et al.*, 1986) $\infty \infty m 0-3 P^c \infty \infty m 3-3$ for piezoresistive pressure sensors (Carmona, Canet & Delhaes, 1987; Yoshikawa, Ota, Newnham & Amin, 1990) and $\infty \infty m 3-3 C^s \infty \infty m 0-3$ for some chemical sensors (Lundberg & Sundqvist, 1986). In the more-complicated three-phase thermistors employed by Brodeur (private communication), as the temperature is raised from absolute zero, the transitions in connectivity can be written as

$$\infty \infty m 3(3-3)-0 T^c \infty \infty m 3(0-3)-0 T^c \infty \infty m 0-3(0-3),$$

where the last transition denotes the change of pentaerythritol from a passive to an active phase [*i.e.* the transition is written as

$$Q(C-M)-P \iff Q(C-M)-P \iff P-Q(C-M).$$

Q = quasi-composite notation, *C* = conductor, *M* = matrix polyethylene, *P* = pentaerythritol].

Finally, the poling of a 0-3(0-3) composite comprised of small particulate carbon and larger grains of PZT in an epoxy matrix would be written as $\infty \infty m 0-3(0-3) P^c E^s \infty m 0-3(3-3) P^c \infty m 0-3(0-3)$ (where the second transition describes the return to ambient pressure) (Sa-gong, Safari, Jang & Newnham, 1985; Sa-gong, Safari & Newnham, 1986).

Summary

Some fundamental aspects of composite symmetry and connectivity and their relation to composite

properties have been reviewed. Connectivity of composites is shown, for several configurations, to be a natural extension from well known crystal structures. The concept of composite scale and its effect on properties is summarized.

A notation for transitions in composites based on Aizu's formulation for ferroelectrics and expanded from Pilgrim's nomenclature is also presented. Three major types of transitions are identified: those which involve changes in the properties of a phase, those which alter the symmetry of the composite, and those which modify the composite connectivity. The transition is then identified by listing the prototype symmetry and connectivity, the driving force for each change (notated to identify the type of change) and the final symmetry and connectivity. This process can be repeated for successive transformations.

References

- AHARONI, S. M. (1972). *J. Appl. Phys.* **43**, 2463-2465.
- AIZU, K. (1965). *Phys. Rev. A*, **140**, 590-596.
- AIZU, K. (1966). *Phys. Rev.* **146**, 423-429.
- ASHTON, J. E., HALPIN, J. C. & PETIT, P. H. (1969). *Primer on Composite Materials: Analysis. Progress in Materials Science Series*, Vol. 3. Stamford, CN, USA: Technomic Publishing Co., Inc.
- BENVENISTE, Y. & ABOUDI, J. (1982). *Int. J. Eng. Sci.* **20**, 193-216.
- BOOMGAARD, J. VAN DEN, TERRELL, D. R., BORN, R. A. J. & GILLER, H. F. J. I. (1974). *J. Mater. Sci.* **9**, 1705-1709.
- BUECHE, F. (1978). *J. Appl. Phys.* **43**, 4837-4838.
- BUTTNER, D. & FRICKE, J. (1985). *Int. J. Sol. Energ.* **3**, 89-94.
- CARMONA, F., CANET, R. & DELHAES, P. (1987). *J. Appl. Phys.* **61**, 2550-2557.
- EGAN, W. G. & ASPNES, D. E. (1982). *Phys. Rev. B*, **26**, 5313-5320.
- GARDOPEE, G. J., NEWNHAM, R. E. & BHALLA, A. S. (1981). *Ferroelectrics*, **33**, 155-166.
- GINIEWICZ, J. R. (1985). *(Pb,Bi)(Ti,Fe)O_x/Polymer 0-3 Composite Materials for Hydrophone Applications*. MS thesis, Pennsylvania State Univ., USA.
- GRONAUER, M. & FRICKE, J. (1986). *Acustica*, **59**, 177-181.
- GUIRE, T. (1987). *Propagation Measurements on Chiral Composites at Microwave Frequencies*. MS thesis, Pennsylvania State Univ., USA.
- GURURAJA, T. R., SCHULZE, W. A., CROSS, L. E. & NEWNHAM, R. E. (1985). *IEEE Trans. Sonics Ultrason. SU-32*, 491.
- GURURAJA, T. R., SCHULZE, W. A., CROSS, L. E., NEWNHAM, R. E., AULD, B. A. & WANG, Y. J. (1985). *IEEE Trans. Sonics, Ultrason. SU-32*, 481.
- HALE, D. K. (1976). *J. Mater. Sci.* **11**, 2105-2141.
- HASEGAWA, H., TANAKA, H., YAMASAKI, K. & HASHIMOTO, T. (1987). *Macromolecules*, **20**, 1651-1662.
- HELLWEGE, K. H. & HELLWEGE, A. M. (1982). Editors. *Landolt-Bornstein Numerical Data and Functional Relationships in Science and Technology, New Series, Vol. 16: Ferroelectrics and Related Substances*. Berlin: Springer-Verlag.
- HOFFMANN, H. & EBERT, G. (1988). *Angew. Chem. Int. Ed. Engl.* **27**, 902-912.
- KAHN, M. (1985). *J. Am. Ceram. Soc.* **68**, 623-628.
- KAHN, M., RICE, R. W. & SHADWELL, D. (1986). *Adv. Ceram. Mater.* **1**, 55-60.
- LACHMAN, I. M., BAGLEY, R. D. & LEWIS, R. M. (1981). *Bull. Am. Ceram. Soc.* **60**, 202-205.
- LUNDBERG, B. & SUNDQVIST, B. (1986). *J. Appl. Phys.* **60**, 1074-1079.
- MILTON, G. W. (1981). *Phys. Rev. Lett.* **46**, 542-545.
- MILTON, G. W. (1982). *J. Mech. Phys. Solids*, **30**, 177-191.
- MOFFATT, D., RUNT, J., SAFARI, A. & NEWNHAM, R. E. (1986). Proc. Sixth IEEE Int. Symp. on Applications of Ferroelectrics, 1986, pp. 673-676.
- MUSSLER, B., SWAIN, M. V. & CLAUSSEN, N. (1982). *J. Am. Ceram. Soc.* **65**, pp. 566-572.
- NAKAYA, C., TAKEUCHI, H. & KATAKURA, K. (1987). *Ultrason. Technol.* pp. 109-116.
- NEWNHAM, R. E. (1975). *Structure-Property Relations*, p. 58. New York: Springer-Verlag.
- NEWNHAM, R. E. (1985). *J. Mater. Ed.* **7**, 605-651.
- NEWNHAM, R. E. (1986). *Annu. Rev. Mater. Sci.* **16**, 47-68.
- NEWNHAM, R. E. (1988). *Crystallogr. Rev.* **1**, 253-280.
- NEWNHAM, R. E., SKINNER, D. P. & CROSS, L. E. (1978). *Mater. Res. Bull.* **13**, 525-536.
- NYE, J. F. (1985). *Physical Properties of Crystals: their Representation by Tensors and Matrices*. Oxford: Clarendon Press.
- PILGRIM, S. M., NEWNHAM, R. E. & ROHLFING, L. L. (1987). *Mater. Res. Bull.* **22**, 677-684.
- ROHLFING, L. L. (1987). *Carbon Black-Polyethylene Composites for PTC Thermistor Applications*. MS thesis, Pennsylvania State Univ., USA.
- ROSS, C. A. & SIERAKOWSKI, R. L. (1975). *Shock Vib. Dig.* **7**, 96-107.
- RUN, A. M. J. G. VAN, TERRELL, D. R. & SCHOLING, J. H. (1974). *J. Mater. Sci.* **9**, 1710-1714.
- SAFARI, A., HALLIYAL, A., NEWNHAM, R. E. & LACHMAN, I. M. (1982). *Mater. Res. Bull.* **17**, 301-308.
- SA-GONG, G., SAFARI, A., JANG, S. J. & NEWNHAM, R. E. (1985). *Ferroelectrics*, **5**, 131-142.
- SA-GONG, G., SAFARI, A. & NEWNHAM, R. E. (1986). Proc. Sixth IEEE Int. Symp. on Applications of Ferroelectrics, 1986, pp. 281-284.
- SHIOSAKI, T. & KAWABATA, A. (1986). Third US: Japan Seminar on Dielectric and Piezoelectric Ceramics. Programs and Abstracts.
- SHIOSAKI, T., TANIZAWA, M., KAMEI, H. & KAWABATA, A. (1983). *Jpn. J. Appl. Phys. Suppl.* **22-2**, 109-112.
- SHROUT, T. R., BOWEN, L. J. & SCHULZE, W. A. (1980). *Mater. Res. Bull.* **15** 1371-1379.
- SHUBNIKOV, A. V. & KOPTSIK, V. A. (1974). *Symmetry in Science and Art*, translated by G. D. ARCHARD, edited by D. HARKER. New York: Plenum Press.
- SMITH, W. A. (1986). Proc. Sixth IEEE Int. Symp. on Applications of Ferroelectrics, 1986, pp. 249-255.
- TAKEUCHI, H. & NAKAYA, C. (1986). *Ferroelectrics*, **68**, 53-61.
- TAKEUCHI, H., NAKAYA, C. & KATAKURA, K. (1984). Proc. IEEE Ultrason. Symp., 1984, pp. 507-510.
- THOMAS, E. L., ALWARD, D. B., KINNING, D. J., MARTIN, D. C., HANDLIN, D. L. JR & FETTERS, L. J. (1986). *Macromolecules*, **19**, 2197-2202.

- THOMAS, E. L., ANDERSON, D. M., HENKEE, C. S. & HOFFMAN, D. (1988). *Nature (London)*, **344**, 598-601.
- TROLIER, S. E., XU, Q. C. & NEWNHAM, R. E. (1987). *Mater. Res. Bull.* **22**, 1267-1274.
- TROLIER, S. E., XU, Q. C. & NEWNHAM, R. E. (1988). *IEEE Trans. Ultrason. Ferroelectr. Freq. Control*, **35**, 839-842.
- UTSUMI, K., SHIMADA, Y., IKEDA, T. & TAKAMIZAWA, H. (1986). *Ferroelectrics*, **68**, 157-179.
- UTSUMI, K., TSUZUKI, M., SUGA, M. & TAKAMIZAWA, H. (1986). IMC 1986 Proc., 28-30 May 1986, pp. 36-42.
- VELDKAMP, J. D. B. (1979). *J. Phys. D*, **12**, 1375-1384.
- WEATHERWAX, R. C. & STAMM, A. J. (1946). US Department of Agriculture and Forest Service, Forest Products Lab. Report R1487.
- YOSHIKAWA, S., OTA, T., NEWNHAM, R. & AMIN, A. (1990). *J. Am. Ceram. Soc.* In the press.

SMART MATERIALS

APPENDIX 4

Smart Electroceramics

Robert E. Newnham* and Gregory R. Ruschau*

Materials Research Laboratory, The Pennsylvania State University,
University Park, Pennsylvania 16802

"Smart" materials have the ability to perform both sensing and actuating functions. Passively smart materials respond to external change in a useful manner without assistance, whereas actively smart materials have a feedback loop which allows them to both recognize the change and initiate an appropriate response through an actuator circuit. Many smart materials are analogous to biological systems: piezoelectric hydrophones are similar in mechanism to the "ears" by which a fish senses vibrations. Piezoelectrics with electromechanical coupling, shape-memory materials that can "remember" their original shape, electro-rheological fluids with adjustable viscosities, and chemical sensors which act as synthetic equivalents to the human nose are examples of smart electroceramics. "Very smart" materials, in addition to sensing and actuating, have the ability to "learn" by altering their property coefficients in response to the environment. Integration of these different technologies into compact, multifunction packages is the ultimate goal of research in the area of smart materials. [Key words: electroceramics, sensors, actuators, memory, transducers.]

I. Introduction

IT HAS been said that life itself is motion, from the single cell to the most complex organism: a human being. This motion, in the form of mobility, change, and adaptation, is what elevates living beings above the lifeless forms.¹ This concept of creating a higher form of materials and structures by providing the necessary life functions of sensing, actuating, control, and intelligence to those materials is the motivation for studying "smart" materials.

Smart materials are part of smart systems—functional materials for a variety of engineering applications. Smart medical systems treat diabetes with blood sugar sensors and insulin delivery pumps. Smart airplane wings achieve greater fuel efficiency by altering their shape in response to air pressure and flying speed. Smart toilets analyze urine as an early warning system for health problems. Smart structures in outer space incorporate vibration cancellation systems that compensate for the absence of gravity and prevent metal fatigue. Smart toys, such as "Altered Beast," awaken from the dead and learn to survive in the hostile environment of a different age. Smart houses have electrochromic windows that control the flow of heat and light in response to weather changes and human activity. Smart tennis rackets have rapid internal adjustments for overhead smashes and delicate drop shots. Smart muscle implants are made from rubbery gels that respond to electric fields, and smart dental braces are made from shape-memory alloys. Smart hulls and propulsion systems for navy ships and submarines detect flow noise, remove turbulence, and prevent detection. Smart water purification systems sense and remove noxious pollutants.

S. M. Wiederhorn—contributing editor

Manuscript No. 197030. Received December 17, 1990; approved January 4, 1991.

Presented in part at the Second International Science and Technology Congress of the American Ceramic Society, Orlando, FL, Nov. 13, 1990 (Symposium on Composites, (Invited) Paper No. 17-SI-90C).

*Member, American Ceramic Society.

feature

A number of smart systems have already been developed for automobiles, but there are many more to come. In a recent newspaper cartoon, Blondie and Dagwood encountered a smart automobile that drives itself back to the finance company when the owner misses a payment!

In this feature paper the idea of "smartness" in a material is discussed, with a number of examples involving electroceramic components. Some of these smart ceramics are in production, whereas others have great potential but are thus far limited to laboratory investigations.

To begin our discussion, we first define "smart" to set the limits for classifying smart materials.

II. How Smart Is Smart?

The short answer is "not very." Webster's dictionary gives several definitions for the word "smart," including "alert, clever, capable," "stylish," and "to feel mental distress or irritation." All three definitions are appropriate for the currently fashionable subject, "smart materials." They are stylish, they are—in some cases—clever, and it does cause some of us mental distress to think that a ceramic might somehow possess intelligence, even in rudimentary form.

There are many words in the English language denoting various degrees of intelligence. Beginning at the bottom, an intelligence scale might look like this: stupid—dumb—foolish—trivial—sensible—smart=clever—intelligent—wise. Many modern-day materials have been cleverly designed to perform useful functions, and, it seems to us anyway, we are justified in calling them smart. They are decidedly better than "sensible" materials, but calling them "intelligent" seems rather presumptuous and self-serving. Perhaps in the future—when we are able to integrate information, processing, and feedback circuitry into our sensor and actuator materials—we will be justified in calling our materials intelligent. As pointed out later, such a time is not far off.

To clarify the concept of smart materials, we describe a few examples of passive and active smartness.

III. Passive Smartness

A passively smart material has the ability to respond to environmental conditions in a useful manner. A passively smart material differs from an actively smart material in that the former has no external fields or forces or feedback systems to enhance its behavior. The "S" words in Table I summarize some of the meanings of passive smartness. Many passively smart materials incorporate self-repair mechanisms or standby phenomena which enable the material to withstand sud-

den changes in its surroundings. The crack-arresting mechanisms in partially stabilized zirconia are a good example. Here the tetragonal-monoclinic phase change accompanied by ferroelastic twin wall motion are the standby phenomena capable of generating compressive stresses at the crack tip. In a similar way, toughness can be improved by fiber pullout or by multiple crack branching as in the structural composites used in aircraft, or in machinable glass-ceramics.

Ceramic varistors and positive temperature coefficient (PTC) thermistors are also passively smart materials. When struck by high-voltage lightning, a zinc oxide varistor loses most of its electrical resistance and the current is bypassed to ground. The resistance change is reversible and acts as a standby protection phenomenon. A varistor also has a self-repair mechanism in which its highly nonlinear current-voltage ($I-V$) relationship can be restored by repeated application of voltage pulses. Barium titanate PTC thermistors show a very large increase in electrical resistance at the ferroelectric phase transformation near 130°C. The jump in resistance enables the thermistor to arrest current surges, again acting as a protection element. The voltage-dependent resistance ($R(V)$) behavior of the varistor and the temperature-dependent resistance ($R(T)$) behavior of the PTC thermistor are both highly nonlinear effects which act as standby protection phenomena, and make the ceramics smart in a passive mode.

Healing mechanisms for electric breakdown are present in both electrolytic and polymer capacitors, enabling them to store as much charge as high-permittivity ceramic capacitors. In electrolytic capacitors, the thin insulating layer of alumina is restored through chemical reaction with the liquid electrolyte. Polymer capacitors restore high resistance by evaporating the electrode near the breakdown path.

Smart composites have been used to solve thermal problems as well. Some rather sophisticated composites made from tungsten, silver, carbon, ceramic, and steel are used as rocket nozzles where the temperatures are very high and dimensional tolerances are critical. Inside the nozzle is an inferno of hot corrosive gas capable of destroying most materials in a fraction of a second, creating severe propulsion problems.

The nozzle insert is made of porous tungsten infiltrated with silver which is very ductile and transmits heat better than tungsten. This protects the tungsten from thermal stress at temperatures below 600°C where it is brittle. When impregnated with silver, tungsten can be machined and is noticeably

Table I. Some Attributes of Passive Smartness

Selectivity
Self-diagnosis
Self-tuning
Sensitivity
Shapeability
Self-recovery
Simplicity
Self-repair
Stability and multistability
Standby phenomena
Survivability
Switchability

lighter. Silver melts and then vaporizes as the nozzle heats up. The heat of vaporization prevents the tungsten from heating too rapidly, and then the silver vapor enters the gas stream where it reduces the convective heat-transfer coefficient.

As the temperature of the porous tungsten rises, heat is transported to the graphite layer which gets stronger as it is heated. Graphite does not resist erosion very well but its high thermal conductivity and specific heat make it an excellent heat sink. Behind the graphite is a layer of refractory ceramic which acts as a thermal insulator to protect the outer steel shell which provides structural strength. Eventually, the ceramic layer overheats, begins to conduct heat, and the shell softens and melts away. The multiphase rocket nozzle is a smart composite that performs a number of thermomechanical functions in a highly imaginative fashion, and enables tungsten to survive above its melting point for a short period of time.

A simpler idea in heat dissipation is that of the thermal delay composite PTC thermistor. Composite thermistors, unlike barium titanate thermistors, undergo no ferroelectric phase transition. They consist of an inert conductive filler, such as carbon black or vanadium oxide, loaded into a semicrystalline polymer (e.g., poly(ethylene)) to form a low-resistivity composite. When the melting point of the polymer is reached, the percolation pathways are disrupted and the composite exhibits a huge increase in electrical resistance. However, further heating beyond the melting point causes severe degradation of the composite PTC thermistor.

Incorporating a third phase into the composite, one with heat-storage capabilities, provides a protection mechanism for the device. Certain organic materials display solid-solid endothermic phase transformation at low temperatures and can be easily dispersed in the PTC thermistors. Degradation caused by overheating can be avoided by using a second filler whose solid-solid transition is slightly greater than the melting temperature of the polymer. Pentaerythritol, with a phase transition at $\sim 185^\circ\text{C}$, is an effective second filler for carbon black-poly(ethylene) ($T_m = 130^\circ\text{C}$) thermistors. The thermal delay in pentaerythritol-doped thermistors has been documented for both externally heated and internally (joule) heated thermistors.²

IV. Active Smartness

A smart ceramic can also be defined with reference to sensing and actuating functions, in analogy to the human body. A smart ceramic senses a change in the environment, and using a feedback system, makes a useful re-

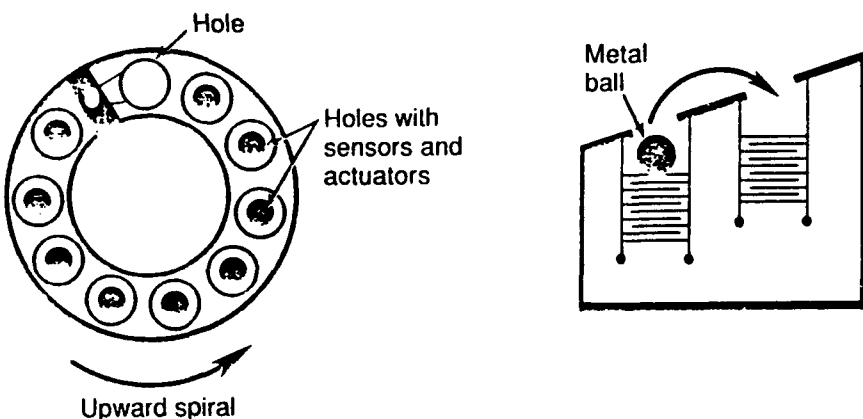


Fig. 1. Piezoelectric Pachinko machine. Smart material is a PZT sensor-actuator stack with a feedback network.

sponse. It is both a sensor and an actuator. Examples of actively smart materials include vibration-damping systems for outer-space platforms and electrically controlled automobile suspension systems using piezoelectric ceramic sensors and actuators.

The piezoelectric Pachinko machine illustrates the principle of an actively smart material. Pachinko parlors with hundreds of vertical pinball machines are very popular in Japan. The piezoelectric Pachinko game constructed by engineers at Nippon Denso (Kariya, Japan) is made from lead zirconate titanate (PZT) multilayer stacks which act as both sensors and actuators. When a ball falls on the stack, the force of impact generates a piezoelectric voltage. Acting through a feedback system, the voltage pulse triggers a response from the actuator stack. The stack expands rapidly throwing the ball out of the hole, and the ball moves up a spiral ramp during a sequence of such events. Eventually, it falls into a hole and begins the spiral climb all over again (see Fig. 1).

The video tape head positioner developed by Piezoelectric Products, Inc. (Metuchen, NJ), operates on a similar principle. A bilaminated bender made from tape-cast PZT ceramic has a segmented electrode pattern dividing the sensing and actuating functions of the positioner. The voltage across the sensing electrode is processed through the feedback system resulting in a voltage across the positioning electrodes. This causes the cantilevered bimorph to bend, following the video tape track path. Articulated sensing and positioning electrodes near the tape head help keep the head perpendicular to the track. The automatic scan tracking system operates at 450 Hz (Fig. 2).

These two examples illustrate how an actively smart ceramic operates. Both sensing and actuating functions are involved in its performance, and al-

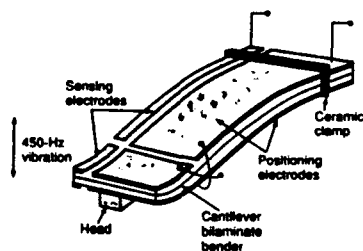


Fig. 2. Video tape head positioner made from PZT bimorph with sensor- and actuator-divided electrodes.

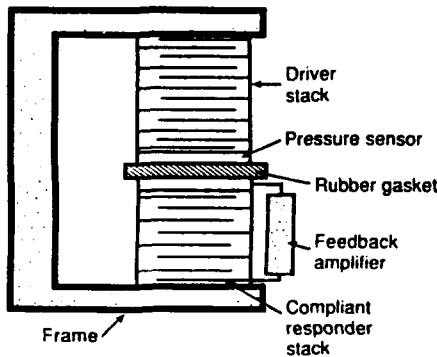


Fig. 3. Test experiment for evaluating smart materials with controlled compliance.

though the Japanese scientists have a somewhat different perspective on smart or intelligent materials (see Panel I), the end results of efforts in this area are very similar.

V. Rubberlike Ceramics

Every baseball player knows the importance of "soft hands." In catching a baseball, it is important to withdraw the hands slightly on making contact with the ball. This reduces the momentum of the ball gradually and creates a soft landing. Soft landings are achieved on ceramics in the same way, making them feel as soft as rubber.

To test the concept, controlled compliance experiments have been conducted using PZT sensors and actuators.⁴ In the test setup (Fig. 3), one actuator is used as the external driver, and the other as the responder. Sandwiched between the two actuator stacks are two sensors and a layer of rubber. The upper actuator is driven at a frequency of 100 Hz and the vibrations are monitored with the upper sensor. The pressure wave emanating from the driver passes through the upper sensor and the rubber separator and impinges on the lower sensor. The resulting signal is amplified using a low-noise amplifier and fed back through a phase shifter to the lower actuator to control the compliance. In this example, the pressure sensor, rubber gasket, responder stack, and feedback amplifier together form what could be termed a smart unit.

A smart sensor-actuator system can mimic a very stiff solid or a very com-

pliant rubber. This can be done while retaining great strength under static loading, making the smart material especially attractive for vibration control.

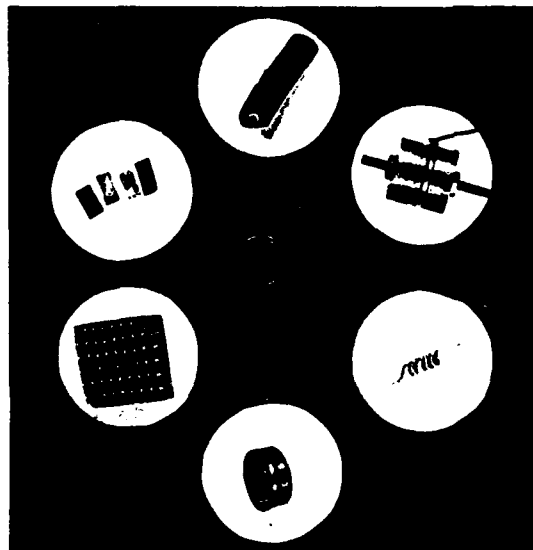
If the phase of the feedback voltage is adjusted to cause the responder to contract rather than expand in length, the smart material mimics a very soft, compliant substance. This reduces the force on the sensors and partially eliminates the reflected signal. The reduction in output signal of the upper sensor is a measure of the effectiveness of the feedback system. As shown in Fig. 4, the compliance of the actuator-sensor composite is reduced by a factor of 6 compared with rubber.⁴

VI. Modulated Suspension Systems

The automobile industry is a very large market in which smart composites and sensors are already widely used. More than 50 electroceramic components can be found in today's high-tech autos, ranging from the air-fuel oxygen sensors used in most autos to the more exotic piezoelectric raindrop sensor, which automatically senses the amount of rain falling and adjusts the windshield wipers to the optimum speed.⁵

Controlled compliance with piezoelectric ceramics is used in Toyota's piezoTEMS (Toyota Electronic Modulated Suspension), a system which has been developed to improve the drivability and stability of the automobile, and at the same time enhance passenger comfort.⁶ The TEMS is basically a road stability sensor and shock adjustor, which detects bumps, dips, rough pavement, and sudden lurches by the vehicle, then rapidly adjusts the shock absorbers to apply a softer or firmer damping force, depending on what is necessary to minimize discomfort while maintaining control of the vehicle. The shock absorbers are continuously readjusted as the road conditions change so that rocking or wobbling on soft shocks is eliminated.

A cross-section view of the shock absorber is shown in Fig. 5. The road surface sensor consists of a five-layer piezoelectric sensor mounted on the piston rod of the shock absorber. When a bump in the road is encountered, the resulting stress applied to the sensor produces a voltage which is fed into an electronic control unit that amplifies the signal and supplies a high voltage to the piezoelectric actuator. The 88-layer PZT actuator produces a 50- μm displacement on the oil system which is hydraulically enlarged to 2 mm, enough to change the damping force from firm to soft; the entire process takes only about 20 ms (not even enough time to slam on the brakes). Also figured into the actuator output are the vehicle speed and the



Ceramics and composites which fall into the category of "smart" materials, clockwise from top: rubber-encased piezoelectric cable; tunable transducer consisting of PZT disks and a rubber-metal laminate between brass plates; PLZT helix with shape-memory capabilities; stress-transforming piezoelectric "moonie" composite (imbedded in resin); 1-3 PZT rod-epoxy resin hydrophone composite; and conductive composite chemical sensor elements (Photograph by Joseph Kearns, Materials Research Laboratory, Pennsylvania State University.)

driver's preference for a generally softer (American) or firmer (European) ride.

Alternatively, it is possible to damp stresses and vibrations without the need for a sensor-actuator feedback loop; materials which can perform this function are called passive damping materials. In a piezoelectric passive damper, a piezoelectric ceramic is connected in parallel with a properly matched resistor. The external stress creates a polarization in the piezoelectric, which induces a current in the resistor, leading to energy dissipation. A high piezoelectric coupling coefficient is required to induce the maximum voltage and energy dissipation.⁷

VII. Actuator Materials

There are many approaches to controlling vibration and structural deformation. Actuation strain can be controlled by piezoelectric materials,⁸ electrostrictive materials,⁹ magnetostrictive materials,¹⁰ shape-memory metal alloys,¹¹ and thermally controllable materials.¹² Using a system with distributed actuators, it is possible to design structures with intrinsic vibration and shape-control capabilities. Among the most important actuator materials are shape-memory metals and ceramics. The shape-memory effect is exhibited by alloys which undergo thermoelastic martensite transformations. This is a first-order displacive transformation in which a body-centered cubic metal transforms by shear on cooling to a martensitic phase. When deformed in the martensitic low-temperature phase, shape-memory alloys recover this deformation and return to the original shape when heated to a temperature where the martensite reverts back to the parent body-centered cubic structure. Unlike most ferroelectric and ferromagnetic transitions, the shape-memory transformation has a large hysteresis which can be troublesome in practice.

Alloys exhibiting the shape-memory effect fall into two general classes: non-ferrous and ferrous. Non-ferrous shape-memory alloys currently in commercial use are Ni-Ti, Cu-Zn-Al, and Cu-Ni-Al. Ferrous shape-memory alloys under development include Fe-Pt, Fe-Ni-C, and Fe-Ni-Co-Ti.

Non-ferrous shape-memory alloys of Ni-Ti alloy (Nitinol) have been developed by Goodyear Aerospace Corporation (Akron, OH) for spacecraft antennae.¹³ A wire hemisphere of the material is crumpled into a tight ball, less than 5 cm across. When heated above 77°C, the ball opens up into its original shape—a fully formed antenna. Although it has been seldom used in service, this antenna demonstrates the magnitude of deformation and reformation possible in shape-memory alloys.

Although shape-memory alloys are more of a solution looking for a problem, it has been suggested that transient and steady-state vibration control can be accomplished with hybrid structures in which the shape-memory alloy is embedded inside the material.¹³

Some ceramic materials also possess a sizeable shape-memory effect: of particular interest are materials which are simultaneously ferroelectric and ferroelastic. Their ferroelasticity ensures that recoverable spontaneous strain is available for contributing to the shape-memory effect, and the ferroelectricity implies that their spontaneous strain can be manipulated not only by mechanical forces but also by electric fields.

Shape memory has been demonstrated in lead lanthanum zirconate titanate (PLZT) ceramics. PLZT is an important ferroelectric-ferroelastic because of the tremendous potential for applications due to the formation of microdomains smaller than the wavelength of light. In one experiment, a 6.5/65/35 PLZT helix was heated to 200°C, well above the transition temperature for recovery ($T_f (= T_c)$), mechanically loaded, then cooled to 38°C (well below T_f)—the "brittle" PLZT helix was deformed by 30% after the load was removed. Upon heating to 180°C (above T_f), the helix transformed back to its original shape, dramatically demonstrating the shape-memory effect in brittle ceramics.¹⁴

Researchers at Sophia University in Tokyo have created a multilayer shape-memory actuator with a $(\text{Pb}, \text{Nb})-(\text{Zr}, \text{Sn}, \text{Ti})\text{O}_3$ ceramic. Twenty rectangular plates of the ceramic are stacked in a multilayer ceramic capacitor-type (MLCC) structure; the magnitude of the strains (3 to 4 μm) that are induced are small by comparison to most shape-memory alloys but are 3 times larger than the strains produced using conventional piezoelectric actuators. In this case, a ferroelectric to antiferroelectric phase change is responsible for the shape change.¹⁵

VIII. Electrorheological Fluids

One of the criteria which separates smart materials from very smart or intelligent materials is the ability of the material to not only sense a change and actuate a response, but to automatically modify one or more of its property coefficients during the sensing-actuating process. In effect, this type of material not only warns the user of a change in its environmental conditions and responds to it, but can, in addition, adjust itself to compensate for future change.

Electrorheological (ER) fluids¹⁶ and their magnetic analog, ferrofluids,¹⁷ are an example of materials that have great potential for use in smart ma-

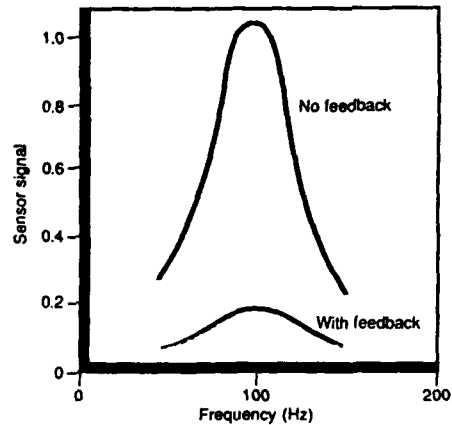


Fig. 4. Reduced subsonic reflectance from smart piezoceramic.

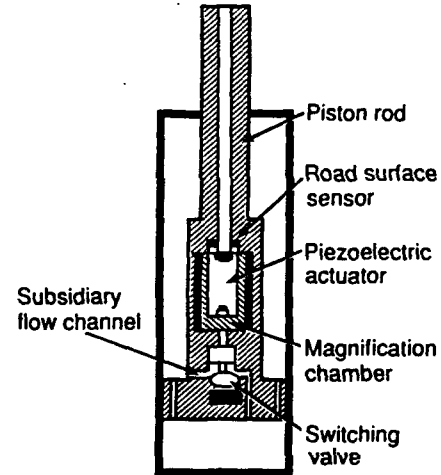


Fig. 5. Cross section of the principal portion of the shock absorber.⁶

terials and systems. ER fluids are typically suspensions of fine particles in a liquid medium; the viscosity of the suspension can be changed dramatically by applying an electrical field. The electric field causes alignment of the particles in fibrillike branches in the direction of the applied field. The alignment disappears when the electric field is removed, thus creating the desired property of complete cyclic reproduc-

bility. Figure 6 shows the microstructure of an ER fluid before and after the application of an electric field.

ER fluids represent an advanced class of composite materials with self-tuning properties that will find considerable use in vibration control applications. In addition, the compatibility of this technology with modern solid-state electronics makes it an attractive component for integration into

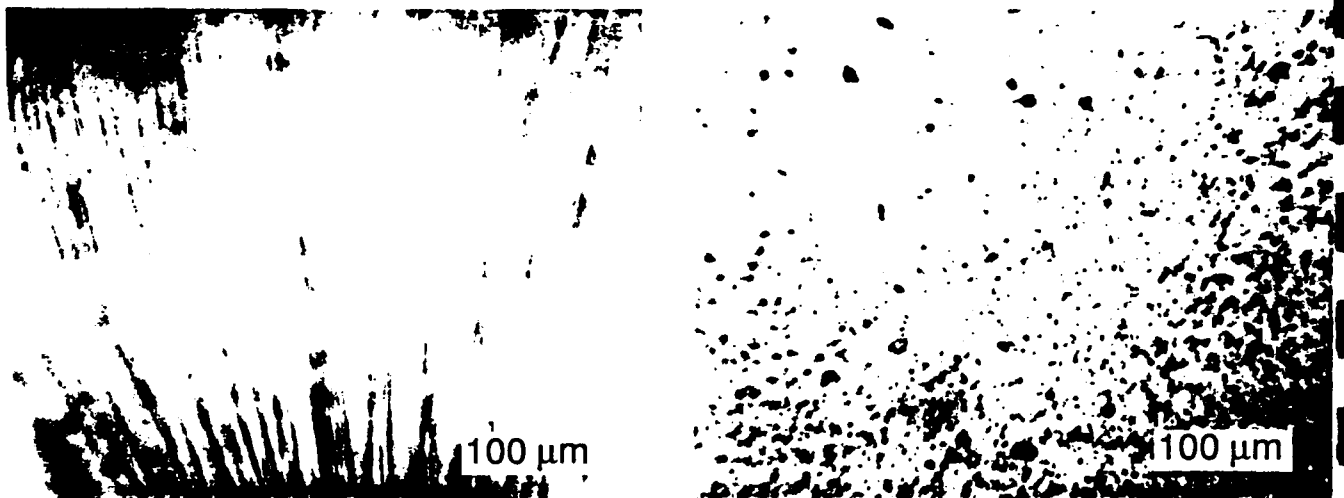
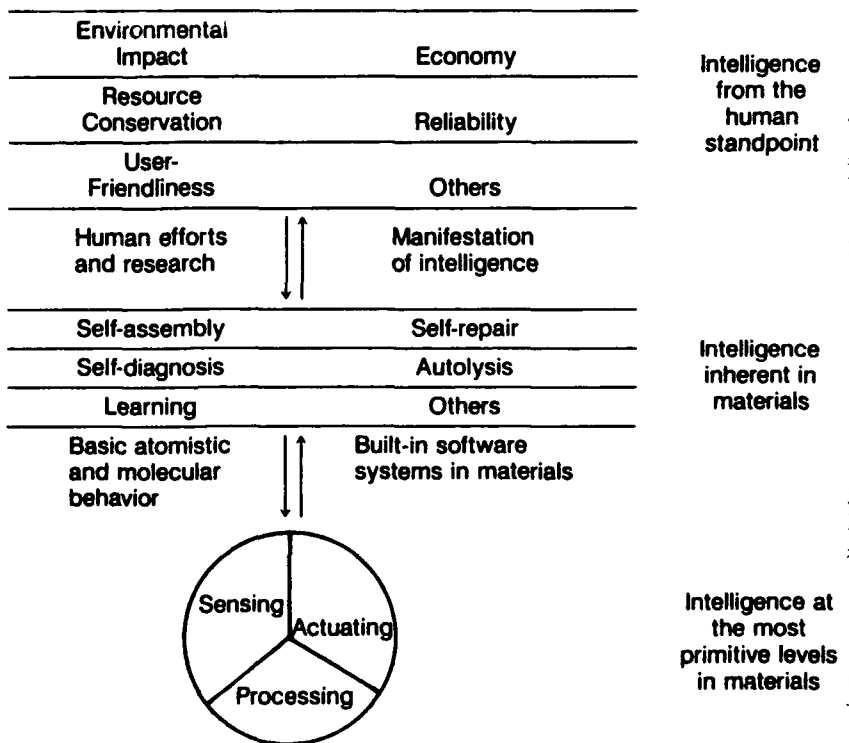


Fig. 6. Optical micrograph of a dispersion of fine particles in ER fluid (A) with no field applied and (B) with an applied direct current bias. (Photograph courtesy of Dr. C. A. Randall, Materials Research Laboratory, Pennsylvania State University.)

Panel I. The Concept of Intelligent Materials—A Japanese Perspective

The development of "intelligent materials" according to the Japanese is a result of understanding the relationship between intelligence from the human standpoint, intelligence inherent in materials, and intelligence at the most primitive levels in materials, as illustrated above.³ Intelligence from the human standpoint is a relative concept, based on the value of a material and its utility in relation to all aspects of society—environmental impact, economy, resource conservation, reliability, etc. Intelligence inherent in materials includes those material properties which may or may not have yet been discovered by humans, regardless of their impact on society; these properties are independent of their evaluation and utilization by man. The primitive functions of intelligence are elementary functions of sensing, processing, and effecting (actuating), all of which must work systematically together to create an intelligent material. Interestingly enough, for every bit of intelligence inherent in inorganic materials, there is a biological analog.



Schematic representation of intelligent materials. Ability of humans to produce intelligent materials is simply a matter of recognizing the intelligence that already exists in materials. It is through the recognition of the intelligence inherent in materials that we will be able to develop a fundamental understanding of the primitive functions of intelligence, and it is at this level that the origins of all the puzzling problems confronting man can be solved.

Panel II. The Replamineform Process—Replicating Nature

Despite the sophistication of modern technology, it often seems that mankind lags behind Mother Nature in producing high-precision, carefully structured materials. Coral skeletons are characterized by (i) a narrow pore-size distribution, (ii) a pore volume approximately equal to the solid-phase volume, and (iii) complete pore interconnectivity making every pore accessible from all other pores. The diameter of the pores/channels varies from species to species, and some types of coral

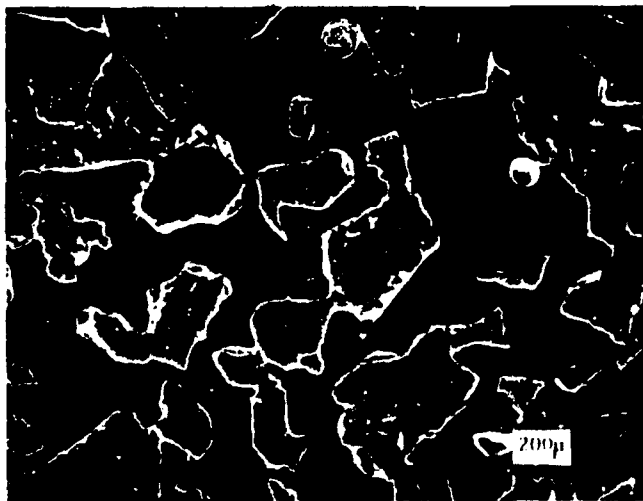
exhibit anisotropy as well, ranging from a 3-1 type connectivity with nearly parallel tubes to highly isotropic 3-3 structures. These features in coral make it an attractive template for making composite biomaterials and transducers.

A method called the replamineform process²⁰ has been developed for reproducing the microstructure of coral in metals, ceramics, and polymers. In the replamineform process, a piece of coral is vacuum-impregnated with wax which is

allowed to harden; the calcium carbonate coral skeleton is leached away with hydrochloric acid, leaving a solid wax negative of the structure. To make transducers, this negative is then reinvested with a lead zirconate titanate (PZT) slip by vacuum impregnation. When the wax negative is burned off at 300°C, a coral-type PZT structure is left. This can be sintered with only minimal (~13%) linear shrinkage, producing a robust PZT skeleton.

Further processing of the skeleton for transducer applications consists of backfilling the PZT with a highly flexible elastomer material, such as silicone rubber. After poling the PZT, the composite can be crushed to yield a highly flexible transducer with low permittivity, or maintained as a rigid solid to be used as a low-density, high-coupling resonator.²¹

Another similar but simpler method of producing porous PZT involves mixing plastic spheres with PZT powder²² then carefully sintering the mixture; this is commonly referred to as the BURPS (burned-out plastic spheres) process. The sintered PZT skeletons can be backfilled with elastomer to produce the same types of composites as with the replamineform process, only with controllable variations on the 50/50 PZT/polymer ratio.



SEM micrograph of wax-impregnated coral. Both the pillars of coral (light sections) and pore channels (dark areas) are connected in three dimensions.

multiplication, self-contained smart material packages.

IX. Biomimetics—Fish Ears

The word "biomimetic" is not found in most dictionaries; therefore, it needs to be defined. It comes from the Greek words "bios," meaning "life," and "mimetikos," meaning "to imitate." Biomimetic means to imitate life, or to use the biological world as a source of ideas for device concepts.

Fish and the other inhabitants of the underwater world have some interesting ways of talking and listening which have been copied using piezoelectric ceramics. Our first composite transducer is copied from coral using a lost-wax process (see Panel II).

For most fish, the principal sensors are the *lateral line* and the *inner ear* coupled to the *swim bladder*. The pulsating swim bladder also acts as a voice, as do chattering teeth in certain fish species.

The lateral line runs from the head to the tail of the fish and resembles a towed array with sensing organs (stitches) spaced at intervals along the nerve fiber. Each stitch contains sev-

eral neuromasts made up of gelatinous cupulae resembling pimples in shape (Fig. 7). Within each cupula are a number of fibers that vibrate as the fish swims through the water and that act as sensors for flow noise. The hairlike fibers are extremely thin in diameter, ranging from 0.5 to 10 μm. When stimulated by turbulence, the motion of the hairs produces changes in the synapses which are in turn connected to the nerve fiber. The electric signal originates from impedance changes in cell walls which modulate the flow of K⁺ ions. The lateral line is especially sensitive to low-frequency fluid motion parallel to the length of the fish. In the 50-Hz range, threshold signals are observed for displacements as small as 30 nm!^{18,19}

The 1-3 composite hydrophones described later are patterned after the hair-filled cupulae of the lateral line. Thin PZT fibers embedded in polymer provide excellent electromechanical coupling to a liquid medium and can be used as both sensors and actuators.

X. Dr. Dolittle and Fish Talk

Among the most popular children's

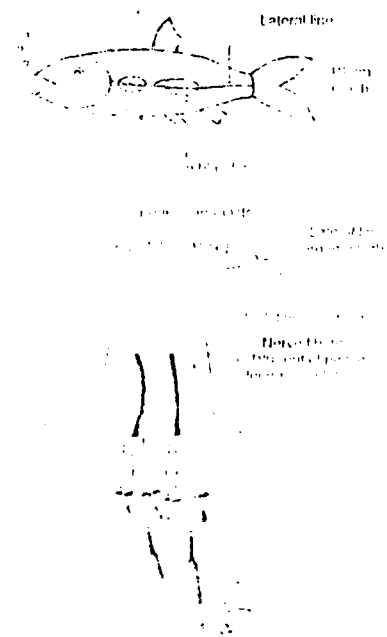


Fig. 7. "Hearing" organs in fish. Lateral line is a series of "stitches," each composed of nerve fibers enclosed in gelatinous cupulae.¹⁶

books of all time are the Doctor Dolittle books written by Hugh Lofting. Doctor Dolittle could talk to the animals. He started with "Pig" and went on to "Duck" and "Cow," and eventually mastered 498 languages. There is a marvelous scene in the movie where young Tommy Stebbins meets Dr. Dolittle in his laboratory:

But the most remarkable thing in the room was the Doctor himself. In some ways, John Dolittle looked very much like an ordinary doctor. He wore a white medical coat and was using a stethoscope. But, the stethoscope was attached only to his right ear, and his patient seemed to be a goldfish in a bowl!

Tommy watched in amazement as the Doctor blew bubbles into the fish bowl through a rubber tube. Between bursts of bubbles he pressed the stethoscope against the bowl and listened intently. Then he actually dipped his left ear in the water!

"Bllrrp!" said Dr. Dolittle, forgetting about the tube. "Tommy! How good to see you! I'm so busy learning Goldfish that I didn't hear you come in. Most exciting this goldfish language. But very difficult—and quite damp."

In recent years, great advances have been made in recording and understanding fish talk, largely because of the development of improved hydrophone arrays and high-speed spectrum analyses. Sound functions in a variety of ways for fish, both in offense and in defense, for warning and intimidation. Many fish speak differently dur-

ing breeding season, and appear to use coded repetition rates to communicate. Our ability to "farm the oceans" could be greatly enhanced by learning how to talk with fish and control their movements and feeding habits. An example of fish talk is shown in Fig. 8.

Although they do not possess a larynx, many species of fish produce high-pitched sound by grinding their teeth, but the vibration of the swim bladder wall provides the greatest repertoire of noises or calls. The croakers of Chesapeake Bay make tapping noises like a woodpecker, by contracting their drumming muscles attached to the swim bladder, and the twilight choruses of sea robins caused great confusion among the operators of anti-submarine echo-location devices during World War II.²⁴

XI. Inner Ears and Swim Bladders

The nature of sound transmission in water has had a great influence on the evolution of hearing in fish. Sound, especially low-frequency sound, travels faster and farther in water than in air. "Near-field" sound consists of small fluid motions or vibrations and are characterized by a displacement direction. They are detected by the inner ear or by the lateral line. The hydrostatic component or "far-field" sound is detected best through the swim bladder.

The inner ear is made up of inertia-sensing chambers resembling accelerometers. Within each chamber is a dense ear stone (otolith) which vibrates in a near-field sound wave (Fig. 9(A)). The inertia of the ear stone causes it to lag behind the motion of the fish, and to push against hair cells which line the chamber (sacculus). On bending, the hair cellular membranes deform, stimulating neural transmissions to the brain. Connections to the swim bladder improve the sensitivity to far-field sound (Fig. 9(B)).

The primary function of the gas-filled swim bladder is to provide buoyancy, but it is also used for sound and pressure reception and in some species is equipped with drumming muscles for sound production (see Fig. 8).

The flexible swim bladder responds to hydrostatic pressure waves by changing volume. Fish with swim bladders can perceive relative pressure changes equivalent to less than 0.5% of the ambient hydrostatic pressure.

Direct or indirect linkages from the swim bladder to the inner ear promote the hearing sensation. Fish with no connections perceive low-frequency sound (less than 500 Hz), whereas those with good connections have an upper frequency response of 5000 Hz. As might be expected, the swim bladder is reduced in size with depth, and loses much of its sensitivity as a sensor.

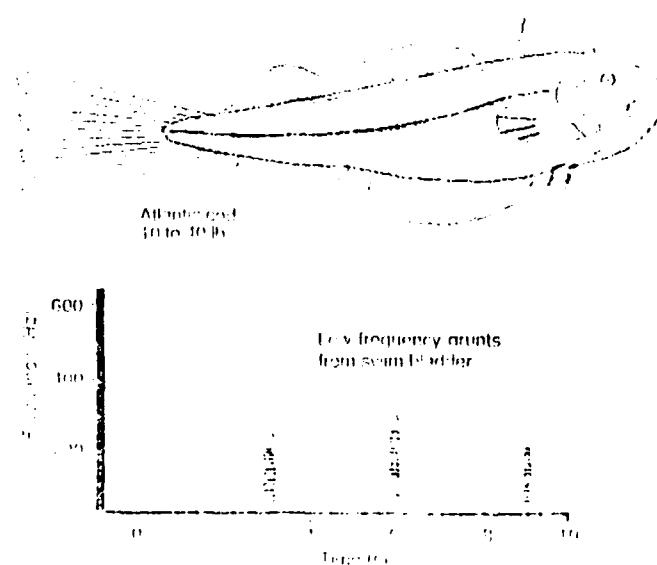


Fig. 8. Sound spectrum of the Atlantic cod. The cod speaks in a series of loud, low-frequency grunts peaking at 500 Hz, with a duration of about 2 s, and repeated three or four times to intimidate intruders and stimulate females. Grunts, growls, and thumps originate from a well-developed swim bladder with many muscle-covered side lobes.²³

XII. Hydrophone Materials

The knowledge which comes from the understanding of "fish talk" can be directly applied to research in materials destined to someday "sleep with the fishes." Hydrophones are underwater listening devices made from piezoelectric materials which respond to hydrostatic pressure waves. Among the applications for hydrophones are sonar systems for submarines, offshore oil platforms, geophysical prospecting equipment, fish finders, and earthquake monitors.

As the earth's population continues to increase, the human race must continue to search for new and efficient sources of food and nutrition. The world's oceans may provide a solution to this problem, not only through fish farming but through the use of new and varied saltwater vegetation that could provide an abundant source of food, especially for third-world countries in which poor soil and harsh climates prohibit conventional farming. Smart hydrophone transceivers could receive and transmit fish talk and monitor the growth of underwater vegetation.

The figure of merit for hydrophone materials is the product of the hydrostatic piezoelectric charge coefficient (d_{31}) and the piezoelectric voltage coefficient (g_h). Although good piezoelectric materials such as PZT have high d_{33} and d_{31} piezoelectric coupling coefficients, the d_{31} value is only about 45 pC/N because d_{33} and d_{31} are opposite in sign, and $d_{31} = d_{33} + 2d_{31}$. $d_{31}g_h$ is also inversely related to the dielectric permittivity (ϵ_{33}), so that low dielectric constants are desirable as well.

Rather than abandon PZT in search of the ultimate hydrophone material, we can avoid the problem of the search by clever (=smart?) engineering of existing materials. Too often in the field of materials research we put too much

emphasis on the synthesis of new materials and too little emphasis on new and unique designs for old materials.

A composite design with 1-3 connectivity is similar in design to the hair-filled gelatinous cupula with thin PZT rods embedded in a polymer matrix. (For a discussion of composites in general, see Panel III.) The 1-3 piezocomposites have excellent sensitivity to pressure waves in water.^{25,26} The large d_{33} value is maintained because the parallel connection results in stress transfer from polymer to piezoceramic, whereas the d_{31} value is destroyed because of series connection in the lateral dimension where the mechanical load is absorbed by the polymer and not transferred to the PZT rods. Finally, ϵ_{33} is minimized because of the large volume of low- ϵ_{33} polymer present. Figure 10 shows the results of the high $d_{31}g_h$, possible, particularly when very thin rods are used.

Another piezoelectric hydrophone composite maximizes d_{31} by simply redirecting the applied stresses using specially shaped electrodes.²⁷ These are flexextensional transducers which mimic the motions of the swim bladder. Shallow air spaces are positioned under the metal electrodes while the PZT ceramic plays the role of the muscle lining the swim bladder. The geometry of these composites, known as "moonies" because of the crescent-shaped cavities, is shown in Fig. 11. When subjected to a hydrostatic stress due to waves, the thick metallic electrodes convert a portion of the z-direction stress into large radial and tangential stresses of opposite signs. The result is that d_{31} changes from negative to positive, so that its contribution now adds to d_{33} rather than subtracting from it. The $d_{31}g_h$ of these composites is approximately 250 times that of pure PZT.

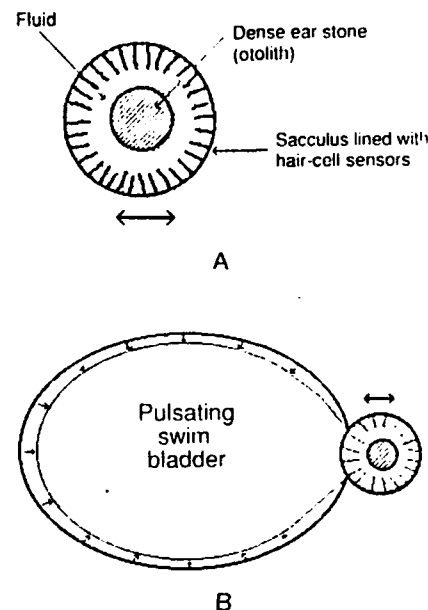


Fig. 9. Structure of the inner ear of a fish, characterized by separate mechanisms for (A) near-field and (B) far-field sensitivities.

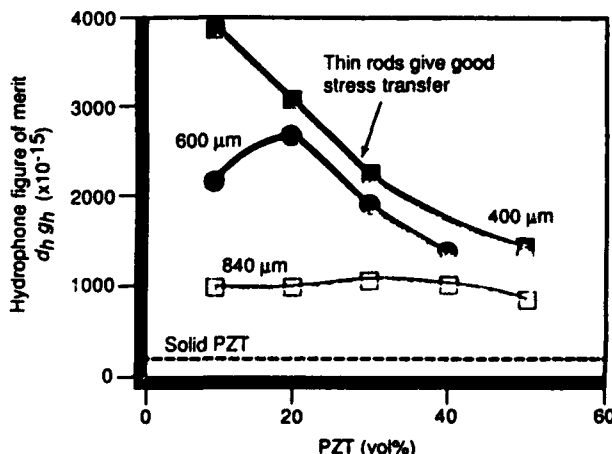


Fig. 10. Figure of merit for 1-3 PZT ceramic-polymer hydrophone composites, comparing rods of different thickness with solid PZT.²⁵

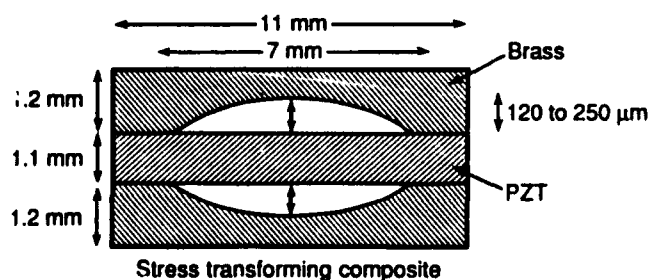


Fig. 11. Geometry of the "moonie" composite, designed to redirect applied stresses. Design is fashioned after the fish swim bladder and functions in a flexextensional mode.

XIII. Underwater Actuation

Using composite designs similar to the PZT fiber and moonie designs, several interesting underwater actuators are being tested. A major goal is the elimination of turbulence and flow noise to achieve streamline flow. The following techniques have been suggested to alter skin friction:²⁸ polymer additions, microbubbles, compliant walls, bursting, coatings, spot forcing, ripples, convex curvature, and outer-

layer devices. Several of these ideas are ideally suited to smart ceramics with sensor-feedback-responder combination. Ink jets could be used to supply microbubbles to dampen sublayer disturbances, or polymer molecules to replenish a surface coating. Bursting is controlled in a similar way by injecting pressure pulses into the fluid stream with a piezopump.

Compliant walls would be flexible surface coating, repositioned with

Panel III.

Composite materials may be defined as two or more dissimilar materials combined to optimize the properties of the composite. Some of the principal ideas governing the properties of composites are as follows:²⁹

(1) *Sum properties* involve the averaging of similar properties in the component phases, with the mixing rules bounded by the series and parallel models. For a simple sum property such as the dielectric constant, the dielectric constant of the composite lies between those of the individual phases. This is not true for combination properties based on two or more properties. Acoustic velocity depends on stiffness and density, and, since the mixing rules for these two properties are often different, the acoustic velocity of a composite is sometimes smaller than those of its constituent phases.

(2) *Product properties* are even more complex because three properties are involved: different properties in the two constituents combine to yield a third property in the composite. In a magnetoelectric composite, for instance, the piezoelectric effect in barium titanate acts on the magnetostrictive effect of cobalt ferrite to produce a composite magnetoelectric effect.

(3) *Connectivity patterns* are a key feature of composite electroceramics. The self-connectiveness of the phases determines whether series or parallel models apply, and thereby minimize or maximize the properties of the composite. The three-dimensional nature of the connectivity patterns makes it possible to minimize some tensor components while maximizing others. Piezoelectric composites made from parallel ferroelectric fibers have large d_{33} values and small d_{31} values. In general, X-Y connectivity refers to one phase self-connected in X dimensions, the other phase self-connected in Y dimensions. Designation of the X phase and Y phase is arbitrary, but must be defined in each

Ten Commandments of Functional Composites

case.

(4) *Concentrated field and force patterns* are possible with carefully selected connectivities. Using internal electrodes, electrostrictive ceramics are capable of producing strains comparable to the best piezoelectrics. Stress concentration is achieved by combining stiff and compliant phases in parallel. A number of different structural engineering designs are based on this principle.

(5) *Periodicity and scale* are important factors when composites are to be used at high frequencies where resonance and interference effects occur. When the wavelengths are on the same scale as the component dimension, the composite no longer behaves like a uniform solid. The colorful interference phenomena observed in opal and feldspar minerals are interesting examples of natural composites. Acoustic analogs occur in the lead zirconate titanate (PZT)-polymer composites used as biomedical transducers.

(6) *Symmetry* governs the physical properties of composites just as it does in single crystals. The Curie principle of symmetry superposition and Neumann's law can be generalized to cover fine-scale composites, thereby elucidating the nature of their tensor properties. As in the case of magnetoelectric composites, sometimes the composite belongs to a symmetry group which is lower than any of its constituent phases. Unexpected product properties occur under such circumstances.

(7) *Interfacial effects* can lead to interesting barrier phenomena in composites. ZnO-Bi₂O₃ varistors and carbon-polymer positive temperature coefficient thermistors are important examples of Schottky barrier effects. Barrier layer capacitors made from conducting grains separated by thin insulating grain boundaries are another example.

(8) *Polychromatic percolation* is an interesting concept which has yet to be fully explored. Composites fabricated from two or more con-

ducting phases can have several kinds of transport paths, both single phase and mixed, depending on percolation limits and volume fractions. Carbon-PZT-polymer composites can be poled because polychromatic percolation establishes flux continuity through ferroelectric grains. The SiC-BeO composites under development as substrate ceramics are another example. These diphasic ceramics are excellent thermal conductors and poor electrical conductors at one and the same time. A thin layer of BeO-rich carbide separates the SiC grains, insulating them from one another electrically, but providing a good acoustic impedance match ensuring phonon conduction.

(9) *Coupled phase transformations* in polyphasic solids introduce additional possibilities. Recently discovered NTC-PTC composites made from V₂O₃ powder and embedded in poly(ethylene) combine matrix and filler materials with complementary properties. At low temperatures the V₂O₃ particles are in a semiconducting state and in intimate contact with one another. On passing through a semiconductor-metal transition, the electrical conductivity increases by 5 orders of magnitude. Further heating brings the polymer to a phase transformation, causing a rapid expansion in volume, and pulling the V₂O₃ particles apart. As a consequence the electrical conductivity decreases dramatically by 8 orders of magnitude.

(10) *Porosity and inner surfaces* play a special role in many electroceramic composites used as sensors. Humidity sensors made from Al₂O₃ and LiF have high inner surface area because of thermally induced fracture. The high surface area and hygroscopic nature of the salt result in excellent moisture sensitivity of the electrical resistance. Chemical sensors based on similar principles can be constructed in a similar manner.

piezoelectric or electrostrictive actuators to smooth out the flow pattern and eliminate flow noise. Spot forcing can be accomplished by localized heating beneath the surface. In this case the responding actuator is a patterned composite resistor.

The remaining methods of reducing drag are mainly passive in nature, although they could be combined with a compliant wall. Semipermeable water-absorbing coatings prevent pressure buildup, allowing molecular interchange between the fluid and wall. Riblets and convex curvature also act to streamline flow, as do the streamlined outer-layer devices called OLDs. Carefully designed geometries like this can be built into smart ceramics.

XIV. Very Smart Composites: The Tunable Transducer

By building-in a learning function, the definition of a smart material can be extended to a higher level of intelligence: A very smart material senses a change in the environment and responds by changing one or more of its property coefficients. Such a material can tune its sensor and actuator functions in time and space to optimize future behavior. With the help of a feedback system, a very smart material becomes smarter with age, something even human beings strive for. The distinction between smart and very smart materials is essentially one between linear and nonlinear properties. The physical properties of nonlinear materials can be adjusted by bias fields or forces to control response.

To illustrate the concept of a very smart material, we describe the tunable transducer recently developed in our laboratory. Electromechanical transducers are used as fish finders, gas igniters, ink jets, micropositioners, biomedical scanners, piezoelectric transformers and filters, accelerometers, and motors.

Five important properties of a transducer are the resonant frequency (f_r), acoustic impedance (Z_A), mechanical damping coefficient (Q), electromechanical coupling factor (k), and electrical impedance (Z_E). The resonant frequency and acoustic impedance are controlled by the elastic constants and density, as discussed in the next section. The mechanical Q is governed by the damping coefficient (α) and is important because it controls "ringing" in the transducer. Definitions of the coefficients are given in Panel IV. Electromechanical coupling coefficients are controlled by the piezoelectric coefficient which, in turn, can be controlled and fine-tuned using relaxor ferroelectrics with large electrostrictive effects. The dielectric "constant" of relaxor ferroelectrics depends markedly on direct-current bias fields, allowing the

electrical impedance to be tuned over a wide range as well. In the following sections we describe the nature of nonlinearity and how it controls the properties of a tunable transducer.

XV. Elastic Nonlinearity: Tuning the Resonant Frequency

Information is transmitted via electromagnetic waves in two ways: amplitude modulation (AM) and frequency modulation (FM). There are a number of advantages to FM signal processing, especially where lower noise levels are important. Atmospheric static is considerably lower in FM radio than in AM radio.

Signal-to-noise ratios are also important in the ultrasonic systems used in biomedical and nondestructive testing systems, but FM is difficult because resonant frequencies are controlled by stiffness (c) and (transducer) dimensions (t). Neither stiffness, dimensions, nor the density (ρ) can be tuned significantly in ceramics and most other materials, but they can be tuned in rubber. To tune the resonant frequency of a piezoelectric transducer, we designed and built a composite transducer incorporating thin rubber layers exhibiting nonlinear elasticity.³⁰

Rubber is a highly nonlinear elastic medium. In the unstressed compliant state, the molecules are coiled and tangled, but under stress the molecules align and the material stiffens noticeably (Fig. 12). Experiments conducted on rubber-metal laminates demonstrate the size of the nonlinearity. Young's modulus ($E=1/s_{1111}$) was measured for a multilayer laminate consisting of alternating steel shim and soft rubber layers each 0.1 mm thick. Under compressive stresses of 200 MPa, the stiffness is quadrupled from about 600 to 2400 MPa.³¹ The resonant frequency (f_r) is therefore doubled, and can be modulated by applied stress.

Rubber-like smart electroceramic is not predictable to have a tuning of the elastic nonlinearity, it is therefore necessary to construct a composite transducer consisting of a piezoelectric ceramic (PZT) transducer, thin rubber layers, and metal head and tail masses, all held together by a stress bolt.

The resonant frequency and mechanical Q of such a sandwich structure was measured as a function of stress bias (Fig. 13). Stresses ranged from 20 to 100 MPa in the experiments. Under these conditions the radial resonant frequency changed from 19 to 27 kHz, increasing in frequency by approximately 50% as predicted from the elastic nonlinearity. At the same time the mechanical Q increased from about 11 to 34 as the rubber stiffened under stress.

Panel IV. Important Characteristics of an Electromechanical Transducer

The fundamental resonant frequency (f_r) of the thickness mode is

$$f_r = \frac{1}{2t} \sqrt{c/\rho}$$

where t is the thickness dimension, c the elastic stiffness, and ρ the density.

The acoustic impedance (Z_A) is

$$|Z_A| = \sqrt{\rho c}$$

The mechanical Q is

$$Q = \pi/\lambda_s \alpha$$

where λ_s is the acoustic wavelength and α the damping coefficient.

The electromechanical coupling coefficient (k) is

$$k = d\sqrt{c/\epsilon}$$

where d is the piezoelectric charge coefficient and ϵ the electric permittivity.

The electrical impedance (Z_E) is

$$|Z_E| = l/\omega A$$

where ω is the angular frequency and A the electrode area.

The changes in resonance and Q can be modeled with an equivalent circuit in which the compliance of the thin, rubber layers is represented as capacitors coupling together the larger masses (represented as inductors) of the PZT transducer and the metal head and tail masses. Under low stress bias, the rubber is very compliant and effectively isolates the PZT transducer from the head and tail masses. At very high stress, the rubber stiffens and tightly couples the metal end pieces to the resonating PZT ceramic. For intermediate stresses the rubber acts as an impedance transformer giving parallel resonance of the PZT-rubber-metal-radiation load.

Continuing the biomimetic theme, it is interesting to compare the change in frequency of the tunable transducer with the transceiver systems used in the biological world. The biosonar system of the flying bat is similar in frequency and tunability to our tunable transducer. The bat emits chirps at 30 kHz and listens for the return signal to locate flying insects. To help it differentiate the return signal from the outgoing chirp, and to help in timing the echo, the bat puts an FM signature on the pulse. This causes the resonant frequency to decrease from 30 to 20 kHz near the end of each chirp. Return signals from the insect target are detected in the ears of the bat where neural cavities tuned to this frequency range measure the time delay and flutter needed to locate and identify its prey. Extension of the bat biosonar principle to automotive, industrial, medical, and entertainment systems is underway.

XVI. Piezoelectric Nonlinearity: Tuning the Electromechanical Coupling Coefficient

The difference between a smart and a very smart material can be illustrated with piezoelectric and electrostrictive ceramics. PZT is a piezoelectric ceramic in which the ferroelectric domains have been aligned in a very large poling field. Strain is linearly proportional to the electric field in a fully poled piezoelectric material which means that the piezoelectric coefficient is a constant and cannot be electrically tuned with a bias field. Nevertheless it is a smart material because it can be used both as a sensor and an actuator.

Lead magnesium niobate (PMN) is not piezoelectric at room temperature because its Curie temperature is near 0°C. Because of the proximity of the ferroelectric phase transformation, however, and because of their diffusive nature, PMN ceramics exhibit very large electrostrictive effects. The nature of this large nonlinear relationship between strain and electric field, and of its underlying atomistic origin, will be described later.

Electromechanical strains comparable to PZT can be obtained with electrostrictive ceramics similar to PMN, and without the troubling hysteretic behavior shown by PZT under high fields. The nonlinear relation between strain and electric field in electrostrictive transducers can be used to tune the piezoelectric coefficient and the dielectric constant.

The piezoelectric d_{33} coefficient is the slope of the strain-electric field curve when strain is measured in the same direction as the applied field. Its value for $\text{Pb}(\text{Mg}_{0.3}\text{Nb}_{0.6}\text{Ti}_0)_3\text{O}_3$ ceramics is zero at zero field and increases to a maximum value of 1300 pC/N (about 3 times larger than PZT) under a bias field of 3.7 kV/cm (Fig. 14).

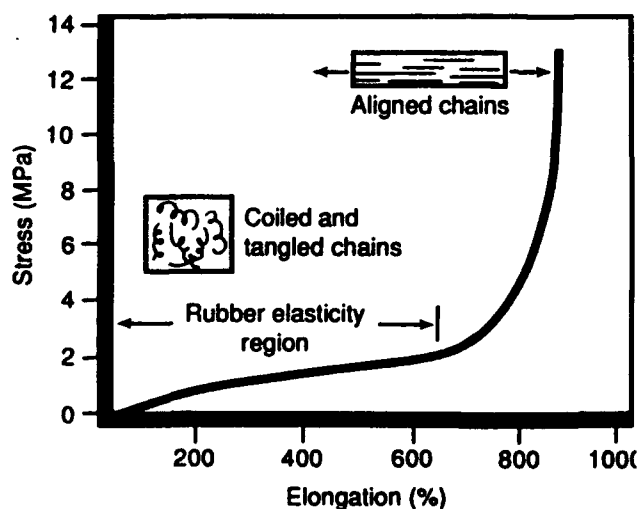


Fig. 12. Stress/strain behavior of rubber. Elasticity is highly nonlinear in rubber which is extremely compliant under small stresses, but stiffens noticeably when the rubber molecules align under large stresses.

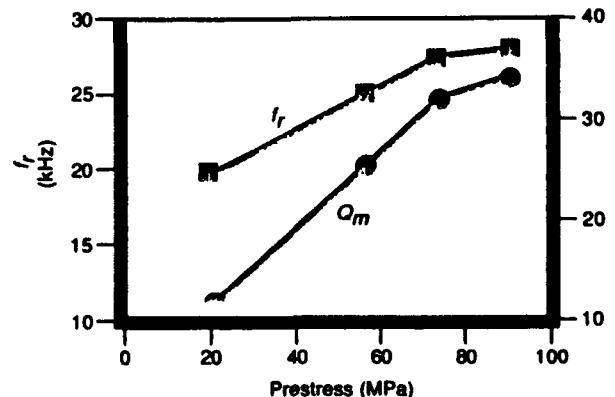


Fig. 13. Stress dependence of resonant frequency and mechanical Q.

This means that the electromechanical coupling coefficient can be tuned over a very wide range, changing the transducer from inactive to extremely active. The dielectric constant also depends on direct-current bias. The polarization saturates under high fields causing decreases of 100% or more in the capacitance. In this way the electrical impedance can be controlled as well.

Electrostrictive transducers have already been used in a number of applications including adaptive optic systems, scanning tunneling microscopes, and precision micropositioners.⁹

To summarize, two types of nonlinearity are utilized in the fully tunable transducer: elastic nonlinearity and piezoelectric nonlinearity. By incorporating thin rubber layers in an electrostrictive transducer, several important properties can be optimized with bias fields and bias stresses. Electromechanical coupling coefficients and electric impedance are tuned with electric field, and mechanical damping, resonant frequency, and acoustic impedance with stress bias.

XVII. Origins of Nonlinearity

What do nonlinear materials have in common? The passively smart PTC thermistor and ZnO varistor have grain boundaries a few nanometers thick, insulating barriers that can be obliterated by the polarization charge accompanying a ferroelectric phase transformation, or, in the case of the varistor, insulating boundaries so thin that they can be penetrated by quantum mechanical tunneling.

Small size is also a key factor in the nonlinear behavior of semiconductors. The thin gate region in a transistor allows charge carriers to diffuse through unimpeded. The *p* region in an *n-p-n* transistor is thin compared with the electron diffusion length in single-crystal silicon. Similar size-related phenomena are observed in quantum well structures made from GaAs and $\text{Ga}_{1-x}\text{Al}_x\text{As}$, where planar structures with nanometer-thick layers show channeling behavior of hot electrons in clear violation of Ohm's law. *I-V* relationships are highly nonlinear in many submicrometer semiconductor structures. Ohm's law is a statistical law which relies upon the assumption that the charge carriers make a sufficiently large number of collisions to enable them to reach a terminal velocity characteristic of the material. When the size of the conduction is sufficiently small, compared with the mean free path between collisions, the statistical assumption breaks down, and Ohm's law is violated.

Nonlinear behavior is also observed in thin-film insulators where even a modest voltage of 1 to 10 V can result

in huge electric fields of 100 MV/m or more. This means that thin-film dielectrics experience a far larger field than do normal insulators, causing the polarization to saturate and electric permittivity to decline. Because of the high fields, electric breakdown becomes a greater hazard, but this is partly counteracted by an increase in breakdown strength with decreasing thickness. This comes about because the electrode equipotential surfaces on a thin-film dielectric are extremely close together, thereby eliminating the asperities that lead to field concentration and breakdown.

The influence of nanometer-scale domains on the properties of relaxor ferroelectrics has already been illustrated with PMN ceramics (Fig. 14). Here the critical size parameter is the size of the polarization fluctuations arising from thermal motions near the broad ferroelectric phase transformation in PMN and similar oxides. The ordering of magnesium and niobium ions in the octahedral site of the PMN structure results in a chemically inhomogeneous structure on a nanometer scale, and this, in turn, influences the size of the polarization fluctuations. Tightly coupled dipoles within each niobium-rich portion of this self-assembling nanocomposite behave like a superparaelectric solid. The dipoles are strongly coupled to one another but not to the crystal lattice, and thus they reorient together under the influence of temperature or electric field. This in turn causes the large electric permittivities and large electrostrictive effects found in relaxor ferroelectrics.

The importance of nanometer-scale fluctuations and the instabilities associated with phase transformations is

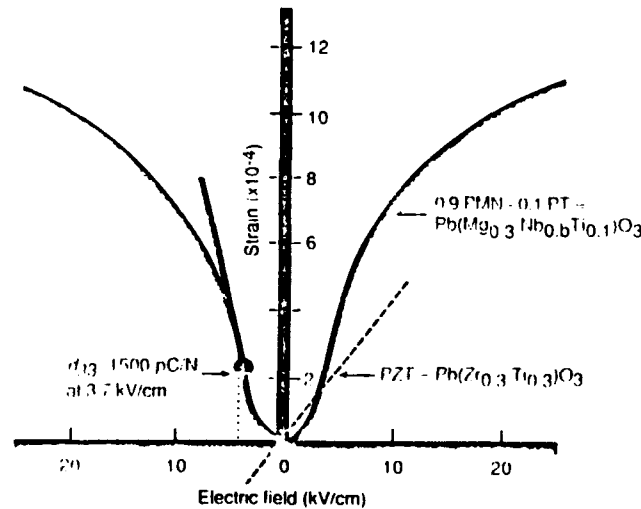


Fig. 14. Strains developed in lead magnesium niobate (PMN) ceramics. Electromechanical coupling coefficient of PMN can be tuned over a wide range with a direct current bias field.¹²

also apparent in the nonlinear elasticity of rubber and other polymeric materials. The thermally assisted movement of the randomly oriented polymer chains under tensional stress results in large compliance coefficients, but rubber gradually stiffens as the chains align with the stress into pseudocrystalline regions. The increase in stiffness with stress gives rise to sizeable third-order elastic constants in many amorphous polymers. The effect depends markedly on temperature. On cooling to lower temperatures, rubber and other amorphous polymers transform from a compliant rubberlike material to a brittle glasslike phase which is of little use in nonlinear devices.

Nonlinear behavior is also observed in magnetic and optical systems. Superparamagnetic behavior, analogous to the superparaelectric behavior of relaxor ferroelectrics, is found in spin glasses, fine powder magnets, and magnetic cluster materials. As in PMN, the magnetic dipoles are strongly coupled to one another in nanometer-sized complexes, but are not strongly coupled to the lattice. Superparamagnetic solids display nonlinear magnetic susceptibilities and unusual ΔE effects in which Young's modulus (E) can be controlled by a magnetic field. The effect is especially large in metallic glasses made from Fe-Si-B-C alloys. The cluster size in spin glasses is in the nanometer range similar to those in PMN.

PLZT perovskites can be prepared as transparent ceramics for electro-optic modulators. Quadratic nonlinear optic behavior is observed in pseudo-cubic regions of the phase diagram which show relaxor-like properties.

A well-known example of a commercial application of nonlinear behavior is the photochromic glass used in ophthalmic lenses for protecting the eyes from ultraviolet radiation, discovered

by Corning, Inc. (Corning, NY), researchers in 1964.³³ This glass darkens when exposed to sunlight, then reverts to the transparent state indoors. The effect is accomplished by incorporating very fine crystallites of silver chloride into an appropriate glass composition. The incident ultraviolet radiation causes reduction of Ag^+ to Ag^0 , resulting in trapped electrons and holes. The Ag^0 atoms cluster together, blocking the incident light and causing the darkening effect; when the ultraviolet radiation is removed, the Ag^0 reverts to Ag^+ , an energetically favorable reaction in the absence of the radiation. The clusters then disperse and fading occurs.³³

In summary, the nonlinear properties of electroceramics are often associated with nanometer-scale structure and diffuse phase transformations. Under these circumstances the structure is poised on the verge of an instability and responds readily to external influences such as electric or magnetic fields, or mechanical stress.

The ready response of nonlinear ceramics allows the properties to be tuned in space or time to optimize the behavior of the sensor-actuator systems.

XVIII. Smart Electroceramic Packages

Up to this point, our discussion has focused primarily on piezoelectric transducers in which the sensing and actuating functions are electromechanical in nature. But the idea of a smart material is much more general than that. There are many types of sensors and many types of actuators, and many different feedback circuits. A few of the possible combinations are shown in Fig. 15.

Many of these sensors and actuators can be fabricated in the form of multilayer ceramic packages. Until recently multilayer packages consisted of low-permittivity dielectric layers with metal circuitry printed on each layer and interconnected through metallized via holes between layers. Buried capacitors and resistors have now been added to the three-dimensional packages, and other components will follow shortly. Smart sensors, adaptive actuators, and display panels, with thermistors and varistors to guard against current and voltage overloads, are next in line for development.³⁴

XIX. Chemical Sensors

The electrochemical response to a change in environment is another material characteristic which, when properly interpreted, can elevate the material to those of other smart materials. One of the smartest and most durable sensors in the human body is the nose, which can easily detect

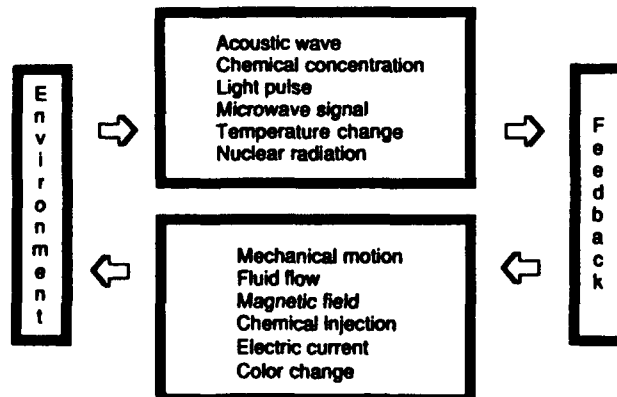


Fig. 15 Schematic of some possibilities for smart electroceramic packages. Smart devices bring together a number of sensor-actuator combinations.

minute amounts of foreign substances and, by feeding this information to the brain, determine the identity of the unseen substance, even in a mixture of components. Although the need for artificial human noses is hardly pressing, the need to identify the presence of potentially harmful or toxic substances is a real one, especially in this age of environmental awareness.

A chemical sensor may be loosely defined as any material (or system) which responds to a change in its chemical environment. The important characteristics of a sensor are its sensitivity (ability to detect species present in small quantities), selectivity (ability to distinguish between two similar chemical species), specificity (ability to measure the same unique property for any species), and reproducibility (ability to obtain high accuracy consistently and repeatedly). The development of useful solid-state chemical sensors is a great challenge to materials scientists. A particularly attractive material property to monitor for chemical sensors is the electrical conductivity because of the tremendous scale associated with this property: more than 24 orders of magnitude (excluding superconductors) separate the best insulators (inert polymers, quartz) from the best conductors (metals—silver, copper, and gold).

In chemical sensors, the ability of the sensor to rid itself of the contamination after exposure is a common problem—as a result, many must be considered disposable, one-time-use devices. For example, humidity detection by porous ZnO is a well-known phenomena, but the self-recovery mechanism in ZnO is quite poor. The resistance of a ZnO sensor decreases with water adsorption, but removal of the water is very slow at room temperature. Thus the measured resistivity may not indicate the correct humidity level because of the large hysteresis observed in the humidity-resistivity characteristic. To obtain accurate results, the ZnO sensor must be regenerated to reactivate the absorption sites.

A somewhat smarter humidity sensor with a self-recovery mechanism has been developed from a two-phase composite of a *p*-type semiconductor (e.g., CuO, NiO) and an *n*-type semiconductor (ZnO).³⁵ The amount of water adsorption near the *p*–*n* heterocontact changes with humidity, and electron holes are ejected from the *p*-type semiconductor into the adsorbed water molecules, giving rise to protons in the water phase. The positive charge is liberated at the *n*-type surface, and, as a consequence, the water is electrolyzed. Consequently, during the *I*–*V* measurements the regeneration process is initiated by the applied voltage, and continues to work during the sensing

process since it is intimately connected to the sensing mechanism. This is a perfect example of self-recovery in a smart sensor.

Semiconducting metal oxides, particularly SnO₂, are known to undergo a remarkable decrease in electrical resistivity in the presence of certain chemical species, usually those associated with oxygen deficiencies or excess electrons at the surface. Often, merely knowing exactly what to look for is all that is necessary to develop a smart sensor from a semiconducting oxide.

A good example of this type of thinking is the so-called sushi sensor, designed to monitor the freshness of fish. The basic component of fish flesh is adenosine triphosphate (ATP), which decomposes into inosine and hypoxanthine when the fish dies. The percentage of these decomposition products in ATP is expressed by a freshness factor *K*. *K* values can be obtained by quantitative analysis of the decomposition process, but this requires considerable effort and time.

Instead, the gaseous components of the decomposition reaction, trimethylamine (TMA) and dimethylamine (DMA) can be monitored by a solid-state ruthenium-doped TiO₂ sensor,³⁶ pictured in Fig. 16(A). Ruthenium aids in catalyzing the decomposition of DMA and TMA gases, as well as acting as an electron acceptor in the space charge region at the surface of the semiconductor. The resistance of the sensor, *R*, can then be related directly to the *K* value, as shown graphically in Fig. 16(B).

Conductive polymers can be quite smart as well. Poly(pyrrole) and poly(vinylpyridine) change conductivity by absorbing and dissociating certain organics, which results in high ionic conductivity.³⁷

Conducting composites, consisting of an inert conductive filler in an insulating polymer matrix, may be used as chemical sensors as well.³⁸ If in the ini-

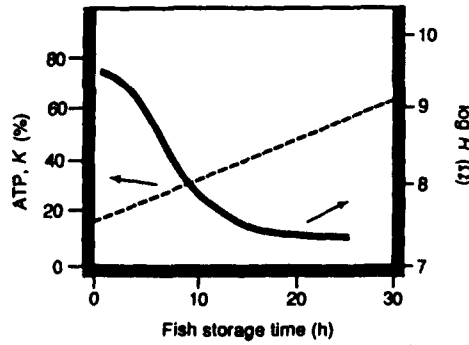
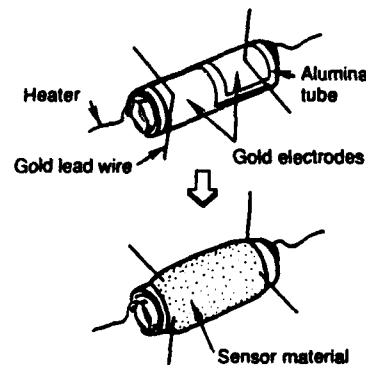


Fig. 16. Fish freshness sensor, showing (A) a diagram of the device and (B) the response of the sensor element.³⁶

tial state a polymer is loaded with conductive filler beyond the percolation threshold, it will have a low resistivity close to that of the pure filler material. All polymers will expand in the presence of the proper chemical solvent; thus, if the correct polymer is chosen for the matrix, the conductor-loaded polymer will expand in the presence of a given chemical vapor, disrupting percolation and increasing the resistance to the level of the pure polymer (see Fig. 17).

The large number of available polymers with a wide range of solubilities in different solvents made this an open-ended field for the discovery of new, selective chemical sensors. Correct choice of the conductive filler material increases the sensitivity while reducing the power consumption, making it possible to develop compact battery-operated sensors for applications such as alcohol "breathalyzer" sensors, leak detectors for fuel storage tanks, and natural-gas leak detectors for the home.

The next level of integration for composite sensors is not difficult to imagine: it is the combination of chemically active filler (e.g., SnO_2) and/or a chemically active polymer (e.g., poly(pyrrole)) into a conductive composite which can change resistivity by either an intrinsic filler reaction, an intrinsic change in the polymer, or an extrinsic change due to percolation disruption upon swelling. Combining the sensor with an actuator circuit (i.e., on a silicon chip) would produce a self-contained, smart sensor package. Actuation might involve removing spoiled food from a conveyor belt, or perhaps identifying the presence of a noxious gas with a color change or an alarm buzzer. As with most smart materials, none of these ideas are especially new: it is only the idea of incorporating these functions inside the material that is new.

XX. Future Developments

Integration and miniaturization of electroceramic sensors and actuators is an ongoing process in the automotive and consumer electronics areas. Multilayer packages containing signal-processing layers made up of low-permittivity dielectrics and printed metal interconnections are in widespread production. Further integration with embedded resistors and capacitors are under development, and it seems likely that intelligent systems will make use of the same processing technology. Tape casting and screen printing are used most often. Varistors, chemical sensors, thermistors, and piezoelectric transducers can all be fabricated in this way, opening up the possibility of multicomponent, multifunction ceramics with both sensor and actuator capabilities. Silicon chips can be mounted on these multifunctional packages to provide all or part of the control network. Processing is a major challenge because of the high firing temperatures of most ceramics, typically in the range 800° to 1500°C. Differences in densification shrinkage and thermal contraction, with adverse chemical reactions between the electroceramic phases, create formidable problems. Nevertheless, the rewards for such an achievement are substantial. An all-ceramic, multifunction package would be small, robust, inexpensive, and sufficiently refractory to withstand elevated temperatures.

Electrodes are both a problem and a challenge. At present, precious metals such as palladium and platinum are used in multilayer ceramic components, greatly adding to the cost of the device. Copper and nickel electrodes require that the ceramic be fired in a reducing atmosphere, which may reduce the electroceramic layers and adversely affect the electrical properties. Copper and silver have high electrical conductivity but the melting points (~1000°C) require lower firing temperatures and make it necessary to alter the ceramic compositions and fabrication procedures. Some headway has been made on this problem, but further work is needed. One interesting approach to the problem is ceramic electrodes. There are a number of ceramic phases with excellent conductivity which could be used, including the copper oxide superconductors. In actuator devices, there are some special advantages in having electrodes and piezoceramics with matched elastic properties.

Composites are another approach to making sensor-actuator combinations. These can be formed at lower temperatures using low-firing ceramics and high-temperature polymers such as polyimides. Sol-gel and chemical precipitation methods are helpful in

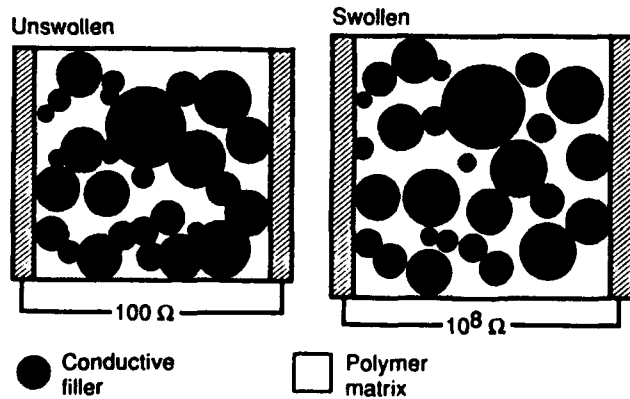


Fig. 17. Schematic of composite chemical sensor response.

preparing ceramic powders with low calcining temperatures, but further work on composite fabrication is required to obtain reliable and reproducible electrical behavior.

To miniaturize the sensors and actuators, and to obtain complex shapes, we recommend the use of photolithography and other processing methods used in the semiconductor industry. Ultraviolet curable polymers incorporated into the tape-casting process make photolithographic processing comparatively easy and should find wide use in preparing ceramic or composite packages for intelligent systems.

The next logical step is to combine the sensor and actuator functions with the control system. This can be done by depositing electroceramic coatings on integrated circuit silicon chips. This is currently a very "hot" area for materials research; many varieties of thin-film sensors and actuators can be produced by a number of techniques.

Reliability is a major requirement in all complex systems. Further research on electrical and mechanical breakdown of sensor-actuator materials is needed to elucidate the mechanisms responsible for failure. Fail-safe and self-repair phenomena would be very helpful.

Intelligent systems for hostile environments is another topic area of interest. Sensor and actuator systems that can operate at high temperatures inside engines or furnaces are required to monitor combustion and to provide pollution controls. Radioactive and chemical waste sensors are another problem. Intelligent systems for oceanographic studies and oil exploration must withstand high pressures and salinity conditions.

Electroceramics have a vital role to play in intelligent systems, and many new developments will take place in the coming decade and the next century.

References

- ¹C. A. Rogers, "From the Editor," *Journal of Intelligent Material Systems and Structures*, **1**, 3 (1990).
- ²S. A. Brodeur, "Phase Change Materials for Thermal Stabilization of Composite Thermistors"; M.S. Thesis Solid State Science, Pennsylvania State University, University Park, PA, 1989.
- ³T. Takagi, "The Concept of Intelligent Materials and the Guidelines on R&D Promotion," Japan Science and Technology Agency Report, Tsukuba Science City, Japan, 1989.
- ⁴R. E. Newnham, Q. C. Xu, S. Kumar, and L. E. Cross, "Smart Ceramics," *Journal of Wave-Material Interaction*, **4**, 3-10 (1989).
- ⁵M. Taguchi, "Applications of High-Technology Ceramics in Japanese Automobiles," *Adv. Ceram. Mater.*, **2**, 754-62 (1987).
- ⁶H. Tsuka, J. Nakomo, and Y. Yokoya, "A New Electronic Controlled Suspension Using Piezoelectric Ceramics," IEEE Workshop on Electronic Applications in Transportation, 1990.
- ⁷A. R. Ramachandran, Q. C. Xu, L. E. Cross, and R. E. Newnham, "Passive Damping with Piezoelectric Ceramics"; presented at the 7th International Symposium on Applications for Ferroelectrics, June 6-8, 1990, Urbana, IL.
- ⁸S. Burke and J. E. Hubbard, "Active Vibration Control of a Simply-Supported Beam Using a Spatially-Distributed Actuator," *IEEE Control Systems Magazine*, **7**, 25-30 (1987).
- ⁹K. Uchino, *Piezoelectric/Electrostrictive Actuators*, Morikita Publishers, Tokyo, Japan, 1986.
- ¹⁰J. L. Butler, *Application Manual for Design of Magnetostrictive Transducers*, Edge Technologies, Extrema Division, North Marshfield, MA, 1988.
- ¹¹L. Schelky, "Shape Memory Alloys," *Sci. Am.*, **241**, 74-82 (1979).
- ¹²D. L. Edberg, "Control of Flexible Structures by Applied Thermal Gradients," *AIAA J.*, **25**, 877-83 (1987).
- ¹³C. A. Rogers, C. Liang, and D. K. Barker, "Dynamic Control Concepts Using Shape-Memory Alloy-Reinforced Plates"; pp. 39-62 in *Smart Materials, Structures, and Mathematical Issues*. Edited by C. A. Rogers. Technomic Publishers, Lancaster, PA, 1989.
- ¹⁴V. K. Wadhawan, M. C. Kernion, T. Kimura, and R. E. Newnham, "The Shape Memory Effect in PLZT Ceramics," *Ferroelectrics*, **37**, 575-78 (1981).
- ¹⁵A. Furuta, K. Oh, and K. Uchino, "Mechanical Clamper Using Shape Memory Ceramics"; presented at the 7th International Symposium on Applications for Ferroelectrics, Urbana, IL, June 6-8, 1990.
- ¹⁶M. V. Ghandi and B. S. Thompson, "A New Generation of Revolutionary Ultra-Advanced Intelligent Composite Materials Featuring Electro-Rheological Fluids"; pp. 63-68 in *Smart Materials, Structures, and Mathematical Issues*. Edited by C. A. Rogers. Technomic Publishers, Lancaster, PA, 1989.
- ¹⁷R. E. Rosenweig, *Ferrohydrodynamics*. Cambridge University Press, New York, 1985.
- ¹⁸C. E. Bond, *Biology of Fishes*. Saunders College Publishing Co., Philadelphia, PA, 1979.
- ¹⁹P. B. Moyle, and J. J. Cech, Jr., *Fishes: An Introduction to Ichthyology*. Prentice Hall, Englewood Cliffs, NJ, 1988.
- ²⁰R. A. White, J. N. Weber, and E. W. White, "Replamineform: A New Process for Preparing Porous Ceramic, Metal, and Polymer Prosthetic Materials," *Science (Washington, D.C.)*, **176**, 922-23 (1972).
- ²¹D. P. Skinner, R. E. Newnham, and L. E. Cross, "Flexible Composite Transducers," *Mater. Res. Bull.*, **13**, 599-607 (1978).
- ²²K. Rittenmyer, T. Shrout, W. A. Schulze, and R. E. Newnham, "Piezoelectric 3-3 Composites," *Ferroelectrics*, **41**, 189-95 (1982).
- ²³M. P. Fish and W. H. Mowbray, *Sounds of Western North Atlantic Fishes*. John Hopkins Press, Baltimore, MD, 1970.
- ²⁴R. J. Urick, *Principles of Underwater Sound*. McGraw-Hill, New York, 1975.
- ²⁵K. A. Klicker, J. V. Biggers, and R. E. Newnham, "Composites of PZT and Epoxy for Hydrostatic Transducer Applications," *J. Am. Ceram. Soc.*, **64**, 5-9 (1981).
- ²⁶T. R. Gurueja, W. A. Schulze, L. E. Cross, R. E. Newnham, B. A. Auld, and J. Wang, "Resonant Modes in Piezoelectric PZT Rod-Polymer Composite Materials"; pp. 523-27 in *Proceedings of IEEE Ultrasonic Symposium*, 1984.
- ²⁷Q. C. Xu, J. Belsick, S. Yoshikawa, T. T. Srinivasan, and R. E. Newnham, "Piezoelectric Composites with High Sensitivity and High Capacitance for Use at High Pressures," *Proc. IEEE*, in press.
- ²⁸P. R. Bandyopadhyay, "Mean Flow in Turbulent Boundary Layers Disturbed to Alter Skin Friction," *J. Fluids Eng.*, **108**, 127 (1986).
- ²⁹R. E. Newnham, "Composite Electroceramics," *J. Mater. Educ.*, **7**, 605-51 (1985).

³⁰Q.C. Xu, R.E. Newnham, M. Blaskiewicz, T.T. Fang, T.T. Srinivasan, and S. Yoshikawa, "Non-linear Multilayer Composite Transducers"; Presented at the 7th International Symposium on Applications for Ferroelectrics, June 6-8, 1990, Urbana, IL.

³¹E.I. Rivin, "Properties and Prospective Applications of Ultra Thin Layered Rubber-Metal Laminates for Limited Travel Bearings," *Tribol. Int.*, **16**, 17-25 (1983).

³²R.E. Newnham, Q.C. Xu, S. Kumar, and L.E. Cross, "Smart Ceramics," *Ferroelectrics*, **102**, 1-8 (1990).

³³I. Ahmad, "Smart' Structures and Materials"; pp. 13-16 in *Smart Materials, Structures, and Mathematical Issues*. Edited by C.A. Rogers. Technomic Publishers, Lancaster, PA, 1989.

³⁴R.E. Newnham, "The Golden Age of Electroceramics," *Adv. Ceram. Mater.*, **3**, 12-16 (1988).

³⁵H. Yanagida, "Intelligent Materials—A New Frontier," *Angew. Chem.*, **100**, 1443-46 (1988).

³⁶M. Egashira, Y. Shimizu, and Y. Takao, "Enhancement of Trimethylamine Sensitivity of Semiconductor Gas Sensors by Ruthenium," *Chem. Lett.*, **17**, 389-92 (1988).

³⁷P.N. Bartlett and S.K. Ling-Chung, "Conducting Polymer Gas Sensors Part III: Results for Four Different Polymers and Five Different Vapours," *Sens. Actuators*, **20**, 287-92 (1989).

³⁸G.R. Ruschau, R.E. Newnham, J. Runt, and B.E. Smith, "0-3 Ceramic-Polymer Composite Chemical Sensors," *Sens. Actuators*, **20**, 269-75 (1989). □



Dr. Robert E. Newnham is Alcoa Professor and Chairman of the Solid State Science Program at the Materials Research Laboratory of The Pennsylvania State University. He is also affiliated with the Ceramic Science Section of the Materials Science and Engineering Department where he teaches courses in crystal chemistry, crystal physics, and electroceramics. Prior to joining the Penn State faculty, Dr. Newnham taught at Massachusetts Institute of Technology where he was a staff member of the Laboratory for Insulation Research. He is a graduate of Hartwick College (B.S., mathematics), Colorado State University (M.S., physics), Penn State (Ph.D., physics and mineralogy), and Cambridge University (Ph.D., crystallography). Dr. Newnham's research interests are in structure-property relations, electroceramics, and composite materials for electronic applications. Recently elected to the National Academy of Engineering, Dr. Newnham is the author or coauthor of more than 300 research papers and is now serving as an Editor of the *Journal of the American Ceramic Society*.



Gregory R. Ruschau graduated from the University of Illinois with a B.S. in ceramic engineering in 1985. Prior to entering the graduate program in Solid State Science at The Pennsylvania State University in 1987, Mr. Ruschau worked for Corning Glass Works in Corning, New York. His research interests include chemical sensors, composites, electroceramics, and ceramic thin-film processes. He is a member of the American Ceramic Society and the Materials Research Society.

APPENDIX 5

TUNABLE TRANSDUCERS: NONLINEAR PHENOMENA IN ELECTROCERAMICS

Robert E. Newnham
Materials Research Laboratory
Pennsylvania State University
University Park, PA 16802

ABSTRACT

The concept of a fully tunable transducer is developed as an example of a very smart material whose sensing and actuating functions can be tuned to optimize behavior. By constructing the composite transducer from an elastically nonlinear material (rubber) and an electrically nonlinear material (relaxor ferroelectric), most of its key properties can be adjusted over wide ranges by applying DC bias fields or mechanical prestress. These properties include resonant frequency, acoustic and electric impedance, damping factors, and electromechanical coupling coefficients.

The origins of nonlinear properties are considered briefly using electrostriction as an example. The nonlinearities usually involve phase transformations and size-dependent phenomena on the nanometer scale.

INTRODUCTION

Much of the recent interest in nonlinear phenomena stems from the desire to build "smart materials" for intelligent systems. The words "smart materials" have different meanings for different people, and can be smart in either a passive sense or an active sense. Passively smart materials incorporate self-repair mechanisms or stand-by phenomena which enable the material to withstand sudden changes in the surroundings.

Ceramic varistors and PTC thermistors are passively smart materials. When struck by lightning or otherwise subjected to high voltage, a zinc oxide varistor loses its electrical resistance and the current is bypassed to ground. The resistance change is reversible and acts as a stand-by protection phenomenon. Barium titanate PTC thermistors show a large increase in electrical resistance at the ferroelectric phase transformation near 130°C. The jump in resistance enables the thermistor to arrest current surges, again acting as a protection element. The

$R(V)$ behavior of the varistor and the $R(T)$ behavior of the PTC thermistor are both highly nonlinear effects which act as standby protection phenomena, and make the ceramics smart in a passive mode.

A smart ceramic can also be defined with reference to sensing and actuating functions, in analogy to the human body. A smart ceramic senses a change in the environment, and using a feedback system, makes a useful response. It is both a sensor and an actuator. Examples include vibration damping systems for space structures and energy-saving windows for homes and factories. The new electronically-controlled automobile suspension systems using piezoelectric ceramic sensors and actuators constitutes an actively smart material.

By building in a learning function, the definition can be extended to a higher level of intelligence: A very smart ceramic senses a change in the environment and responds by changing one or more of its property coefficients. Such a material can tune its sensor and actuator functions in time and space to optimize behavior. The distinction between smart and very smart materials is essentially one between linear and nonlinear properties. The physical properties of nonlinear materials can be adjusted by bias fields or forces to control response.

TUNABLE TRANSDUCER

To illustrate the concept of a very smart material, we describe the tunable transducer recently developed in our laboratory. Electromechanical transducers are used as fish finders, gas igniters, ink jets, micropositioners, biomedical scanners, piezoelectric transformers and filters, accelerometers, and motors.

Four important properties of a transducer are the resonant frequency f , the acoustic impedance Z_A , the mechanical damping coefficient Q , the electromechanical coupling factor k , and the electrical impedance Z_E . The resonant frequency and acoustic impedance are controlled by the elastic constants and density, as discussed in the next section. The mechanical Q is governed by the damping coefficient ($\tan \delta$) and is important because it controls "ringing" in the transducer. Electromechanical coupling coefficients are controlled by the piezoelectric coefficient which, in turn, can be controlled and fine-tuned using relaxor ferroelectrics with large electrostrictive effects. The dielectric "constant" of relaxor ferroelectrics depends markedly on DC bias fields, allowing the electrical impedance to be tuned over a wide range as well. In the following sections we describe the nature of nonlinearity and how it controls the properties of a tunable transducer.

ELASTIC NONLINEARITY: TUNING THE RESONANT FREQUENCY

Information is transmitted on electromagnetic waves in two ways: amplitude modulation (AM) and frequency modulation (FM). There are a number of advantages to FM signal processing, especially where lower noise levels are important.

Signal-to-noise ratios are also important in the ultrasonic systems used in biomedical and nondestructive testing systems, but FM-modulation is difficult because resonant frequencies are controlled by stiffness (c) and sample dimensions (t):

$$f = \frac{1}{2t} \sqrt{c / \rho}$$

Neither c , t , or the density ρ can be tuned significantly in most materials, but rubber is an exception. To tune the resonant frequency of a piezoelectric transducer, we have designed and built a composite transducer incorporating thin rubber layers exhibiting nonlinear elasticity.

Rubber is a highly nonlinear elastic medium. In the unstressed compliant state, the molecules are coiled and tangled, but under stress the molecules align and the material stiffens noticeably. Experiments carried out on rubber-metal laminates demonstrate the size of the nonlinearity. Young's modulus ($E = 1/s_{1111}$) was measured for a multilayer laminate consisting of alternating steel shim and soft rubber layers each 0.1 mm thick. Under compressive stresses of 200 MN/m², the stiffness is quadrupled from about 600 to 2400 MN/m². The resonant frequency f is therefore double, and can be modulated by applied stress.

Rubber, like most elastomers, is not piezoelectric. To take advantage of the elastic nonlinearity, it is therefore necessary to construct a composite transducer consisting of a piezoelectric ceramic (PZT) transducer, thin rubber layers, and metal head and tail masses, all held together by a stress bolt.

The resonant frequency and mechanical Q of such a triple sandwich structure was measured as a function of stress bias. Stresses ranged from 20 to 100 MPa in the experiments. Under these conditions the radial resonant frequency changed from 19 to 37 kHz, approximately doubling in frequency as predicted from the elastic nonlinearity. At the same time the mechanical Q increases from about 11 to 34 as the rubber stiffens under stress.

The changes in resonance and Q can be modeled with an equivalent circuit in which the compliance of the thin, rubber layers are represented as capacitors coupling together the larger masses (represented as inductors) of the PZT transducer and the metal head and tail masses. Under low stress bias, the rubber is very compliant and effectively isolates the PZT transducer from the head and tail masses. At very high stress, the rubber stiffens and tightly couples the metal end pieces to the resonating PZT ceramic. For intermediate stresses the rubber acts as an impedance transformer giving parallel resonance of the PZT - rubber - metal - radiation load.

It is interesting to compare the change in frequency of the tunable transducer with the transceiver systems used in the biological world. The biosonar system of the flying bat is similar in frequency and tunability to our

tunable transducer. The bat emits chirps at 30 kHz and listens for the return signal to locate flying insects. To help it differentiate the return signal from the outgoing chirp, and to help in timing the echo, the bat puts an FM signature on the pulse. This causes the resonant frequency to decrease from 30 to 20 kHz near the end of each chirp. Return signals from the insect target are detected in the ears of the bat where neural cavities tuned to this frequency range measure the time delay and flutter needed to locate and identify its prey. Extension of the bat biosonar principle to automotive, industrial, medical and entertainment systems is obvious.

PIEZOELECTRIC NONLINEARITY: TUNING THE ELECTROMECHANICAL COUPLING COEFFICIENT

The difference between a smart and a very smart material can be illustrated with piezoelectric and electrostrictive ceramics. PZT (lead zirconate titanate) is a piezoelectric ceramic in which the ferroelectric domains are aligned in a poling field. Strain is linearly proportional to electric field in a piezoelectric material which means that the piezoelectric coefficient is a constant and cannot be electrically tuned with a bias field. Nevertheless it is a smart material because it can be used both as a sensor and an actuator.

PMN (lead magnesium niobate) is not piezoelectric at room temperature because its Curie temperature lies near 0°C. Because of the proximity of the ferroelectric phase transformation, and because of its diffuse nature, PMN ceramics exhibit very large electrostrictive effects. The nature of this large nonlinear relationship between strain and electric field, and of its underlying atomistic origin, will be described later.

Electromechanical strains comparable to PZT can be obtained with electrostrictive ceramics like PMN, and without the troubling hysteretic behavior shown by PZT under high fields. The nonlinear relation between strain and electric field in electrostrictive transducers can be used to tune the piezoelectric coefficient and the dielectric constant.

The piezoelectric d_{33} coefficient is the slope of the strain-electric field curve when strain is measured in the same direction as the applied field. Its value for $\text{Pb}(\text{Mg}_{0.3}\text{Nb}_{0.6}\text{Ti}_{0.1})\text{O}_3$ ceramics is zero at zero field and increases to a maximum value of 1300 pC/N (about three times larger than PZT) under a bias field of 3.7 kV/cm.

This means that the electromechanical coupling coefficient can be tuned over a very wide range, changing the transducer from inactive to extremely active. The dielectric constant also depends on DC bias. The polarization saturates under high fields causing decreases of 100% or more in the capacitance. In this way the electrical impedance can be controlled as well.

Electrostrictive transducers have already been used in a number of applications including adaptive optic systems, scanning tunneling microscopes, and precision micropositioners.

To summarize, two types of nonlinearity are utilized in the fully tunable transducer: elastic nonlinearity and piezoelectric nonlinearity. By incorporating thin rubber layers in an electrostrictive transducer several important properties can be optimized with bias fields and bias stresses. Electromechanical coupling coefficients and electric impedance are tuned with electric field, and mechanical damping, resonant frequency, and acoustic impedance with stress bias.

RELAXOR FERROELECTRICS

In the three remaining sections we consider the atomistic origin of nonlinear behavior in ceramics. The magnesium - niobium distribution in PMN ceramics have been studied by transmission electron microscopy. Images formed from superlattice reflections show that the size of the regions with 1:1 ordering is approximately 3 nm ($=30\text{\AA}$). The ordered regions are small islands separated by narrow walls of niobium - rich PMN.

A simple energy argument explains the scale of the ordered regions. The chemical formula of PMN can be divided into 1:1 ordered regions with niobium-rich coatings as follows:



assuming all ions have their usual valence states, the ordered regions will be negatively charged and the coatings positive. The ordering must therefore be on a very fine scale in order to minimize coulomb energy.

A cubes model is adopted to estimate the size of ordered islands. Let each island be a cube n unit cells on edge. Then there will be $n^3/2$ Mg atoms and $n^3/2$ Nb atoms within the island. This means that $n^3/2$ Nb atoms are excluded from the island because the Mg:Nb ration is 1:1 in the ordered island and 1:2 in the chemical formula. We assume the excluded niobiums form a thin monolayer coating on the cubes then $n^3/2 = 3n^2$, where $3n^2$ is the number of surface atoms per cube, neglecting edges and corners. By keeping the coating as thin as possible, charge is neutralized on a local scale, and electrostatic energy is minimized.

Solving the equation gives $n=6$, or 24\AA , surprisingly close to the 30\AA observed by TEM. It is also interesting to compare this result with the behavior observed of small ferroelectric particles. X-ray studies of very fine-grained PbTiO_3 show that the polar tetragonal phase becomes unstable below about 200\AA , the so-called ferroelectric - superparaelectric transformation. Relaxor ferroelectrics like PMN exhibit many of the characteristics of superparaelectric solids where the dipole moments are strongly coupled to one another, but not to a

crystallographic axis. The coupled electric dipoles oscillate in orientation and respond readily to applied fields giving rise to large dielectric constants and massive electrostriction coefficients.

SEVEN MISCONCEPTIONS ABOUT ELECTROSTRICKTION

Perhaps the best way to describe the basic features of nonlinear physical properties is to first dispel some of the common misconceptions. Some of the key ideas are described in this section using electrostriction as an example.

Misconception #1: Electrostrictive strain is proportional to the square of the electric field.

When an electric field E is applied to an insulator it develops a polarization P and a strain ϵ . In tensor notation the strain can be written as a power series in E or in P .

$$(1) \quad \epsilon_{ij} = d_{ijk}E_k + M_{ijkl}E_kE_l + \dots$$

$$(2) \quad \epsilon_{ij} = d_{ijk}P_k + Q_{ijkl}P_kP_l + \dots$$

The first term in both equations represents piezoelectricity, the second electrostriction. Piezoelectricity is a third rank tensor property found only in noncentrosymmetric materials. It is absent in most ceramic materials, but electrostriction is not. The electrostriction coefficients M_{ijkl} or Q_{ijkl} constitute a fourth rank tensor which, like the elastic constants, are found in all materials, regardless of symmetry. In the discussion which follows, we deal with centrosymmetric media for which the piezoelectric coefficients are zero.

Returning to equations (1) and (2), which of these equations is the correct way to describe electrostriction, or can both be used? For normal low permittivity materials, the polarization P is proportional to the applied electric field E , and therefore both expressions are correct, but for high permittivity solids only one is correct. Under high fields, the polarization saturates in high permittivity materials, especially in ferroelectric ceramics just above T_c , the Curie temperature. In capacitor dielectrics, it is not unusual to observe a decrease in dielectric constant of 100% under high electric fields. In this situation P is not proportional to E , and therefore electrostrictive strain cannot be proportional to both E^2 and P^2 .

When strain is plotted as a function of electric field for PMN-PT, a typical electrostrictive transducer ceramic, it is not proportional to E^2 except for small fields where the shape is parabolic. When plotted as function P^2 , a straight line is obtained for the $\epsilon(P^2)$ relationship. Therefore the correct way to formulate electrostriction is

$$(3) \quad \boxed{\epsilon_{ij} = Q_{ijkl} P_k P_l} \quad (i,j,k,l = 1,2,3)$$

The M_{ijkl} coefficients in eq. (1) are not good constants except in linear dielectrics.

It is instructive to convert the fourth rank tensor coefficients to the more manageable matrix form

$$(4) \quad \epsilon_i = Q_{ij} P_j^2 \quad (i,j = 1-6)$$

When written out in full for cubic point group m3m, this becomes

$$(5) \quad \begin{pmatrix} \epsilon_1 \\ \epsilon_2 \\ \epsilon_3 \\ \epsilon_4 \\ \epsilon_5 \\ \epsilon_6 \end{pmatrix} = \begin{pmatrix} Q_{11} & Q_{12} & Q_{12} & 0 & 0 & 0 \\ Q_{12} & Q_{11} & Q_{12} & 0 & 0 & 0 \\ Q_{12} & Q_{12} & Q_{11} & 0 & 0 & 0 \\ 0 & 0 & 0 & Q_{44} & 0 & 0 \\ 0 & 0 & 0 & 0 & Q_{44} & 0 \\ 0 & 0 & 0 & 0 & 0 & Q_{44} \end{pmatrix} \begin{pmatrix} P_1^2 \\ P_2^2 \\ P_3^2 \\ P_2 P_3 \\ P_3 P_1 \\ P_1 P_2 \end{pmatrix}$$

In this expression ϵ_1 , ϵ_2 and ϵ_3 represent tensile strains along the [100], [010], and [001] axes, respectively. ϵ_4 , ϵ_5 and ϵ_6 are shear strains about the same three axes.

To understand the structure-property relationship underlying electrostriction, it is helpful to visualize the atomistic meaning of coefficients Q_{11} , Q_{12} , and Q_{44} . The high temperature structure of PbTiO₃ is pictured in Fig. 1 a. Lead ions are located at the corners of the cubic unit cell, titanium ions at the body-centered position, and oxygens at the face-center positions.

When an electric field is applied along [100], polarization component P_1 develops along the same axis. This in turn causes the unit cell to elongate by an amount Δa , and the resulting tensile strain is $\epsilon_1 = \Delta a/a$. Electrostrictive coefficient Q_{11} is equal to ϵ_1/P_1^2 . The drawing in Fig. 1b makes it clear why electrostrictive strain is proportional to electric polarization rather than electric field. Polarization and strain are both controlled by atomic displacement.

The atomistic meaning of Q_{12} and Q_{44} are pictured in figs. 1 c and 1 d, respectively.

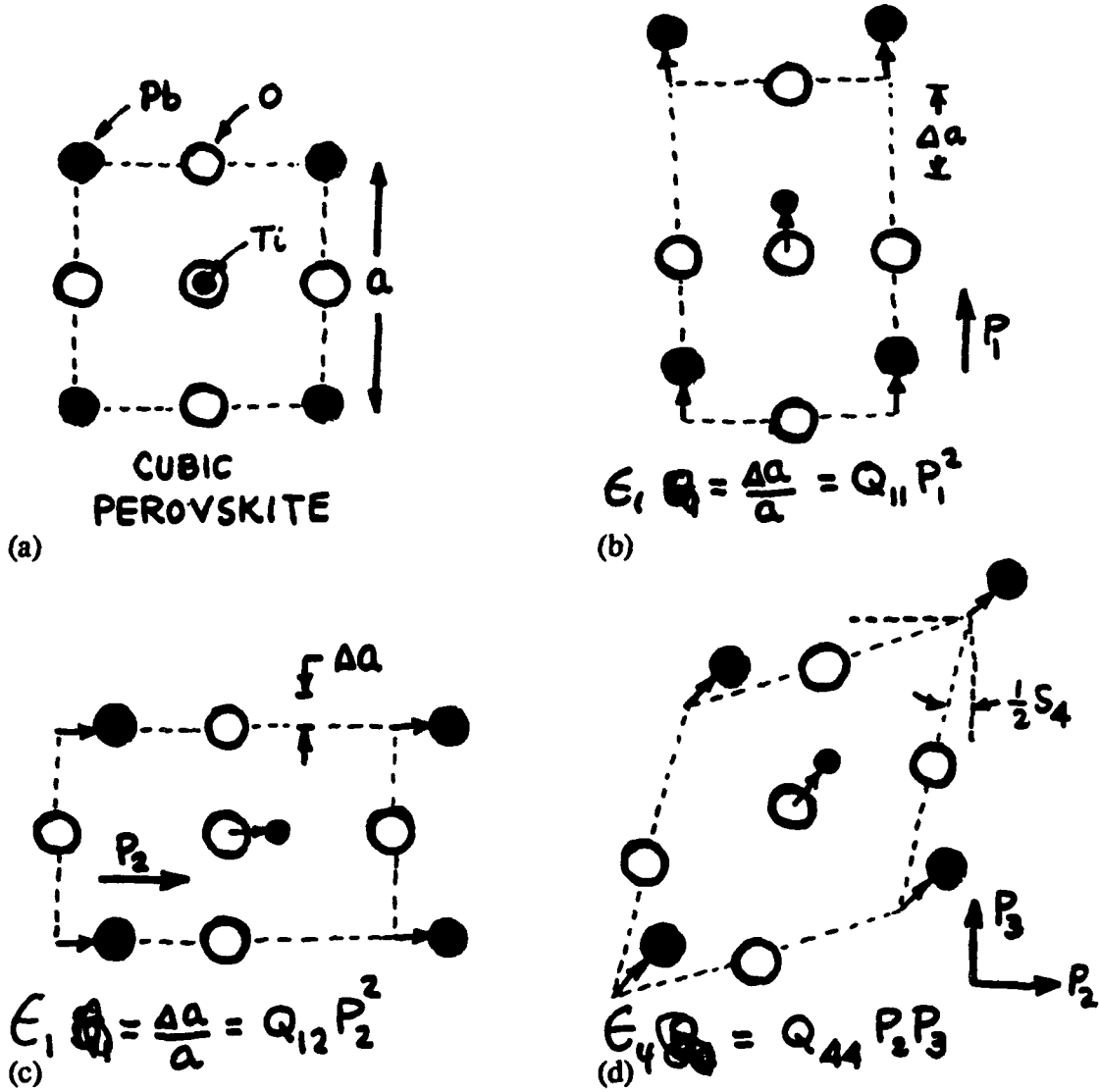


Fig. 1 Electrostriction in cubic perovskite showing the physical origin of coefficients Q_{11} , Q_{12} , and Q_{44} .

Misconception #2. Large voltages are required to observe electrostriction.

This misconception arises from the fact that historically, the first electroceramics were high voltage insulators made from low permittivity oxides such as porcelain, glass, steatite, and alumina. To prevent breakdown, the insulators were fabricated in large sizes, typically with 1-10 cm separation between electrodes. Under these conditions the voltages required to induce measurable electrostriction are huge, but the picture has changed in the last decade.

Two factors have made the difference: smaller electrode separation and higher permittivity. The introduction of thin and thick film technology, together with tape-casting, has reduced the thickness of the dielectric constants to less than 50 μm with corresponding increases in the electric field levels. Fields of megavolts/meter are common under these circumstances. At the same time, new ferroelectric ceramics with dielectric constants in excess of 10,000 have raised the polarization levels to new heights, further contributing to electrostriction strain. As a result, strains of 10^{-3} to 10^{-2} are observed with relatively modest voltages.

Misconception #3 Electrostriction coefficients are about the same size for all materials.

Misconception #4 Electrostriction coefficients are largest in ferroelectric solids with high dielectric constants.

Q_{11} coefficients measured for normal oxides are several orders of magnitude or more larger than those of ferroelectrics.

	$Q_{11} (\text{m}^4/\text{C}^2)$
Silica	+12.8
Barium Titanate	+0.11
Lead Magnesium Niobate	+0.009

Misconception #5 Materials with large electrostrictive coefficients produce the biggest strains.

The Q coefficients are largest for non-ferroelectrics but relaxor ferroelectrics like PMN have the largest strains. The following table lists typical values of the electrostriction coefficients Q , the dielectric constant K , and electrostrictive strain ϵ computed for a field of 1 MV/m.

	Q	K	ϵ
non-ferroelectric	~ 10	~ 10	$\sim 10^{-7}$
normal ferroelectric	$\sim 10^{-1}$	$\sim 10^3$	$\sim 10^{-5}$
relaxor ferroelectric	$\sim 10^{-2}$	$\sim 10^4$	$\sim 10^{-4}$

Note that the product $QK \sim 100 \text{ m}^4/\text{C}^2$ is approximately a constant for all three classes. To see why this is so, consider the following argument based on the atomistic models in Fig 1.

Under the action of an applied electric field, the cations and anions in a crystal structure are displaced in opposite directions by an amount Δr . It is this displacement which is responsible for electric polarization (P), the dielectric constant K , and the electrostrictive strain ϵ . To a first approximation, all three are proportional to Δr . The electrostriction coefficient Q is therefore proportional to $1/K$:

$$Q = \frac{E}{P^2} \sim \frac{(\Delta r)}{(\Delta r)^2} = \frac{1}{\Delta r} \sim \frac{1}{K}$$

This means then, that QK is approximately constant, as indicated earlier. Materials with high permittivity have small electrostriction coefficients but large electrostrictive strain.

Misconception #6. Unlike piezoelectricity there is no converse electrostriction effect.

In the direct piezoelectric effect an applied mechanical stress σ_{kl} produces an electric polarization $P_i = d_{ijk} \sigma_{kl}$. The converse effect relates mechanical strain to applied electric field, $\epsilon_{ij} = d_{ijk} E_k$. The piezoelectric coefficients d_{ijk} are identical in the direct and converse effect because both originate from the same term in the free energy function:

$$F = \dots + d_{ijk} P_i \sigma_{jk} + \dots$$

Electrostriction and its converse effects arise from the free energy term

$$F = \dots + Q_{ijkl} P_i P_j \sigma_{kl} + \dots$$

Taking the partial derivatives in different order leads to three equivalent effects. The first is the normal electrostriction effect, the variation of strain with polarization:

$$\frac{\partial}{\partial P_i} \left(\frac{\partial}{\partial P_j} \left(\frac{\partial F}{\partial \sigma_{kl}} \right) \right) = \frac{\partial^2 \epsilon_{kl}}{\partial P_i \partial P_j} = Q_{ijkl}$$

The second is the stress dependence of the dielectric stiffness β_{ij} , better known as the reciprocal electric susceptibility:

$$\frac{\partial}{\partial \sigma_{kl}} \left(\frac{\partial}{\partial P_i} \left(\frac{\partial F}{\partial P_j} \right) \right) = \frac{\partial \beta_{ij}}{\partial \sigma_{kl}} = Q_{ijkl}$$

The third effect is the polarization dependence of the piezoelectric voltage coefficient g_{jkl} :

$$\frac{\partial}{\partial P_i} \left(\frac{\partial}{\partial \sigma_{kl}} \left(\frac{\partial F}{\partial P_j} \right) \right) = \frac{\partial g_{jkl}}{\partial P_i} = Q_{ijkl}$$

Thus there are two converse effects for electrostriction, and there are three ways of evaluating the electrostrictive coefficients.

The three effects are used in three different applications: (1) the electrostrictive micropositioner, (2) a capacitive stress gauge, and (3) a field-tunable piezoelectric transducer.

Misconception #7 Thermal expansion effects make electrostrictive micropositioners and stress gauges impractical.

This is true for normal oxide insulators but not for relaxor ferroelectrics. For a normal oxide such as silica, the electrostrictive coefficient $Q \sim 10 \text{ m}^2/\text{C}^2$, the dielectric constant $K \sim 10$, and the thermal expansion coefficient $\alpha \sim 10^{-5} \text{ K}^{-1}$. For such a material the strain produced by an electric field of 1 MV/m is about 10^{-7} , which is equivalent to a temperature change of only 10^{-2} degrees. This would pose severe problems in an actuator or micropositioner, but the situation is quite different for a ferroelectric.

For PMN, $Q \sim 10^{-2}$, $K \sim 10^4$ and $\alpha \sim 10^{-6} \text{ K}^{-1}$. Therefore the electrostrictive strain for a field of 1 MN/m is about 10^{-3} which is equivalent to a temperature rise of 1000° ! Relaxor ferroelectrics sometimes have an abnormally low thermal expansion coefficient near the diffuse phase transformation where the dielectric constant and the electrostrictive strain are unusually large. Micropositioners made from ferroelectric ceramics are not troubled by small variations in temperature.

ORIGINS OF NONLINEARITY

What do nonlinear materials have in common? The passively-smart PTC thermistor and ZnO varistor have grain boundaries a few nm thick, insulating barriers that can be obliterated by the polarization charge accompanying a ferroelectric phase transformation, or, in the case of the varistor, insulating boundaries so thin they can be penetrated by quantum mechanical tunneling.

Small size is also key factor in the nonlinear behavior of semiconductors. The thin gate region in a transistor allows charge carriers to diffuse through unimpeded. The p-region in an n-p-n transistor is thin compared to the diffusion length in single crystal silicon. Similar size-related phenomena are observed in quantum well structures made from GaAs and $\text{Ga}_{1-x}\text{Al}_x\text{As}$. Planar structures with nm-thick layers show channeling behavior of hot electrons in clear violation of Ohm's law. Current - voltage relationships are highly nonlinear in many submicron semiconductor structures. Ohm's law is a statistical law which relies upon the assumption that the charge carriers make a sufficiently large number of collisions to enable them to reach a terminal velocity characteristic of the material. When the size of the conduction is sufficiently small, compared to the mean free path between collisions, the statistical assumption breaks down, and Ohm's law is violated.

Nonlinear behavior is also observed in thin film insulators where even a modest voltage of 1-10 volts can result in huge electric fields of 100 MV/m or more. This means that thin film dielectrics experience a far larger field than do normal insulators, and causing the polarization to saturate and electric permittivity to decline. Because of the high fields, electric breakdown becomes a greater hazard, but this is partly counteracted by an increase in breakdown strength with decreasing thickness. This comes about because the electrode equipotential surfaces on a thin film dielectric are extremely close together, thereby eliminating the asperities that lead to field concentration and breakdown.

The influence of nanometer-scale domains on the properties of relaxor ferroelectrics has already been made plain. Here the critical size parameter is the size of the polarization fluctuations arising from thermal motions near the broad ferroelectric phase transformation in PMN and similar oxides. The ordering of Mg and Nb ions in the octahedral site of the PMN structure results in a chemical inhomogeneous structure on a nm-scale, and this, in turn, influences the size of the polarization fluctuations. Tightly coupled dipoles within each Nb-rich portion of this self-assembling nanocomposite behave like a superparaelectric solid. The dipoles are strongly coupled to one another but not to the crystal lattice, and thus they reorient together under the influence of temperature or electric field. this in turn causes the large electric permittivities and large electrostrictive effects found in relaxor ferroelectrics.

The importance of nanometer-scale fluctuations and the instabilities associated with phase transformations is also apparent in the nonlinear elasticity of rubber and other polymeric materials. The thermally-assisted movement of the randomly oriented polymer chains under tensional stress results in large compliance coefficients, but rubber gradually stiffens as the chains align with the stress into pseudo-crystalline regions. The increase in stiffness with stress gives rise to sizeable third order elastic constants in many amorphous polymers. The effect depends markedly on temperature. On cooling, to lower temperatures rubber and other amorphous polymers transform from a compliant rubber-like material to a brittle glass-like phase which is of little use in nonlinear devices.

Nonlinear behavior is also observed in magnetic and optical systems. Superparamagnetic behavior, analogous to the superparaelectric behavior of relaxor ferroelectrics, is found in spin glasses, fine powder magnets, and magnetic cluster materials. As in PMN, the magnetic dipoles are strongly coupled to one another in nanometer-size complexes, but are not strongly coupled to the lattice. Superparamagnetic solids display nonlinear magnetic susceptibilities and unusual " ΔE " effects in which Young's modulus E can be controlled by magnetic field. The effect is especially large in metallic glasses made from Fe-Si-B-C alloys. The cluster size in spin glasses is in the nanometer range like those in PMN.

Lead lanthanum zirconate titanate (PLZT) perovskites can be prepared as transparent ceramics for electrooptic modulators. Quadratic nonlinear optic behavior are observed in pseudocubic regions of the phase diagram which show relaxor-like properties.

In summary, the nonlinear properties of electroceramics are often associated with nanometer-scale structure and diffuse phase transformations. Under these circumstances the structure is poised on the verge of an instability and responds readily to external influences such as electric or magnetic fields, or mechanical stress.

The ready response of nonlinear ceramics allows the properties to be tuned in space or time to optimize the behavior of the sensor-actuator systems referred to by some as "very smart ceramics."

ACKNOWLEDGEMENTS

Numerous discussions with Q.C. Xu, M. Blaskiewicz, L.E. Cross, K. Uchino, S.J. Jang and S. Yoshikawa are gratefully acknowledged. Carol Foster typed the manuscript with great skill.

DISCUSSION

P. Davies: Concerning the relaxor ferroelectric with cation ordering in the nanodomains, the charge imbalance between the ordered and disordered regions bothers me a little bit. Are we sure there are no oxygen deficiencies in these domains? Why are the ordered domains stable?

R. Newnham: Well, that's a good question. If you examine various ordered configurations, say by model-building, you find the one-to-one pattern goes together very nicely because there are six unit cells around each perovskite unit cell, making it easy to pair things off. If you try, two-to-one ordering corresponding to the overall composition, you find it is necessary to position niobium ions in neighboring octahedral sites. This violates Paulings electrostatic valence rule and leads to charge imbalance on the atomic scale.

What I'm pointing out is that if you look at other possible ordering schemes there are problems with them, too, so it comes down to which is least unfavorable.

P. Davies: Are we sure there are no oxygen deficiencies in the domains?

R. Newnham: Well, I'll let Prof. Smyth comment on that, but I can tell you that these relaxors are excellent insulators which will withstand very high voltages, and I think if there were a lot of oxygen vacancies which were present we would be seeing conduction and degradation phenomena which are not observed.

D. Smyth: Well, that's a question of continuity. You might have some motion within the domain, but whether it would transport throughout the entire system, I don't know. I don't think we have any direct evidence on that because it is difficult to probe these very small areas.

D. Kolar: What is the effect of grain size?

R. Newnham: The samples we have prepared have normal grain sizes on the micron scale. There have been studies of small grain sizes in ferroelectric ceramics and studies of nanocomposite materials showing transitions from the multidomain regime, to single domain, and to the superparaelectric regime. You have to ask in what temperature range and in which size regime are you operating. In the high temperature regime, the electrostrictive material behaves like a normal paraelectric, then on cooling, there is a broad diffuse phase region with relaxor phenomena, and then at low temperatures it is a normal ferroelectric with normal domain structure. Then PMN behaves pretty much like other ferroelectrics, but it is this broad diffuse range which comes about because of nanometer scale structure, and which we think is analogous to similar phenomena observed when ferroelectrics are prepared in very small particle sizes. This is what is often called superparaelectricity with very large dielectric constants and very large electrostrictive effects.

APPENDIX 6

ELECTROSTRRICTIVE AND PIEZOELECTRIC MATERIALS
FOR ACTUATOR APPLICATIONS

D. Damjanovic and R.E. Newnham

*Materials Research Laboratory
The Pennsylvania State University,
University Park, PA 16802*

A Section in Chapter 5 - Intelligent Material Systems.
ASME/NASA Monograph on Flight-Vehicle Materials, Structures
and Dynamics Technologies - Assessment and
Future Directions
Edited by Ahmed K. Noor and Samuel L. Venneri

ABSTRACT

The piezoelectric and electrostrictive effects in ferroelectric ceramics are reviewed with an emphasis on those properties that are relevant for applications in actuators. Various contributions to the piezoelectric effect in ferroelectric ceramics, especially lead zirconate titanate ceramics, are discussed in some detail. Relaxor ferroelectrics such as lead magnesium niobate are shown to be a unique family of materials with very attractive electrostrictive effects as well as piezoelectric properties. Finally, several actuator systems that employ piezoelectric and electrostrictive ceramics are briefly discussed.

INTRODUCTION

Piezoelectric and electrostrictive materials are a natural choice for precision displacement transducers or actuators. They utilize the strain induced by an electric field, an external parameter which can be easily controlled. Achievable strains are on the order of 10^{-4} - 10^{-3} for realizable fields ($\sim 10^6$ V/m), which for samples with dimensions on the order of 1 cm, translates into 10 μm displacements. At the same time, the expected accuracy may be as good as 0.01 μm . This, together with high speeds (1 - 10 μs), low power requirements, relatively high generative forces and possibility of miniaturization makes electrostrictive and piezoelectric actuators far superior to the conventional electromagnetic methods as well as to the newer types of actuators that are controlled by temperature (shape memory effect) or magnetic field (magnetostrictive effect) (22).

Formally, the relationship between the induced strain and electric field is simple, even in highly anisotropic piezoelectric and electrostrictive materials. The coupling coefficients (piezoelectric and electrostrictive coefficients), however, depend on the impurities present in the material, on the preparation procedure, on the size and frequency of applied electric and mechanical fields, on the temperature, and on aging time. Thus, a materials engineer has a challenging task when designing a material which will deliver the reproducible displacements required by the new generation of ultraprecise actuators. This paper deals with some of the properties of piezoelectric and electrostrictive ceramics that are important in the successful performance of an actuator assemblage.

FUNDAMENTAL RELATIONS

Piezoelectric Effect

Piezoelectricity describes the first order (linear) coupling between dielectric and elastic phenomena. For an anisotropic, homogeneous solid, under isothermal conditions and neglecting the magnetic field effects, the components of the elastic strain tensor x_{ij} are given by the following relation (16):

$$x_{ij} = s^E_{ijkl} X_{kl} + d_{ijk} E_k + \text{higher order terms} \quad (1)$$

where X_{kl} and E_k are the components of the stress tensor and the electric field vector, respectively. The s^E_{ijkl} coefficients are the components of the elastic compliance tensor measured at constant electric field. The components d_{ijk} of the piezoelectric tensor define the linear electromechanical coupling. In the first approximation, all the higher order terms in Eq. (1) are considered to be negligible. If a static electric field is applied to a piezoelectric material that is free to change its shape, the total stress X is zero and Eq. (1) reduces to $x_{ij} = d_{ijk} E_k$. The piezoelectric term thus relates the mechanical strain developed in a material as a consequence of the electric field applied to the material. For this reason d is called the piezoelectric strain coefficient and the effect is known as the converse piezoelectric effect. Alternatively, for a linear, anisotropic, homogeneous, polarizable solid the components of the dielectric displacement vector D_i are given by the relation:

$$D_i = d_{ijk} X_{jk} + \epsilon^X_{ij} E_j + \text{higher order terms} \quad (2)$$

where ϵ^X_{ij} are the components of the dielectric permittivity tensor measured at constant stress. As before, the higher order terms are neglected. If an elastic field (stress) is applied to a piezoelectric material that is short-circuited, the total electric field across the material is zero.

and Eq. (2) becomes $D_i = d_{ijk}X_{jk}$. In this case, the piezoelectric term relates the charge developed on the material's surface upon application of stress. The d coefficient is now called the piezoelectric charge coefficient and the corresponding electromechanical coupling is known as the direct piezoelectric effect. It can be shown that the components of the piezoelectric tensors for the direct and converse effects are equivalent. In matrix form one can write $d_{\text{converse}} = (d_{\text{direct}})^t$, where t denotes the transpose matrix.

The piezoelectric coupling between the elastic and dielectric parameters of a material can be readily introduced using the thermodynamic approach. One can arbitrarily choose a set of the independent variables in the appropriate thermodynamic potential to derive the so-called constitutive piezoelectric equations. In addition to Eqs. (1) and (2), the other three sets of constitutive equations are (3)

$$X = c^E x - e^E E \quad (3a)$$

$$D = ex + e^x E \quad (3b)$$

$$X = c^D x - h^D D \quad (4a)$$

$$E = -hx + \beta^x D \quad (4b)$$

$$x = s^D X + g^D D \quad (5a)$$

$$E = -gX + \beta^X D \quad (5b)$$

In these equations the indices for the tensorial components are dropped for simplicity. The piezoelectric tensors e , g and h are respectively known as the stress (or charge), voltage (or strain) and stress (or voltage) piezoelectric coefficients. c is the elastic stiffness tensor, and the superscript denotes whether it is measured at constant field E or constant displacement D . s^D is the elastic compliance at constant electric displacement. The difference between the two types of coefficients will be discussed in a subsequent section. e^x is the dielectric permittivity at constant strain. β^x and β^X are the dielectric impermittivities at constant strain and constant stress, respectively. Matrices of the dielectric impermittivity tensors are defined as $\beta^x = (\epsilon^x)^{-1}$ and $\beta^X = (\epsilon^X)^{-1}$. Relationships between the four piezoelectric coefficients are as follows:

$$d_{ijk} = e_{ilm}s^E_{lmjk} = g_{ljk}\epsilon^X_{il} \quad (6a)$$

$$e_{ijk} = d_{ilm}c^E_{lmjk} = h_{ljk}\epsilon^x_{il} \quad (6b)$$

$$g_{ijk} = d_{ljk}\beta^X_{li} = h_{ilm}s^D_{lmjk} \quad (6c)$$

$$h_{ijk} = e_{ljk}\beta^x_{il} = g_{ilm}c^D_{lmjk} \quad (6d)$$

The choice of which of Eqs. (1)-(5) is to be used in the particular problem depends on the elastic and electric boundary conditions. Furthermore, the constitutive equations may be derived for isothermal or adiabatic conditions. For nonpolar materials, the isothermal and adiabatic coefficients are equal. For the polar materials (pyroelectric and ferroelectric) the difference between the isothermal and adiabatic coefficients is usually negligible (3).

Symmetry Arguments

Because of the symmetry of the stress and strain tensors the third rank tensor of the piezoelectric coefficients d_{ijk} (as well as e, g and h) is also symmetrical in indices j and k . This leaves only 18 independent piezoelectric coefficients. To convert the tensor coefficients to matrix form, the pair of indices jk is replaced with a single index $m = 1, 2, 3$ if $j=k$ and $jj=11, 22,$ or 33 , respectively. If $j \neq k$ then $jk = 23$ or $32, 13$ or 31 and 12 or 21 is replaced with $m = 4, 5, 6$, respectively. In matrix notation (16), d_{ijk} are written as $d_{ijk} = d_{im}$ when $m = 1, 2, 3$ and $d_{ijk} = 1/2d_{im}$ when $m = 4, 5, 6$. Hence, the direct and converse piezoelectric effects may be written in the following matrix form:

$$D_i = d_{im} X_m \quad (7a)$$

$$x_m = d_{im} E_i \quad (7b)$$

where a corresponding reduction is made in the subscripts of the components of the stress and strain tensors (16).

Neumann's principle states that the symmetry elements of a physical property of a crystal must include the symmetry elements of the point group of the crystal (16). The principle can be extended to include not only the 32 crystallographic point groups but also the Curie point groups which contain the infinite symmetry axes (19). The most important consequence of Neumann's principle is that certain physical properties may be absent in a material because of its symmetry. Thus, in the eleven centrosymmetric point groups and in point group 432 all the components of the piezoelectric tensor (and all odd-rank tensors) are equal to zero. The remaining 20 point groups are potentially piezoelectric. Neumann's principle, however, gives only necessary conditions for a material to exhibit the piezoelectric effect. Whether a material that belongs to one of the piezoelectric point groups exhibits measurable piezoelectricity has to be verified experimentally.

Of the 20 piezoelectric point groups, 10 are polar. These are 1, m, 2, mm2, 3, 3m, 4, 4mm, 6, and 6mm. Crystals that belong to these point groups possess spontaneous electrical polarization P_s and exhibit a pyroelectric effect. If there is more than one equilibrium direction along which the vector of the spontaneous polarization may be oriented the material is also ferroelectric, provided that switching between states can be achieved by a realizable electric field.

Among the polycrystalline materials only ferroelectric materials and polar glass ceramics show piezoelectricity. The polycrystalline materials with a random orientation of grains belong to the Curie point group $\infty\infty\infty m$ which has spherical symmetry (14). This point group has a center of symmetry and all odd-rank tensor properties of polycrystalline materials with random distribution of grains are equal to zero. In ferroelectric materials, however, a strong electric field can permanently reverse the directions of the polarization vector P_s within many of the domains inside each grain, leading to a nonzero macroscopic polarization. Polarized or poled polycrystalline ferroelectric materials possess conical symmetry ∞m . This symmetry has the same nonzero components of the dielectric, elastic and piezoelectric tensors as the point group 6mm. Therefore, poled ferroelectric ceramics exhibit the piezoelectric effect. The polycrystalline ferroelectric piezoelectrics are by far the largest and the most important group of the piezoelectric materials. Matrices for the elastic compliance s , the dielectric permittivity ϵ , and the piezoelectric coefficient d are given in Table I for poled ceramics.

Table I. Matrices of the elastic compliance s , dielectric permittivity ϵ and piezoelectric coefficient d for poled ceramic.

$$\left(\begin{array}{ccccccc}
 s_{11} & s_{12} & s_{13} & 0 & 0 & 0 & 0 & d_{31} \\
 s_{12} & s_{11} & s_{13} & 0 & 0 & 0 & 0 & d_{31} \\
 s_{13} & s_{13} & s_{33} & 0 & 0 & 0 & 0 & d_{33} \\
 0 & 0 & 0 & s_{44} & 0 & 0 & 0 & d_{15} \\
 0 & 0 & 0 & 0 & s_{44} & 0 & d_{15} & 0 \\
 0 & 0 & 0 & 0 & 0 & s_{66} & 0 & 0 \\
 0 & 0 & 0 & 0 & d_{15} & 0 & \epsilon_{11} & 0 \\
 0 & 0 & 0 & d_{15} & 0 & 0 & 0 & \epsilon_{11} \\
 d_{31} & d_{31} & d_{33} & 0 & 0 & 0 & 0 & \epsilon_{33}
 \end{array} \right) = \begin{pmatrix} s & d' \\ d & \epsilon \end{pmatrix}$$

schematic

$$s_{66} = 2(s_{11} \cdot s_{12})$$

Electrostrictive Effect

In the section on piezoelectricity the relationships between strain and electric field (converse piezoelectricity) and between electric displacement and stress (direct piezoelectricity) are developed assuming a linear dependence of strain on electric field and electric displacement on stress. This assumption is valid only if the applied stress or electric field is small. Otherwise, higher order terms in the expansion of the corresponding thermodynamic functions must be taken into account (16). Thus, for a nonlinear solid one may write the following expression for the total strain:

$$x_{ij} = s^E_{ijkl} X_{kl} + d_{ijk} E_k + M_{klji} E_k E_l + \text{higher order terms} \quad (8)$$

As before, the first term in Eq. (8) describes Hooke's law, the second term is the converse piezoelectric effect and the third term is called the electrostrictive effect. The components M_{klji} of the fourth rank tensor M are the electrostrictive coefficients and the corresponding matrix has the same nonzero elements as that of the elastic compliance (see Table 1). For a zero stress ($X = 0$) and neglecting the higher order terms, Eq. (8) reduces to (16):

$$x_{ij} = d_{kij} E_k + M_{klji} E_k E_l = (d_{kij} + M_{klji} E_l) E_k \quad (9)$$

The electrostrictive effect can therefore be classified as an electric-field dependent contribution to the linear piezoelectric effect. In principle, however, the two effects are separable because the piezoelectric effect is possible only in noncentrosymmetric materials. Being described by an even rank tensor, the electrostrictive effect is not limited by symmetry and is in fact present in all materials, even those that are amorphous. Hence, the electrostrictive effect describes the nonlinear (second order or quadratic) dependence of the strain on the applied electric field.

If the strain in Eq. (8) is expressed in terms of the components of the polarization vector P , one obtains another commonly used set of electrostrictive coefficients Q_{ijkl} :

$$x_{ij} = g_{ljk} \epsilon^X_{il} P_k + Q_{ijkl} P_k P_l, \quad M_{ijmn} = \epsilon^X_{km} \epsilon^X_{ln} Q_{ijkl} \quad (10)$$

In addition to the direct electrostrictive effect, the second order coupling between stress and polarization leads to a converse electrostrictive effect. The direct and converse effects are thermodynamically equivalent. However, in materials with non-zero spontaneous polarization there is an additional coupling term caused by the dependence of the dielectric permittivity on the spontaneous polarization, which in turn is dependent on pressure. For this reason the interpretation of the experimentally determined values of the electrostrictive coefficients in ferroelectric materials is not always straightforward (24). Similarly, the equivalence between the direct and converse piezoelectric coefficients as derived thermodynamically breaks down in materials with non-zero spontaneous polarization (12,13). A unique piezoelectric tensor can still be defined if there is an external surface charge compensation of the internal polarization. In the absence of such charge compensation new piezoelectric relations ought to be used.

Electromechanical Coupling Factors

The constitutive piezoelectric equations (1 - 5) show that the elastic or dielectric response of a piezoelectric material depends not only on its piezoelectric properties but also on its elastic and dielectric parameters. Therefore, a figure of merit of a piezoelectric material must include its elastic, dielectric and piezoelectric coefficients and at the same time should be independent of external forces. Clearly such a figure of merit or, as it is most often called, a coupling factor, is not uniquely defined. Berlincourt et al. (3) define the piezoelectric coupling factor as "the ratio of the mutual elastic and dielectric energy density to the geometric mean of the elastic and dielectric self-energy density." For a linear system the internal energy is given by:

$$U = 1/2 (x_m X_m + D_i E_i) \quad (11)$$

which together with Eq. (1) gives

$$U = 1/2 (X_m s_{mn} X_n + X_m d_{mi} E_i + E_i d_{im} X_m + E_i \epsilon_{ij} E_j) \\ = U_e + 2U_m + U_d \quad (12)$$

where U_e is elastic contribution to the internal energy, U_d is dielectric and U_m is the mutual or coupled contribution to the internal energy U . According to this definition, the electromechanical coupling factor k is given by the absolute value of the following expression:

$$k = U_m / (U_e U_d)^{1/2} \quad (13)$$

Each term in Eq. (11) involves generally a summation over six stress and three electric field components. Eqs. (11) and (13) depend on the constitutive piezoelectric relationships used, i.e. they depend on boundary conditions of the particular problem.

For a one-dimensional ceramic bar (point group ∞m) with electric field perpendicular to its length, Eq. (11) becomes

$$U = 1/2 (X_I^2 s E_{II}) + E_3 X_I d_{3I} + 1/2 (\epsilon^X_{33} E_3^2) \quad (14)$$

and the corresponding coupling factor is

$$k_{3I} = d_{3I} / (\epsilon^X_{33} s E_{II})^{1/2} \quad (15)$$

For a ceramic bar with electric field along its length the coupling factor is

$$k_{33} = d_{33} / (\epsilon^X_{33} s E_{33})^{1/2} \quad (16)$$

Similarly, coupling factors can be obtained for other configurations of stress and electric field or any other set of independent variables and for all piezoelectric point groups.

As defined by Eq. (13), coupling factors are, however, meaningful only in the static limit. In a dynamic case, for example near a resonant frequency, the coupling factor is dependent on stress and strain, which show spatial variations (20). Furthermore, for two- or three-dimensional cases, the distribution of strains and stresses is usually more complicated, and the stress components in the numerator and denominator in Eq. (13) do not always cancel even in a static situation. Hence, the coupling coefficients are dependent on external variables and often do not describe intrinsic properties of the material. Despite these drawbacks, the concept of electromechanical coupling factors as defined by Berlincourt is very widely used.

The factor $k^2 = d^2/(s\epsilon)$ involving the piezoelectric, elastic, and dielectric constants that is found in all the coupling factors is a fundamental characteristic of a piezoelectric material and appears in many piezoelectric relations independent of Eq. (13). Thus, if a static electric field E is applied to a clamped piezoelectric material the strain x is zero and Eq. (1) gives $X s^E = -dE$. Replacing the stress X in Eq. (2) with $X = -dE/s^E$, the following expression for the dielectric displacement D is obtained:

$$D = -d^2 E / s^E + \epsilon^X E = \epsilon^X (1 - d^2 / (s^E \epsilon^X)) E \quad (17)$$

The dielectric permittivity $\epsilon^x = \epsilon^X (1 - d^2 / (s^E \epsilon^X))$ is called the clamped dielectric constant. Similarly, under open-circuit conditions, the dielectric displacement D in Eq. (2) is zero, and $dX = -\epsilon^X E$. Replacing the electric field E in Eq. (1) with $E = -dX/\epsilon^X$, the strain x becomes

$$x = s^E X - d^2 X / \epsilon^X = s^E (1 - d^2 / (s^E \epsilon^X)) X \quad (18)$$

and the elastic compliance $s^D = s^E (1 - d^2 / (s^E \epsilon^X))$ at constant (zero) displacement D is obtained. It follows that the velocity of acoustic waves, $v = (\rho s)^{1/2}$ where ρ is density, in a piezoelectric material depends on electric boundary conditions. The velocity of elastic waves at constant electric field E (short-circuit condition) and constant electric displacement D (open-circuit condition) are thus related to each other through the electromechanical coupling factors. For

materials such as PZT with electromechanical coupling factor k close to 0.7, the difference between clamped and free dielectric constant or between the short- and open-circuit elastic compliances may be as high as 50%.

PIEZOELECTRIC AND ELECTROSTRRICTIVE CERAMIC MATERIALS

The only requirement for a nonconductive material to exhibit the piezoelectric effect is that the material belongs to one of the 20 piezoelectric point groups. It is not surprising then that piezoelectricity is often encountered in nature. It is found in many organic materials, single crystals and ceramics, but also in hybrid materials such as polymer/ceramic composites and polar glass ceramics. Clearly then, an answer to the question of what mechanisms contribute to piezoelectricity is not a simple one.

Contributions to the Piezoelectric Effect

Single Crystal vs. Ceramic Properties. Ferroelectric Domains. The complexity of the coupling between the electric and elastic properties can be comprehended when ferroelectric materials are considered. The origin of the intrinsic piezoelectricity in most ferroelectric materials can be explained in terms of the electrostriction of the paraelectric phase using thermodynamic phenomenological theory (8). In principle then, it is possible to predict a complete set of the values of the piezoelectric coefficients of, for example, single crystal $BaTiO_3$, knowing the corresponding electrostrictive coefficients and the value of the spontaneous polarization at the temperature of interest.

In practice, however, ferroelectric materials are usually used in polycrystalline or ceramic form. Each grain consists of domains which are oriented along the directions dictated by the symmetry of the parent phase. Ferroelectric domains form as the ferroelectric material is cooled through its Curie temperature. In ceramics, the individual grains tend to assume anisotropic shapes determined by the orientation of the crystallographic axes. The shape change of each grain induces large stresses upon adjacent grains. In order to minimize the total elastic energy, a complex domain structure forms within each grain adjusting its shape to the immediate environment. Thus, all the tensor properties of a ceramic material are averages of the corresponding single crystal values represented by the individual grains and domains (11).

The poling process required to induce piezoelectricity only partly aligns the polar vectors of the domains and the resulting property values are always different than those for the single crystal. The averaging procedure used to calculate the components of a tensor property of a poled ferroelectric ceramic must include not only the degree of the orientation of the domains, and the structure, size, and shape of grains, but also the boundary conditions on the grains and domains. For coupled properties such as piezoelectricity this means that the elastic and dielectric boundary conditions on the grains and domains must be known. Furthermore, when the response of a piezoelectric ceramic is examined under weak alternating electric fields or mechanical stress, the domain walls will move in a reversible fashion. The effect of the domain wall dynamics on the dielectric, elastic and piezoelectric properties may be considerable and must be taken into account (2).

Role of Defects. The spontaneous polarization P_s carried by the domains interacts with polar defects (point defects) present in the crystal structure. The defects may be induced in the material either accidentally during preparation, or may be purposely added with the aim of controlling the conductivity and the poling behavior of material. Defects also influence the domain wall mobility, the diffusion properties and the sintering of the ceramic. The interaction of the domains and defects leads to so called "soft" and "hard" piezoelectric compositions. Piezoelectrically soft materials are characterized by relatively mobile domain walls and high piezoelectric constants. In the hard compositions the domain wall motion is more inhibited resulting in lower piezoelectric constants but a more stable remnant polarization (15). Some examples of the mechanisms which lead to soft and hard compositions will be given in the section on PZT piezoelectric ceramics.

Piezoelectric Relaxation. Recently, there has been an increasing evidence that the piezoelectric constants of ferroelectric ceramics exhibit nonzero phase angle, i.e. they may be described as complex quantities. This should be expected since the piezoelectricity represents a coupling between the elastic and dielectric properties of a material, both of which are known to be major sources of energy dissipation. Although the piezoelectric relaxation in ferroelectric ceramics is not yet fully understood, it is clear that it does not originate from an independent loss mechanism in the material but is a result of an electromechanical coupling between the dielectric and mechanical losses operating in the material. The loss mechanisms may lead to a large and unwanted dependence of piezoelectric coefficients on frequency often characterized as relaxation-type behavior (1).

Summing up, the piezoelectric constants of a ferroelectric ceramic may be written in the following form:

$$d = d[d_{ij}(s.c.), \theta] + \Sigma \Delta d' - i\Sigma d'' + \Sigma_{\text{other}} \quad (19)$$

where $d/d_{ij}(s.c.), \theta$ is a function of intrinsic single crystal piezoelectric coefficients, $d_{ij}(s.c.)$, and also a function of the degree of polarization of ceramic, described by an orientation parameter θ . $\Sigma \Delta d' - i\Sigma d''$ describes the sum of all relaxation contributions, and Σ_{other} is a sum of all nonrelaxational extrinsic contributions to the total piezoelectric coefficients of ceramics. The various competing mechanisms to piezoelectricity in ferroelectric ceramics are sometimes of comparable strength and may even lead to a change of sign of the piezoelectric constant with temperature or frequency (7,10).

Hysteresis. The complex changes in the configuration of domain walls in ferroelectric materials under an AC electric field lead to the characteristic hysteretic relationships between polarization and electric field and between electric field and strain, Fig. 1. Those domains that do not return to their initial random configuration after the electric field is removed, but remain oriented to a certain degree, are responsible for the remnant (residual) strain and polarization. Since the remnant strain and polarization are functions of the maximum applied field, it is clear that there is a range of possible strain and polarization states for zero field. Fig. 1 (Refs. 4 and 9).

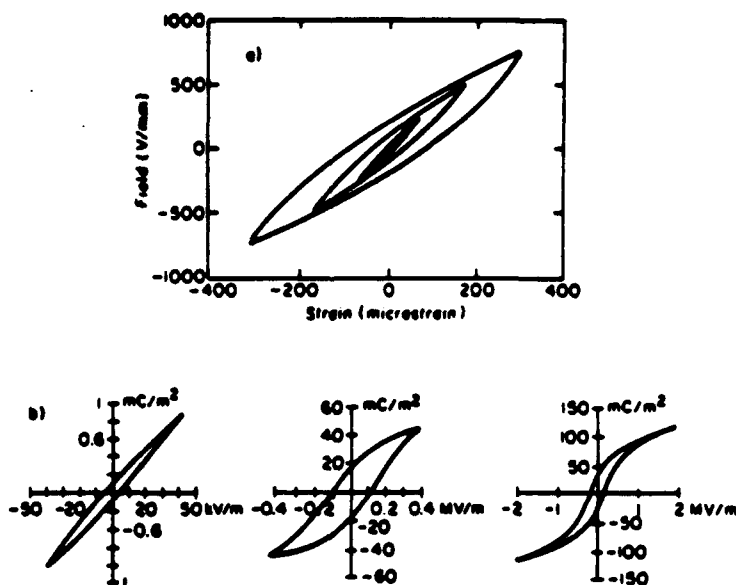


Fig. 1. (a) Strain-electric field and (b) polarization-electric field hysteresis loops for typical ceramic ferroelectrics.

Aging. One of the most complex properties of the ferroelectric ceramics is the time dependence of their elastic, dielectric and piezoelectric coefficients. This phenomenon, known as aging, follows the poling of ceramics, even in the absence of external forces or temperature changes. Aging occurs in all ferroelectric ceramics although its degree varies greatly from one composition to another. The effect is closely related to the mobility of the domain walls. An important contribution to the aging is the slow relaxation of the high stresses that are introduced into ceramic during poling at elevated temperatures. The poling is accompanied by anisotropic shape changes of the grains, which are caused by the reorientation of domains under the poling field. When the external field is removed and the ceramic is cooled to room temperature, the domain configuration will tend to reach a new equilibrium state relieving some of the stresses (11).

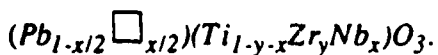
Aging is affected by the internal fields created by defect dipoles which, under certain conditions, may stabilize the domain configuration by interacting with the spontaneous polarization within domains. Thus, the aging in for example PZT ceramics, may be controlled by doping the ceramics with suitable aliovalent cations (15). In relaxor ferroelectrics, such as lead magnesium niobate (PMN), ageing seems to be fully controlled by the impurities and may be completely absent in pure, stoichiometric material (17).

Lead Zirconate Titanate (PZT) Ceramics

The phase diagram of the lead zirconate titanate ($Pb(Zr,Ti)O_3$ or PZT) system is shown in Fig. 2a. A complete solid solution forms at high temperature with Zr and Ti randomly distributed over the octahedral sites of the cubic perovskite structure. On cooling, the structure undergoes a displacive phase transformation into a distorted perovskite structure. Titanium-rich compositions favor a tetragonal modification with a sizeable elongation along [001] and a large spontaneous polarization in the same direction. There are six equivalent polar axes in the tetragonal state corresponding to the [100], [100], [010], [010], [001] and [001] directions of the cubic paraelectric state. A rhombohedral ferroelectric state is favored for zirconium-rich compositions. Here the distortion and polarization are along [111] directions, giving rise to eight possible domain states: [111], [111], [111], [111], [111], [111], [111] and [111].

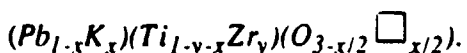
The compositions which pole best lie near the morphotropic boundary between the rhombohedral and tetragonal ferroelectric phases. For these compositions there are fourteen possible poling directions over a very wide temperature range. This explains why the piezoelectric coefficients are the largest near the morphotropic boundary (Fig. 2b). Typical values are $d_{33} \approx 400$, $d_{31} = -170$ and $d_{15} = 500$ pC/N. The magnitudes depend markedly on dopants and defect structure because of their influence on domain wall motion.

Donor ions create Pb vacancies in the PZT structure. As an example, when Nb^{5+} is substituted for Ti^{4+} , vacancies on the lead site result:



Donor doping is not effective in pinning domain walls. Pinning is believed to result from the alignment of defect dipoles with the spontaneous polarization within a domain. The defect dipoles come from the negatively charged Pb vacancies paired with dopant Nb^{5+} ions. Since the defect dipoles are formed at high temperature, the dipoles are not aligned with P_s initially because the spontaneous polarization is zero in the cubic paraelectric state. Alignment can only take place below the Curie temperature (~350°C for PZT) where diffusion rates are low. Such is the case for donor-doped PZT, a so-called "soft" PZT. In a soft PZT, domain wall motion contributes to the size of the dielectric and piezoelectric coefficients. Adversely, however, soft PZT ceramics are easily depoled because the domain walls are not pinned.

Acceptor doping with lower valent ions such as K^+ (for Pb^{2+}) or Fe^{3+} (for Ti^{4+}) is employed to produce "hard" PZT. Oxygen vacancies are generated by acceptor doping:



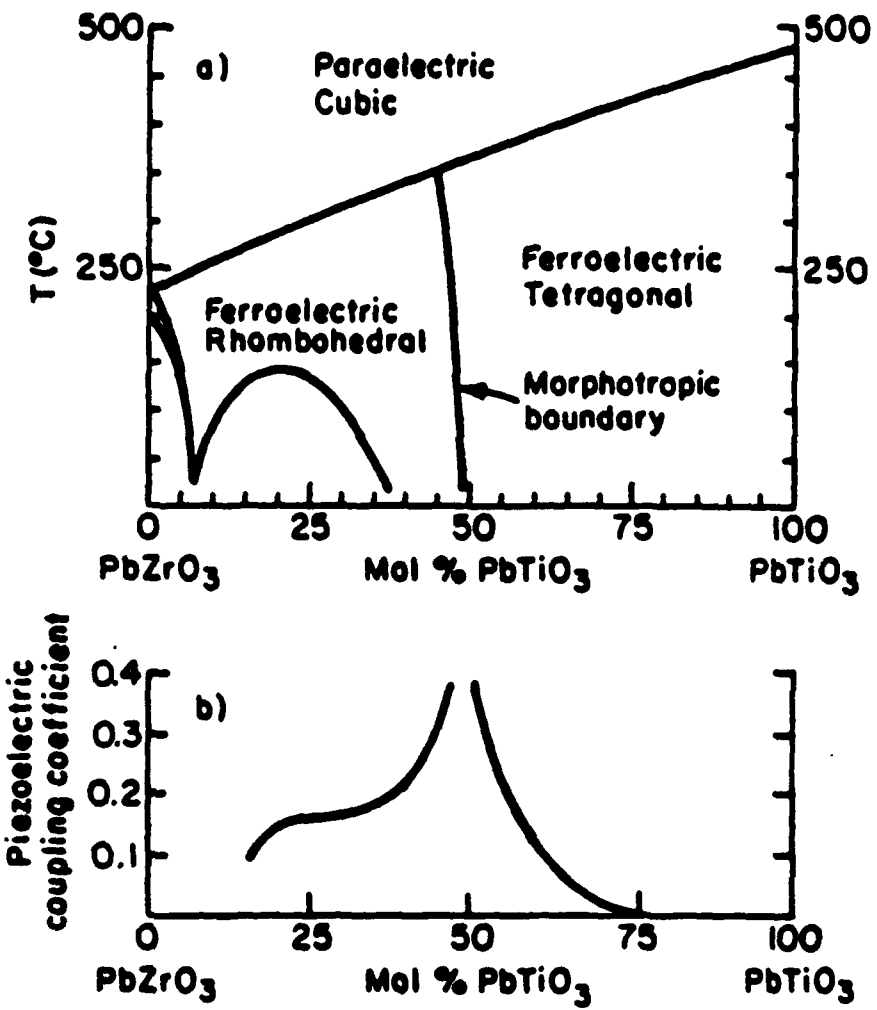


Fig. 2. (a) Binary phase diagram of the lead zirconate-titanate ceramics. (b) Large piezoelectric coefficients are obtained for poled ceramics with compositions near the morphotropic phase boundary.

Domain walls are pinned in hard *PZT* because the defect dipoles are able to align in accordance with the domain structure. Dipoles consisting of oxygen vacancies and associated dopant ions are able to reorient more easily in a hard *PZT*. The explanation lies in the ease with which oxygen vacancies diffuse at temperature below T_c .

Examination of the perovskite structure makes it clear why oxygen vacancies diffuse faster than cation vacancies. Cations are completely surrounded by oxygens and are separated from the nearest cation site by an entire unit cell ($\sim 4 \text{ \AA}$), making diffusion very difficult. Oxygen sites, on the other hand, are adjacent to one another, only 2.8 \AA apart. Hence oxygens can easily move into nearby oxygen vacancies, realigning defect dipoles and pinning domain walls.

Since their discovery in the 1950s, *PZT* based ceramics have become, along with quartz, the most widely studied and used piezoelectric material. Because of its high piezoelectric coefficients, simple preparation, ease of poling and low cost the *PZT* family is used more than any other piezoelectric material for transducer, sensor, and actuator applications. The only exception is quartz which, owing to the excellent stability of its piezoelectric properties with time and temperature, has not been surpassed by *PZT* in the field of frequency control.

Electric Field Induced Piezoelectricity in Relaxor Ferroelectrics

The relaxor-type ferroelectrics are discussed in detail in this section. For the present purpose, it is sufficient to say that relaxor ferroelectrics cannot be poled, even at temperatures considerably below the so-called diffuse phase transition. However, in this temperature range, relaxor materials show high dielectric constants and very large electrostrictive effects, Fig. 3 (Refs. 5 and 6). The piezoelectric d_{33} coefficient is the slope of strain-electric field curve, Eq. (8). The nonlinearity between strain and electric field in a relaxor ferroelectric can be used to tune the piezoelectric coefficient. From Fig. 3, the value of d_{33} for lead magnesium niobate ($\text{Pb}(\text{Mg}_{1/3}\text{Nb}_{2/3})\text{O}_3$ or *PMN*) with 10-mole% lead titanate (PbTiO_3 or *PT*) ($0.9\text{PMN} - 0.1\text{PT}$) at room temperature is zero at zero field and increases to a maximum value of $\sim 1500 \text{ pC/N}$ (about three times larger than *PZT*) under a bias field of about 3.7 kV/cm . Recent measurements with a laser interferometer show that transverse piezoelectric coefficient (d_{31}) in $0.9\text{PMN} - 0.1\text{PT}$ ceramics also exhibits very high values under bias field, with a maximum of about $\sim -400 \text{ pC/N}$ at bias field of $\sim 3 \text{ kV/cm}$, Fig. 4 (Ref. 21).

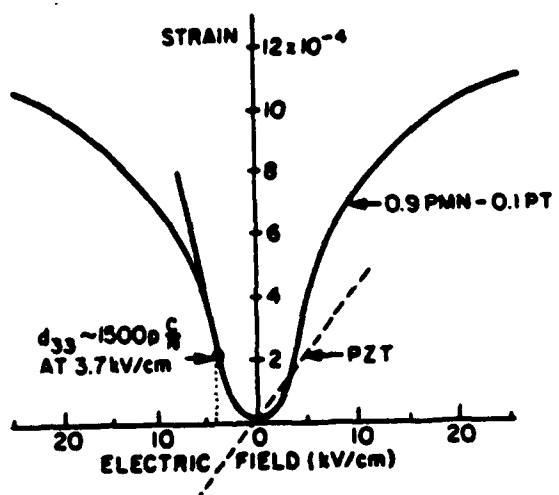


Fig. 3. Electromechanical coupling in electrostrictive (PMN-PT) and piezoelectric (PZT) ceramics.

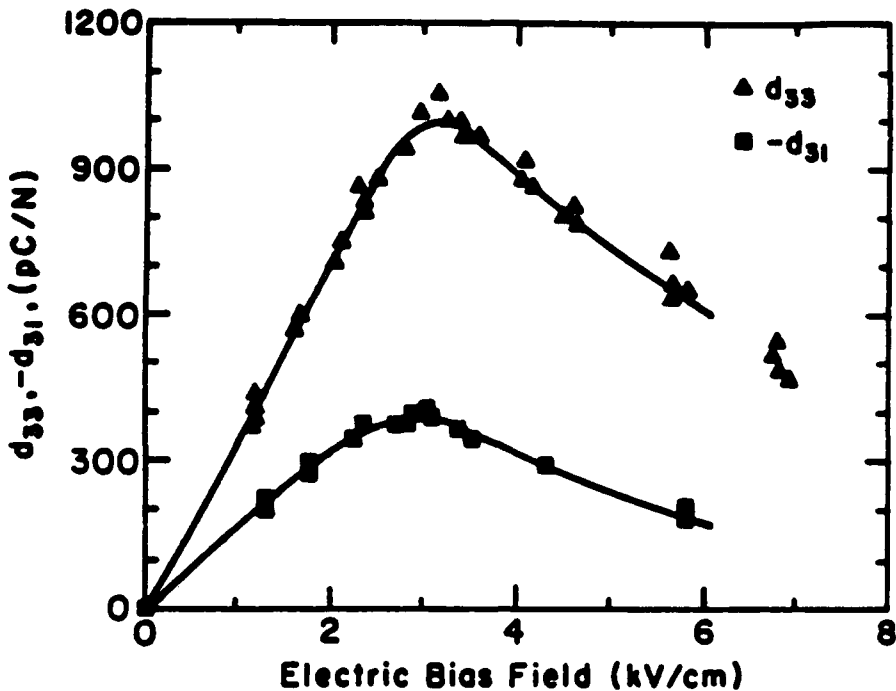


Fig. 4. Piezoelectric coefficients d_{33} and d_{31} of 0.9PMN-0.1PT as a function of DC electric bias field, measured at 500 Hz using a laser interferometer.

Electrostrictive Materials

The electrostrictive effect is often believed to be too small for exploitation in devices. This is indeed true for most conventional nonferroelectric materials as well as for many ferroelectrics. The magnitude of the polarization related electrostrictive coefficients Q in nonferroelectric materials is on the order of $10 \text{ m}^4/\text{C}^2$ and in most "normal" ferroelectrics $Q \sim 10^{-1} \text{ m}^4/\text{C}^2$. Eq. (10) however indicates that the electrostrictive strain x is equal to QP^2 , where $P = \kappa\epsilon_0 E$ is the induced polarization, κ is the dielectric constant of the material and ϵ_0 permittivity of free space. Thus, for a given electric field E , the materials with a very large dielectric constants exhibit large electrostrictive strains, even though their electrostrictive coefficients are relatively small. In most nonferroelectric materials dielectric constant is about 10 and for a typical field, say $E = 10^6 \text{ V/m}$, the achievable strain is only 10^{-7} . In normal ferroelectric materials near the ferroelectric-paraelectric phase transition dielectric constant may reach high values (10^3) but the electrostrictive strain ($\sim 10^{-5}$) is still smaller than that in piezoelectric ceramics.

Over the past 20 years, however, the development of high permittivity capacitor dielectrics have led to the discovery of many partially disordered structures, such as the relaxor ferroelectrics, with extremely large dielectric constants. The values of electrostrictive coefficients in relaxor ferroelectrics are relatively small, on the order of $10^{-2} \text{ m}^4/\text{C}^2$, but dielectric constants on the order of 10^4 are observed over a wide range of temperatures near the diffuse phase transition. Thus, electrostrictive strains in a typical relaxor material are on the order of 10^{-4} , and are comparable in size to those in piezoelectric ceramics.

Relaxor Ferroelectrics. Relaxor ferroelectrics are characterized by a strong dispersion of the dielectric permittivity with frequency, Fig. 5, and the absence of macroscopic polarization even at temperatures much below the temperature of the maximum dielectric constant (5). This unusual dielectric response of relaxor ferroelectrics is explained by a statistical inhomogeneity in the distribution of the B_1 and B_2 cations in the B sites of the $A(B_1, B_2)O_3$ perovskite structure. This chemical disorder is responsible for formation of microregions (microdomains) within the material which have widely different Curie temperatures. Relaxor ferroelectrics thus do not have a well-defined Curie temperature but rather exhibit a Curie range over which the material is a statistical mixture of paraelectric and ferroelectric regions. As temperature decreases from the high-temperature paraelectric state the

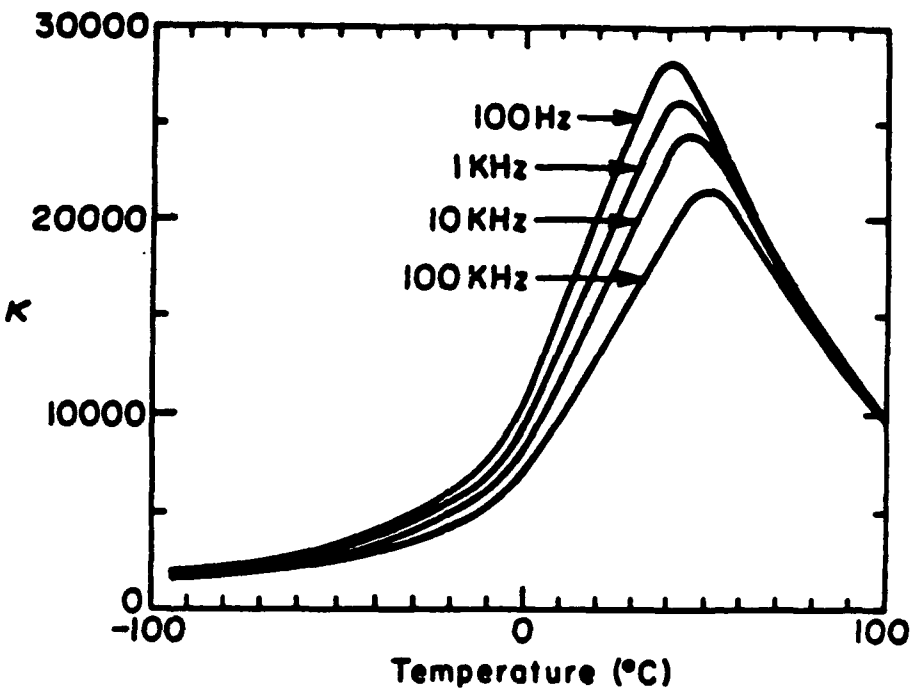


Fig. 5. Dielectric constant of 0.9PMN-0.1PT as a function of temperature for selected frequencies.

microdomains gradually coalesce to macrodomains giving rise to a diffuse phase transformation. The polarization fluctuations associated with the polar microregions are dependent on the electric bias field and measurement frequency. The dielectric constant drops off rapidly with frequency (hence the name "relaxor") because it takes time for the polarization fluctuations to respond. DC bias fields favor coalescence, having the same effect as lowering the temperature. This classical interpretation of the relaxor behavior is not completely successful in explaining all the complex properties of relaxor ferroelectrics as several recent studies suggest (5,23). Relaxor behavior is very common among Pb-based perovskites, suggesting that Pb^{+2} and its "lone-pair" electrons play a role in the microdomain process, possibly by adjusting the orientation of the lone pair.

Lead Magnesium Niobate - Lead Titanate Relaxor Ferroelectrics. Lead magnesium niobate ($Pb(Mg_{1/3}Nb_{2/3})O_3$ or PMN) is a typical relaxor ferroelectric and perhaps the most studied. Its solid solution with lead titanate (PT) has a morphotropic phase boundary near 35-mole% PT. All compositions on the PMN rich side of the morphotropic phase boundary exhibit relaxor behavior. The most recent studies of this system suggest that the relaxor ferroelectric is a polar-glassy system, analogous to a spin-glass rather than being "superparaelectric", as suggested in the past (23).

It has been pointed out that for temperatures within the Curie range, the relaxor ferroelectric may be driven into polar form by an electric bias field. The induced piezoelectric effect is thus tunable by the bias field. On removal of the field relaxor reverts back to a random arrangement of microregions with no net remnant polarization or strain (6). The absence of hysteresis in the field-strain curve on the high-temperature side of the Curie range is another advantageous feature of relaxor ferroelectrics.

PMN-PT relaxor ferroelectrics are a unique family of materials with a remarkable set of properties: (1) electrostrictive strains are comparable to that of the best conventional piezoelectric ceramics, (2) nonhysteretic behavior is responsible for excellent positional reproducibility (3) no poling is required, and (4) the magnitude of piezoelectric coefficients may be adjusted by electric bias field, and the maxima values of the piezoelectric coefficients are 2-3 times higher than those in PZT ceramics.

PIEZOELECTRIC AND ELECTROSTRRICTIVE ACTUATORS

There are presently more than 20 practical devices that employ piezoelectric and electrostrictive actuators (22), and it seems likely that the range of applications for solid state displacement transducers will continue to grow in the future. Table 2 lists some of the applications of piezoelectric/electrostrictive actuators. Properties that are essential for the performance of one type of actuator, for instance a linear response, are often irrelevant for others. Thus, each application demands carefully defined figure of merit for the actuator material.

Table 2. Actuator applications

Tracking Optical and Magnetic Heads
Drivers for Relays and Switches
Wire-Dot Printers and Via Punches
Fuel Injection Valves
Adaptive Optic Systems
Micropositioners for Robots and Machine Tools
Cone Vibrators for Speakers
Fans and Conical Air Movers
<u>Ink Jet Printers</u>

Classification of Electrostrictive and Piezoelectric Actuators

The strain of a displacement transducer may be controlled by an electric field in different ways (17,22). Fig. 6. In the first case, the strain of the actuator is controlled directly by electric field, as illustrated in Fig. 6a. The waveform of the electric field depends on the required waveform of the displacement. The displacement will follow the field only with a linear relationship between strain and electric field. This type of actuator requires a transducer material with a reproducible, nonhysteretic, field-independent relationship between strain and field. The second type, Fig. 6b, of displacement transducer is used in the situations in which the displacement is affected by an external parameter, such as a mechanical disturbance or temperature change. A feedback system is then necessary to adjust the magnitude of the electric bias field and bring the displacement to the desired value. In this type of transducer nonlinearities between strain and electric field are tolerable, but the hysteretic behavior is still detrimental. If the displacement drifts away from the desired value, longer times and large variations in bias field are required to bring the displacement back to the desired value for an actuator with hysteresis.

In the third type, Fig. 6c, strain is controlled by electric field in an on/off manner. There are two variations of this type of actuators: in one, the field induced displacement disappears as soon as the field is switched off; in the other, the induced strain may remain, but its level has to be controlled in some other way after the field is removed. For an actuator of this type only the reproducibility of the maximum strain induced by the electric field pulse is critical and it is not of a great importance how the strain reaches its optimum value. Since the pulses are usually very short, the response of actuator must also be very fast. The

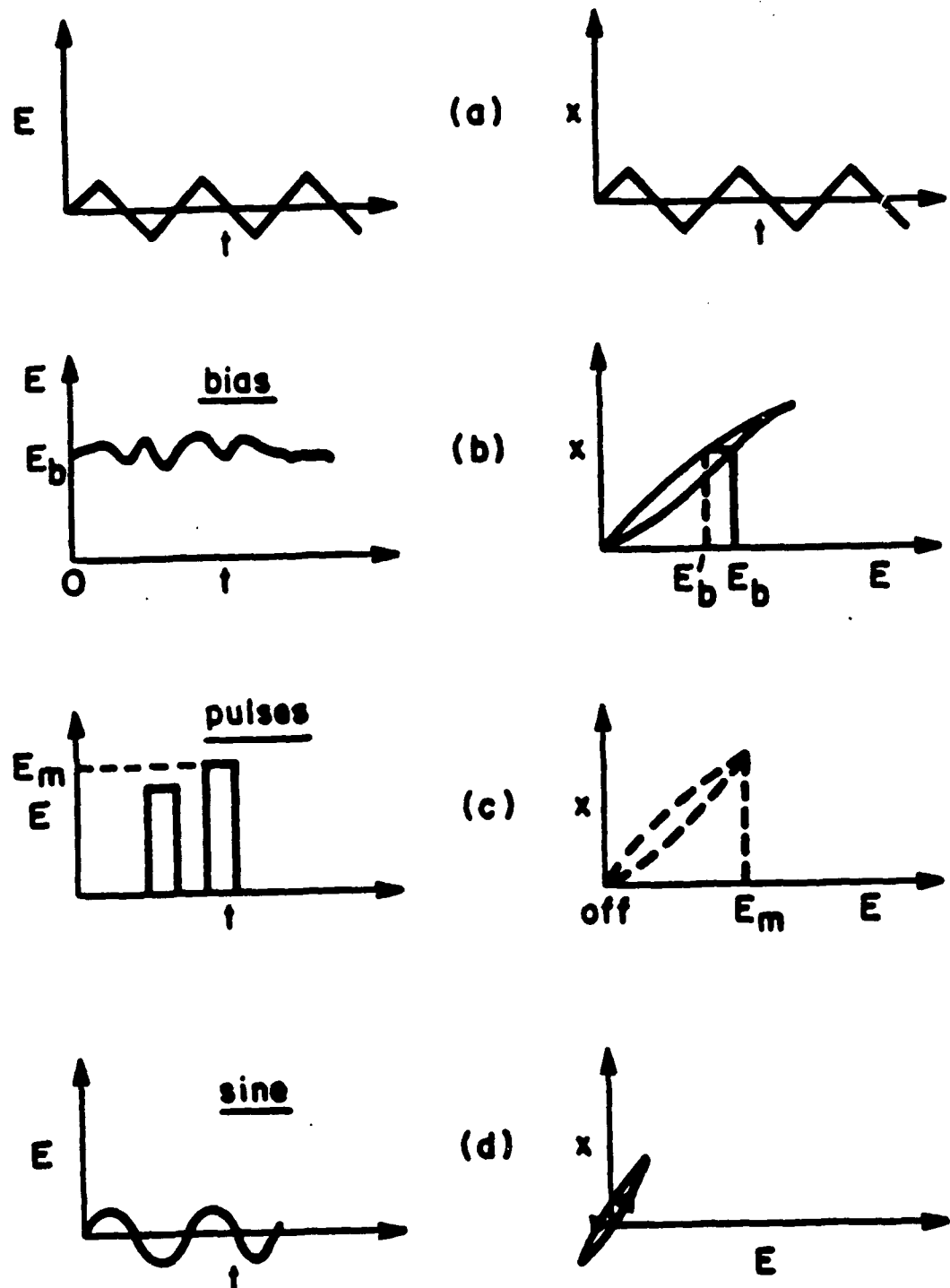


Fig. 6. Classification of piezoelectric and electrostrictive actuators according to the modes of driving. (a) Strain is controlled directly by electric field. (b) Displacement is controlled by a feedback system and electric bias field. (c) Strain is controlled by electric field in an on/off manner. (d) Resonating strain in ultrasonic motors.

driving mechanism for ferroelectric actuators that perform in an on/off mode does not necessarily have to involve a piezoelectric or electrostrictive effect. Certain compositions in the $PbZrO_3$ - $PbTiO_3$ - $PbSnO_3$ ternary system undergo phase transitions from an antiferroelectric to a ferroelectric phase under applied electric field (18). The phase transition is accompanied by a large volume change since the antiferroelectric phase has the smaller lattice volume than the ferroelectric form. Associated strains are as large as 1% but the electric fields required for switching are very high.

Finally, in ultrasonic motors, an alternating electric field is applied to the actuator with a frequency equal to the resonant frequency of the actuator. In this way, larger strains may be induced under relatively smaller fields compared to the other types of actuators. Since the actuator operates at its resonant frequency, the material properties of greatest importance are a high mechanical quality factor and a high electromechanical coupling coefficient. There are several types of ultrasonic motors. The most widely studied type uses surface acoustic waves to move an object that is in contact with the transducer surface. The surface acoustic waves are generated by superimposing two standing waves of equal amplitude but with a phase difference of 90° with respect to both time and space. The waves are caused by a combination of longitudinal and shear motions governed by the stress-free boundary conditions at the surface (11). The particles at the surface describe elliptical motions with amplitudes that decrease with thickness and become insignificant below $\sim 1\mu m$. The horizontal component of the elliptical motion is responsible for the force acting on an object in contact with the surface.

Applications of Electrostrictive and Piezoelectric Actuators

There are four major groups of applications of electrostrictive/piezoelectric actuators. These are briefly reviewed below (17,22).

Deformable Mirrors. In the field of adaptive optics, a mirror surface is dynamically controlled using a feedback system to adjust the phase of the light wave and eliminate atmospheric turbulence, thermally induced stresses or gravitational forces. Applications of active optical systems include large ground-based and space telescopes, high energy lasers, laser communication systems, and highly sensitive AC interferometric dilatometers. Typical requirements for deformable mirrors are a maximum throw of $\pm 20\mu m$, small volumes, long term stability, good reproducibility and low thermal expansion.

Mechanical Micropositioners. Precision actuators are often required to position mechanical parts very accurately and reproducibly on a micron or even submicron level. The displacement of the actuators used for these purposes is usually controlled by a feedback system. Applications are found in the fields of optical microscopy, cutting-error corrections, micropositioners for robots, and in the tracking of optical and magnetic heads. Excellent reproducibility and anhysteretic behavior of the strain-electric field relation are important requirements for actuators used in these applications.

Impact Devices. The impact type actuators are driven in an on/off manner. They move parts to a desired position by making an impact with them. Typical applications are drivers for relays and switches, via punches, wire-dot printers, and ink jet printers. Clearly, such actuators should have a quick response, large electromechanical coupling factors and large generative forces.

Ultrasonic Motors. Ultrasonic motors are mainly at the development stage (22), but they have considerable potential because they are compact and light weight, with a self-locking mechanism, relatively high torque at low speeds and motion in both forward and reverse directions. Two of the problems with ultrasonic motors are the maintenance of frictional forces between the surface and the moving object at the contact points, and the need for high frequency power supplies. A typical application is the automatic focusing unit in a movie camera.

REFERENCES

1. Arlt, G., "Piezoelectric Relaxation," *Ferroelectrics*, Vol. 40, 1982, p. 149.
2. Arlt, G., Dederichs, H., and Herbeit, R., "90°-Domain Wall Relaxation in Tetragonally Distorted Ferroelectric Ceramics," *Ferroelectrics*, Vol. 74, 1987, pp. 37-53.
3. Berlincourt, D., Curran, D.R., and Jaffe, H., "Piezoelectric and Piezomagnetic Materials and Their Function in Transducers," *Physical Acoustics*, Vol. 1, Part A, ed. by W.P. Mason, Academic, New York, 1964, pp. 169-270.
4. Crawley, E.F. and Anderson, E.H., "Detailed Models of Piezoceramic Actuation of Beams," *J. of Intell. Mater. Syst. and Struct.*, Vol. 1, No. 1, January 1990, pp. 4-25.
5. Cross, L.E., "Relaxor Ferroelectrics," *Ferroelectrics*, Vol. 76, 1987, pp. 241-267.
6. Cross, L.E., Jang, S.J., Newnham, R.E., Nomura, S. and Uchino, K., "Large Electrostrictive Effects in Relaxor Ferroelectrics," *Ferroelectrics*, Vol. 23, 1980, pp. 187-192.
7. Damjanovic, D., Gururaja, T.R., and Cross, L.E., "Anisotropy in Piezoelectric Properties of Modified Lead Titanate Ceramics," *Am. Ceram. Soc. Bull.*, Vol. 66, No. 4, April 1987, p. 699.
8. Devonshire, A.F., "Theory of Barium Titanate - Part I," *Phil. Mag.*, Vol. 40, 1949, p. 1040.
9. Herbert, J.M., "Ferroelectric Transducers and Sensors," *Electrocomponent Science Monographs*, Vol. 3, Gordon and Breach, New York, 1982.
10. Jimenez, B. and De Frutos, J., "Piezoelectric Relaxation Studies of Ferro-Piezoelectric Ceramics," *Ferroelectrics*, Vol. 109, 1990, pp. 107-112.
11. Moulson, A.J. and Herbert, J.M., "Electroceramics," Chapman and Hall, London, 1990, pp. 265-318.
12. Nelson, D.F. and Lax, M., "New Piezoelectric Contributions to Piezoelectricity," *Phys. Rev. Lett.* Vol. 31, 1973, p. 763.
13. Nelson, D.F. and Lax, M., "Linear Elasticity and Piezoelectricity in Pyroelectrics," *Phys. Rev.* Vol. B13, 1976, p. 1785.
14. Newnham, R.E., "Structure-Property Relations," Springer-Verlag, Berlin, 1975.
15. Newnham, R.E., "Electroceramics," *Rep. Prog. Phys.*, Vol. 52, 1989, pp. 123-156.
16. Nye, J.F., "Physical Properties of Crystals," Clarendon, Oxford, 1985.
17. Pan, W.Y., "Ferroelectric Materials for Actuator Applications," PhD Thesis, The Pennsylvania State University, University Park, PA., 1988.
18. Pan, W.Y., Zhang, Q.M., Bhalla A., and Cross, L.E., "Field-Forced Antiferroelectric -to-Ferroelectric Switching in Modified Lead Zirconate Titanate Stannate Ceramics," *J. Am. Ceram. Soc.*, Vol. 72, No. 4, April 1989, pp. 571 - 578.
19. Sirotin, Yu. I. and Shaskolskaya, M.P., "Fundamentals of Crystal Physics," Mir, Moscow, 1982.
20. Smits, J.G., "Eigenstates of Coupling Factors and Loss Factor of Piezoelectric Ceramic," PhD Thesis, Twente University of Technology, Netherlands, 1978.
21. Taylor, D.J., Damjanovic, D., Bhalla A.S., and Cross, L.E. "Large Hydrostatic Piezoelectric Coefficient in Lead Magnesium Niobate - Lead Titanate Ceramics," *J. Mater. Sci. Lett.* submitted for publication.
22. Uchino, K., "Electrostrictive Actuators: Materials and Applications," *Am. Cer. Soc. Bull.* Vol. 65, No. 4, April 1986, pp. 647-652.
23. Viehland, D., Jang, S.J., Cross, L.E., and Wuttig, M., "Freezing of the Polarization Fluctuations in Lead Magnesium Niobate Relaxors," *J. Appl. Phys.*, Vol. 68, No. 16, September 1990, pp. 2916-2921.
24. Zhang, Q.M., Pan, W.Y., Jang, S.J. and Cross, L.E., "The Pressure Dependence of the Dielectric Response and Its Relation to the Electrostriction," *Ferroelectrics*, Vol. 88, 1988, pp. 147 - 154.

APPENDIX 7

Large displacement transducers based on electric field forced phase transitions in the tetragonal $(\text{Pb}_{0.97}\text{La}_{0.02})(\text{Ti},\text{Zr},\text{Sn})\text{O}_3$ family of ceramics

W. Y. Pan, C. Q. Dam, Q. M. Zhang, and L. E. Cross

Materials Research Laboratory, The Pennsylvania State University, University Park, Pennsylvania 16802

(Received 21 June 1989; accepted for publication 24 August 1989)

Several properties associated with the field-induced phase change between the antiferroelectric and ferroelectric states in tetragonal $(\text{Pb}_{0.97}\text{La}_{0.02})(\text{Sn},\text{Ti},\text{Zr})\text{O}_3$ antiferroelectric ceramic family were investigated for high-strain displacement transducer applications. The longitudinal field-induced strain accompanying the phase change is in the range of 0.2%–0.9%. The single-shot switching time between the two states is on the order of 1–2 μs . Under continuous ac field driving, the hysteretic heating effect introduces a temperature rise, changing the original room-temperature switching behavior. The ceramics degrade under ac field excitation, the average life cycles is in the range of 10^6 – 10^7 cycles which can be greatly improved by carefully polishing the sample surfaces.

I. INTRODUCTION

Ceramics of lead zirconate titanate stannate and further modified forms have been studied in the past 20 years for many potential applications in energy conversion.^{1,2} In these ceramics, the free-energy difference between the antiferroelectric and ferroelectric states may be modified compositionally to such an extent that a phase change between the antiferroelectric state and the ferroelectric state can be forced by an electric field or a hydrostatic pressure. More specifically, a phase transition from a stable antiferroelectric to a ferroelectric form can be accomplished by an electric field, while a phase change from a ferroelectric (or a metastable ferroelectric) state to an antiferroelectric state can be accomplished by a hydrostatic pressure. The pressure switching has been extensively investigated.² Upon inversion into the antiferroelectric state, a poled ferroelectric ceramic releases all polarization charges and therefore can supply very high instantaneous current. The electric field forced phase transitions were also studied for different applications. The first systematic study was done at Clevite laboratories in the 1960s to explore the use of phase change compositions in capacitive energy storage.³ Later on, Uchino and Nomura⁴ studied this effect for the shape memory application. Because of the limited field-induced strain level (0.1%) in normal piezoelectric and electrostrictive ceramics,⁵ a study was recently carried on several compositions of modified $\text{Pb}(\text{Ti},\text{Zr},\text{Sn})\text{O}_3$ ceramics for high-strain compact displacement transducer application.⁶ One composition of the $(\text{Pb}_{0.97}\text{La}_{0.02})(\text{Ti},\text{Zr},\text{Sn})\text{O}_3$ ceramics showed a longitudinal field-induced strain greater than 0.5%; such a strain level motivated us to study more thoroughly the $(\text{Pb}_{0.97}\text{La}_{0.02})(\text{Ti},\text{Zr},\text{Sn})\text{O}_3$ system. In this paper, we report the three properties which are important for displacement transducer applications: the field-induced polarization and strain, the kinetics of the phase change between the antiferroelectric and ferroelectric states and the ac field excitation degradation in this family of antiferroelectric ceramics.

II. COMPOSITION SELECTION AND SAMPLE PREPARATION

The phase diagram of the $(\text{Pb}_{0.97}\text{La}_{0.02})(\text{Sn},\text{Ti},\text{Zr})\text{O}_3$ system (Fig. 1) was studied by Berlincourt.⁷ The F_R (LT) region is the low-temperature ferroelectric rhombohedral region, the A_O region is the antiferroelectric orthorhombic region, and the A_T region is the antiferroelectric tetragonal region. The compositions in the A_O region are not suitable for this study because the transition field from the antiferroelectric state to the ferroelectric state is so high that the transition is difficult to be accomplished by a realizable applied electric field. However, in the antiferroelectric tetragonal region, the compositions are so energetically close to those of the ferroelectric form that the switching between the antiferroelectric and ferroelectric form can be accomplished by an applied electric field. The function of Sn is very obvious as may be observed from the phase diagram: As the Sn increases, the antiferroelectric tetragonal region expands greatly. The compositions chosen for this study and their locations in the phase diagram are shown in Fig. 2. The chemical compositions are listed in Table I with their reference numbers of the selected compositions. The reference numbers of the compositions start from 4 in order to be consistent to that of the earlier study.⁶ These numbers will be referred to in the text here on.

The above compositions were made from reagent grade oxides using conventional solid-state sintering technique. Calcining temperatures were in the range of 750–900 °C. Green disks were cold pressed using small amounts of polyvinyl alcohol binder and fired in the temperature range of 1250–1350 °C in an excess PbO atmosphere. The density of the fired disks is in the range of 7.5–8 g/cm³.

III. FIELD-INDUCED POLARIZATION AND STRAIN

A. Measurements

The samples for polarization and strain measurement were cut into dimensions of 0.6×0.4 cm with thickness

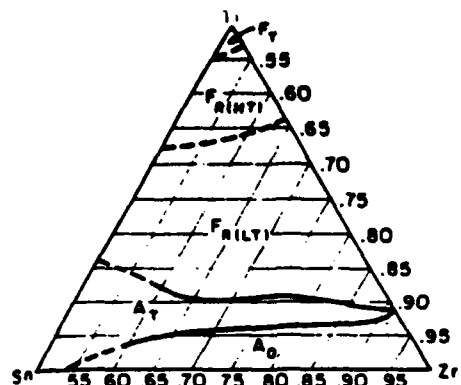


FIG. 1. Phase diagram of the $(\text{Pb}_{0.9}, \text{La}_{0.02})(\text{Sn}, \text{Ti}, \text{Zr})\text{O}_3$ system.

ranging from 0.15 to 0.3 mm. The polarization was measured using a modified Sawyer and Tower circuit. The longitudinal field-induced strain was measured by a laser interferometer which is described in an earlier paper.⁷ The sample was mounted in a manner as shown in Fig. 3. The laser beam strikes the mirror attached at one end of the rod of which another end is in contact with the sample. If the sample changes thickness due to the field-induced strain, the displacement can be measured by measuring the displacement of the front mirror. For such a mounting, the sample could be wet by silicone oil to prevent the surface breakdown of the sample. The transverse strain was measured using the bonded strain gauge technique. The temperature variation for polarization and transverse strain measurements were accomplished by a hot stage immersed in a liquid-nitrogen container. Temperature was controlled by a transformer in series with a temperature controller (Model 76K-1 RFL Industries Inc.).

B. Experimental results

1. Composition dependence of field-induced polarization and strain

The dielectric hysteresis loops for different compositions are sketched in the phase diagram shown in Fig. 2. Some parameters in polarization and strain hysteresis loops

TABLE I. Chemical compositions and the reference numbers.

No.	Composition
4	$(\text{Pb}_{0.9}, \text{La}_{0.02})(\text{Zr}_{0.66} \text{Ti}_{0.06} \text{Sn}_{0.25})\text{O}_3$
5	$(\text{Pb}_{0.9}, \text{La}_{0.02})(\text{Zr}_{0.55} \text{Ti}_{0.12} \text{Sn}_{0.25})\text{O}_3$
6	$(\text{Pb}_{0.9}, \text{La}_{0.02})(\text{Zr}_{0.66} \text{Ti}_{0.11} \text{Sn}_{0.25})\text{O}_3$
7	$(\text{Pb}_{0.9}, \text{La}_{0.02})(\text{Zr}_{0.66} \text{Ti}_{0.105} \text{Sn}_{0.25})\text{O}_3$
8	$(\text{Pb}_{0.9}, \text{La}_{0.02})(\text{Zr}_{0.66} \text{Ti}_{0.06} \text{Sn}_{0.25})\text{O}_3$
9	$(\text{Pb}_{0.9}, \text{La}_{0.02})(\text{Zr}_{0.66} \text{Ti}_{0.11} \text{Sn}_{0.25})\text{O}_3$
10	$(\text{Pb}_{0.9}, \text{La}_{0.02})(\text{Zr}_{0.62} \text{Ti}_{0.11} \text{Sn}_{0.27})\text{O}_3$
11	$(\text{Pb}_{0.9}, \text{La}_{0.02})(\text{Zr}_{0.66} \text{Ti}_{0.06} \text{Sn}_{0.25})\text{O}_3$
12	$(\text{Pb}_{0.9}, \text{La}_{0.02})(\text{Zr}_{0.66} \text{Ti}_{0.10} \text{Sn}_{0.10})\text{O}_3$
13	$(\text{Pb}_{0.9}, \text{La}_{0.02})(\text{Zr}_{0.55} \text{Ti}_{0.1125} \text{Sn}_{0.1125})\text{O}_3$
14	$(\text{Pb}_{0.9}, \text{La}_{0.02})(\text{Zr}_{0.55} \text{Ti}_{0.10} \text{Sn}_{0.25})\text{O}_3$

are marked in Fig. 4 and will be referred to in the text. The E_{A-F} is the field required to induce an antiferroelectric to ferroelectric phase transition, and E_{F-A} represents the reverse transition field below which the metastable ferroelectric state converts to the antiferroelectric state again. In the compositions studied, the induced polarization and strain are dominated by the phase transition between the antiferroelectric and ferroelectric forms. Far above the E_{A-F} , the polarization induced due to the permittivity of the ferroelectric phase and the strain induced due to the piezoelectric effect of the ferroelectric phase are much less than the polarization and strain due to the phase transition.

The room-temperature switching data for all the studied compositions are divided, according to the locations in the phase diagram and the shape of the dielectric hysteresis loops, into two groups. Group 1 is compositions which are close to the morphotropic phase boundary (MPB) between the ferroelectric rhombohedral and the antiferroelectric tetragonal. These compositions have dielectric hysteresis loops similar to those of the ferroelectrics. The members in this group include Nos. 5, 6, 7, 9, and 10. On the other hand, group 2 compositions which are further away from the (MPB) show classic double-hysteresis loops with transition fields significantly higher than those of the group 1 compositions. The members in this group include Nos. 4, 8, 11, and 14. The room-temperature switching data for group 1

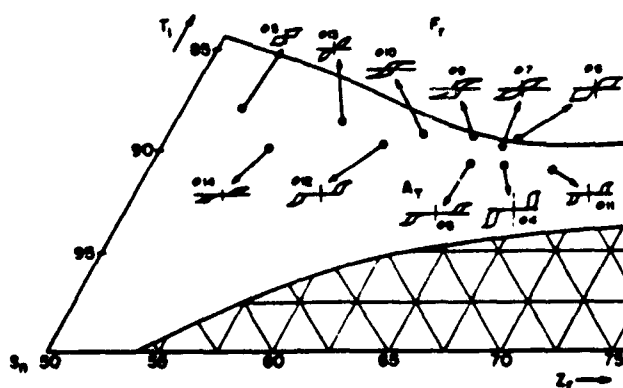


FIG. 2. Antiferroelectric tetragonal compositions selected for study and their dielectric hysteresis loops.

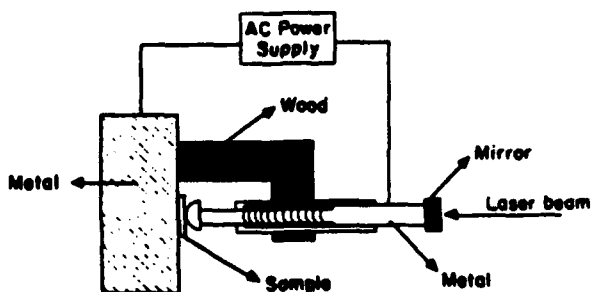


FIG. 3. Schematic drawing of sample holder and sample mounting for longitudinal strain measurement.

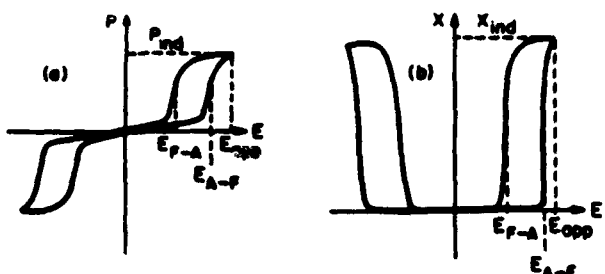


FIG. 4. Typical polarization and strain hysteresis loops (composition No. 4) and some illustrated parameters.

and group 2 compositions are listed in Table II. It is observed that the field-induced longitudinal strain amounts to 0.87% for composition No. 6.

Figure 5 shows the field-induced strain, polarization, and transition field as a function of Sn/Zr ratio variation for group 1 compositions. It may be noted that as Sn/Zr ratio decreases, the field-induced strain increases, while the transition field ($E_{A,F}$) decreases. For the compositions in group 2, the field-induced strains are comparable to those of group 1 compositions; however, the transition fields are significantly higher. The field-induced strain for group 2 compositions does not change with Sn/Zr as regularly as that for the group 1 compositions, however, the average strain level for Zr-rich compositions is larger than that of the Sn-rich compositions. Comparing the transition fields of the group 1 and group 2 compositions, we also find that the transition field $E_{A,F}$ is more sensitive to the Ti content change for Zr-rich compositions than for Sn-rich compositions. For example, the transition field E_{AF} difference for Nos. 4 and 7 is 28 kV/cm while for Nos. 5 and 14 is only 1 kV/cm.

2. Temperature dependence of field-induced polarization and strain

For this family of antiferroelectric ceramics, the antiferroelectric form is only stable over a finite temperature range

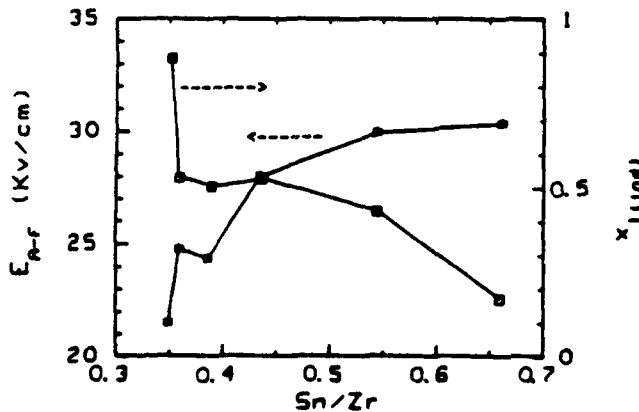


FIG. 5. Field-induced longitudinal strain and E_{AF} value as a function Sn/Zr ratio for group 1 compositions.

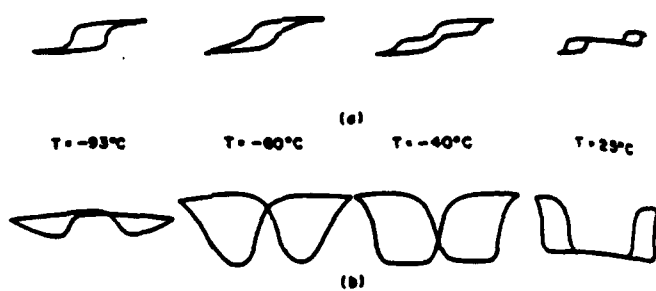


FIG. 6. Polarization and strain hysteresis loops at four different temperatures for composition No. 4.

below which the ferroelectric form is stable and above which the paraelectric form is stable. The dielectric hysteresis loop and field-induced strain for composition 4 is shown in Fig. 6. At low temperatures, the composition shows a ferroelectric hysteresis loop and small field-induced strain. At the higher-temperature range, the composition shows a classical double-hysteresis loop characteristic for antiferroelectrics. However, the field-induced strain is largest at the temperature range from -60 to -40 °C within which the double-hysteresis loop just begins to emerge. The temperature dependence of the field-induced polarization and strain for composition No. 4 is shown in Fig. 7. One feature of the temperature dependence on the field-induced polarization and strain immediately comes to one's attention. It may be seen that the field-induced polarization is almost constant with respect to temperature, while the field-induced strain changes greatly with temperature. The induced strain increases with temperature until it reaches a maximum value, after this point, the strain decreases with increasing temperature.

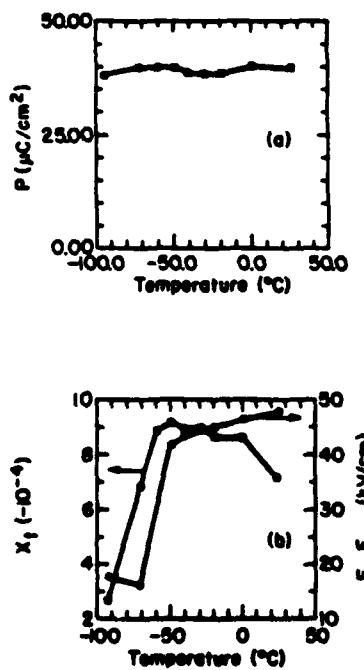


FIG. 7. Field (52 kV/cm) induced ferroelectric polarization as a function of temperature and (b) transition field E_{AF} or coercive field E_C and field-induced transverse strain as a function of temperature for composition No. 4.

TABLE II. Switching data for different compositions.

(a) Group 1 compositions				
No.	P (uC/cm ³)	E _{EF} (kV/cm)	E _{PP} (kV/cm)	x _{Hind}
5	30	30	35	0.18%
13	28	30	43	0.45%
10	36	28	60	0.5%
9	36	24	60	0.59%
7	36	22	58	0.52%
6	40	21	46	0.87%

(b) Group 2 compositions				
No.	P (uC/cm ³)	E _{EF} (kV/cm)	E _{PP} (kV/cm)	x _{Hind}
14	31	44	56	0.35%
12	32	49	59	0.42%
8	30.5	52	68	0.37%
4	43	50	75	0.55%
11	33	45	60	0.45%

C. Discussion

1. Temperature dependence of field-induced polarization and strain

In order to explain the temperature dependence and the compositional dependence of the field-induced strain, we turn to the phenomenological treatment which was adopted by Uchino, Cross, and Newnham⁶ to explain the pressure dependence of antiferroelectric Néel temperature. For the antiferroelectric compositions studied here, the temperature dependence of the free energy with respect to that of the paraelectric form is shown schematically in Fig. 8.

When the temperature is increased, the stable form changes from the ferroelectric form to the antiferroelectric form and then to the paraelectric form. Pervoskite ferroelectrics are derived from a centric point group *m3m* which is free from piezoelectric effect. To simplify the matter, let us consider the spontaneous polarization occurring only along axis 3 under the presence of hydrostatic pressure. The general expression for ΔG is:

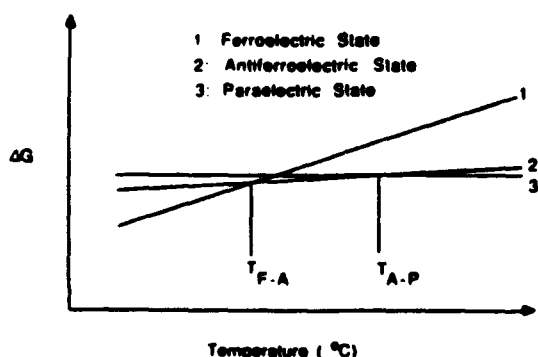


FIG. 8. Free energy with respect to the paraelectric state for the antiferroelectric state and ferroelectric state of the antiferroelectric system.

$$\begin{aligned} \Delta G = & \frac{1}{2}\alpha(T)(P_a^2 + P_b^2) + \frac{1}{2}\beta(P_a^4 + P_b^4) \\ & + \frac{1}{2}\gamma(P_a^6 + P_b^6) \\ & + \eta P_a P_b - \frac{1}{2}s_h \sigma^2 \\ & + Q_h \sigma(P_a^2 + P_b^2 + 2\Omega P_a P_b). \end{aligned} \quad (1)$$

where P_a and P_b denote the two-sublattice polarizations, η is the dielectric stiffness constant, s_h is the hydrostatic compressibility, σ is the hydrostatic pressure, and Ω is a scalar electrostrictive coefficient for the coupling between the two sublattices.

Introducing the transformation $P_F = (P_a + P_b)/\sqrt{2}$ and $P_A = (P_a - P_b)/\sqrt{2}$ leads to the following expression:

$$\begin{aligned} \Delta G = & \frac{1}{2}\alpha(T)(P_F^2 + P_A^2) + \frac{1}{2}\beta(P_F^4 + P_A^4 + 6P_F^2 P_A^2) \\ & + \frac{1}{2}\gamma(P_F^6 + P_A^6 + 15P_F^4 P_A^2 + 15P_F^2 P_A^4) \\ & + \frac{1}{2}\eta(P_F^2 - P_A^2) \\ & - \frac{1}{2}s_h \sigma^2 + Q_h \sigma(P_F^2 + P_A^2) + \Omega(P_F^2 - P_A^2). \end{aligned} \quad (2)$$

The elastic equation of the state follows as

$$\frac{\partial \Delta G}{\partial \sigma} = \frac{\Delta v}{v} = s_h \sigma + Q_h(1 + \Omega)P_F^2 + Q_h(1 - \Omega)P_A^2. \quad (3)$$

If the stress $\sigma = 0$ (sample is unclamped), then we have

$$\Delta v/v = Q_h(1 + \Omega)P_F^2 + Q_h(1 - \Omega)P_A^2. \quad (4)$$

In the polar state, $P_A = 0$, then

$$(\Delta v/v)_F = Q_h(1 + \Omega)P_F^2. \quad (5)$$

When $\Omega = 1$, $(\Delta v/v)_F = 2P_F^2 = Q_h P_{ind}^2$, where P_{ind} is the field induced polarization, the volume change is the normal electrostrictive effect in ferroelectrics. In the antipolar state, $P_F = 0$, then

$$(\Delta v/v)_A = Q_h(1 - \Omega)P_A^2. \quad (6)$$

When the coupling between the two sublattices lowers the free energy of the system, $\Omega > 1$. Thus volume decreases when the antipolar state is developed from the paraelectric state.

In a low-temperature range, a stable ferroelectric form persists, and the polarization reversal is the main contributor to the field-induced polarization. Therefore, the field-induced strain is very small. In the stable antiferroelectric temperature range, if the piezoelectric strain is neglected, the volume change associated with the field-induced antiferroelectric-ferroelectric phase should be

$$(\Delta v/v)_F - (\Delta v/v)_A = Q_h(1 + \Omega)P_F^2 - Q_h(1 - \Omega)P_A^2. \quad (7)$$

Since $P_F^2 = P_A^2$, the equation becomes

$$\begin{aligned} (\Delta v/v)_F - (\Delta v/v)_A &= 2Q_h \Omega P_F^2 = 2Q_h \Omega (1/\sqrt{2}P_{max})^2 \\ &= Q_h \Omega P_{ind}^2, \end{aligned} \quad (8)$$

where P_{ind} is the polarization induced by the electric field. It is observed that the volume change accompanying the field-forced antiferroelectric-ferroelectric phase transition is proportional to the Ω coefficient. The stronger the coupling between the two sublattices, the larger the volume change.

... paraelectric temperature range, the field-induced volume change should be a pure hydrostatic electrostrictive effect as described by

$$(\Delta v/v)_{\text{ind}} = Q_A P_{\text{ind}}^2. \quad (9)$$

Comparing Eqs. (8) and (9), we may observe that for the same polarization induced, the induced volume change is greater if the ferroelectric polarization is induced from an antiferroelectric state than if it is induced from a paraelectric state because $\Omega > 1$. In Fig. 7(a), we see that the induced polarization is almost constant with respect to temperature, but the strain decreases when the temperature is above 50 °C. To explain this, we may consider the temperature dependence of the Ω constant. Below $T_{F,A}$ and above $T_{A,F}$ the Ω constant should be equal to one. In the temperature range $T_{F,A} - T_{A,F}$ the Ω constant should be greater than one and may be assumed to vary with temperature with the maximum occurring somewhere between $T_{F,A}$ and $T_{A,F}$. In Fig. 7 the decrease of the strain with increasing temperature may be the result of the decrease of the Ω constant.

2. Composition dependence of field-induced polarization and strain

For the composition dependence of the field-induced polarization and strain, two points are worthwhile to point out: As Sn is added to the system, the tetragonal region expands to a wider and wider Ti content range. Thus, for an equal amount of Ti added to the system, the change of the stability of the antiferroelectric form is much smaller for Sn-rich compositions than Zr-rich compositions. The addition of the Sn to the system is also believed to decrease the Ω coefficient of the composition. This may explain the reduced strain level for Sn-rich compositions. For group 1, it is interesting to note that the Zr-rich compositions not only have a larger strain level but also a smaller $E_{A,F}$ value. The reduced $E_{A,F}$ value is, of course, because the compositions are closer to the MPB. This point can be further supported by comparing the average strain level and the $E_{A,F}$ value between the group 1 and group 2 compositions. The $E_{A,F}$ value for group 1 compositions is significantly smaller but the strain level is slightly larger. The advantage is, therefore, doubled. It is natural for one to think that a composition with a large Ω constant should be accompanied by a larger $E_{A,F}$ value. However, one must remember that Ω constant, an electro-mechanical property, may not have a 1:1 correlation to the $E_{A,F}$ value, which is a dielectric parameter.

IV. SPEED OF THE FIELD-INDUCED PHASE CHANGE

A. Measurement

1. Forward switching speed

The forward switching is referred to as the switching from a stable antiferroelectric to a ferroelectric state. The switching current as a function of the switching time was measured by the square pulse technique adopted by Merz for measuring the speed of polarization reversal in ferroelectric crystals.⁹ The rectangular pulse was generated by an HP 204 pulse generator and amplified by a Cober 604A high-power pulse amplifier. The rise times for both pulse generators are

shorter than 20 ns. The high-amplitude pulse was then applied to the sample as the switching current was picked up by a small resistor in series with the sample. The area of the sample was kept small enough so that switching current maximum did not exceed the current limit of the high-power pulse generator. The signal pickup resistor was also kept small enough to keep the RC time constant of the resistor and sample capacitor within the rise time of the pulse. The switching current was measured using an HP 54201A digital oscilloscope with "single-shot" bandwidth of 50 MHz. The switching time was recorded at the point when the switching current dropped to 10% of the maximum switching current.

2. Backward switching speed

The backward switching is referred to as the switching from the ferroelectric to the antiferroelectric state upon the decrease of the applied electric field. The principle utilized in the measurement is to induce a ferroelectric polarization by applying a dc electric field above $E_{A,F}$, then quickly release the applied electric field and measure the current due to the discharge of the ferroelectric polarization as a function of time. The block diagram for the measuring system is shown in Fig. 9. The transistor used is a SIPMOS power field-effect transistor (FET) with a drain-source breakdown voltage of 1000 V, an "on" resistance 5 Ω , and a "turn-on" time of 45 ns. The oscilloscope used for the measurement was a Nicolet 204A digital oscilloscope with a bandwidth of 20 MHz and the pulse generator used was a Hewlett Packard type 214B pulse generator with a rise time of 20 ns. When no voltage is applied to the gate of the FET and ground, the FET is "off" and thus the applied voltage drops across the sample to induce a large ferroelectric polarization. When the pulse generator is manually triggered, a square pulse is applied to the gate-source junction to turn the FET "on" and the field across the sample is reduced to nearly zero. The discharge then takes place through the small resistor R3. Since R1 is very large, the current flow to the dc power supply could be neglected. The purpose of putting the resistor R2 in the discharging loop is to damp the high-frequency piezoelectric resonance modes.¹⁰ The switching time was also measured at the time when the current dropped to 10% of the maximum switching current.

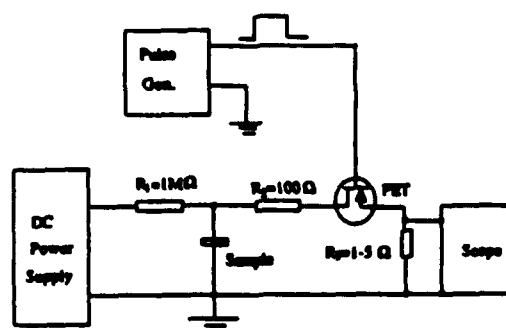


FIG. 9. Block diagram of the backward switching measuring system.

3.3.1.1
The switching under continuous ac field driving is measured by the simple Sawyer and Tower technique; the dielectric hysteresis loop was recorded by a digital oscilloscope as a function of the driving frequency.

3. Experimental results and discussions

3.1. Forward switching

The switching current as a function of time for composition 5 under different applied fields is shown in Fig. 10. The shapes of the switching current-time curves are similar to those for the polarization reversal in ferroelectric crystals. An *RC* peak is followed by the switching current maximum. The maximum switching current I_{\max} increases and the switching time t_s decreases with increasing applied field. These switching times are less than 1 μ s for an applied field level about 30 kV/cm. The switching time is comparable to that of the polarization reversal in a BaTiO₃ single crystal except that the applied field level is higher. Figure 11(a) shows $1/t_s$ vs E and $\ln(1/t_s)$ vs $1/E$, and Fig. 11(b) shows I_{\max} vs E and $\ln(I_{\max})$ vs $1/E$. The field dependence of the switching is not the same as that for the polarization reversal in ferroelectric crystals which was studied by Merz.⁹ For polarization reversal in ferroelectric crystals, the switching under low applied field level is controlled by the nucleation of new domains. The switching time t_s and maximum switching current I_{\max} can be expressed by the following relations under the low applied electric field

$$I_{\max} \sim e^{-\alpha/E}, \quad t_s \sim e^{\alpha/E}, \quad (10)$$

where α is the so-called activation field, a measure of the ease with which new domains are nucleated. Under a high applied field, the switching is controlled by domain wall motion; the switching time t_s and maximum switching current I_{\max} can be expressed by the following relations under the high applied field:

$$I_{\max} \sim KE, \quad 1/t_s \sim KE, \quad (11)$$

where K is a constant which is a measure of the ease with which the domain walls move. When I_{\max} or $1/t_s$ is plotted against E , an exponential relation holds in the low-field region within which the nucleation of new domains controls the switching and a linear relation holds in the high-field region where the domain wall motion controls the switching.

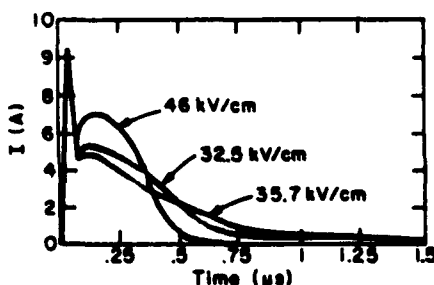


FIG. 10. Forward switching current-time curve under three different applied pulse fields for composition No. 5.

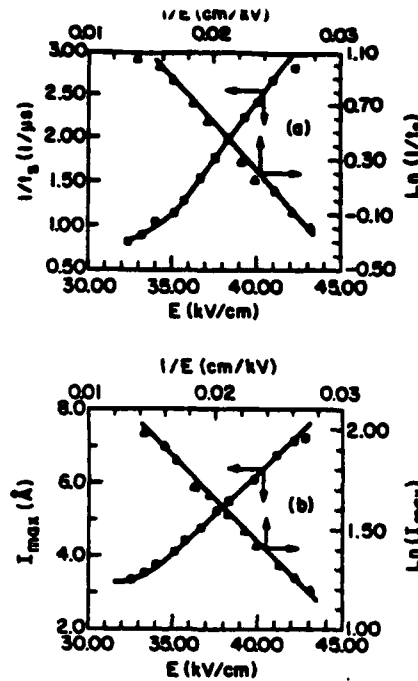


FIG. 11. (a) $1/t_s$ (forward switching speed) vs E and (b) $\ln(I_{\max})$ vs $1/E$ for composition No. 5.

On the other hand, when $\ln(I_{\max})$ or $\ln(1/t_s)$ is plotted against $1/E$, a linear relation should hold in the low-field region where the nucleation of the new domains controls the switching but not in the high-field region where the domain wall growth controls the switching.

In Fig. 11(a) the nucleation-controlled switching seems to be ended at about 36 kV/cm from either $1/t_s$ -vs- E or I_{\max} -vs- E plots. Above this field level, the points seem to follow a linear relation. However, this is not true for either $\ln(1/t_s)$ vs $1/E$ or $\ln(I_{\max})$ vs $1/E$ because the points for the field above 36 kV/cm still seem to follow the linear relation, indicating that the nucleation may still control the switching. It must be remembered that the switching here is different from the polarization reversal in ferroelectric crystals. There is no domain wall movement but there is a phase boundary movement during the switching. We were unable to observe the phase boundary movement controlled field range because of the voltage limitation of the pulse generator and electric breakdown problem of the sample. The activation field calculated from the slope of $\ln(1/t_s)$ vs $1/E$ is 200 kV/cm, while that calculated from the slope of $\ln(I_{\max})$ vs $1/E$ is 150 kV/cm. Although this is not a perfect agreement, we believe that the activation field falls between 150 and 200 kV/cm. The activation field for the polarization reversal in PLZT and PZT family of ferroelectric ceramics have been reported by Li, Pan, and Cross.^{10,11} The activation field for PLZT 8/65/35 is about 5 kV/cm and that for PZT5 is about 10 kV/cm. Therefore, the activation field here is much higher compared to those observed for ferroelectric ceramics which indicate that nucleation of a new phase is more difficult than the nucleation of new domains.

2. Backward switching

The backward switching current for composition 4 under three different applied dc poling field levels is shown in Fig. 12(a). It is surprising to find that the switching current-time curves are very similar to that of the forward switching. The I_{max} can also be observed. The switching time as a function of the applied dc field is shown in Fig. 12(b). The switching time t_s increases with the applied dc field, then reaches an almost constant value at about 70 kV/cm. When the applied field is below 70 kV/cm, the area under the switching current-time curve (a measure of the total induced charge) decreases appreciably with decreasing applied field.

The initial increases and subsequent "level off" of the switching time with the applied field may be explained by the sharpness of the forward transition field. The forward transition field for composition 4 is not perfectly defined and distributed over a field range as may be seen from Fig. 4. Within this field range, the ferroelectric polarization is not fully induced and the ferroelectric phase is not fully stabilized. Imagine that the stability of the ferroelectric phase increases with increasing applied electric field and thus the energy barrier for the recovery of the antiferroelectric phase increases with increasing applied field. As a result, the switching time increases with increasing applied electric field. When the applied field is high enough to complete the anti-

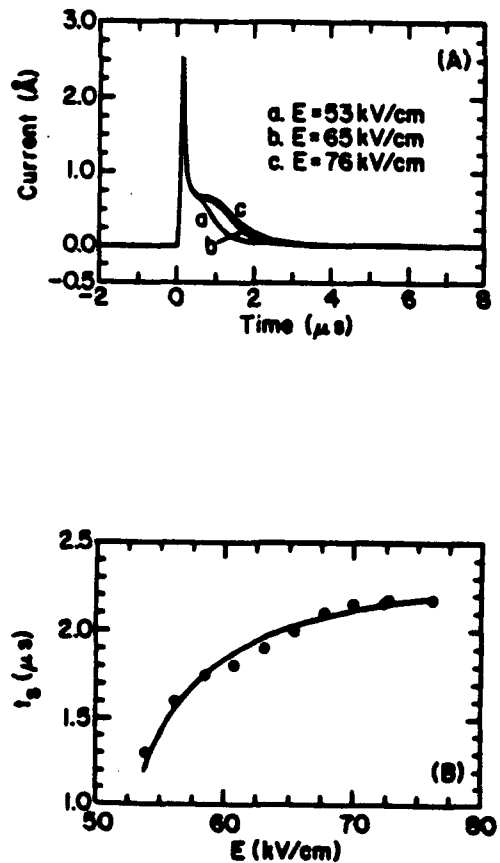


FIG. 12. (a) Backward switching current under different dc poling fields and (b) backward switching time as a function of dc poling field for composition No. 4.

ferroelectric-to-ferroelectric phase transition, a further increase in the applied field would not increase the stability of the induced ferroelectric phase significantly and thus the switching time levels off with increasing applied field.

The backward switching time is observed to depend on the backward switching field $E_{F,A}$. Figure 13(a) shows the comparison of switching current-time curves for composition 4 and 11. The switching current is divided by the charge induced for the purpose of comparison. The applied field is 75 kV/cm for composition 4 and 67 kV/cm for composition 11, respectively. The fields are high enough to reach the plateau regions of switching time versus applied field curves. It can be seen that the area under the switching current-time curves for the two compositions are roughly equal, but the switching time for composition 11 is significantly longer. We think that the difference in the switching time is caused mainly by the different backward switching field $E_{F,A}$. In Fig. 13(b), the switching time at the plateau region is plotted against the $E_{F,A}$ value for different compositions. The applied poling field and compositions for different $E_{F,A}$ values

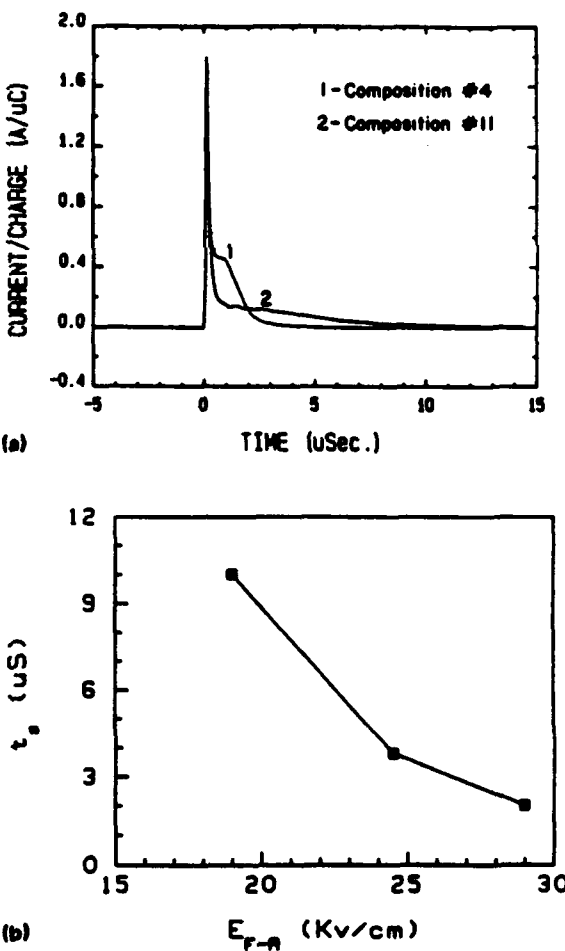


FIG. 13. (a) Comparison of backward switching current-time curve for composition Nos. 4 and 11. Composition No. 4 has a backward switching field $E_{F,A}$ of 29 kV/cm and composition No. 11 has a $E_{F,A}$ of 19 kV/cm. (b) The backward switching time in the plateau region vs the backward switching field: three different backward switching fields are 19 kV/cm of composition No. 11, 24.5 kV/cm of composition No. 12 and 29 kV/cm of composition No. 4.

are as illustrated in the figure caption. One qualitative nature is apparent, the switching time decreases with increasing $E_{F,A}$ value of the compositions. It must be mentioned that when the $E_{F,A}$ value of the composition becomes very small, the switching current is so spread out on the time axis that the switching time is very difficult to be ascertained by the present technique. So, the data for low $E_{F,A}$ compositions were not plotted.

3. Switching under ac field

The switching times presented above are obtained from a "single shot," i.e., the transition from the ferroelectric phase to antiferroelectric phase occurred just once or vice versa. When the sample is driven continuously by an ac field, the heat generated from the $P-E$ hysteresis may modify the original switching behavior. Figure 14 shows the $P-E$ hysteresis loops for composition 4 and 6. For both compositions, the forward switching field increases slightly with the driving frequency, while the backward switching field increases significantly with increasing driving frequency above 10 Hz. For the hysteresis loops at 300 Hz, the $E_{F,A}$ values are increased greatly and the ferroelectric polarization values decreased appreciably with respect to those of the low-frequency values. Clearly, these phenomena cannot be explained by the kinetics of the phase switching because the switching time from "single shot" measurements is of the order of microseconds. It is observed from the temperature dependence of the ferroelectric polarization (Fig. 7) that the behavior of the phase transition differs with temperature. Because the hysteresis heating effect increases with increasing driving frequency, the effect of high driving frequency at room tem-

perature is similar to the effect of low driving frequency at higher temperatures. Thus, the dielectric hysteresis loops at high driving frequencies are not room-temperature dielectric hysteresis loops. The variation of the dielectric hysteresis loop with temperature is most pronounced near the anti-ferroelectric-to-ferroelectric phase transition temperature. From Fig. 2 it may be seen that composition 6 is closer to the MPB than composition 4, therefore, its antiferroelectric-to-ferroelectric phase transition temperature should be closer to room temperature than that of composition 4. This is why the change of $P-E$ loop is more pronounced for composition 6 than for composition 4. The shape of the hysteresis loop for composition 6 and some of the other MPB compositions depends critically on the heat transport condition. When the sample is in contact with a large heat sink, the sample remains cold, and the hysteresis loop shows the low-temperature form. When the electric connection is accomplished by two thin wires and is thermally isolated, the hysteresis loop shows the high-temperature form.

V. FIELD EXCITATION DEGRADATION EFFECT

A. Measurement

The ac field excitation induced degradation is evaluated by measuring the ac field-induced ferroelectric polarization as a function of switching cycles. The ferroelectric polarization was measured using the Sawyer and Tower technique. The $P-E$ hysteresis loops were recorded using a x-y digital oscilloscope at different switching cycles. The driving frequency of the ac field was kept at 60 Hz. The applied electric field varies with composition to accommodate the differences of the transition field of each composition. The fields applied to the samples were approximately 25% above the $E_{A,F}$ transition fields of the compositions.

B. Experimental results

1. Effect of sample surface

To test the effect of sample surface on the degradation behavior of the ceramic composition, we kept the applied electric field level and the driving frequency of the applied field constant for each composition. The rough surfaces were prepared by grinding with 400 grit sand paper and the smooth surfaces were prepared by polishing with $1 \mu\text{m}$ diamond paste.

Figure 15 shows the comparison of normalized field-induced ferroelectric polarization as a function of driving cycles for composition 5 and 6. The difference between the rough surfaces and polished surfaces is astonishing. Furthermore, the difference for composition 6 is even larger. The degree of the smoothness that can be accomplished depends on the density of the composition. The sample surfaces of composition 6 are smoother than those of composition 5 because the density of composition 6 is 8 g/cm^3 and that of the composition 5 is 7.6 g/cm^3 .

2. Effect of electrodes

The equal potential surfaces were accomplished by applying different metal electrodes to the major surfaces of the samples. The gold electrode was applied by sputtering, the

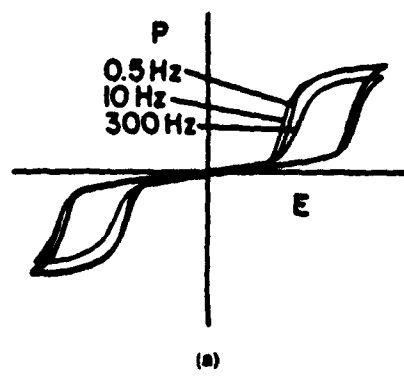
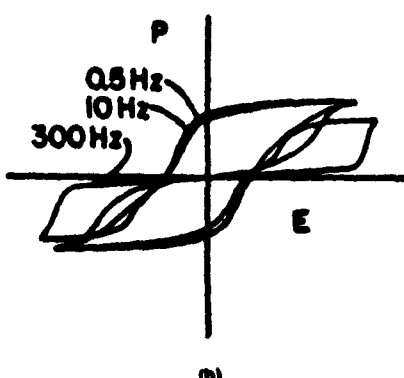
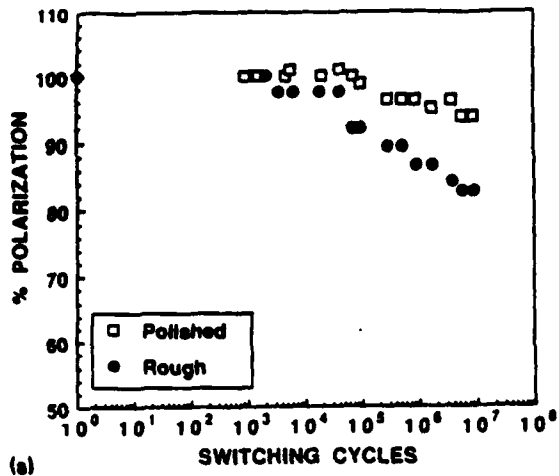
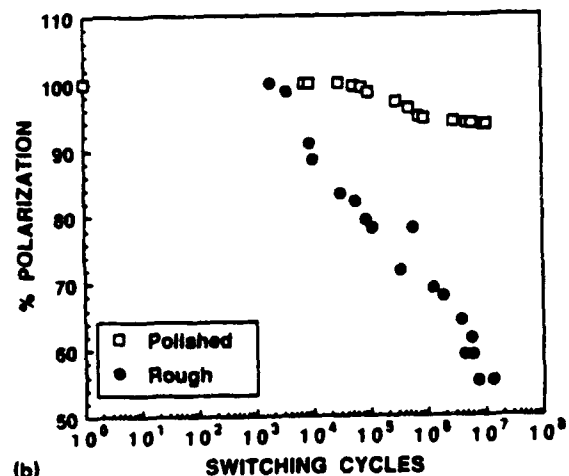


FIG. 14. $P-E$ hysteresis loops of composition Nos. 4 and 6 as a function of frequency.





(a) SWITCHING CYCLES



(b) SWITCHING CYCLES

FIG. 15. Normalized field-induced ferroelectric polarization as a function of driving cycles for (a) composition No. 5 and (b) composition No. 6; the polished sample surfaces and ground sample surfaces are as illustrated.

indium electrode was coated by evaporation under controlled filament current condition and silver electrodes were applied by brushing air-dry silver paste on to the samples.

Figure 16 shows a comparison of degradation effect of the composition 5 with different metal electrodes. Surprisingly, the degradation behavior are very similar.

3. Effect of compositions

The degradation behavior of different compositions was tested. The samples for this comparison were all polished although the surfaces were not all at the same degree of smoothness because of the density difference among the compositions.

Figure 17 shows the maximum field-induced ferroelectric polarization as a function of the driving cycles for group 1 and group 2 ceramic compositions. It is very difficult to correlate the degradation systematically to the variation of composition, but we can see in general that group 1 has a lower degradation rate. The average reduction of the normalized ferroelectric polarization for group 2 composition is

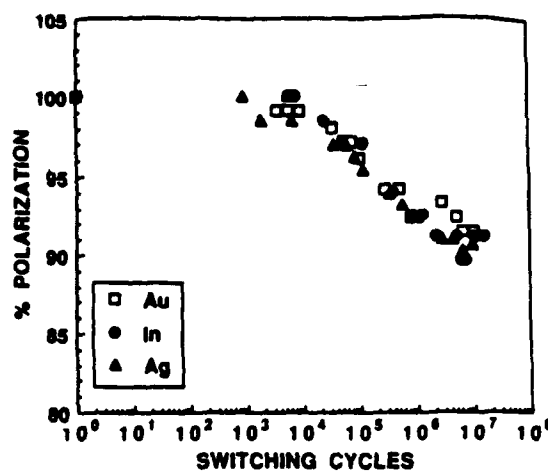
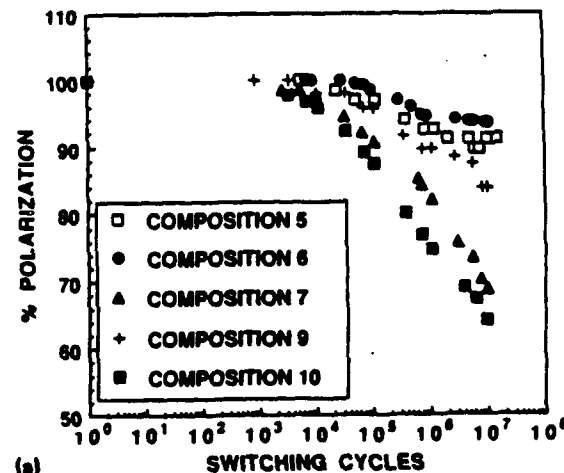
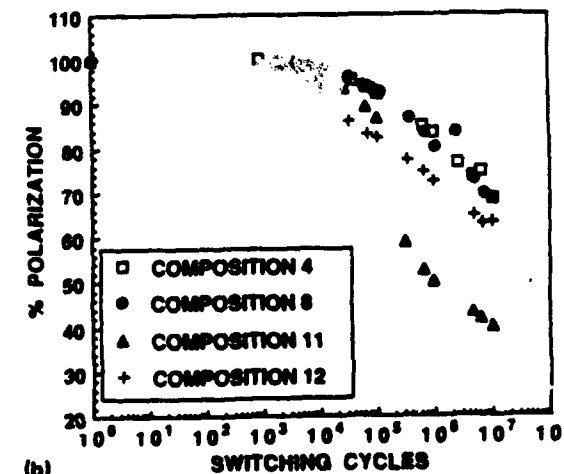


FIG. 16. Normalized field-induced polarization vs driving cycles of composition No. 5 for different metal electrodes.



(a) SWITCHING CYCLES



(b) SWITCHING CYCLES

FIG. 17. Normalized field-induced ferroelectric polarization vs driving cycles for (a) group 1 and (b) group 2 compositions; the compositions are as illustrated.

38% at 10^7 cycles, while group 1 has an average of 21%. For group 1, composition 10 and 7 have a larger degradation rate than the rest of the compositions and for group 2 compositions; No. 11 clearly has the largest degradation rate.

C. Discussion

The degradation effect of the composition appears to depend on the distance of the composition away from the MPB. Group 2 compositions, on the average, are further away from the MPB than group 1 compositions, and accordingly, the average degradation rate for group 1 compositions is less than that for group 2 composition. The degradation rate seems also to depend on the Sn/Zr ratio. From Fig. 2, composition 5 is farthest away from the phase boundary, however, this composition is richest in Sn, the degradation rate is smaller than most of the composition in group 1. In group 2, composition 11 is closest to the phase boundary among the group members. However, this composition is richest in Zr, and the degradation rate is thus most severe. It may be said that the degradation effect depends on the easiness of the antiferroelectric-ferroelectric phase transition. Close to the phase boundary, the energy difference between the antiferroelectric phase and ferroelectric phase is small, and the degradation rate is less. However, this effect cannot be compared simply by measuring the distances of the compositions away from the morphotropic phase boundary. For two compositions which are the same distance away from the MPB, the Sn-rich composition is easier to be switched into the ferroelectric phase and the degradation rate is correspondingly less.

The surface finishing condition has a profound effect on the degradation rate of the antiferroelectric ceramics. This result is very different from that reported by Fraser and Maldonado who observed significantly reduced ac field excitation degradation effect by using indium electrode.¹² The dependence of the degradation rate on the surface finishing condition is not clear at the moment. However, if the fatigue is mechanical in origin, we speculate that the cracks may initiate from the surfaces and propagate into the bulk under ac field driving, resulting in the degradation. Different surface finishing conditions yield different amount of flaws on the surface and might affect the degradation differently. On the other hand, if the fatigue is electric in origin, different

surfaces can give a different charge injection because of the electric field concentration at the flaws. The injected charges can then interact with the polarization discontinued region, trap there, and stabilize the regions. This mechanism can also give rise to the observed degradation effect. Further work is carrying on to sort out and verify the mechanisms of the degradation effect.

VI. SUMMARY AND CONCLUSION

The longitudinal field-induced strain accompanying the phase change in this family of antiferroelectric ceramics is in the range of 0.2%–0.9%. The temperature and composition dependencies of the field-induced strain are explained by the temperature dependence of the sublattice coupling related electrostrictive coefficient Ω . The Sn/Ti ratio dependence of the strain level is explained by the possible decrease of Ω due to the addition of the Sn to the system.

The single-shot switching time between the two states is on the order of 1–2 μ s. The kinetics is controlled by the nucleation of the new phase under the realizable applied field range. Under continuous ac field driving, the hysteretic heating effect introduces temperature rise, changing the original room-temperature switching behavior.

The ceramics degrade under ac field excitation, the average life cycles is in the range of 10^6 – 10^7 cycles which can be greatly improved by carefully polishing the sample surfaces. The compositions close to the phase boundary and rich in Sn degrade more slowly than the compositions away from the phase boundary and rich in Zr.

¹B. Jaffe, W. R. Cooke, Jr., and H. Jaffe, *Piezoelectric Ceramics*, edited by J. P. Roberts and P. Popper, (Academic, London, 1971).

²D. Berlincourt, H. Jaffe, H. H. A. Krueger, and B. Jaffe, *Appl. Phys. Lett.* **3**, 90 (1963).

³D. Berlincourt, *IEEE Trans. Sonics Ultrason.* **SU-13**, 116 (1966).

⁴K. Uchino and S. Nomura, *Ferroelectrics* **50**, 517 (1987).

⁵L. E. Cross, S. J. Jang, R. E. Newnham, S. Nomura, and K. Uchino, *Ferroelectrics* **23**, 187 (1980).

⁶W. Y. Pan, Q. M. Zhang, A. S. Bhalla, and L. E. Cross, *J. Am. Ceram. Soc.* **72**, 571 (1989).

⁷Q. M. Zhang, W. Y. Pan, and L. E. Cross, *J. Appl. Phys.* **63**, 2492 (1988).

⁸K. Uchino, L. E. Cross, and R. E. Newnham, *Jpn. J. Appl. Phys.* **19**, L425 (1980).

⁹W. J. Merz, *J. Appl. Phys.* **27**, 938 (1956).

¹⁰Q. Li, W. Y. Pan, and L. E. Cross, *J. Wave Mater. Interact.* **1**, 257 (1986).

¹¹Q. Li, W. Y. Pan, and L. E. Cross, *Mater. Lett.* **5**, 51 (1986).

¹²D. B. Fraser and J. R. Maldonado, *J. Appl. Phys.* **41**, 2172 (1970).

COMPOSITE MATERIALS

APPENDIX 8

**PIEZOELECTRIC COMPOSITES WITH HIGH SENSITIVITY AND
HIGH CAPACITANCE FOR USE AT HIGH PRESSURES**

Q.C. Xu, J. R. Belsick, S. Yoshikawa and R.E. Newnham
Materials Research Laboratory
The Pennsylvania State University
University Park, PA 16802, USA

Abstract

A new type of piezoelectric composite has been developed for oceanographic applications. The composites have a large figure of merit ($d_3 \cdot g_3$ or $d_3 \cdot g_3/\tan \delta$); a large dielectric constant (K) and low dielectric loss, as well as great mechanical strength. A shallow cavity between the PZT ceramics and thick metallic electrode is designed to convert a portion of the z-direction stress into a large radial and tangential stress of opposite sign, thereby causing the d_{33} and d_{31} contributions to d_3 to add rather than subtract, and raising the figure of merit. Theoretical stress analysis was carried out using an axisymmetric finite element method. Experimental results show that the $d_3 \cdot g_3$, K and withstandable pressure are extremely high.

I. Introduction

For many hydrophone applications, there is a great demand for piezoelectric composites with a high hydrostatic piezoelectric charge coefficient (d_3), high hydrostatic piezoelectric voltage coefficient (g_3), and high dielectric constant (K) as well as a high pressure tolerance. In the last decade, several piezoelectric ceramic-polymer composites with different connectivity patterns has been developed for hydrophone and medical transducer applications¹⁻⁴. The advantages of these composites over ceramics include higher figure of merit $d_3 \cdot g_3$ to enhance the sensitivity, increased the mechanical compliance, smaller acoustic impedance for matching to water or tissue, and lower transverse electromechanical coupling coefficient to reduce cross-talk noise and improve directivity of the transducer array. Disadvantages of these ceramic-polymer composite transducers however, are lower dielectric constant and lower pressure tolerance than their ceramic counterparts.

Flextensional transducers composed of a piezoelectric ceramic and a shell structure exhibit good electroacoustic performance⁵⁻⁹ in which the extensional vibration mode of a piezoelectric ceramic is coupled to the flexural vibration mode of a metal or polymer shell. The shell is used as a mechanical transformer for transforming the high acoustic impedance of the ceramic to the low acoustic impedance of the medium and for producing large volume velocity. Or, when operated in the reverse direction, the large velocity in the medium produces a high stress in the ceramic. All five types of flextensional transducers described in ref. 5 and 6 are designed to operate in the low frequency range below 10 kHz.

This paper describes a new type of piezoelectric ceramic-metal composite based on the principle

of a flextensional transducer. The basic structure is described in sec. II. A computer analysis for stress analysis in the composite was performed using the Finite Element Method (FEM). The stress contours are described in sec. III. In sec. IV, the experimental results are presented to show that this type of composite can provide very high $d_4 \cdot g_1$ or $d_4 \cdot g_1 / \tan \delta^{[7]}$, together with a large capacitance and high withstandng pressure.

II. Basic Principle

As is well known, PZT ceramics have high d_{33} and d_{31} , but its $d_4 (= d_{33} + 2d_{31})$ value is only about 45 pC/N because d_{31} and d_{33} have opposite signs. To enhance d_4 , we have developed a PZT-metal composite with very shallow cavities between the PZT ceramic and thick metallic electrodes which convert a portion of z-direction stress into a large radial and tangential stresses of opposite signs, thereby causing the d_{33} and d_{31} contribution to d_4 to add rather than to subtract, leading to high d_4 .

A cross section view of the PZT-metal composite is shown in Fig. 1. The symmetrical structure is designed to obtain an extensional vibration mode of PZT, and high hydrostatic pressure tolerance. The height of the shallow cavity h is less than 150 μm . The shallow cavity allows deformation of the metal electrode toward the ceramic disk by closing the cavity which reduces stress amplification in the PZT and prevents breakdown during shockwaves or very high hydrostatic pressure. A simplified explanation is shown in Fig. 1 and the following equations.

Let T_x be the x-direction stress in PZT.

$$T_x \approx P_a - N \frac{d}{h} \approx T_x$$

Where P_a is the acoustic pressure and N is a stress amplification parameter. N is approximately equal to $1/\tan \alpha$. Where α is the shallow cavity angle shown in Fig.1.

T_z is the z-component of stress in PZT and is given by

$$P_a \frac{S}{S_2}$$

Where S is the surface area of the disk and S_2 is the surface area of the metal-PZT bond. The resulting polarization is $d_{31}T_z + d_{31}T_y + d_{33}T_z S_2/S$.

Therefore,

$$(d_e)_{\max} \equiv d_{33} + 2d_{31} \left[1 - \frac{Nd_e}{h_p} \right]$$

This representation of $(d_e)_{\max}$ is only for explaining the basic principle for designing the composite. In fact, the experimental result of d_e is much smaller than $(d_e)_{\max}$, because N is much less than $1/\tan \alpha$ for the thick metal electrode.

The basic idea is to attempt to use both the d_{33} and d_{31} to obtain high d_e . Thick metal plates are used as a mechanical transformer to transform the stress direction and amplitude, and also adjust the acoustic impedance from a low impedance in the z-direction to high impedance in planar direction.

The lowest vibration mode of the composite is a flexural mode determined mainly by the stiffness of the PZT in planar mode and the equivalent mass of the metal plate. This equivalent mass is much larger than the real mass of the metal plate, because the vibration velocity at the central portion of the metal is much larger than the reference velocity on the PZT. The operating frequency range of the composite is dependent on this flexural mode which is related to the cavity diameter d_c , the height of the cavity h , the thickness of the metal h_m and the stiffness of the ceramic in planar mode.

Since the withstanding hydrostatic pressure P_w is another important parameter for the undersea application, the stress amplification coefficient N cannot be designed too high. Transducers with large cavity diameters (d_c) have low flexural resonant frequency, low P_w and high d_e .

The capacitance of the composite can be changed by adjusting the electrode area on the PZT surfaces.

III. Stress Analysis with FEM

A theoretical analysis of the brass-PZT composite was performed using the finite element analysis program, ANSYS version 4.3TM. A one-quarter axially-symmetric model is shown in Fig. 2. The mesh contained 640 quadrilateral-shaped elements with 729 nodal points. Half of

them are in the PZT. The sign of triangles are used to "pin" the object and allow only parallel direction movement on the boundary when stresses are employed.

For simplicity of analysis, the metal bonding layer is neglected, and a hydrostatic reference pressure of $P_0 = 1$ is applied to the model. Fig. 3 shows the stress contours in radial (R) direction with quadrupole pattern in the brass, and the stress concentration with a factor of about 20 is at the tip point of the PZT and the brass. In the PZT, there are only extensional stresses in the radial R direction and very small stresses in the center part. The tangential stresses in Fig. 4 shows that there are bending stresses in the brass, and extensional stresses in the PZT. The stress contours in the z-direction shown in Fig. 5 indicate that there are undesirable extensional stresses in the PZT, and the stresses are concentrated with a factor of about 15 at the tip line of the PZT and the brass. This stress analysis shows that the material used as a bonding layer between the PZT and the brass should have greater compliance than brass or PZT in order to reduce the stress concentration factor and to obtain compressive stresses in the PZT along the z-direction.

IV. Experiment and Results

Brass-PZT composite samples with dimensions (Fig 1): $d = 11$ mm, $h_m = 1.2$ mm, $h_s = 1.1$ mm, $h = 100\text{-}150 \mu\text{m}$ and four different cavity diameters d_c , 7.6 mm (large cavity), 5.8 mm (middle cavity), 4.1 mm (small cavity), 2.5 mm (very small cavity) were machined for the experiment. In order to obtain a thick bonding layer, the brass plates with silver paste applied over the bonding area were fired at 600 °C for 10 minutes. Then the brass plates were bonded to a PZT-5 disk with the silver-glass paste and fired at 600 °C for 10 minutes. Brass was chosen for its low thermal expansion coefficient (approximately 15 ppm/°C). After cooling the composite was encapsulated around its circumference with Spurrs epoxy resin and cured at 90 °C for more than 8 hours. The composite was poled in oil at 150 °C with a 2.5 kV/mm electric field for about 15 minutes.

Piezoelectric coefficients g_{31} and d_{31} were measured in a closed oil cavity using a low frequency (approximately 53 Hz) comparative method with the hydrostatic pressures up to 1000 psi (7 MPa). The experimental results presented in Fig. 6 and Fig. 7 show that large cavity size leads to large d_{31} and g_{31} . The dielectric constant was larger than 1500 and $\tan \delta$ less than 0.025. Fig. 8 shows the relationship between the d_{31} value measured at center point of the sample with a Berlincourt d_{31}

meter and the d_{31} value measured by the low frequency comparative method. The d_{33} value also increased markedly with cavity diameter. Fig. 9 shows that the frequency of the lowest flextensional mode decreases as the cavity diameter increases. Therefore, the larger cavity diameter composites possess a lower operating frequency range.

Because the thermal expansion coefficient of brass is larger than the PZT (approximately 5.7 ppm/ $^{\circ}$ C), compressive prestresses are applied to PZT in R and ϕ directions perpendicular to the poling direction. These prestresses help to maintain the polarization in the PZT. Fig. 10 shows that the aging under hydrostatic pressure at 350 psi (about 2.5 MPa) was very small.

A planar array was made for testing by embedding four composite samples with large cavities in epoxy resin (Eccogel 1365-25, Emerson & Cuming Inc.) (Fig. 11). The admittance and conductance of the array in air and in water presented in Fig. 12 and Fig. 13 show that the lowest flextensional mode was higher than 30 kHz and the resonant peak in water was very flat. Therefore its flat receiving response is more than 20 kHz.

V. Conclusions

1. A PZT-brass composite with redirected stresses exhibits a very high figure of merit ($d_3 \cdot g_b$ or $d_3 \cdot g_b / \tan \delta$) as well as high dielectric constant K and withstanding pressure P_w . Its $g_b \cdot d_b \equiv 50000 \times 10^{-15} \text{ m}^2/\text{N}$. For PZT ceramic its $g_b \cdot d_b \equiv 110 \times 10^{-15} \text{ m}^2/\text{N}$. For PbTiO₃ ceramic its $g_b \cdot d_b \equiv 1800 \times 10^{-15} \text{ m}^2/\text{N}$. For voided thick PVDF $g_b \cdot d_b \equiv 5000 \times 10^{-15} \text{ m}^2/\text{N}$.
2. Larger cavity sizes lead to large d_b and g_b , but lower operating frequencies.
3. Little aging was observed under hydrostatic pressure (350 psi).
4. An experimental four-element flexible array shows flat frequency response.

VI. Acknowledgements

The authors wish to thank The Office of Naval Research and Professor L.E. Cross, Professor V. Varadan and Dr. W. Smith for their advice and support of this research, Patrick A. Marlowe for his help for preparation of this manuscript.

References

- [1] R.E. Newnham, "Composite Electroceramics," Ann. Rev. Mater. Sci., pp. 47-68, Annual Reviews Inc. (1986).
- [2] T.R. Gruraja, A. Safari, R.E. Newnham and L.E. Cross, "Piezoelectric Ceramic-Polymer Composites for Transducer Application," Electronic Ceramics, ed. L. Levison, pp. 92-128, Marcel Dekker, Inc., New York (1987).
- [3] H. Banno and S. Saito, "Piezoelectric Properties of Composites of Synthetic Rubber and PbTiO₃ or PZT," Int. J. Appl. Phys., vol. 22, supp.22-2, p. 67 (1983).
- [4] Y.Q. Zhuang, Y.G. Heu and Q.C. Xu, "Sandwich PZT/Polymer Composite Transducer," Ferroelectrics, vol. 49, pp. 241-249 (1983).
- [5] G.A. Brigham and L.H. Roystor, "Present Status in the Design of Flextensional Underwater Acoustic Transducer," J. Acou. S. Amer., vol. 46, N° 1 (part 1), p. 92 (1969).
- [6] K.D. Rolt, "History of the Flextensional Electroacoustic Transducer," J. Acou. S. Amer., vol. 87, N° 3, pp. 1340-1349 (1990).
- [7] A.S. Bhalla and R.Y. Ting, "Hydrophone Figure of Merit," Sensors and Materials, vol. 4, pp. 181-185 (1988).
- [8] K.L. Swain, "Crescent-Shaped 3-0 Piezoelectric Transducers," B.S. Thesis, Department of Materials Science and Engineering, The Pennsylvania State University, (1988).
- [9] T.J. Meyer, "3-0 Crescent Shaped Composite Hydrophones," B.S. Thesis, Department of Materials and Engineering, The Pennsylvania State University, (1989).

Figure List:

Fig. 1. The Geometry of the Composite

Fig. 2. Meshed Area For Brass/PZT Composite

Fig. 3. Finite Element Model of Stress in R Direction

Fig. 4. Finite Element Model of Stress in ϕ Direction

Fig. 5. Finite Element Model of Stress in z Direction

Fig. 6. Hydrostatic Pressure Dependence of d_s and g_s

Fig. 7. Hydrostatic Pressure Dependence of d_s and g_s

Fig. 8. d_s Dependence of d_{33} at Center Point

Fig. 9. The First Flextensional Frequency Dependence of Cavity Diameter

Fig. 10. Aging Under Hydrostatic Pressure

Fig. 11. Testing Flexible Composite Array

Fig. 12. Conductance and Admittance of the Array in Air

Fig. 13. Conductance and Admittance of the Array in Water

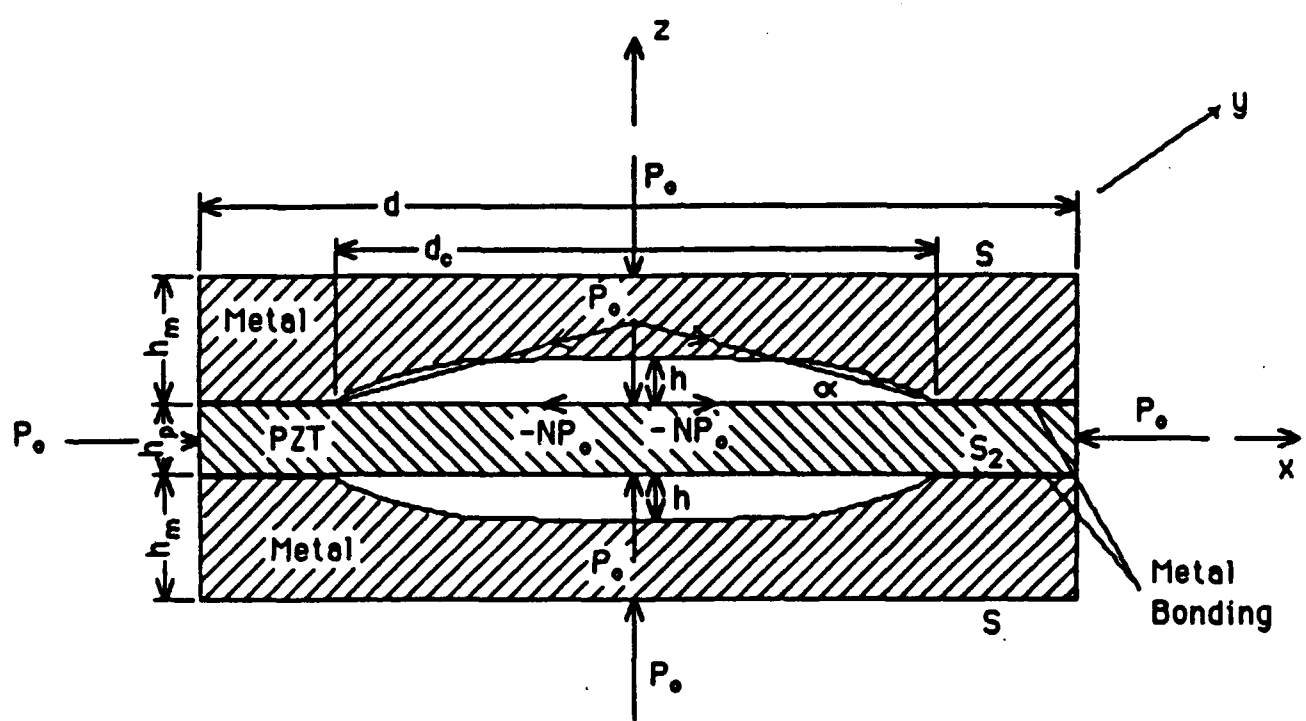


Fig.

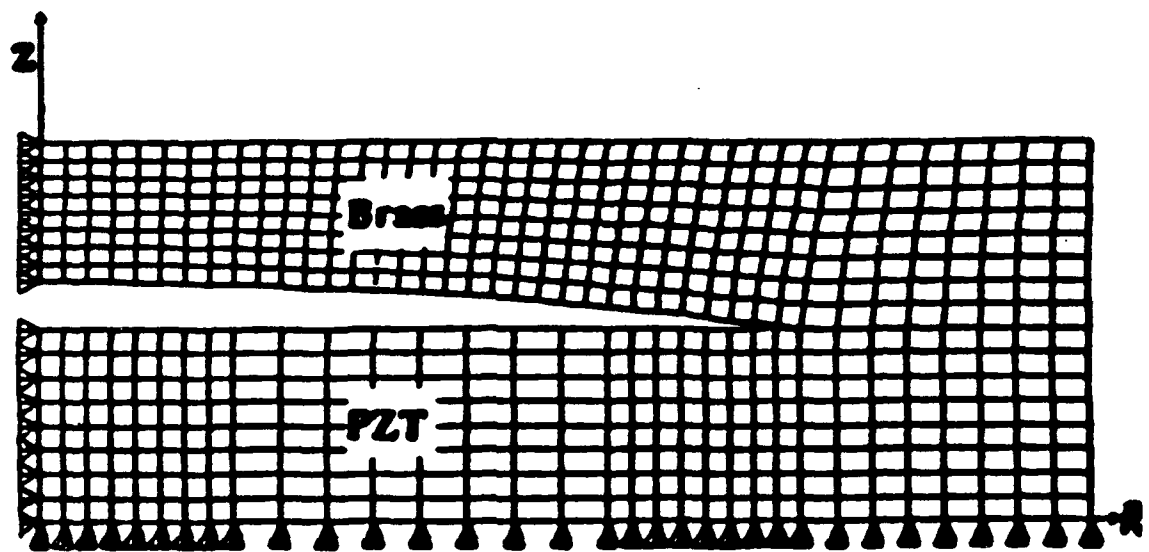
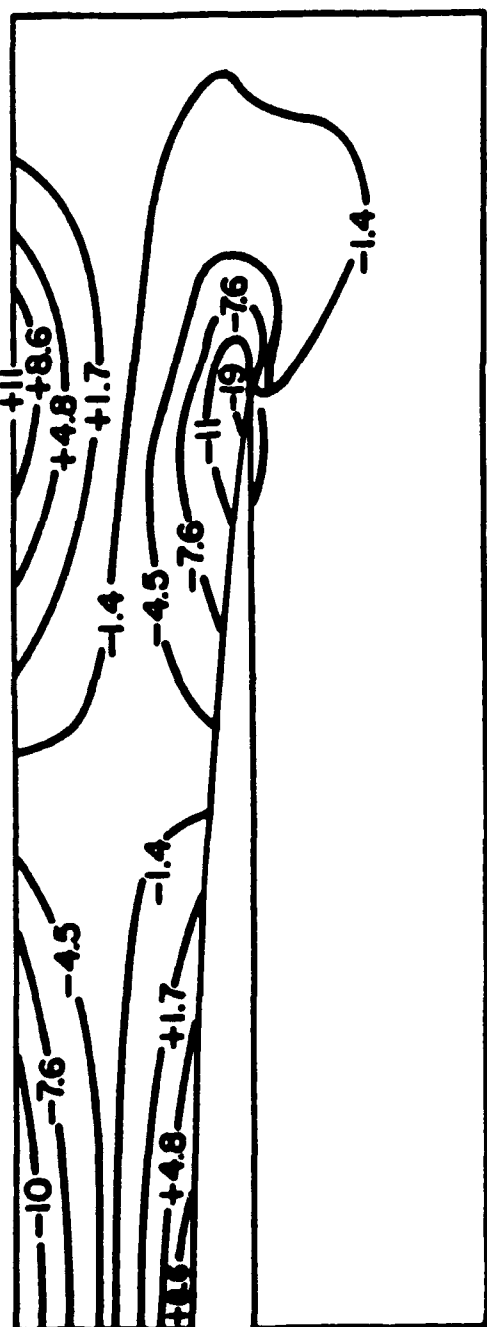


Fig. 2

Fig. 3



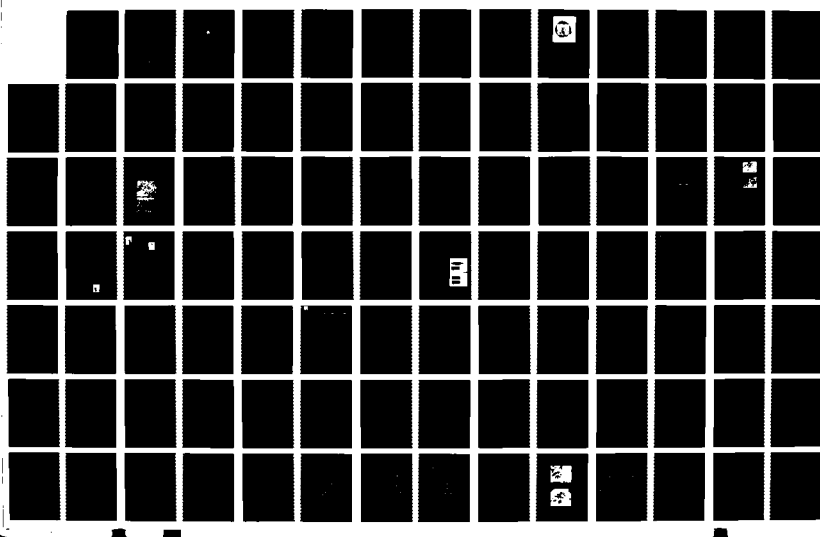
AD-A236 219

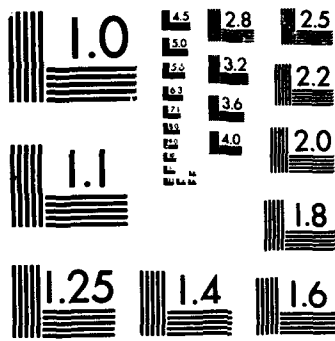
PIEZOELECTRIC AND ELECTROSTRICITIVE MATERIALS FOR
TRANSDUCER APPLICATIONS. (U) PENNSYLVANIA STATE UNIV
UNIVERSITY PARK MATERIALS RESEARCH LAB.

3/4

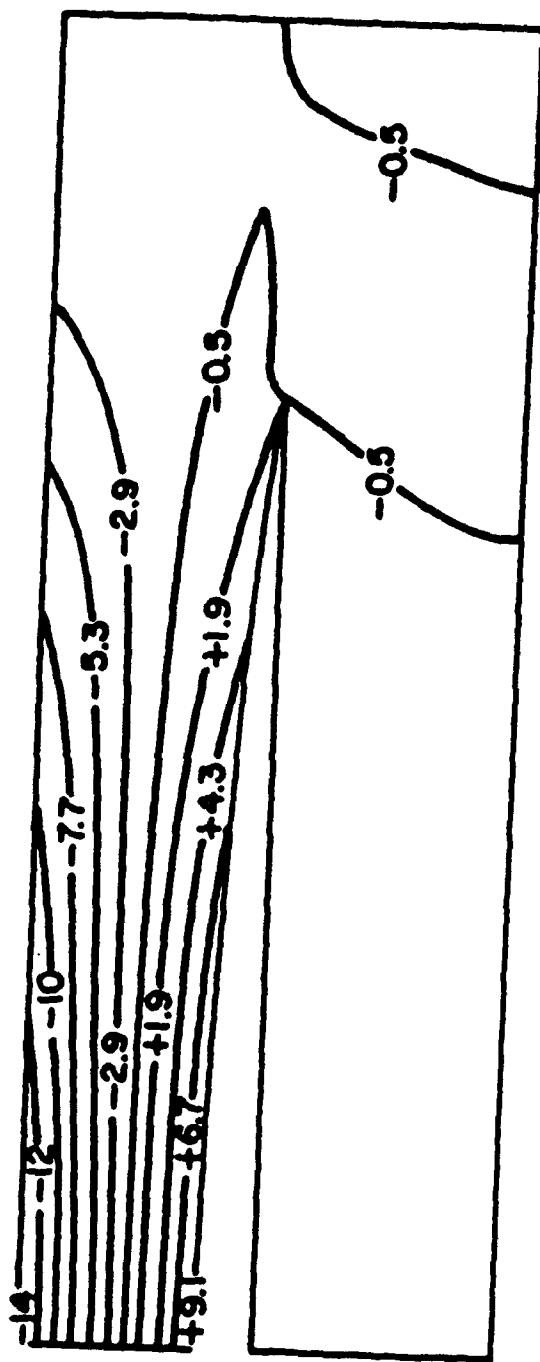
UNCLASSIFIED L E CROSS ET AL. 31 JAN 91 XN-DNR

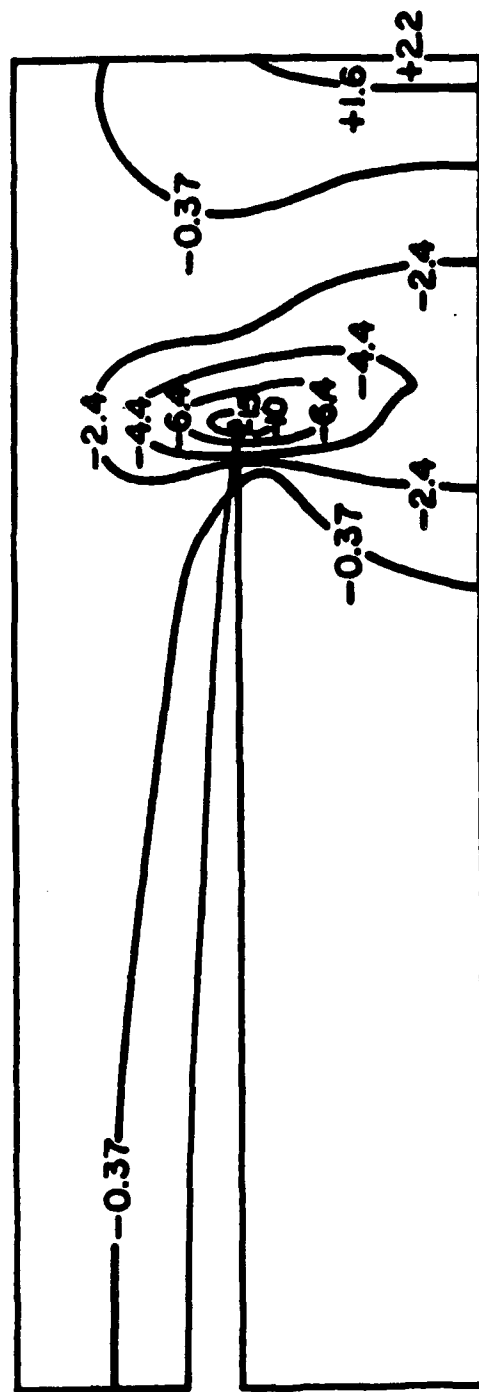
NL

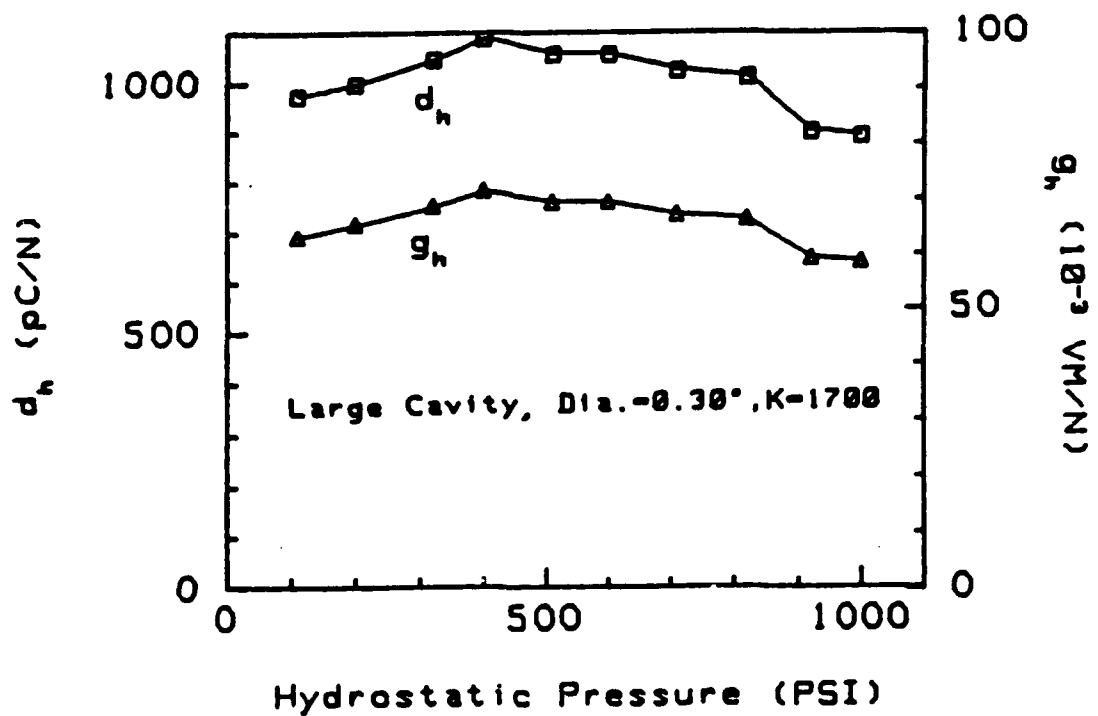




MICROCOPY RESOLUTION TEST CHART
NATIONAL BUREAU OF STANDARDS-1963-A







Fig

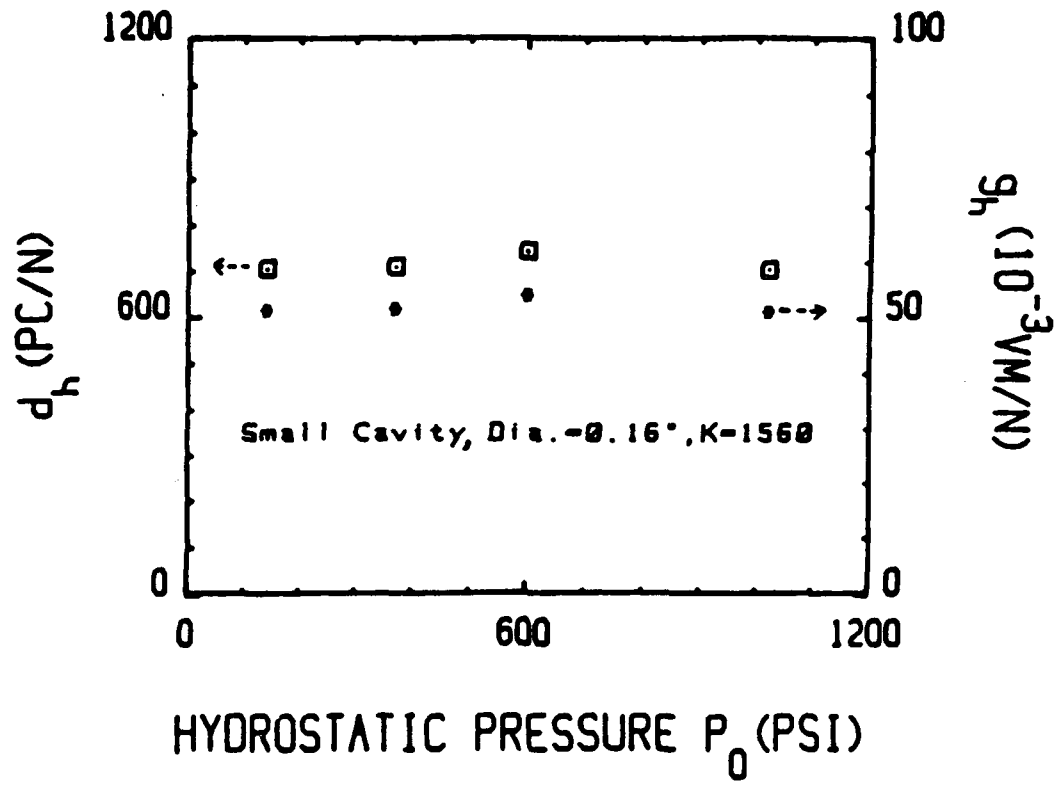


Fig.

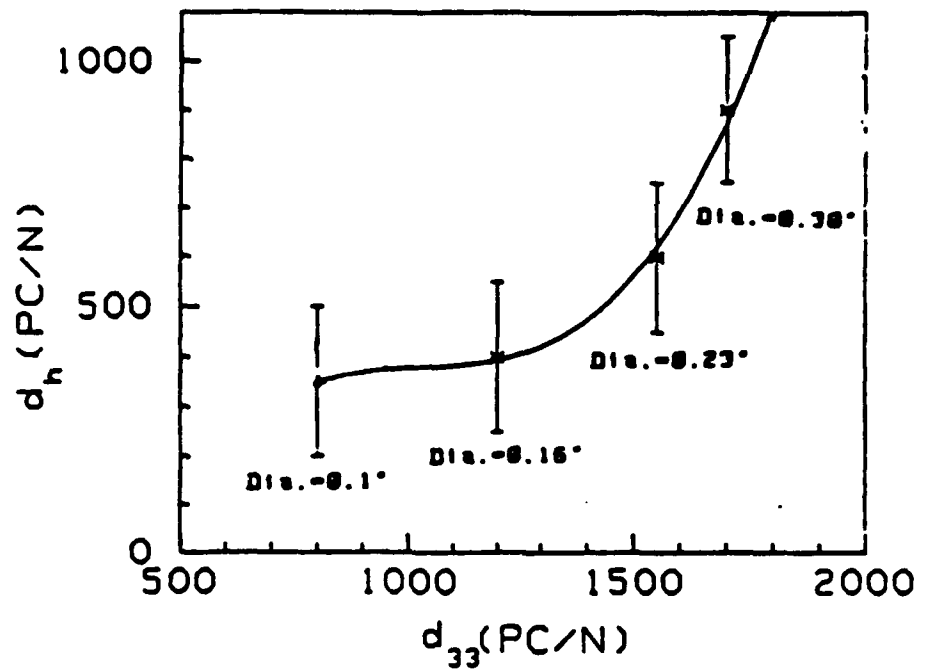


Fig. 8

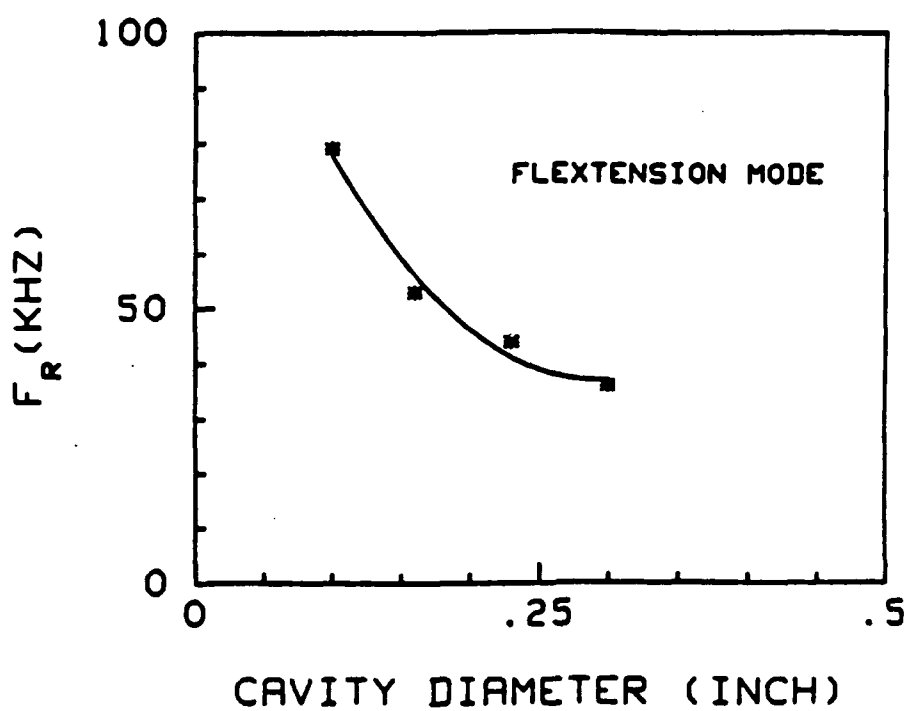


Fig 9

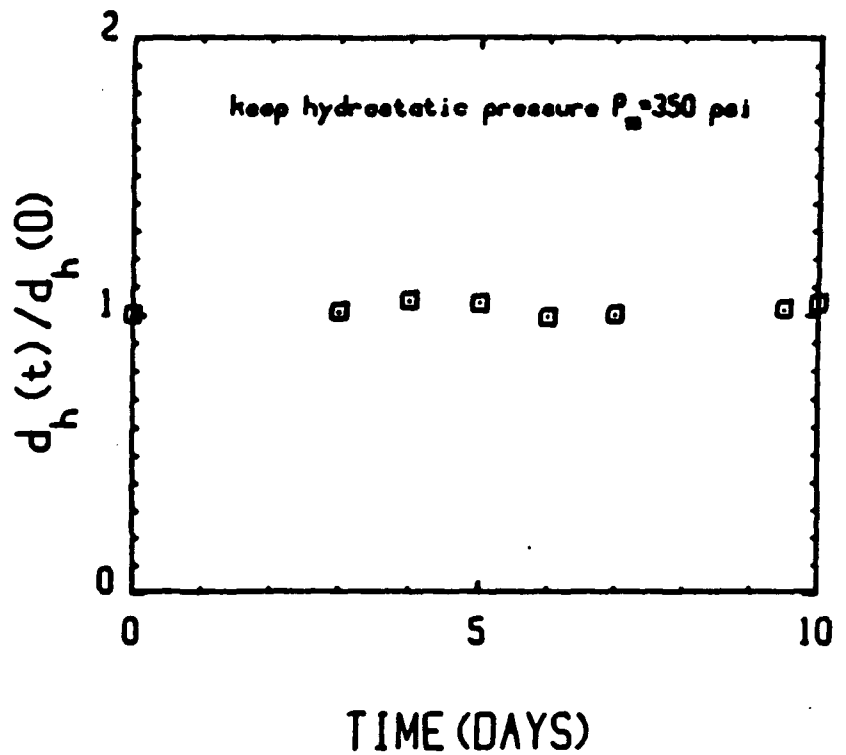


FIG. 1



Fig.:

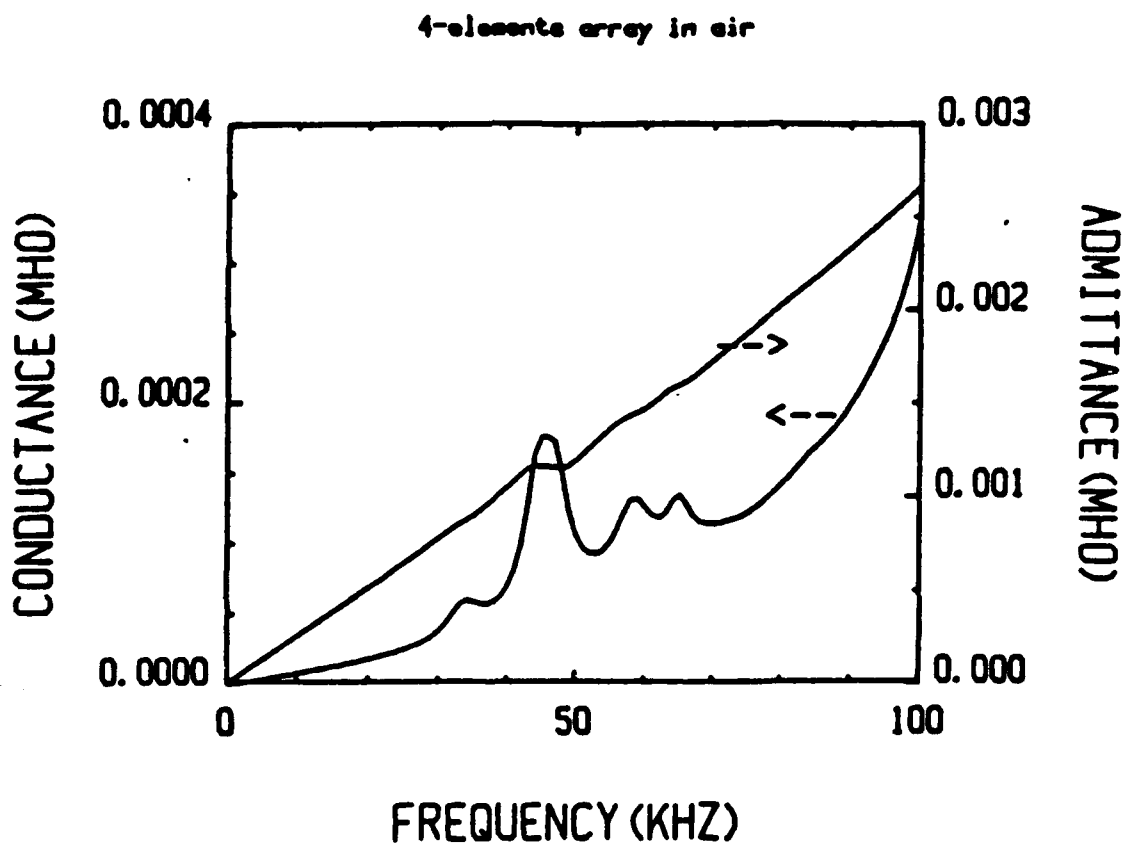


Fig. 12

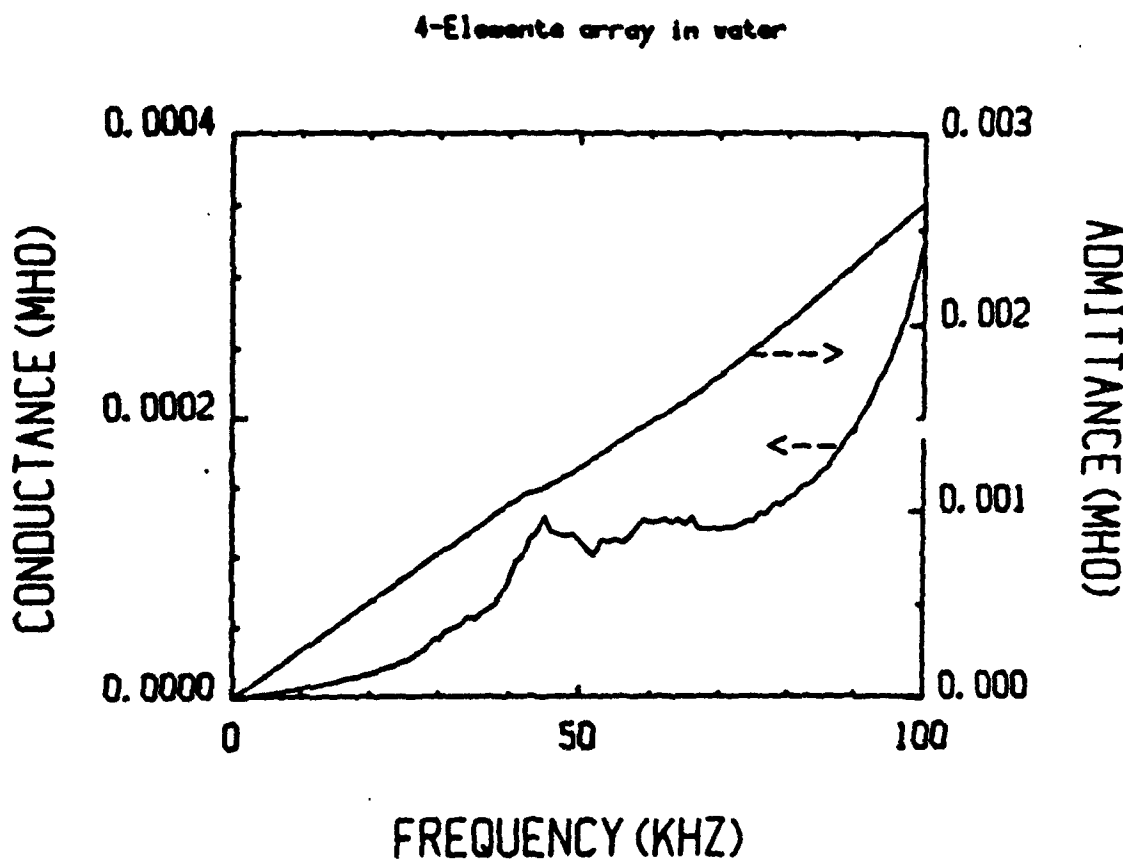


Fig. 13

APPENDIX 9

Hydrophone Figure of Merit

A. S. Bhalla and R. Y. Ting¹

Materials Research Laboratory, The Pennsylvania State University,
University Park, Pennsylvania 16802, USA

¹Naval Research Laboratory, Underwater Sound Reference Division, Orlando,
Florida 32856, USA

(Received May 2, 1989; accepted May 8, 1989)

Key words: hydrostatic pressure sensor, hydrophone figure of merit, composites, sources of noise in pressure sensors, piezoelectrics

The potential of a number of hydrophone sensor materials is assessed by considering the sensitivity requirement and various noise contributions in the design of a hydrophone element. Noises originating from the loss tangent and pyroelectricity of the material can be serious factors. By considering the free-field voltage sensitivity and a proposed figure of merit $g_h d_h / \tan \delta$, it is shown that composites and glass ceramics are the more promising candidates for new sensor applications. The self-noise factors can be minimized by designing sensor materials that have large $g_h t$ and low $\tan \delta$ values. Pyroelectric noises can also be greatly reduced by appropriate composite designs.

For a crystal belonging to one of the piezoelectric classes, there is no guarantee that the crystal in actual measurements will display the piezoelectricity in all the stress conditions. In a particular stress environment, piezoelectric effects are permissible for some piezoelectric crystals. For a crystal used as a stress sensor, the change in polarization, ΔP_i , (or charge, ΔQ , developed on the per unit surface area of a sensor) is given by⁽¹⁾

$$\Delta P_i = \frac{\Delta Q_i}{A} = \frac{d_{ij} \Delta \sigma_j}{d_{ij}} \quad (i = 1, 2, 3 \text{ and } j = 1-6), \quad (1)$$

where A is the area and d_{ij} are the piezoelectric coefficients of the sensing element. For a hydrostatic stress environment ($\sigma_1 = \sigma_2 = \sigma_3 = -P_h$, $\sigma_4 = \sigma_5 = \sigma_6 = 0$)

$$\Delta Q_i = d_{i(h)} \Delta P_h A. \quad (2)$$

Table 1
Nonzero $d_{(h)}$ expression for active piezoelectric crystal classes (\mathbf{l} is a direction vector)

System	Class	$d_{(h)} \equiv d_h$	Example
Triclinic	1	$(d_{11} + d_{12} + d_{13})l_1 + (d_{21} + d_{22} + d_{23})l_2 + (d_{31} + d_{32} + d_{33})l_3$	
Monoclinic	$m \perp x_2$	$(d_{11} + d_{12} + d_{13})l_1 + (d_{31} + d_{32} + d_{33})l_3$	
Monoclinic	$2/\!/x_2$	$(d_{21} + d_{22} + d_{23})l_2$	$\text{Li}_2\text{SO}_4 \cdot \text{H}_2\text{O}$
Orthorhombic	$mm2$	$(d_{31} + d_{32} + d_{33})l_3$	PVF_2
Tetragonal	4,4 mm		$\text{Li}_2\text{B}_4\text{O}_7$
Rhombohedral	3,3 m		Relaxor Ferroelectrics
Hexagonal	6,6 mm	$(2d_{31} + d_{33})l_3$	ZnS, CdS
Poled Ceramics	$\infty, \infty m$		PZT, PT, Composites
			Glass Ceramics
			PVF_2

It can be shown that $d_{(h)}$ (or d_h) for all piezoelectric crystal classes, except for those belonging to the pyroelectric or polar classes, is zero (Table 1).

From eq. (2), the hydrostatic voltage sensitivity, M , (M.K.S. units) of a lossless capacitor (or a crystal) is defined as

$$M = \frac{d_{(h)}}{K\epsilon_0} \cdot t \left[\frac{\text{V} \cdot \text{m}}{\text{N}} \right] \cdot \text{m}$$

or

$$M = g_h \cdot t \left[\text{V} \cdot \frac{\text{m}^2}{\text{N}} \right] \quad (3)$$

where K is the dielectric constant of a material, ϵ_0 the permittivity of vacuum and N/m^2 the stress in Newton per square meter. M is defined as the free-field voltage sensitivity (volt per pascal) and thus depends on the sensing element thickness, t . The g_h coefficient for most practical materials falls in the range $10 - 200 \times 10^{-3} \text{ V} - \text{m}/\text{N}$. Thus, from the material designer's point of view, the g_h coefficient is the most direct and important consideration for hydrophones of high sensitivities. In practice, besides the intrinsic material properties ($K, d_h, g_h, \tan \delta$), the device development also depends upon the fabrication parameters (e.g., sample preparation, electrodes, mounting, sensor dimensions, single crystal or polycrystalline material, etc.) and operational conditions (temperature, pressure, frequency, and other environmental conditions). The material property which is also highly affected by the fabrication and operational parameters is the intrinsic $\tan \delta$ of the sensing element. The loss tangent generally depends heavily on the material preparation and its state, for example, it being a single crystal, polycrystalline, thin film or composite, and often on the poling conditions and aging effects in the ceramics.

Hence, there are various sources of noise in a practical hydrostatic sensing device. Some of the other sources of noise are due to flow noise, temperature fluctuations or pyroelectric noise, open circuit input noise of an amplifier, short circuit input noise, etc. The self-noise (which in general $\propto \tan \delta / \omega C$), depending upon the operational conditions, must be seriously considered in the design of hydrostatic sensors.

Therefore, the figure of merit of a (Johnson noise limited) hydrostatic sensor could be expressed as

$$\text{F.O.M.} \propto \frac{M^2 C}{\tan \delta}$$

or

$$\propto \frac{g_{(h)} d_{(h)}}{\tan \delta} \cdot t \cdot A \quad (4a)$$

or

$$\propto \frac{d_{(h)}^2}{\epsilon_0 K \tan \delta} \cdot t \cdot A. \quad (4b)$$

For a sensor with given dimensions A and t , the hydrostatic figure of merit of the sensor material is directly related to $(g_h \cdot d_h)/\tan \delta$. The values of g_h , d_h , and FOM for a hydrostatic sensor material are expressed in units of

$$g_h \sim 10^{-3} \frac{V - m}{N}$$

$$d_h \sim 10^{-12} \frac{C}{N}$$

$$d_h g_h \sim 10^{-15} \frac{m^2}{N} \quad \text{or} \quad \frac{10^{-15}}{\text{pascal}}$$

Generally, $\tan \delta$ for most materials is $\sim 10^{-2}$. By including $\tan \delta$ in the FOM, we can express $g_h d_h / \tan \delta$ as $\sim 10^{-13} \text{ m}^2/\text{N}$.

For hydrophone materials with $d_h g_h \sim (10 \text{ to } 1000) \times 10^{-15} \text{ m}^2/\text{N}$, the FOM of the order of $(1 \text{ to } 100) \times 10^{-12} \text{ m}^2/\text{N}$ has the units and range of elastic compliance of most common materials. This allows one to draw an elastic analogy to the situation as if the material were behaving like an elastic media. A higher FOM gives an analogy to a highly compliant material whereas a lower FOM reflects the highly stiff behavior of the material. For comparison, typical values of compliance, s_{13} , in some cases are

Spurr Epoxy $- 122 \times 10^{-12} \text{ m}^2/\text{N}$

$$\begin{array}{ll} \text{Stycast Epoxy} & -32 \times 10^{-12} \\ \text{PbTiO}_3 & -1.4 \times 10^{-12}. \end{array}$$

Table 2 lists the hydrostatic figures of merit g_h , d_h , and $(g_h d_h)/\tan \delta$ for various important piezoelectric ceramics and composites.⁽²⁻¹⁰⁾ It clearly indicates that composite and glass ceramic sensor materials are superior to any other single-phase piezoelectric sensor materials. It is also clear from expressions (3) and (4) that the thickness of the sensing element is an important parameter in the hydrostatic pressure sensor design. In many instances, the available thickness of a material becomes the limiting factor for the design of sensitive hydrophones. For example, in order to achieve a design goal of sensitivity -192 dB re Volt/ μ Pa, and 2nF capacitance, for a $10 \times 10 \text{ cm}^2$ sensor, the best PVDF ($K = 12$) can provide is ~ 0.6 mm thickness, and therefore it requires a minimum g_h of 150×10^{-3} Vm/N. Thus composites and glass ceramics offer additional possibilities to meet the design goal for hydrophones. It should be noted that greater thicknesses of the piezoelectric elements usually translate into greater degree of difficulty for poling and reduce the net capacitance of the sensing element at the same time.

Table 2
Hydrostatic figures of merit g_h , $g_h d_h$, and $d_h^2/(K\epsilon_0 \tan \delta)$ for various important materials.

Sample	Ref.	K^*	d_h $\times 10^{-12}$ C/N	g_h $\times 10^{-3}$ Vm/N	$d_h g_h$ $\times 10^{-15}$ m ² /N	$\tan \delta_e$	$d_h^2/\epsilon_0 K \tan \delta$ $10^{-12} \text{ m}^2/\text{N}$
PZT4	7	1300	43	4	172	0.02	9
PZT5	7	1690	21	2	42	0.02	2
PVdF (1983) I	7,8	10	10	112	1,120	0.011	101
PVdF II		8	18	270	4,860	0.015	324
<i>Composites</i> ⁺	2,10						
A. 3-3 Mitsubishi	5,9	200	92	53	4,876	0.019	256
B. 0-3 NTK 304	10	54	22	47	1,034	0.058	17
306		38	27	81	2,187	0.016	137
305		37	41	124	5,084	0.023	221
307		51	69	153	10,557	0.035	302
N 3-0	7		150	19	2,850 (0.02)		143
K1	4,5	41	30	82	2,460	0.012	205
K2 3-1	4,5	356	220	72	15,840	0.02	792
K3 3-2	4,5	360	153	52	7,956	0.02	398
P1 Philips 1-3		45	28	71	1,988	0.02	100
K4 510b		478	200	48	9,600	0.018	533
Edo PbTiO ₃		210	48	26	1,248	0.007	178
BST Glass-Ceramics	6,7	12	10	83	830	0.001	830

⁺For details see refs. 2 and 3.

*Measurements at 1 kHz.

Another noise source which is to be considered in the hydrophone performance and can be eliminated in the composite material design is related to pyroelectric noises.⁽¹¹⁾ Since the pyroelectric coefficients are much larger than the piezoelectric coefficients of hydrostatic piezoelectric materials, even a small temperature fluctuation is a matter of concern in the operation of hydrostatic pressure sensors, especially at lower frequencies. For a constant $\delta V/V$, a 3×10^{-3} K temperature variation produces an equivalent effect of one psi in a typical PVDF sensor. Such effects can be successfully eliminated by proper design of the composite material.⁽¹²⁾

Acknowledgement

We dedicate this paper to Professor Robert E. Newnham on the occasion of his sixtieth birthday. He has devoted over a decade of his active research career to developing and advancing the principles of connectivity and applications of composite electromaterials in the field of ferroic research. We wish him great and everlasting happiness in the coming years.

References

- 1 J. F. Nye: *Physical Properties of Crystals* (Clarendon Press, Oxford, 1957).
- 2 R. E. Newnham, D. P. Skinner, L. E. Cross: *Mat. Res. Bull.* 13 (1978) 525.
- 3 D. P. Skinner, R. E. Newnham and L. E. Cross: *Mat. Res. Bull.* 13 (1978) 599.
- 4 R. Y. Ting: *Ferroelectrics* 67 (1986) 143.
- 5 R. Y. Ting: *Ferroelectrics* 65 (1985) 11.
- 6 R. Y. Ting, A. Halliyal and A. S. Bhalla: *Appl. Phys. Lett.* 44 (1984) 852.
- 7 R. Y. Ting, A. Halliyal and A. S. Bhalla: *Jap. J. Appl. Phys. Suppl.* 24 (1985) 982.
- 8 J. C. McGrath, L. Holt and D. M. Jones: *Ferroelectrics* 50 (1983) 13.
- 9 H. Hikita, K. Yamada, M. Nishioka and M. Ono: *Ferroelectrics* 49 (1983) 265.
- 10 H. Banno, K. Ogura, H. Sobue and K. Ohya: *Jap. J. Appl. Phys. Suppl.* 26 (1987) 153.
- 11 A. Bhalla, R. E. Newnham and L. E. Cross: *Ferroelectrics* 33 (1981) 139.
- 12 A. Bhalla: "Polar Glass Ceramics" presented at the ECAP-ISAF 1988, Zürich, to be published in *Ferroelectrics*.

APPENDIX 10

THIN FILM 0-3 POLYMER/PIEZOELECTRIC CERAMIC COMPOSITES : PIEZOELECTRIC PAINTS

K. A. HANNER[†], A. SAFARI[‡], R. E. NEWNHAM and J. RUNT

Materials Research Laboratory, The Pennsylvania State University, University Park, PA 16802 USA

(Received 29 April 1989)

In this paper we summarize our investigation of the electrical properties of thin-film 0-3 polymer-ceramic composites. The main objective of this study was to demonstrate the principle that a piezoelectric 'paint' can indeed be prepared. Two polymers, an acrylic copolymer and a polyurethane, were utilized in our research. Both were loaded with 60-70 volume percent PZT and a coprecipitated PbTiO₃. The addition of various surfactants and dispersing agents to the acrylate-based composites was necessary to aid in dispersing the ceramic particles in the polymer matrix. The hydrostatic strain and voltage coefficients, along with the 'figures of merit' for PZT-filled acrylic and polyurethane composites were found to be significantly larger than values reported previously for other 0-3 polymer-PZT composites. For acrylic copolymer-coprecipitated PbTiO₃ composites, the hydrostatic coefficients were found to be roughly 50% larger than the comparable PZT-filled materials. For example, g_3 , d_3 ranged from about $1260-1380 \times 10^{-15} \text{ m}^2/\text{N}$ for PZT-filled and from about $1970-2140 \times 10^{-15} \text{ m}^2/\text{N}$ for PbTiO₃-loaded acrylic composites. The electrical properties of the PbTiO₃-filled polyurethane were comparable to those of the corresponding PZT composites.

INTRODUCTION

Piezoelectric ceramic/polymer composites possessing various connectivity patterns have been the focus of much study in the past ten years [e.g., 1-3]. Among the composites examined, the simplest types are those with so-called 0-3 connectivity. These consist of piezoelectrically-active ceramic particles dispersed in a 3-dimensionally connected polymer matrix. One of the more attractive features of polymer composites based on the 0-3 connectivity pattern is their versatility in assuming a variety of forms, including thin sheets, molded shapes, and extruded bars and fibers. By choosing the appropriate polymer matrix, these composites can also be made flexible, to conform to curved surfaces. A number of elastomeric and rigid polymers have been utilized in 0-3 composites in the past. These have been loaded with various piezoceramics, the most documented of which being lead zirconate titanate (PZT). In general, the 0-3 composite family has been found to exhibit high hydrostatic piezoelectric voltage coefficients and 'figures of merit' when compared to the properties of conventional single phase materials. Consequently, these composites have the potential for use in a number of applications such as hydrophones or ultrasonic transducers.

As an extension of this work, 0-3 composites have been examined for the development of piezoelectric (or pyroelectric) 'paints'. In this case, the term 'paint' refers to a thin-film polymer/ceramic composite which can be applied to large

[†]Present address: Dow Chemical Company, Midland, MI 48640.

[‡]Present address: Rutgers University, Piscataway, NJ 08854.

surface areas. The initial question that must be addressed is: is it feasible to load a typical paint vehicle to the levels required to obtain good piezoelectric or pyroelectric activity in the final, dry film? In fact, it is common in flat and ceiling paints to load to 60–80 volume percent pigment.⁴ Our research has focused on the preparation and electrical properties of piezoelectric 0–3 composites in the form of relatively thin films (~200–500 μ microns thick), cast onto brass plates.

EXPERIMENTAL

A. Materials and sample preparation

The polymers used in this study were an acrylic copolymer (in the form of a suspension in water) and a polyurethane. The copolymer (random) consisted of methyl methacrylate and 2-ethylhexyl acrylate (44 wt. % methyl methacrylate) dispersed in water (60% solids). Various surfactants and rheological agents such as sodium carboxy methyl cellulose, hydroxyethylcellulose, and polyethylene oxide (a nonionic surfactant) were purchased from Polysciences, Inc. "Foammaster" defoamer was obtained from Rohm Haas, Inc. The polyurethane composites incorporated only one additive: a dispersing agent, Anhydrous Aerosol OT-100 (100% solids), obtained from American Cyanamid, Inc. The glass transition temperatures (T_g) of the acrylate ($T_g \sim 3^\circ\text{C}$) and the polyurethane ($T_g \sim 31^\circ\text{C}$) were obtained using a Perkin Elmer differential scanning calorimeter (Series 7).

A series of 0–3 composites were prepared using PZT or coprecipitated PbTiO_3 powder as the electroceramic filler. The PbTiO_3 powder was prepared by a two step precipitation from aqueous solution.⁵ The final dry powder was ground, then calcined at 900°C for one hour to yield highly crystalline PbTiO_3 particles with a narrow particle size distribution. An additional calcination was carried out at 850°C for four hours to produce a powder with a particle size of 4–5 μ as measured by a Quantachrome Monosorb Surface Area Analyzer, Model MS-12. The 'original' PZT powder (501A-Ultrasonic Powders, Inc.) was also calcined at 850°C to yield a powder with an average particle size of 1–2 μ .

Films were prepared by combining the copolymer emulsion or the polyurethane with their respective surfactants and dispersing agents. For the acrylic copolymer case this was done in the proportions designated in Reference 6. The electroceramic filler was loaded into the polymer mixture and allowed to stir at room temperature for approximately two hours. A sufficient amount of defoamer was then added to eliminate the formation of bubbles while stirring. The polyurethane/electroceramic composites were prepared in a similar fashion. The polyurethane plus approximately 10% solvent (toluene) was combined with either 1.5% (for PbTiO_3) or 2.5% (for PZT) anhydrous aerosol OT-100 at room temperature. Defoamer was then added and the materials were mixed at room temperature.

The final films were prepared by casting the mixtures onto brass plates. The surface of the brass was made rough to ensure good adhesion between the composites and the metal. The films were initially dried in air at room temperature for 24 hours then placed in a vacuum oven at 110°C for an additional 24 hours to ensure removal of all residual water or solvent.

Air-dry silver paint was used to electrode the final, dry films on one side, while the brass plate acted as the second electrode. The resultant film thicknesses ranged from about 200–500 μ . The internal microstructure of each composite type was determined using an I.S.I. Super IIA Scanning Electron Microscope. The samples (minus the brass) were fractured in liquid nitrogen and the fracture surface of each composite examined.

B. Poling and dielectric and piezoelectric measurements

Poling of the composites was accomplished by both the conventional and the Corona discharge techniques. The conventional poling apparatus consisted of an oil bath and an external power supply. The temperature of the bath was maintained at 75°C for the acrylate-based composites and at 100°C for the polyurethane composites. The voltage was applied stepwise; the composite was allowed to remain at a particular voltage for ten minutes, then the electric field was increased. This process was repeated until the maximum field for a given composite was reached (100–150 kV/cm). This procedure minimized the possibility of electrical breakdown of the composites.

The Corona discharge method of poling involved the application of a large d.c. field to a set of needles, causing an ionization of surrounding gas molecules. The composite was electrodeed and placed on a grounded metal plate and a charge from the needles was sprayed onto the unelectroded surface. The temperatures used during Corona poling were the same as for the conventional method.

Initially, the breakdown strengths of the candidate polymer matrices were evaluated to assess their capability of withstanding electric fields of 100–150 kV/cm, i.e., those normally required to pole 0-3 composites. This was done by placing samples of the pure polymers into the conventional poling apparatus and increasing the applied field until breakdown occurred. The acrylic copolymer withstood an applied electric field of ~150 kV/cm whereas the dielectric strength of the polyurethane was found to be ~120 kV/cm. The breakdown strength of the polymer matrices plus their respective additives were also evaluated. The addition of the ionic surfactant to the acrylic copolymer greatly lowered the breakdown strength (to approximately 50 kV/cm) and, consequently, was removed from the composite formulation. The dielectric breakdown strength without the ionic surfactant was found to be ~130 kV/cm. The polyurethane with the added dispersing agent possessed a breakdown strength identical to that found for the pure polyurethane.

Dielectric constant and loss were measured using a Hewlett-Packard Model 4274A Multi-frequency LCR Meter. Measurements were taken at room temperature and 1 kHz for all the composites to obtain $\tan \delta$ and the dielectric constant.

Measurements of d_{33} were made using a Berlincourt Piezo d_{33} -meter at 100 Hz for each poled sample. The d_{33} values reported here are the average of 10 random point measurements (5 on each electrodeed surface). The hydrostatic strain coefficient (d_h) was evaluated using a static technique and from this, the hydrostatic voltage coefficient (g_h) was subsequently derived. The apparatus consists of an oil chamber within which a sample holder is immersed. The sample holder contains the test samples along with a standard (PZT). A hydraulic press to provide static pressure to the oil bath, an AC stress generator within the chamber, and a spectrum

analyzer (Hewlett-Packard 3585A) to monitor the voltage produced by the sample were also employed. All hydrostatic measurements were made approximately 2–3 days after polarization.

RESULTS AND DISCUSSION

The dispersion of both the PZT and PbTiO_3 in the acrylic copolymer was found to be excellent, indicating that the combination of surfactants and rheological agents utilized were appropriate for this type of composite. The dielectric constants for these composites (Table I) are comparable to those found in previous studies on piezoelectric 0–3 composites.^{7–9} The values reported in Table I represent an average of measurements taken on several random samples. The standard deviation for the dielectric constant and $\tan \delta$ were ± 5 and ± 0.01 respectively. As expected, the dielectric constant increased with increasing volume fraction of ceramic due to the large dielectric constants of PZT ($K \sim 1800$) and PbTiO_3 , ($K \sim 230$) compared to those of the polymer matrices. The dissipation factors of the composites at room temperature and 1 kHz are 0.04–0.06, similar to that of the pure polymer (0.05). The losses are relatively high because room temperature is within the temperature range encompassed by the α -relaxation at 1 kHz of this particular copolymer.

The d_{33} values for the PZT-filled composites were found to be 25–28 pC/N, while those for the coprecipitated PbTiO_3 /acrylic copolymer composites were 35–38 pC/N. Epoxy elastomer composites fabricated by Safari, *et al.*, loaded with 67% coprecipitated PbTiO_3 , were reported to exhibit a d_{33} of approximately 60 pC/N.⁵ This is substantially larger than the values for the PbTiO_3 /acrylic copolymer composites (as well as the PbTiO_3 /polyurethane composites) reported here. The reason for this discrepancy is unclear at this time. The difference in d_{33} between the PZT and PbTiO_3 -acrylic copolymer composites could stem from the lower dielectric constant of PbTiO_3 compared to PZT. From a consideration of the influence of the dielectric constant of the phases in an 0–3 composite on the electric field acting on an isolated spherical grain during poling, it becomes apparent that the electric field acting on the PZT particles should be about a factor of 10 less than for PbTiO_3 particles in a typical polymer matrix. Consequently, the overall polarization of the PZT should be less, giving rise to lower d_{33} . In addition, it is possible that the

TABLE I
Dielectric and Piezoelectric Response of Acrylic Copolymer Composites

	K_{33}	$\tan \delta$	d_{33} (10^{-12} C/N)	d_h (10^{-12} C/N)	g_h (10^{-3} V·m/N)	$d_h g_h$ (10^{-15} m 2 /N)
60 vol% PZT	29 ± 5	0.04	26 ± 6	18 ± 5	70 ± 10	1260 ± 390
70 vol% PZT	51 ± 5	0.05	28 ± 5	25 ± 6	55 ± 11	1380 ± 430
60 vol% PbTiO_3	48 ± 5	0.05	35 ± 5	29 ± 5	68 ± 10	1970 ± 450
70 vol% PbTiO_3	54 ± 5	0.06	38 ± 6	32 ± 5	67 ± 10	2140 ± 470
70 vol% PbTiO_3 (corona poled)	54	0.06	39	30	63	1890

difference in particle size of the PbTiO_3 and PZT also contributes to the differences in d_{33} .¹⁰

The d_h (and the hydrostatic voltage coefficient, g_h) values reported in Table I are an average of measurements on five samples. d_h for the PbTiO_3 /acrylic copolymer composites were found to be in the range of 29–32 pC/N, somewhat lower than those reported previously by Safari, *et al.* for a coprecipitated PbTiO_3 /flexible epoxy 0–3 composite (43 pC/N).⁵ d_h and g_h for the PZT-filled composites are substantially larger than values reported previously for unmodified 0–3 PZT composites and comparable to 0–0–3 PZT composites where a second conductive filler was added to aid in poling.⁹ The hydrostatic figure of merit ($d_h g_h$) ranged from $1260\text{--}1380 \times 10^{-15} \text{ m}^2/\text{N}$ for the PZT-filled and from $1970\text{--}2140 \times 10^{-15} \text{ m}^2/\text{N}$ for the PbTiO_3 -filled composites.

Conventional oil bath poling is not necessarily the most ideal way of pole a polymer-based composite. The polymer portion may be susceptible to dissolution or swelling in the oil, which will undoubtedly interfere with the poling. In a preliminary experiment, the Corona discharge method was utilized to pole a 70 volume percent PbTiO_3 /acrylic copolymer composite. As shown in Table I, d_{33} was found to be 39 pC/N, the same within experimental error as the conventionally poled samples. The corresponding d_h , g_h and figure of merit were also similar to the composites poled by the conventional method. Although immersion in oil does not appear to be of concern for this particular polymer matrix, one must be aware of the possible difficulties that oil immersion may cause.

Microscopic analysis indicates that both PZT and the coprecipitated PbTiO_3 are well dispersed in the polyurethane matrix. Compared to the acrylic composites, the dissipation factors are somewhat lower for the polyurethane compositions, reflecting the lower loss at room temperature of the polyurethane ($\tan \delta \sim 0.01$) compared to the acrylic copolymer matrix. Dielectric constants and the piezoelectric coefficients are the same within experimental error for all composites of a given volume fraction. While the hydrostatic piezoelectric properties of the 70 volume percent polyurethane composites are comparable to the acrylic copolymer-based materials, those with 60 volume percent ceramic (especially PbTiO_3) are significantly less. For 60 volume percent PZT, this is a result of the higher dielectric constant for the polyurethane composite. In addition, d_{33} for the PbTiO_3 -polyurethane composites are significantly less than the corresponding PbTiO_3 -acrylic composites. The reason for this is unknown at present. Both types of composites were poled at a similar T-Tg and there is no difference in the x-ray diffraction patterns of composites poled in the presence of either polymer (i.e., the degree of poling is similar).

TABLE II
Dielectric and Piezoelectric Response of Polyurethane Composites

	K_{33}	Tan δ	(10^{-12} C/N)	d_h (10^{-12} C/N)	$(10^{-3} \text{ V}\cdot\text{m}/\text{N})$	$d_h g_h$ $(10^{-15} \text{ m}^2/\text{N})$
60 vol% PZT	51 ± 5	0.02	25 ± 5	18 ± 5	40 ± 10	720 ± 270
70 vol% PZT	45 ± 5	0.04	28 ± 5	26 ± 6	65 ± 11	1690 ± 480
60 vol% PbTiO_3	42 ± 5	0.03	25 ± 5	17 ± 5	47 ± 10	800 ± 290
70 vol% PbTiO_3	44 ± 5	0.03	27 ± 6	25 ± 5	67 ± 10	1680 ± 420

ACKNOWLEDGEMENTS

The authors would like to express their appreciation to the Office of Naval Research for their support of this work through contract N00014-82-K-0039 and to Dr. Steven Pilgrim for many helpful discussions.

REFERENCES

1. R. E. Newnham, D. P. Skinner and L. E. Cross, *Mater. Res. Bull.*, **13**, 525 (1978).
2. R. E. Newnham, A. Safari, J. Giniewicz and B. H. Fox, *Ferroelectrics*, **60**, 15 (1984).
3. H. Banno and S. Saito, *Jpn. J. Appl. Phys.*, **22** (Supp 22-2), 67 (1983).
4. T. C. Patton, *Paint Flow and Pigment Dispersion*, New York, John Wiley and Sons (1979).
5. A. Safari, Y. H. Lee, A. Halliyal and R. E. Newnham, *Am. Ceram. Soc. Bull.*, **66**, 668 (1987).
6. C. Bondy and M. M. Coleman, *J. Col. Chem. Assoc.*, **53**, 555 (1970).
7. W. B. Harrison, "Flexible Piezoelectric Organic Composites," Proceedings of the Workshop on Sonar Transducer Materials, Naval Research Laboratories (Feb. 1976).
8. L. A. Pauer, "Flexible Piezoelectric Material," IEEE Conf. Res., **1** (1973).
9. G. Sa-Gong, A. Safari, S. J. Jang and R. E. Newnham, *Ferroelectrics Letters*, **5**, 131 (1986).
10. M. H. Lee, A. Halliyal and R. E. Newnham, *Proc. Amer. Cer. Soc. Mtg.*, **121** (1987).

APPENDIX 11

Fabrication of 0-3 Piezoelectric-Glass Composites

Gye Song Lee, Sunuk Kim* and Thomas R. Shrout

Materials Research Laboratory, The Pennsylvania State University
University Park, PA 16802, U.S.A

(Received October 9, 1989; accepted December 22, 1989)

Key words: piezoelectrics, 0-3 composites, glass, PbTiO₃, sintering

Piezoelectric 0-3 glass composites for high temperature and wide area applications were developed by firing a mixture of modified PbTiO₃ and lead-based glass powder. Sintering of the 0-3 piezoelectric composites was dependent upon the firing temperature and the amount of glass phase. Piezoelectric 0-3 composites with 41-72 vol% ceramic, fired at 450°C, showed dielectric constants, K , ~45-100, piezoelectric g_{33} coefficients $\sim 13-20 \times 10^{-3}$ Vm/N and piezoelectric d_{33} coefficients $\sim 5-15 \times 10^{-12}$ C/N which were found to be comparable to those of polar glass-ceramics.

1. Introduction

Electroceramic composites are frequently designed to provide the desired electromechanical properties through the combination and connectivity of different phases.⁽¹⁻⁹⁾ Design concepts of numerous electroceramic composites have been well documented.⁽²⁾ Fabrication and characterization of piezoelectric composites, which are based on polymer and piezoelectrically active ceramic particles such as pure or modified PbTiO₃ and PZT, have been reported.⁽⁴⁻⁷⁾ Such composites which possess the 0-3 connectivity, i.e., piezoelectrically active ceramic particles are dispersed in the 3-dimensionally interconnected polymer phase, offer many advantages such as easy processing of various shapes, i.e., sheets and fibers, flexibility and high hydrostatic piezoelectric coefficients. Effects of piezoelectric ceramic content, particle sizes of the piezoelectric ceramic and poling conditions on the 0-3 composite properties have been investigated.^(6,7) However, the application of these polymer

*Visiting Scientist from RIST, Pohang, Korea.

matrix composites is limited to relatively low temperatures due to low processing temperatures characteristic of the polymers used.

Novel grain-oriented glass-ceramics based on fresnoite ($\text{Ba}_2\text{TiSi}_2\text{O}_8$) and related polar crystals for pyroelectric and piezoelectric applications were developed by temperature gradient crystallization.⁽⁸⁾ Advantages of such polar-glass composite structures include no need for poling, low aging because of their nonferroelectric nature, and the possibility of high-temperature usage. The intrinsic nature of grain-oriented glass-ceramic composites and their associated poor mechanical integrity, however, may limit their practical implementation.

To overcome the inconvenience in polar glass-ceramics processing, conventional glass-ceramic processing was adopted to fabricate piezoelectric/pyroelectric glass-ceramics based on PbTiO_3 .⁽⁹⁾ The ease of processing together with the notable piezoelectric/pyroelectric properties of poled glass-ceramics indicates a useful method for large-area piezoelectric/pyroelectric applications. It also seems to be possible to produce piezoelectric glass-ceramics for high-temperature applications by modifying the glass composition.

The purpose of this work was to develop 0-3 piezoelectric composites through conventional firing of a mixture of modified PbTiO_3 and lead-based glass powders. Some of the advantages of the 0-3 piezoelectric-glass composites are as follows: (1) a wide variety of shapes and geometries can be fabricated by using both powder and conventional glass-forming technologies including screen printing and glazing/frits, (2) the glass composites will be relatively mechanically robust and capable of operating at moderately high use temperatures and (3) low cost and ease of fabrication. In this paper, the initial results of processing and property characterization of 0-3 piezoelectric-glass composites will be described.

2. Experimental Procedure

2.1 Materials

The modified PbTiO_3 , $[(\text{Pb}_{0.85}\text{Sm}_{0.10})(\text{Ti}_{0.98}\text{Mn}_{0.02})\text{O}_3]$ composition, whose reported dielectric and piezoelectric properties are shown in Table 1, was selected for the piezoelectric ceramic. As discussed earlier, this material was chosen for many previously reported composites due to its relatively low dielectric constant and high piezoelectric g_{33} coefficient.⁽¹⁰⁾ In the selection of glass composition, the following characteristics were felt to be necessary: chemical compatibility with the ceramic particle, good wettability for good densification, relatively low softening point for low-temperature processing, and electrical insulation such as to allow ease of poling. In addition, a low dielectric constant is favorable to obtain the high piezoelectric g_{33} coefficient but inhibits poling. Based on these requirements, a high lead-based glass composition, which was developed for solder glass and whose reported properties are shown in Table 1, was selected. As shown in the table, the low softening point (i.e., 440°C) and the low resistivity of the glass should allow low-temperature processing and poling, respectively.

Table I
Properties of the glass and the piezoelectric components.

Material	Composition (wt%)	Density (g/cm ³)	T_c^1 or T_s^2 (°C)	$\log \rho$ (Ω·cm, RT)	K (RT, 1 kHz)	D (%)	d_{33} ($\times 10^{-12}$ C/N)	g_{33} ($\times 10^{-3}$ Vm/N)
Corning glass #7570	PbO B ₂ O ₃ (11) Al ₂ O ₃ SiO ₂	74.0 12.0 11.0 3.0	5.4 440°C	>17	14	0.1		
Modified PbTiO ₃	PbO Sm ₂ O ₃ (10) TiO ₂ MnO ₂	66.7 6.0 26.7 0.6	7.7 320°C	>12	200	2.5	-60	-33

¹Curie temperature.

²Softening point.

2.2 Processing

The high purity oxides[†] were weighed according to the above chemical formula, and about 3 wt% of excess PbO was added to compensate for the loss during calcination and sintering.⁽¹⁰⁾ The oxides were ball milled in ethyl alcohol for 24 hours using zirconia as the milling medium. The dried powder was calcined at 900°C for 4 hours in an alumina crucible. The loosely packed calcined powder was further heat-treated at 1200°C for 24 hours to increase the grain size for better polishing. The powder slug, whose primary particle size was determined to be 3–5 μm, was crushed and sieved through 325 mesh. This powder was used in the preparation of the composites.

The commercially available high-lead glass frit^{††} was milled in a vibratory mill for 48 hours to increase the sinterability of the glass powder. To determine the compatibility, the glass and 41 vol% piezoelectric ceramic powders were wet-mixed in an agate mortar. Pellets were fabricated at 88 MPa using 4 wt% of binder^{†††} solution. The binder was burnt out by heating at 2°C/minute to 400°C (<softening temperature) and holding for 30 minutes. The pressed samples were fired for 60 minutes in the range of 430–490°C. The compatibility of the glass with the piezoelectric ceramic was confirmed by XRD of the fired composites.

As for all 0-3 composites, the properties were found to depend on the amount of the functional components.⁽¹⁶⁾ Piezoelectric-glass composites with a ceramic content in the range of 41–72 vol% were prepared. The composites were fired for 60

[†]PbO: Hammond Lead Products, Inc., MnO₂, Sm₂O₃, and TiO₂: Alfa Products.

^{††}Corning #7570, Corning Glass Works.

^{†††}Dupont Binder 5200.

minutes at 450°C, this having previously been found to be the optimum sintering condition. Characterization of the fired samples included the geometric density and microstructural analysis of fracture surfaces using scanning electron microscopy (SEM).[†] Fired samples were polished and electrode by gold sputtering and further coated by an air-dry silver paste[‡] to insure electrical contact. The dielectric constant and loss were determined as a function of temperature (RT-400°C) and frequency (100, 200, 1000, 10000 and 100000 Hz) using a LCR meter.[§] Samples were poled at 10-30 KV/cm during cooling in air from 335 to 150°C in a box furnace.^{||} The effectiveness of the poling was determined by measuring the piezoelectric d_{33} coefficient using a Berlincourt Piezo d_{33} Meter.^{||||}

3. Results and Discussion

3.1 Firing

To investigate the densification behavior of the 0-3 piezoelectric-glass composites, samples of 41 vol% ceramic were fired for 60 minutes at 430, 450, 470 and 490°C, respectively. Figure 1 presents the percent theoretical density of the fired composites at various temperatures. As shown, the density exhibited a peak value

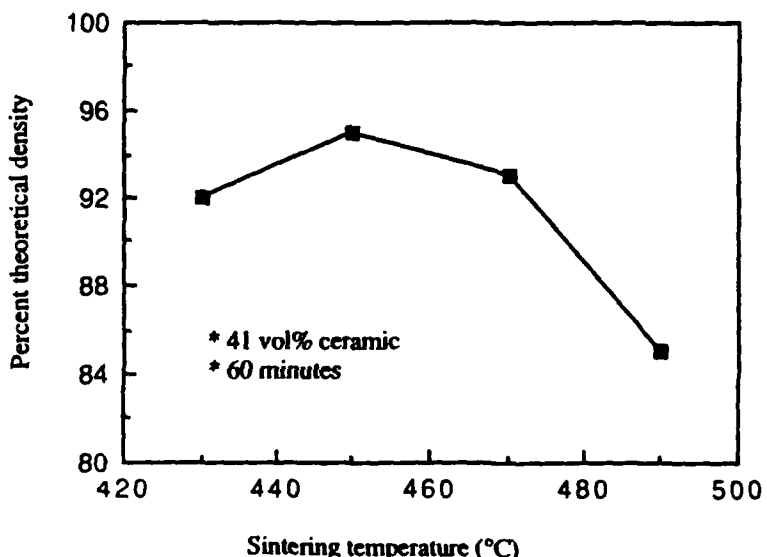


Fig. 1. Fired density (percent theoretical) of the 0-3 piezoelectric-glass composites of 41 vol% ceramic as a function of firing temperature.

[†]Super-IIIA, ISI.

[‡]Materials for Electronics, Inc.

[§]HP 4274A, Multi-frequency LCR Meter.

^{||}Delta Design.

^{||||}Channel Products, Inc.

of ~95% theoretical at 450°C, decreasing as the temperature increased. To understand the decrease in fired density above 450°C, microstructures were examined. Fig. 2A and 2B show SEM micrographs of fracture surfaces of samples fired at 450 and 490°C, respectively. Figure 2A indicates good wettability of the glass and a dense microstructure with a few spherical pores ranging from 0.5 to 10 µm. In contrast, the microstructure observed from the sample fired at 490°C (Fig. 2B) possesses large spherical pores which are uniformly distributed throughout the body.

The reason for the spherical pores present in the fired composites was not clear

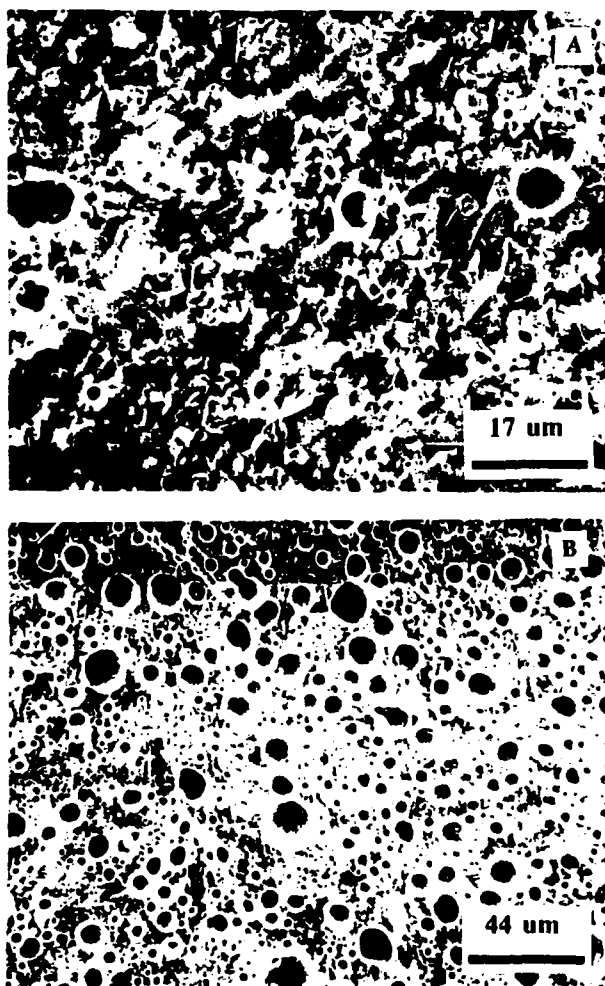


Fig. 2. Fracture surfaces of 0-3 piezoelectric-glass composites of 41 vol% ceramic fired for 60 minutes A at 450°C and B at 480°C.

but may be attributed to the rapid entrapment of air bubbles inside the body due to rapid flow at the sample surface preventing the escape of the air in pores. At 490°C, expansion of the air bubbles in the samples was made easier due to the low viscosity of the glass, resulting in larger pores ($\sim 30 \mu\text{m}$). From this firing study, it is suggested that the firing temperature should be limited to a narrow range around the softening point of the glass, i.e., 440°C in this work.

The effect of the amount of the piezoelectric ceramic on firing at 450°C of the 0-3 piezoelectric-glass composites is presented in Fig. 3. As the piezoelectric ceramic content increased, the fired density decreased. The observed strong dependence of densification upon the glass content in the piezoelectric-glass composites was in good agreement with the aluinina-glass composites (II). Relatively dense (> 93% theoretical) composites with up to ~ 50 vol% ceramic could be obtained. However, this level of ceramic loading in the piezoelectric-glass 0-3 composites is relatively low compared to the ~ 70 vol% achievable in 0-3 polymer composites.^(5,7)

3.2 Dielectric/piezoelectric properties

The dielectric constant K (unpoled) of 0-3 composites of 41 vol% ceramic was determined to be ~ 48 , which is close to the calculated value (~ 42) based on the logarithmic mixing rule⁽¹²⁾ from known values of 14 and 200 for the glass and the ceramic, respectively. As a function of temperature, both dielectric constant and loss exhibited maxima near the Curie temperature of the modified PbTiO₃ (i.e., 320°C). The transition could only be observed at high frequencies due to conduction.

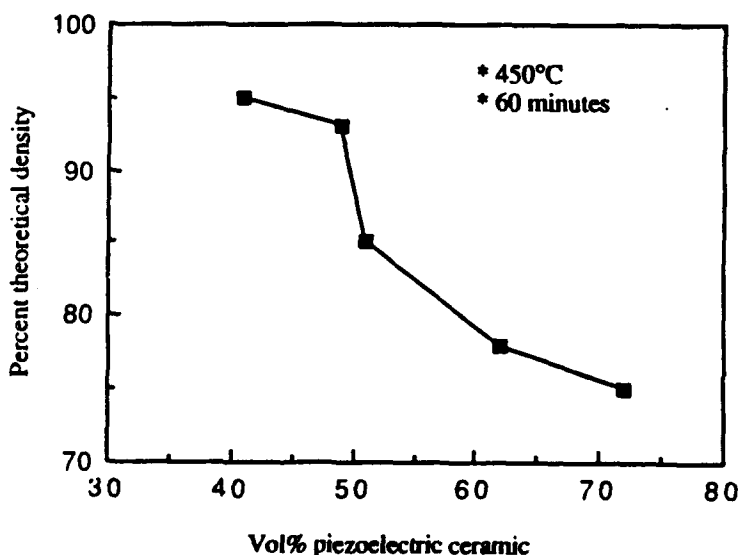


Fig. 3. Fired density (percent theoretical) of the 0-3 piezoelectric-glass composites as a function of the amount of piezoelectric ceramic, fired for 60 minutes at 450°C.

tion mechanism contributing to loss. Along with XRD data, the same Curie temperature as that of the starting piezoelectric ceramic indicated little chemical interaction between the ceramic and the glass during firing. The dielectric constant at the Curie temperature was found to be only 90 (at 1 KHz), which is very low compared to ~ 7000 of the piezoelectric bulk ceramic.⁽¹⁰⁾ The sharp increase in dielectric constant of the composite above Curie temperature of the piezoelectric ceramic is attributed to the high conductivity of the glass as indicated by the large dielectric loss above Curie temperature. Figure 4 presents the dielectric constant and loss curves drawn up to 250°C to show the dielectric losses clearly. As shown, the dielectric losses of 0-3 piezoelectric-glass composites were much lower than that of the piezoelectric bulk ceramic over a very wide temperature range (see Table 1), i.e., 0.05 vs 0.2 at 250°C (at 1 KHz), respectively.

The poling temperature was found to be limited to below 300°C due to conductivity. Figure 5 shows the measured piezoelectric d_{33} values as a function of the amount of piezoelectric ceramic. Piezoelectric d_{33} values of the composites increased almost linearly from 5 to 15×10^{-12} C/N with increasing amount of piezoelectric ceramic. The piezoelectric g_{33} coefficients were calculated to be in the range of $13-20 \times 10^{-3}$ Vm/N. The dielectric and piezoelectric properties of the 0-3 piezoelectric-glass composites are presented in Table 2, together with those of other related composites, i.e., grain-oriented polar glass ceramics and PbTiO_3 -polymer 0-3 composites, for comparison. The measured d_{33} values of the piezoelectric-glass composites were relatively low compared with those of polymer composites but comparable to those of polar-glass ceramics.⁽⁶⁾ The low d_{33} values of the piezoelectric-glass composites were believed to be attributable to the limited poling efficiency

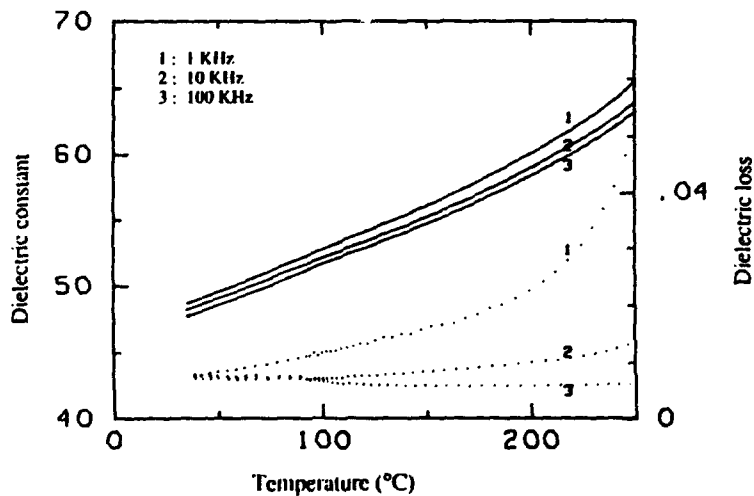


Fig. 4. Dielectric constants and losses of the 0-3 piezoelectric-glass composite of 41 vol% ceramic, fired for 60 minutes at 450°C, as a function of temperature and frequency.

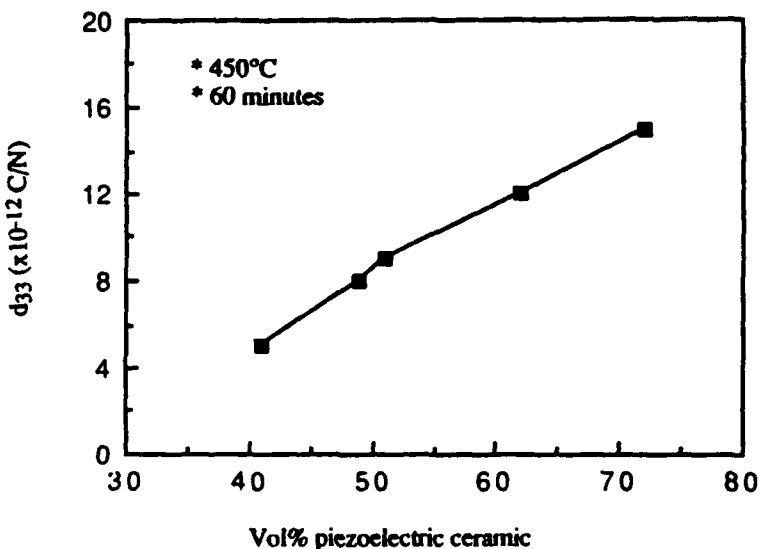


Fig. 5. Piezoelectric d_{33} coefficients of the 0-3 piezoelectric-glass composites fired for 60 minutes at 450°C, as a function of piezoelectric ceramic content.

Table 2
Dielectric and piezoelectric properties of various piezoelectric composites.

Material		K (RT, 1 kHz)	D (%)	$d_{33} (\times 10^{-12} \text{ C/N})$	$g_{33} (\times 10^{-3} \text{ Vm/N})$
Piezo/glass 0-3 composites					
41 vol%	poled	45	1.0	-5	~13
	unpoled	48	1.0		
49 vol%	poled	52	1.1	-8	~17
	unpoled	55	1.2		
Polar-glass ceramics⁽⁸⁾					
		-10	<0.1	-8-10	~100
PbTiO₃/polymer 0-3 composites⁽⁹⁾					
~70 vol%		-60	>5	~30	~20

due to the low DC resistivity at those temperature ranges where poling was carried out, i.e., $\rho_{225}=10^{12.5}$ and $\rho_{200}=10^9 \text{ ohm}\cdot\text{cm}$.⁽¹³⁾ In addition, some kind of clamping of the piezoelectric particles by the stiff glass matrix may limit the poling of the piezoelectric-glass composites.

4. Summary and Future Work

1. It was demonstrated that a new type of 0-3 piezoelectric-glass composite could be obtained by firing of a mixture of piezoelectric ceramic and glass powders.
2. The firing temperatures of the 0-3 piezoelectric-glass composites were found to be limited around the softening point of the glass (i.e., 440°C) due to the increased porosity at higher temperatures.
3. Firing of 0-3 piezoelectric-glass composites was also found to depend on the amount of glass content, i.e., >51 vol% glass in this composition for dense composites (i.e., >93% theoretical density).
4. Poled dense piezoelectric composites (i.e., 49 vol% ceramic) showed g_{33} coefficients of $\sim 17 \times 10^{-3}$ Vm/N, and d_{33} values ($\sim 8 \times 10^{-12}$ C/N) which were relatively low compared to those of polymer composites but comparable to those of polar-glass ceramics.
5. Further optimization of the composite properties may be achieved through particle size variation of the piezoelectric ceramic powder and its effect on firing, selection of glass compositions to allow ease of poling (i.e., higher resistivity near the Curie point of the piezoelectric ceramic) and densification, and methods to incorporate more piezoelectric ceramic content. Also, high-temperature piezoelectric property measurements are required to characterize these materials to determine their use temperature range.

Acknowledgements

This study was supported by RIST, Pohang, Korea.

References

- 1 W. B. Harrison: Proc. Workshop on Sonar Transducer Materials. Naval Research Laboratory (1976).
- 2 R. E. Newnham, D. P. Skinner and L. E. Cross: Mat. Res. Bull. 13 (1978) 525.
- 3 K. A. Klicker, J. V. Biggers and R. E. Newnham: J. Am. Ceram. Soc. 64 (1981) 5.
- 4 H. Banno: Ferroelectrics 5 (1983) 3.
- 5 R. E. Newnham, A. Safari, J. Giniewicz and B. H. Fox: Ferroelectrics 60 (1984) 15.
- 6 J. Mendiola, C. Alemany, B. Jimenez and E. Maurer: J. Mat. Sci. Lett. 4 (1986) 1383.
- 7 M. H. Lee, A. Halliyal and R. E. Newnham: Ferroelectrics 87 (1988) 71.
- 8 A. Halliyal, A. Safari, A. S. Bhalla and R. E. Newnham: Ferroelectrics 50 (1983) 45.
- 9 W. Mianxue and Z. Peinan: J. Non-Cryst. Solids 84 (1986) 344.
- 10 D. M. Damjanovic, Ph. D: Thesis, The Pennsylvania State University (1987).
- 11 K. Kawakami, M. Takabatake, T. Minowa, J. Chiba and M. Sasaki: A Low-Temperature Cofired Multilayer Ceramic Substrate, eds. J. B. Blum and R. Cannon, Advances in Ceramics vol. 19 (The American Ceramic Society, 1986) 95.
- 12 W. D. Kingery, H. K. Bowen and D. R. Uhlmann: Introduction to Ceramics (2nd ed. A Wiley-Interscience Publication, 1976) Chap. 18.
- 13 J. S. Nordyke: Lead in the World of Ceramics (The American Ceramic Society, 1984) 35.

APPENDIX 12

Acoustic Properties of Particle/Polymer Composites for Ultrasonic Transducer Backing Applications

MARTHA G. GREWE, T. R. GURURAJA, THOMAS R. SHROUT, AND ROBERT E. NEWNHAM

Abstract—The acoustic impedance and attenuation in composites made of particle fillers loaded in polymer matrices for transducer backing applications is explored. The acoustic impedance of tungsten/vinyl composites was modeled and an experimental matrix identifying variables that contribute to composite attenuation was established. The variables included the particle type, the particle size and volume fraction of a filler, the physical characteristics of the polymer matrix, and the processing route that determined the composite connectivity. Experimental results showed that with an increase in filler particle size or a decrease in volume fraction of filler, there is an increase in composite attenuation. Overall, the various types of filler, the polymer matrix, and the interface between the two contribute to attenuation in the composite as confirmed by the acoustic properties and the microstructural analysis.

I. INTRODUCTION

THE ACTIVE PART of an ultrasonic transducer typically has a low ultrasonic absorption that causes it to ring when the transducer is excited. While the transducer is ringing, the long pulse durations degrade the axial resolution or the ability to distinguish between different structures along the axis of the transducer. The waveform can be damped by attaching an acoustically absorbing material on the back of the transducer that couples the ultrasonic energy out of the active element. Ideally, this backing material should provide high attenuation and it should match the acoustic impedance of the transducer for efficient coupling [1], [2]. If the acoustic impedance of the backing is close to that of the transducer, most of the ultrasonic energy will be coupled into the backing. As a result, the transducer will have a shorter pulse duration with decreased sensitivity. By using a backing with a lower acoustic impedance, greater sensitivity is achieved because less energy is absorbed into the backing [3]. Unfortunately, the transmitted and received pulses are longer due to increased ringing in the transducer. A compromise must be made in choosing the acoustic impedance of the backing [2].

The two most important materials parameters of ultrasonic transducer backings are the acoustic impedance and the attenuation. The acoustic impedance of the backing

for piezoelectric ceramic transducer materials generally range from a high value of approximately 30 MRayl to a low value of 2 to 4 MRayl, depending on the transducer design [4]. Attenuation is the loss of acoustical energy and is mainly due to two mechanisms: 1) scattering of acoustic energy (Rayleigh, diffusion, and stochastic) and 2) absorption losses from thermoelastic effects, inelastic hysteresis, relaxation, and dislocation damping [5]–[7].

In the past, backings have been composed of a filler in a polymer matrix [2], [8], [9]. The backings have impedances that are matched to the PZT type piezoelectric material (about 30 MRayl) and are typically made of composites of tungsten and an epoxy resin or rubber [9]. These backings typically have high specific densities and thus have been named accordingly, “heavy backings.” In order to match the impedance of PZT, about 60 volume percent loading of tungsten is required [1], [10]. Light backings that possess relatively low acoustic impedance have been fabricated from epoxy or rubber.

An important aspect to explore in composite attenuation is the role of the polymer matrix and filler phases, especially those properties that contribute to acoustic loss in the composites [10]. For example, the acoustics loss in polymers is dependent on the degree of crystallinity; with an increase in crystallinity, there is typically a decrease in attenuation. Similarly, acoustical loss decreases with increasing cross-linkage [7], [11].

In the case of solid specimens of metals or ceramics, an inhomogeneity in the material will cause scattering of ultrasonic waves determined by the difference in density and elastic modulus from the surrounding media [12], [13]. In a similar way, fillers in a polymer matrix contribute to the attenuation depending on the particle size, shape, and the acoustic impedance relative to the polymer matrix.

Another important contributor to attenuation in composites is the interaction between the polymer and filler. One study cited poor adhesion between the filler and matrix as causing loss mechanisms that included scattering, antiphase vibrations, and interfacial friction [14].

The main purpose of this study has been to develop an understanding of these various contributions to composite attenuation to aid in optimization of the material compositions for ultrasonic transducer backings. The study explores modeling methods and experimental verification of the acoustic impedance. Experimental results demon-

Manuscript received December 28, 1989; revised April 23, 1990; accepted May 10, 1990.

M. G. Grewe and T. R. Gururaja are with the Imaging Systems Division, Hewlett-Packard, Andover, MA 01810.

T. R. Shroud and R. E. Newnham are with the Materials Research Laboratory, Pennsylvania State University, University Park, PA 16802.

IEEE Log Number 9038495.

ng the importance of polymer phase, filler type, particle size, volume fractions of each phase, and fabrication routes are reported. In the end, various trends are identified and a better understanding of composite attenuation is developed.

II. MODELING OF COMPOSITE ACOUSTIC IMPEDANCE

When exploring modeling of composites, it is important to understand how the various phases are interconnected and their effects. Each phase in a composite is connected in either one, two, or three dimensions, or not connected at all, which can be described by the term connectivity and its nomenclature developed by Newnham [15]. Composites containing a small amount of filler in a polymer matrix, as in this study, have a 0-3 connectivity pattern in which the "0" phase is the filler material which is not self connected in any dimension and the "3" phase is the polymer matrix that is interconnected in all three dimensions [15].

The velocity of a longitudinal sound wave, c_L , is related to the mechanical properties of the medium through the expression

$$c_L = \left(\frac{K}{\rho} \right)^{0.5} \quad (1)$$

where K is the elastic bulk modulus, ρ is the density [4], and the acoustic impedance Z is related to the elastic properties by

$$Z = (K\rho)^{0.5}. \quad (2)$$

The density of a two phase system increases steadily with the increase in volume percent of filler and can be calculated as

$$\rho_{\text{composite}} = \rho_{\text{particle}} V_{\text{particle}} + \rho_{\text{polymer}} V_{\text{polymer}} \quad (3)$$

where ρ is the density and V is the volume fraction of each phase.

When describing the elastic properties of two phase composites, three different models are most commonly examined: the Reuss, Voigt, and logarithmic models [16]. The two extremes are the lower bound Reuss Model which assumes constant stress throughout the solid and the upper bound Voigt Model, which assumes constant strain in the solid. The lower bound corresponds to a parallel connection and is defined as

$$K_{\text{composite(Reuss)}} = \left(\frac{K_1 K_2}{V_1 K_2 + V_2 K_1} \right) \quad (4)$$

where K_1 and K_2 are the elastic bulk modulus of each phase and V_1 and V_2 are the volume fractions of each phase. The upper bound corresponds to a series of connection as shown here:

$$K_{\text{composite(Voigt)}} = V_1 K_1 + V_2 K_2. \quad (5)$$

The logarithmic model is an empirical model that falls between the two extremes and is defined as

$$\ln(K_{\text{composite}}) = V_1 \ln(K_1) + V_2 \ln(K_2). \quad (6)$$

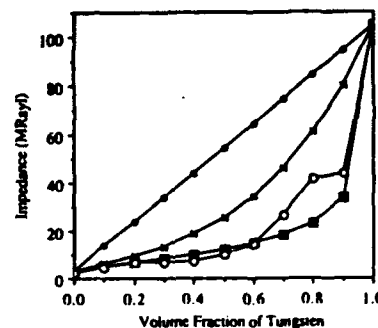


Fig. 1. Acoustic impedance models. $Z = \sqrt{\rho K} \wedge 0.5$. —●— shows Voigt K . —○— shows Logarithmic K . —■— shows Reuss K . —□— shows actual Z data. $\log = *$.

For this study, the bulk modulus at a particular volume fraction was estimated using all three models and then multiplied by the composite density to calculate the impedance at that volume fraction. The composites which were modeled were composed of tungsten particles in vinyl matrices. The models were compared to results from Lees *et al.* and are shown in Fig. 1 [17]. The values for the material properties are as follows: $Z_{\text{tungsten}} = 103 \times 10^6$ Rayl, $Z_{\text{vinyl}} = 2.3 \times 10^6$ Rayl, $c_{\text{tungsten}} = 5400$ m/s, $c_{\text{vinyl}} = 2000$ m/s, $K_{\text{tungsten}} = 5.65 \times 10^{11}$ N/m², $K_{\text{vinyl}} = 5.0 \times 10^9$ N/m². Similar results have been calculated for tungsten/araldite composites [1], [2], [18].

The most accurate fit or closest approximation was found to be the impedance calculated with the Reuss Bulk Modulus ((4)) and the composite density ((3)). Thus, from this point on, the acoustic impedance will always be estimated using this model calculated using (2).

III. EXPERIMENTAL DESIGN

The experimental part of this study was divided into four groups of samples: 1) pure polymer samples, 2) composites made of the same filler, but various polymer phases, 3) composites composed of different fillers, yet the same polymer phase, 4) composites fabricated by dissimilar processing routes to create microstructures with different connectivity patterns. Each group of samples were fabricated and their acoustic properties and microstructures were observed.

A. Fabrication of Samples

Typical thermoplastic and thermoset polymers used in engineering applications were processed into samples using the most appropriate route for each polymer. Table I lists these polymers. The thermoplastics were warm pressed into two inch disks. The solution thermosets and rubbers were poured into 40-mm-diameter sample holders and cured according to the manufacturer's recommended directions.

The composites with the same filler (5-μm tungsten powder),¹ but various polymers were fabricated using dif-

¹Teledyne Wah Chang, Huntsville, AL.

TABLE I
LISTING OF POLYMERS MEASURED IN THE ATTENUATION STUDY

Polymer	Classification of the Polymer	Company
High density Polyethylene	Purely aliphatic, nonpolar crystalline thermoplastic	Philips Chemical
Poly(methyl methacrylate)	Amorphous thermoplastic	Rohm and Haas
Polypropylene	Purely aliphatic, nonpolar semicrystalline thermoplastic	Hercules, Inc.
Poly(butylene terephthalate)	Semicrystalline thermoplastic	Shell Chemical
Polycarbonate	Engineering thermoplastic	Dow Chemical
Polyurethane CA 118	Linear, hydroxyl terminated polyester urethane thermoplastic	Morton Chemical
CA 128	Linear, hydroxyl terminated urethane thermoplastic	Morton Chemical
Estane Polyester	Ester urethane thermoplastic	B.F. Goodrich
Epoxy		
Spurr epoxy	Organic glass—thermoset	Polysciences, Inc.
Eccogel 1365-80	Organic glass—thermoset	Emerson and Cumming
Silicone rubber Dispersion 236	Rubber	Dow Corning
RTV-141	Rubber	Rhone-Poulenc, Inc.

ferent processing routes depending on the polymer type. The thermoplastic composites were fabricated by homogeneously mixing the tungsten powder in a Brabender high temperature shear mixer (Model #SP-TP25).² The mixtures were next warm pressed into 25-mm-diameter slugs at temperatures governed by the polymer. The solution thermosets were hand mixed with the tungsten powder in a 40-mm-diameter sample holder and then cured. All of the composites were hand polished using various grit polishing paper to form flat surfaces.

Composites with the same polymer phase (Spurr epoxy),³ but different fillers were also fabricated. Spurr epoxy was chosen for its low viscosity and low attenuation. The multiple composites had varying volume fractions between 5 and 40 volume percent of filler and particle sizes ranging from 0.3 μm to 50 μm of various fillers: tungsten,¹ lead zirconate titanate (PZT),⁴ and alumina (Al_2O_3).⁵ First, the desired amount of powder was hand mixed with low viscosity Spurr epoxy in a 40-mm-diameter sample holder and then cured. The samples were next removed from the sample dish and polished to an even thickness.

Two additional processing routes were used to fabricate composites with microstructures with different connectivities. In one process, tungsten powder with an average particle size of 5 μm was hot uniaxially pressed (HUP) in a nitrogen atmosphere. The pellets were partially sintered so that the porosity remained interconnected. The final sintered pellets were then vacuum impregnated with Spurr epoxy and polished to even thicknesses.

In the second process, the filler powder and poly(methyl methacrylate) (PMMA) microspheres³ were mixed with a polyvinyl alcohol (PVA) binder for adhesion and then cold pressed into pellets. The samples were then placed in a furnace to remove the PVA and PMMA microspheres during a burn-out cycle at 500°C for one hour and then the temperature was raised to 1100°C for one hour to start the sintering process. A porous network with 3-3 connectivity would be developed. The process is referred to as burnable polymeric spheres (BURPS). The final pellets were then vacuum impregnated with Spurr epoxy and polished. Ideally, a uniform two phase composite microstructure made of the filler and Spurr epoxy would be created.

B. Experimental Testing

The density of each composite was calculated by measuring the volume and weight. The actual volume fraction of filler was then calculated with the assumption that no voids were present. Next, the velocity through each composite was calculated by measuring the time of flight of a sound wave through each sample by sandwiching the sample with ultrasonic coupling gel between the transmitter and receiver transducers. The velocities were measured at 1, 3, and 5 MHz. The experimental values of the acoustic impedance were obtained by multiplying the densities with the velocities.

Attenuation was measured by the insertion loss technique that compares the transmission through the sample to the transmission without a sample present. Two focused 5-MHz transducers, a transmitter and receiver, were used for the measurement as shown in the experimental arrangement in Fig. 2 [10]. With this method, the amplitude of the pulse received with and without the sample present are measured. The amplitude of the pulse with the

¹C. W. Brabender, NJ.

²Polysciences, Inc., Warrington, PA.

³Ultrasonics, Inc., South Plainfield, NJ.

⁴Buehler, LTD, Evanston, IL.

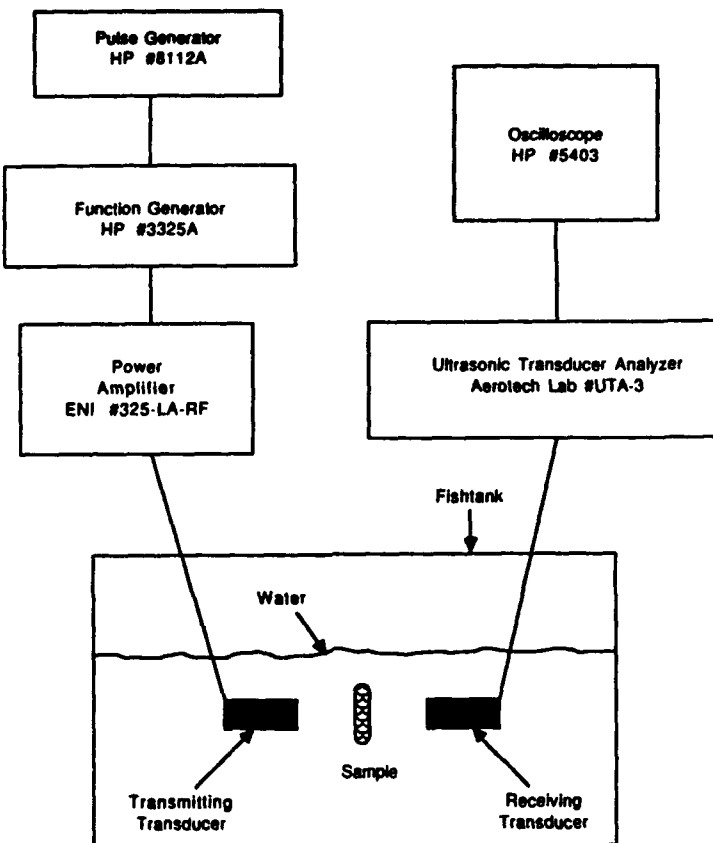


Fig. 2. Attenuation measurement scheme.

TABLE II
AVERAGE ACOUSTIC PROPERTIES OF THE TUNGSTEN ($<3 \mu\text{m}$) FILLED POLYMER COMPOSITES AT 5 MHz

Polymer	Pure Polymer		Composites		
	Impedance Z (MRayl)	Attenuation (dB/cm)	Volume % Tungsten	Impedance Z (MRayl)	Attenuation (dB/cm)
Spurr epoxy	2.5	19	19.3 \pm 0.5	7.2 \pm 0.1	36 \pm 2
Eccogel 1365-80 epoxy	2.5	120	20.6	6.5	175
CA-118 Polyurethane	2.1	24	18.7 \pm 0.5	6.9 \pm 0.1	48 \pm 1
CA-128 Polyurethane	2.0	37	18.7 \pm 0.4	6.0 \pm 0.2	94 \pm 7
Estane Polyurethane	2.1	27	18.5 \pm 0.8	6.6 \pm 0.1	64 \pm 0
Polyethylene	1.7	9	18.7 \pm 0.2	6.9 \pm 0.0	68 \pm 14
Poly (methyl methacrylate)	2.5	7	22.0 \pm 0.2	9.1 \pm 0.0	41 \pm 2
Polypropylene	1.7	28	18.8 \pm 0.6	7.2 \pm 0.2	38 \pm 2
Poly (butylene terephthalate)	2.4	54	21.7	8.9	58
Polycarbonate	2.0	24	23.0 \pm 0.4	7.8 \pm 0.1	34 \pm 4
Dispersion-236 rubber	2.1	139			
RTV-141 rubber	1.1	14			

sample present is corrected for the reflection loss at the sample-water interfaces. Thus, by comparisons of the amplitude of the pulses, the attenuation was determined.

IV. ACOUSTIC PROPERTY RESULTS

A. Single Phase Polymer Samples

The results of the acoustic properties of the pure polymer samples are summarized in the first two columns of Table II. The pure polymer samples had very similar

acoustic impedances that ranged from 1.1 to 2.5 MRayl. In contrast, the attenuation values had a much broader range from 7 to 139 dB/cm. A comparison of the polymer structures indicated that the most attenuating polymers measured (Eccogel 1365-80 and Dispersion-236) have very elastic matrices since they are both lightly cross-linked network structures. On the other end, the least attenuating polymers (polyethylene, PMMA, and RTV-141) have rather dissimilar structures. Polyethylene has a crys-

talline structure, PMMA is amorphous, while RTV-141 is a rubber. By comparing the two epoxies, Spurr epoxy (a heavily cross-linked structure) and Eccogel (a lightly cross-linked structure), the data confirmed the expectations that a decrease in cross-linkage increases attenuation.

B. Same Filler/Different Polymer Composite

As discussed earlier, attenuation in a composite is related to three main factors: the polymer matrix, the filler, and the interface between the two. For this part of the study, the 5- μ tungsten was the filler in all of the samples and the attenuation contributions from the pure polymer have been previously determined. Thus, the main observation in this part of the study was the contribution of the interface to attenuation which would include characteristics such as wettability. It should be noted that since the polymer was the major phase (80 volume percent), all of the composites in this part of the study were assumed to have a 0-3 connectivity, which would mean that each particle was surrounded by the polymer matrix.

Table II lists the acoustic property results of both the pure polymer samples and the tungsten-filled composites to help establish some comparison between the systems. The results for the tungsten-filled polymer composites showed that the Eccogel-80 and CA-128 polyurethane composites were the most attenuating. Yet, the increase in attenuation between the polymer samples and the composites was not the largest increase. On the other extreme, the least attenuating polymer samples (PMMA and polyethylene) had proportionally the largest change in attenuation when the filler was added. In another case, the tungsten-filled polycarbonate and Spurr epoxy composites were the least attenuating, yet their unfilled polymer systems displayed average amounts of attenuation. This shows that the adhesion between the polymer and particle also contributes to attenuation in a composite.

To help in the understanding of attenuation, the microstructures were examined. The composites were cut by a diamond saw and polished using diamond polishing paste and then observed using a scanning electron microscope. Each microstructure had a characteristic appearance, however there were two distinct types of structures that are shown in the example micrographs in Figs. 3 and 4. Fig. 3 shows the CA-128 polyurethane composite which had a high attenuation value (94 dB/cm at 5 MHz). The polyurethane appeared to coat the tungsten particles, yet the particles looked as if they could shift within the matrix. Whereas, Fig. 4 is a micrograph of a PMMA composite that had a low attenuation value (41 dB/cm at 5 MHz). The particles appeared to be fixed in the PMMA matrix.

In conclusion, the bond between the particle and the polymer plays an important role in the attenuation of the composites. If the adhesion between the polymer and the particle is strong, the particle is unable to vibrate freely when the ultrasonic wave is incident on the particle. Thus, the attenuation should be low due to less interfacial friction.

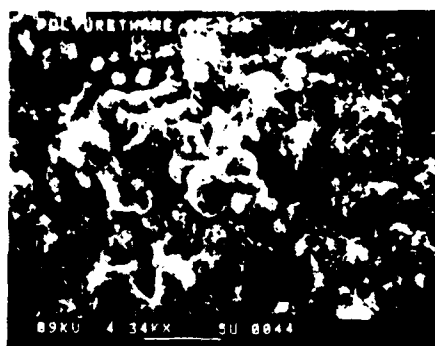


Fig. 3. SEM of 18.7 volume percent 1- μ m tungsten - 81.3 volume percent CA-128 polyurethane.

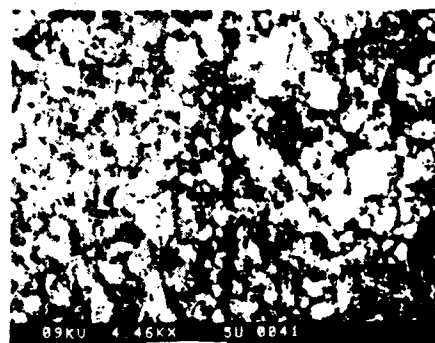


Fig. 4. SEM of 22.0 volume percent 1- μ m tungsten - 78.0 volume percent PMMA.

However, if it is a weak bond, the particle may vibrate which may cause friction and then absorption of energy into the polymer matrix that would increase attenuation.

C. Different Filler/Same Polymer Composites

Multiple 0-3 composite samples composed of Spurr epoxy and various fillers were fabricated and tested as shown in Tables III-V. Since Spurr epoxy has a fairly low attenuation, the effects of the particle size, volume fraction and filler powder characteristics were determined using Spurr epoxy as the matrix. The average values at 5 MHz and standard deviations are listed in the tables. The standard deviation of the measured acoustic impedance ranged from <1% to 8% of the average values, while the standard deviation of the attenuation coefficient had a much broader range of values ranging from 5% to 20%. The reasoning for the difference was the accuracy level of the attenuation measurement and the presence of possible defects such as porosity in the different composites.

The acoustic impedance values that were calculated using the model are also listed in the tables. The calculated impedances of the composites with 20 volume percent filler or less were consistent with the measured values. Yet, the impedances calculated for composites with increasing volume fraction of filler (>20 volume percent) are increasingly lower than the measured impedances.

TABLE III
AVERAGE ACOUSTIC PROPERTIES OF TUNGSTEN/SPURR EPOXY COMPOSITES

Filler	Averages → Volume %	Measured Impedance (MRayl)	Calculated Impedance (MRayl)	Attenuation at 5 MHz (dB/cm)
Spurr Epoxy	100	2.5		19
Tungsten	100	103		
Tungsten 1 μm	10.6 ± 0.7 18.8 ± 0.6	4.9 ± 0.2 7.0 ± 0.2	5.0 6.5	45 ± 8 40 ± 5
3 μm	11.2 ± 1.2 19.6 ± 0.4 28.2 ± 0.6	5.1 ± 0.4 7.0 ± 0.2 9.7 ± 0.2	5.1 6.7 8.0	47 ± 8 39 ± 6
5 μm	9.9 ± 0.3 18.9 ± 0.7 31.9 ± 0.7	4.7 ± 0.2 6.7 ± 0.3 10.8 ± 0.4	4.9 6.5 8.7	69 ± 12 65 ± 8 42 ± 5
50 μm	36.4 ± 0.9 40.1 ± 0.9	12.8 ± 0.2 14.6 ± 0.7	9.4 10.2	246 ± 17 178 ± 17

TABLE IV
AVERAGE ACOUSTIC PROPERTIES OF PZT/SPURR EPOXY COMPOSITES

Filler	Averages → Volume %	Measured Impedance (MRayl)	Calculated Impedance (MRayl)	Attenuation at 5 MHz (dB/cm)
Spurr Epoxy	100	2.5		19
PZT	100	30		
PZT 1.5 μm	9.8 ± 0.5 19.0 ± 0.6 27.8 ± 0.7 37.0 ± 1.1	3.4 ± 0.1 4.4 ± 0.1 6.1 ± 0.1 7.5 ± 0.2	3.8 4.5 5.4 6.4	61 ± 12 61 ± 8 34 ± 4 35 ± 6
>75 μm	28.6	6.6	5.5	164

TABLE V
AVERAGE ACOUSTIC PROPERTIES OF ALUMINA/SPURR EPOXY COMPOSITES

Filler	Averages → Volume %	Measured Impedance (MRayl)	Calculated Impedance (MRayl)	Attenuation at 5 MHz (dB/cm)
Spurr Epoxy	100	2.5		19
Alumina	100	25		
Alumina 0.3 μm	5.8 ± 0.6	3.3 ± 0.1	3.2	38 ± 6
1.0 μm	11.8 ± 0.8	4.0 ± 0.1	3.6	36 ± 4
3.0 μm	3.9 ± 0.3 10.4 ± 0.5	2.6 ± 0.0 3.1 ± 0.0	3.0 3.5	40 ± 6 25 ± 3
12.5 μm	4.4 ± 0.9 10.8 ± 0.4 40.6 ± 1.0	2.6 ± 0.1 3.1 ± 0.0 7.0 ± 0.2	3.1 3.5 5.4	3.5 ± 9 23 ± 2 22 ± 2

Some fabrication variations occur when mixing the composites thus making it difficult to compare between the various types of fillers. There was a maximum volume fraction (20 volume percent) of the fine tungsten particles ($\leq 5 \mu\text{m}$) that could be added to the epoxy due to the particles' high surface areas that caused the viscosity to

increase. Furthermore, the composites with the large particles tended to have settling problems which made it difficult to fabricate low filler volume composites.

A plot of the frequency dependence of attenuation of pure Spurr epoxy and tungsten, PZT, and alumina-filled composites is shown in Fig. 5. The slope of frequency dependence of attenuation is higher for the composites compared to the pure epoxy sample due to the attenuation contribution from the fillers. Most of the impedance values were nearly independent of frequency.

Table III lists the acoustic properties of the tungsten-filled composites. In order to isolate and observe the influence of volume fraction of filler on attenuation, the particle size was kept the same while the volume fraction was varied. There was a decrease in attenuation with an increase in volume fraction of filler. Next, the particle size effect was characterized by comparing composites with the same filler volume fractions. The attenuation increased with an increase in particle size. For example, the attenuation increased from 45–69 dB/cm for the 10 volume percent tungsten-filled composites with only a slight increase of a few microns in the average particle size. The effect of the particle size is seen more prominently when the attenuation of the 50-μm tungsten particle composite is compared with other composites since the particle is closer in size to the wavelength.

Table IV shows the data for the PZT-filled composites. Similar trends in comparison to the tungsten composite data were seen. The attenuation of the 1.5-μm PZT-filled composites dropped from 61 dB/cm to 35 dB/cm with an increase in volume fraction of PZT (10 to 37 volume fraction). A comparison of the 28 volume percent of 1.5 μm PZT and >75 μm PZT composites showed an increase in attenuation from 34 dB/cm to 164 dB/cm.

The alumina-filled composite data are shown in Table V. The observed values showed a slight decrease in attenuation with an increase in volume fraction of alumina. However, with about 11 volume percent of alumina, there was a decrease in attenuation from 36 dB/cm to 23 dB/cm with an increase in particle size of alumina from 1 μm to 12.5 μm. The reverse trend from the PZT and tungsten composites might have been due to the large difference in the acoustic impedance of the alumina in comparison to the PZT and tungsten.

At the particle interface, part of the wave will be transmitted and part will be reflected depending on the impedance mismatch. This is one reason why the tungsten composites are more attenuating than the PZT and alumina composites as shown in Fig. 5. Overall, the very large tungsten (~50 μm) and PZT (>75 μm) particle-filled composites were the most attenuating since the particle size was close to the size of the wavelength (400 μm at 5 MHz), thus creating multiple reflections and/or scattering. Generally, the alumina-filled composites were the least attenuating.

The composites were cut and examined under a scanning electron microscope to see the particle wettability, dispersion, and the presence of porosity and micro cracks.

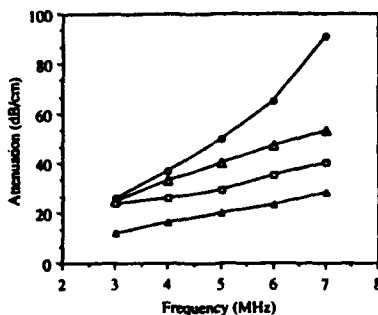


Fig. 5. Attenuation versus frequency of epoxy and filled-epoxy composites. 10 volume % filler ($\sim 1 \mu\text{m}$). —○— shows tungsten. —△— shows PZT. —□— shows alumina. —▲— shows Spurr epoxy.

TABLE VI
ACOUSTIC PROPERTIES OF THE HOT UNIAXIALLY PRESSED TUNGSTEN/EPOXY COMPOSITES

Sample number	Particle Size (μm)	Pressure (psi) (Hot pressing conditions)	Temp ($^{\circ}\text{C}$)	Volume %	Impedance (MRayl)	Attenuation @ 5 MHz (dB/cm)
HUP-3	50	3000	1700	62.4	38.8	23
HUP-4	87.5% 50 μm 12.5% 5 μm	3000	1700	74.3	59.7	6
HUP-5	87.5% 5 μm 12.5% 5 μm	3000	1600	75.4	54.0	13

For these composites, the Spurr epoxy appeared to wet the particles and create a fairly well dispersed matrix.

In summary, the general trends of the acoustic properties for the 0-3 composites with the same epoxy matrix are recapitulated as follows.

- 1) Acoustic impedance is independent of frequency.
- 2) Acoustic impedance increases with an increasing volume fraction of filler material.
- 3) Attenuation generally decreases with increasing volume percent of filler material.
- 4) As the particle size of the filler material increases and surface to volume ratio decreases, the attenuation increases for the tungsten and PZT-loaded composites and decreases for the alumina-loaded composites.
- 5) In general, the tungsten composites appear to be more attenuating than the alumina and PZT composites. This is probably due to the large impedance mismatch at the interface between the polymer and tungsten that make the tungsten particles a product of stronger scattering sites.
- 6) The acoustic impedance given by the square root of the composite density and the Reuss Bulk Modulus is an accurate model for composites with less than 40 volume percent filler.

D. Composites Processed in Different Ways

To achieve higher densities, the samples were hot uniaxially pressed (HUP) using a mix of tungsten particles of various sizes to create better packing. In addition, the combination of pressure and temperature promoted

sintering as observed in the microstructures. The acoustical results are presented in Table VI. The higher volume fraction samples achieved impedances of greater than 50 MRayl. The attenuation of these HUP composites was less than 24 dB/cm. This value is low compared to the attenuation obtained with large particles loaded to approximately 40 volume percent.

A comparison between the HUP composites and the large 50 micron tungsten particle/Spurr epoxy composites shows that with an increase of approximately 20 volume fraction of tungsten, a decrease in attenuation of about 180 dB/cm occurred. One explanation is that the composites followed the trend that attenuation typically decreases with increasing volume fraction of filler. Another explanation is that the different processing route resulted in a change in the typical 0-3 composite connectivity to 1-3 and 3-3 composite connectivities that were seen in the microstructural analysis.

The BURPS process was used to create a uniform two phase microstructure. The results of the acoustic properties of the BURPS samples are listed in Table VII. The attenuation of the tungsten BURPS samples were found to be greater than for any other sample except for the 50- μm tungsten/Spurr epoxy composites. The attenuation was higher than 214 dB/cm at 5 MHz and the impedance was about 8.7 MRayl. The alumina and PZT BURPS composites also had high attenuation values of 48 dB/cm and 111 dB/cm, respectively.

A look at the internal structure helped to provide some possible answers to the high attenuation. The composites appeared to have 0-3 connectivity as seen in the microstructural analysis. There were severe microcracks

TABLE VII
ACOUSTIC PROPERTIES OF THE BURNABLE POLYMER SPHERES COMPOSITES

Filler	Particle Size (μm)	Averages \rightarrow Volume % Filler	Impedance (MRayl)	Attenuation at 5 MHz (dB/cm)
Tungsten	5	19.6 ± 0.4	8.3 ± 0.0	$>217 \pm 13$
	50	21.9 ± 0.2	8.8 ± 0.0	$>219 \pm 9$
Alumina	1.0	15.9 ± 1.3	4.1 ± 0.2	48 ± 5
PZT	1.5	20.8 ± 0.7	5.4 ± 0.1	111 ± 3

throughout each microstructure that may have occurred during the polymer burn-out step. Thus, the high attenuation values may have resulted from the increased scattering sites due to the cracks and the additional phases in the composites such as any porosity, or PMMA and PVA, that was not completely burned off. Nonetheless, more studies should be conducted to understand this unpredicted observation.

V. CONCLUSION

The backing plays an important role in optimizing the impulse response of an ultrasonic transducer. The emphasis of this study was to be able to improve the understanding and predictability of the acoustic impedance and attenuation of composite backings.

The main conclusion from the theoretical modeling of the acoustic impedance is that the model which uses the square root of the composite density and the Reuss Bulk Modulus is a fair estimate for the composites with lower volume fractions of filler. However, as the volume fraction of filler was increased (>40 volume %), the model did not accurately predict the impedance.

The major conclusion from the experimental portion of this study showed that both the polymer matrix and particle filler contribute to composite attenuation. It was shown that certain polymer matrices tend to attenuate sound waves more than others. For example, a decrease in crosslinkage or crystallinity in the structure tends to create more acoustically lossy matrices.

General trends concerning the influence of the particle size, volume fraction, and type of filler on the acoustical properties were established. In summary, the larger particles and low volume fractions of filler tend to create better scattering sites that increased attenuation. In addition, the larger impedance mismatch due to the differences in phases caused an increase in reflections at the interfaces that in turn created more acoustical loss.

The adhesion between the polymer and particle is another important contributor to attenuation. Wetting characteristics appear to be correlated with attenuation, yet more studies need to be performed.

Finally, a recommendation for the materials design of a highly attenuating backing is a composite of a fairly low volume fraction of dense, large particles such as the 50- μm tungsten in a soft, lightly cross-linked polymer matrix such as Eccogel 1365-80 or Dispersion-236. In

conclusion, the physical characteristics of the filler particles and the polymer matrix, plus their ability to interact, control attenuation in composites.

IV. REFERENCES

- [1] K. F. Bainton and M. G. Silk, "Some factors which affect the performance of ultrasonic transducers," *Brit J. NDT*, vol. 22, no. 1, pp. 15-20, 1980.
- [2] C. M. Sayers and C. E. Tait, "Ultrasonic properties of transducer backings," *Ultrason.*, vol. 18, no. 3, pp. 57-60, 1984.
- [3] H. W. Persson and C. H. Hertz, "Acoustic impedance matching of medical ultrasound transducers," *Ultrason.*, vol. 23, no. 3, pp. 83-89, 1985.
- [4] M. G. Silk, *Ultrasonic Transducers for Nondestructive Testing*. Bristol: Adam Hilger, 1984.
- [5] A. Vary and H. E. Kautz, "Transfer function concept for ultrasonic characterization of material microstructures," *Analytical Ultrasonics in Materials Research and Testing*, NASA Conference Publication 2383, pp. 257-297, 1986.
- [6] I. I. Perepechko, *Acoustic Methods to Investigating Polymers*. Moscow: MIR Publishers, 1975.
- [7] J. N. Lange, Jr., "A study of ultrasonic attenuation and wave propagation in solids," Ph.D. thesis, Pennsylvania State Univ., University Park, PA, 1964.
- [8] G. Kossoff, "The effects of backing and matching on the performance of piezoelectric ceramic transducers," *IEEE Trans Sonics Ultrason.*, vol. SU-13, no. 1, pp. 20-30, 1966.
- [9] A. Lutsch, "Solid mixtures with specified impedances and high attenuation for ultrasonic waves," *J. Acoust Soc. Am.*, vol. 34, pp. 131-132, 1962.
- [10] M. G. Grewe, "Acoustic matching and backing layers for ultrasonic transducers," M.S. thesis, Dept. Solid State Sci., Pennsylvania State Univ., University Park, PA, 1989.
- [11] I. I. Perepechko, *An Introduction to Polymer Physics*. Moscow: MIR Publishers, 1981.
- [12] W. P. Mason and H. J. McSkimin, "Attenuation and scattering of high frequency waves in metals and glasses," *J. Acoust. Soc. Am.*, vol. 19, no. 3, pp. 464-473, 1947.
- [13] *Physical Acoustics, Vol. IV-Part B*, W. P. Mason, Ed. New York: Academic Press, 1968.
- [14] S. M. Pilgrim, "Application of piezoelectric polymer composites to passive and active vibration absorption," Ph.D. thesis, Dept. Solid State Sci., Pennsylvania State Univ., University Park, PA, 1987.
- [15] R. E. Newnham, "Composite electroceramics," *Ferroelectrics*, vol. 68, pp. 1-32, 1986.
- [16] J. M. Pelmore, "Acoustic impedance of composite materials," *Acoust. Lett.*, vol. 3, no. 3, pp. 65-68, 1979.
- [17] S. Lees, R. S. Gilmore, and P. R. Kranz, "Acoustic properties of tungsten-vinyl composites," *IEEE Trans. Sonics Ultrason.*, vol. SU-20, no. 1, pp. 1-2, 1973.
- [18] L. Sidney and C. L. Davidson, "Ultrasonic measurement of some mineral filled plastics," *IEEE Trans. Sonics Ultrason.*, vol. SU 24, no. 3, pp. 222-225, 1977.



Martha G. Grewe was born in Minneapolis, Minnesota on November 24, 1964. She earned a B.S. degree in materials science engineering in 1986 at Rensselaer Polytechnic Institute, Troy, NY. She earned the M.S. degree in solid state science in 1989 from Pennsylvania State University, University Park, PA.

She has worked at the Imaging Systems Division of Hewlett-Packard in Andover, MA, since February 1989. She works in the Research and Development Lab as a Transducer Development Engineer. Her main research interests are in the area of composites and piezoelectric materials.

Ms. Grewe is a member of the American Ceramic Society and the Materials Research Society.



T. R. Gururaja was born on September 24, 1954, in Bangalore, India. He received the B.Sc. and M.Sc. in physics from the University of Mysore, India, in 1974 and 1976, respectively. He received the M.Tech. degree in materials science from the Indian Institute of Technology, Kanpur in 1978 and Ph.D. degree in Solid State Science from the Pennsylvania State University in 1984.

He is currently a Transducer Design Engineer at Hewlett-Packard in Andover, MA. He worked as a Research Associate at the Pennsylvania State University from 1984 to 1987. His research activities have been in the area of dielectric and piezoelectric crystals, ceramics, and composites.

ration and characterization of electronic ceramics with emphasis on power processing and fabrication.

Dr. Shrout is a member of the Electronics Division of the American Ceramic Society and I.S.H.M.



Robert E. Newnham received the B.S. degree in mathematics in 1950 from Hartwick College, Oneonta, NY, the M.S. degree in physics in 1952 from Colorado State University, Fort Collins, CO, the Ph.D. degree in physics and mineralogy in 1956 from Pennsylvania State University, University Park, PA, and the Ph.D. degree in crystallography in 1969 from Cambridge University, Cambridge, England.

He is Alcoa Professor and Chairman of the Solid State Science program at the Materials Research Laboratory of the Pennsylvania State University. He is also affiliated with the Ceramic Science Section of the Materials Science and Engineering Department where he teaches courses in crystal chemistry, crystal physics, and electroceramics. His research interests are in structure-property relations, electroceramics, and composite materials for electronic applications.

Dr. Newnham was recently elected to the National Academy of Engineering. He is the author of more than 300 research papers, and is now serving as co-editor of the *Journal of the American Ceramic Society*.

Thomas R. Shrout was born in Kingwood, WV, in 1954. He received a B.S. degree in ceramic science in 1976 from Pennsylvania State University and the Ph.D. degree in ceramic science in 1981.

After working several years at the R&D Laboratories of Sprague Electric Co. and AVX, he returned to Pennsylvania State University in 1986 where he is presently an Associate Professor of Solid State Science at the Materials Research Laboratory. His research interests include the prepa-

APPENDIX 13

PASSIVE PIEZOELECTRIC DAMPING

A.R. Ramachandran, Q.C. Xu, L.E. Cross and R.E. Newnham,
 Materials Research Laboratory, The Pennsylvania State University,
 University Park, PA 16802.

Abstract

It is possible to make passive damping materials using piezoelectric materials. The term "passive" is used to indicate the absence of sensor-actuator combinations using feedback loops. Structural stress can be transferred to a piezoelectric material with a high coupling coefficient to cause currents to flow through electrically resistive elements, thereby leading to energy dissipation. Based on theoretical considerations, it should be possible to design a damping material with high stiffness ($\sim 2 - 10 \times 10^{10} \text{ N/m}^2$), along with high a damping coefficient ($\tan \delta \sim 0.3$). To show the feasibility of such a damper, we will present results based on resonance measurements made using the LE mode, where k_{33} is the operative coupling coefficient.

Introduction

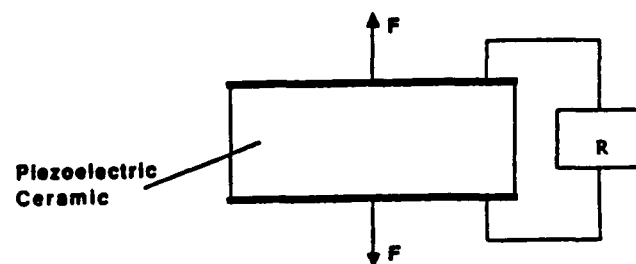
Materials with good vibration damping capabilities find applications in structures where vibration and noise are to be reduced. In this work, we have investigated the possible use of piezoelectric materials with large electromechanical energy conversion efficiencies, (large coupling coefficients) for passive vibration damping applications. In order to attenuate mechanical vibrations in a passive absorbing element, it is essential to convert a major fraction of mechanical/elastic energy into heat. The idea behind passive piezoelectric vibration damping is to convert a large fraction of elastic energy into electrical energy using the piezoelectric coupling coefficient and then dissipate the electrical energy using a simple resistive element. For efficient damping characteristics, the coupling coefficient must be large. Similar work aimed at designing a piezoelectric mechanical damper has been reported by Uchino and Ishii[1].

Theory

The attenuation of an elastic plane wave in a semiconducting, piezoelectric material - the electroacoustic effect, has been studied by Hutson and White[2]. In this case, the mechanism for energy dissipation is the local charge carrier current that accompanies the elastic wave. In the present work, we have attempted to duplicate a semiconducting piezoelectric material by connecting resistors across disks of poled PZT. By selecting a piezoelectric ceramic with low compliance and a high coupling coefficient, it is possible to obtain a

material with a large Young's modulus and good mechanical damping characteristics.

Consider the following schematic (Fig. 1) which shows a block of poled Lead-Zirconate-Titanate (PZT) ceramic being subjected to an oscillatory (sinusoidal) stress. The poling direction is along the vertical (3-direction) as shown. The PZT block is shunted by a resistance R which is connected to the electrodes.



F = Force applied

Figure 1: Schematic diagram showing the principle of piezoelectric damping.

The constitutive equations of state for a piezoelectric material relating the stress, strain, electric field and electric displacement in matrix form are[3]:

$$S = sE T + d_t E \quad (1a)$$

$$D = \epsilon^T E + d T \quad (1b)$$

where,

S = strain matrix

T = stress matrix

E = electric field matrix

D = electric displacement matrix

sE = elastic compliance matrix under constant E -field condition

ϵ^T = dielectric permittivity matrix under constant stress condition

d = piezoelectric coefficient matrix

d_t = transpose of above matrix

Assuming low frequencies so that the fields are not position dependent and only S_3 , T_3 , E_3 and D_3 are non-zero, the following one-dimensional equations can be obtained.

$$S_3 = s_{33} E T_3 + d_{33} E_3 \quad (2a)$$

$$D_3 = \epsilon_{33}^T E_3 + d_{33} T_3 \quad (2b)$$

Since D_3 is related to the current through the resistor, one can arrive at the following equation relating the strain S_3 to the stress T_3 :

$$S_3 = s_{33} \left(1 - \frac{k_{33}^2}{1 + j/\omega RC} \right) T_3 \quad (3)$$

where,

$$k_{33} = \frac{d_{33}}{\sqrt{\frac{E}{s_{33} \epsilon_{33}}}}$$

is the piezoelectric coupling coefficient, and

$$C = \frac{T}{\frac{E_{33} A}{L}}$$

is the capacitance of the PZT block.

Thus we obtain a complex compliance coefficient s_{33}^* , given by,

$$s_{33}^* = s_{33} \left(1 - \frac{k_{33}^2}{1 + j/\omega RC} \right) = s' - js'' \quad (4)$$

where, s' and s'' are respectively the real and imaginary compliance coefficients.

$$s' = s_{33}^* \left(\frac{1 - k_{33}^2 + (1/\omega RC)^2}{1 + (1/\omega RC)^2} \right) \quad (5)$$

and

$$s'' = s_{33}^* \frac{k_{33}^2 / \omega RC}{1 + (1/\omega RC)^2} \quad (6)$$

We can then define a mechanical loss tangent $\tan \delta = s''/s'$;

$$\tan \delta = \frac{k_{33}^2 / \omega RC}{1 - k_{33}^2 + (1/\omega RC)^2} \quad (7)$$

The complex compliance coefficient is obviously a function of frequency and the loss tangent is a maximum when the following condition holds,

$$\omega = 1/RC \sqrt{1 - k_{33}^2} \quad (8)$$

The maximum in energy dissipation occurs when s'' is maximum i.e., when $\omega = 1/RC$. A maximum value of $s'' = (k_{33}^2/2)s_{33}^E$ can be attained.

A plot of the real part of the compliance s' and $\tan \delta$ as a function of frequency is shown in Fig. 2. It has been assumed that $k_{33} = 0.7$, which is typical for PZT-5. As can be seen the system shows classical Debye relaxation behaviour with a single time constant. The maximum value of $\tan \delta$ is 0.35. In addition, by controlling the shunt resistor, we can design the damper to have the desired optimum properties at any frequency of interest.

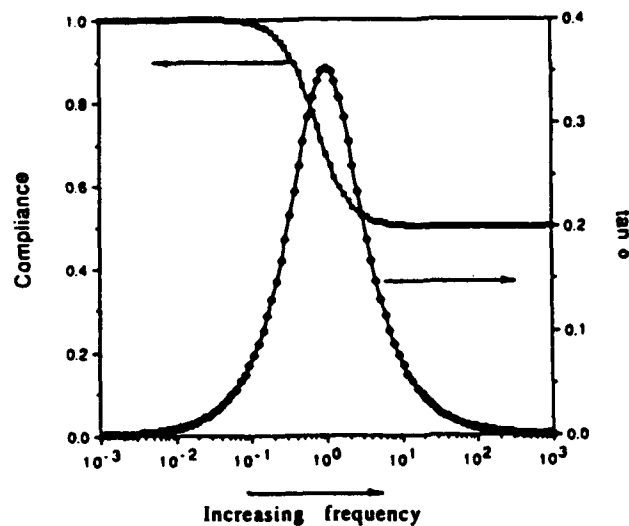


Figure 2: Expected mechanical behaviour of piezoelectric damper. The real part of the compliance s' is plotted on a normalized scale (left y-axis) with unit value assigned to s_{33}^E . The mechanical loss tangent $\tan \delta$ is plotted with reference to the right y-axis. -- $\tan \delta_{max} = 0.35$ if $k_{33} = 0.7$. The logarithmic x-axis is normalized with respect to a "tuning frequency", $\omega_0 = 1/RC$.

Experimental

Sample preparation

It has been seen that the damping efficiency of a piezoelectric damper is directly linked to the coupling coefficient pertaining to the stresses and strains produced by the pertinent modes of vibration. In this work, the experiments were performed around the resonance frequency using the lengthwise 3-3 vibration mode[3], since the k_{33} coefficient of PZT is the largest available coupling coefficient. The configuration of such a 3-3 mode sample for resonance measurements is a long bar or cylinder with the poling and vibration directions

coinciding with the major dimension. Due to the enormous voltage that would be required to pole a sample of sufficient length, such a sample was made up using a large number of PZT toroids as shown in the schematic (Fig. 3).

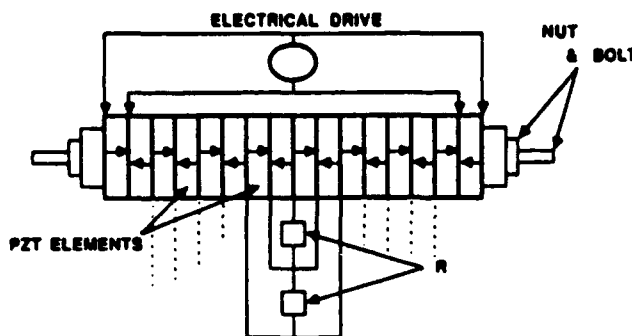


Figure 3: Schematic of PZT stack sample.

Sintered PZT disks, 0.8 cm. in radius were made by conventional ceramic processing using commercially available PZT-501A powder purchased from Ultrasonic Powders Inc. A central, axial hole, 0.3 cm. in radius was drilled through each disk using a diamond core drill to obtain the toroids. These toroids were then ground and polished to the same thickness, 0.33 cm., using a diamond polishing wheel. Silver termination ink (DuPont Corp.) was then painted on the flat surfaces of the toroids which were then fired at 600°C to obtain well bonded electrodes. The PZT toroids were then poled along the thickness direction in a silicone oil bath at 120°C using an electric field of 25 kV/cm. The dielectric constant of these toroids was measured using a HP 4275A Multi-Frequency LCR meter and the piezoelectric coefficient d_{33} was measured using a Berlincourt d_{33} meter (Channel Products Inc.) to obtain the following results.

$$K_{33}^T \text{ (Dielectric Constant)} = 1950$$

$$d_{33} = 430 \text{ pC/N}$$

The 3-3 mode vibrator was made by stacking 32 such PZT toroids alternating with brass electrodes on a 12 cm. long threaded steel rod. The brass electrodes were circular disks of thin (1 mil thickness) shim material with a 0.3 cm. radius hole punched through the center. The thin brass layers were of slightly larger diameter than the PZT toroids to facilitate external electrical connection. A thin layer of a hard epoxy (Spurrs Epoxy manufactured by Polysciences Inc.) was applied to the electrode surfaces before assembly and care was taken to see that all surfaces were clean and free from oil or grease. One 0.5 cm. thick brass toroid was also stacked on each end of the assembly. Steel nuts screwed onto the threaded rod at each end held the assembly in place and also provided a compressive pre-stress. The stack was

kept in an oven set at 90°C to cure the epoxy for 24 hours.

Measurements and Results

First, the integrity of the sample was checked with regard to the quality of the epoxy bond at the PZT-brass interfaces. In order to do this, all the PZT elements were connected in parallel and the stack was set into vibration through electrical excitation by means of a HP 4192A LF Impedance Analyser and the electrical admittance vs. frequency curve, obtained. A sharp resonance peak corresponding to the fundamental resonance mode of the stack (~11 kHz) together with the absence of any spurious vibration modes showed that there were no cracks or other impedance mismatch problems at the interfaces. It may also be noted here, that since the thickness of each PZT element is much smaller than the wavelength at the resonance frequency ($< \lambda/50$) at which all the data were obtained, the assumptions in the model developed in the theory section hold.

The mechanical stiffness and the loss tangent $\tan \delta$, were measured using an electrical resonance technique by measuring the electrical impedance over a frequency range about the fundamental resonance frequency. The stiffness coefficient E , was estimated from the resonance frequency - (due to the type of electrical excitation used, the electrical resonance frequency was equal to the mechanical resonance frequency) - using the relation,

$$E = \rho f_r^2 \lambda^2 \quad (9)$$

where, ρ is the density; f_r is the resonance frequency; and λ ($= 2 \times$ length) is the wavelength.

The loss tangent was estimated using the half-bandwidth technique modified for application to low Q (high mechanical loss) materials[4]. The use of a resonance technique only estimates the mechanical parameters especially in a material with a high, frequency dependent loss factor. However, the stiffness is estimated quite accurately and the loss tangents estimated are lower limiting values since this method[4] actually leads to an underestimation.

In a bar vibrator excited symmetrically about the center at the fundamental resonance mode, one expects the contribution to the overall coupling coefficient to be different from different regions depending on the location since the stress and the strain are maximum in the center and drop down to near zero at the ends. Therefore an effective coupling coefficient[5], k_{eff} which is determined by k_{33} was measured by electrically exciting only parts of the sample symmetrically from the center towards the ends. The effective coupling coefficient

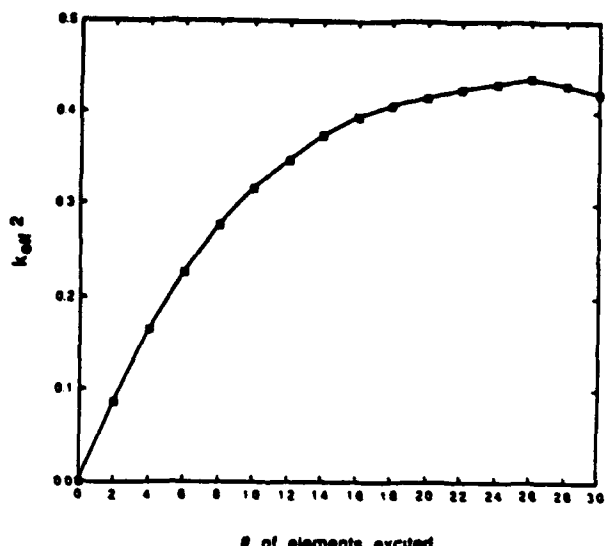


Figure 4: Plot of k_{eff}^2 shown as a function of the number of PZT elements excited symmetrically about the center of the stack.

is related to the measured values of the resonance and antiresonance frequencies, f_r and f_a as follows;

$$k_{eff}^2 = 1 - (f_r/f_a)^2 \quad (10)$$

The relation of k_{eff}^2 to the number of excited elements is shown in Fig. 4. It can be seen that the regions of high strain in the center contribute the most toward the overall coupling coefficient.

In the first set of experiments, the effective damping contribution from different regions of the sample was determined. In order to do this, the whole PZT stack was set into vibration by electrically exciting with the impedance analyzer, only one element at each end and obtaining the admittance vs. frequency curve. Optimally tuned resistors ($-7\text{ k}\Omega$) were connected across the central two elements, then across an additional two elements on either side and so on upto the ends of the stack, and the stiffness E , and the loss tangent $\tan \delta$ were estimated from the admittance plot. The results are shown in Fig. 5. The similarity between the k_{eff}^2 and $\tan \delta$ curves (Figs. 4 and 5) is obvious showing that most of the contribution towards the damping arises from the central parts of the stack.

In the second set of experiments, the stack sample was set into resonance again by electrically exciting one PZT element at each end using a sufficiently long gated sine wave. The voltage output from one of the central elements was measured using an oscilloscope; this voltage being proportional to the strain in that element. At the end of the exciting signal, the time decay in the vibration amplitude is observed as the decay in this voltage output. The experiments were conducted

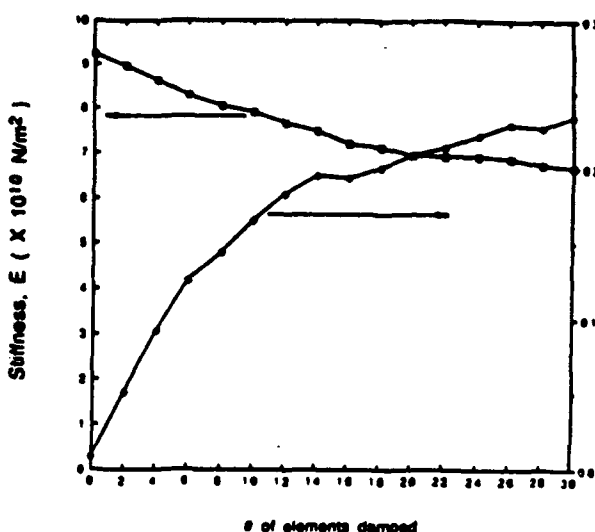


Figure 5: Plot of mechanical stiffness and $\tan \delta$ against number of disks shunted by optimally tuned resistors.

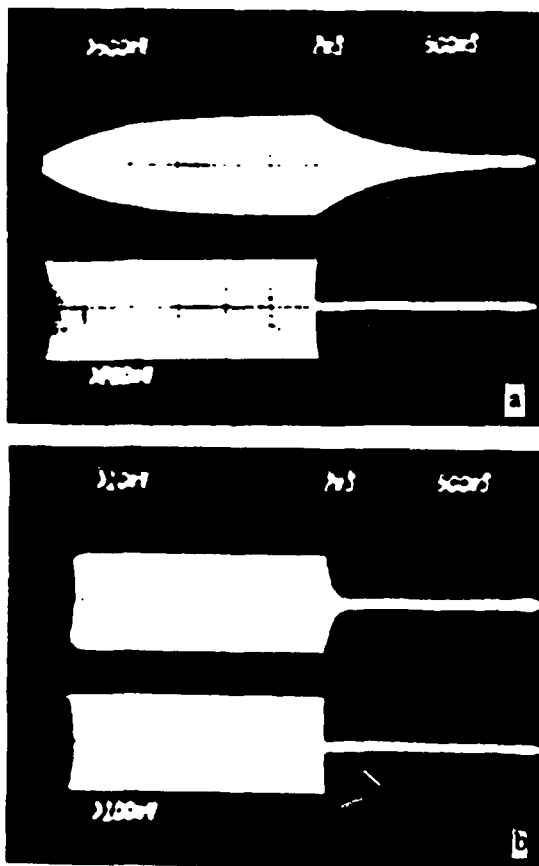


Figure 6: Oscilloscope photographs showing attenuation of vibrations of the stack sample when no resistors are connected (a) and when four central elements are shunted by optimum resistances (b). Also shown is the exciting gated sine wave.

without any shunt resistor as well as with optimally tuned resistors connected across some or all the elements as described previously. Some results are shown in Fig.6.

Conclusions

In conclusion we find that it is possible to obtain high stiffness and high damping characteristics using a simple passive electrically resistive element in conjunction with a piezoelectric ceramic material (PZT) with a high coupling coefficient. By optimum tuning of the resistors, it should be possible to shift the peak damping to any frequency of interest. Proper placement of piezoelectric elements at regions of high stress in a vibrating structure will optimise the damping capability.

Future Work

The use of a mechanical, non-resonant, transfer function technique is proposed to measure the property coefficients more accurately over a range of frequencies (500 Hz to 5 kHz) and variable resistance values. Incorporation of other passive electrical elements should lead to better control and design of properties tailored to suit specific applications.

References

1. K. Uchino and T. Ishii, "Mechanical Damper using Piezoelectric Ceramics," J. Japan Ceramic Society, vol. 96, pp. 863-867, 1988.
2. A.R. Hutson and D.L. White, "Elastic Wave Propagation in Piezoelectric Semiconductors," J. Appl. Phys., vol. 33(1), 1962.
3. D.A. Berlincourt, D.R. Curran and H. Jaffe, "Piezoelectric and Piezomagnetic Materials and Their Function in Transducers," Physical Acoustics, vol. 1, Part A, W.P. Mason, ed. Academic Press, pp. 169-270, 1964.
4. Q.C. Xu, A.R. Ramachandran and R.E. Newnham, "Resonance Measurement Technique for Complex Coefficients of Piezoelectric Composites," J. Wave-Material Interaction, vol. 2, pp. 105-122, 1987.
5. W.J. Toulis, "Electromechanical Coupling and Composite Transducers," J. Acoustical Society of America, vol. 35(1), 1963.

THEORETICAL STUDIES

APPENDIX 14



ANHARMONIC PERTURBATION THEORY OF ELECTROSTRCTION IN A PEROVSKITE OXIDE AT FINITE TEMPERATURE†

B.N. NARAHARI ACHAR* AND G. R. BARSCH**

*Memphis State University, Department of Physics, Memphis, TN 38152 USA

**The Pennsylvania State University, Department of Physics and Materials Research Laboratory, University Park, PA, 16802 USA

(Received January 1 1990 by R.H. Silsbee)

The hydrostatic electrostriction coefficient of SrTiO_3 and its temperature dependence have been calculated on the basis of anharmonic many-body perturbation theory. Contributions from several lowest order diagrams have been evaluated using an anharmonic shell model originally used for calculating the electrostriction coefficients of the static crystal. The calculated temperature dependence is in agreement with experiment.

The electrostriction (ES) coefficients determine the strain dependence of the dielectric constant; those most directly amenable to lattice dynamical calculation are defined as the derivatives of the dielectric susceptibility (x_{rs}) with respect to the Lagrangian strain tensor η_{kl} :

$$e_{rs,kl} = (\partial x_{rs} / \partial \eta_{kl}) \quad (r,s,k,l = 1,2,3)$$

They are related to the more conventional Q-coefficients familiar to experimentalists and defined in a rotationally invariant form by

$$Q_{rs,ij} = \frac{1}{2} (\partial^2 V_{ij} / \partial P_r \partial P_s)$$

where V_{ij} and P_r denote the components of the displacement gradient and the dielectric polarization respectively. The relationship between the two sets of coefficients is given by (tensor notation; summation convention)

$$\begin{aligned} Q_{rs,ij} &= -\left(\frac{1}{2}\right) S_{ijkl} (b_{rubs} v_{uv,kl} \\ &\quad + b_{rk\delta sl} + b_{sk\delta ri} - 2b_{rs\delta kl}) \end{aligned}$$

Here S_{ijkl} represent the components of the elastic compliance tensor and $b_{rs} = (x_{rs})^{-1}$. For a cubic crystal there are only three independent coefficients Q_{1111} , Q_{1122} and Q_{2323} . In this paper, we are primarily concerned with the hydrostatic coefficient $Q_h = Q_{1111} + 2Q_{1122}$ and the shear coefficient $Q_s = Q_{1111} - Q_{1122}$.

It was generally believed that the Q-coefficients are temperature independent, an idea supported in part by the microscopic theory of Silverman for ferroelectric soft-mode materials in the paraelectric phase. However, more recent experimental data for several perovskite oxides [3a-3c] indicate a linear variation with temperature. Phenomenological approaches based on a properly constructed Landau-Devon-

shire free energy function also lead to a similar linear variation of the Q-coefficients with temperature.⁴ However, a microscopic theory which would explain this linear variation of the Q-coefficients with temperature is still lacking. It is the purpose of this paper to present the results of an atomistic calculation of the temperature variation of the ES Coefficients on the basis of an anharmonic many-body theory^{5,6}.

Room temperature values of the ES coefficients have been calculated for SrTiO_3 from a shell model by Bruce and Cowley⁷. However, in their model, the anharmonicity from Coulomb interactions is neglected. It has been shown^{8a,8b} that for a consistent description of the first order anharmonic properties it is essential to include Coulomb anharmonicity. We have reported preliminary results for the temperature variation of Q_h that we obtained from a harmonic shell model with anharmonicity in the short range and Coulomb forces included in the rigid ion approximation. However, these results were based only on the contribution from the lowest order diagram in the anharmonic perturbation expansion and did not account for the observed temperature variation of Q_h . In the present paper, we have extended the work of Ref. 9 by treating anharmonicity in the full shell model and by including the contributions from three additional diagrams.

Outline of Theoretical Method

According to standard anharmonic perturbation theory⁶, the dielectric properties of a crystal can be calculated by considering the total Hamiltonian H to consist of a harmonic part H_0 , an anharmonic part H_A and an interaction $H_I = -\vec{M} \cdot \vec{E}$ between an external electric field \vec{E} and the dipole moment of the crystal \vec{M} :

$$H = H_0 + H_A + H_I$$

† Work supported in part by US Office of Naval Research Contract No. N00014-82-D-0339.

The electric field is turned on adiabatically as $\vec{E} = \vec{E}_0 \exp(-i\omega t + ct)$ and the dielectric susceptibility can be expressed as

$$\chi_{rs}(\Omega) = P_{rs}(\Omega) + (S/Nv)G(M_rM_s,\Omega + i\epsilon)$$

where $P_{rs}(\omega)$ is the electronic susceptibility and G is the thermodynamic Greens function for dipole moment operators M_r and M_s . For a strained crystal, the Hamiltonian H and the dipole moment M can be expanded in a double series in terms of the phonon coordinates $A(\lambda)$ and the deformation parameters V_{ij} , and a diagram technique employed to evaluate the electrostriction coefficients $\epsilon_{rs,ij}$.

Figure 1 shows the lowest order diagrams considered here in the anharmonic perturbation expansion contributing to the ES coefficients and the corresponding contributions. In the expressions given, $M_r(\lambda)$ denotes the r-component of the dipole moment arising from the normal mode λ , $\omega_r(\lambda)$ and $\omega_T(\lambda)$ the corresponding bare and renormalized temperature dependent eigenfrequencies, respectively. $V_{kl}(\lambda, -\lambda')$ denotes the double Fourier transform of products of linear combinations of third order coupling parameters and components of the eigenvectors of the bare normal modes λ and λ' . The mode index λ entails both the wave vector and the branch index, and the sums are over the modes at the zone center only. The quantities $M_r(\lambda)$, $V_{kl}(\lambda, -\lambda')$, $M_{r,s}\delta$, and P_{rs} have all been defined by Cowley¹⁰.

The quantities in the numerators of all expressions pertain to the bare reference state in the perturbation expansion. The temperature dependence of the ES coefficients arises only via the self-energy corrections to the phonon frequencies giving rise to the renormalized frequencies $\omega_T(\lambda)$ appearing in the denominators. The evaluation of the self-energy corrections is a separate problem and a knowledge of the mode softening mechanism is a prerequisite for a more complete understanding of the temperature variation of the ES coefficients. For purposes of the present paper, it is sufficient to use experimental zone center frequencies as functions of temperature. However, the scope of the present paper entails the calculation of the numerators in the expressions given above, from a shell model, in which Coulomb anharmonicity and anharmonicity of the short range interactions are included. The model parameters used are identical to the ones used before for the calculation of the first order anharmonic quantities at the zone center of the static crystal⁸. In the spirit of the pseudoharmonic

$$\begin{aligned} M_r &\rightarrow V_{r\beta} \\ M_s &\rightarrow V_{s\beta} \end{aligned} \quad \frac{8}{\hbar^2 \lambda'} \sum \frac{M_r^{(\lambda)} M_s^{(\lambda')} V_{r\beta}^{(-\lambda, -\lambda')} \omega_r^{(\lambda)} \omega_T^{(\lambda')}}{\omega_T^{2(\lambda)} \omega_T^{2(\lambda')}}$$

$$\begin{aligned} M_{r,s}\delta &\rightarrow M_s \\ M_{r,s}\delta &\rightarrow M_{s,r}\delta \end{aligned} \quad \frac{2}{\hbar \lambda} \sum \frac{M_{r,s}\delta^{(-\lambda)} M_{s,r}\delta^{(-\lambda)} \omega_r^{(\lambda)}}{\omega_r^{2(\lambda)} \omega_T^{2(\lambda)}}$$

$$P_{rs} \quad \boxed{V_{r\beta}} \quad \frac{2}{\hbar^2 \lambda'} \sum \frac{P_{rs}^{(\lambda, \lambda')} V_{r\beta}^{(-\lambda, -\lambda')} \omega_r^{(\lambda)} \omega_T^{(\lambda')}}{\omega_T^{2(\lambda)} \omega_T^{2(\lambda')}}$$

Figure 1. Electrostriction Diagrams and Their Contributions

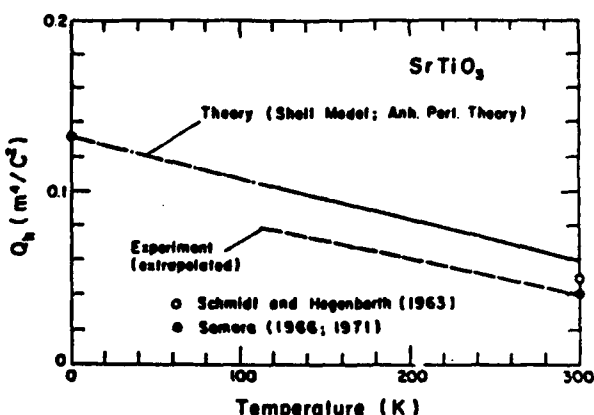


Figure 2. Variation of Q_h with Temperature

approximation of Cowley⁶ the numerators are evaluated by using the eigenvectors of the model RT of Ref. 8a.

In Fig. 2, are plotted the results for the hydrostatic ES coefficient Q_h versus temperature. It can be seen that there is good agreement with experiment so far as the temperature dependence is concerned, but that there is some discrepancy in the absolute value. There is, however, poor agreement for the other ES coefficients. The latter poor agreement is attributed to the neglect of many-body forces.

In conclusion, a calculation based on anharmonic many-body perturbation theory using the lowest order diagrams and an anharmonic shell model yields results in good agreement with the experimental temperature variation of Q_h . This good agreement arises as a result of both the improvement in the model and the inclusion of additional diagrams.

References

1. G. R. Barsch, B. N. N. Achary and L. E. Cross, *Ferroelectrics* 35, 187 (1981).
2. B. D. Silverman, *Phys. Rev.* 131, 2478 (1963).
- 3a. G. A. Samara, *Phys. Rev.* 151, 378 (1966); *Ferroelectrics* 2, 177 (1971).
- 3b. G. Schmidt and E. Hegenbarth, *Physica Status Solidi* 3, 329 (1963).
- 3c. G. Sorge, H. Beige and G. Schmidt, *Physica Status Solidi* a 26, K153 (1974).
- 3d. G. Ruprecht and W. H. Winter, *Phys. Rev.* 155, 1019 (1967).

- 3a. H. Beige and G. Schmidt, *Exp. Technik der Physik* 22, 393 (1974).
4. G. R. Barsch, B. N. N. Achar and L. E. Cross, *Ferroelectrics* 35, 191 (1981).
5. A. A. Maradudin and A. E. Fain, *Phys. Rev.* 128, 2589 (1962).
6. R. A. Cowley, *Adv. Phys.* 12, 421 (1963).
7. A. D. Bruce and R. A. Cowley, *J. Phys.* C6, 2422 (1973).
8. B. N. N. Achar, G. R. Barsch and L. E. Cross, (a) *Phys. Rev.* B24, 1209 (1981); (b) *Ferroelectrics* 37, 495 (1981).
9. B. N. N. Achar and G. R. Barsch, *Ferroelectrics* 37, 491 (1981).
10. R. A. Cowley, *Proc. Phys. Soc.* 84, 281 (1964).

APPENDIX 15

Origin of the first-order phase change at the Curie temperature in KNbO₃

L. Eric Cross

Materials Research Laboratory, Pennsylvania State University, University Park, Pennsylvania 16802

George A. Rossetti, Jr.^{a)}

Mitsubishi Kasei Corporation, Research Center, 1000 Kamoshida-cho, Midori-ku, Yokohama 227 Japan

(Received 26 March 1990; accepted for publication 9 October 1990)

As judged by the difference between Curie temperature T_c and Curie-Weiss temperature Θ ($T_c - \Theta \sim 53^\circ\text{C}$) KNbO₃ goes through a very strongly first-order phase change at T_c into a tetragonal ferroelectric phase. For BaTiO₃, it is known that the weaker first-order change at T_c ($T_c - \Theta \sim 10^\circ\text{C}$) derives from the electrostrictive coupling and that the strain-free crystal would go directly to rhombohedral symmetry by a second-order transition. It is the purpose of this note to point up the fact that in spite of the much stronger first-order change in KNbO₃, the origin is again in the electrostrictive coupling, and that the cubically clamped crystal would go through a second-order phase change.

I. INTRODUCTION

The ferroelectric perovskite KNbO₃ is qualitatively analogous to BaTiO₃, exhibiting the same ferroelectric phase transition sequence on cooling from high temperature (ie. Pm3m → P4mm → Bmm2 → R3m). As with BaTiO₃, all of these transitions are first order. If the difference $\Delta = (T_c - \Theta)$ is regarded as a measure of the first-order character of the ferroelectric-paraelectric (FE-PE) transition, however, this difference in KNbO₃ ($\Delta \sim 53^\circ\text{C}$) is seen to be significantly greater than that in BaTiO₃ ($\Delta \sim 10^\circ\text{C}$). Consequently, it might be suspected that the nature of the first-order FE-PE transition in the two crystals may be fundamentally different.

Consideration of a simple Devonshire free-energy formalism for KNbO₃ provides insight into the nature of the FE-PE transition. For BaTiO₃, Devonshire¹ showed that the weaker first-order change at T_c ($\Delta \sim 10^\circ\text{C}$) derives from the electrostrictive coupling and that the strain-free crystal would go directly to rhombohedral symmetry by a second-order transition. Consequently, by examining the sign of the fourth-rank dielectric stiffness coefficient in the Helmholtz free-energy expansion, it is possible to determine whether the first-order nature of the FE-PE transition in KNbO₃ arises as in BaTiO₃ due to the elastic coupling, or if it is in fact intrinsic to the strain-free crystal.

II. THERMODYNAMICS

To examine the origin of the FE-PE transition in KNbO₃, we consider the thermodynamic potential functions A and G , for the crystal subject to the constraints of constant elastic strain (x) and constant elastic stress (X), respectively. The Helmholtz (A) and elastic Gibbs (G) free-energy functions are defined by:

$$A = U - TS$$

and

$$G = U - TS - xX,$$

(1)

where U is the internal energy, S is the entropy, and T the absolute temperature. Appropriate Taylor series expansions of Eq. (1) yield expressions for the free-energy density wherein the sign of the fourth-rank dielectric stiffness tensor determines the order of the FE-PE phase transition.¹ Naturally, the thermodynamic potential functions of Eq. (1) are not independent, so that by finding the spontaneous strain matrix ($\delta G_i / \delta X_j$), defining $X = 0$, and substituting into the expression for A , the relationship between the fourth-rank dielectric stiffness coefficients in the two free-energy expansions can be readily obtained. Using standard reduced tensor notation, the desired relationships are:

$$\alpha_{11}^x = \alpha_{11}^x + 2(Q_{11}^2 + 2Q_{12}^2)c_{11} + 4Q_{12}(2Q_{11} + Q_{12})c_{12}$$

and

$$(2)$$

$$\alpha_{12}^x = \alpha_{12}^x + 2Q_{12}(2Q_{11} + Q_{12})c_{11} + 2(Q_{11}^2 + 3Q_{12}^2 + 2Q_{11}Q_{12})c_{12} + Q_{44}^2c_{44},$$

where α_{ij}^x and α_{ij}^y are the fourth-rank dielectric stiffness coefficients at constant strain and constant stress, respectively; the Q_{ij} are the cubic electrostrictive constants in polarization notation; and the c_{ij} are the cubic elastic stiffnesses at constant electric displacement. For a tetragonal crystal of symmetry P4mm derived from a cubic prototype of symmetry Pm3m, only the coefficient α_{11}^x requires evaluation. A positive value of the Helmholtz coefficient α_{11}^x would indicate that the strong first-order character of the FE-PE transition in KNbO₃ results from the electrostrictive coupling, while a negative value would imply that this behavior is intrinsic to the strain-free crystal. The constants in the expression for α_{11}^x are evaluated below.

A. Elastic Gibbs function coefficients

At constant and zero stress, an appropriate expression for the elastic Gibbs free-energy density for the tetragonal phase of KNbO₃ is:

$$G_1 = G_0 + 1/2\chi_0(T - \Theta)P_3^2 + 1/4\alpha_{11}^xP_3^4 + 1/6\alpha_{111}^xP_3^6,$$

(3)

where

$$G_0 = 0,$$

^{a)} Permanent address: Materials Research Laboratory, Pennsylvania State University, University Park, Pennsylvania 16802.

and

$$\chi_0 = 1/\epsilon_0 C.$$

In Eq. (3), P_i is a vector component of spontaneous polarization (P_s), ϵ_0 is the permittivity of free space, and C is the Curie constant. At T_c , we have from the equilibrium condition

$$G_1 = G_0 = 0, \quad (4)$$

which, when combined with the first partial derivative stability condition

$$\delta G_1 / \delta P_i = 0 \quad (5)$$

gives for the higher-order dielectric stiffness constants:

$$\alpha_{11}^Y = -4\chi_0(T_c - \Theta)/P_{sc}^2$$

and

$$\alpha_{111}^Y = 3\chi_0(T_c - \Theta)/P_{sc}^4, \quad (6)$$

where P_{sc} is the spontaneous polarization at T_c . From Eq. (5) we also have

$$P_i^2 = [-\alpha_{11}^Y + ((\alpha_{11}^Y)^2 - 4\alpha_{111}^Y\chi_0(T - \Theta))^{1/2}] / 2\alpha_{111}^Y. \quad (7)$$

From dielectric data on single crystals, Triebwasser² has previously determined the values of the higher-order dielectric stiffnesses and discussed their possible temperature dependence. Indeed, using Triebwasser's data, insertion of the experimental value of P_{sc} into Eq. (6) gave good agreement between the experimental spontaneous polarization ($P_s = P_i$) values and those obtained from Eq. (7) only at temperatures near T_c . Alternatively, P_{sc} can be chosen so as to provide the best fit of Eq. (7) to the experimental data over the complete temperature range. The latter procedure yielded

$$\alpha_{11}^Y = -1.7 \times 10^{-10} \text{ m}^2/\text{C}^2\text{F}$$

and

$$\alpha_{111}^Y = 2.1 \times 10^{-10} \text{ m}^6/\text{C}^4\text{F}.$$

The use of the experimental value of P_{sc} at T_c as opposed to the best-fit value resulted in only a modest (15%) difference in the associated values of α_{11}^Y . It will be seen that this difference is not sufficient to influence the result of the Helmholtz coefficient calculation. Therefore, any temperature dependence of the higher-order dielectric stiffnesses was neglected.

B. Spontaneous strains and electrostriction constants

The x-ray data of Shirane, Newnham, and Pepinsky³ were used to calculate the spontaneous strains and electrostriction constants in the tetragonal phase. The spontaneous strains (x_s) were calculated from:

$$x_s = (a_s - a'_c)/a'_c \text{ and } x_s = (c_s - c'_c)/a'_c, \quad (8)$$

where a_s and c_s are the tetragonal lattice constants and a'_c is the extrapolated cubic cell constant. The value a'_c was determined following the method of Haun, *et al.*⁴ by assuming that the electrostrictive constant ratio Q_{12}/Q_{11} is independent of temperature. This assumption, along with the electrostrictive strain equations

$$x_s = Q_{12}P_i^2 \text{ and } x_s = Q_{11}P_i^2, \quad (9)$$

gives the following relation for a'_c :

$$a'_c = [a_s - (c_s - c'_c)Q_{12}/Q_{11}] / (1 - Q_{12}/Q_{11}). \quad (10)$$

The Q_{12}/Q_{11} ratio was determined by extrapolating the experimental cubic cell constant (a_s) 15 °C to the first set of tetragonal lattice constant data (410 °C) using:

$$a_c(\text{\AA}) = aT(\text{°C}) + a_0, \quad (11)$$

where

$$a = 4.47598 \times 10^{-3} \text{ \AA/°C}$$

and

$$a_0 = 4.00237 \text{ \AA}.$$

A linear least squares correlation coefficient of 1.00 was obtained for the cubic cell data. Using Eqs. (8) and (9), this procedure gave a Q_{12}/Q_{11} ratio of -0.354. The extrapolated values of a'_c obtained using this ratio are plotted along with experimental values of a_s , c_s , and a_c in Fig. 1. Figure 2 shows the spontaneous strains determined from the x-ray data.

The spontaneous strain data of Fig. 2 were used along with the experimental spontaneous polarization data² to calculate the electrostriction constants from Eq. (9). The results are shown in Fig. 3. To the extent of the validity of the initial assumption regarding the Q_{12}/Q_{11} ratio, the values of the electrostriction constants obtained are seen to be relatively insensitive to temperature. The average values over the temperature range examined are

$$Q_{11} = 0.13 \text{ and } Q_{12} = -0.046 [\text{m}^4/\text{C}^2],$$

which are in excellent agreement with the room-temperature values of $Q_{11} = 0.13$ and $Q_{12} = -0.047$ obtained by Günter⁵ from piezoelectric measurements. Weisendanger⁶ obtained values of $Q_{11} = 0.13$ and $Q_{12} = -0.055$ by assuming a room-temperature value for P_s of 0.42 C/m², which is about 30% higher than the P_s value measured by Triebwasser.² The electrostriction constants obtained from the x-ray strain data were used in the remainder of the calculation.

C. Elastic constants

From piezoelectric measurements made on orthorhombic crystals, Weisendanger⁶ obtained the following room-temperature values for the elastic stiffness constants at constant electric displacement (c_y^0):

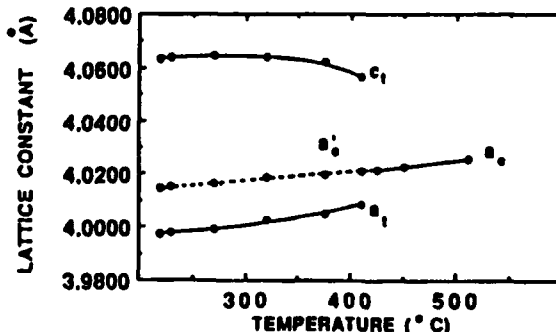


FIG. 1. Experimental lattice constants (from Ref. 3) of KNbO₃ against temperature. The extrapolated cubic cell constants a'_c were calculated from Eq. (10).

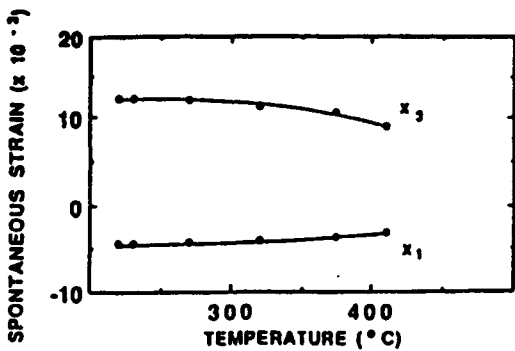


FIG. 2. Spontaneous strains x_3 and x_1 of KNbO_3 against temperature.

$$c_{11}^D = 2.800 \times 10^{11} \text{ N/m}^2, c_{44}^D = 0.940 \times 10^{11} \text{ N/m}^2, \\ \text{and } c_{33}^D = 1.135 \times 10^{11} \text{ N/m}^2.$$

The relations between the cubic and orthorhombic constants

$$c_{33}^D = 1/2(c_{11} + c_{12} + 2c_{44}), \\ c_{44}^D = c_{44}, \text{ and } c_{55}^D = 1/2(c_{11} - c_{12}) \quad (12)$$

gave the cubic stiffnesses at constant electric displacement (c_{ii}) as⁶

$$c_{11} = 3.00 \times 10^{11} \text{ N/m}^2, c_{12} = 0.71 \times 10^{11} \text{ N/m}^2, \\ \text{and } c_{44} = 0.95 \times 10^{11} \text{ N/m}^2.$$

Alternatively, the data of Nunes, Axe, and Shirane⁷ gave the following values from phonon dispersion curves measured at 460 °C:

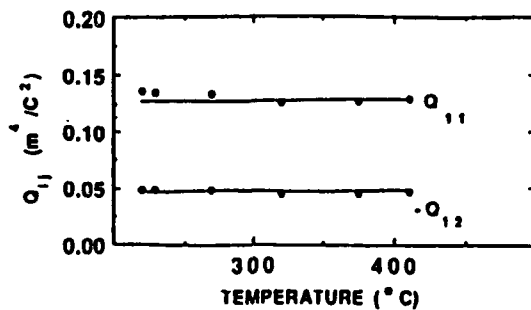


FIG. 3. Electrostriction constants Q_{11} and Q_{12} of KNbO_3 against temperature.

$$c_{11} = 2.55 \times 10^{11} \text{ N/m}^2, c_{12} = 0.80 \times 10^{11} \text{ N/m}^2, \\ \text{and } c_{44} = 0.90 \times 10^{11} \text{ N/m}^2.$$

While the two data sets are in reasonably good agreement, the data of Nunes, *et al.* more closely satisfies the isotropy condition ($2c_{44} = c_{11} - c_{12}$) and the Cauchy relation ($c_{44} = c_{12}$). The latter data set was selected for use in the present calculation, although the choice is not critical to the final result.

D. Helmholtz coefficient

Substituting $\alpha_{11}^X = -1.7 \times 10^9 \text{ m}^3/\text{C}^2\text{F}$ into Eq. (2) along with the electrostrictive and elastic constants given above we find that:

$$\alpha_{11}^X = -1.7 \times 10^9 + 7.6 \times 10^9$$

or

$$\alpha_{11}^X = +5.9 \times 10^9 \text{ m}^3/\text{C}^2\text{F},$$

where the magnitude of the positive elastic term is found to be more than four times greater than the magnitude of the negative Gibbs coefficient.

III. CONCLUSIONS

From the finding that the contribution of the positive elastic term to the Helmholtz coefficient is much larger than the contribution of the negative Gibbs term, it is inferred that like BaTiO_3 , the first-order nature of the transition in KNbO_3 (at T_c) results from the electrostrictive coupling. Consequently, despite the fact that the FE-PE transition exhibits anomalously strong first-order character ($T_c - \Theta \sim 53^\circ\text{C}$), this behavior is apparently not an intrinsic property of the strain-free crystal. It is therefore expected that the crystal subject to cubic clamping would undergo a second-order transition at Θ .

¹A. F. Devonshire, *Adv. Phys.* **3**, 85 (1954).

²S. Triebwasser, *Phys. Rev.* **101**, 993 (1956).

³G. Shirane, R. E. Newnham, and R. Pepinsky, *Phys. Rev.* **96**, 581 (1954).

⁴M. J. Haun, E. Furman, S. J. Jang, H. A. McKinstry, and L. E. Cross, *J. Appl. Phys.* **62**, 3331 (1987).

⁵P. Günter, *Jpn. J. Appl. Phys.* **16**, 1727 (1977).

⁶E. Weisendanger, *Ferroelectrics* **6**, 263 (1974).

⁷A. C. Nunes, J. D. Axe, and G. Shirane, *Ferroelectrics* **2**, 291 (1971).

APPENDIX 16

Thermodynamic Theory of Single-Crystal Lead Titanate with Consideration of Elastic Boundary Conditions

George A. Rossetti, Jr.,* K. R. Udayakumar,* Michael J. Haun,*† and L. Eric Cross*

Materials Research Laboratory, The Pennsylvania State University, University Park, Pennsylvania 16802

A phenomenological free-energy function including the effects of elastic boundary conditions was presented and used to investigate the single-domain, single-crystal properties of the ferroelectric perovskite, PbTiO_3 . In particular, the effects of tensile and compressive hydrostatic stress on the spontaneous polarization, Curie point, dielectric susceptibility, and piezoelectric property coefficients were examined. The calculated shift of the Curie point with hydrostatic stress, along with the entropy and enthalpy of the ferroelectric-paraelectric phase transition, was found to be in good agreement with experimental measurements. The isothermal variation of the relative dielectric susceptibility and piezoelectric coefficients with hydrostatic stress exhibited the expected behavior near the ferroelectric-paraelectric phase transition. [Key words: thermodynamics, lead titanate, single crystals, stress, electrical properties.]

I. Introduction

EXPERIMENTAL studies of the effect of hydrostatic stress on the single-crystal properties of technologically important ferroelectric perovskites such as BaTiO_3 and PbTiO_3 , have proven useful in understanding their ferroelectric properties, particularly in the region near the ferroelectric-paraelectric (FE-PE) phase transition.¹ Although the effects of hydrostatic stress on the properties of BaTiO_3 have been extensively investigated,^{2,3} accurate measurements of the single-crystal properties for pure PbTiO_3 are difficult because Pb^{2+} losses at temperatures near the Curie point result in high electrical conductivity.⁴ This has dictated the use of samples doped with U or Nb charge compensators to enhance resistivity,¹ so that, even at ambient pressure, considerable discrepancies in reported property data exist because of differences in crystal quality. As a consequence, few data are available regarding the effect of hydrostatic stress on the phase transitions and properties of pure single-domain, single-crystal PbTiO_3 .

For U-doped crystals below 407°C, Samara⁴ successfully measured the pressure dependence of the permittivity and Curie point at hydrostatic stresses up to 3 GPa. Other less extensive examinations of doped crystals under hydrostatic stress have also been reported.^{5,6} The pressure dependence of the dielectric and piezoelectric properties for pure, single-crystal PbTiO_3 was calculated by Amin *et al.*⁷ from a phenomenological free-energy function. These results were obtained as part of a more extensive investigation involving PbZrO_3 - PbTiO_3 (PZT) solid solutions,⁸ wherein the polarization interaction coefficients of the energy function for PbTiO_3 were determined by extrapolation from values obtained by fitting the morphotropic phase boundary. Since Amin *et al.* primar-

ily considered morphotropic PZT compositions, no data were reported regarding the effects of elastic boundary conditions on the Curie point and energetics of the FE-PE phase transition for pure PbTiO_3 . Recently, however, the coefficients in the energy function for PbTiO_3 have been refined by Haun *et al.*⁹ from high-temperature X-ray strain measurements made on pure, sol-gel-derived powders. Using these coefficients, a more thorough investigation of the effect of elastic boundary conditions on pure, single-crystal PbTiO_3 is possible.

In the present study, therefore, a simple phenomenological free-energy function that includes the effects of elastic boundary conditions is presented and used along with the coefficients of Haun *et al.*⁹ to predict the properties of pure, single-domain, single-crystal PbTiO_3 . In particular, the effects of tensile and compressive hydrostatic stress on the spontaneous polarization, Curie point, dielectric susceptibility, and piezoelectric property coefficients are investigated.

II. Theoretical Approach

Using reduced tensor notation, the Landau-Ginsburg-Devonshire (LGD)¹⁰ free-energy function of a proper ferroelectric derived from a phase of prototypic symmetry $Pm\bar{3}m$ may be expressed as a Taylor series in dielectric polarization as follows:

$$\begin{aligned}
 G_1 = & \alpha_1(P_1^2 + P_2^2 + P_3^2) + \alpha_{11}(P_1^4 + P_2^4 + P_3^4) \\
 & + \alpha_{12}(P_1^2 P_2^2 + P_2^2 P_3^2 + P_3^2 P_1^2) \\
 & + \alpha_{111}(P_1^6 + P_2^6 + P_3^6) \\
 & + \alpha_{112}[P_1^4(P_2^2 + P_3^2) + P_2^4(P_1^2 + P_3^2) \\
 & \quad + P_3^4(P_1^2 + P_2^2)] \\
 & + \alpha_{123}(P_1^2 P_2^2 P_3^2) - \frac{1}{2} s_{11}(X_1^2 + X_2^2 + X_3^2) \\
 & - s_{12}(X_1 X_2 + X_2 X_3 + X_3 X_1) \\
 & - \frac{1}{2} s_{14}(X_4^2 + X_5^2 + X_6^2) \\
 & - Q_{11}(X_1 P_1^2 + X_2 P_2^2 + X_3 P_3^2) \\
 & - Q_{12}[X_1(P_2^2 + P_3^2) + X_2(P_1^2 + P_3^2) \\
 & \quad + X_3(P_1^2 + P_2^2)] \\
 & - Q_{44}(X_4 P_2 P_3 + X_5 P_1 P_3 + X_6 P_1 P_2) \quad (1)
 \end{aligned}$$

where P_i and X_i are the polarizations and stresses, respectively; α_i , α_{ij} , and α_{ijk} are the dielectric stiffness and higher order stiffness coefficients at constant stress; s_{ij} are the elastic compliances at constant polarization; and Q_{ij} are the cubic electrostrictive constants in polarization notation.

In the reduced notation, the tensile stresses are denoted by X_1 , X_2 , X_3 , and the shear stresses by X_4 , X_5 , X_6 . Consequently, for a hydrostatic stress (σ)

$$X_1 = X_2 = X_3 = \sigma$$

$$X_4 = X_5 = X_6 = 0$$

W. A. Schulze — contributing editor

Manuscript No. 197808. Received January 30, 1990; approved July 5, 1990.

*Member, American Ceramic Society.

†Now at DuPont Experimental Station, Electronics Department, Building 334, Wilmington, DE 19880.

and Eq. (1) then takes the form

$$\begin{aligned} G_1 = & -(3s_{11} + 6s_{12})\sigma^2/2 \\ & + [\alpha_1 - (Q_{11} + 2Q_{12})\sigma](P_1^2 + P_2^2 + P_3^2) \\ & + \alpha_{11}(P_1^4 + P_2^4 + P_3^4) \\ & + \alpha_{12}(P_1^2 P_2^2 + P_2^2 P_3^2 + P_3^2 P_1^2) \\ & + \alpha_{111}(P_1^6 + P_2^6 + P_3^6) \\ & + \alpha_{112}[P_1^4(P_2^2 + P_3^2) + P_2^4(P_1^2 + P_3^2) \\ & + P_3^4(P_1^2 + P_2^2)] + \alpha_{123}(P_1^2 P_2^2 P_3^2) \end{aligned} \quad (2)$$

Since the elastic and electrostrictive terms both carry negative signs, the appropriate sign convention is adopted such that compressive stress is denoted by negative values of σ .¹¹ Equation (2) has two solutions of interest for PbTiO₃, corresponding to the cubic (*Pm3m*) and tetragonal (*P4mm*) states. These are

$$\begin{aligned} P_1^2 = P_2^2 = P_3^2 = 0 & \quad (\text{cubic}) \\ P_1^2 = P_2^2 = 0, P_3^2 \neq 0 & \quad (\text{tetragonal}) \end{aligned} \quad (3)$$

By applying Eq. (3) to Eq. (2) the free energy functions for the cubic and tetragonal states are obtained as

$$G_1 = -(3s_{11} + 6s_{12})\sigma^2/2 \quad (\text{cubic}) \quad (4)$$

$$\begin{aligned} G_1 = & -(3s_{11} + 6s_{12})\sigma^2/2 + [\alpha_1 - (Q_{11} + 2Q_{12})\sigma]P_3^2 \\ & + \alpha_{11}P_3^4 + \alpha_{111}P_3^6 \quad (\text{tetragonal}) \end{aligned} \quad (5)$$

The spontaneous polarization in Eq. (5) is determined from the first partial derivative stability condition

$$\delta G/\delta P_i = 0 \quad (6)$$

which together with Eqs. (2) and (3) yields for the tetragonal state

$$\begin{aligned} P_3^2 = & \{-\alpha_{11} + [\alpha_{11}^2 - 3\alpha_{111}] \\ & \times (\alpha_1 - (Q_{11} + 2Q_{12})\sigma)\}^{1/2}/3\alpha_{111} \end{aligned} \quad (7)$$

The shift in the Curie point (T_c) with hydrostatic stress was determined by finding the intersections of the cubic and tetragonal free-energy curves given by Eqs. (4) and (5). At each intersection, the prevailing stress (σ_c) is defined as the stress required to induce the FE-PE transition at the temperature specified. The shift in T_c with hydrostatic stress had been previously estimated for BaTiO₃, by imposing the condition to Eq. (7) that the spontaneous polarization in the paraelectric state is no longer real.¹² This is equivalent to assigning a value of zero to the square root in Eq. (7) above the Curie point, such that

$$\begin{aligned} \alpha_{11}^2 - 3\alpha_{111}[\alpha_1 - (Q_{11} + 2Q_{12})\sigma] &= 0 \\ \sigma_c^* = [3\alpha_1\alpha_{111} - \alpha_{11}^2]/[3\alpha_{111}(Q_{11} + 2Q_{12})] & \end{aligned} \quad (8)$$

where σ_c^* is the approximate stress at the FE-PE transition. For a first-order transition, however, it is more rigorous to find the transition stress by equating the energies of the cubic and tetragonal phases as described above. In the present case, the value of σ_c^* determined from Eq. (8) exceeds σ_c by approximately 0.05 GPa. At a specified stress, this corresponds to a difference in the calculated values of T_c of $\sim 4.5^\circ\text{C}$.

Appropriate second partial derivatives of Eq. (2) give the reciprocal dielectric susceptibilities (χ_{ij}) (i.e., dielectric stiffnesses) and the piezoelectric constants (b_{ij})

$$\begin{aligned} \delta^2 G/\delta P_i \delta P_j &= \chi_{ij} \\ \delta^2 G/\delta P_i \delta X_j &= -b_{ij} \end{aligned} \quad (9)$$

The relative dielectric susceptibilities (η_{ij}) of the tetragonal state are obtained from Eqs. (2), (3), and (9), and are given by

$$\begin{aligned} \eta_{11} &= (2\epsilon_0[\alpha_1 - (Q_{11} + 2Q_{12})\sigma] + \alpha_{12}P_3^2 + \alpha_{112}P_3^4)^{-1} \\ \eta_{33} &= (2\epsilon_0[\alpha_1 - (Q_{11} + 2Q_{12})\sigma] + 6\alpha_{11}P_3^2 \\ & + 15\alpha_{111}P_3^4)^{-1} \end{aligned} \quad (10)$$

where ϵ_0 is the permittivity of free space.

The piezoelectric charge coefficients (d_{ij}) are defined by

$$d_{ij} = b_{ij}\eta_{ij} \quad (11)$$

and are therefore given for the tetragonal state by

$$d_{33} = 2\epsilon_0\eta_{33}Q_{11}P_3$$

$$d_{31} = 2\epsilon_0\eta_{33}Q_{12}P_3$$

$$d_{13} = 2\epsilon_0\eta_{11}Q_{11}P_3 \quad (12)$$

The piezoelectric voltage coefficients (g_{ij}) are proportional to the b_{ij} coefficients by a factor of $(K - 1)/K$, where K is the dielectric constant. Since $K \gg 1$ for PbTiO₃, the piezoelectric voltage coefficients of the tetragonal state may be approximated by

$$g_{33} = b_{33} = 2Q_{11}P_3$$

$$g_{31} = b_{31} = 2Q_{12}P_3$$

$$g_{13} = b_{13} = 2Q_{11}P_3 \quad (13)$$

Equation (2) shows that the effect of hydrostatic stress on the free-energy function enters primarily through the term involving the electrostriction constants since the purely elastic contribution to the relative free energies of the cubic and tetragonal states is the same (Eqs. (4) and (5)). The effect of temperature on the free-energy function enters through the dielectric stiffness constant (α_1) which was given a linear temperature dependence based on the Curie-Weiss law.

$$\alpha_1 = (T - \theta)/2\epsilon_0 C \quad (14)$$

where C is the Curie constant and θ is the Curie-Weiss temperature. All other coefficients were assumed independent of temperature and stress and have the values given in Table I. Although this assumption may not be strictly valid,³ Goswami¹² has shown the approximation to give excellent results for single-crystal BaTiO₃. With the exception of the elastic compliances,¹³ the values of the coefficients in Table I were determined by spontaneous strain measurements¹ made on pure, sol-gel-derived PbTiO₃ powders.¹⁴

III. Results and Discussion

(I) Spontaneous Polarization, Curie Point, and Relative Phase Stabilities

The hydrostatic stress dependence of the spontaneous polarization (P_i) for single-domain, single-crystal PbTiO₃ in the

Table I. Constants Used with Eq. (2)*

Parameter	Value
T_c ($^\circ\text{C}$) ($\sigma = 0$)	492.2
θ ($^\circ\text{C}$)	478
C ($10^{-3} \text{ }^\circ\text{C}$)	1.5
Q_{11} ($10^{-2} \text{ m}^4/\text{C}^2$)	8.9
Q_{12} ($10^{-2} \text{ m}^4/\text{C}^2$)	-2.6
Q_{44} ($10^{-2} \text{ m}^4/\text{C}^2$)	6.75
s_{11} ($10^{-12} \text{ m}^2/\text{N}$)	6.785 ^t
s_{12} ($10^{-12} \text{ m}^2/\text{N}$)	-2.5 ^t
α_1 (10^6 m/F) at T_c ($\sigma = 0$)	5.045
α_1 (10^6 m/F) at 25°C ($\sigma = 0$)	-1.708
α_{11} ($10^7 \text{ m}^5/(\text{C}^2 \cdot \text{F})$)	-7.252
α_{12} ($10^8 \text{ m}^5/(\text{C}^2 \cdot \text{F})$)	7.5
α_{111} ($10^8 \text{ m}^9/(\text{C}^4 \cdot \text{F})$)	2.606
α_{112} ($10^8 \text{ m}^9/(\text{C}^4 \cdot \text{F})$)	6.1
α_{123} ($10^9 \text{ m}^9/(\text{C}^4 \cdot \text{F})$)	-3.36

*From Ref. 9. ^tFrom Ref. 13.

tetragonal state is shown at various temperatures in Fig. 1. Under hydrostatic compression, the polarization decreases with increasing stress and drops discontinuously to zero at σ_c , the stress required by Eq. (8) above the FE-PE transition. At room temperature, σ_c takes a value of 4.8 GPa. Under hydrostatic tension, the spontaneous polarization increases gradually from the zero stress value. Although no experimental polarization versus stress data for PbTiO₃ are available for comparison, the general shapes of the curves in the compressive region of Fig. 1 are similar to those experimentally determined for single-crystal BaTiO₃.²

The hydrostatic stress dependence of the Curie point determined from Eqs. (4) and (5) is shown along with the experimental data of Samara⁴ in Fig. 2. The value of $-dT_c/d\sigma = 98^\circ\text{C/GPa}$ was determined from the theory, as compared to the value of 84°C/GPa determined by Samara from the initial slope of a smooth curve drawn as a least-squares fit to the high-pressure data and the ambient-pressure value. A value of 84°C/GPa was also obtained from high-pressure structural studies.⁵ The positive deviation from linearity in the experimental T_c vs σ curve of Fig. 2 might suggest that true hydrostatic conditions may not have prevailed at the higher stresses, thereby artificially lowering the observed value of $-dT_c/d\sigma$.³ Alternatively, this deviation may be indicative of a transition to second-order behavior with increasing hydrostatic stress.⁴ It is clear that the simply formulated free-energy function of Eq. (2) (with pressure independent coefficients) will not predict such a transition. For the present purposes, however, it is sufficient to consider that the main effect of an applied hydrostatic stress is to shift the P_s vs T curve along the T -axis. The implication is then that the dipole moment is relatively insensitive to stress, such that the chief effect of hydrostatic stress on the properties of pure, single-crystal PbTiO₃ lies in its influence on T_c . Recognizing the limitations of such a treatment, predictions of the energetics of the FE-PE transition made on this basis are nevertheless found to be in quite good agreement with the experimental measurements, as discussed below.

The calculated value of $-dT_c/d\sigma$ was used along with the Clausius-Clapeyron equation to determine the enthalpy and entropy change at the first-order FE-PE transition.

$$dT_c/d\sigma = T_c \Delta V / \Delta H = \Delta V / \Delta S \quad (15)$$

The value of $\Delta V(\text{FE-PE}) = -0.2041 \times 10^{-6} \text{ m}^3/\text{mol}$, obtained from high-temperature X-ray measurements,⁹ gives $\Delta S = 2.1 \text{ J}/(\text{mol} \cdot \text{K})$ and $\Delta H = 1590 \text{ J/mol}$. These values are in excellent agreement with the experimentally determined values⁴ of $\Delta S = 1.9 \pm 0.2 \text{ J}/(\text{mol} \cdot \text{K})$ and $\Delta H = 1460 \pm 190 \text{ J/mol}$. Consequently, it is expected that calculations made using Eq. (2), with the coefficients of Table I, will provide rea-

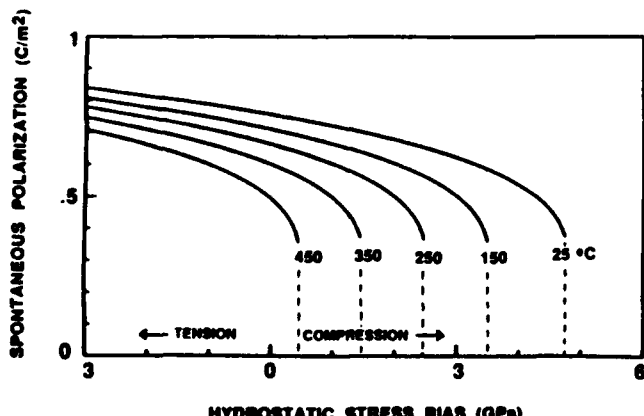


Fig. 1. Calculated spontaneous polarization versus hydrostatic stress at various temperatures.

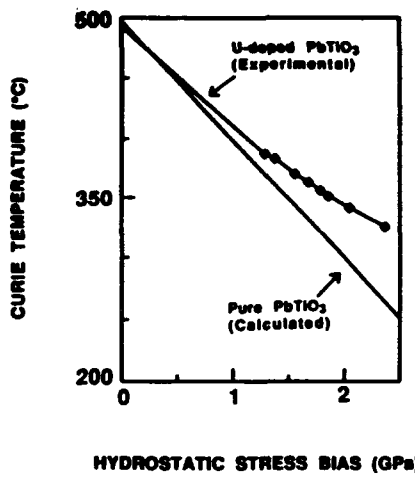


Fig. 2. Comparison of experimental and calculated shift of the Curie point with hydrostatic stress. Experimental data are for U-doped crystals (after Samara, Ref. 4).

sonable approximations of the dielectric and piezoelectric properties.

In the foregoing, it was tacitly assumed that the tetragonal phase is the stable phase at all hydrostatic stresses below σ_c . Although BaTiO₃ transforms to an orthorhombic phase on cooling,² no such transformation has been observed for PbTiO₃. Since the orthorhombic phase would be expected to occupy a larger volume relative to the tetragonal phase, the possibility exists of destabilizing the tetragonal phase under a sufficiently large hydrostatic tensile stress.

To examine this possibility, the appropriate solution for the orthorhombic (*Bmm2*) state (i.e., $P_1^2 = P_2^2 \neq 0, P_3^2 = 0$) was used with Eq. (2) to calculate the relative free energies of the tetragonal and orthorhombic states as a function of hydrostatic stress and temperature. It has been previously shown⁹ that, under zero stress conditions, the value of $\phi = -\alpha_{12}/\alpha_{11}$ primarily controls the relative stability of the orthorhombic and tetragonal phases at temperatures down to -273°C . The free-energy calculations made using Eq. (2) showed that, even at -273°C , the value of ϕ is sufficiently large to destabilize the orthorhombic phase to hydrostatic tensile stresses of up to $\sim 530 \text{ GPa}$. Consequently, under physically realizable conditions, the calculations suggest that only the properties of the tetragonal state require consideration.

(2) Dielectric Susceptibility and Piezoelectric Coefficients

The pressure dependence at 25°C of the relative dielectric susceptibility coefficients is shown in Fig. 3. In accordance with Fig. 2, similar curves displaced along the σ -axis are obtained at other temperatures. Consistent with experiment,⁴ the dielectric susceptibility increases rapidly close to σ_c . Near the transition, the susceptibility (η_{33}) parallel to the polar axis is much greater than the perpendicular susceptibility (η_{11}), but at stresses below $\sim 3.5 \text{ GPa}$, the two curves intersect. As with the tetragonal phase stability, the value of ϕ controls the dielectric anisotropy.⁹ Following from the earlier discussion of Fig. 2, the isothermal variation of the dielectric anisotropy with hydrostatic stress is in all respects analogous to the isobaric variation with temperature.⁹

The pressure dependence at 25°C of the piezoelectric charge and voltage coefficients is shown in Figs. 4 and 5, respectively. The charge coefficients increase rapidly near σ_c because of the strong pressure dependence of the dielectric susceptibilities. The voltage coefficients vary only with polarization and therefore decrease with stress and drop discontinuously to zero near σ_c . As with the dielectric susceptibilities, curves similar to those in Figs. 4 and 5 shifted along the σ -axis are obtained at other temperatures. Again, the isothermal variation of the piezoelectric coefficients with

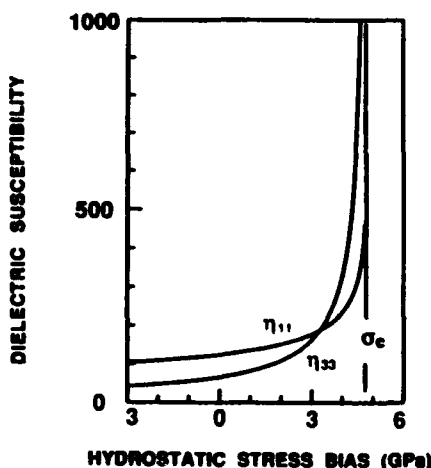


Fig. 3. Calculated relative dielectric susceptibility coefficients versus hydrostatic stress at 25°C. Compressive region is to the right of the origin, tensile region to the left.

hydrostatic stress is analogous to the isobaric variation with temperature.⁹

IV. Summary

A phenomenological free-energy function including the effects of elastic boundary conditions was presented and used to predict the properties of single-domain, single-crystal PbTiO₃. In the present theory, the hydrostatic stress dependence of the single-domain, single-crystal properties can be interpreted in terms of the displacement with stress of the spontaneous polarization (P_s) versus temperature (T) curve along the T -axis. The calculated shift of the Curie point with hydrostatic stress ($-dT_c/d\sigma = 98^\circ\text{C/GPa}$), along with the calculated entropy ($\Delta S = 2.1 \text{ J}/(\text{mol}\cdot\text{K})$) and enthalpy ($\Delta H = 1590 \text{ J/mol}$) of the ferroelectric-paraelectric phase transition, was found to be in good agreement with experimental measurements. Also in agreement with experiment, the orthorhombic phase was found to be metastable relative to the tetragonal phase. At absolute zero, the metastability of the orthorhombic phase was calculated to persist even under the application of high hydrostatic tensile stresses. Predictions of the isothermal variation of the relative dielectric susceptibility and piezoelectric coefficients with hydrostatic stress showed the expected behavior near the ferroelectric-paraelectric phase transition.

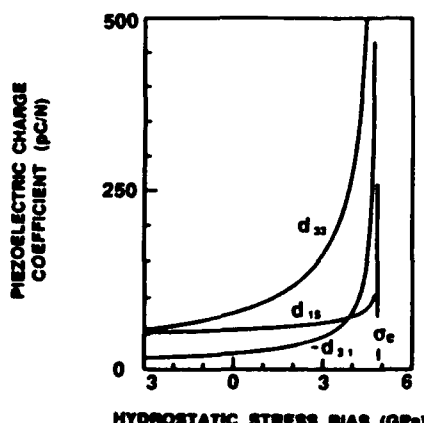


Fig. 4. Calculated piezoelectric charge coefficients versus hydrostatic stress at 25°C. Compressive region is to the right of the origin, tensile region to the left.

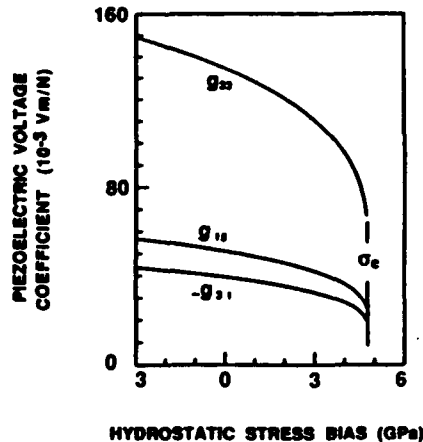


Fig. 5. Calculated piezoelectric voltage coefficients versus hydrostatic stress at 25°C. Compressive region is to the right of the origin, tensile region to the left.

The present calculations confirm the utility of the simply formulated Landau-Ginsburg-Devonshire (LGD) formalism, as well as the validity of the associated coefficients used, in describing the static, single-domain, single-crystal properties of PbTiO₃, subject to elastic boundary conditions. In subsequent work, we intend to extend the present calculations using the coefficients recently determined¹⁵⁻¹⁹ for the PbZrO₃-PbTiO₃ solid-solution system to investigate the effects of elastic boundary conditions on technologically important compositions near the morphotropic phase boundary.

Acknowledgments: The authors appreciate the helpful suggestions of the reviewers for improving the manuscript.

References

- M. E. Lines and A. M. Glass, *Principles and Applications of Ferroelectrics and Related Materials*; pp. 160, 249. Oxford University Press, Oxford, U.K., 1979.
- G. A. Samara, "Pressure and Temperature Dependences of the Dielectric Properties of the Perovskites BaTiO₃ and SrTiO₃," *Phys. Rev.*, **151** [2] 378-86 (1966).
- G. A. Samara, "The Effects of Hydrostatic Pressure on Ferroelectric Properties"; pp. 155-239 in *Advances in High-Pressure Research*, Vol. 3. Edited by R. S. Bradley. Academic Press, New York, 1969.
- G. A. Samara, "Pressure and Temperature Dependence of the Dielectric Properties and Phase Transitions of the Ferroelectric Perovskites: PbTiO₃ and BaTiO₃," *Ferroelectrics*, **2**, 277-89 (1971).
- T. Ikeda, "Effect of Hydrostatic Pressure on the Phase Transition of Ferroelectric PbTiO₃," *Solid State Commun.*, **16**, 103-104 (1975).
- R. J. Nelmes and A. Katrusiak, "Evidence for Anomalous Pressure Dependence of the Spontaneous Strain in PbTiO₃," *J. Phys. C: Solid State Phys.*, **19**, L725-30 (1986).
- A. Amin, R. E. Newnham, and L. E. Cross, "Effect of Elastic Boundary Conditions on Morphotropic Pb(Zr,Ti)O₃ Piezoelectrics," *Phys. Rev. B: Condens. Matter*, **34** [3] 1595-98 (1986).
- A. Amin, M. J. Haun, B. Badger, H. A. McKinstry, and L. E. Cross, "A Phenomenological Gibbs Function for the Single-Cell Region of the PbZrO₃-PbTiO₃ Solid Solution System," *Ferroelectrics*, **65**, 107-30 (1985).
- M. J. Haun, E. Furman, S. J. Jang, H. A. McKinstry, and L. E. Cross, "Thermodynamic Theory of PbTiO₃," *J. Appl. Phys.*, **62** [8] 3331-38 (1987).
- A. F. Devonshire, "Theory of Barium Titanate, Part I," *Philos. Mag.*, **40**, 1040-63 (1949).
- A. Amin, L. E. Cross, and R. E. Newnham, "Sign Notation in Ferroelectric Free-Energy Functions," *Ferroelectrics*, **99**, 145-48 (1989).
- A. K. Goswami, "Theory on the Effect of Hydrostatic Pressure on the Permittivity and Curie Point of Single-Crystal Barium Titanate," *J. Phys. Soc. Jpn.*, **21**, 1037-40 (1966).
- H. Landolt and B. Bornstein, *Ferroelectric and Antiferroelectric Substances*. Springer Verlag, Berlin, FRG, 1975.
- Z. Q. Zhuang, M. J. Haun, S. J. Jang, and L. E. Cross, "Fabrication and Characterization of Pure Homogeneous PZT Ceramics from Sol-Gel-Derived Powders," *Adv. Ceram. Mater.*, **3** [5] 485-97 (1988).
- M. J. Haun, E. Furman, S. J. Jang, and L. E. Cross, "Thermodynamic Theory of the Lead Zirconate-Titanate Solid Solution System, Part I: Phenomenology," *Ferroelectrics*, **99**, 13-25 (1989).
- M. J. Haun, E. Furman, H. A. McKinstry, and L. E. Cross, "Thermo-

dynamic Theory of the Lead Zirconate-Titanate Solid Solution System, Part II: Tricritical Behavior," *Ferroelectrics*, **99**, 27–44 (1989).

¹⁷M. J. Haun, Z. Q. Zhuang, E. Furman, S. J. Jang, and L. E. Cross, "Thermodynamic Theory of the Lead Zirconate-Titanate Solid Solution System, Part III: Curie Constant and Sixth-Order Polarization Interaction Dielectric Stiffness Coefficients," *Ferroelectrics*, **99**, 45–54 (1989).

¹⁸M. J. Haun, E. Furman, T. R. Halemane, and L. E. Cross, "Thermodynamic Theory of the Lead Zirconate-Titanate Solid Solution System, Part IV: Tilting of the Oxygen Octahedra," *Ferroelectrics*, **99**, 55–62 (1989).

¹⁹M. J. Haun, E. Furman, S. J. Jang, and L. E. Cross, "Thermodynamic Theory of the Lead Zirconate-Titanate Solid Solution System, Part V: Theoretical Calculations," *Ferroelectrics*, **99**, 63–86 (1989). □

APPENDIX 17

(submitted to Journal of Applied Physics)

**X-RAY AND PHENOMENOLOGICAL STUDY OF LANTHANUM
MODIFIED LEAD ZIRCONATE - TITANATE COMPOSITIONS INCIPENT
TO THE RELAXOR FERROELECTRIC PHASE TRANSITION REGION**

G. A. Rossetti, Jr.^{a)} and T. Nishimura
Research Center, Mitsubishi Kasei Corporation
1000 Kamoshida-cho, Midori-ku, Yokohama, 227 Japan

L. E. Cross
Materials Research Laboratory, Pennsylvania State University
University Park, Pennsylvania 16802 U.S.A.

X-ray diffraction analyses of chemically derived $Pb_{1-x}La_x(Zr_{0.65}Ti_{0.35})_{1-x/4}O_3$ (PLZT) powders were combined with a phenomenological theory to investigate the corresponding single-crystal ferroelectric properties of compositions incipient to the relaxor phase transition region ($x = 0 - 0.04$). The powder diffraction analyses served to quantify the temperature and composition dependences of two types of strain arising in these materials: 1) strain that is electrostrictive in origin (spontaneous strain) and 2) the strain associated with composition and/or structure-state fluctuations (lattice strain). The combined results suggested that small deviations from the average composition (x) may result in significant inhomogeneities in the internal strain field. The temperature dependence of the electrostrictive strain component x_4 was found to be well described by the Landau-Ginsburg-Devonshire theory taking $T_c = 357^\circ C$ independent of La content (x). This result allowed for the calculation of the single-domain, single-crystal elastic Gibbs free-energy density as a function of temperature and composition. Based on a simple superparaelectric model of relaxor behavior involving the temperature stabilization of noninteracting polar microregions, the calculations suggested that the stability of the polar regions against thermal agitation becomes strongly composition dependent when their size is reduced below the range of 5 - 15 nm.

^{a)} Permanent Address: Materials Research Laboratory, Pennsylvania State University, University Park, Pennsylvania 16802 U. S. A.

I. INTRODUCTION

Ferroelectrics showing relaxor phase transition behavior are of considerable theoretical as well as practical interest. These materials find a variety of applications in ceramic form, particularly as electrostrictive actuators and capacitor dielectrics. The best studied class of relaxor ferroelectrics are compounds and solid solutions of oxides crystallizing with the simple perovskite structure. Although the mechanisms underlying relaxor behavior in the perovskite-based systems are not yet clear, frustration of the normal ferroelectric transition appears to arise in general due to nanostructural lattice imperfections which locally lower, but do not destroy entirely, the translational symmetry. Smolenski¹ first proposed the widely held view that the origin of the symmetry lowering lies in chemical microheterogeneity, which in turn results in a broad distribution of local Curie temperatures. Alternatively, from a series of transmission electron microscope (TEM) studies², it now appears that for the complex $A(B_1B_2)O_3$ perovskite compounds, the origin lies in the coherence length of the long range B-site ordering. Other structural features involving defect dipoles, inhomogeneous order, and incommensurate phase transitions may also play a role in relaxor behavior³.

Cross⁴ has pointed out that the development of a stable ferroelectric polarization within a postulated microregion of a relaxor crystal requires that the energy barrier separating symmetry equivalent polarization orientation states be sufficient to stabilize the region against thermal agitation. Since ferroelectricity is a cooperative phenomenon, all energies scale with volume. Consequently, by analogy with ferromagnetism, superparaelectric behavior may result if the microregions cannot develop sufficient volume stabilization or electrocrystalline anisotropy energy with respect to other degrees of freedom. Although the superparaelectric model accounts for many of the observed properties of relaxor ferroelectrics, such as the frequency dependence of the permittivity and dielectric aging^{5,6}, few quantitative estimates have been reported regarding the microregion size and/or composition dependence of the energy barriers separating equivalent polarization orientation states for actual relaxor crystals.

The Landau-Ginsburg-Devonshire (LGD) free-energy formalism provides a realistic macroscopic thermodynamic description of the single-domain, single-crystal elastodielectric properties of normal (proper) ferroelectric materials⁷. In the absence of suitable quality single-crystal samples, high-temperature cell parameter measurements have proved invaluable in the development of the phenomenological thermodynamic theories for several perovskite ferroelectrics and their solid solutions^{8,9}. These measurements establish the temperature dependence of the spontaneous elastic strain, which is related through the electrostrictive strain equations to the spontaneous polarization. The spontaneous polarization is the macroscopic order parameter for the paraelectric-ferroelectric (PE-FE) phase transition, and its temperature dependence can be used to determine the higher-order polarization interaction coefficients needed to evaluate the elastic Gibb's free-energy density function.

Previous investigations have utilized this approach extensively in phenomenological studies of the $\text{PbZr}_y\text{Ti}_{1-y}\text{O}_3$ (PZT) solid solution system^{10,11}. In the present work, we extend the X-ray measurements to the $\text{Pb}_{1-x}\text{La}_x(\text{Zr}_y\text{Ti}_{1-y})_{1-x/4}\text{O}_3$ ^{b)} (PLZT) system and consider compositions where $y = 0.65$ and $x = 0 - 0.04$ (also denoted X/65/35 with X = 0 - 4). As judged from the published phase diagram¹² shown in Figure 1, compositions in this series begin to assume significant relaxor ferroelectric character at compositions near $x = 0.04$. Although the nanostructural features leading to relaxor behavior in PLZT solid solutions are not yet entirely understood, it is clear that they are intimately associated with the La content (x). This observation does not necessarily imply the distribution of Curie temperatures (and the corresponding predictions) of the Smolenski model¹. Alternatively, recent studies¹³ suggest that nanostructural features potentially modulated through the La content, such as the distribution and/or ordering of Pb vacancies and the associated defect dipoles, may break the translational symmetry sufficiently to localize the polarization to

^{b)} The choice of the B-site vacancy formula for the synthesis of these compositions was arbitrary and not meant to imply a particular defect structure.

superparaelectric regions on a size scale appropriate to interpretation on the basis of a spin-glass model¹⁴.

It is the purpose of the present paper to describe an initial X-ray and phenomenological study of the La-modified PZT system. For this study, alkoxy-derived PLZT powders were prepared with compositions approaching those in the relaxor ferroelectric phase transition region ($x = 0.00 - 0.04$). Precise cell parameter and X-ray line broadening measurements were combined to quantify the composition and temperature dependences of both the spontaneous and root mean square (RMS) lattice strains. The temperature dependence of the spontaneous strain was modelled using the LGD free-energy formalism. The results are discussed on the basis of a simple superparaelectric model of relaxor behavior.

II. EXPERIMENTAL PROCEDURE

The PLZT powders were prepared from lead acetate trihydrate, lanthanum isopropoxide, zirconium n-butoxide, and titanium isopropoxide according to a modification of a procedure described earlier¹⁵. All manipulations of the starting chemicals and reaction mixtures were carried out in a glove box under dry nitrogen. Initially, 1:8 (m/m) solutions of the lead compound and of the combined alkoxides in 2-methoxyethanol (2-MOE) were prepared. The Pb solution was dehydrated by boiling and the combined alkoxide was refluxed (≈ 1 hr in each case) prior to mixing at approximately 100 °C. The mixed solution was then refluxed until a constant boiling temperature of 124 °C (the boiling point of pure 2-MOE) was attained. At this stage, the H₂O content of the solution, as measured by Karl Fisher titration, had been reduced to < 5 ppm. The refluxed solution was then concentrated, cooled, filtered through a 0.5 μm filter, and adjusted in concentration to 0.6 M. Prior to hydrolysis, 6 mol % Pb in excess of the formula amount was introduced as a dehydrated solution of lead acetate in 2-MOE. The resulting solution was chilled to -25 °C and excess water for hydrolysis (> 4:1 mol H₂O/mol alkoxide) was added as a 1:2 (v/v) solution in 2-

MOE. The hydrolyzed solution was gelled by heating in sealed vials to 80 °C. The gels were then air dried for 2 days at 90 °C, ground in an agate mortar and pestle, and calcined to a maximum temperature of 1100 °C for 1 hr with intermediate holds on heating at 250 °C (30 min), 500 °C (2 hrs), and 800 °C (6 hrs). The final concentration of the volatile Pb component was verified using inductively coupled plasma atomic emission spectroscopy, and agreed with the expected (B-site vacancy formula) values to within a few percent.

As shown in Figure 2, the resulting powders were well crystallized and showed very sharp diffraction peaks for the rhombohedral perovskite phase. No secondary phases were detected by X-ray diffraction. The splitting associated with the rhombohedral 111 and 220 peaks ($2\theta \approx 38^\circ$ and 64° , respectively) became quite small at compositions near $x = 0.04$, making high temperature cell parameter measurements for higher La content samples difficult using standard X-ray techniques, and requiring that careful attention be paid to the details of the measurement conditions.

All analyses of the X-ray data were performed using commercially available software. The high temperature diffraction experiments were carried out on a carefully aligned automated diffractometer employing CuK α radiation. The temperature stability of the sample hot stage was ± 0.1 °C over the measurement range (-50 - 300 °C). For the cell parameter measurements, a 0.1 mm receiving slit and 0.5 ° divergence and scattering slits were used. The rhombohedral cell parameters were determined by refinement over four pairs of reflections. The step size (in degrees 2θ) and count times were varied according to the diffraction angle of these peaks as follows: 111/11-1 (0.005°/2s); 220/20-2 (0.01°/5s); 222/22-2 (0.02 °/10s); 420/40-2 (0.02 °/15s). Accurate assignment of the peak positions was facilitated by fitting with a Marquardt least squares routine that properly accounted for the K α splitting. In this routine, the only fixed parameter was the peak width, which was held constant at the room temperature value. This procedure generally permitted the cell constants to be refined with an absolute angular precision of better than 0.025 ° 2θ although,

especially for the higher La content samples, the relatively broad, low intensity 420/40-2 peaks occasionally had to be omitted from the analysis.

Semiquantitative estimates of the RMS lattice strains $\langle \varepsilon^2 \rangle^{1/2}$ were obtained using a modified Warren-Averbach analysis¹⁶ of the 100 and 200 line profiles using the 100 and 201 reflections of quartz as an external reference standard. For the line profile measurements, a 0.2 mm receiving slit and 1° divergence and scattering slits were used. The profiles were obtained as step scans using a step size of 0.005 ° 2θ and count times of 2 - 10 s to ensure ≈10,000 counts on the peak maxima. The profiles were corrected for background and Kα2 prior to analysis. Peak positions were determined using the best fit to the maxima chosen from among parabolic, Gaussian and Cauchy functions. The error in the analysis was estimated from the error in determining the effective crystallite size D_{eff} .

To assess the PE-FE phase transition character for these compositions, differential scanning calorimetry (DSC) was performed at a heating rate of 10 °C/min under flowing N₂. The DSC traces showed only a flat, featureless baseline in the temperature range of 25 - 450 °C, consistent with the expectation of second-order phase transition behavior¹⁷.

III. RESULTS AND DISCUSSION

A. Spontaneous Strain

The room temperature rhombohedral angle and associated shear strain component are shown for various La contents (x) in Table I. The shear strain component x_4 was related to the rhombohedral angle α by¹⁸

$$x_4 = (90 - \alpha)/90 \quad (1)$$

The temperature dependence of x_4 in the region of R3m phase stability is shown for x = 0.00, 0.02, and 0.04 in Figure 3. The terminus of each curve represents the temperature

above which the cell parameters could no longer be refined with the desired precision, nor the temperature of transition to cubic symmetry. Figure 3 shows that the addition of even small amounts of La resulted in a large decrease in x_4 relative to unmodified PZT. The relative change of x_4 with La content shown in Figure 3 is much larger than the change with Zr/Ti ratio observed for unmodified PZT compositions across the entire rhombohedral phase field¹⁸.

The temperature dependence of the spontaneous strain was modelled using the Landau-Ginsburg-Devonshire (LGD) free-energy formalism⁷. Using reduced tensor notation, an appropriate expression for the elastic Gibbs free-energy density of a ferroelectric of rhombohedral symmetry derived from a prototype of symmetry Pm3m is¹¹:

$$\begin{aligned}
 G_1 = & 3\chi_0(T-T_0)P_3^2 + \zeta P_3^4 + \xi P_3^6 + \beta\theta_3^2 + v\theta_3^4 + \phi P_3^2\theta_3^2 \\
 & - 1/2s_{11}(X_1^2+X_2^2+X_3^2) - s_{12}(X_1X_2+X_2X_3+X_3X_1) - 1/2s_{44}(X_4^2 + X_5^2 + X_6^2) \\
 & - (Q_{11} + 2Q_{12})(X_1 + X_2 + X_3)P_3^2 - Q_{44}(X_4+X_5+X_6)P_3^2 \\
 & - (R_{11} + 2R_{12})(X_1 + X_2 + X_3)\theta_3^2 - R_{44}(X_4+X_5+X_6)\theta_3^2
 \end{aligned} \tag{2}$$

where P_3 is a vector component of spontaneous polarization; θ_3 is a component of the oxygen octahedral tilt angle; X_i is a tensor component of elastic stress; χ_0 , ζ , ξ are related to the dielectric stiffness and higher-order stiffness coefficients at constant stress; β, v are related to the octahedral torsion coefficients; ϕ is related to the coupling coefficients between polarization and tilt angle; s_{ij} are the elastic compliances at constant polarization; Q_{ij} are the cubic electrostriction constants in polarization notation; and R_{ij} are the rotostrictive coefficients coupling tilt angle and stress.

Considering initially only the phase of R3m symmetry ($\theta_3 = 0$), from the first partial derivative stability condition

$$\delta G_1 / \delta P_3 = 0 \tag{3}$$

the spontaneous polarization for a second-order transition ($T_0 = T_c$) may be obtained as

$$P_3^2 = \{-\zeta + [\zeta^2 - 9\chi_0(T - T_c)\xi]^{1/2}\}/3\xi \quad (4)$$

with $\chi_0 = 1/(2\epsilon_0 C)$ where C is the Curie constant and ϵ_0 is the permittivity of free space.

Rearranging to eliminate the explicit dependence on C and simplifying gives

$$P_3^2 = A \{1 - [1 - B(T - T_c)]^{1/2}\} \quad (5)$$

with $A = -\zeta C/3\xi C$ and $B = 9\xi C/[2\epsilon_0(\zeta C)^2]$. The spontaneous strain ($X_i \equiv 0$) is given by the appropriate partial derivative of Eq. (2)

$$-\delta G_1/\delta X_4 = x_4 = Q_{44} P_3^2 \quad (6)$$

Combining with Eq. (5) yields

$$x_4 = A' \{1 - [1 - B(T - T_c)]^{1/2}\} \quad (7)$$

where $A' = AQ_{44}$.

It is worth noting here that the polarization enters in Eq. (6) as the square and so the strain does not depend on the sign of P . Furthermore, fluctuations of the polarization among the symmetry equivalent orientation states are unimportant provided the time spent by the polarization vector along the $<111>$ is long compared to the time spent between states. The strain determined from the X-ray measurements and Eq. (1) therefore reflects the time and space averaged value of the spontaneous polarization *i.e.*, the spontaneous strain associated with the net polarization component along the symmetry equivalent $<111>$ orientations for a corresponding hypothetical single-crystal of average composition (x).

Eq. (7) was used to fit the spontaneous strain data in Figure 3 using a Marquardt nonlinear regression analysis with A' , B , and T_c as adjustable constants. Taking T_c from the radio frequency dielectric measurements (Figure 1), values of A' and B could not be found to adequately describe the data for the $x = 0.02$ and 0.04 compositions. Convergence

could be achieved for these compositions by allowing A', B, and T_c to vary simultaneously, although for the $x = 0.04$ sample, the value of T_c so obtained had no obvious physical significance and the values of A' and B became unacceptable (*i.e.* B became very large and $A' \rightarrow 0$). The refractive index results of Burns and Dacol¹⁹, and the X-ray scattering results of Darlington²⁰, have shown that the onset of local polarization is independent of x for $x = 0.07 - 0.095$ and occurs at a temperature $T_c \approx 350 - 360$ °C (hereinafter termed T_{Burns}) of the unmodified PZT end member. Rapid convergence to the fits shown by the solid lines in Figure 3 that also yielded reasonable values of A' and B was attained using a composition independent value of $T_c = T_{Burns} \approx 357$ °C. The excellent fit to the data in Figure 3 suggests that the onset of local polarization for the lower La compositions ($x \leq 0.04$) also occurs near 360 °C, and that the relaxor behavior observed for the higher La contents is incipient from the introduction of even small amounts of La. The values of the fitting constants A' and B are listed along with the associated values of the higher-order dielectric stiffness - Curie constant products, ζC and ξC , in Table II.

Considering now the phase of R3c symmetry ($\theta_3 \neq 0$), the spontaneous strain becomes

$$-\delta G_1/\delta X_4 = x_4 = Q_{44}P_3^2 + R_{44}\theta_3^2 \quad (8)$$

For the PZT system, R_{44} has been shown to be negative²¹, and so the rotostrictive contribution to the strain lowers the value relative to electrostriction alone. Apparently, this is also the case for the PLZT compositions studied here, as shown in Figure 4. The solid lines in Figure 4 represent an extrapolation of the electrostrictive strain for the R3m phase according to Eq. (7), while the dashed lines are smoothed fits to the experimental data over the complete measurement range. The arrows indicate the rhombohedral - rhombohedral phase transition temperatures from Figure 1. The points of departure of the data from the calculated lines for electrostriction alone are roughly in agreement with the acoustic

measurement results shown on the phase diagram. This result supports the choice of $T_c = T_{Burns}$ used in fitting the electrostrictive strain data for the R3m phase since, to a good approximation, the transition temperature to R3c symmetry is also correctly predicted.

B. Lattice Strain

The effective crystallite size and RMS lattice strain for samples of various La content (x) are shown in Table I. Within the error of the analysis, the effective crystallite size was a constant 53 nm. Figure 5 shows scanning electron micrographs of the $x = 0.00$ sample. At the lower magnification it is apparent that each agglomerate is composed of relatively uniform, acicular primary particles. On higher magnification it is seen that the size of these particles is ≈ 60 nm, and so is in good qualitative agreement with the effective crystallite size determined from the Warren-Averbach analysis. The corresponding RMS lattice strains for these compositions were also nearly constant, although there was a small but distinct increase for the sample with composition $x = 0.04$. As judged from the radio frequency dielectric measurements¹², this composition marks the onset of the relaxor phase transition region. Although the absolute magnitude of the lattice strains estimated from line profile analyses must be interpreted with great care, it is interesting to note that the values obtained (≈ 0.001) are on the same order of magnitude as the difference in the electrostrictive strain Δx_4 between samples of different La content in the range of $x = 0.00 - 0.04$. Consequently, the data in Figure 3 and Table I may suggest that small deviations from the average composition (x) lead to significant inhomogeneities in the electrostrictive strain field. Based on a spin-glass model, inhomogeneity in the internal strain field has recently been proposed as a possible frustration mechanism leading to freezing of the polarization in these materials²².

The RMS lattice strain for a sample of composition $x = 0.04$ is shown as function of temperature in Figure 6. The lattice strain was constant from -50 to 200 °C, but dropped sharply between 200 and 250 °C, very near the temperature of the radio frequency permittivity maximum (Figure 1). Also in this temperature range, the rhombohedral angle

became too small to accurately measure (220°C). Based on lattice softening and dielectric measurements, Viehland *et al.*²² have recently proposed a revised version of the phase diagram of Figure 1 and defined a temperature $T_{\text{perc}} \approx 250^{\circ}\text{C}$ at which thermally fluctuating polar microregions can begin to deform electrostrictively into the surrounding matrix. Since the freezing temperature T_f (the temperature determined by extrapolating the collapse of the remanent polarization to $P = 0$) for the $x = 0.04$ composition is also close to this temperature ($T_f \approx T$ at K_{max}), the internal strain associated with this deformation should also saturate near 250°C . The data in Figures 3 and 6 are consistent with this suggestion; the lattice strain increased and rapidly saturated in the same narrow temperature regime where a well defined rhombohedral shear became evident under interrogation by X-ray wavelength probing radiation.

In summary, the combined results of spontaneous and lattice strain measurements on alkoxy-derived PLZT powders with compositions incipient to the relaxor phase transition region indicate that: 1) the electrostrictive strain for the $\text{R}3\text{m}$ phase can be well described using a simple LGD formalism by taking $T_c = T_{\text{Burns}} \approx 357^{\circ}\text{C}$ independent of La content (x); this result implies the existence of a local (RMS) polarization up to T_{Burns} and 2) small deviations from the average composition (x) and thermal fluctuations of the local polarization may both contribute to significant inhomogeneities in the internal strain field. Both observations are better interpreted on the basis of a superparaelectric model involving localized polarization as opposed to a distribution of local Curie points on the Smolenski model.

IV. PHENOMENOLOGICAL ANALYSIS

Under conditions of constant and zero stress, the spontaneous strain measurements described above allow evaluation of the spontaneous polarization and single-domain, single-crystal elastic Gibbs free-energy as a function of composition and temperature up to T_{Burns} .

It has recently been recognized²³ that Curie-Weiss behavior is obeyed for relaxor ferroelectrics above T_{Burns} , and this is an inherent assumption of the LGD formalism when $T_c \equiv T_{Burns}$. Calculations made using Eq. (2) therefore reflect the free-energy density that a hypothetical crystal of average composition (x) would have if it underwent a second-order transition to a Devonshire ferroelectric at T_{Burns} . Recognizing that this does not in actuality occur, the deviation from Devonshire behavior is interpreted on the basis of an idealized superparaelectric model⁴. In this model it is assumed that small deviations from the average composition (x) localize the polarization to regions on a size scale where thermal fluctuations of the orientation of the polar vector between different permissible variants become possible. The dependence of the relative stability against thermal agitation of an isolated region on its size, composition, and temperature can then be evaluated. Clearly, the dielectric response of the crystal would depend in a complex way on interactions between regions, the kinetics of the available relaxational processes, as well as on any associated distortions of the free-energy surface. These calculations estimate only how the volume stabilization energy of a postulated microregion with symmetry equivalent polarization orientation states compares with the thermal energy. Surface effects, elastic boundary constraints, and the cell doubling transformation are neglected. For these calculations we take $C = 2.0 \times 10^5 \text{ }^\circ\text{C}$ and $Q_{44} = 0.06 \text{ m}^4/\text{C}^2$, typical values for the rhombohedral PZT-based perovskites²⁴.

The spontaneous polarization determined from the X-ray strain measurements and Eq. (6) is shown for various compositions (x) in Figure 7. The upper portion of the figure shows that even for the $x = 0.04$ composition, the values of the polarization measured from the X-ray strain can be extrapolated quite plausibly to T_{Burns} using Eq. (4). The lower portion of Figure 7 compares the spontaneous polarization determined from Eq. (6) for the $x = 0.02$ composition with the remanent polarization determined by Haertling²⁵ from hysteresis loops measured on ceramic samples. At low temperatures the two measurements are in good agreement, but begin to differ substantially above $\approx 75 \text{ }^\circ\text{C}$ where the remanent polarization starts to collapse. As discussed earlier, the polarization enters in Eq. (6) as the

square, and so the differences in the two curves primarily reflect the difference between the reversible macropolarization (\bar{P}) and local (RMS) polarization ($\langle \bar{P}^2 \rangle^{1/2}$). Since the spontaneous polarization is the macroscopic order parameter in Eq. (2), we expect the calculated free-energy density to be correct only at low temperatures where thermally activated processes are frozen out.

The elastic Gibbs free-energy density versus polarization curves for various compositions (x) are shown at two temperatures in Figure 8. The energy barriers shown represent the energy barrier E_c for the polarization passing through the center of the energy surface, *i.e.* heterophase fluctuations. While the electrocrystalline anisotropy energy barrier E_{ec} separating adjacent orientation states would in general be smaller, for an undeformed energy surface, both scale with volume in the same way. As a relative measure, it is sufficient to consider E_c . At 25 °C, the height of the energy barrier separating equivalent orientation states is quite large for all x , so that even at the smallest sizes amenable to a macroscopic treatment, the energy barriers substantially exceed $k_B T$. Near T_{Burns} , however, the energy barriers become a factor of 1000 smaller, and a sizeable composition dependence develops, as discussed below.

The free-energy density curves of Figure 8 suggest that increasing the La content eventually leads to a phase of cubic symmetry. Assuming that the free-energy densities are linear functions of composition, the La content required to induce the transition was estimated at various temperatures. The calculated results are compared with the experimental phase diagram in Figure 9. As expected, the predicted and measured values are in good agreement only at low temperature where, judging from Figure 7, freezing of the polarization is nearly complete. The calculations suggest that at low temperatures, the structure becomes truly cubic at a La content near 14 mol %. Since the calculation involved no adjustable parameters, the agreement of this prediction with the experimental measurements¹² suggests that the simply formulated LGD formalism, with $T_c \equiv T_{Burns}$, is valid for this system at low temperatures. At higher temperatures, where the remanent polarization collapses and

thermal fluctuations become much more important, the macroscopic properties will no longer be described by Eq. (2). Instead, an idealized superparaelectric model is assumed, and Eq. (2) is used to investigate the effects of size and composition on the stability of a postulated single-domain polar microregion.

In Figure 10, the energy barrier height E_c is plotted as a function of temperature and composition for two postulated microregion sizes. The line representing $k_B T$ is shown to indicate the minimum conditions for stability against thermal agitation. At the larger size ($n = 1000$ unit cells) the temperature range over which the various x become stable with respect to $k_B T$ is relatively narrow (≈ 15 °C) and close to T_{Burns} . At the smaller size ($n = 100$ unit cells) this range becomes considerably broader (≈ 35 °C) and shifts down about 100 °C in temperature. The shift of the curves can be attributed to the size effect alone, while their relative separation relates to the way the free-energy densities for the different x depend on temperature.

The separation ΔT of the energy barrier curves along the line $k_B T$ is plotted against the log of the postulated microregion size in Figure 11. The difference ΔT is taken as a relative (minimum) measure of the stability against thermal agitation of regions with different x . At macroscopic sizes, $\Delta T \rightarrow 0$, so that a stable ferroelectric polarization is expected for all x very near T_{Burns} . Consistent with the original observation of Burns and Dacol¹⁹, regions deficient in La are predicted to be first to develop a detectable polarization. As the microregion size is decreased, ΔT increases, eventually increasing exponentially as the size is reduced below 1000 unit cells. Since the lattice constant $a \approx 0.4$ nm, this result implies that in the lower limit, composition effects become important for microregions with equivalent spherical diameters ≤ 5 nm.

To obtain a reasonable estimate of the size scale on which composition effects may become important on a simple superparaelectric model (*i.e.* noninteracting microregions), it is necessary to recall that the polarization flipping frequency is given by

$$v = v_0 e^{-H/k_B T} \quad (9)$$

where v_0 is characteristic of a softened lattice mode ($\approx 10^{12}$ Hz) and H is the energy barrier separating equivalent polarization orientation states. If, instead of taking the minimum value of $H = k_B T$ as above, we now take a more realistic value of $H \approx 18 k_B T$, the depolarization frequency v becomes 15 kHz, which is sufficient to influence the dielectric properties for measuring fields at 10 kHz. Repeating the calculations of Figure 11 using $18 k_B T$ as the stability criterion, the microregion size at which composition effects become important is then predicted to be ≈ 15 nm. This prediction is quite plausible in light of direct TEM observations²⁶ that place the size of the polar microregions in PLZT 9/65/35 near 10 nm below 0°C. Furthermore, heterogeneities on this scale are not unreasonable given that the effective crystallite size was estimated to be substantially larger (50 - 60 nm). The scale on which composition effects become important relative to size effects alone may be an important factor distinguishing solid solutions with diffuse transitions (broad but not frequency dispersive) from those with relaxor (broad and frequency dispersive) phase transition behavior.

V. CONCLUSIONS

X-ray diffraction analyses of chemically derived $Pb_{1-x}La_x(Zr_{0.65}Ti_{0.35})_{1-x/4}O_3$ (PLZT) powders were combined with a phenomenological theory to investigate the corresponding single-crystal ferroelectric properties of compositions incipient to the relaxor phase transition region ($x = 0 - 0.04$). The results were consistent with the existence of a local (RMS) polarization up to ≈ 360 °C independent of composition (x). The predictions of the phenomenological theory regarding the polarization and relative phase stabilities were in good agreement with experimental measurements at low temperatures. At higher temperatures, where thermal fluctuations of the polar vector among the symmetry permitted variants may become important, the calculations suggested that the stability of an isolated

polar microregion against thermal agitation becomes strongly composition dependent when reduced in size below the range of 5 - 15 nm.

ACKNOWLEDGEMENTS

The authors thank the Mitsubishi Kasei Corporation for financial support of this study. One of us (GAR) would like to express special appreciation for the kindness and hospitality shown to him by so many people during his stay at the MKC Research Center. It is a pleasure to acknowledge Y. Matsumoto, K. Mori, and M. Sakaguchi for technical assistance, T. Matsuzaki, S. Nakamura and Y. Oguri for their support of this study, and C. Randall and D. Viehland for illuminating discussions.

REFERENCES

1. G. Smolenski and A. Agranovska, *Sov. Phys. Sol. State*, **1** 1429 (1960).
2. C. A. Randall and A. S. Bhalla, *Jap. J. Appl. Phys.*, **29** 327 (1990).
3. C. A. Randall, A. S. Bhalla, T. R. Shrout, and L. E. Cross, *J. Mater. Res.*, **5** 829 (1990).
4. L. E. Cross, *Ferroelectrics*, **76** 241 (1987).
5. W. A. Schulze, J. V. Biggers, and L. E. Cross, *J. Mater. Sci.*, **15** 2478 (1978). *Am. Ceram. Soc. 61 46*
6. W. Pan, E. Furman, G. O. Dayton, and L. E. Cross, *J. Mater. Sci. Lett.*, **5** 647 (1986).
7. A. F. Devonshire, *Philos. Mag.*, **40** 1040 (1949).
8. M. J. Haun, E. Furman, S. J. Jang, H. A. McKinstry, and L. E. Cross, *J. Appl. Phys.*, **62** 3331 (1987).
9. M. J. Haun, T. J. Harvin, M. T. Lanagan, Z. Q. Zhuang, S. J. Jang, and L. E. Cross, *J. Appl. Phys.*, **65** 3173 (1989).
10. A. Amin, M. J. Haun, B. Badger, H. A. McKinstry, and L. E. Cross, *Ferroelectrics*, **65** 107 (1985).
11. M. J. Haun, E. Furman, S. J. Jang, and L. E. Cross, *Ferroelectrics*, **99** 13 (1989).
12. A. Meitzler and H. O'Bryan, *Proc. IEEE*, **61** 959 (1973).
13. M. Kuwabara, K. Goda, and K. Oshima, *Phys. Rev.*, **B42** 10012 (1990).
14. D. Viehland, S. J. Jang, L. E. Cross, and M. Wuttig, *J. Appl. Phys.*, **68** 2916 (1990).
15. J. B. Blum and S. R. Gorkovich, *J. Mater. Sci.*, **20** 4479 (1985).
16. B. E. Warren, "X-ray Diffraction", Addison - Wesley, Reading, MA (1969).
17. M. J. Haun, E. Furman, H. A. McKinstry, and L. E. Cross, *Ferroelectrics*, **99** 27 (1989).

18. M. J. Haun, Y. H. Lee, H. A. McKinstry, and L. E. Cross, *Adv. X-ray Anal.*, **30** 473 (1987).
19. G. Burns and F. Dacol, *Phys. Rev.*, **B28** 2527 (1983).
20. C. N. W. Darlington, *J. Phys.*, **C21** 3851 (1988).
21. M. J. Haun, E. Furman, T. R. Halemane, and L. E. Cross, *Ferroelectrics*, **99** 55 (1989).
22. D. Viehland, S. J. Jang, L. E. Cross, and M. Wuttig, *J. Appl. Phys.*, (accepted).
23. D. Viehland, S. J. Jang, L. E. Cross, and M. Wuttig, *Phys. Rev.*, (submitted).
24. M. J. Haun, Z. Q. Zhuang, E. Furman, S. J. Jang, and L. E. Cross, *Ferroelectrics*, **99** 45 (1989).
25. G. H. Haertling, *J. Am. Ceram. Soc.*, **54** 303 (1971).
26. C. A. Randall, D. J. Barber, and R. W. Whatmore, *J. Micro.*, **145** 275 (1986).

TABLE I. Rhombohedral angle (α), spontaneous strain (x_4), effective crystallite size (D_{eff}), and RMS lattice strain ($\langle \varepsilon^2 \rangle^{1/2}$) for $Pb_{1-x}La_x(Zr_{0.65}Ti_{0.35})_{1-x/4}O_3$ at 27 °C.

x	α (degrees)	x_4	D_{eff} (nm)	$\langle \varepsilon^2 \rangle^{1/2}$	$\langle \varepsilon^2 \rangle^{1/2}$ Error Range
0.00	89.684	0.00351	52.6 ± 1.7	0.00129	0.00123 - 0.00135
0.01	89.695	0.00339	53.6 ± 1.7	0.00118	0.00112 - 0.00125
0.02	89.708	0.00324	54.1 ± 2.5	0.00120	0.00111 - 0.00131
0.04	89.764	0.00262	52.0 ± 1.5	0.00148	0.00142 - 0.00155

TABLE II. Constants used to evaluate Equation (2).

x	$A'(X \cdot 10^{-4})$	$B(X \cdot 10^{-3})$	$\zeta C(X \cdot 10^{14})$ (J m ⁵ °C/C ⁴)	$\xi C(X \cdot 10^{15})$ (J m ⁹ °C/C ⁶)
0.00	- 3.92	294.4	0.85	4.21
0.02	-7.73	77.73	1.64	4.10
0.04	-25.33	9.92	3.91	2.99

FIGURE CAPTIONS

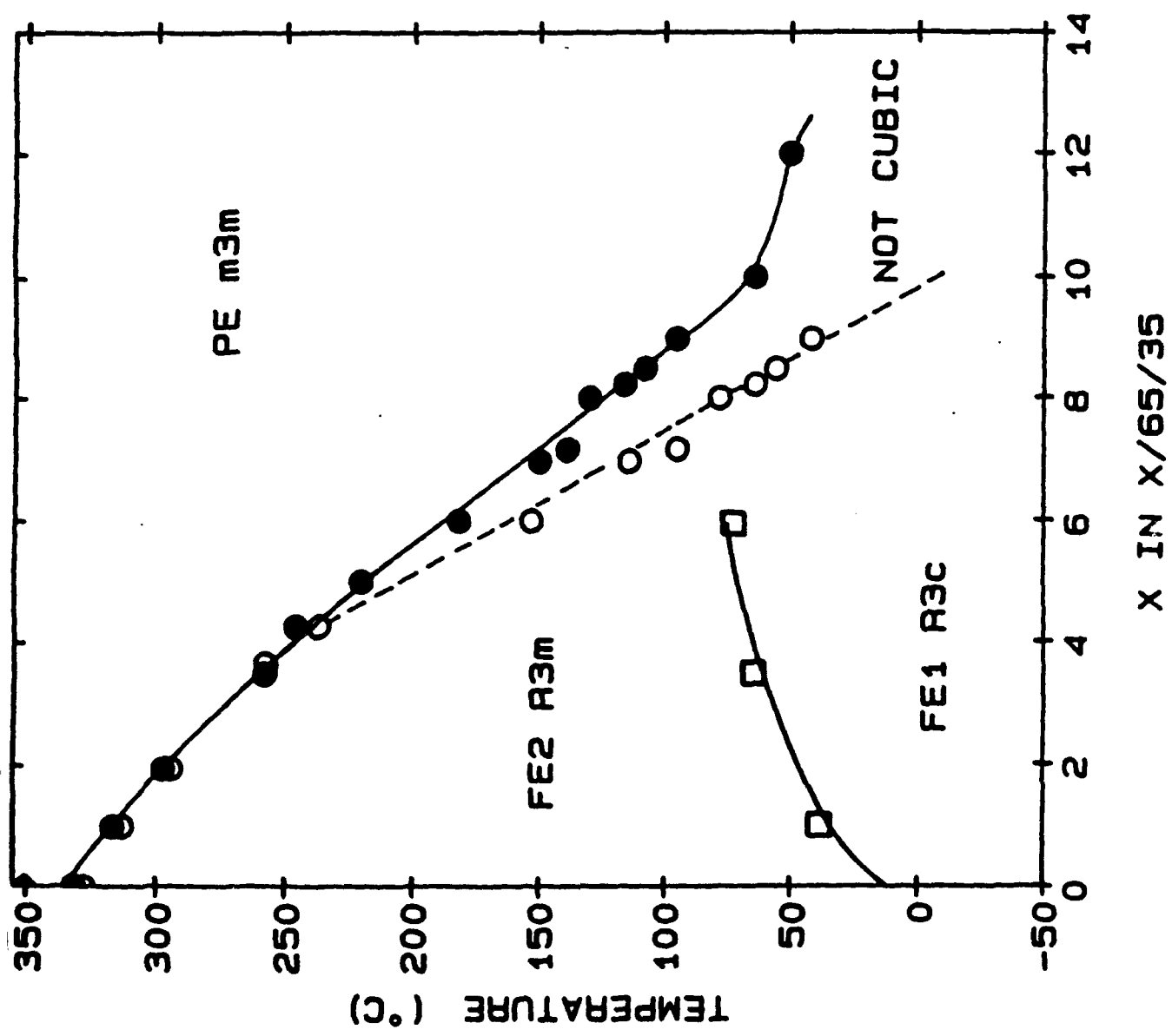
- Figure 1. Phase diagram for PLZT X/65/35 (after reference 12).
- Figure 2. Powder X-ray diffraction patterns for $Pb_{1-x}La_x(Zr_{0.65}Ti_{0.35})_{1-x/4}O_3$.
- Figure 3. Spontaneous elastic strain data for $Pb_{1-x}La_x(Zr_{0.65}Ti_{0.35})_{1-x/4}O_3$ (R3m phase). The solid lines were calculated using Equation (7) of the text and the constants of Table II.
- Figure 4. Low temperature spontaneous strain data for $Pb_{1-x}La_x(Zr_{0.65}Ti_{0.35})_{1-x/4}O_3$. The solid lines are an extrapolation of the electrostrictive strain for the R3m phase using Equation (7) of the text. The dashed lines are smoothed fits to the experimental data points over the complete measurement range. The arrows indicate the R3m - R3c phase transition temperatures taken from Figure 1.
- Figure 5. Scanning electron micrographs of $Pb_{1-x}La_x(Zr_{0.65}Ti_{0.35})_{1-x/4}O_3$ ($x = 0.00$).
- Figure 6. RMS lattice strain against temperature for $Pb_{1-x}La_x(Zr_{0.65}Ti_{0.35})_{1-x/4}O_3$ ($x = 0.04$).
- Figure 7. Polarization against temperature for $Pb_{1-x}La_x(Zr_{0.65}Ti_{0.35})_{1-x/4}O_3$. The data points were determined from spontaneous strain measurements. The solid lines were extrapolated to T_{Burns} using Equation (4) of the text. The curve labelled P_r is taken from the remanent polarization data of reference 25.
- Figure 8. Free-energy density against polarization for $Pb_{1-x}La_x(Zr_{0.65}Ti_{0.35})_{1-x/4}O_3$.
- Figure 9. Comparison of calculated and experimental phase diagrams. The experimental data are taken from Figure 1. The predicted and measured values are in good agreement only at low temperatures where thermally activated processes are expected to freeze out.

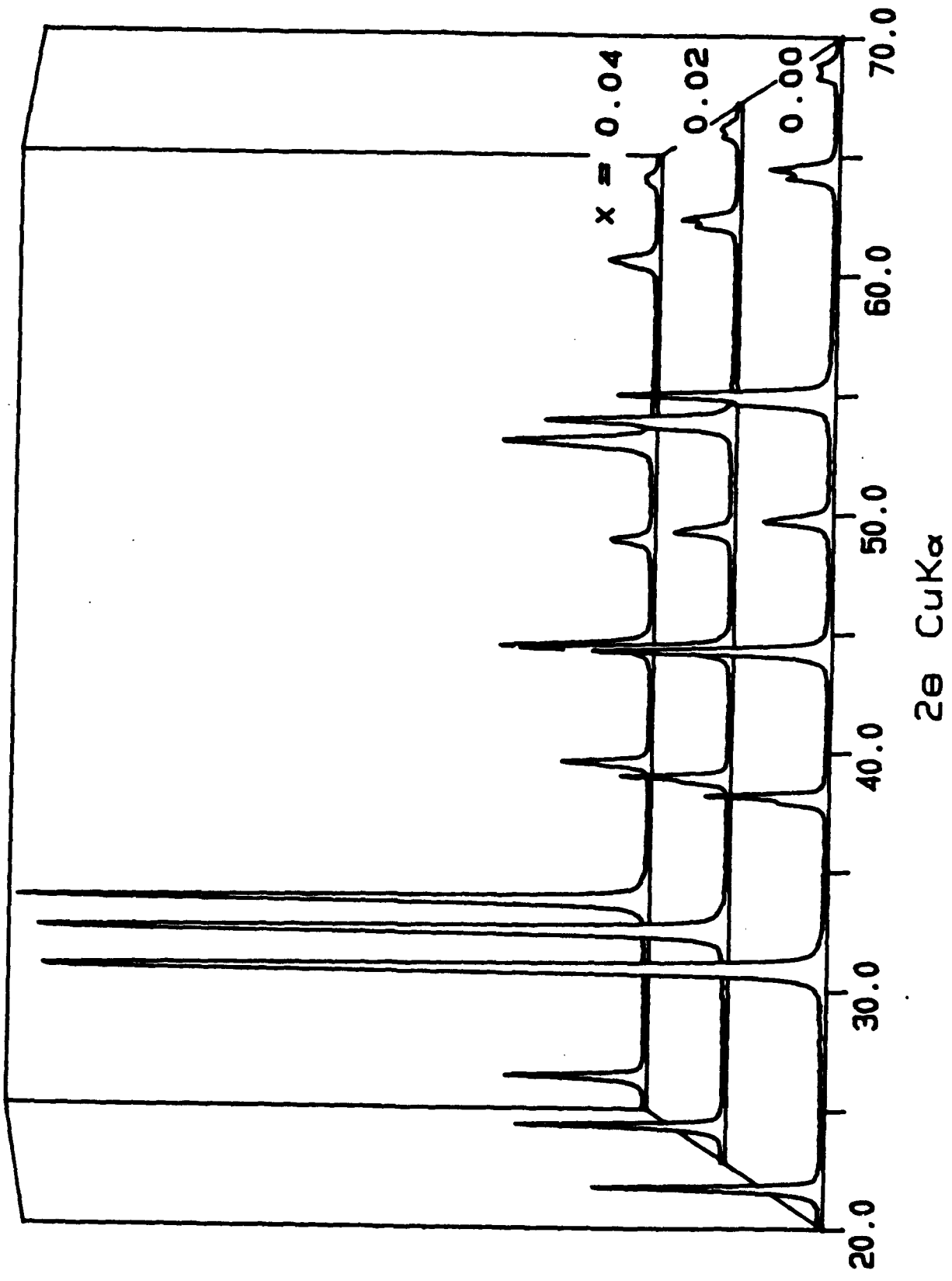
Figure 10. Energy barrier height against temperature for $Pb_{1-x}La_x(Zr_{0.65}Ti_{0.35})_{1-x/4}O_3$. n is the number of unit cells in a postulated microregion.

Figure 11. ΔT against the log of the postulated microregion size n. ΔT is the separation of the energy barrier curves of Figure 10 along the line $k_B T$. The designations 2 - 0 and 4 - 0 refer to the ΔT of the energy barrier height curves for $x = 0.02$ and 0.04 relative to that for $x = 0.00$.

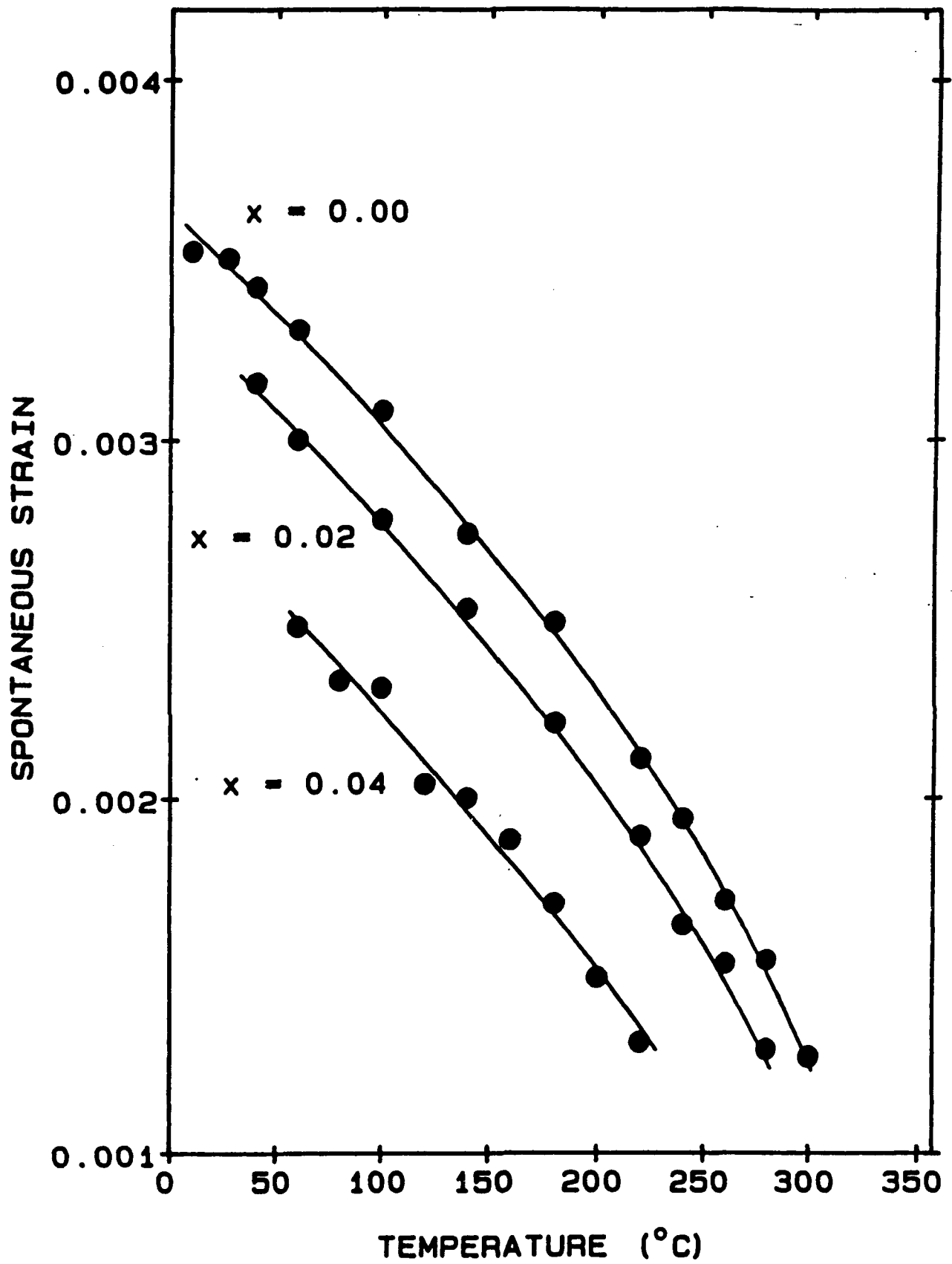
DIELECTRIC SUSCEPTIBILITY
 DIELECTRIC LOSS
 PZT PHASE DIAGRAM
 LONGITUDINAL SOUND VELOCITY

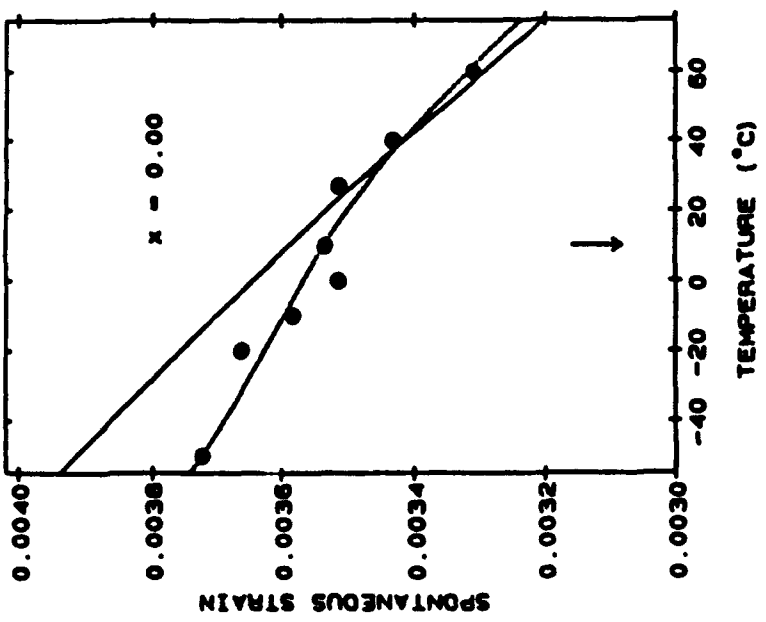
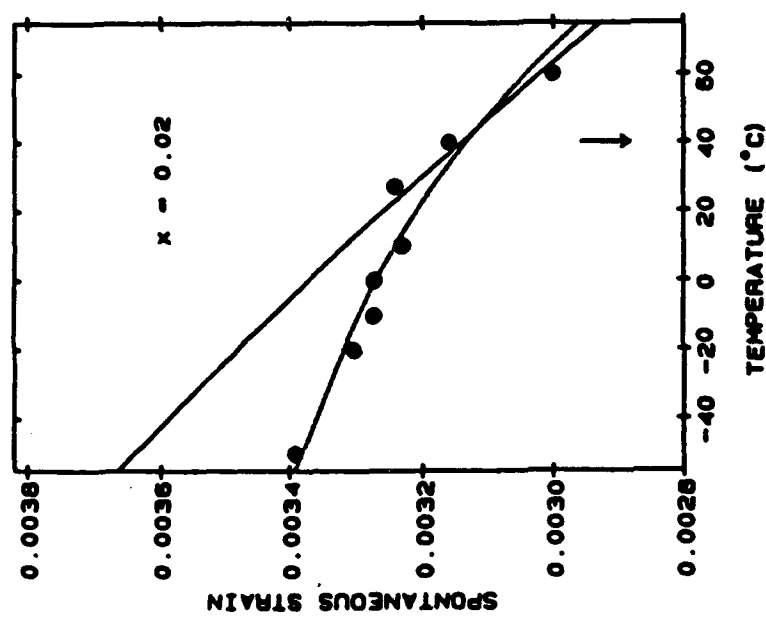
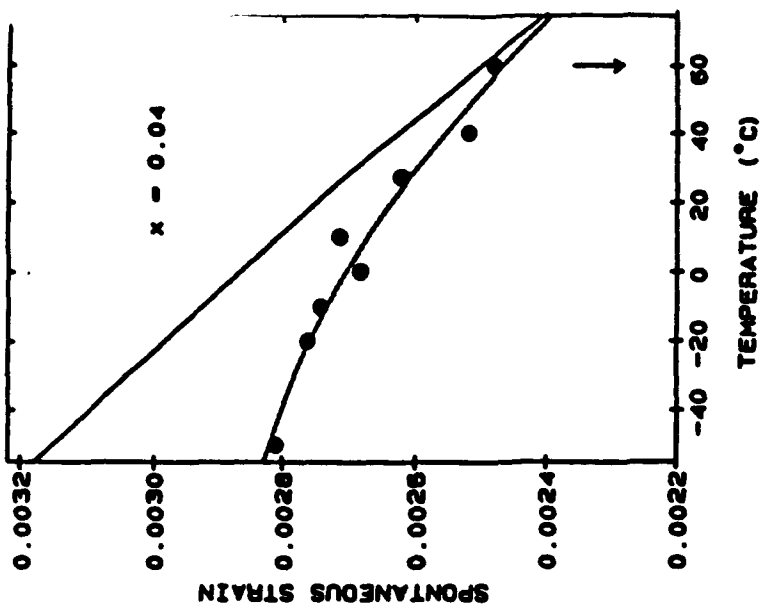
● ○ ◆ □

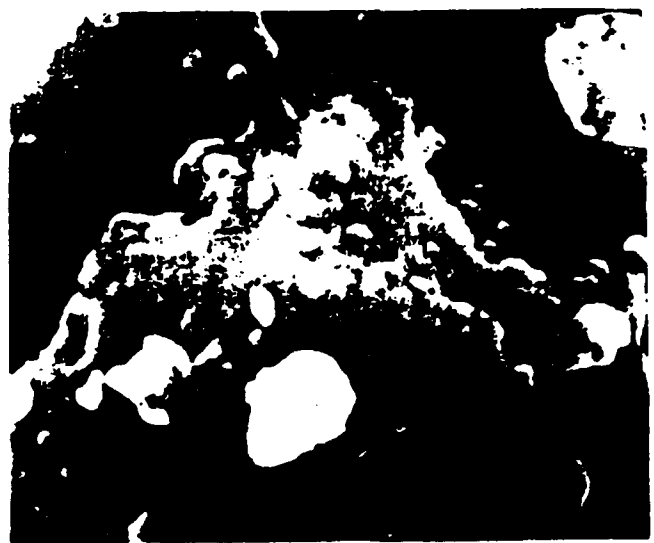


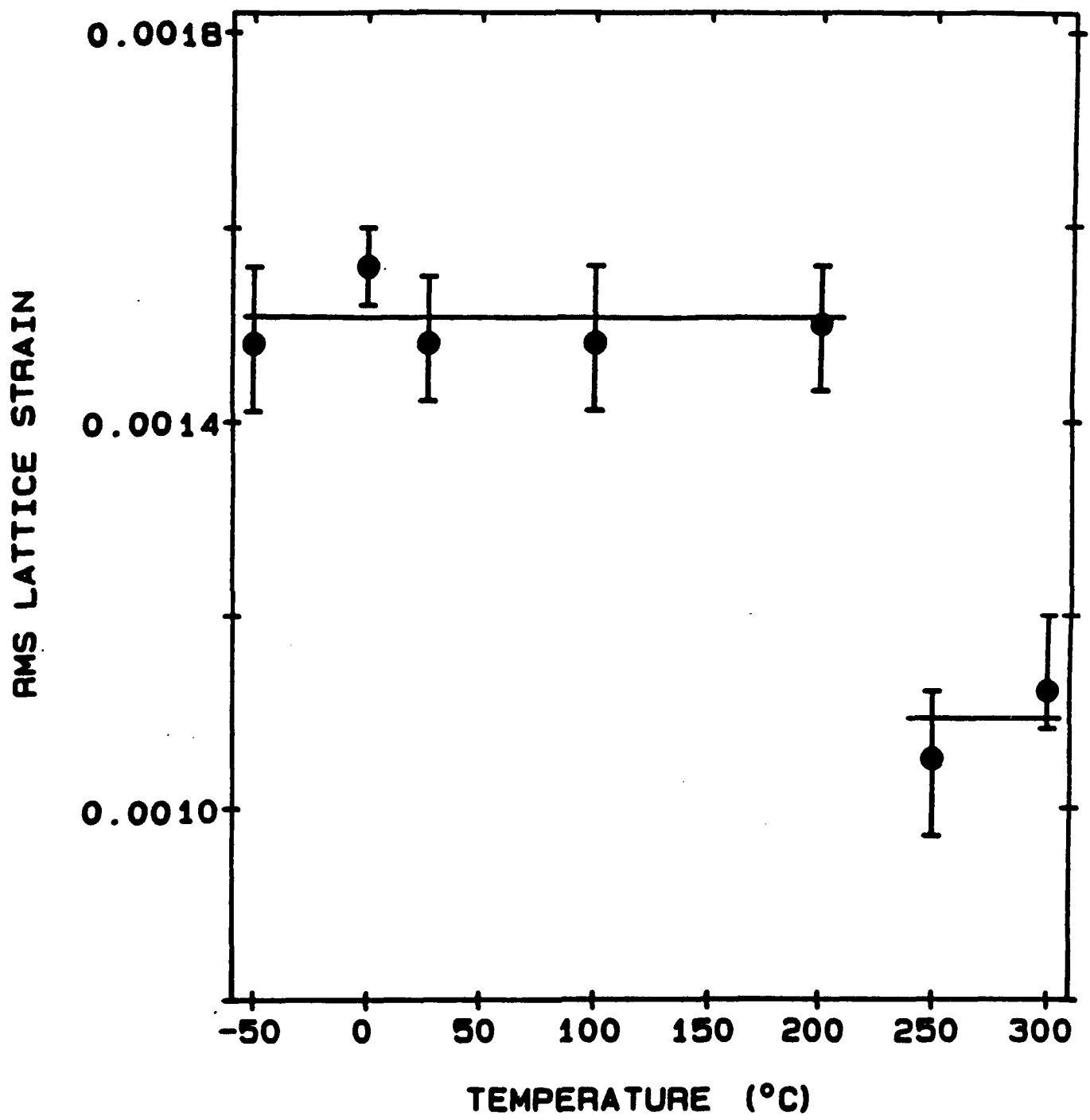


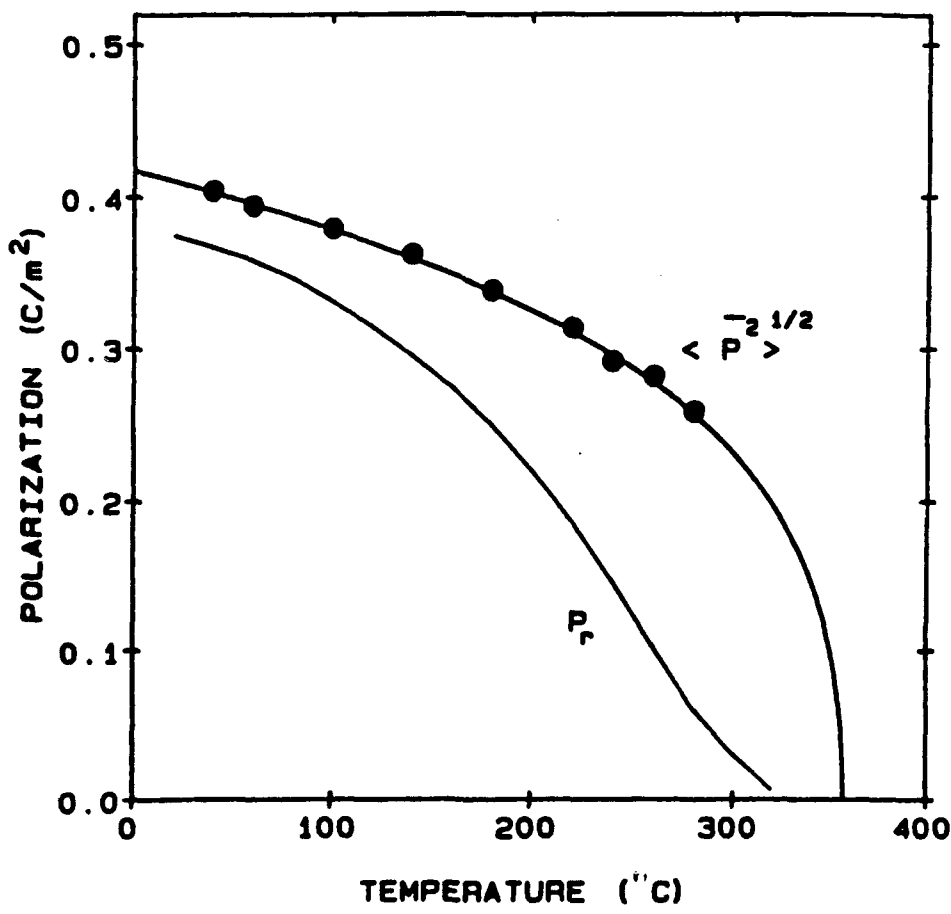
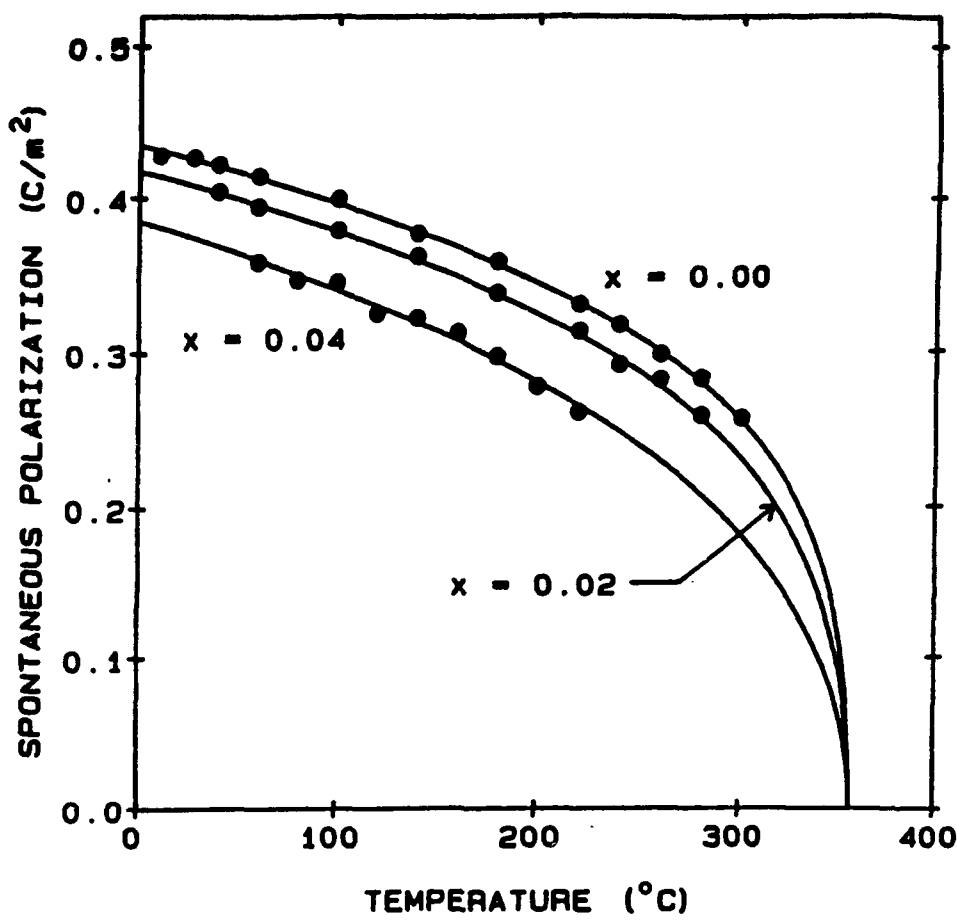
INTENSITY (ARBITRARY UNITS)

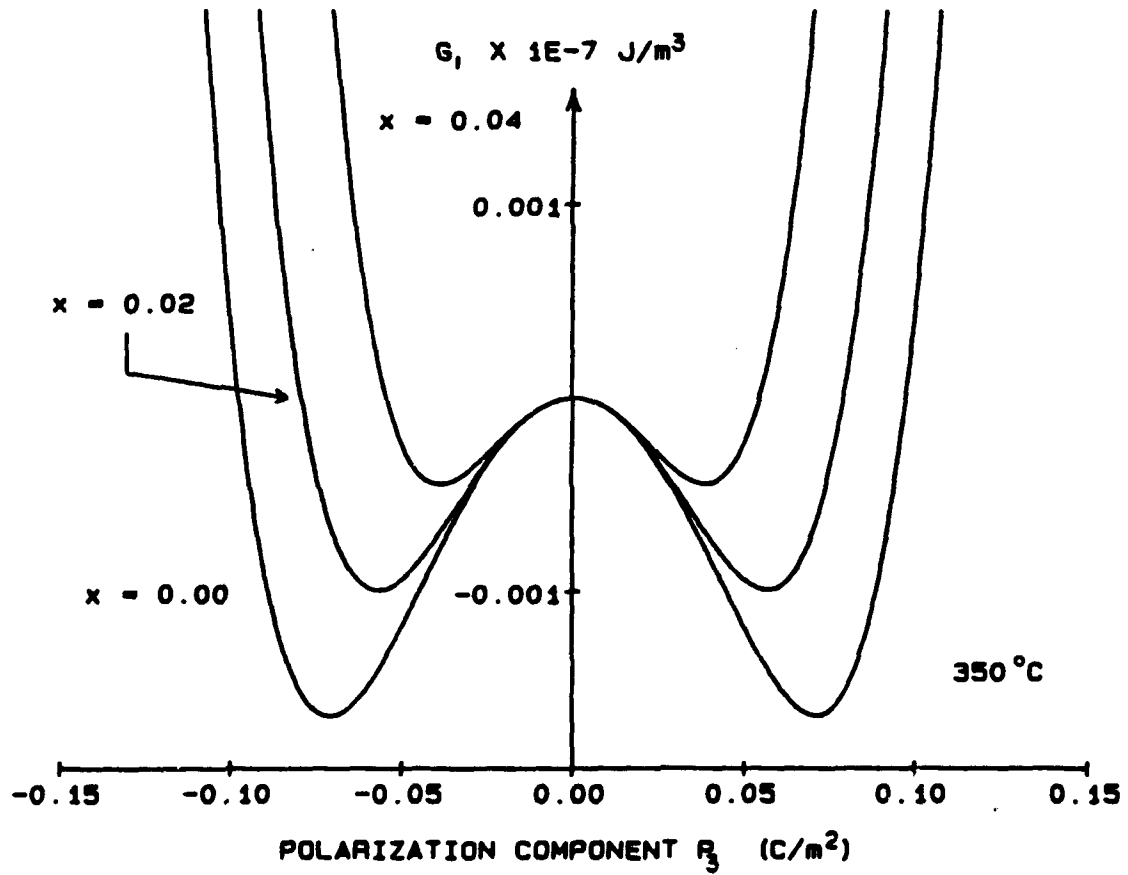
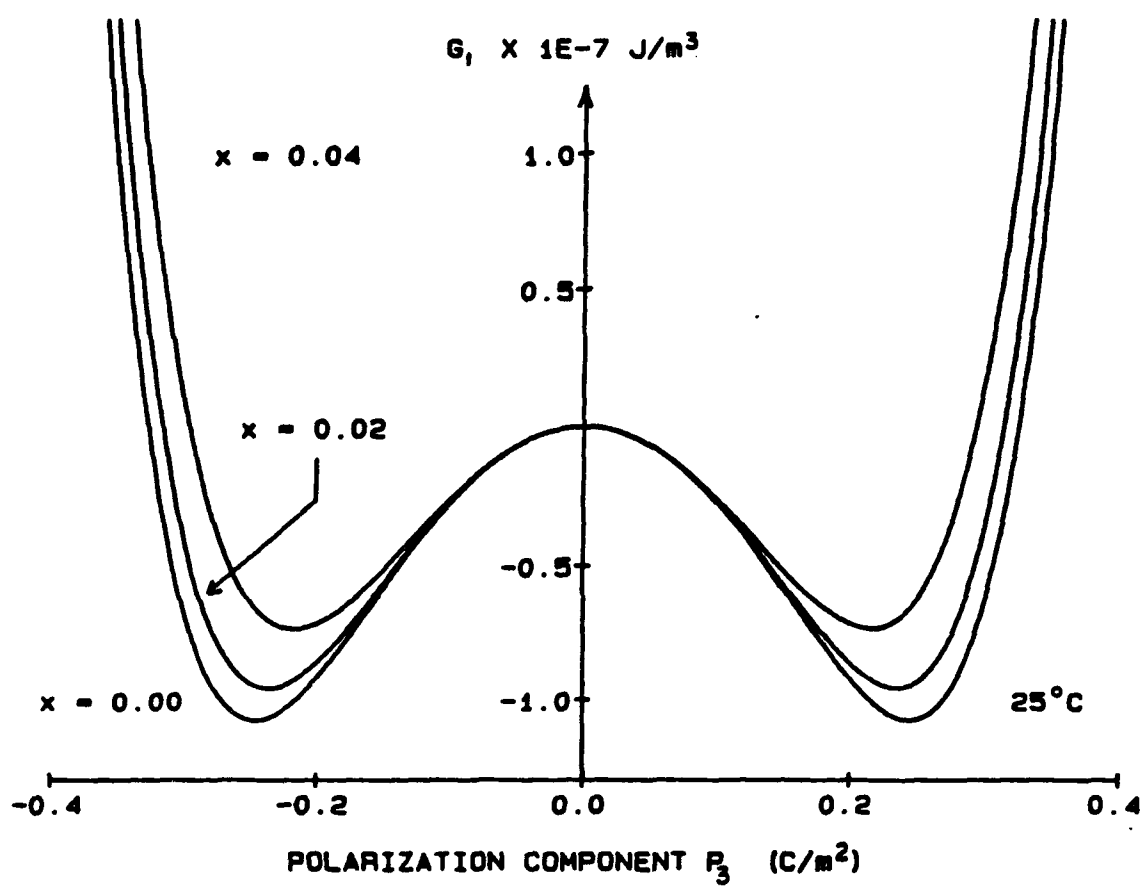


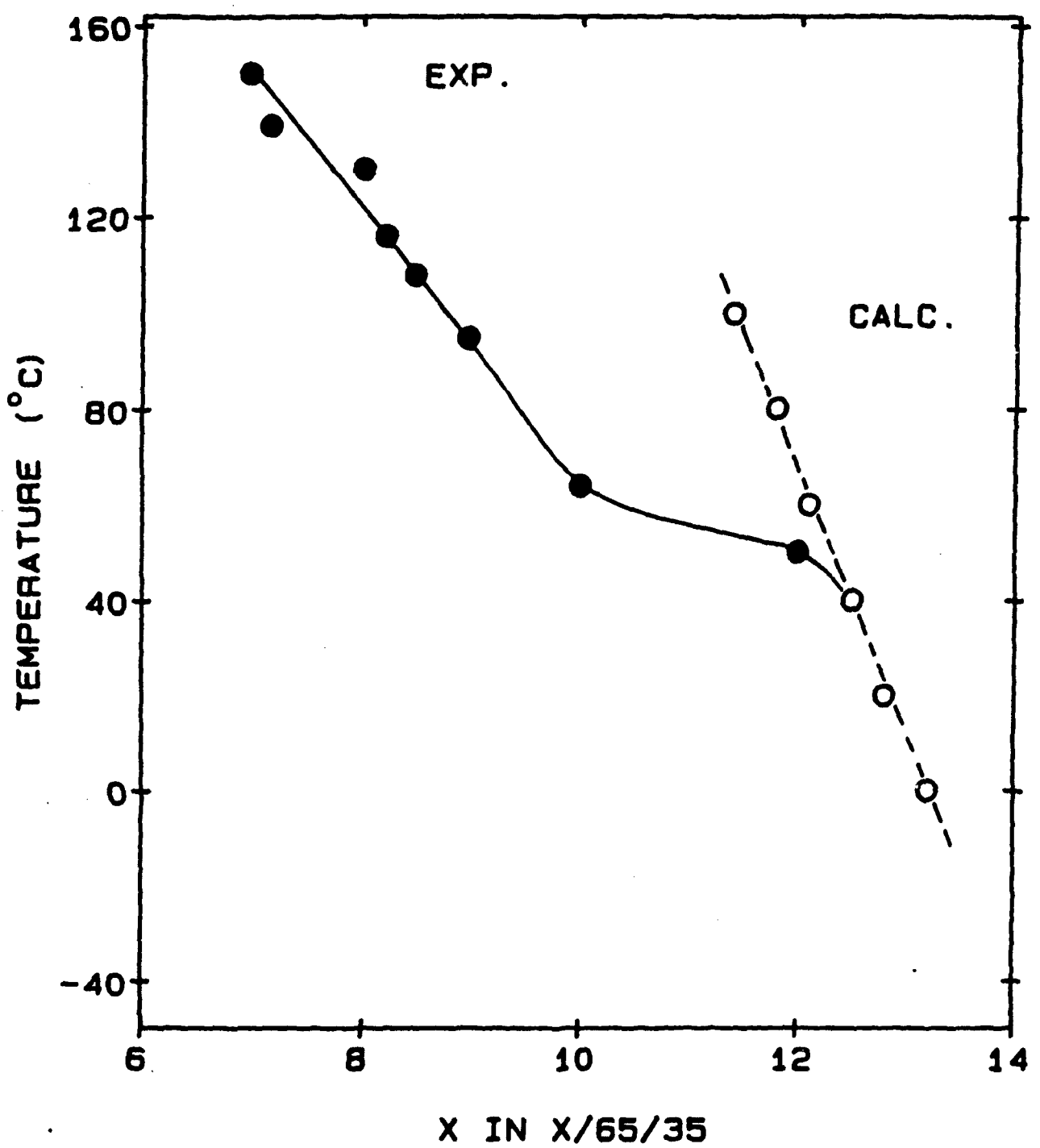












AD-A236 219

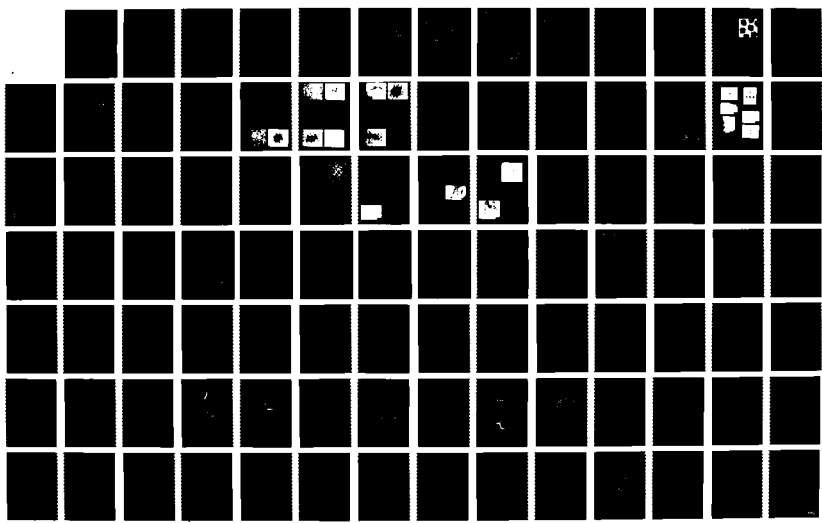
PIEZOELECTRIC AND ELECTROSTRRICTIVE MATERIALS FOR
TRANSDUCER APPLICATIONS. (U) PENNSYLVANIA STATE UNIV
UNIVERSITY PARK MATERIALS RESEARCH LAB.

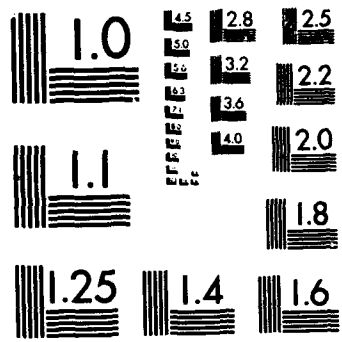
474

UNCLASSIFIED

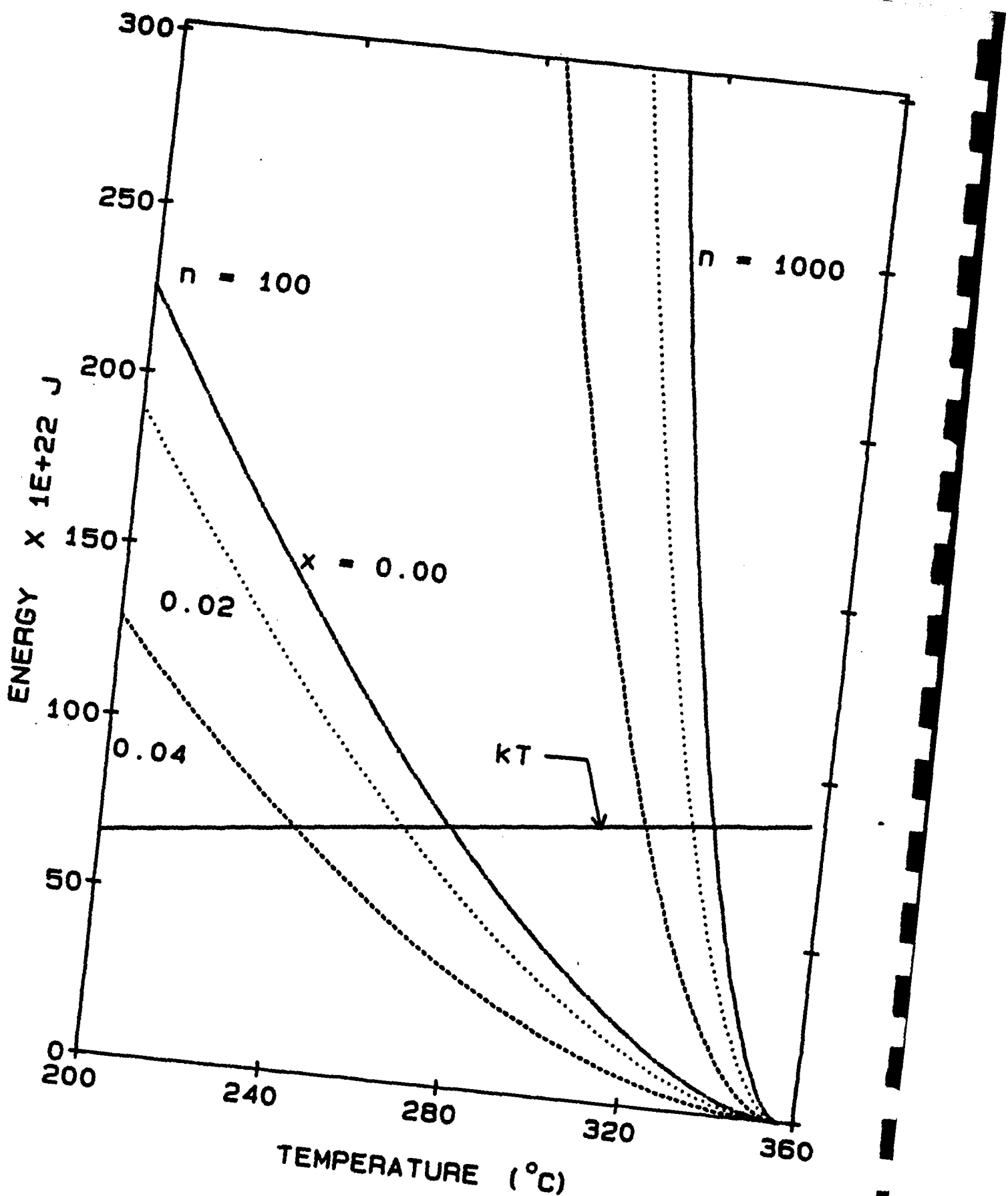
L E CROSS ET AL. 31 JAN 91 XN-ONR

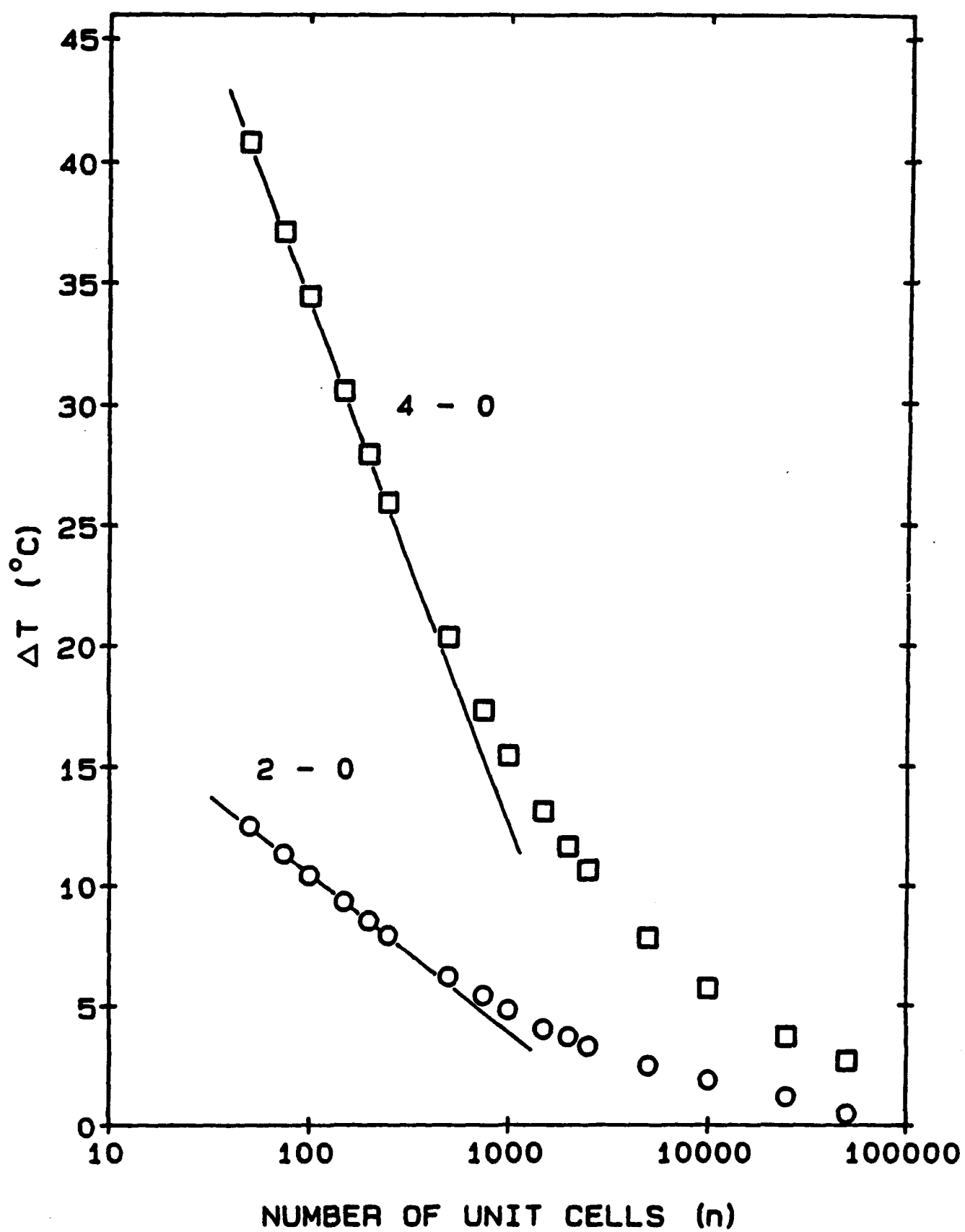
NL





MICROCOPY RESOLUTION TEST CHART
NATIONAL BUREAU OF STANDARDS-1963-A





**ELECTROSTRICTION/
RELAXOR FERROELECTRICS**

APPENDIX 18

RELAXOR FERROELECTRIC MATERIALS

Thomas R. Shrout and Joseph Fielding, Jr.

Pennsylvania State University
Materials Research Laboratory
University Park, PA 16802

ABSTRACT

Complex lead-based perovskites having the general formula $Pb(B' B'')O_3$ exhibiting broad and frequency dispersive phase transitions are known as relaxor ferroelectrics. Their anomalously large dielectric constants (K) make them ideal for MLCs, electrostrictive actuators, and recently E-field induced piezoelectrics for low frequency sonar and high frequency bio-medical transducers. The presence of morphotropic phase boundaries (MPB) in various solid solutions gives rise to a new family of high K piezoelectrics. Microstructurally, relaxors offer less grain size dependency than normal PZTs allowing finer scale devices. Commonalities in dielectric and related behavior of relaxors suggests an inter-relationship of the underlying intrinsic phenomena of these so-called nanocomposites.

compounds with $PbTiO_3$ (PT) similar to that in the well known $Pb(Zr_{1-x}Ti_x)O_3$ (PZT) system, also makes these materials excellent candidates for piezoelectric transducers.⁽⁷⁾ It will be discussed in this paper, that relaxor ferroelectrics offer additional device potential as E-field induced piezoelectrics for applications including low frequency sonar and high frequency bio-medical transducers.

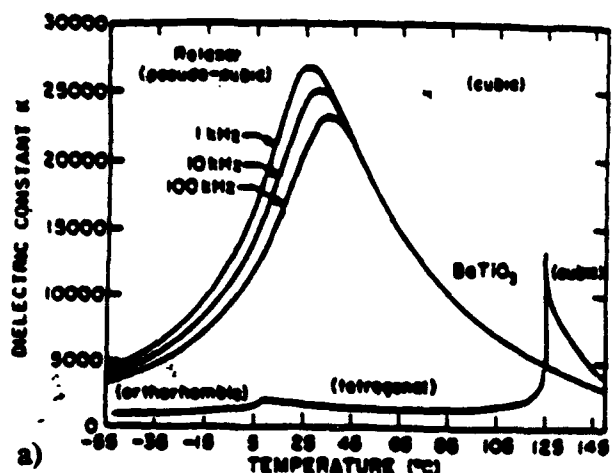
Included in the following discussion, we will review relaxor ferroelectrics and associated phenomena and commonalities that materials in this large family share. Advantages of relaxors in contrast with conventional "normal" type ferroelectrics, e.g., PZTs and $BaTiO_3$ will be clearly evident. It will also be presented that microstructurally, these materials offer further benefits.

Background

The general characteristics of relaxor ferroelectrics are presented in Fig. 1, using the well known relaxor $Pb(Mg_{1/3}Nb_{2/3})O_3$ (PMN) as the example. Differences between normal and relaxor ferroelectrics are also reviewed in Table I. As given, relaxors are distinguished from "normal" ferroelectrics, such as PZT and $BaTiO_3$, by the presence of a broad-diffuse and dispersive phase transition (Fig. 1a). The dielectric constant (K) peaks at T_m , but because of the dispersion in the Curie temperature can only be defined in reference to the frequency at which the measurements are made. The remanent polarization, P_R , is not lost at T_m but gradually decays to zero with increasing temperature above T_m (Fig. 1b). It is important to point out that the temperature of depolarization (T_d) occurs well below T_m as

INTRODUCTION

The largest group of relaxor ferroelectrics are found in the family of complex lead-based perovskites having the general formula $Pb(B' B'')O_3$, where B' is a low-valence cation, such as Mg^{+2} , Ni^{+2} , Fe^{+3} , C^{+3} , or Zn^{+2} , and B'' is a high valence cation, such as Nb^{+5} , Ta^{+5} , or W^{+6} . First discovered by Smolenskii et al.,⁽¹⁾ these materials exhibit broad and anomalously large dielectric maxima which make them ideal candidates for multilayer capacitors (MLCs),⁽²⁾ electrostrictive actuators,^(3,4) pyroelectric bolometers,⁽⁵⁾ and for electro-optics.⁽⁶⁾ The existence of a morphotropic phase boundary (MPB) in various solid solutions of relaxor



a)

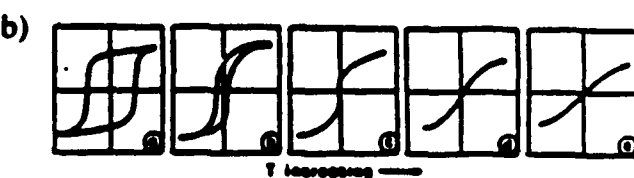
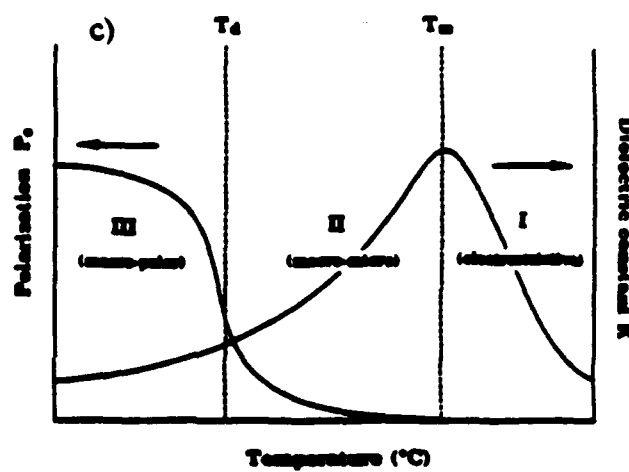
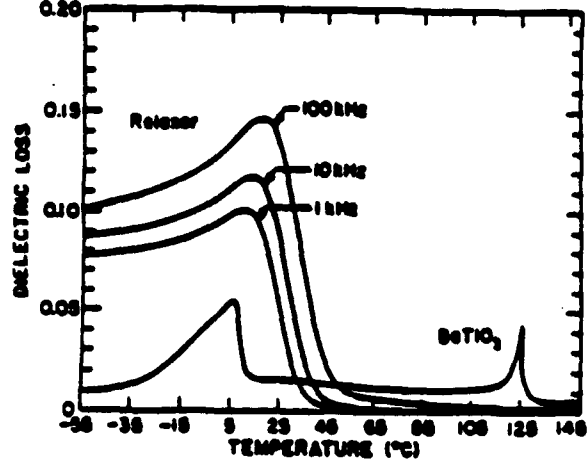


Figure 1. a) Typical Dielectric Behavior for a relaxor ferroelectric (0.93PMN:0.07PT) at 1 kHz, 10 kHz, and 100 kHz and a normal ferroelectric (BaTiO_3) at 1 kHz.⁽¹⁰⁾ b) Dielectric hysteresis in PMN as a function of temperature.⁽⁹⁾ c) Dielectric and polarization behavior for PMN as a function of temperature.

Table I. Property differences between relaxor and normal perovskite ferroelectrics.⁽⁹⁾

Property	Normal	Relaxor
Dielectric temperature dependence $K = K(T)$	Sharp 1st or 2nd order transition about Curie temperature (T_c)	Broad-diffuse phase transition about Curie maxima (T_{max})
Dielectric temperature and frequency dependence $K = K(T, \omega)$	Weak frequency dependence	Strong frequency dependence
Dielectric behavior in paraelectric range ($> T_c$)	Follow Curie-Weiss law Equation: $1/K = C/(T - T_c)$	Follow Curie-Weiss square law Equation: $1/K = 1/K_{max} + (T - T_{max})^2/2K_{max}\delta^2$
Remanent polarization, (P_R)	Strong remanent polarization, (P_R)	Weak remanent polarization
Scattering of light	Strong anisotropy (birefringent, Δn)	Very weak anisotropy to light (pseudo-cubic)
Diffraction of x-rays	Line splitting owing to spontaneous deformation from paraelectric \rightarrow ferroelectric phase	No x-ray line splitting giving a pseudo-cubic structure

δ = diffuse coefficient describing breadth of statistical distribution of Curie temperatures.

shown in Fig. 1c. Relaxor materials also show no evidence of optical anisotropy or x-ray line splitting (pseudo-cubic structural changes) even well below T_m .

The most widely accepted models for the understanding of relaxor ferroelectric phenomena come from Smolenskii⁽⁸⁾ and Cross.⁽⁹⁾ The generally accepted inhomogeneous micro-region model postulated by Smolenskii et al., bases the origin of the diffuse phase transition on local compositional fluctuations associated with B-site cation disorder, resulting in a distribution of Curie temperatures. Cross further enhanced the understanding of relaxor dielectric behavior suggesting that localized polar micro-regions are analogous to spin cluster behavior in superparamagnets. Cross's "superparaelectric" concept accounts for many of the observed properties of relaxors including the frequency dependence of the permittivity, dielectric aging, and also metastable switching from micro-macrodomains. Common to the above models, is the fact that the structural origin of relaxor behavior is on the scale of ~ 10 nm well below normal microstructural features such as grain size. Hence, grain size effects normally seen in PZTs and other piezoelectrics, due to domain wall clamping effects, are not expected for relaxor materials.

APPLICATIONS AND ASSOCIATED PHENOMENA OF RELAXORS

The most widely investigated and potentially useful family of relaxors can be found in the PMN-PT solid solution system. The phase diagram for PMN-PT is presented in Fig. 2. As shown, the role of PbTiO_3 ($T_c \sim 490^\circ\text{C}$) shifts T_m upwards around 5 °C/mole% addition. As reported by Choi et al.,⁽⁷⁾ a MPB boundary separating pseudo-cubic and tetragonal phases exists at approximately 33% PT. The strong curvature is unlike that found for the MPB in the PZT system. Presented in the Figure 3, the role of PT enhances K_m while decreasing the dispersive dielectric response, exhibiting normal ferroelectric-like behavior beyond the MPB (PT ≥ 35%).

In terms of applications, relaxor ferroelectrics in the PMN-PT system can be placed into three groups as related to their polarization/polar behavior, as shown earlier in Fig. 1c. The regions are: I) electrostrictive, II) micro-macro, and III) macro-polar. Group I compositions are those with T_m near room temperature possessing unusually high dielectric maxima ($K_m > 20,000$). This high dielectric permittivity makes them attractive for MLGs and electrostrictive strain actuators.

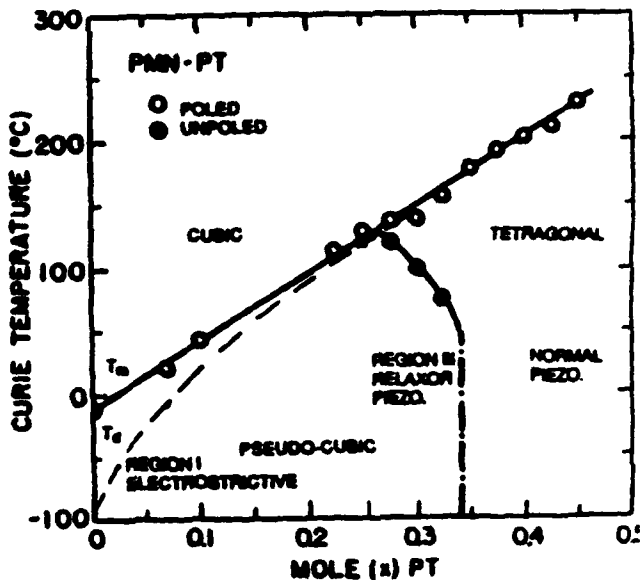


Figure 2. The phase diagram for the $(1-x)\text{Pb}(\text{Mg}_{1/3}\text{Nb}_{2/3})\text{O}_3-(x)\text{PbTiO}_3$ solid solution system showing the morphotropic phase boundary region.⁽⁷⁾

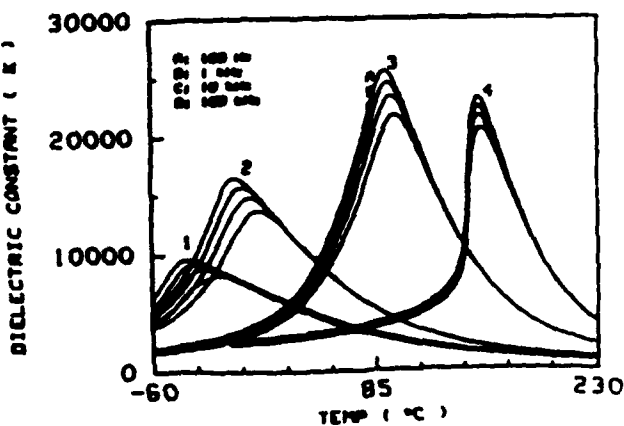


Figure 3. Dielectric constant K at various frequencies for La-doped (1 mole %) PMN:PT (X/Y): 1) 100/0; 2) 93/07; 3) 80/20 and 4) 65/35 for compositions sintered at $1200^\circ\text{C}/2\text{h}$.⁽¹¹⁾

The fundamental expressions for both piezoelectricity and electrostrictive phenomena are contrasted in Table II. As presented, electrostrictive strain (s) is proportional to the square of the polarization (P) or the applied E-field. Being a forth ranked tensor quantity, electrostriction occurs in all dielectrics, but large strains are only possible in highly polarizable materials. From the expression relating polarization (P_{induced}) with E-field, the level of strain is proportional to the dielectric constant squared ($s \propto K^2$), hence, the origin of the large strain in PMN-based relaxors. Figure 4 shows the classic quadratic strain-E-field relationship for PMN also reflecting hysteresis free behavior. Strain levels > 0.1% can be obtained, being comparable to the best piezoelectric ceramics. From this curve, electrostriction can be thought of as a non-linear E-field induced piezoelectric. As such, Fig. 5 presents the E-field induced piezo coefficient (slope of strain-E-curve) for several PMN-PT compositions of varying T_m , showing the possibility of enormously high effective piezo (strain d) coefficients. Characteristic of relaxors, however, the induced piezoelectric effect is dependent on frequency, particularly as you approach the micro-macro region below T_m .

In contrast to conventional piezoelectrics, Group I relaxors offer the following advantages: 1) large strains, 2) higher force capability (large K_s), and 3) excellent position reproducibility, i.e., no hysteresis or aging nor do they need to be poled. In addition to these advantages electrostrictors exhibit fast responses (~ 1 μsec) again since no macro domains are involved. These characteristics make them ideal for

^{*}Note: Force (F) = $V P_i \partial E_i / \partial X_j \approx$
(volume)(polarization)(Grad-E-field) ≈
 $V (\epsilon_0 K_{ij})(E_i)(\text{Grad-}E_i)$

Table II. Introduction to Piezoelectric and Electrostrictive Phenomena

Relaxors	Piezoelectricity	Electrostriction
Strain-Gauge Field	$d_{33} = \epsilon_{33} P_{33}$	$s_{ij} = M_{ij} \epsilon_{ij} E_i$
Strain-Polarization	$d_{33} = \epsilon_{33} P_{33}^2 \alpha$	$s_{ij} = C_{ijkl} P_l P_j$ (Note: $P = \epsilon_0 K E \rightarrow \text{m}^{-2}$)
Crystal Classes	Non-cubic-symmetric (permanent electric dipole)	* All Paraelectric (E-field induced dipole)
Polycrystalline Ceramics	Piezoelectric (Hysteretic P-E)	All Ceramics (No Hysterisis)

Induced Piezoelectric Effect: $d_{33} = 20(1 + \epsilon_0 K) P_{33}$ ($P_{33} = 0.4 \text{ C/cm}^2$ assumed)

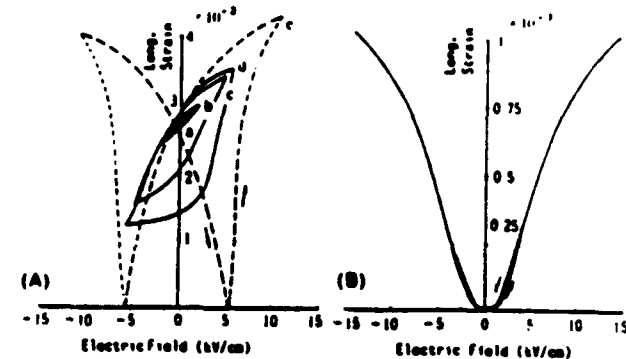


Figure 4. Field induced strains in the piezoelectric PLZT (7/62/38) and b) in the electrostrictive PMN-based ceramics. (12)

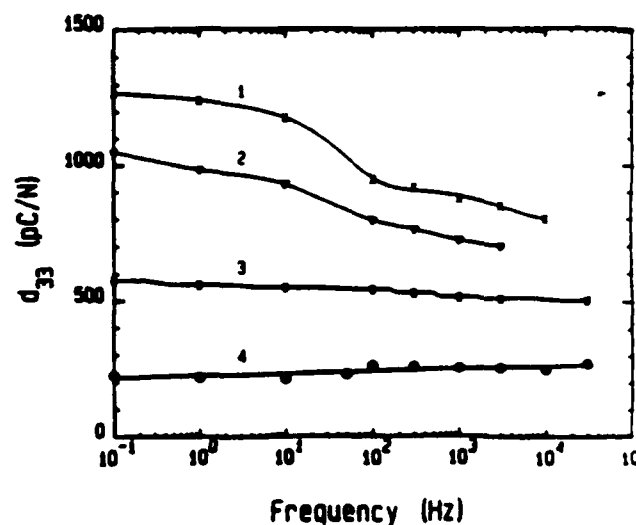


Figure 5. The d_{33} coefficient at the piezoelectric maximum vs. the AC frequency: 1) 0.93 PMN-0.07 PT ($T_m \sim 20^\circ\text{C}$); 2) 0.90 PMN-0.10 PT ($T_m \sim 40^\circ\text{C}$); 3) 0.91 PMN-0.07 PT+0.01 La ($T_m \sim 5^\circ\text{C}$); 4) PMN ($T_m \sim 10^\circ\text{C}$). (13)

micropositioners in optics where high stability is required.⁽¹⁴⁾ New applications of Group I relaxors include low frequency sonar transducers whereby large E-field induced strains are required in non-resonant structures.⁽¹⁵⁾

In addition to the more conventional usages of Group I electrostrictors, (e.g., low frequency actuators) they have been reportedly shown to have potential for high frequency resonant type devices,⁽¹⁶⁾ and more recently for bio-medical transducers.⁽¹⁷⁾ As given in the equations in Table II, piezoelectricity is induced by the application of an E-field. The induced piezoelectric phenomena is a function of E-field and frequency, depending on reference point of T_m and level of induced polarization (Fig. 5). Typical E-field dependency of the dielectric constant, piezoelectric coupling coefficients k_p and k_t and mechanical Q are presented in Fig. 6. As shown and reported in Table III, coupling coefficients comparable to that exhibited by PZTs can be achieved. Mechanical Q's can go from hard to soft, being very sensitive to T_m proximity, i.e., above "hard" and below "soft" where micro- and macro-domains are present. Though induced k_t 's and k_{ps} are only comparable to that of PZTs, these materials offer several distinct advantages:

- E-field tunability
- On-off device capability
- Large dielectric constants (impedance matching)

The ability to "tune" a transducer offers the potential of sensing reflected acoustic waves of various times or depth profiles. As the frequency of these devices increases and subsequent device size gets smaller, the need for higher capacitance becomes apparent for impedance matching to the electronics.

Group III relaxor compositions are not unlike that of conventional PZTs. As a note, all relaxor compositions are piezoelectric well below T_m (see Fig. 1b) possessing E-field induced macro-domains. In reference to room temperature, anomalously high piezo properties are observed near the MPB, as found in the PZT system. Dielectric and piezoelectric

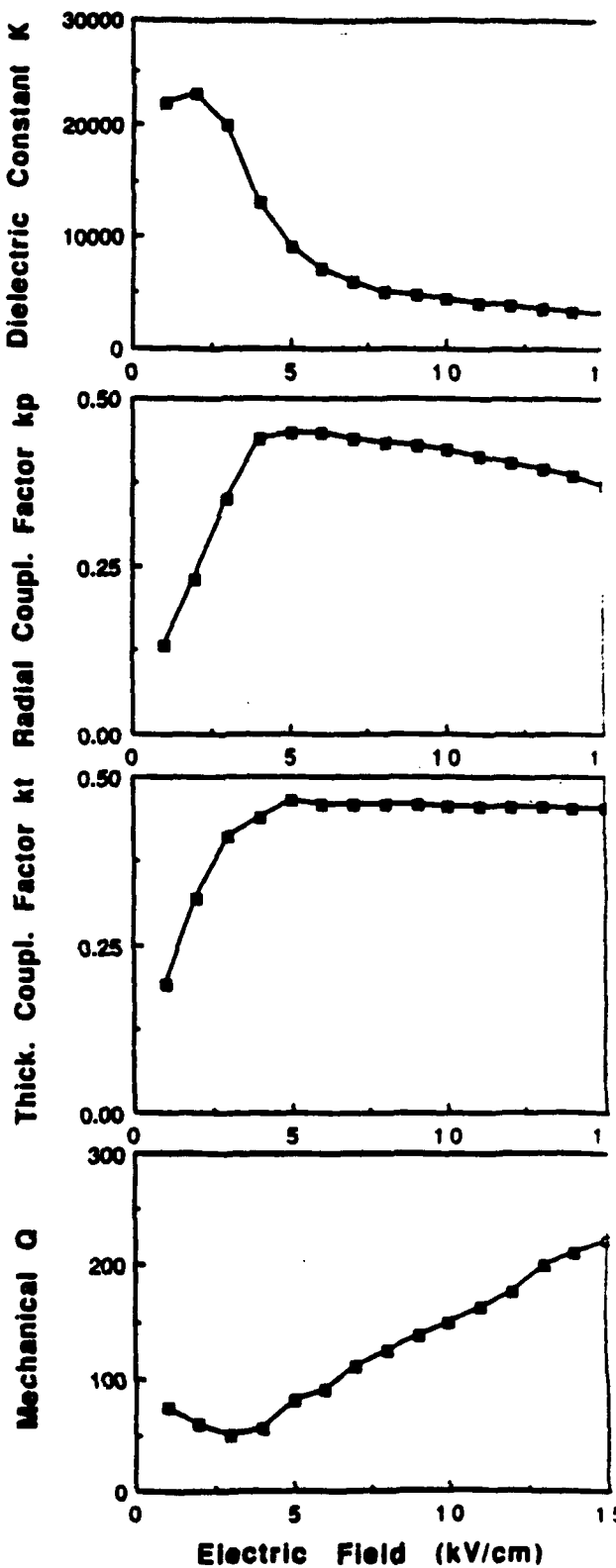


Figure 6. Electric Field dependence of dielectric constant K_3 , piezoelectric coupling coefficients k_p , k_t and mechanical Q for 0.9 PMN-0.1 PT at 25°C.

Table III. Induced Piezoelectric Properties of PMN-PT^a Based Relaxor Ferroelectrics as Compared to Conventional "Soft" and "Hard" Piezoelectrics PZTs^(14,18) (Room Temperature).

Material (T_m)	d_{33} (10^{-12} C/N)	K	k_p (%)	k_t (%)	Q_{mech}	Response Time
Group I PMN (-15°C)	200-300	18,000 *(15,000)	16	32	> 1000	~ 1 μ s
	~ 1000-1500	25,000 *(15,000)	45	48	- 50-100	
Group III PMN-PT (MPB)	660	5,000	- 65		70-100	
	270	1200	- 58	51	≥ 500	
	220	1000	- 50	44	≥ 1000	
	~ 400	~ 2,000	- 60	49	75	
	~ 590	~ 3,500	- 65	50	65	≥ 10 μ s

^aNote: Dielectric and piezoelectric properties are E-field dependent values at ~ 10 KV/cm

properties of MPB compositions are reported in Table III. As presented, these materials are superior to very "soft" PZTs such as PZT-5. Group III relaxor piezoelectrics also offer certain advantages, particularly in terms of microstructural dependences. In conventional PZT piezo-materials, large piezoelectric effects are not possible in fine grain size materials (typically 3-10 μ m) owing to grain boundary clamping of extrinsic contributions to polarizability such as domain wall motion.⁽¹⁹⁾ Since the underlying intrinsic phenomena associated with relaxor ferroelectric behavior is on the order of ~ 10 nm, little grain size dependency and thermal degradation (aging) is observed.⁽²⁰⁾ Reported by Kim et al.,⁽²¹⁾ fine grain relaxors using La modification to inhibit grain growth resulted in highly dense piezoelectrics with grain sizes < 1 μ m. The significance of this is evident as the "scale" of devices including MLCs, actuators, and piezo transducers continue to decrease. The higher dielectric constants, once again offer improved impedance matching.

Group II relaxor compositions have not been fully exploited for device applications. Though these compositions do not exhibit stable macro-polar domains above T_d , the thermal depolarization temperature, the P-T behavior shown (see Fig. 1c) is essentially a low frequency phenomena. As such, large E-field induced strains are possible, but minimal hysteresis is obtained only at low frequencies, typically < 1 Hz. Essentially this behavior couples both electrostrictive and piezoelectric phenomena, whereby macro-polar domains can be stabilized under an applied E-field. In terms of actuators, Group II relaxors offer lower dielectric constants than Group I materials, placing less demands on power supplies used to drive the devices. Also, depending on the temperature width, $\Delta T = T_m - T_d$, the temperature range of usage is broad in comparison. The width (micro-macro) region is the widest for PMN decreasing continuously with increasing PbTiO₃, reaching $\Delta T \approx 0$ at the MPB as shown in Fig. 2. Recent work by Kim et al.,⁽²²⁾ found that the micro-macro temperature width (ΔT) could be broadened by compositionally modifying on the A-site of the perovskite structure using La making this Group II family of relaxors more promising for transducer applications.

COMPOSITIONAL RELATIONSHIPS AND COMMONALITIES

In recent years, substantial improvements have been made in the processing, fabrication, and understanding of relaxor ferroelectrics and their underlying phenomena.^(8,9) Once again, most of this work has been focused on the PMN-PT system. The question arises, is PMN-PT representative of other relaxor systems? Though the role of compositional modifications on relaxor behavior is not yet clear, work by Randall et al.,^(23,24) suggests a commonality among all $Pb(B_1B_2)O_3$ relaxors in that short range B-site cation order must be present. For example, no B-site order is evident in normal ferroelectrics such as PZT's and fully ordered compounds such as $Pb(Mg_{1/2}W_{1/2})O_3$ which exhibit normal antiferroelectric behavior. As supported by transmission electron microscopy (TEM), the compositional ordering in relaxors is on the nanoscale (~ 10-100 nm). As depicted in Figure 7, relaxor ferroelectrics can be thought of as nanocomposites! Interestingly, the scale of these regions appears to correlate to the relaxor dielectric behavior. The larger the regions the more diffuse the transition. This observation is supported by the work of Hilton et al.⁽²⁶⁾, whereas with increasing $PbTiO_3$ in the PMN-PT system the size of the ordered regions (Mg:Nb) decreases, disappearing at the MPB. Further support comes from non-stoichiometric modifications such as La^{+3} , increasing the size of the ordered regions and subsequently broadening the transition.⁽²⁷⁾

In contrast to the above observations, enhanced ordering in the relaxor compounds $Pb(Sc_{1/2}Ta_{1/2})O_3$ (PST)⁽²⁸⁾ and $Pb(In_{1/2}Nb_{1/2})O_3$ ⁽²⁹⁾ (PIN) by thermal annealing, results in more normal ferroelectric and antiferroelectric behavior, respectively. Though all relaxors possess B-site ordering, Mg:Nb ordering in $Pb(Mg_{1/3}Nb_{2/3})O_3$ is non-stoichiometric since the ideal ratio is actually 1:2. Common to the observed ordering effects in PMN and the relaxors above is the level or degree of compositional inhomogeneity. In other words, decreasing the non-stoichiometric ordered regions of Mg:Nb and increasing the stoichiometric regions in PST and PIN both

lead to overall compositional uniformity. Once again, the key to relaxor phenomena is the presence of distinct or abrupt compositional regions on a nanoscale. Commonalities in relaxor dielectric behavior are also observed.

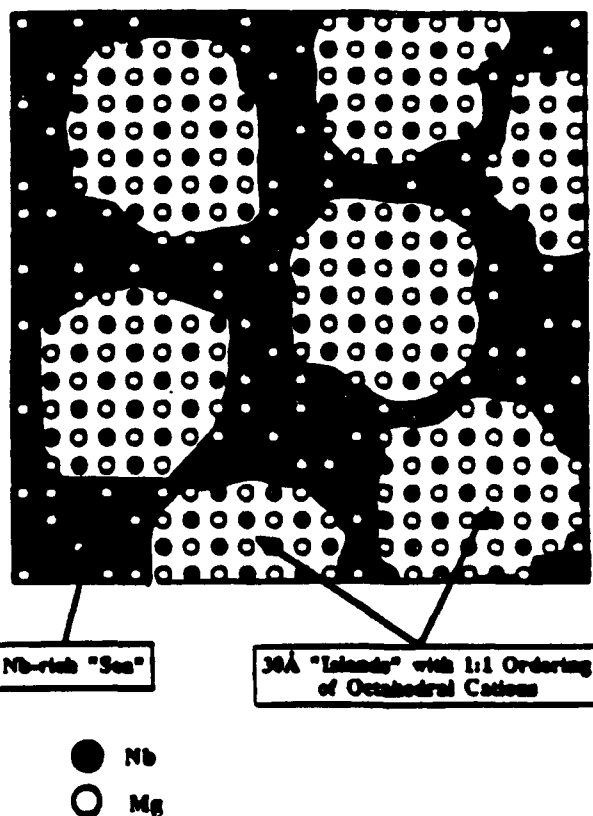


Figure 7. Schematic representation of the nanostructure of $Pb(Mg_{1/3}Nb_{2/3})O_3$ showing regions with 1:1 ordering of the B-site.⁽¹⁰⁾

Along with $PbTiO_3$, Voss⁽³⁰⁾ and others,⁽³¹⁾ reported that the Curie temperature T_m of PMN could be adjusted both upwards and downwards with a wide range of B-site substitutions as shown in Fig. 8. Of importance is the fact that the value of K_{max} is dependent on T_m . More recent work by Hilton et al., and Papet^(32,33) found that for a given relaxor system the value $K_{max}\delta^2$, where δ reflects the diffuseness of the transition, is nearly constant regardless of processing variables, such as grain size, firing temperature, etc. The above commonalities of relaxors goes beyond the Group I types, as evident by the observation that nearly all MPB relaxor-based compositions exhibit comparable dielectric and piezoelectric properties (see Table IV). Interestingly these MPB relaxors possess

similar T_c 's (~ 150-170°C) reflecting the temperature limitation of relaxor (Group III) piezoelectrics.

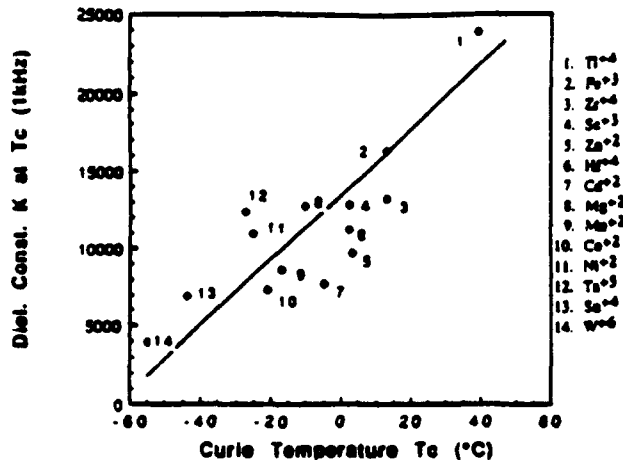


Figure 8. Dielectric Constant K at T_c or T_m for various compositionally modified PMN ceramics (1 kHz data for fourteen compositions).⁽³⁰⁾

Table IV. Dielectric and Piezoelectric Properties of Pb-Based Relaxor Ceramics with Compositions Near MPB.^(17,34,35,36)

Composition	Curie Temp. (°C)	$K \oplus 25^\circ\text{C}$ and 1 kHz	d_{33} (pC/V)	k_p
0.6 Pb(Mg _{1/3} Nb _{2/3})O ₃ - 0.4 Pb(Zr _{0.8} Ti _{0.2})O ₃ (Ouchi, et al., 1985)	170	--	--	0.50
0.5 Pb(Ni _{1/3} Nb _{2/3})O ₃ - 0.5 Pb(Zr _{0.9} Ti _{0.1})O ₃ (Chung, et al., 1989)	130	3,000	370	0.45
0.87 Pb(Zr _{1/3} Nb _{2/3})O ₃ - 0.03 BaTiO ₃ -0.06 PTIO ₃ (Sommer, 1986)	150	5,000	640	0.52
0.70 Pb(Mg _{1/3} Nb _{2/3})O ₃ - 0.30 PTIO ₃ (Chen, et al., 1989)	145	4,900	670	0.50

The consequences of the above findings is summarized in the following statement.

"Given equivalent and adequate processing, optimum relaxor compositions are compositionally independent given the same T_m ."

Hence, selection of the "ideal" relaxor formula should be based on ease of processing and cost of raw materials.

SUMMARY

Complex lead-based perovskites with the general formula $\text{Pb}(\text{B}'\text{B}^{\prime\prime})\text{O}_3$ encompass the largest family of relaxor ferroelectrics. Distinguished from "normal" ferroelectrics, relaxors exhibit broad-diffuse frequency dispersive phase transitions. As such, relaxors can be classified into three distinct groups based on their polar behavior and transition proximity (T_m). They are as follows: I. micro-polar (electrostrictive) near T_m ; II. micro-macro $T_m - T_d$, when T_d is the depolarization temperature; and III. macro-polar (piezoelectric) $\ll T_m$. Group III relaxor piezoelectrics are found to be optimum at morphotropic phase boundaries, e.g., 0.65 PMN-0.35 PT, similar to the well known $\text{Pb}(\text{Zr}_{1-x}\text{Ti}_x)\text{O}_3$ system. Subsequently, applications of relaxors can also be subdivided into various classes. Applications of Group I relaxors take advantage of their high K_s and broad transitions making them ideal for MLCs and electrostrictive actuators. The ability to induce large piezoelectric effects with an E-field offers interesting device potential for low frequency sonar and high frequency biomedical transducers. In contrast to conventional PZTs, these materials offer minimal hysteresis, little aging, large E-field induced strains, E-field variable properties, on-off capability and high dielectric constants for improved impedance matching. Group III relaxors offer enhanced piezoelectric activity again with high dielectric constants.

Commonalities in terms of dielectric and related properties of all relaxors suggest a strong inter-relationship of the short range B-site ordering found in these so-called nanocomposites. Hence, given equivalent and adequate processing, one relaxor family, such as PMN-PT, is representative. Given the same T_m , the ideal relaxor material is thus compositionally independent.

Further enhancements of relaxor materials will come through continued understanding of the intrinsic relaxor phenomena. It is believed that significant advancements will come through the combined relaxor phenomena associated with the PLZT perovskite family as evident by the work of N.

Kim using A-site modifications of La doped PMN-based relaxors. It is believed that through future R & D efforts, relaxor ferroelectrics will play an important role in the next generation of electronic ceramics.

References

1. G.A. Smolenskii, A.I. Agranovskaya. "Dielectric Polarization and Losses of Some Complex Compounds," Sov. Phys. Tech. Phys., 3, pp. 1380-82 (1958).
2. T.R. Shrout, A. Halliyal. "Preparation of Lead-Based Ferroelectric Relaxors For Capacitors," Am. Ceram. Soc. Bulletin, Vol. 66, No. 4, pp. 704-711 (1987).
3. S.J. Jang. Ph.D. Thesis, The Pennsylvania State University (1979).
4. K. Uchino. "Electrostrictive Actuators: Materials and Applications," Cer. Bull., 65, No. 8, pp. 647-652 (1986).
5. R.W. Whatmore, P.C. Osbond, N.M. Shorrocks. "Ferroelectric Materials For Thermal IR Detectors," Ferroelectrics, Vol. 76, pp. 351 (1987).
6. D.A. McHenry, J. Giniewicz, S.J. Jang, A.S. Bhalla, T.R. Shrout. "Optical Properties of Hot Pressed Relaxor Ferroelectrics," Ferroelectrics, 93, pp. 1137-1143 (1989).
7. S.W. Choi, T.R. Shrout, S.J. Jang, A.S. Bhalla. "Dielectric and Pyroelectric Properties in the Pb(Mg_{1/3}Nb_{2/3})O₃-PbTiO₃ System," Ferroelectrics, 100, pp. 29-38 (1989).
8. G.A. Smolenskii. "Physical Phenomena in Ferroelectric with Diffused Phase Transition," Journal Phys. Soc. of Japan, Vol 28. Supplement, p. 26 (1970).
9. L.E. Cross. "Relaxor Ferroelectrics," Ferroelectrics, Vol. 76, pp. 241-267 (1987).
10. J.P. Dougherty and T.R. Shrout. "Lead Based Pb(B1B2)O₃ Relaxors vs. BaTiO₃ Dielectrics for Multilayer Capacitors," Proc. Symp. on Ceramic Dielectrics, Ed. H.C. Ling, Am. Ceram. Soc. (1989).
11. N. Kim. "The Role Of Lanthanum Modification On The Fabrication and Properties of Lead Magnesium Niobate-Lead Titanate Ceramics," M.S. Thesis, The Pennsylvania State University (1990).
12. K. Uchino, S. Nomura, L.E. Cross, S.J. Jang and R.E. Newnham. "Electrostrictive Effect in Lead Magnesium Niobate Single Crystals," J. Appl. Phys., Vol. 51, No. 2, pp. 1142-45 (1980).
13. W.Y. Pan, W.Y. Gu, D.J. Taylor and L.E. Cross. "Large Piezoelectric Effect Induced by Direct Current Bias in PMN:PT Relaxor Ferroelectric Ceramics," Japanese Journal of Applied Physics, Vol. 28, No. 4, pp. 653-661 (1989).
14. S. Nomura, K. Uchino. "Electrostrictive Effect in Pb(Mg_{1/3}Nb_{2/3})O₃-Type Materials," Ferroelectrics, Vol. 41, pp. 117-132 (1982).
15. Robert Ting (private communication).
16. T.R. Shrout, W.A. Schulze, J.V. Biggers. "Temperature Compensated Composite Resonator," Ferroelectrics, 34, pp. 105-111 (1981).
17. H. Masuzawa, Y. Ito, C. Nakaya, et al. "Electrostrictive Materials For Ultrasonic Probes in the Pb(Mg_{1/3}Nb_{2/3})O₃-PbTiO₃ System," Japanese Journal of Applied Physics, Vol. 28, Supplement 28-2, pp. 101-104 (1989).
18. H. Jaffe and D.A. Berlincourt. "Piezoelectric Transducer Materials," Proc. IEEE, Vol. 53, No. 10, pp. 1372-1386 (1965).
19. K. Okazaki and K. Nagata. "Effects Of Density and Grain Size On The Elastic And Piezoelectric Properties of Pb(Zr,Ti)O₃," J. Soc. Mater. Sci. Japan, Vol. 4, pp. 404-12 (1972).
20. J.T. Fielding, Jr., S.J. Jang and T.R. Shrout. "Thermal Degradation Of Relaxor-Based Piezoelectric Ceramics," presented at ISAF '89, to be published in Ferroelectrics.
21. N. Kim, S.J. Jang, and T.R. Shrout. "Relaxor Based Fine Grain Piezoelectric Ceramics," presented at ISAF '89, to be published in Ferroelectrics.
22. N. Kim, W. Huebner, S.J. Jang and T.R. Shrout. "Dielectric and Piezoelectric Properties of Lanthanum Modified Lead Magnesium Niobate Ceramics," Ferroelectrics, Vol. 93, pp. 341-49 (1989).

23. C.A. Randall, A.S. Bhalla, "Nanostructural-Property Relations in Complex Lead Perovskites", Jap. J. Appl. Phys., Vol. 29, No. 2, pp. 327-333 (1990).
24. C.A. Randall, A.S. Bhalla, T.R. Shrout and L.E. Cross, "Classification and Consequences of Complex Lead Perovskite Ferroelectrics With Regard To B-Site Cation Disorder", submitted for publication to Mat. Res. Bulletin.
25. T.R. Shrout, W. Huebner, C.A. Randall and A.D. Hilton, "Aging Mechanisms In -Based Relaxor Ferroelectrics", Ferroelectrics, Vol. 93, pp. 361-372 (1989).
26. A.D. Hilton, D.J. Barber, C.A. Randall and T.R. Shrout, "On Short Range Ordering in The Perovskite Lead Magnesium Niobate", J. Mat. Sc., Vol. 25, No. 8, pp. 3461-3466 (1990).
27. J. Chen, H.M. Chan, and M.P. Harmer, "Ordering Structure and Dielectric Properties of Undoped and La/Na Doped $Pb(Mg_{1/3}Nb_{2/3})O_3$ ", presented at the 89th Annual Meeting of the Am. Ceram. Soc. (1987).
28. N. Setter and L.E. Cross, "The Role of B-Site Cation Disorder In Diffuse Phase Transition Behavior of Perovskite Ferroelectrics", J. Appl. Phys., Vol. 51, No. 8, pp. 4356-60 (1980).
29. U. Kodama, M. Osada, O. Kumon and T. Nishimoto, "Piezoelectric Properties and Phase Transition of $PbIn_{1/2}Nb_{1/2}O_3$ - $PbTiO_3$ Solid Solution Ceramics", Am. Ceram. Soc. Bulletin, Vol. 48, No. 12, pp. 1122-4 (1969).
30. D.J. Voss, S.L. Swartz, T.R. Shrout, "The Effect of Various B-Site Modifications On The Dielectric And Electrostrictive Properties Of Lead Magnesium Niobate Ceramics", Ferroelectrics, Vol. 50, pp. 203-208 (1983).
31. Landolt-Bornstein, Ferroelectrics and Related Substances, New Series, Vol. 16 (1981).
32. P. Papet, J.P. Dougherty, T.R. Shrout, "Particle and Grain Size Effects On The Dielectric Behavior Of The Relaxor Ferroelectric $Pb(Mg_{1/3}Nb_{2/3})O_3$ ", accepted for publication in the Journal of Materials Research.
33. A.D. Hilton, C.A. Randall, D.J. Barber, T.R. Shrout, "The Influence Of Processing On Dielectric Properties Of PMN:PT Based Ceramics," to be published.
34. H. Ouchi, K. Nagano, and S. Hayakawa, "Piezoelectric Properties of $Pb(Mg_{1/3}Nb_{2/3})O_3$ - $PbTiO_3$ - $PbZrO_3$ Solid Solution Ceramics," J. Amer. Ceram. Soc., Vol. 48, No. 12, pp. 630-635 (1965).
35. S. Baumler, "The Dielectric and Piezoelectric Properties of PZN:PT:BT Ceramics", M.S. Thesis, The Pennsylvania State University (1986).
36. S.T. Chung, K. Nagata, and H. Igarishi, "Piezoelectric and Dielectric Properties of $Pb(Ni_{1/3}Nb_{2/3})O_3$: $Pb(Zn_{1/3}Nb_{2/3})O_3$: $Pb TiO_3$ System Ceramics", Ferroelectrics, Vol. 94, pp. 243-7 (1989).

APPENDIX 19

On short range ordering in the perovskite lead magnesium niobate

A. D. HILTON, D. J. BARBER

Department of Physics, University of Essex, Wivenhoe Park, Colchester, Essex, UK

C. A. RANDALL, T. R. SHROUT

Materials Research Laboratory, Pennsylvania State University, PA 16802, USA

The structural ordering characteristics of lead magnesium niobate (PMN) and solid solutions (PMN-PT) of PMN with lead titanate have been investigated using transmission electron microscopy (TEM). It is proposed that short range, non-stoichiometric 1:1 ordering of the Mg and Nb cations on an F-centred superlattice generates space charges which dominate the kinetics of the ordering process and inhibit the development of long-range order. Furthermore, it is demonstrated that by introducing off-valent La³⁺ ions on to the A-site sublattice, the local charges can be at least partially-compensated and an increase in the extent of structural ordering is consequently observed.

1. Introduction

Most of the ferroelectric relaxors which crystallize with the perovskite structure and correspond to the general formula A(B'⁺B''⁺)O₃ can undergo at least short-range structural ordering of the B-site cations. In the B-site order-disorder-perovskites the degree of long-range order can be varied by means of suitable thermal treatments. This has been shown to have important consequences since the dielectric properties of this class of relaxor are directly dependent on the degree of B-site order (e.g. lead scandium tantalate (PST), lead scandium niobate (PSN), lead indium niobate (PIN) [1-4]), thereby providing another variable for the tailoring of properties. In most ferroelectric relaxors, however, the degree of order is not so readily altered and often can only be brought about by modifying the bulk composition [5, 6]. In some instances, such as in lead iron niobate (PFN), even short-range order is undetectable by conventional experimental techniques and a homogeneous disorder is believed to exist [7]. Nevertheless, in relaxors which exhibit some degree of short-range order, it is reasonable to suppose that even subtle changes in the state of structural order may also affect dielectric response (in addition to any effect resulting from necessary compositional modification) particularly if the two species of B-site cations are very different in electronic character.

The ideal perovskite structure can be considered as BO₆ octahedra centred on the corners of a simple cubic lattice and linked by the sharing of oxygen ions. The A-site cations are located in the interstitial positions between these octahedra. Ordering takes place in some of the $x = 1/2$ perovskites by the diffusion of B' and B'' cations to nearest neighbour positions on the B-site sublattice. This results in the formation of an F-centred $2a_0 \times 2a_0 \times 2a_0$ superlattice (where a_0 is the lattice parameter). This superstructure can easily be identified by the presence of

superstructure reflections in X-ray and electron diffraction patterns.

The ordering characteristics of most complex A(B'⁺B''⁺)O₃ perovskites can largely be understood by considering the electrostatic and mechanical forces generated, respectively, by differences in electronic charge and in ionic radii of the B' and B'' ions. Broadly speaking, materials possessing large differences in both valence and ionic size between the B' and B'' cations show a strong tendency for order [8]. These empirical guidelines can be used successfully to predict the degree of order that is actually observed in a large number of relaxors that have the perovskite structure. Some perovskite materials, however, do not exhibit the long-range order that is to be expected from the above considerations of electrostatic and mechanical forces. Most materials falling into this category correspond to $x \neq 1/2$ in the general perovskite formula A(B'⁺B''⁺)O₃ and PMN, where $x = 1/3$, is exemplary.

By means of TEM dark field and electron diffraction techniques, the behaviour of PMN-PT [Pb(Mg_{1/3}Nb_{2/3})O₃-PbTiO₃] solid solutions and the effect of La substitutions in the PMN [Pb(Mg_{1/3}Nb_{2/3})O₃] structure have been studied in order to elucidate the special ordering characteristics of this class of perovskite relaxor.

2. Experimental procedure

Samples examined in this study included PMN, PMN + 2 wt % La₂O₃ and solid solutions corresponding to (1 - y)PMN-y PT with y ranging from 0.07 to 0.4.

Ceramic samples were prepared via the columbite route [9] in order to avoid formation of parasitic pyrochlore phases. Both conventionally sintered (prepared by T. R. Shroud, Pennsylvania State University, USA) and hot pressed (prepared by P. Osbourn,

Northants, UK) ceramic materials were examined. The hot pressed ceramic was prepared with a small excess of PbO.

Samples for TEM observation were mechanically polished to a thickness of $\sim 30 \mu\text{m}$ prior to ion beam thinning. Examination of the samples was carried out using a Jeol-200CX transmission electron microscope which was operated at an accelerating voltage of 200 kV. The use of 200 keV electrons enhances sample penetration, thus enabling thicker regions, more representative of the bulk, to be examined. A Hexland low temperature goniometer stage was used to vary the sample temperature within the range $-176^\circ\text{C} < T^* < 150^\circ\text{C}$ where T^* represents the temperature indicated by the thermocouple. Slight differences between the sample temperature and the temperature indicated are expected because of local heating effects from the electron beam.

3. Results

With the exception of the 0.6 PMN-0.4 PT samples, $\{h + 1/2, k + 1/2, l + 1/2\}$ superstructure reflections (F-spots) were observed in all samples for both $\langle 110 \rangle$ and $\langle 211 \rangle$ zone axis diffraction patterns. The intensities of the F-spots were assessed by comparison with the intensities of the matrix reflections. Dark field (DF) imaging using one of the F-type reflections gives regions of light contrast associated with domains of B-site structural order. Figs 1a and b show respectively a DF image formed with the $\{3/2, 3/2, 3/2\}$ reflection and the corresponding $\langle 110 \rangle$ zone axis diffraction pattern, obtained from undoped PMN. In Fig. 1a the ordered domains have an average size of $\sim 6 \text{ nm}$ and only small deviations in this size are present across the whole grain. The F-spots associated with these domains are indicated in Fig. 1b. As the concentration of PbTiO_3 is increased within the PMN-PT solid solution both the intensities of the F-spots and the sizes of associated domains diminish. Fig. 2a shows domains of about 3 nm in dimension within the 0.93 PMN-0.07 PT solid solution. Fig. 2b is the $\langle 110 \rangle$ electron diffraction pattern from the

superstructure reflections than those observed in undoped PMN. The reduction in the intensities of superstructure reflections is associated with the reduction in domain size. No significant spread of domain sizes is observed. Fig. 3 shows the $\langle 110 \rangle$ diffraction pattern of 0.8 PMN-0.2 PT. The F-spots are significantly weaker than that in undoped PMN and it proved impossible to obtain DF images with them. In the 0.6 PMN-0.4 PT sample (Fig. 4) the F-spots are completely absent. However, when only 2 wt % of lanthanum is substituted for lead an increase in both the intensity of the F-reflections and the domain size is observed (Figs 5a and b). In most grains a range of domain sizes from 5 to 35 nm is present. However, certain grains (as in Fig. 5a) were observed to exhibit domains up to 150 nm in size. The larger ordered domains frequently exist near the grain boundaries but clusters of large domains are occasionally found in the grain interior.

The F-spots become slightly more diffuse on heating the specimens from -176°C through to 150°C , but no abrupt change in intensity is observed. Undoped, hot pressed PMN samples, annealed for 7 days at 970°C in a lead-oxide-rich atmosphere do not differ markedly in microstructure from PMN samples which have not been annealed.

Zone axis diffraction patterns exposed for long periods of time reveal the presence of very weak $\{h + 1/2, k + 1/2, 0\}$ reflections (referred to as α' -spots). These reflections are strongest in the $\langle 100 \rangle$ zone but proved to be too weak to produce DF images. The $\{h + 1/2, k + 1/2, 0\}$ reflections in the $\langle 100 \rangle$ zone for undoped PMN are indicated in Fig. 6. This figure also shows the presence of weak diffuse scattering parallel to the $\langle 110 \rangle$ direction.

The relative intensity variation of the α' -spots with respect to composition and temperature is similar to the intensity variation observed for the F-spots. Additions of PbTiO_3 to the PMN-PT solid solution produces weaker α' -reflections but small La substitutions increase their intensity. No abrupt change in

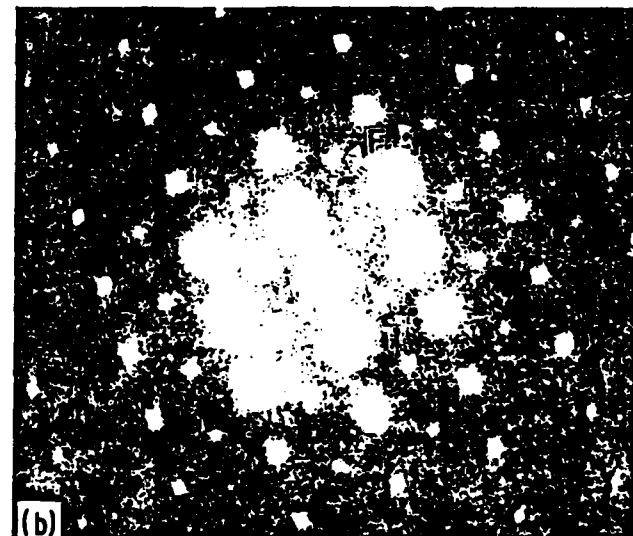
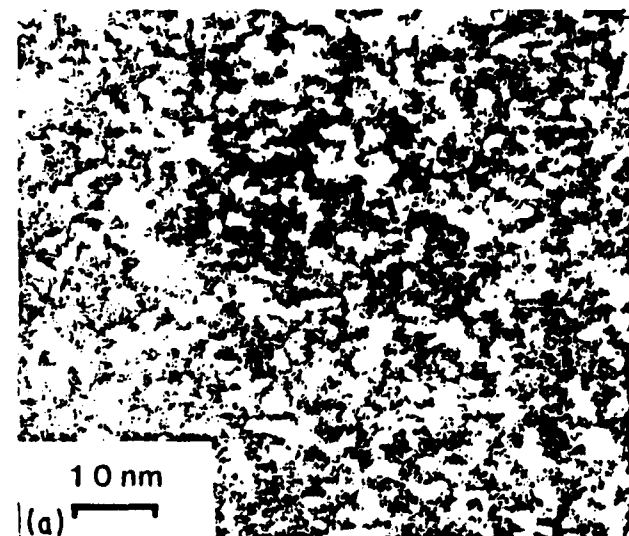


Figure 1 (a) Dark field image showing B-site ordered domains (bright areas) in undoped hot pressed PMN. (b) $\langle 110 \rangle$ zone axis selected area diffraction pattern taken from the grain in Fig. 1a. The F-spots are indicated.

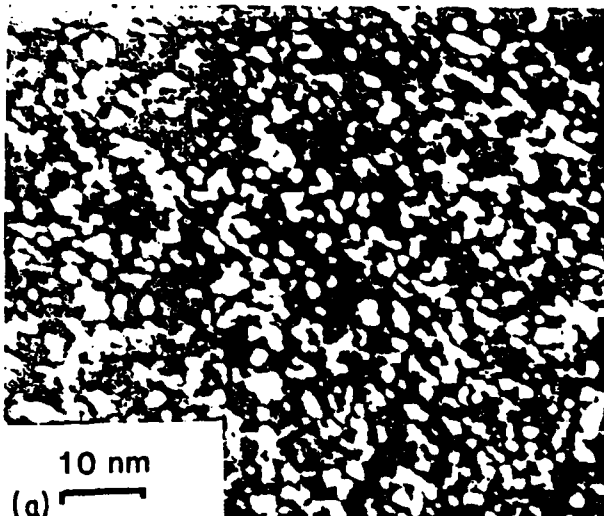
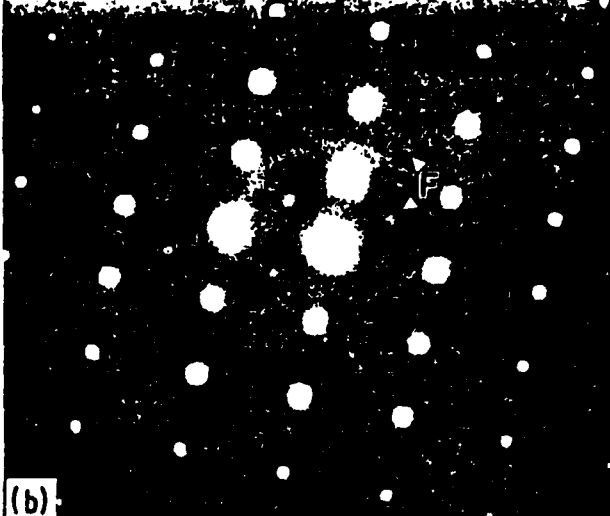


Figure 2 (a) Dark field image showing B-site ordered domains in conventionally sintered 0.93PMN-0.07PT.



(b) $\langle 110 \rangle$ selected area diffraction pattern taken from Fig. 2a.

intensity of the x' -reflections is observed in the temperature range $-176^\circ\text{C} < T < 150^\circ\text{C}$.

4. Discussion

4.1. Ordering

The presence of F-spots indicates that an F-centred $2a_0 \times 2a_0 \times 2a_0$ superlattice exists in all samples with the exception of the 0.6 PMN-0.4 PT sample. Since the intensities of the F-spots do not change significantly with temperature it can be concluded that they are not associated specifically with either the ferroelectric phase or with tilting of the oxygen octahedra [10] but are chemical in origin.

The F-centred superstructure in PMN has previously been identified using high resolution [11] and dark field [12] imaging techniques. On the basis of X-ray data it has also been pointed out that a number of $x = 1/3$ and other $x = 1/2$ perovskites can order stoichiometrically provided the appropriate superlattice can develop [13, 14]. However, the ordering schemes proposed for such systems necessarily generate particular superlattice reflections. These

superlattice reflections were not present within electron diffraction patterns observed in the current study.

We believe that our results demonstrate that non-stoichiometric 1:1 ordering of Mg and Nb cations takes place on an F-centred $2a_0 \times 2a_0 \times 2a_0$ superlattice in the PMN system. For the $x = 1/2$ materials such as PST, it is interesting to note that a charge imbalance which would accompany a non-stoichiometry between B-site cations would be reduced by the diffusion of these cations to alternate B-sites. In the case of a perovskite where $x \neq 1/2$, as in PMN (where $x = 1/3$ in the ideal compound), the implications of 1:1 order are less straightforward. In this case, the nucleation and growth of ordered domains implies the outward diffusion of B" (excess) ion species into the circumferential zones which become enriched in element B" (Nb in PMN). Thus in the absence of compensating charge effects, large electric fields would be generated in the lattice between ordered and disordered regions (with effective positive and negative charge respectively). These charge effects would become more severe as the ordered regions increase in



Figure 3 $\langle 110 \rangle$ selected area diffraction pattern from hot pressed 0.8PMN-0.2PT.

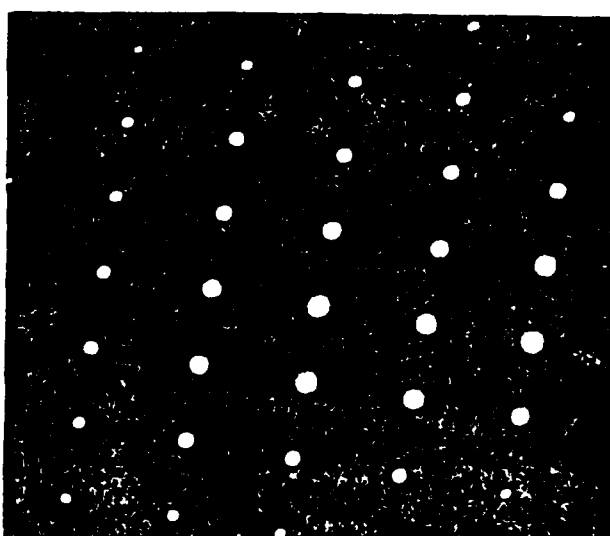


Figure 4 $\langle 110 \rangle$ selected area diffraction pattern from conventionally sintered 0.6PMN-0.4PT. The F-spots are absent.

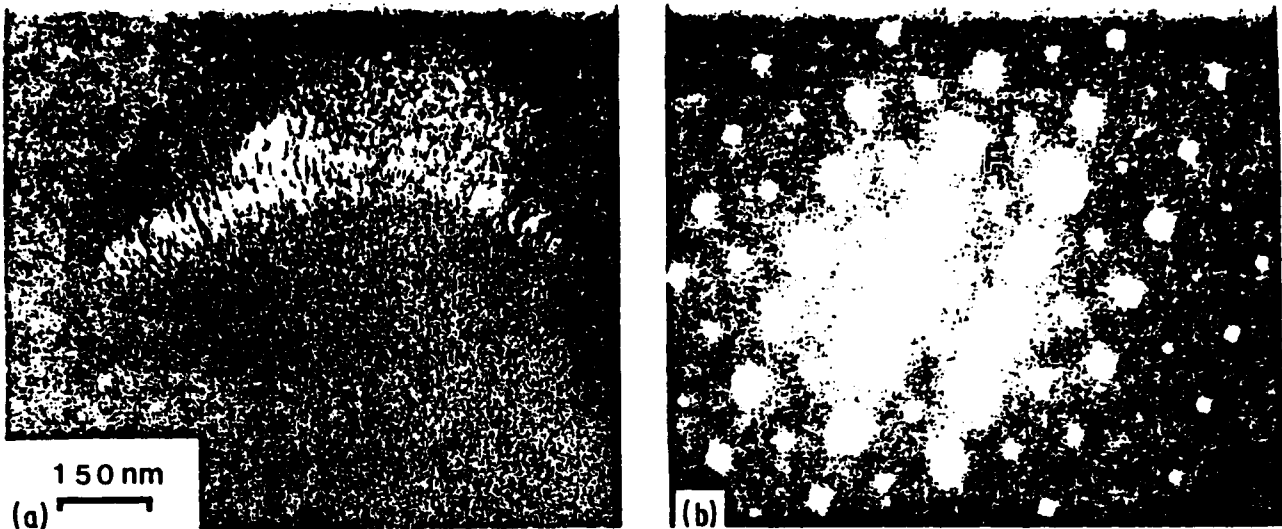


Figure 5 (a) Dark field image showing the influence of grain boundaries on the sizes of B-site ordered domains in hot pressed PMN + 2 wt % La_2O_3 . Domains ranging from 5 to 150 nm in dimensions are present. (b) $\langle 110 \rangle$ selected area diffraction pattern taken from Fig. 5a.

size. In this case one may anticipate that an equilibrium domain size will be reached when the driving forces for B cation ordering (electrostatic and mechanical) are balanced by forces tending to disorder B-site cations (from the interactions between local space charges generated by the expansion of non-stoichiometrically ordered regions). In the case where space charges can be compensated by lattice defects, an equilibrium size of ordered domains is also anticipated when the space charges become too large to be compensated by existing defects. These views are supported by the observation that an equilibrium size for ordered domains of 6 nm is found in undoped PMN even after prolonged annealing. Exaggerated growth of ordered domains at grain boundaries has been reported in PST [15] and PSN [16] annealed ceramics. The existence of enhanced vacancy concentrations [17] which facilitate cation diffusion near grain boundaries was invoked to explain this phenomenon. No such effect has been found in PMN or 0.93 PMN-0.07 PT samples.

From considerations of ionic radii it is generally accepted that Ti ions occupy B-sites in PMN-PT solid

solutions. It is not believed, however, that Ti ions are directly involved with the ordering process. Consideration of the possible 1:1 ordering of Mg and Ti ions yields an average B-site valency of +3 and is therefore electrostatically less favourable than Mg:Nb order. Nb:Ti ion order is unlikely since the degree of order would be expected to increase with increasing PbTiO_3 content. Since a progressive decrease in B-site order is observed with increasing PbTiO_3 content it is possible that Ti ions 'dilute' the electrostatic and mechanical interactions which exist between Mg and Nb cations thus reducing their tendency to order.

It is interesting to note that small substitutions of lanthanum oxide to PMN promote the formation of larger ordered domains and a non-uniformity of domain size. We believe that La^{3+} ions, which probably occupy Pb^{2+}/A -sites, aid in reducing the charge imbalance generated by non-stoichiometric ordering although the exact mechanism for this process is presently unclear. The associated lead vacancies may also relax bonding constraints thereby enhancing diffusion and facilitating ordering. The anomalously large ordered domains frequently observed near grain boundaries in La-doped PMN suggests that charge heterogeneity is no longer the limiting factor on domain size, as in PMN and PMN-PT systems, but that the kinetics of ordering is then governed by the usual factors constraining diffusion. Alternatively, the non-uniformity of domain sizes observed could be attributed to the segregation of La ions to the grain boundaries or to improper mixing during processing. Clusters of large ordered domains sometimes found in grain interiors also imply that a non-uniform distribution of La ions exists within these regions.

The origin of α' -spots observed in the current study is presently uncertain. α' -spots have previously been reported to be present within electron diffraction patterns of PST [15]. Since the intensities of α' -spots in PMN do not change significantly with temperature it is likely that they are chemical in origin. Furthermore, since the intensities of the α' -spots reduce with PbTiO_3 additions and increase with La substitutions.

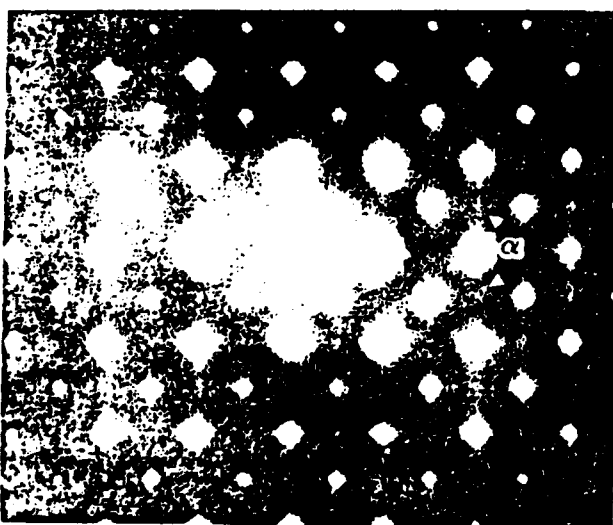


Figure 6 $\langle 100 \rangle$ selected area diffraction pattern of undoped hot pressed PMN. Weak α' -spots are indicated.

structural order. However, we note that the intensity dependence of the x' -spots with temperature is different for PMN and PST systems. It is therefore possible that the origin of the x' -spots in these two systems is different.

4.2. Electrical properties

Ordering may be anticipated to change either or both the amplitudes of compositional fluctuations and the sizes of the chemically distinct regions with which the broad phase transitions of relaxors have been associated [18, 19]. However, TEM studies have so far failed to reveal the mechanism by which the degree of order modifies the dielectric characteristics. No strong interactions are observed between macro-ferroelectric domains and the antiphase boundaries which define the ordered domains [15, 20]. This supports the view that the process of structural ordering influences the diffuse nature of relaxor paraelectric-ferroelectric (PE-FE) phase transitions only indirectly. However, the relationship between ordered domains and the micro-polar domains, which can be observed in unpoled relaxors [21, 22], is still ambiguous. Studies of the order-disorder relaxors, for which $x = 1/2$, has shown that an increase in the degree of structural order is associated with a less diffuse PE-FE phase transition and a reduction in frequency dispersion. Such observations therefore fit into the existing framework for relaxor behaviour. However, it has been shown that phase transitions exhibited by PMN become less diffuse and less frequency dependent (i.e. the relaxor tends to "normal" ferroelectric behaviour) with increasing PbTiO_3 content [23]. The present study illustrates that the size of ordered domains is reduced with increasing PbTiO_3 additions. There does therefore seem to be a basic antagonism in the relationship between stoichiometric order in $x = 1/2$ materials, non-stoichiometric 1:1 order in $x = 1/3$ materials and the corresponding trends in dielectric properties. In brief, an increase in order in the $x = 1/2$ relaxors reduces chemical inhomogeneity and therefore favours more "normal" dielectric behaviour. An increase in non-stoichiometric order in $x = 1/3$ relaxors promotes space charge fluctuations and the corresponding dielectric data shows an enhancement of the relaxor characteristics. In the latter case it is possible that some interaction may exist between the dipoles formed in the FE state and any uncompensated fluctuations in charge. Alternatively, it is apparent that the complete or partial compensation of charge fluctuations would involve significant alteration of the local defect chemistry. This suggests that although only small ordered domains may be able to form in relaxors like PMN, they may have a more significant effect on the dielectric permittivity as compared to the effect of a similar degree of order in a $x = 1/2$ relaxor. It is interesting to note however, that both systems appear to follow a common trend in that more "normal" ferroelectric behaviour is favoured as charge fluctuations are reduced. This is necessarily the result of a reduction in the variation between local B-site chemistry and bulk stoichiometry. We therefore

should be further investigated in relation to the influence of order on the dielectric behaviour of relaxors.

5 Conclusions

Using TEM techniques the ordering characteristics of PMN and PMN-PT solid solutions have been investigated. The restricted dimensions of the ordered domains which are observed in these systems are believed to be the result of charge fluctuations which develop as Mg and Nb ions order on alternate B-lattice sites. The ordering process is arrested when the space charges become too large to be accommodated by the structure or when the lattice is no longer able to compensate for such charges with existing lattice defects. A reduction in the ability to order is observed on adding PbTiO_3 to the PMN-PT solid solution. Ti ions are believed to 'dilute' the forces responsible for the ordering process. Substitution of off-valence La^{3+} ions on the Pb^{2+} sublattice enhance order by aiding in the charge compensating mechanisms. It is suggested that charge fluctuations which occur in relaxor materials affect both ordering and dielectric behaviour.

Acknowledgements

This work was carried out with the assistance of a SERC CASE studentship (ADH). Samples used in the work were kindly supplied by P. Osbond and R. W. Whatmore of the Allen Clark Research Centre, and by T. R. Shrout of M.R.L., Pennsylvania State University. We also acknowledge helpful discussions with R. W. Whatmore and K. Z. Baba-Kishi.

References

1. N. SETTER and L. E. CROSS, *J. Mater. Sci.* 15 (1980) 2478.
2. L. G. F. STENGER, F. L. SCHOLTEN and A. J. BURGRAAF, *Solid State Commun.* 32 (1979) 989.
3. L. G. F. STENGER and A. J. BURGRAAF, *Phys. Status. Solidi. (a)* 61 (1980) 275.
4. P. GROVES, *J. Phys. C: Solid State Phys.* 19 (1986) 111.
5. F. S. GALASSO, in "Structure, Properties and Preparation of Perovskite Type Compounds" (Pergamon, New York, 1969).
6. T. R. SHROUT, S. L. SWARTZ and M. J. HANN, *Bull. Amer. Ceram. Soc.* 63(6) (1984) 80R.
7. S. ABDUL MABAD, *Phase Transitions* 4 (1984) 183.
8. V. A. ISUPOV, *Izvestia Akademii Nauk SSSR, Seriya Fizicheskaya* 47(3) (1983) 559.
9. S. Z. SWARTZ and T. R. SHROUT, *Mater. Res. Bull.* 17 (1982) 1245.
10. A. M. GLAZER, *Acta Crystallogr.* B28 (1972) 3384.
11. H. B. KRAUSE, J. M. COWLEY and J. WHEATLEY, *ibid.* A35 (1979) 1015.
12. H. CHAN and M. HARMER, presented at the meeting of the American Ceramic Society, Chicago, 1986.
13. F. GALASSO and J. PYLF, *Inorg. Chem.* 2 (1963) 482.
14. J. A. ALONSO, E. MZAYEK and I. RASINES, *Mater. Res. Bull.* 22 (1987) 69.
15. C. A. RANDALL, D. J. BARBER, R. W. WHATMORE and P. GROVES, *J. Mater. Sci.* 21 (1986) 4456.
16. D. J. BARBER, A. D. HILTON and K. Z. BABA-KISHI, *Proc. Brit. Ceram. Soc.* 41 (1989) 139.
17. A. ATKINSON and R. I. TAYLOR, *Phil. Mag.* A43 (1981) 979.
18. G. A. SMOLENSKII, *J. Phys. Soc. Jap. (suppl.)* 28 (1970) 26.
19. V. A. ISUPOV, *Soviet Phys. Solid State* 5 (1963) 136.

20. Y. CHAN and Z. CHEN, *Ferroelectr. Lett.* 4 (1985) 13.
21. C. A. RANDALL, D. J. BARBER and R. W. WHATMORE, *J. Microscopy* 145 (1987) 275.
22. A. D. HILTON, C. A. RANDALL, D. J. BARBER and R. W. WHATMORE, in *Proceedings of EMAG '87*, Manchester, Conference Series No. 90, edited by L. M. Brown (Institute of Physics, London, 1987) p. 315.
23. S. L. SWARTZ, T. R. SHROUT, W. A. SCHLUZER and L. E. CROSS, *J. Amer. Ceram. Soc.* 67(5) (1984) 311.

*Received 11 May
and accepted 12 September 1988*

APPENDIX 20

Nanostructural-Property Relations in Complex Lead Perovskites

C. A. RANDALL and A. S. BHALLA

Materials Research Laboratory, The Pennsylvania State University,
University Park, PA 16802, USA

(Received July 4, 1989; accepted for publication November 18, 1989)

From transmission electron microscopy studies on several complex lead perovskite compounds $Pb(B'B'')O_3$, and their solid solutions a classification can be obtained based on B-cation order. This classification divides the complex lead perovskites into three subgroups; random occupation or disordered, nanoscale or short coherent long-range order and long coherent long-range order of B-site cations. A correlation between the nanoscale B-site order and relaxor on glassy ferroelectric behavior is found in these lead perovskites. An hypothesis is suggested which relates 0-3 polar connectivity to 0-3 order-disorder connectivity. This hypothesis is discussed with relation to present theories [G. A. Smolenskii: J. Phys. Soc. Jpn. (1970) Suppl., p. 26, L. E. Cross: Ferroelectrics 76 (1987) 241, T. L. Renieke and K. L. Ngai: Solid State Commun. 18 (1973) 1543] and reported experimental results of the perovskite relaxor ferroelectrics.

KEYWORDS: relaxor materials, dielectric properties, nanocomposite, electron microscopic study, model for relaxor behavior

§1. Introduction

1.1 Ferroelectric background

For the past thirty years there has been much work, both pure and applied, on the oxide ferroelectric materials and their properties.¹⁻³ One of the most complex ferroelectrics class is those characterized by a diffuse and dispersive phase transition of the so-called relaxor ferroelectrics.^{4,5} The permittivity (ϵ') and $\tan \delta (\epsilon''/\epsilon')$ vs temperature show a diffuse phase transition over a so-called Curie range. There is a Curie maximum temperature, which is frequency dependent over a wide frequency range, and increases in temperature with increasing frequency. Also, the maximum in the permittivity (ϵ') does not correspond with the maximum in the dielectric loss ($\tan \delta$). Figure 1 shows a typical permittivity vs temperature for a relaxor ferroelectric. This transition behavior is very different from the 'normal-like' ferroelectrics which usually shows a sharp 1st or 2nd order phase transition.

The most widely accepted models for the understanding of the relaxor ferroelectrics have come from Smolenskii⁴ and Cross.⁵ The Smolenskii model notes that ferroelectric relaxors have a common characteristic where two or more cations occupy equivalent crystallographic sites. It is the distribution of these cations which gives rise to chemical microregions with various compositions and in turn differing Curie temperatures. The summed distribution of these microregions give the broad phase transition. As a relaxor ferroelectric crystal is cooled, these microregions undergo the paraelectric \rightarrow ferroelectric phase transition and local polar microregions are created ($\sim 100 \text{ \AA}$).

The Smolenskii model⁴ is a very successful model but it has its weaknesses:

- 1) There is no discrimination between compounds and solid-solutions with mixed cation sites and their tendency to show relaxor or normal dielectric characteristics.
- 2) With a Gaussian distribution of chemical microregions with their differing Curie temperatures there must exist very subtle changes in chemical compositions from area to area for the major volume of the crystal. This would not appear to give sufficient gradients necessary for the localization of polar microregions or clusters.

Two independent studies on the order-disorder perovskite, $Pb(Sc_{1/2}Ta_{1/2})O_3$, were performed by Setter and Cross^{6,7} and also Stenger and Burggraaf⁸ in which the key role of the cation distribution and its effect on the dielectric properties was demonstrated.

An understanding of the relaxor dielectric properties was enhanced by the superparaelectric theory as suggested by Cross.⁹ Basically, the superparaelectric theory describes the relaxor and its localized polar microregions analogous to the spin cluster behavior in superparamagnets. Considering two polarization states, $+P$ and $-P$, superparaelectric potential, as illustrated in Fig. 2, these polarization states of a polar microregion are separated by an activation barrier. The height of the

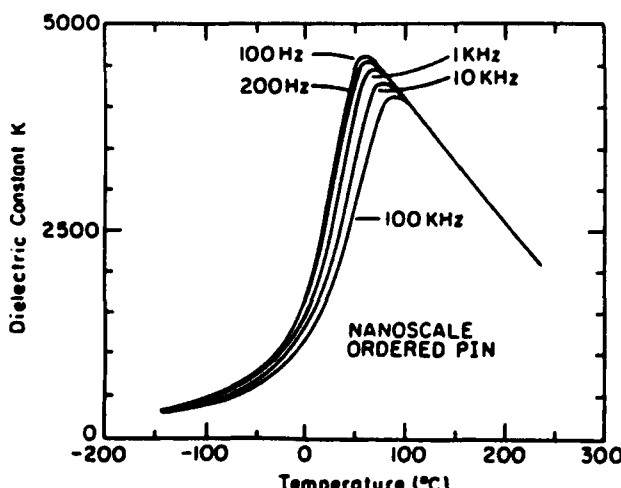


Fig. 1. A schematic representation of the permittivity versus temperature relationship for a complex lead perovskite relaxor.

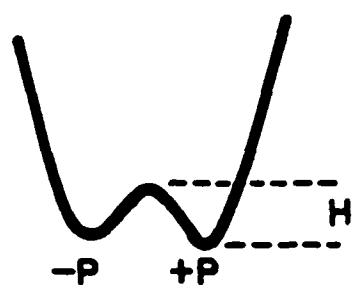


Fig. 2. Schematic representation of a superparaelectric potential describing the polarization states $+P$ and $-P$.

barrier, H , is directly proportional to the volume of the polar microregion itself. This indicates thermal energy, $k_B T$, and the frequency of polarization flipping, v , are related in a simple relation:

$$v = v_D \exp\left(\frac{-H}{k_B T}\right)$$

where,

H is the activation height between $-P$ and $+P$,
 k_B is the Boltzmann constant,
 T is the absolute temperature,
 v is the flipping frequency between $-P$ and $+P$,
and v_D is the Debye frequency ($\sim 10^{11}$ – 10^{13} Hz).

However, for low thermal energies the polarization will 'lock-in' to a particular orientation, thus forming a polar microdomain or a polar cluster. This feature distinguishes the polar microregion from the polar microdomain (which is static and not a strong frequency dependent feature).

The superparaelectric concept accounts for many of the observed properties of the ferroelectric relaxor such as the frequency dependence of the permittivity, the dielectric aging,^{9,10} and also the metastable switching from micro→macrodomain.^{11–13} It also reflects the nonlinear behavior of the thermal and optical properties as observed in these materials.^{14–16}

1.2 Cation order background

Within a given crystal structure the arrangement of various cations and point defects on particular crystallographic sites depends on the relative magnitude of the interaction energy for possible configurations. If this interaction is sufficiently low there are no detectable correlations between the occupancy of nearest neighbor sites. However, if there exists a diffuse but distinct superlattice reflection the cations have long range order (LRO) between unlike cations on nearest neighbor sites. Since, in this study the scale of this LRO is important to observed physical properties we describe a coherence length based on the size of ordered domains as imaged with transmission electron microscopy (TEM). A short coherence length of LRO is associated with order domain in a range ~ 20 – 800 Å in diameter, and long coherence lengths corresponding to order domains much greater than 1000 Å. For excellent reviews on cation order see Cowley (1976) and Reynaud (1982).^{17,18}

As discussed above in §1.1 and 1.2, there is a need to better understand the nanostructure property relationship in these important class of ferroelectric materials. In view of this we carried out studies on a wide selection of important and well characterized complex lead perovskites (single crystals and ceramics). Based on our TEM observations a new insight is gained in the understanding of the nanostructure of these relaxor materials. In this paper we present an approach relating B-site cation order to the ferroic properties in complex lead perovskites. This approach has been discussed in light of present theories and satisfies experimental results.

§2. Results and Discussion

The results discussed here on the structural ordering are made from TEM analysis. Major advantages of this technique include: small coherence length of high energy electrons, the very strong scattering power of electrons with atom ($\sim 10^4$ times greater than X-rays) and also direct imaging of nanostructures with contrast and high resolution methods.

Within the complex perovskites $Pb(B;B'_{-x})O$ ($x=1/2$) family many of the compounds have shown long-range B-site ordering of the cations, as documented by Galasso.¹⁹ The ordering of B-site cations in these systems gives rise to an F-centered $2a_0 \times 2a_0 \times 2a_0$ superstructure, see Fig. 3(a). This additional symmetry consideration gives a set of superlattice lines/spots, F-spots in electron diffraction. However, if the B-cations are randomly occupying the lattice there is no superstructure and the ordinary perovskite cell $a_0 \times a_0 \times a_0$ describes the compound in the paraelectric state, see Fig. 3(b).

Examples of some of the TEM results obtained from complex lead perovskites: Fig. 4(a) shows a weak-diffuse but distinct F-spots in $Pb(Sc_{1/2}Ta_{1/2})O$ (PST); 4(b) shows the corresponding dark-field image revealing the contrast of the nanoscaled ordered domains; and 4(c) demonstrates long-range order in normal PST being broken by an antiphase boundary. Figure 5 shows strong F-spot in $\langle 211 \rangle$ zone axis pattern from $Pb(Co_{1/2}W_{1/2})O$, corresponding to an ordered grain also observed are incommensurate satellite reflections. Nanoscale order domains in PMN:PT (0.9/0.1) and the corresponding $\langle 110 \rangle$ zone axis pattern with superstructural F-spots is shown in Figs. 6(a) and 6(b) respectively.

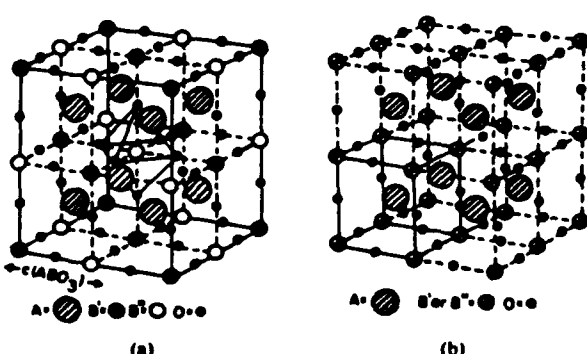


Fig. 3. (a) Ordered B-site superstructure of $Pb(B;B'_{-x})O$ ($x=1/2$) complex perovskite; (b) disorder B-site with primitive perovskite cell.

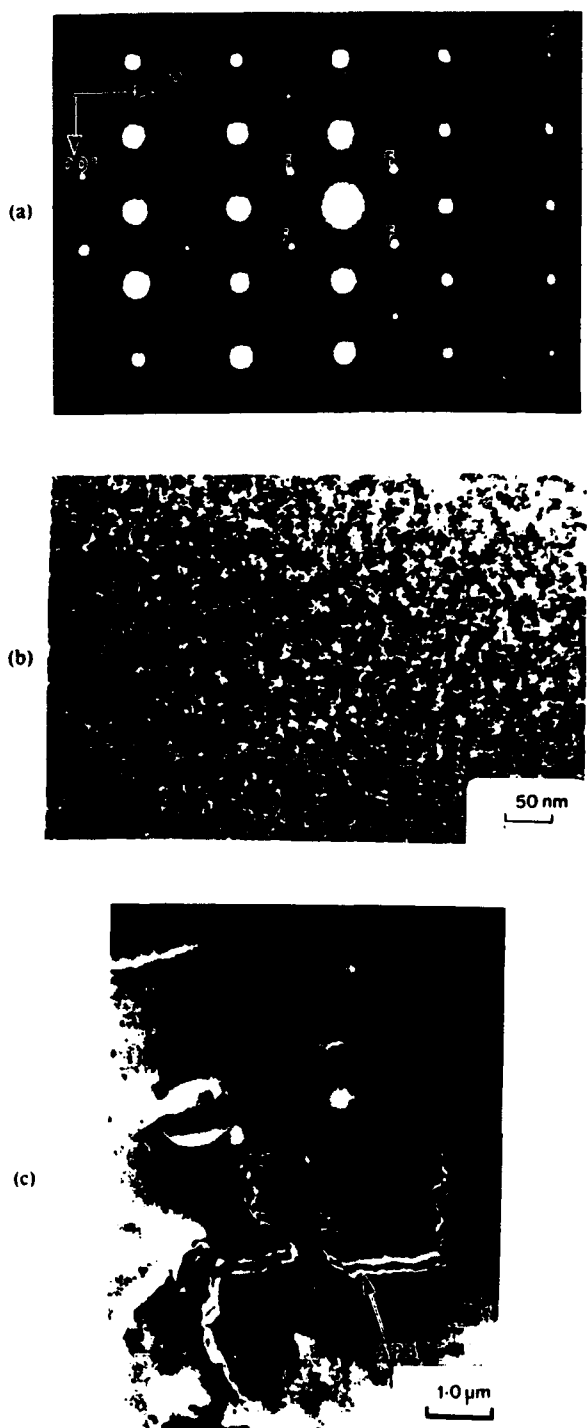


Fig. 4. (a) $\langle 110 \rangle$ zone axis pattern from relaxor $Pb(Sc_{1-x}Ta_{1/2})_xO_3$, the diffuse and weak but discrete order spots are marked F-spots; (b) corresponding dark field image with nanoscale order domains (bright contrast); and (c) long-range order being broken by antiphase boundaries in normal $Pb(Sc_{1-x}Ta_{1/2})_xO_3$.

So within the complex lead-perovskites $Pb(B'_{1/2}B''_{1/2})O_3$, ($x=1/2$) systems there are several examples where the B-site cations B' and B'' have a driving force sufficiently large from valence and ionic radii differences as to order the cations and give superstructure. For instance, $Pb(Co_{1/2}W_{1/2})O_3$, has a strong driving force and grows with almost complete ordering between Co^{+2} and W^{+6} ca-

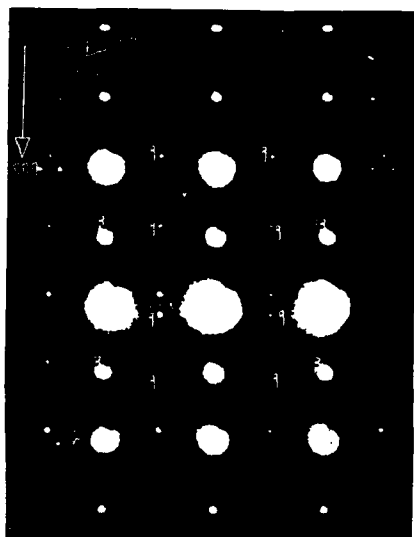


Fig. 5. $\langle 211 \rangle$ zone axis pattern in $Pb(Co_{1/2}W_{1/2})O_3$ taken at $-160^\circ C$; a strong order F-spot is indicated along with incommensurate satellites (I).

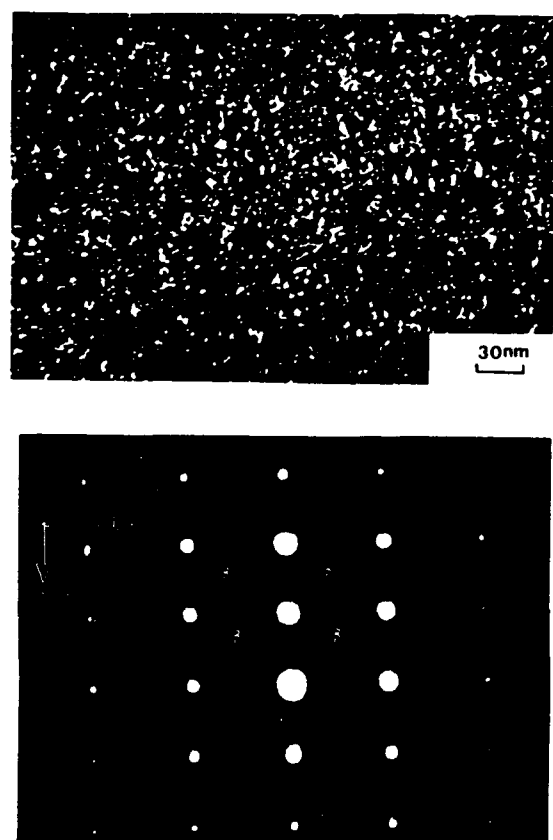


Fig. 6. (a) $\langle 110 \rangle$ zone axis diffraction pattern from 0.9 PMN-0.1 PT showing an order spot (F) and (b) the corresponding dark field image reveals nanoscale order domains ($\sim 100 \text{ \AA}$).

tions. Perovskites such as PST and $Pb(In_{1/2}Nb_{1/2})O_3$ (PIN) have lower driving forces close to the critical limit of disorder and order occupancy of the B-sites. This is inferred by various annealing, quenching, and growth condition effects which shows differing scales (LRO).⁶⁻⁸ In

Table I. Property differences between relaxor and normal perovskite ferroelectrics.

Property	Normal	Relaxor
permittivity temperature dependence $\epsilon = \epsilon(T)$	sharp 1st or 2nd order transition about Curie temperature	broad-diffuse phase transition about Curie maxima (T_{max})
permittivity temperature and frequency dependence $\epsilon = \epsilon(T, \omega)$	weak frequency dependence	strong frequency dependence
remanent polarization	strong remanent polarization	weak remanent polarization
scattering of light	strong anisotropy (birefringent)	very weak anisotropy to light (pseudo-cubic)
diffraction of X-rays	line splitting owing to spontaneous deformation from paraelectric \rightarrow ferroelectric phase	no X-ray line splitting giving a pseudo-cubic structure

the $x=1/2$ ordered perovskites there is an average B-site valence of +4 in the superstructure which gives rise to so-called stoichiometric ordering.

In the complex lead-perovskites $Pb(B_{1/3}^{+3}B_{2/3}^{+5})O_3$ ($x=1/3$) systems there is a LRO with short coherence length of a 1:1 non-stoichiometric ordering between cations which gives an average valence not equal to +4. The local field and charge compensation mechanisms associated with non-stoichiometric order is not well understood in these systems, but the fact remains that the nanoscale order domains $\sim 100 \text{ \AA}$ do exist in $x=1/3$ systems, as observed by a number of authors.²⁰⁻²⁴

In our TEM study we are able to classify a number of complex perovskites based on their B-site cation order and respective dielectric, X-ray, and optical properties. The compounds and solid-solutions are then assigned to the normal ferroelectrics (antiferroelectrics) or relaxor ferroelectrics (Table I) as based on their characteristics outlined by Cross.⁵¹ The relations of the cation order in the complex lead perovskites to the respective dielectric behavior (normal or relaxor) are summarized in Table II and in Fig. 7.

We observed that in the solid-solutions of $Pb(Mg_{1/3}Nb_{2/3})O_3:PbTiO_3$, (PMN:PT), and $Pb(Zn_{1/3}Nb_{2/3})O_3:PbTiO_3$, (PZN:PT), there is a gradual disappearance of the F-spot close to the morphotropic phase boundary which separates strong relaxor ferroelectric behavior from normal ferroelectric behavior in the phase diagram of solid solutions. So on the relaxor side of the phase diagram there exists nanoscale cation order and in the normal side of the diagram there is a cation distribution which is atomically random or disordered with no distinct superstructure. Also, we have included $Pb(Fe_{1/2}Nb_{1/2})O_3$ (PFN) and $Pb(Fe_{1/2}Ta_{1/2})O_3$ (PFT) as "normal" ferroelectrics in Table II and Fig. 7. In a number of studies on these compounds with both ceramics and single crystals the results point towards a normal ferroelectric behavior despite a broad phase transition in the permittivity versus temperature data.²⁵ X-ray, birefringence, and D.T.A. (differential-thermal-analysis) point to normal behavior.^{26,27} Brunskill *et al.*²⁶ and Brixel *et al.*²⁷ have extrapolated from the temperature dependence of spontaneous birefringence, a polarization order parameter in PFN and PFT respectively. This, as Brixel *et al.* concludes, suggests these materials behave like normal or proper ferroelectrics. So those complex lead perovskites $Pb(B_xB_{1-x}^{+5})O_3$ and solid solutions which have classical relaxor behavior also possess nanoscale B-site order. This strong correlation is thought to be very

Table II. Analysis of order and their corresponding dielectric behavior in a number of $Pb(B_xB_{1-x}^{+5})O_3$ systems.

Compound	Relative coherence length of B-site long range order	Dielectric description
$Pb(Fe_{1/2}Nb_{1/2})O_3$ (PFN)	disordered	normal
$Pb(Fe_{1/2}Ta_{1/2})O_3$ (PFT)	disordered	normal
$Pb(Mg_{1/3}Nb_{2/3})O_3$ (PMN)	short	relaxor
0.9 PMN:0.1 PT (PT-PbTiO ₃)	short	relaxor
0.8 PMN:0.2 PT	short	relaxor
0.7 PMN:0.3 PT	short	relaxor
0.6 PMN:0.4 PT	disordered	normal
$Pb(Zn_{1/3}Nb_{2/3})O_3$ (PZN)	short	relaxor
0.915 PZN:0.085 PT	short	relaxor
0.9 PZN:0.1 PT	short	relaxor
0.885 PZN:0.115 PT	disordered	normal
$Pb(Ni_{1/3}Nb_{2/3})O_3$ (PNN)	short	relaxor
$Pb(Sc_{1/2}Ta_{1/2})O_3$ (PST)	short	relaxor
$Pb(Sc_{1/2}Ta_{1/2})O_3$	long	normal
$Pb(In_{1/2}Nb_{1/2})O_3$ (PIN)	short	relaxor
$Pb(In_{1/2}Nb_{1/2})O_3$	long	normal
$Pb(Mg_{1/2}W_{1/2})O_3$ (PMW)	long	normal
$Pb(Co_{1/2}W_{1/2})O_3$ (PCW)	long	normal
$Pb(Cd_{1/2}Nb_{1/2})O_3$ (PCN)	short	relaxor

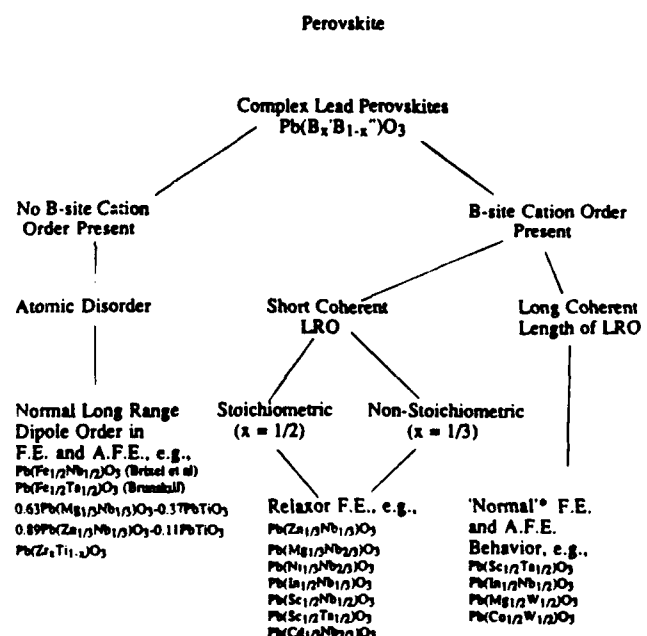


Fig. 7. Flow diagram showing the classification of complex lead perovskites with respect to B-site cation order and dielectric behavior.

*Incommensurate Superstructural Satellites are found in some members of this sub-group, e.g., $Pb(Co_{1/2}W_{1/2})O_3$ and $Pb(Sc_{1/2}Ta_{1/2})O_3$

important in localizing polar regions or clusters as will be discussed below.

The complex lead-perovskite $\text{Pb}(\text{B}_x\text{B}'_{1-x})\text{O}_3$ ($x=1/2$) and long coherence cation (LRO) and having ferroelectric or antiferroelectric properties are traditionally regarded as normal ferroelectrics or normal antiferroelectrics with long range co-operative interactions between the dipoles. However, the authors here are cautious on this point in light of new experimental evidence of incommensurate satellite reflections observed in TEM studies on some of these materials.²⁸ Some of those compounds found in this subgroup such as PCW, PST, and PIN have subtle incommensurate dipole modulations associated with the paraelectric → ferroelectric phase transition; these may not strictly be classified as normal ferroelectrics or normal antiferroelectrics. More research is on-going within this interesting subgroup of long-range B-site order lead-based perovskites in order to classify these materials.

2.1 An hypothesis for the relaxor ferroelectrics as a nanocomposite

Let us introduce the perovskite relaxor ferroelectrics in terms of a nanocomposite. These relaxor compounds as nanocomposites can be considered by two differing but fundamentally related ways.

(i) We may consider the relaxor nanocomposite through its chemical connectivity.²⁹ According to the above results the nanoscale LRO has a 0-3 connectivity within a 3-dimensionally interconnected disordered matrix, as schematically represented by Fig. 8.

(ii) We can also consider the relaxor nanocomposite on its mixing of polar and non-polar regions. The connectivity of these two phases is very much a question of the temperature of the system. At higher temperatures, $T > T_0$, (T is a temperature where the total crystal is paraelectric) then we have a material which is chemically heterogeneous as described in (i) but electrically homogeneous (or paraelectric). However, lower temperatures below T_0 , optical and thermal expansion experiments indicates the on-set of a polarization through non-linear index of refraction and thermal strain effects:¹⁴⁻¹⁶

$$\Delta\eta_{ii} \propto g_{ijkl} P_{kl}^2$$

$$\Delta x_{ii} \propto Q_{ijkl} P_{kl}^2$$

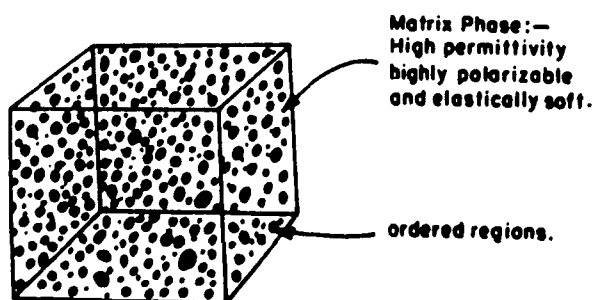


Fig. 8. Schematic representation of nanoscale order domains (dark regions) in a disordered matrix in the form of a 0-3 connected nanocomposite.

Where $\Delta\eta_{ii}$ is the optical birefringence, g_{ijkl} the quadratic electro-optic coefficients, P_{kl}^2 mean square polarization, Δx_{ii} thermal strain and Q_{ijkl} are electrostrictive coefficients of the material.

At temperatures in the range ($T < T_0$), the nonpolar-polar connectivity is described in 0-3. At lower temperatures ($T \ll T_0$) as more and more of the crystals volume becomes ferroelectric, the connectivity may change to other forms e.g., 3-3, 3-0, etc. The mechanisms of the kinetics involving stabilizing and equilibration of dynamic polar regions and clustering of neighboring polar regions through local strain and local electric field effects in the matrix phase is not well understood. But, a direct freezing in of the polar microdomain in the cold-stage TEM studies on 8.2/70/30 PLZT has been observed by Randall *et al.*^{13,30} indicating the existence of such polar domains. Also, the 'in-situ' switching of the polar microdomains to an aligned macrodomain state confirming their metastable phase transition in relaxors.

The new hypothesis suggests an intimate connection between the 0-3 chemical order distribution (i) and 0-3 polar distribution (ii) in the complex lead perovskites at high temperatures $T < T_0$, provided the chemically ordered regions are associated with a much higher transition than the surrounding matrix.

In the following text we will test the 0:3 nanocomposite approach in relation to various existed models for explaining the relaxor behavior.

2.2 Reneike-Ngai theory (1976)³¹

This model was originally postulated with 'disorder' phonon modes originating at highly defective regions of the lattice and coupling with the matrix soft mode and locally perturbing the Curie temperature. This is suggested to give rise to 0-3 polar microregion distributions with various Curie temperatures and local polarization order parameters. One of the major objections to the Reneike-Ngai theory was discussed by Isupov.³² He pointed out that the theory did account for the broad phase transition and described local polar microregions but it was based on a homogeneous crystal matrix with locally distributed defects. According to Isupov, a homogeneous matrix does not exist in relaxors and all microscopic parts of the crystal are inhomogeneous.

We suggest here that the Reneike-Ngai theory should be reconsidered in light of the present nanostructural observations. The new hypothesis suggests an disordered matrix surrounding nanoscale order-domains; it is conceivable that the order domains have additional phonon modes which could couple to the soft mode of the matrix. The strength of the coupling and its perturbation on the local soft mode transition give rise to local various Curie temperatures. This in turn may be related to the size of the cation order domains themselves.

2.3 The superparaelectric model (1987)³³

The superparaelectric model (1987) satisfactorily accounts for the nature of the polarization behavior in polar microregions. The sites of cation order in the disordered matrix may give potential wells ~ 100 Å within the lattice in which to localize the superparaelectric poten-

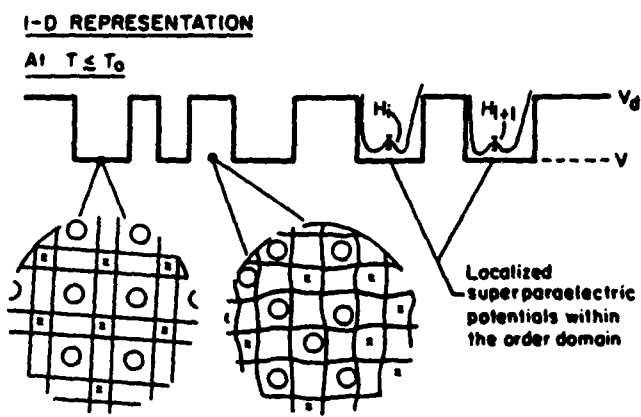


Fig. 9. Schematic representation demonstrating how nanoscale ordered regions giving rise to local strain barriers within the perovskite lattice. These barriers are the suggested sites to localize superparaelectric potentials of the polar regions at high temperatures.

tials, as schematically represented in Fig. 9. The lattice potential differences between LRO and disorder regions are owing to strain and electrostatic energy differences between these respective regions. This difference in lattice potential then can act as a barrier to localize short-range dipolar domains which, of course, are described by the superparaelectric model. Which in turn explains the dielectric, optical, X-ray, and thermal properties of relaxor ferroelectrics.

§3. Summary

In summary the present approach of cation order which is based on the TEM observations and the available experimental data on various complex lead oxide perovskites can be highlighted as follows:

(i) Separates the complex lead perovskite family into three subgroups based on B-site cation order:

- a) random or fully disordered distributions,
- b) short coherence LRO distributions,
- c) long coherence LRO distributions.

(ii) The above approach links these discrete nanoscale order domains to the relaxor ferroelectrics in the complex lead perovskites. This change in B-site distribution from nanoscale order to random occupation is observed very close to the morphotropic phase boundary in solid solution PZN:PT and PMN:PT. Also, scale of LRO accounts for the difference in the macroscopic behavior of PST and PIN. The disorder in PFN and PFT accounts for the normal characteristics in the temperature dependence of the spontaneous birefringence.

(iii) The nanoscale order domains are natural sites for localizing the superparaelectric polar clusters within a paraelectric matrix. This is supported by the work of Smolenskii and Cross who both predicted a size of ~ 100 Å for the polar microregion from the dielectric relaxations in the permittivity measurements.

(iv) However, despite the apparent successes of this qualitative hypothesis, there are still points of conjecture we wish to relay to the reader:

- a) There is no knowledge of which part of the order-disorder 0-3 nanocomposite is ferroelectric and paraelectric at higher temperatures.
- b) There is, so far, no statistical analysis of the scale of LRO distribution or volume percentage within these materials.
- c) We have only a limited understanding of non-stoichiometric order in the $x=1/3$ complex lead perovskites.^{33,34)}

Acknowledgements

The authors wish to thank DARPA and ONR for their support of this study. Many thanks go to Professor L. E. Cross and Professor D. J. Barber, Dr. G. Burns, Drs. T. R. Shroud, K. Baba-Kishi and A. D. Hilton and many others for useful discussions and encouragement throughout this work. Thanks to Joyce Baney for typing this manuscript.

References

- 1) M. A. Lines and A. M. Glass: *Principles and Applications of Ferroelectrics and Related Materials* (Clarendon Press, Oxford, 1977).
- 2) B. Jaffe, W. R. Cook and H. Jaffe: *Piezoelectric Ceramics* (Academic Press, New York, London, 1971).
- 3) F. Jona and G. Shirane: *Ferroelectric Crystals* (Macmillan, New York, 1962).
- 4) G. A. Smolenskii: *Proc. 2nd Meet. Ferroelectricity, Kyoto, 1969*, J. Phys. Soc. Jpn. **28** (1970) Suppl. p. 26.
- 5) L. E. Cross: *Ferroelectrics* **76** (1987) 241.
- 6) N. A. Setter and L. E. Cross: *J. Mater. Sci.* **15** (1980a) 2478.
- 7) N. A. Setter and L. E. Cross: *J. Appl. Phys.* **51** (1980b) 4356.
- 8) C. G. Stenger and A. F. Burggraaf: *Phys. Status Solidi (a)* **61** (1980) 275.
- 9) W. A. Schulze, J. V. Biggers and L. E. Cross: *J. Mat. Sci.* **15** (1978) 2478.
- 10) P. Wuji, E. Furman, G. O. Dayton and L. E. Cross: *J. Mater. Sci. Lett.* **51** (1983) 3399.
- 11) V. A. Bokov and I. E. Myl'nekova: *Sov. Phys. Solid State* **3** (1961) 613.
- 12) X. Yao, Z. L. Chen and L. E. Cross: *J. Appl. Phys.* **54** (1984) 3399.
- 13) C. A. Randall, D. J. Barber, R. W. Whatmore and P. Groves: *Ferroelectrics* **76** (1987) 00.
- 14) G. Burns and B. A. Scott: *Solid State Commun.* **13** (1973) 417.
- 15) G. Burns and F. M. Dacol: *Phys. Rev. B* **28** (1980) 2527.
- 16) S. J. Jang, K. Uchino, S. Nomura and L. E. Cross: *Ferroelectrics* **27** (1980) 31.
- 17) J. M. Cowley: *Advances in High Temperature Chemistry* (Academic Press, London, New York, 1971) Vol. 3, p. 36.
- 18) F. Reynaud: *Phys. Status Solidi (a)*, **72** (1982) 11.
- 19) F. S. Galasso: *Structure, Properties, and Preparation of Perovskite Type Compounds* (Pergamon Press, Oxford, London, Edinburgh, New York, Toronto, Sidney, Paris, Branschweig, 1969).
- 20) B. Krause, J. M. Cowley and J. Wheatley: *Acta Cryst. A* **35** (1979) 1015.
- 21) A. D. Hilton, C. A. Randall and D. J. Barber: *Inst. Phys. Conf. Series*, No. 90 (1987) Chapter 9, 315.
- 22) A. D. Hilton, C. A. Randall, D. J. Barber and T. R. Shroud: *Ferroelectrics* **93** (1989) 379.
- 23) J. Chen, H. Chen and M. A. Harmer: *J. Am. Ceram. Soc.*, **72** (1989) 593.
- 24) E. Hussan, M. Chubb and A. Morell: *Mater. Res. Bull.* **33** (1988) 357.
- 25) Landolt-Bornstein: *New Series III/16a*, ed. T. Mitsumi and S. Nomura (Springer-Verlag, Berlin, 1981).
- 26) I. H. Brunskill, H. Schmid and P. Tissot: *Ferroelectrics* **37** (1981) 547.

- 27) W. Brixel, J. P. Rivera and H. Schmid: *Ferroelectrics* **55** (1984) 181.
- 28) C. A. Randall, S. A. Markgraf, A. S. Bhalla and K. Baba-Kishi: *Phys. Rev. B* **40** (1989) 413.
- 29) R. E. Newham, D. Skinner and L. E. Cross: *Mater. Res. Bull.* **13** (1978) 525.
- 30) C. A. Randall, D. J. Barber and R. W. Whatmore: *J. Micro.* **145** (1987) 235.
- 31) T. L. Renieke and K. L. Ngai: *Solid State Commun.* **18** (1973) 1543.
- 32) G. A. Smolenskii, V. A. Bokov, V. A. Isupov, N. N. Kranik, P. E. Pasynkov and A. I. Sokolov: *Ferroelectrics and Related Materials*, ed. G. Taylor and G. A. Smolenskii (Gordon and Breach, New York, London, Paris, Montreux, Tokyo, 1984).
- 33) T. R. Shrout, W. Huebner, C. A. Randall and A. D. Hilton: *Ferroelectrics* **93** (1989) 361.
- 34) D. M. Smyth, M. P. Harmer and P. Peng: American Ceramic Society Meeting, Indianapolis, IN (1989).

APPENDIX 21

Classification and consequences of complex lead perovskite ferroelectrics with regard to B-site cation order

C. A. Randall, A. S. Bhalla, T. R. Shroud, and L. E. Cross

Materials Research Laboratory, The Pennsylvania State University, University Park, Pennsylvania 16802

(Received 27 October 1989; accepted 8 December 1989)

From a number of studies on ferroelectric and related materials based on complex lead perovskites $[Pb(B'_x B''_{1-x})O_3]$, it is apparent that the B-site cation order influences the crystallography, phase transitions, and other physical properties. A classification of complex lead perovskites is presented based on the relative scale of long-range cation order. In particular, we discuss the implications of cation order in relation to relaxor and normal ferroelectric behavior.

I. INTRODUCTION

The largest group of ferroelectric and related materials is based on the simple perovskite structure, ABO_3 .^{1,2} In the cubic perovskite structure A-cations occupy the corner positions of the cube, the B-cations occupy the body-center position, and oxygen anions are situated at the face-centered positions. Within the perovskite family there are many differing types of ferroic phases including ferroelectrics, antiferroelectrics, ferroelastics, ferromagnetics, and coupled forms of these. Using the perovskite structural tolerance factor (t) where,

$$t = \frac{R_A + R_X}{\sqrt{2}(R_B + R_X)} \quad \text{after Megaw}^3 \quad (1)$$

and R_A : ionic radii of A-site cation

R_B : ionic radii of B-site cation

R_X : ionic radii of anion

a distribution of ferroelectrics (FE) and antiferroelectrics (AFE) in the perovskite family were determined by Ven'skev and Zhdanov.⁴ The AFEs are found to have a limited distribution $0.78 \leq t \leq 1.00$, while the FE's cover the whole perovskite range $0.78 \leq t \leq 1.05$; the tolerance factors were recalculated using ionic radii from Shannon and Prewitt.^{4b}

Of particular interest are complex lead-based perovskites having the general formula $Pb(B'_x B''_{1-x})O_3$, where B' is typically a low valence cation, e.g., Mg^{+2} , Zn^{+2} , Fe^{+3} , Ni^{+2} , In^{+3} , and Sc^{+3} and B'' a high valence cation, e.g., Ti^{+4} , Nb^{+5} , Ta^{+5} , and W^{+6} . Within this perovskite subgroup there are many variations of the type of FE or AFE phase transition, but only two forms, normal and relaxor, will be discussed. In contrast to normal FE (or AFE), relaxors exhibit a broad and strongly frequency dependent phase transition. The major property differences which distinguish relaxor versus normal type ferroelectrics are summarized in Table I.⁵

In addition to using the tolerance factor (t) to categorize ferroic behavior in perovskites, Halliyal and Shroud⁶ found that plotting t versus the average electronegativity as expressed by

$$\bar{x} = (x_{AO} + x_{BO})/2 \quad (2)$$

where x_{BO} = electronegativity difference between B cation and oxygen and

x_{AO} = electronegativity difference between A cation and oxygen

for a range of both simple and complex perovskites, resulted in information about the stability of the per-

TABLE I. Property differences between relaxor and normal perovskite ferroelectrics and antiferroelectrics.

Property	Normal	Relaxor
Permittivity temperature dependence $\epsilon = \epsilon(T)$	Sharp 1st or 2nd order transition about Curie temperature	Broad-diffuse phase transition about Curie maxima (T_{max})
Permittivity temperature and frequency dependence $\epsilon = \epsilon(T, \omega)$	Weak frequency dependence	Strong frequency dependence
Remanent polarization in ferroelectrics	Strong remanent polarization	Low remanent polarization
Birefringence	Strongly anisotropy	Very weak anisotropy (pseudo-cubic)
Diffraction of x rays	Line splitting owing to spontaneous deformation from paraelectric \rightarrow ferroelectric (AFE) phase	No x-ray line splitting (pseudo-cubic)

ovskite phase (see Fig. 1). Perovskite compounds with both low t and x tended to form pyrochlore phase(s), and the perovskite phase was stabilized by solid solutions in which t or x was increased. It is interesting to note that many of the "unstable" complex compounds are those which exhibit relaxor behavior.

In this paper we propose to further classify the complex lead perovskites based on nanostructural features which in turn are believed to be the fundamental cause for distinction between relaxor and normal FE (or AFE) behavior.

II. LONG-RANGE ORDER IN COMPLEX LEAD PEROVSKITES, $Pb(B_{1-x}B'_{1-x''})O_3$

Ordering of the B-site cations in complex perovskites occurs, providing there exists a sufficiently large interaction energy between neighboring cations. This interaction is based on valence and ionic radii differences between the respective B' and B'' cations. The cations are said to be ordered when nearest neighbors on the B-sublattice are unlike and next-nearest neighbors are similar; see Fig. 2. If the ordering has sufficiently large coherency, the translational periodicity of B' and B'' gives rise to a distinct superlattice as detected by x rays, electrons, or neutrons inferring long-range order (LRO).⁷

It is of significance to point out that B-site order in $Pb(B_{1-x}B'_{1-x''})O_3$ compounds can be either stoichiometric or nonstoichiometric. For example, B-site order in $x = 1/2$ compounds, e.g., $Pb(Sc_{1/2}Ta_{1/2})O_3$ (PST) and $Pb(Mg_{1/2}W_{1/2})O_3$ (PMW), results in an average valence of (+4) and thus is referred to as stoichiometric ordering. In contrast, nonstoichiometric ordering is found in

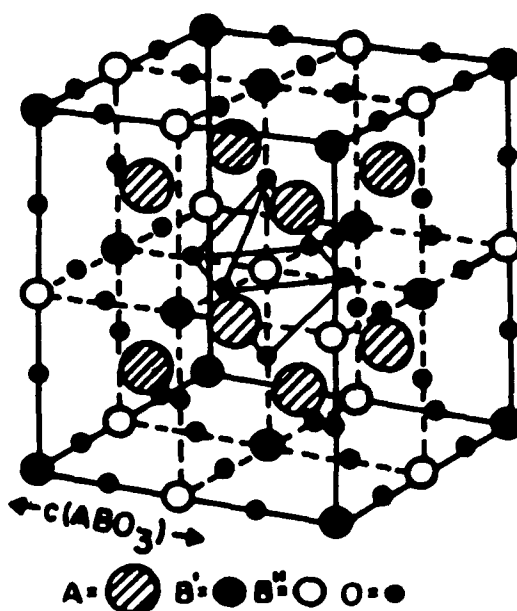


FIG. 2. The F-centered ordering of B-site cations in $Pb(B_{1/2}B'_{1/2})O_3$.

$x = 1/3$ compounds, e.g., $Pb(Mg_{1/3}Nb_{2/3})O_3$ (PMN) and $Pb(Cd_{1/3}Nb_{2/3})O_3$ (PCN) where the observed $B'B''$ order is 1:1 and as such the average charge value is lower than the expected valence of (+4). The overall defect chemistry and average compensation mechanisms of the nonstoichiometric ordering are not well understood at this time.^{8,9}

Transmission electron microscopy (TEM) studies on complex lead perovskites¹⁰⁻¹⁵ have also been performed on a wide variety of compounds, as summarized in Fig. 3. The scale of the ordering of B-site cations has been classified and correlated to relaxor or normal FE (or AFE) behavior observed from experimental data using Table I. As shown in Fig. 3, the complex perovskites were divided into three columns: (I) perovskites possessing no detectable order (<2 nm), (II) ordered with long coherency (≥ 100 nm), and (III) ordered but on a nanoscale (2–50 nm) or short coherency. As presented, both columns I and II contain complex lead perovskites with normal FE (or AFE) characteristics whereas column III contains many of the relaxor type materials. A typical example of nanoscale order is shown in Fig. 4 for the relaxor ferroelectric 0.9 PMN-0.1 PT ($PbTiO_3$), where white contrast regions correspond to the order domains ~ 10 nm.

Though relaxor 'like' behavior has been observed for compounds such as $Pb(Fe_{1/2}Nb_{1/2})O_3$ (PFN) and $Pb(Fe_{1/2}Ta_{1/2})O_3$ (PFT) (column I), in the form of a broad dielectric transition, other physical properties such as spontaneous birefringence^{16,17} and x-ray line splitting point to normal FE behavior.¹⁸ In certain compounds, the driving force for cation order energy is such that long-range coherency of B-cations (LRO) and corresponding normal FE (or AFE) behavior can be

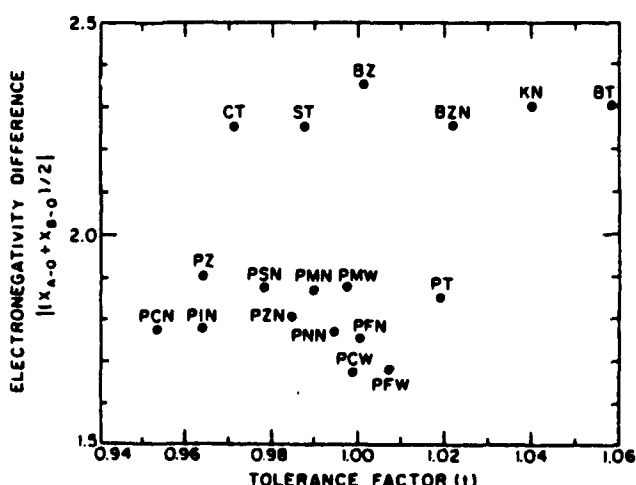


FIG. 1. Plot of average electronegativity (x) versus tolerance factor (t), where BT = $BaTiO_3$, KN = $KNbO_3$, BZN = $Ba(Zn_{1/2}Nb_{2/3})O_3$; BZ = $BaZrO_3$, ST = $SrTiO_3$, CT = $CaTiO_3$, PT = $PbTiO_3$, PMN = $Pb(Mg_{1/2}Nb_{2/3})O_3$, PSN = $Pb(Sc_{1/2}Nb_{1/2})O_3$, PZ = $PbZrO_3$, PFN = $Pb(Fe_{1/2}Nb_{1/2})O_3$, PNN = $Pb(Ni_{1/2}Nb_{2/3})O_3$, PZN = $Pb(Zn_{1/2}Nb_{2/3})O_3$, and PIN = $Pb(In_{1/2}Nb_{1/2})O_3$, and PCN = $Pb(Cd_{1/2}Nb_{2/3})O_3$.

CLASSIFICATION OF COMPLEX LEAD PEROVSKITES

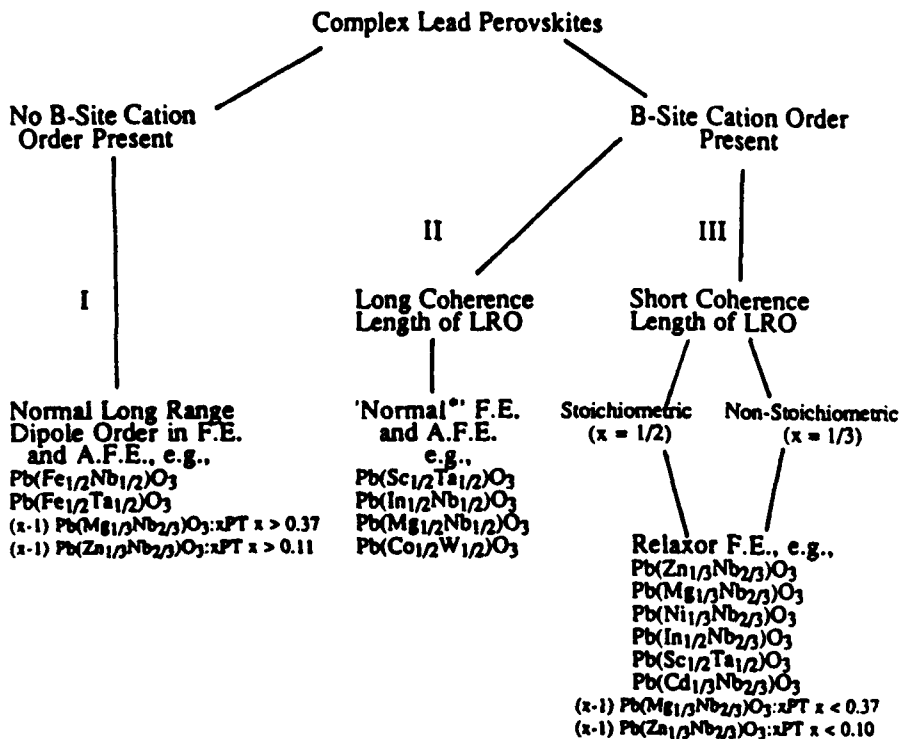


FIG. 3. Flow chart showing the relationship between long-range cation order and dielectric characteristics in complex lead perovskites.

*Incommensurate superstructural satellites found in some members of subgroup II, e.g., $Pb(Co_{1/2}W_{1/2})O_3$ and $Pb(Sc_{1/2}Ta_{1/2})O_3$.

achieved through thermal annealing as found for both $Pb(Sc_{1/2}Ta_{1/2})O_3$ (PST) and $Pb(In_{1/2}Nb_{1/2})O_3$ (PIN); thus they are reported in both columns II and III.

Along with individual perovskite compounds, various solid solutions are reported in the various columns. In solid solutions of $(1-x) PbMg_{1/3}Nb_{2/3}O_3, xPbTiO_3$ (PMN:PT) and $(1-x) PbZn_{1/3}Nb_{2/3}O_3, xPbTiO_3$ (PZN:PT) there is a weakening of the superlattices as the

$PbTiO_3$ (PT) content increases. Eventually, there is a point where a superlattice cannot be detected, and thus the solid solution is disordered or possesses only short-range order (≤ 2 nm).^{13,14} This has been found to occur in compositions very close to the morphotropic phase boundaries (MPB) which separate relaxor from normal FE behavior.^{19,20} These MPB compositions are approximately 0.65 PMN:0.35 PT and 0.9 PZN:0.1 PT and hence higher PT compositions are listed in column I since there is no detectable order and correspondingly normal FE behavior exists. Based on the cation order and its relative coherency and ferroelectric behavior, a correlation is suggested within a variety of compounds and solid solutions in the complex lead perovskites.

III. DISCUSSION

A. Consequences of long-range order

The consequences of nanoscale order for relaxor behavior in lead-based perovskites have been recently discussed by Randall and Bhalla.²¹ The authors state that regions of nanoscale order act as sites to localize superparaelectric polar potentials, schematically represented in Fig. 5. The superparaelectric model, as proposed by Cross, accounts for the dielectric and struc-

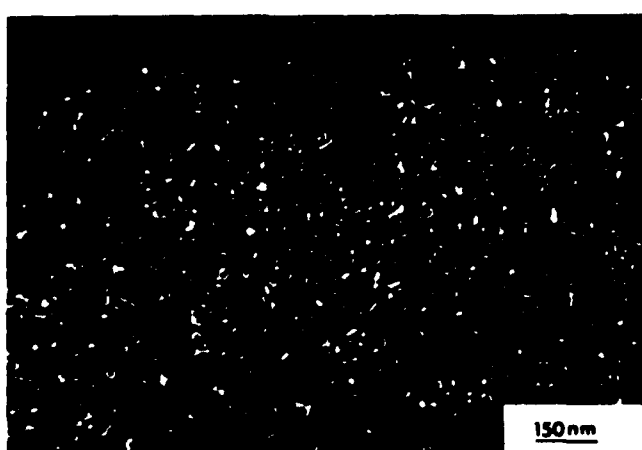


FIG. 4. B-site order domains in 0.9 PMN:0.1 PT.

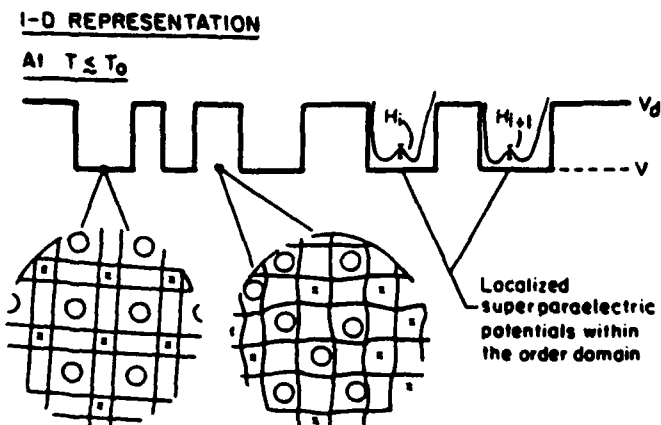


FIG. 5. Schematic representation of superparaelectric potentials localized in a nanoscale LRO domain (~ 10 nm) of a complex perovskite relaxor. The superparaelectric potential in the i th order domain has an activation barrier of height H_i .

tural characteristics of relaxor compounds.⁵ Basically, the superparaelectric model is analogous to superparamagnetism and refers to thermal agitations of the orientation of spontaneous dipolar polarization in polar clusters. The size of the polar clusters determines the size of the activation barrier, H , between degenerate dipolar states. Then for sufficient thermal energy, a flipping of the orientation from one state to another can occur. The flipping frequency, v , is expressed as:

$$v = v_D \exp - \frac{H(V)}{k_B T} \quad (3)$$

where v_D = Debye frequency ($\sim 10^{11}$ - 10^{13} Hz),

$H(V)$ = Height of the activation barrier is directly related to the volume of the polar cluster, V ,

k_B = Boltzmann constant, and

T = Absolute temperature.

The superparaelectric model interprets many of the relaxor features including broad dielectric dispersion, nonlinear optical and thermal properties, dielectric aging, etc.⁵ The superparaelectric model and the concept of the polar clusters about nanoscale order domains have three important attractions in contrast to the generally accepted inhomogeneous chemical microregion model postulated by Smolenskii:²²

(1) Nanostructural B-cation ordered regions and not inhomogeneous chemical fluctuations link relaxor ferroelectricity in complex lead perovskites. The scale of this B-site order allows for discriminations to be made with the complex perovskites for those exhibiting either relaxor or normal type behavior.

(2) The nanoscale order domains act as natural sites to localize the high temperature superparaelectric polar clusters within a paraelectric matrix on a scale (~ 10 nm) consistent with the predictions of Smolenskii²² and Cross,⁵ as previously deduced from dielectric relaxation calculations.

(3) A distribution of the size of ordered domains (e.g., 10–1000 nm) may account for the broad phase transitions observed in relaxors. However, little statistical inference in this area has yet been established.

B. Inhomogeneous order

It is generally accepted that variations in dielectric and related properties for a given material are microstructurally related. Such features include grain size, porosity, grain boundary, chemical homogeneity, and domain/twin structure with a scale on the micron level with 1–100 μ grains at the upper level and domain size in the range of 0.1 μ to 10 μ at the lower level.

In complex lead perovskites, variations in the dielectric properties reported in the open literature for a given material may also be the result of variations in the scale of nanosized ordered regions. For example, inhomogeneities of the scale of ordering in flux grown PST single crystals, as shown in Fig. 6(a), are believed

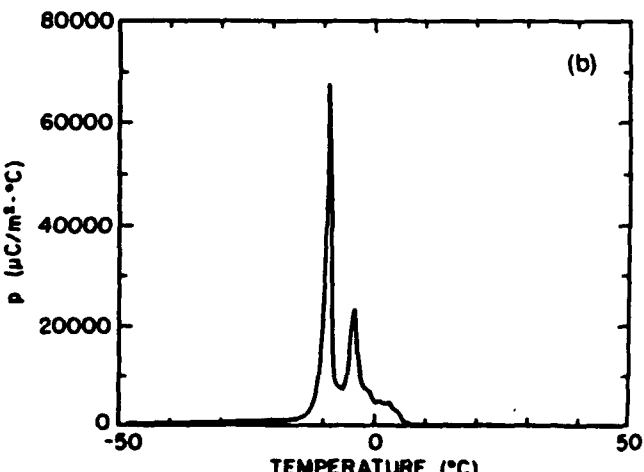


FIG. 6. (a) Inhomogeneous order in single crystal PST. (b) Multiple transitions in the pyroelectric coefficient temperature dependence in single crystal PST.

to be the cause of multiple transitions which occur in PST crystals as manifested by variations in the pyroelectric behavior; see Fig. 6(b). Inhomogeneous order in polycrystalline PST has also been observed, whereby larger ordered domains tend to be observed near the grain boundaries with smaller ones at the center of the grains (see Fig. 7). In the case of PIN, where increases of order give rise to changes in the dipole arrangements from FE to AFE, inhomogeneous order results in mixed FE and AFE phases and corresponding dielectric mixing behavior.^{15,23-25}

C. Dipolar incommensurates and long-range order

X-ray and TEM studies on large-scale ordered $\text{Pb}(\text{Co}_{1/2}\text{W}_{1/2})\text{O}_3$ (PCW) and $\text{Pb}(\text{Sc}_{1/2}\text{Ta}_{1/2})\text{O}_3$ (PST) compounds have revealed evidence of incommensurate displacive ferroic phase transitions in the form of superlattices and satellites.²⁶⁻²⁹ Dark-field imaging of these satellites revealed discommensurate microstructures, as presented earlier.²⁸ Figure 8 shows incommensurate satellites in the $\langle 001 \rangle$ zone axis pattern of PCW. The detection of a subtle incommensurate dipole modulation in some of the highly ordered $\text{Pb}(\text{B}_{1/2}\text{B}_{1/2''})\text{O}_3$ compounds of column II raises questions regarding local dipole symmetry within the nanoscale ordered domains of the relaxor perovskites in column III.

IV. SUMMARY

A classification of complex lead perovskites is presented on the basis of scale of B-cation LRO and is correlated to reported physical properties. The consequences of this classification give rise to new insights into the perturbations on the long-range cooperative

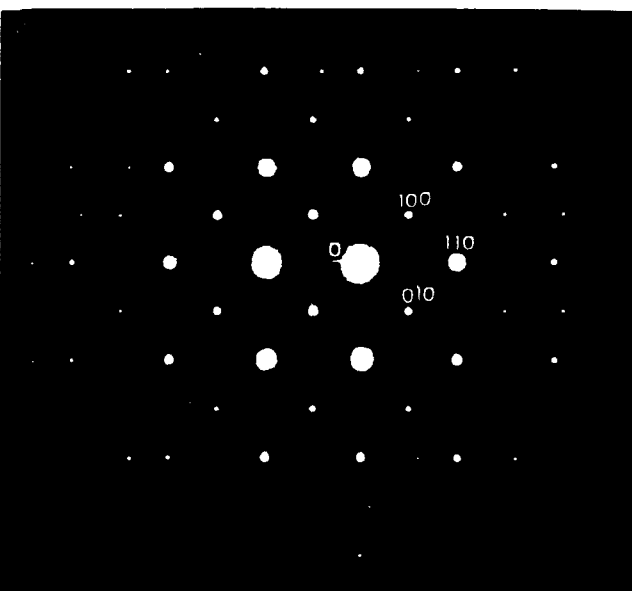


FIG. 8. Displacive incommensurate superlattices and satellites in $\langle 001 \rangle$ zone axis patterns of ferroic PCW.

alignment of ferroelectric dipoles. The existence of B-site LRO to form ordered domains on the scale of 2–50 nm appears to be an important structural link between the chemical distribution and the relaxor ferroelectric behavior. These ordered domains with short coherency are suggested as the sites on which to localize superparaelectric polar clusters of relaxors.

Additionally, other consequences of LRO include inhomogeneous distributions of its scale, giving rise to transitions over a wide temperature range. Also, recent findings of an incommensurate modulation of the dipolar alignment in perovskites such as PCW and PST show other ways in which the B-site order influences the crystallography of the dipole alignment in ferroic phases.

ACKNOWLEDGMENTS

The authors wish to thank ONR and DARPA for their financial support. It is a pleasure to acknowledge discussions with Professor D. J. Barber, Dr. K. Baba-Kishi, Dr. A. D. Hilton, and Dr. G. Burns. Also many thanks to Joyce Baney for the typing of this manuscript.

REFERENCES

- ¹M. E. Lines and A. M. Glass, *Principles and Applications of Ferroelectrics and Related Materials* (Clarendon Press, Oxford, 1977).
- ²G. A. Smolenskii, V. A. Bokov, V. A. Isupov, N. N. Kranik, P. E. Paslyakov, and A. I. Sokolov, *Ferroelectrics and Related Materials* (Gordon and Breach, New York, 1984).
- ³H. A. Megaw, Proc. Phys. Soc. **58**, 133 (1946).
- ⁴Y. N. Venskev and G. S. Zhdanov, Acad. Sci. USSR **20**, 161 (1956).
- ⁵R. D. Shannon and C. T. Prewitt, Acta Cryst. **B25**, 925 (1969).
- ⁶L. E. Cross, Ferroelectrics **76**, 241–267 (1987).



FIG. 7. Inhomogeneous order in a PST ceramic grain.

- ⁴A. Halliyal and T. R. Shrout, *Am. Ceram. Conf. (Regional)*, New Orleans (1986).
- ⁵J. M. Cowley, *Advances in High Temperature Chemistry* 3, 36-82 (1971).
- ⁶T. R. Shrout, W. Huebner, C. A. Randall, and A. D. Hilton, *Ferroelectrics* (1989).
- ⁷D. M. Smyth, M. P. Harmer, and P. Peng, *Am. Ceram. Soc. Meeting*, Indianapolis, IN (1989).
- ⁸B. Krause, J. M. Cowley, and J. Wheatly, *Acta Cryst.* A35, 1015 (1979).
- ⁹C. A. Randall, D. J. Barber, R.W. Whatmore, and P. Groves, *J. Mat. Sci.* 23, 4456 (1988).
- ¹⁰C. A. Randall, D. J. Barber, and R.W. Whatmore, *J. Micro.* MS, 235 (1987).
- ¹¹J. Chen, H. Chen, and M. A. Harmer, *J. Am. Ceram. Soc.* 72, 593 (1989).
- ¹²A. D. Hilton, C. A. Randall, and D. J. Barber, *J. Mater. Sci.* (in press) (1989).
- ¹³C. A. Randall, D. J. Barber, P. Groves, and R.W. Whatmore, *J. Mater. Sci.* 23, 3678-3682 (1988).
- ¹⁴I. M. Brunskill, H. Schmid, and P. Tissot, *Ferroelectrics* 37, 547-550 (1984).
- ¹⁵W. Brixel, J. P. Rivera, and H. Schmid, *Ferroelectrics* 55, 181-184 (1984).
- ¹⁶Landolt-Börnstein, *New Series III, 16a* (Springer-Verlag, Berlin, 1981).
- ¹⁷S. W. Choi, T. R. Shrout, S. J. Jang, and A. S. Bhalla, *J. Mater. Lett.* (to be published).
- ¹⁸J. Kuwata, K. Uchino, and S. Nomura, *Jpn. J. Appl. Phys.* 21, 1298 (1982).
- ¹⁹C. A. Randall and A. S. Bhalla, submitted to *Jpn. J. Appl. Phys.*
- ²⁰G. A. Smolenskii, *J. Phys. Soc. Jpn. (Suppl.)* 28, 26 (1970).
- ²¹A. V. Turik, M. F. Kupriyanov, V. F. Zhestkov, N. B. Slevchenko, and V. A. Kogan, *Sov. Phys.-Solid State* 27, 1686 (1986).
- ²²P. Groves, *J. Phys. C: Solid State Phys.* 19, 5103 (1986).
- ²³A. A. Bokov, *Ferroelectrics* 54, 241 (1984).
- ²⁴H. Tamura, *Ferroelectrics* 21, 449 (1978).
- ²⁵W. Brixel, M. L. Werk, P. Fischer, W. Buhrer, J. P. Rivera, P. Tissot, and H. Schmid, *Jpn. J. Appl. Phys. (Suppl.)* 24, 242 (1985).
- ²⁶C. A. Randall, S. A. Markgraf, A. S. Bhalla, and K. Baba-Kishi, *Phys. Rev. B* 40, 413 (1989).
- ²⁷P. Sciau, K. Krushe, P. A. Buffatt, and H. Schmid, Proc. 7th Int. Meeting on Ferroelectricity, Saarbrücken, F. R. Germany (1989).

APPENDIX 22

ELECTRICAL BEHAVIOR OF DIFFUSED PHASE FERROELECTRICS IN THE MICROWAVE REGION

D. C. DUBE and S. C. MATHUR

*Physics Department, Indian Institute of Technology, Delhi,
New Delhi 10016, India*

and

S. J. JANG and A. S. BHALLA

*Materials Research Laboratory, The Pennsylvania State University,
University Park, PA 16802, USA*

(Received January 15, 1989; in final form Feb. 15, 1989)

High permittivity and varying degrees of losses in diffused phase ferroelectrics negate the use of conventional techniques for their study at microwave frequencies. Therefore, frequency difference and quarter wave plate matching techniques have been employed. Results are presented on lead-magnesium niobate-lead titanate (PMN-PT) solid solutions of several compositions. It has been suggested that partial charge compensation at the grain boundaries on solid dilution may play a major role on the dielectric properties.

Complex perovskite ferroelectrics demonstrate interesting electrical properties. They exhibit diffuse phase transition of a relaxor type. In solid solutions, the diffusion of phase transition generally may result from macroscopical non-equilibrium inhomogeneity of composition. But diffused phase transition observed for compound $\text{PbMg}_{1/3}\text{Nb}_{2/3}\text{O}_3$ (designated PMN) is due to the micro- to nanosize order-disordered ferroelectric regions.¹ Therefore, these microscopic scale of chemical inhomogeneities of composition are the source of diffusion of relaxor type phase transition. The situation is expected to change for solid solutions of PMN with other proper ferroelectric PbTiO_3 (designated PT and having a first order phase change at 495°C). We report here our investigations on dielectric behavior of PMN-PT solid solutions of varying compositions.

Perovskite solid solutions of PMN-PT were prepared in different compositions using the two-step method discussed in detail by Swartz *et al.*² The absence (<2%) of pyrochlore phase in samples of all compositions was established by measuring x-ray diffraction peak intensities.

The procedure adopted for experimental determination of dielectric properties of PMN-PT in the microwave region as well as low frequencies has been described elsewhere.^{3,4}

Four different compositions of $x\text{-PMN}$ ($1-x\text{-PT}$) (where $x = 0.9, 0.8, 0.7$, and 0.6) were selected for the present studies. Figure 1 shows the room temperature permittivity and dielectric loss in 0.6 PMN-0.4 PT and 0.7 PMN-0.3 PT in the 8-12 GHz microwave frequency region. These results were obtained using the frequency difference techniques.⁵ Other compositions of PMN-PT showed similar

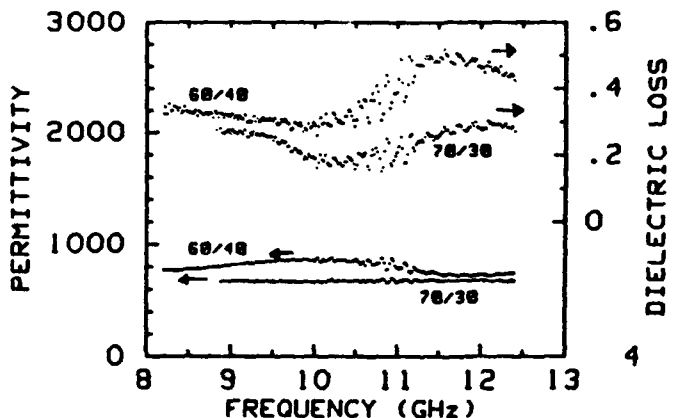


FIGURE 1 Dielectric properties of 60/40 and 70/30 PMN-PT ceramics in the microwave region at room temperature.

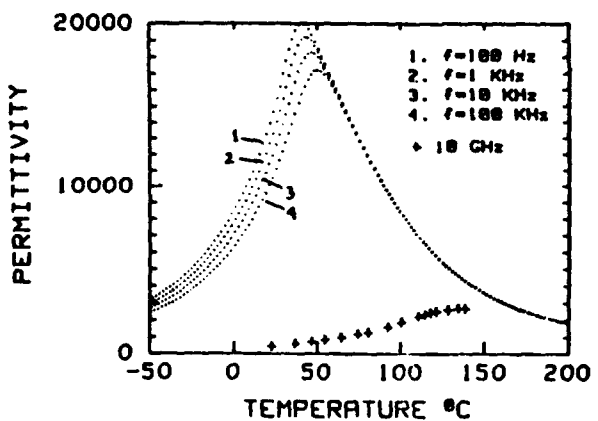


FIGURE 2 Temperature dependence of the dielectric permittivity of 0.9 PMN 0.1 PT ceramic at microwave (10 GHz) and low frequencies 100 Hz, 10 kHz, and 100 kHz.

behavior. The flat frequency response of PMN-PT is in tune with the true nature of ferroelectric relaxors.

Plots shown in Figure 1 were obtained, as mentioned earlier, by frequency difference techniques. In Figure 1, scatter in K vs. f experimental data is seen at room temperature and found to increase at higher temperatures. Therefore, temperature studies were conducted with quarter wave plate technique.^{3,4} This technique negates the facility of sweeping the frequency and the investigations were restricted to a single frequency.

Figure 2 illustrates the permittivity of 0.9 PMN-0.1 PT at 10 GHz as a function of temperature. A broad dielectric maximum at 140°C is observed. For comparison purposes, Figure 2 also contains low frequency data which exhibit less broad maxima in the vicinity of 50°C. The reduction in permittivity and shifting of maxima towards

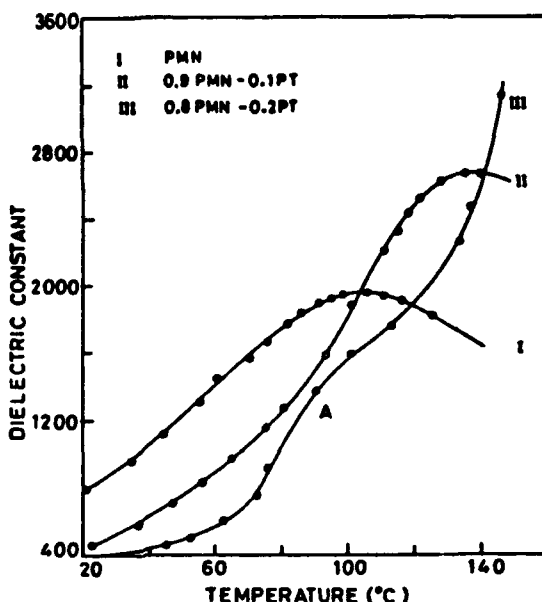


FIGURE 3 Dielectric constant as function of temperature for PMN, 0.9 PMN-0.1 PT and 0.8 PMN-0.2 PT at 10 GHz.

higher temperature side at microwave frequencies is typical of relaxation processes in the system.

The permittivity as a function of temperature at 10 GHz for pure PMN as well as for PMN-PT are shown in Figure 3 and corresponding loss data are plotted in Figure 4.

From the dielectric peaks observed or from the trends of permittivity variation with temperature (Figure 3) one finds that as the PT content in PMN-PT becomes higher the dielectric peak moves to higher temperature side. The peak value of permittivity ϵ_{\max} becomes higher and the peaks get sharper for samples with higher PT content.

The increase in the value ϵ_{\max} as well as the shifting of T_c to higher temperature side on increasing the PT content is consistent with the expected general behavior of solid solutions. However, the decrease in the width of the peak with increase in the PT content does not follow the expected pattern. For solid solutions, compositional fluctuations are more probably giving rise to more diffused phase transition. But sharper peaks for solid solutions with higher content of PT may be due to the fact that PT is a proper ferroelectric. There is yet another possibility. PMN relaxor materials are considered as composites of nanoregions of chemically different composition. These regions are of ferroelectric nature. This results in charge imbalance at grain boundaries. It is likely that PT partly balances the surface charges. As the PT content is increased the charge imbalance decreases and thus favoring the growth of larger macro ferroelectric regions. Thus the increase of PT content may be considered as a move towards creating a large ferroelectric region. This may give rise to less diffused phase transition peaks with increased PT content.

A little hump in the dielectric response of 0.8 PMN-0.2 PT (region A in Figure

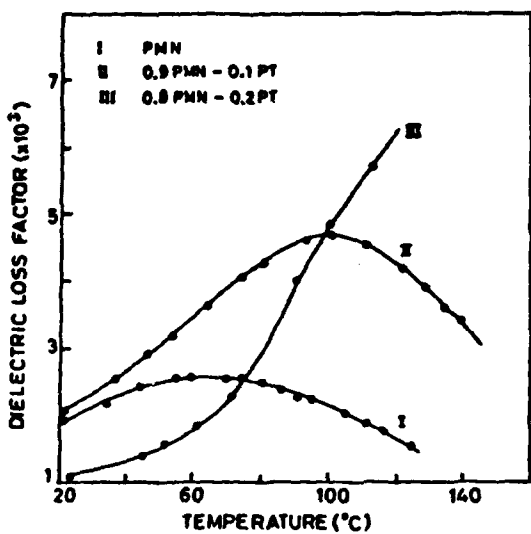


FIGURE 4 Dielectric loss factor as a function of temperature for PMN, 0.9 PMN-0.1 PT and 0.8 PMN-0.2 PT at 10 GHz.

3) indicates the on-set of morphotropic boundary. The morphotropic phase boundary becomes more pronounced in 0.7 PMN-0.3 PT composition.³

From Figure 4, it may be noted that dielectric loss maxima do not fall at the same temperature as permittivity maxima (Figure 3). Loss peaks are observed at lower temperatures. This observation is consistent with the typical behavior of relaxor materials.^{1,6}

ACKNOWLEDGEMENTS

The authors wish to thank Professor L. E. Cross for the various stimulating discussions on relaxor materials.

REFERENCES

1. G. A. Smolenskii, *J. Phys. Soc. Jap.*, **28**, Suppl. 26 (1970).
2. S. L. Swartz and T. R. Shroud, *Mat. Res. Bull.*, **17**, 1245 (1982).
3. M. T. Lanagan, N. Yang, D. C. Dube, and S. J. Jang, *Am. Ceram. Soc. Bull.*, **67**, (1988).
4. D. C. Dube, S. J. Jang, and A. S. Bhalla, *Ferroelectrics*, (to appear).
5. M. T. Lanagan, J. H. Kim, D. C. Dube, S. J. Jang, and R. E. Newnham, *Ferroelectrics*, **82**, 91 (1988).
6. N. P. Khuchua, *Proc. Inter. Meeting Ferroelectricity*, Prague, Vol. 2, p. 161 (1966).

APPENDIX 23

Freezing of the polarization fluctuations in lead magnesium niobate relaxors

Dwight Viehland, S. J. Jarig, and L. Eric Cross^{a)}

Materials Research Laboratory, Pennsylvania State University, University Park, Pennsylvania 16802

Manfred Wuttig

Engineering Materials Program, University of Maryland, College Park, Maryland 20742

(Received 7 March 1990; accepted for publication 31 May 1990)

The dielectric relaxation of a solid solution of 10-mol % lead titanate in lead magnesium niobate is found to be similar to the magnetic relaxation in spin-glass systems.¹⁻³ Based on this analogy, it is proposed that the relaxor ferroelectric is a polar-glassy system which has thermally activated polarization fluctuations above a static freezing temperature. An activation energy and freezing temperature of 0.0407 eV and 291.5 K, respectively, were found by analyzing the frequency dependence of the temperature of the dielectric maximum using the Vogel-Fulcher relationship.^{4,5} It has also been shown that a macroscopic polarization is sustained on heating up to this freezing temperature. A coupling between nanometer scale clusters is believed to control the kinetics of the fluctuations and the development of a frustration as the system freezes into states of local equilibrium. The possibility of an orientational freezing associated with the ferroelastic nature of the nanosized polar regions in the rhombohedral relaxor families as well as a polar freezing is discussed. A diffuse phase transformation is believed to arise due to a dispersion in the fluctuation frequency of the polarization. A qualitative model for the relaxation time spectrum is also proposed in which the width of the spectrum broadens strongly near the freezing temperature.

I. INTRODUCTION

Lead magnesium niobate (PMN) is the classic relaxor ferroelectric. It easily forms a solid solution with lead titanate (PT), and relaxor behavior persists up to the morphotropic phase boundary at a composition containing 35 at % PT. Relaxors are characterized by a strong frequency dispersion of the dielectric maxima (K_{\max}), and the absence of macroscopic polarization and anisotropy at temperatures significantly below K_{\max} . It is commonly recognized that all relaxors are highly inhomogeneous materials. Smolenski⁶ originally proposed that underlying the relaxor behavior was a chemical inhomogeneity on a cation site giving rise to a diffuse phase transformation (DPT). He postulated that the DPT arose due to a multitude of local first order phase transition temperatures. Smolenski's concept failed to explain why many nonrelaxor ferroelectrics have a DPT. Randall⁷ has found evidence for short range chemical order on the nanoscale level using transmission electron microscopy (TEM). Randall and Cross⁸ have subsequently proposed that it is the scale of the inhomogeneity which underlies the relaxor behavior. Cross⁹ has proposed that these nanometer scale clusters are dynamical in nature with the dipole moment thermally fluctuating between equivalent directions. In the absence of interactions between regions this model would be analogous to superparamagnetism,¹⁰ and consequently the frequency dependence of the temperature of the dielectric maximum should be governed by a simple Debye relationship. Activation energies and preexponential factors of approximately 7 eV and 10^{40} s^{-1} , respectively, have been obtained from analysis with the Debye equation¹¹ both of which are physically unrealistic for simple thermally acti-

vated polarization fluctuations. Isupov,¹¹ however, obtained an activation energy on the order of kT with a preexponential factor of 10^9 s^{-1} by extrapolating Cole-Cole plots. He then explained the dielectric relaxation as a temperature dependence of the number of polar regions.

A spin-glass state is generally viewed as a system of interacting superparamagnetic clusters,^{12,13} and not as a system of clusters with independent localized behavior. The universal characteristic of a spin glass, and in general any glassy behavior, is the existence of a static freezing temperature. In structural glasses the freezing temperature, commonly known as the glass transition temperature, is determined by the onset of measurable visco-elastic behavior on observable time scales.^{4,5} In spin glasses a static freezing temperature can be determined from the frequency dependence of the permittivity¹⁻³ which approaches a constant value at lower frequencies. The freezing of the magnetic moment in spin glasses is believed to arise due to competing interactions, both ferromagnetic and antiferromagnetic, between neighboring clusters preventing the establishment of conventional long-range ordering.¹⁴ Instead, these systems become frustrated by establishing only local ordering, ferromagnetic and antiferromagnetic, between clusters. Several other types of competing interactions have been found to lead to glassy behavior. A dipolar glass is believed to exist in $\text{Rb}_{1-x}(\text{NH}_4)_x\text{H}_2\text{PO}_4$ due to a competition between ferroelectric and antiferroelectric couplings.¹⁵ A quadrupolar or orientational glass is believed to exist in KCN-KBr due to a competition between elastic interactions amongst different orientational states.^{16,17} A competition between a random strain field or anisotropy with a ferromagnetic coupling has been predicted to lead to freezing.¹⁸ All known glassy systems to date possess two key elements: (1) randomness due to an underlying disorder usually with clustering, and (2) frustration leading to freezing.

^{a)} Also in the Electrical Engineering Department.

The purpose of this work was to investigate the dielectric relaxation of PMN-10PT and to determine if the data give evidence for a static freezing temperature. The dielectric relaxation has been modeled by analogy to spin-glass systems. The expectation was to establish that significant interactions do exist between the ferroelectric clusters, and to try to determine the nature of these interactions and their implications in the understanding of the diffuse phase transformation in relaxors.

II. EXPERIMENTAL PROCEDURE

The samples used in this study were PMN ceramics with 10 at % PT (PMN-10PT). They were prepared as described by Pan and Cross.¹⁹ The 100 Hz dielectric maximum was near 40 °C. The samples were free of aging as described by Pan,¹⁹ were free of pyrochlore as described by Shroud,²⁰ were of dimensions $1 \times 0.5 \times 0.03$ cm, and were electrode with gold. Stoichiometric aging free samples were used to avoid a potential complication of the relaxation mechanism by a time varying defect structure.

The dielectric constant was measured as a function of frequency (ω) between 100 and 0 °C at a cooling rate of 1 °C/min. The frequencies used were 0.1, 0.2, 0.4, 1, 2, 4, 10, 20, 40, 100, 200, 400, 1000 KHz. The dielectric curve for each frequency was smoothed and interpolated to find the most accurate temperature of the dielectric maximum (T_{\max}) to within 0.02 °C. The pyroelectric current was also measured as a function of temperature, and the polarization was calculated by integration for comparison with the dielectric data.

III. RESULTS

An illustration of the frequency dependence of the dielectric response is shown in Fig. 1. These curves demonstrate typical relaxor behavior with the magnitude of the dielectric constant decreasing with increasing frequency and the maximum shifting to higher temperatures. The values of T_{\max} and the corresponding frequency are tabulated in Table I. Figure 2 shows a plot of the $\ln(\omega)$ vs $1/T_{\max}$, where the open squares are the experimental data. It is obvious from

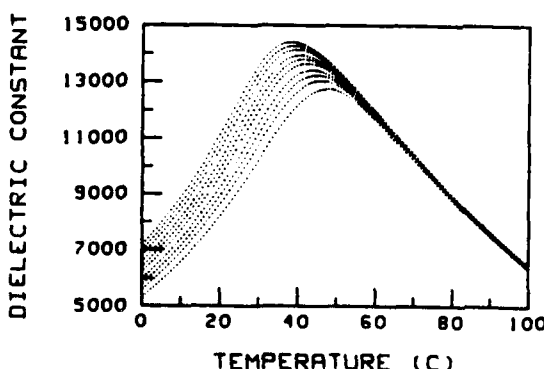


FIG. 1. Dielectric constant as a function of temperature at measurement frequencies of 0.1, 0.2, 0.4, 1, 2, 4, 10, 20, 40, 100 KHz. The highest dielectric response is the 0.1 KHz curve, the lowest is the 100 KHz curve, and the other curves between are in order of increasing frequency.

TABLE I. Temperature of the dielectric maximum in Kelvin tabulated along side the corresponding measurement frequency.

Frequency (kHz)	T_{\max} (K)
0.1	311.9
0.2	312.75
0.4	313.4
1	314.35
2	315.05
4	315.82
10	317.38
20	318.21
40	318.98
100	320.59
200	321.71
400	323.51
1000	325.98

Fig. 2 that the frequency derivative of $1/T_{\max}$ is smaller at lower frequencies in the observed range. This figure visually illustrates that as $\omega \rightarrow 0$ a static freezing temperature is approached. The polarization as a function of temperature is shown in Fig. 3. An extrapolation of the slope at the inflection point to zero yielded a critical temperature near 290 K shown in Fig. 3 as T_f .

IV. DISCUSSION

The magnetic relaxation in spin-glass systems¹⁻³ can be described by a relationship attributed to Vogel⁴ and Fulcher⁵ given in Eq. (1)

$$\omega = f_0 \exp[-E_a/k(T_{\max} - T_f)] \quad (1)$$

where T_f is the static freezing temperature, E_a the activation energy, f_0 the Debye frequency, and T_{\max} the temperature of the permittivity maximum. The activation energy is generally believed to be the product of an anisotropy energy, K_{anis} , and the cluster volume, V , as originally described by Neel.¹⁰ Analysis of the thirteen pairs of (ω, T_{\max}) , given in Table I, with a Levenberg-Marquadt nonlinear analysis program us-

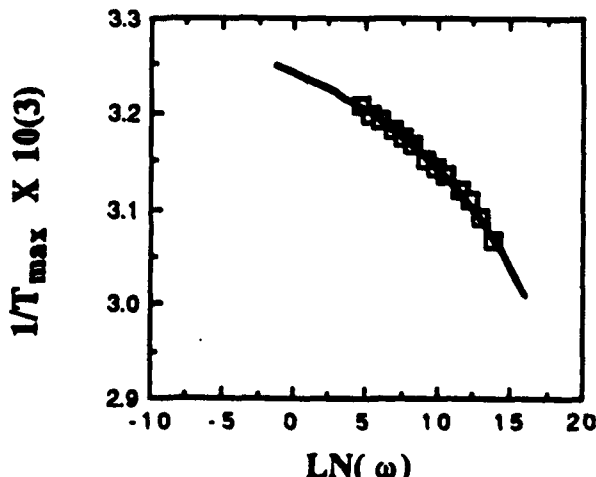


FIG. 2. Inverse of the temperature of the dielectric maximum as a function of the measurement frequency.

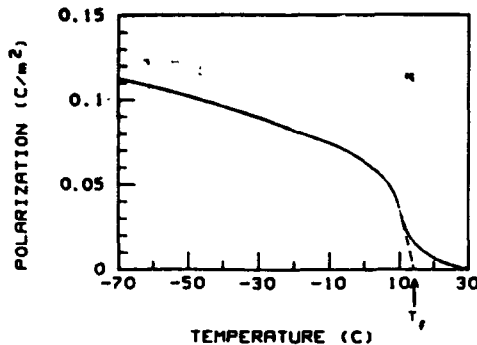


FIG. 3. Remanent polarization as a function of temperature.

ing Eq. (1) gave an activation energy of 0.0407 eV, a preexponential factor of 1.03×10^{12} Hz, and a static freezing temperature of 291.5 K. The curve fitting to the data is shown as the solid line in Fig. 2. The close agreement of the data with the Vogel-Fulcher relationship, suggests that the relaxor behavior in the PMN system is analogous to a spin glass with polarization fluctuations above a static freezing temperature. The activation energy and preexponential factor are both consistent with thermally activated polarization fluctuations. The most probable fluctuation mechanism is the rotation of the polarization in an isothermal plane between equivalent orientations as the electrocrystalline anisotropy energy is generally smaller than the paraelectric free energy, i.e., the polar fluctuations are not heterophase fluctuations. The PMN family of relaxors are rhombohedral,²¹ and consequently the fluctuations will occur between (111) variants. K_{min} , then, is probably the electrocrystalline anisotropy energy which represents the barrier for a rotation of the polarization between adjacent (111) variants as shown in Fig. 4(a), rather than the paraelectric free energy representing the barrier through the center (paraelectric state) which is more consistent with heterophase fluctuations (paraelectric to ferroelectric) as shown in Fig. 4(b). It is difficult to comment with certainty on whether or not fluctuations may occur between other minima, such as between (111) and (110) variants. Recent x-ray refinement results by Bonneau *et al.*²² give evidence in support of this idea. A complete phenomenological description, then, may have to include variants along other crystallographic orientations. It may be characteristic of relaxors that many of the minima are close to the same depth, i.e., the energy surface is near spherical. The fluctuation mechanism in the tungsten bronze family of relaxors should be significantly different than the PMN family because the structure in the prototypic form is tetragonal with only two domain states. The fluctuations in tungsten bronzes probably occur through the center and are more closely related to a heterophase fluctuation than a superparaelectric relaxation. The static freezing temperature for PMN-10PT was in close agreement with the temperature of the collapse in the remanent polarization (290 K). The static freezing temperature is large relative to those of spin-glass systems^{23,24} and the $\text{Rb}_{0.65}(\text{NH}_4)_{0.35}\text{H}_2\text{PO}_4$ polar-glass system.¹⁵

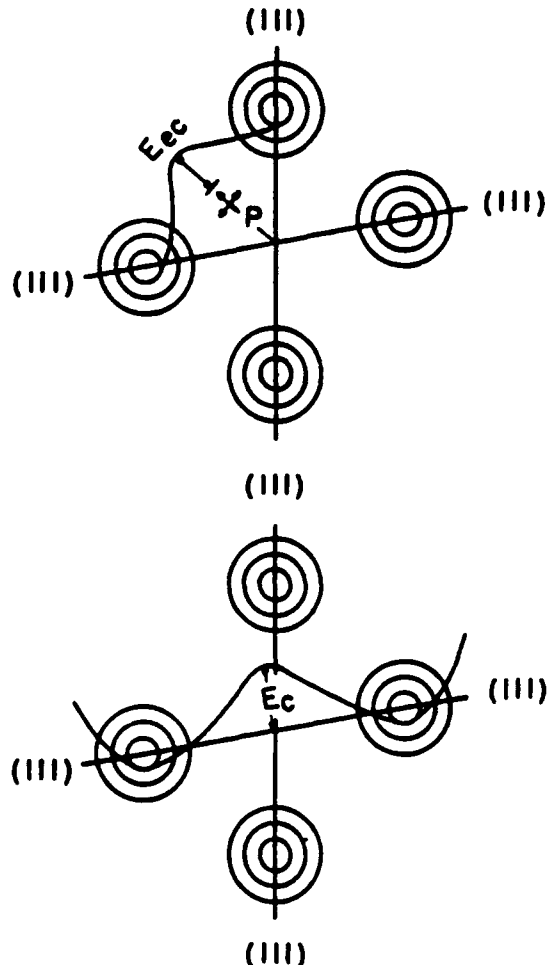


FIG. 4. (a) Potential well diagram which illustrates the activation energy for a superparaelectric relaxation where E_c is the electrocrystalline anisotropy and P is the polarization. (b) Potential well diagram which illustrates the activation energy for a heterophase fluctuation where E_r is the paraelectric free energy.

The Vogel-Fulcher relationship may be interpreted as a normal Debye relaxation with a temperature-dependent activation energy. The activation energy increases as the temperature decreases becoming undefined at the freezing temperature. A more realistic interpretation of this relationship, in reference to relaxors, is that E_a represents the activation energy for polarization fluctuations of an isolated cluster with the temperature dependence arising from the development of short-range order between neighboring clusters with kT_f being a measure of the interaction energy. It is certainly possible that the ferroelectric clusters interact via dipole and dipole-induced dipole exchanges. The possibility also exists that the clusters could interact elastically through local rhombohedral distortions implying that the clusters may freeze into an orientational glassy state and are superparaelectric above the freezing temperature. The close agreement of the frequency dependence of T_{max} with the Vogel-Fulcher relationship and the reasonable values obtained from the analysis imply that the mean E_a does not significantly change in the temperature interval investigated. The mean E_a would be expected to decrease with increasing tempera-

ture if the frequency dependence of T_{\max} was a reflection of the inability of the larger clusters to follow the drive with increasing frequency. The evidence presented here indicates that to a close approximation the kinetics of the polarization fluctuations in the radio frequency range are controlled by the interactions between the clusters and the development of local correlations, and not by a change in the number of ferroelectric clusters or their size. Careful inspection of the data did reveal a slow decrease in E_s as the higher frequencies values of T_{\max} were added in the analysis, and also the 10 GHz T_{\max} (125 °C) as reported by Jang²⁵ was approximately 10 °C higher than predicted from the radio frequency data using Eq. (1).

The PMN system partitions into nanoscale clusters of 1:1 ordering between Mg and Nb and into disordered regions which are Mg deficient.⁶ Because of this "fossil" chemistry left over from the processing, relaxors may not be able to establish a homogeneous order of the polarization but only short-range order between neighboring clusters. It is generally believed that for the development of glassy behavior competing interactions are necessary in addition to a chemical disorder. This may not necessarily be the case in relaxors, but there are previous results in the literature which lend support to such a hypothesis. It is well known that the antiferroelectric phase boundary on the lead zirconate side of the lead zirconate titanate (PZT) phase diagram extends towards the morphotropic phase boundary with increasing La²⁺ (PLZT), and there have been reports that PLZT relaxors are in a mixed phase region of ferroelectric and antiferroelectric members.^{27,28} Randall⁷ has recently found evidence which indicates that some nanoscale clusters in PLZT are ferroelectric and others antiferroelectric. Also, lead scandium tantalate (PST) and lead indium niobate (PIN) are both relaxor ferroelectrics of the PMN family with similar properties whose positional order can be controlled by thermal treatment. The ordered PST is ferroelectric,^{29,30} but the PIN orders into an antiferroelectric state.⁽³¹⁻³³⁾ These results imply that there may be tendencies for both ferroelectricity and antiferroelectricity in the PMN and PLZT families. A possible explanation for this tendency may be that the potential wells along the (111) directions are very shallow, and hence other wells representing different orientations or order parameters may make a significant contribution to the overall free energy. The implication is that the development of a frustration on freezing may occur due to the complex nature of the free energy phase space. Another possible mechanism by which conflicting interactions may arise is via a perturbation on a potential well of a micropolar region due to interactions with neighboring regions. In this situation the dipole moment of a micropolar region would not be able to fluctuate independently of its neighbors. The dipole moments, then, would not freeze randomly into a variant, but the freezing process would be cooperative and the direction in which one dipole freezes influences its neighbors. The macroscopic effect may be that some regions energetically favor a ferroelectric coupling with their neighbors, while the other regions favor antiferroelectric or ferroelastic couplings. It is too early to speculate effectively any further upon the exact nature of the interactions responsible for

freezing, or for the frustration which prevents the onset of long-range polar order. These questions may be resolved when current studies to explore the separate nonlinearities in both dielectric and elastic responses are completed. The most definite statement that can presently be said is that PMN relaxors probably possess both key ingredients for a glassy state: (1) disorder with clustering, and (2) a competition between interactions leading to freezing. It may be suggested that the differences between various relaxors is a reflection of the different nanoscale interactions and the corresponding competitions which dominate the freezing process.

The fundamental difference between spin-glass freezing and a thermal blocking process as observed in superparamagnetism is that freezing is a collective or cooperative phenomena, whereas a thermal blocking process is a local or independent phenomena. The cooperative phenomena is believed to be a reflection of interactions which are "in conflict" due to inhomogeneities. The implication is that the relaxor behavior is also a collective phenomena where short range interactions between the micropolar regions control the kinetics of the polarization fluctuations and the freezing process. Because of the cooperative nature of the freezing process the field-cooled relaxor state has a macroscopic polarization and is hysteretic below T_f . The agreement of the extrapolated temperature of zero polarization with the freezing temperature indicates that the collapse of the remanent polarization is a result of the kinetics of the fluctuations. When the kinetics approach observable time periods, the polar axes of the clusters begin to randomize and consequently a poled sample loses its macroscopic polarization and anisotropy. Figure 5 illustrates the expected agreement of the near-zero frequency dielectric response and the collapse of the remanent polarization at T_f . The difference between the zero-field-cooled (unpoled) and field-cooled (poled) states might be that the properties of the zero-field-cooled state correspond to a single minimum in phase space representing the average local equilibrium, whereas the properties of the

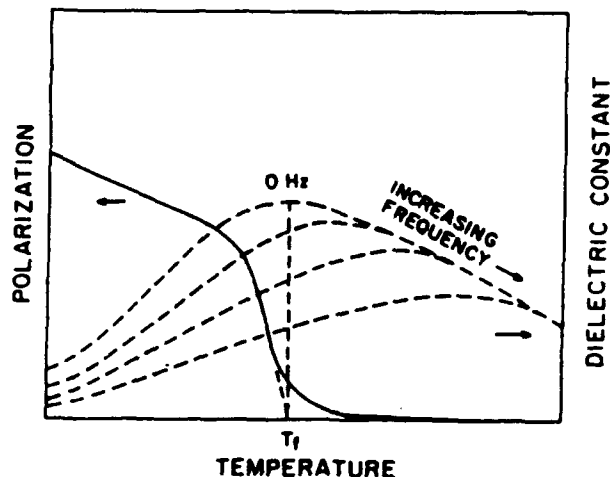


FIG. 5. Diagram illustrating the proposed agreement of the collapse in the remanent polarization and the static freezing temperature as calculated from the dielectric data.

field-cooled state correspond to the average over all minima representing a global equilibrium. The establishment of the global equilibrium would only occur through a forced electrical or electroelastic alignment of the polarization vectors of the clusters. On subsequent cooling below T_f , the dipoles would stay aligned after the field is removed.

The clusters have a size dispersion which determines the width of the relaxation time spectrum. A significant size dispersion was found by Randall⁸ and Harmer³⁴ using TEM. A relatively small difference in the cluster volume would make a large change in its fluctuation frequency. Assuming a temperature of 50 °C, spherical regions with an average diameter of 50 Å which is in agreement with the mean size found by TEM,^{8,34} and accepting the activation energy and freezing temperature presented in this work, an electrocrystalline anisotropy of 6.22×10^{-4} eV/nm³ and a value for $k(T - T_f)$ of 0.00271 eV can be approximated. Using Eq. (1), it can be shown that regions of diameter 45 and 55 Å would have fluctuation frequencies of approximately 2×10^7 and 2×10^3 Hz, respectively. The freezing process, then, may be related to a strong broadening of the relaxation time spectrum whose mean extends into the regime of macroscopic times at T_f . The faster end of this time spectrum, i.e., smaller clusters, would control the relaxation observed below T_f which subsequently must be cooled to lower temperatures to reach macroscopic time periods. An implication of the relaxation below T_f is that the system may freeze into a state which has nonequilibrium characteristics such as a time-dependent order parameter. It is possible that other relaxation mechanisms are becoming important below T_f . For example, a relaxation associated with domain wall vibration or a relaxation due to the cooperative motion of a group of clusters.

In an ideal superparaelectric the clusters are independent and the frequency dependence of T_{max} is governed by the Debye equation ($\omega = f_i e^{-E_a/kT_{max}}$). The Vogel-Fulcher relationship can be rearranged to $\omega = f_i e^{-E_a/kT(1 - T/T_{max})}$ where T_f/T_{max} is a measure of the nonideality of a superparaelectric state due to interactions. As the temperature is increased T_f/T_{max} decreases and the clusters behave more ideally. At the 10 GHz T_{max} (125 °C),²⁵ T_f/T_{max} is approximately 0.7 suggesting that strong correlations between clusters exist even at high fluctuation rates, but significant deviation from the Vogel-Fulcher relationship with respect to the radio frequency data was evident. At 900 K T_f/T_{max} is predicted to be 0.3 which is physically unrealistic. Obviously, the Vogel-Fulcher relationship cannot be used to model the dielectric relaxation near and above 10 GHz. The deviation from this relationship can be explained by conceptually adjusting the static picture of the diffuse phase transformation. Instead of having polar and nonpolar regions co-existing over a broad temperature interval with the volume fractions continuously changing,³⁵ local polar regions which have a dispersion in their fluctuation frequencies may co-exist over a significant part of this interval. The dispersion in the fluctuation frequency is a reflection of the cluster size dispersion. A cluster will remain ferroelectric until the temperature at which its polarization fluctuates at a frequency approaching (but below) the Debye frequency above which point the dipoles of a cluster can

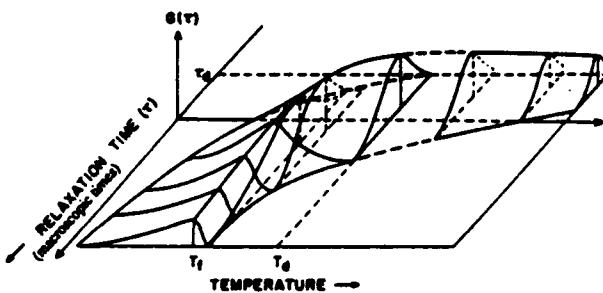


FIG. 6. Diagram illustrating the proposed temperature-dependent relaxation time spectrum. $G(\tau)$ is the number of micropolar regions having a relaxation time τ .

only move individually. The response of the smaller clusters which fluctuate more rapidly will "clamp out" at lower temperatures becoming paraelectric. When this occurs, the average distance between the remaining ferroelectric clusters will increase decreasing their interaction. Above this temperature, polar and nonpolar regions co-exist with the volume fraction of the polar regions decreasing with increasing temperature as more clusters become paraelectric. Below a critical percolation threshold, the correlation between the remaining ferroelectric clusters will be destroyed. At this point the clusters become isolated behaving as an ideal superparaelectric. The deviation of the frequency dependence of T_{max} from the Vogel-Fulcher relationship at high temperatures may then be explained by a change in T_f/T_{max} as the distribution of relaxation times extends into the regime of the Debye frequency.

A model of a temperature-dependent relaxation time spectrum is presented in Fig. 6. This model is not quantitative, but is qualitatively consistent with the experimental observations. The isothermal width of the spectrum is shown to become very broad at T_f with the mean value (τ_{ave}) approaching macroscopic time periods. Below T_f a noticeable fraction of the relaxations is shown to occur at shorter times. The shortest relaxation time (τ_{min}) is shown to approach macroscopic times only at temperatures far below T_f . Above T_f the isothermal width of the relaxation time spectrum continuously sharpens as the temperature is increased with τ_{ave} and τ_{min} approaching the microscopic time regime. Upon further increment of the temperature τ_{min} approaches τ_d , and at T_d becomes larger than τ_d . T_d can be viewed as the start temperature of the diffuse phase transformation in which polar and nonpolar regions co-exist. At temperatures greater than T_d , τ_{ave} , and τ_{max} begin to approach τ_d indicating that the volume fraction of the polar regions is decreasing.

V. CONCLUSION

Strong evidence for a static freezing temperature of thermally activated polarization fluctuations in PMN-10PT was found by modeling the dielectric relaxation using the Vogel-Fulcher relationship. The activation energy and static freezing temperature obtained were 0.0407 eV and 291.5 K, respectively. The macroscopic polarization was also found to collapse near the static freezing temperature on heating. A

polar-glassy model for relaxors was then proposed on the basis of these results with the interaction between the micro-polar regions controlling the kinetics of the fluctuations and the development of a frustration near the freezing temperature.

ACKNOWLEDGMENT

This work has been supported in full by contracts administered through the Office of Naval Research.

- ¹J. Tholence, *J. Appl. Phys.* **50**, 7369 (1979).
- ²J. Tholence, *Solid State Commun.* **35**, 113 (1980).
- ³S. Shtrikman and E. Wohlfarth, *Phys. Lett.* **85 A**, 467 (1981).
- ⁴H. Vogel, *Phys. Z.* **22**, 645 (1921).
- ⁵G. Fulcher, *J. Am. Cer. Soc.* **8**, 339 (1925).
- ⁶G. Smolenski and A. Agranovskaya, *Sov. Phys. Solid State* **1**, 1429 (1960).
- ⁷C. Randall, PhD dissertation, University of Essex, 1987.
- ⁸C. Randall, A. Bhalla, T. Shrout, and L. E. Cross, *J. Mater. Res.* **5**, 829 (1990).
- ⁹L. E. Cross, *Ferroelectrics* **76**, 241 (1987).
- ¹⁰L. Neel, *Compt. Rend. Acad. Sci.* **228**, 664 (1949).
- ¹¹V. Kirillov and V. Isupov, *Ferroelectrics* **5**, 3 (1973).
- ¹²A. Morgenownik and J. Mydosh, *Solid State Commun.* **47**, 321 (1983).
- ¹³K. Binder, *Z. Phys. B* **26**, 339 (1977).
- ¹⁴K. Binder and K. Schroder, *Solid State Commun.* **18**, 1361 (1976).
- ¹⁵E. Courtena, T. Rosenbaum, S. Nagel, and P. Horn, *Phys. Rev. B* **29**, 515 (1984).
- ¹⁶A. Loid, R. Feile, and K. Knorr, *Phys. Rev. Lett.* **48**, 1263 (1982).
- ¹⁷S. Bhattacharya, S. Nagel, L. Fleishman, and R. Susman, *Phys. Rev. Lett.* **48**, 1267 (1982).
- ¹⁸Y. Imry and S. Ma, *Phys. Rev. Lett.* **35**, 1399 (1975).
- ¹⁹W. Pan, Q. Jiang, and L. E. Cross, *J. Am. Cer. Soc.* **71**, C-17 (1988).
- ²⁰S. Swartz and T. Shrout, *Mater. Res. Bull.* **17**, 1245 (1982).
- ²¹L. A. Shebanov, P. Kapostina, and J. Zvirgzds, *Ferroelectrics* **56**, 105 (1984).
- ²²P. Bonneau, P. Garnier, E. Husson, and A. Morell, *Mater. Res. Bull.* **24**, 201 (1989).
- ²³E. Gyot, S. Foner, S. Hansanian, R. Guertin, and K. Westerholz, *Phys. Lett. A* **79**, 339 (1980).
- ²⁴J. Ferre, J. Rajchenbach, and H. Maletta, *J. Appl. Phys.* **52**, 1697 (1981).
- ²⁵M. Lanagan, N. Yang, D. Dube, and S. Jang, *J. Am. Cer. Soc.* **72**, 481 (1989).
- ²⁶G. Haertling and C. Land, *J. Am. Cer. Soc.* **54**, 1 (1971).
- ²⁷V. Ishchuk, E. Zavadskii, and O. Presnyakova, *Sov. Phys. Solid State* **26**, 437 (1984).
- ²⁸V. Ishchuk and O. Presnyakova, *Inorganic Mater.* **21**, 1047 (1985).
- ²⁹N. Setter and L. E. Cross, *Am. J. Appl. Phys.* **51**, 4356 (1980).
- ³⁰N. Setter and L. E. Cross, *Phys. Status Solidi A* **61**, k71 (1980).
- ³¹M. Kuprianov, A. Turik, S. Zaitser, and E. Fesenko, *Phase Transitions* **4**, 65 (1984).
- ³²A. Bokov, I. Rayevskii, V. Smotrakov, and I. Talyshova, *Sov. Phys. Solid State* **26**, 369 (1984).
- ³³P. Groves, *J. Phys. C* **19**, 111 (1984).
- ³⁴J. Chen, H. Chan, and M. Harmer, *J. Am. Cer. Soc.* **72**, 593 (1989).
- ³⁵B. Rolov, *Sov. Phys. Solid State* **6**, 1676 (1965).

APPENDIX 24

Local polar configurations in lead magnesium niobate relaxors

Dwight Viehland, S. J. Jang, and L. Eric Cross^{a)}

Materials Research Laboratory, Pennsylvania State University, University Park, Pennsylvania 16802

Manfred Wuttig

Engineering Materials Program, University of Maryland, College Park, Maryland 20742

(Received 21 June 1990; accepted for publication 21 June 1990)

The field dependence of the dielectric response has been measured for lead magnesium niobate relaxors. The frequency dispersion of the temperature of the permittivity maximum, T_{\max} , was analyzed using the Vogel-Fulcher relationship. The field dependence of the permittivity at various temperatures was also modeled using a phenomenological expansion in the electric field. The activation energy and a softening of the dielectric response were found to be maximum under a small bias. The freezing temperature was found to be minimum near this same bias. These results are interpreted to mean that the moments of the polar clusters do not freeze in random orientations, but rather locally preferred configurations of moments are proposed to exist. Evidence is presented that the scale of these configurations is approximately 100 Å. At higher biases the relaxation mechanism was shut down; consequently, the nonlinear response was stiffened and T_{\max} increased. The nonlinear response was also found to be maximum near the freezing temperature.

I. INTRODUCTION

Lead magnesium niobate (PMN) was the first ferroelectric discovered which exhibited a classic dielectric relaxation¹ and consequently was designated a relaxor ferroelectric. Since that time, many relaxors have been identified in mixed oxide systems, primarily in the perovskite and tungsten bronze structure families. Relaxors are unable to sustain a macroscopic polarization until temperatures significantly below the dielectric maximum (K_{\max}), but a local polarization is known to exist until much higher temperatures.² These locally polarized regions are believed to have rhombohedral symmetry³ and, consequently, eight equivalent variants. In consideration of these findings, Cross⁴ suggested that the polar clusters are superparaelectric with the polarization thermally fluctuating between equivalent directions. The density of the polar clusters as observed by transmission electron microscopy^{5,6} (TEM) is high enough that collective effects between clusters may be significant. Viehland *et al.*⁷ have consequently suggested that the fluctuations have a freezing temperature similar to spin glasses. Similar behavior in which long-range polar order is in conflict with random freezing has been reported in $\text{KTa}_1\text{Nb}_x\text{O}_{1-x}$,^{8,9} $\text{K}_{1-x}\text{Li}_x\text{TaO}_3$,¹⁰ and $\text{K}_{1-x}(\text{NH}_4)_x\text{H}_2\text{PO}_4$.¹¹ Burns and Dacol¹² and Bovton *et al.*¹³ have previously discussed the similarities of PMN relaxors to dipole and spin glasses.

Relaxors are known to be strongly nonlinear materials. The dielectric permittivity^{14,15} and elastic constants¹⁶⁻¹⁸ have both been reported to be altered by an electric field. It is generally believed that the nonlinearities are a reflection of the macroscopic polarization which can be sustained by an electric field to much higher temperatures. The polarization is completely reversible and collapses when the field is removed. Pan *et al.*¹⁵ have investigated the field dependence of the room-temperature dielectric constant in PMN; they

found strong nonlinearities and a suppression of the frequency dispersion at higher biases. Xi, Zhili, and Cross¹⁹ proposed an electric-field-induced micro-macro domain transition in La-modified lead zirconate titanate with 8 at. % La and a Zr/Ti ratio of 65/35 near the temperature of the onset of a macroscopic polarization to account for the field dependence of the dielectric response.

Spin glasses can be viewed as interacting superparamagnetic clusters.²⁰ These materials are characterized by a freezing temperature at which the fluctuations of the magnetic moment condense and by conflicting interactions. Spin glasses are also known to be strong nonlinear materials magnetically. It is generally believed that the change in properties is a reflection of an alignment of spins and an ordering of nearest-neighbor interactions, leading to a change in the dynamics of the freezing process. The magnetic permittivity,²¹ temperature of the permittivity maximum,²² and the onset of irreversibility²³ have all been reported to be altered by magnetic fields. The purpose of this work was to investigate the field dependence of the freezing process and the nonlinear permittivity in PMN relaxors. The field dependence of the dielectric response has been comprehensively measured up to bias levels above saturation.

II. EXPERIMENTAL PROCEDURE

The samples used in this study were PMN ceramics with 10 at% PT (PMN-10PT). They were prepared as described by Pan.²⁴ The 100 Hz dielectric maximum was near 40 °C. The samples were free of aging as described by Pan,²⁴ free of pyrochlore as described by Swartz and Shroud,²⁵ of dimensions 1 cm × 0.5 cm × 0.05 cm, and electrode with gold. Stoichiometric aging free samples were used to avoid a potential complication of the relaxation mechanism by a defect structure.

The dielectric response was measured as a function of frequency and temperature at bias levels of 0, 0.5, 1, 2, 3, 4, 5, 6, 7, 8, 10, 12, 14, 20, and 28 kV/cm. The frequencies used

^{a)} Also in the Electrical Engineering Department.

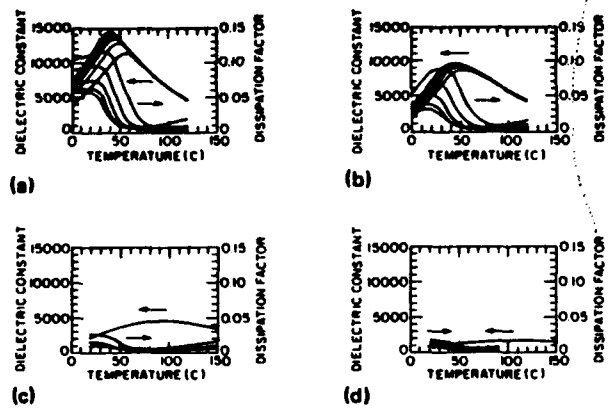


FIG. 1. Dielectric constant and dissipation factor as a function of temperature at measurement frequencies of 0.1, 1, 10, 100, and 1000 kHz. The largest dielectric constant and dissipation factor are the 0.1 kHz, the smallest are the 1000 kHz, and the other curves between are in order of increasing frequency. (a)–(d) are at bias levels of 0, 8, 20, and 28 kV/cm respectively.

were 0.1, 0.2, 0.4, 1, 2, 4, 10, 20, 40, 100, 200, 400, and 1000 kHz. Measurements were made in the temperature range of 0–150 °C by cooling at a rate of 1 °C/min. The measurements were made using an HP4275A and 4274A LCR meters. Two large blocking capacitors were used to protect the dielectric bridge from possible dielectric breakdown of the sample. A 20-MΩ resistor was put in series with the dc power supply so as not to bypass the ac current from the capacitance bridge.

III. RESULTS

The field dependencies of the dielectric responses, both real and imaginary, are illustrated in Figs. 1(a)–1(d) for bias levels of 0, 8, 20, and 28 kV/cm, respectively. It can be seen that an electric field reduces the dielectric constant, suppresses the frequency dispersion, and increases the temperature of the dielectric maximum. Also, the dielectric loss was reduced and showed a more pronounced maximum. Under larger biases, Maxwell–Wagner losses are evident at high temperatures as shown in Figs. 1(c) and 1(d). The loss is not shown in Fig. 1(d) above 80 °C in order to make the graph distinguishable.

The field dependence of K_{max} is shown in Fig. 2(a). The 0.1-kHz K_{max} was approximately 15 000 under 0 kV/cm, decreased slowly at lower bias levels, and then decreased quadratically to approximately 1500 under 28 kV/cm. At higher frequencies, K_{max} showed less field dependence, but no dispersion of K_{max} was observed above 10 kV/cm. The field dependence of the temperature of the dielectric maximum (T_{max}) is shown in Fig. 2(b). The 0.1-kHz T_{max} went through a minimum of approximately 38 °C under 3 kV/cm and then increased to approximately 110 °C under 28 kV/cm. Similar results were obtained for the other frequencies. At higher measurement frequencies, T_{max} was less dependent on the bias, but no dispersion was observed above 10 kV/cm in the frequency domain investigated.

IV. DISCUSSION

The strong field dependence of the dielectric permittivity can be interpreted in terms of an alignment of the mo-

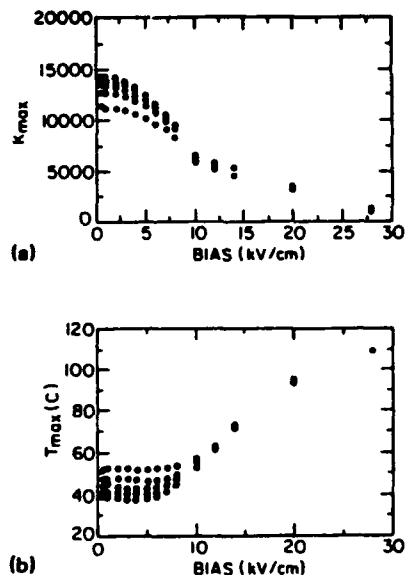


FIG. 2. (a) Permittivity maximum (K_{max}) as a function of dc bias level. The measurement frequencies were 0.1, 1, 10, 100, and 1000 kHz. The largest K_{max} 's are the 0.1 kHz, the smallest are the 1000 kHz, and the other curves between are in order of increasing frequency. (b) Temperature of permittivity maximum (T_{max}) as a function of bias level. The measurement frequencies were 0.1, 1, 10, 100, and 1000 kHz. The lowest temperatures are the 0.1 kHz, the highest are the 1000 kHz, and the other curves between are in order of increasing frequency.

ments of polar clusters. The permittivity decreased by approximately an order of magnitude under a bias level of 28 kV/cm relative to 0 kV/cm. At higher biases, the sample probably has reached saturation with nearly all moments aligned, and consequently the dielectric response ($\delta P/\delta E$) is lower. The polarization behavior for PMN-10PT has recently been modeled by modifying Néel's equilibrium equation for superparamagnetic clusters to include an effective internal field.²⁶ A more complete understanding of the field dependence of the relaxor behavior might be obtained by a careful analysis of the kinetics of the dielectric response and its nonlinear contribution.

The frequency dependence of the temperature of the permittivity maximum can be modeled using the Vogel–Fulcher relationship^{7,27,28} given in Eq. (1):

$$\omega = f_0 \exp\left(\frac{-E_a}{k(T_{max} - T_f)}\right) \quad (1)$$

where f_0 is the Debye frequency, E_a is the activation energy, T_{max} is the temperature of the permittivity maximum, and T_f is the freezing temperature. The 13 pairs of (ω, T_{max}) for each bias level below 10 kV/cm were analyzed using a Levenberg–Marquardt nonlinear fitting to Eq. (1) solving for f_0 , E_a , and T_f . The analysis was done assuming that f_0 was constant at all bias levels. A value of $1.03 \times 10^{12} \text{ s}^{-1}$ resulted in minimum variance. The resultant values for E_a and T_f are given in Table I along with the corresponding bias level. Figures 3(a) and 3(b) show E_a and T_f as a function of bias, respectively. E_a went through a maximum near 3 kV/cm and then decreased quadratically to zero near 10 kV/cm. T_f went through a minimum near 3 kV/cm and then increased

TABLE I. Activation energy (E_a) and freezing temperature (T_f) tabulated along side the corresponding bias level.

Bias (kV/cm)	E_a (eV)	T_f (K)
0.00	0.0407	291.50
1.00	0.0419	290.25
2.00	0.0426	289.37
3.00	0.0430	288.79
4.00	0.0425	288.85
5.00	0.0395	290.80
6.00	0.0363	293.51
7.00	0.0287	299.56
8.00	0.0217	306.20

dramatically above 10 kV/cm. The field dependence of the permittivity was modeled with a phenomenological expansion in the electric field as given in Eq. (2):

$$\chi(E, T) = \chi_0(T) + \chi_2(T)E^2 + \chi_4(T)E^4 + \dots, \quad (2)$$

where $\chi_0(T)$ is the zero-field permittivity, $\chi_2(T)$ is the second-order nonlinearity, and $\chi_4(T)$ is the fourth-order nonlinearity. The fitting of the data is shown as the solid lines in Figs. 4(a)–4(d), and the experimental data as the solid circles. χ_2 and χ_4 as a function of temperature at measurement frequencies of 0.1 and 100 kHz are shown in Figs. 5(a) and 5(b), respectively. Both nonlinear components had anomalous behavior near 15 °C, which is close to T_f . The second-order nonlinearity was positive (soft) near T_f , but became negative (stiff) at higher and lower temperatures. The fourth-order nonlinearity was soft above 60 °C and became stiff at lower temperatures. Similar results were obtained at the other measurement frequencies, but are not shown in order to make the graph distinguishable. The magnitude of both nonlinear components decreased with increasing frequency.

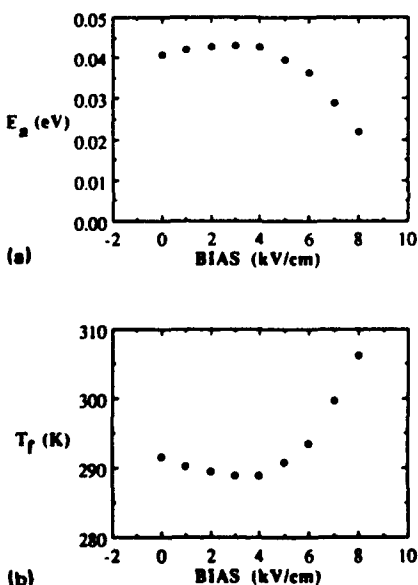


FIG. 3. (a) Activation energy (E_a) as a function of bias level. (b) Freezing temperature (T_f) as a function of bias level. E_a and T_f were calculated using Eq. (1).

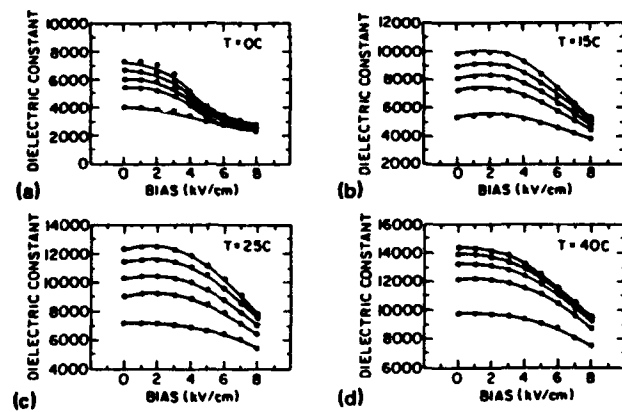


FIG. 4. Permittivity as a function of bias level at various temperatures for measurement frequencies of 0.1, 1, 10, 100, and 1000 kHz. The solid points are the experimental data, and the solid line is the curve fitting to Eq. (2). The highest dielectric response is the 0.1 kHz, the lowest is the 1000 kHz, and the other curves between are in order of increasing frequency. (a)–(d) are at measurement temperatures of 0, 15, 25, and 40 °C, respectively.

The strong decrease in E_a indicates that a large dc bias shuts down the relaxation mechanism. The electric field may split the degeneracy of the eight equivalent rhombohedral states and significantly change the depths of the potential wells. As a consequence, the polarization can no longer rotate between neighboring directions near this “pinch-off.” The degeneracy of the variants is not split in normal ferroelectrics because, before the required field level is reached, domain wall motion sets in. The field dependence of E_a for a rotation of the magnetic moment of a superparamagnetic cluster was derived by Néel.¹⁹ A similar expression in terms of the electric field for a superparaelectric cluster is given in Eq. (3):

$$E_a = E_a(0) \left(1 \pm \frac{E}{E_k} \right)^2, \quad (3)$$

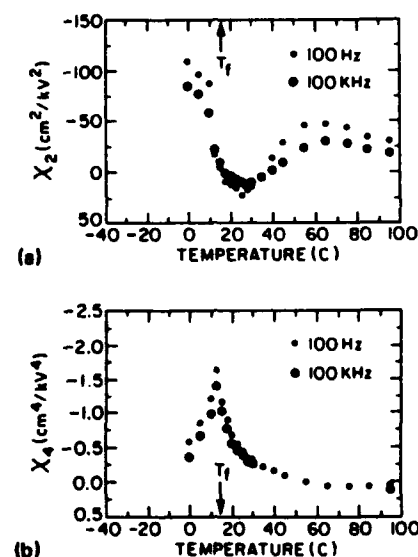


FIG. 5. (a) Second-order nonlinear dielectric response (χ_2) as a function of temperature where T_f is the freezing temperature. (b) Fourth-order nonlinear dielectric response (χ_4) as a function of temperature. Both figures show data for measurement frequencies of 0.1 and 100 kHz.

where E is the applied field, and E_a is the anisotropy field. E_a can be approximated as $2E_a(0)/P_{\text{local}}V$,³⁰ where P_{local} is the local polarization, and V is the cluster volume. $E_a(0)$ was 0.0407 eV, and the cluster diameter of PMN has been reported to be between 2 and 5 nm.^{5,6} The mean cluster diameter can be assumed to be the average of these two values, and assuming spherical regions, the volume can be approximated as $2.5 \times 10^{-20} \text{ cm}^3$. The local polarization has been found to be approximately 0.25 C/m^2 ,² and E_a can then be estimated as 22 kV/cm. The fluctuation frequencies at 40 °C under 10 kV/cm for the 0°, 70°, 110°, and 180° variants are then 2×10^{-8} , 0.5, 2.5×10^5 , and 1.5×10^9 Hz, respectively. Some relaxation may be detected due to rotations between the 110° and 70° variants at measurement frequencies above 100 kHz, but the population of these states is relatively small. The average relaxation time under 10 kV/cm, then, is so long compared to the half-cycle of the measurement that the system is essentially kinetically frozen. This model can qualitatively describe the shut down of the relaxation mechanism, but it predicts that E_a should decrease significantly at low bias levels. The measured E_a actually increased until a threshold bias.

To more accurately describe the field dependence of E_a , the effect of cluster interactions needs to be included. Interactions have recently been accounted for by including an internal field.²⁶ The internal field was treated as a macroscopic average, but there will also be local dipole fields between cluster moments in the unelectrified state which are probably randomly orientated as evidenced by a lack of macroscopic polarization and anisotropy. One of the effects of a local field will be to change the depths of the potential wells and to make them dependent on the configurations of neighboring clusters. A possible explanation of the maximum in E_a at 3 kV/cm then is that the sample becomes internally biased by finding locally preferred configurations of moments. Under a small electric field, then, a threshold is reached where on the global average the difference between the potential minima is smallest. Assuming that the local internal biases have a net direction along one of the rhombohedral orientations the 0°, 70°, 110°, and 180° variants are lowered by ΔE_a , $\Delta E_a \cos 70^\circ$, $\Delta E_a \cos 110^\circ$, and $-\Delta E_a$, respectively. The average relaxation time (τ_{ave}) can be approximated by a statistical average over the entire set of relaxation times if the splitting of the degeneracy is much smaller than E_a . An approximation for τ_{ave} is given in Eq. (4):

$$\begin{aligned} \tau_{\text{ave}} = & \frac{\tau_0}{8} \left[\exp\left(\frac{\bar{E}_a + \Delta E_a}{k(T_{\text{max}} - T_f)}\right) + \exp\left(\frac{\bar{E}_a - \Delta E_a}{k(T_{\text{max}} - T_f)}\right) \right. \\ & + 3 \exp\left(\frac{\bar{E}_a + \Delta E_a \cos 70^\circ}{k(T_{\text{max}} - T_f)}\right) \\ & \left. + 3 \exp\left(\frac{\bar{E}_a - \Delta E_a \cos 70^\circ}{k(T_{\text{max}} - T_f)}\right) \right], \end{aligned} \quad (4)$$

where \bar{E}_a is the activation energy under 3 kV/cm, at which point E_a was maximum and presumably the energy difference between the variants smallest. Equation (4) was modeled using a nonlinear analysis program solving for $\Delta \bar{E}_a$,

which yielded a value of 0.005 eV. The analysis was done simultaneously for all measured frequencies under zero bias in order to obtain the best estimate.

The decrease in T_f and the softening of the dielectric response can be understood in terms of an enhanced fluctuation kinetics under small biases. The magnitude of χ_2 and ΔT_f were small, which is undoubtedly a reflection of the small value of ΔE_a . An approximation for an internal bias in the unelectrified state can be obtained by setting ΔE_a equal to an electrical energy as given in Eq. (5):

$$\frac{1}{2} E_a P_{\text{local}} V = \Delta E_a, \quad (5)$$

where E_a is an internal bias. E_a is not the mean value of the random dipole field, but rather reflects the dependence of E_a on the configurations of neighboring moments. V and P_{local} were approximated above as $2.5 \times 10^{-20} \text{ cm}^3$ and 0.25 C/m^2 , respectively. E_a can then be estimated as 2.5 kV/cm, which is nearly equal to the field level at which χ was maximum and T_f minimum. This indicates that the maximum softening of the dielectric response and minimum T_f may occur at a threshold field which overrides the local configurations. The local dipole fields may tend to locally align the cluster moments, consequently slowing down the fluctuations. If the scale of the local configurations is small, the preferred alignment will average out over a macroscopic scale, but the effect on the fluctuation kinetics will not. A small applied bias adjusts the potential wells and on a global average decreases ΔE_a ; consequently, the fluctuation kinetics are enhanced. The maximum softening and minimum T_f then occurs when the potential variants are closest to being equivalent.

A potential-well model which describes the field dependence of the equivalent variants is shown in Figs. 6(a)–6(c). Figure 6(a) represents the unbiased state and illustrates that the degeneracy of the equivalent variants is inherently split. The splitting energy is shown as ΔE . Figure 6(b) represents the average potential well under 3 kV/cm. This figure shows that the variants are essentially all of the same depth. At this point the moment can most readily access all variants. Figure 6(c) shows the average potential well near "pinch-off" where the relaxation mechanism has essentially been shut down. This figure shows that the variant antiparallel to the field has been raised by nearly E_a and the variant parallel to the field lowered by E_a .

The glassy nature of relaxors in the unelectrified state probably arises due to the random dipole fields between cluster moments. If the dispersion in the local dipole field is of the same order as the mean local field, then the macroscopic system may try to partially order the cluster moments. If the mean local field cannot override the inhomogeneity, a global equilibrium cannot be established. Vugnerister and Glinchuk³¹ have proposed a dipole interaction theory for strongly polarizable solids with soft phonon modes. The prediction of this theory is that if $Nr_c^3 \gg 1$, then the dipoles will favor a ferroelectric ordering, and if $Nr_c^3 \ll 1$, then the dipoles will freeze randomly, where N is the dipole density and r_c is the correlation radius. N can be approximated as V_f/V , where V_f is the volume fraction of the polar clusters. V_f is not known precisely, but will be roughly estimated here as $\frac{1}{3}$ from

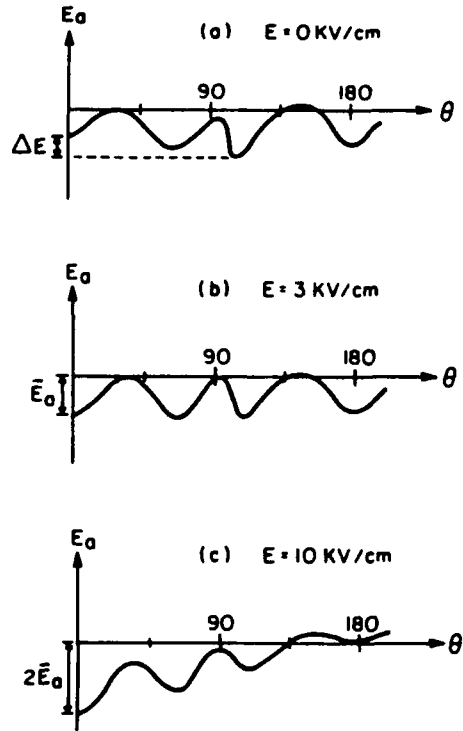


FIG. 6. Diagram illustrating the proposed potential-well model which describes the field dependence of the dielectric response. E_a is the activation energy, ΔE is the inherent zero field splitting of the equivalent variants, and \bar{E}_a is the activation energy, at which point the energy difference between the variants is smallest. (a)-(c) are for dc bias levels of 0, 3, and 10 kV/cm.

TEM micrographs.^{5,6} The correlation length has been found to saturate near freezing at 200 Å,¹² and the correlation radius may be approximated as 100 Å. Nr_c^3 can then be estimated for PMN as 10. This indicates that relaxors are not ideal dipole glasses, but have some tendency towards ferroelectric ordering of the cluster moments. This ordering obviously does not go to completion; the macroscopic system may instead establish preferred configurations of orientations of cluster moments. Below T_f , the macroscopic system is stuck in these configurations and cannot establish a normal polar state. The implication is that relaxors freeze into configurations which have a texture on the nanometer scale and that this texture is the "precursor" to long-range polar order of a macrodomain state. The scale of these configurations below T_f can be assumed to be approximately the same as the maximum correlation length. This scale is such that on a global average the preferred alignment averages out, and no macroscopic polarization or anisotropy is observed.

Locally preferred configurations could arise by the macroscopic system balancing the configurations of nearest and next-nearest cluster moments. The local effect may be that the potential minima of the variants are split by dipole-dipole interactions in such a manner that on a global average the 0° variant is lower for nearest-neighbor configurations and the 70° or 180° variant is lower for next-nearest-neighbor configurations. The macroscopic system may minimize its frustration by partially satisfying the drive for an ordering of the moments. It is generally believed that spin-glass behavior is a reflection of competing interactions which lead to freez-

ing. The implication is that the freezing in relaxors may occur when the correlation length reaches a value where polar clusters have multiple neighbors which are mutually polarizing. Other nanoscale interactions could lead to freezing in relaxors, and in fact recent results indicate that the freezing in PLZT could be due in part to strain fields.

The results suggest that there may be a hierarchy of relaxation processes associated with a complex phase space having many local energy minima associated with different configurations of moment orientations. The splitting of the degeneracy of the equivalent variants can serve as a driving force for a subsequent search for an optimum configuration suppressing the fluctuation kinetics. The cluster moments may then be able to relax below T_f when the moments of neighboring polar clusters are in certain improbable configurations. The implication is that the relaxational process is not truly stochastic in that the "random walk" has favored local minima which drives the relaxation. The measured value of ΔE should be slightly different for measurements made on heating as compared to cooling, and in fact the dielectric response has been found to be different.¹⁹ At the start of a cooling run, the moments may be thermally randomized, destroying the local configurations, whereas on a heating run the initial state is not disturbed. The low-field aging of the dielectric permittivity in PMN²⁴ can also be interpreted using this model. The aging occurs over long time periods near the maximum in the permittivity. The relaxation time of the aging process is much longer than that of the polarization fluctuations at this temperature, indicating that there is a hierarchy of mechanisms. Defects may be able to significantly change the optimum configuration, and consequently the permittivity decreases with time because the kinetics of the fluctuations are suppressed as more favorable configurations are found.

At biases above 3 kV/cm, the dielectric response became stiff, which indicates that the fluctuations are slowed down by large electric fields. The maximum nonlinearities occurred near T_f , which is close to the temperature where the remanent polarization collapsed.⁷ It is perhaps logical to anticipate the nonlinear response to be optimal at this point because an electric field can most effectively repopulate the orientations of the moments in its direction. Consequently, the randomness of the dipole fields between cluster moments would be unstable to an ordering field which would effectively give a nonlinear feedback to the dielectric response. At bias levels above pinch-off, T_f and T_{max} increased rapidly, approximately 80 °C between 10 and 28 kV/cm, and seemed to be saturating at the highest bias levels. The correlation length is known to be field dependent.¹² As the correlation length increases, the effective cluster volume increases, and consequently the interactions between polar clusters are longer range and the kinetics of the fluctuations are slower. At bias levels above the point where the fluctuations have condensed, the electrification may override the chemical inhomogeneity which normally prevented long-range polar ordering. T_{max} then approaches the value of the homogeneous state. Near saturation, the correlation length may reach the macroscopic scale, and T_{max} saturates. The glassy character of relaxors is then destroyed by a large applied electric field

which orders the local dipole fields and establishes a global equilibrium.

V. CONCLUSION

Evidence for local configurations of the moments of polar clusters in PMN relaxors was found. A small applied field is believed to override these configurations, enhancing the kinetics of the polarization fluctuations. Large biases are believed to order the local dipole fields between cluster moments, destroying the dipole-glass character of relaxors.

ACKNOWLEDGMENT

This work has been supported in full by contracts administered through the Office of Naval Research.

- ¹G. Smolenski and A. Agranovska, Sov. Phys. Solid State **1**, 1429 (1960).
- ²G. Burns and F. Dacol, Solid State Commun. **48**, 853 (1983).
- ³L. Shebanov, P. Kapostius, and J. Zvirgzds, Ferroelectrics **56**, 1057 (1984).
- ⁴L. Cross, Ferroelectrics **76**, 241 (1987).
- ⁵C. Randall and A. Bhalla, J. Mater. Sci. **29**, 5 (1990).
- ⁶J. Chen, H. Chan, and M. Harmer, J. Am. Cer. Soc. **72**, 593 (1989).
- ⁷D. Viehland, S. Jang, L. Cross and M. Wuttig, J. Appl. Phys. **68**, 2916 (1990).
- ⁸G. Samara, Jpn. J. Appl. Phys. **24**, Suppl. 24-2, 80 (1985).
- ⁹K. Lyon, P. Fleury, J. Negron, and H. Carter, Phys. Rev. B **36**, 2465 (1987).
- ¹⁰U. Hochli, P. Kofel, and M. Maglione, Phys. Rev. B **32** 4546 (1985).
- ¹¹E. Courtens, T. Rosenbaum, S. Nagler, and P. Horn, Phys. Rev. B **29**, 515 (1984).
- ¹²G. Burns and F. Dacol, Solid State Commun. **58**, 567 (1986).
- ¹³V. Bovtun, N. Krainik, L. Markova, Y. Poplavko, and G. Smolenski, Sov. Phys. Solid State **25**, 225 (1984).
- ¹⁴A. Glass, J. Appl. Phys. **40**, 4699 (1969).
- ¹⁵W. Pan, W. Gu, D. Taylor and L. Cross, Jpn. J. Appl. Phys. **28**, 653 (1989).
- ¹⁶T. Shroud, Ph.D. dissertation, The Pennsylvania State University (1980).
- ¹⁷G. Schmidt, H. Beige, G. Borchhardt, J. Cieminski, and R. Rossbach, Ferroelectrics **22**, 683 (1978).
- ¹⁸T. Shroud, W. Schulze, and J. Biggers, Ferroelectrics **34**, 105 (1981).
- ¹⁹Y. Xi, C. Zhili, and L. Cross, Ferroelectrics **54**, 163 (1983).
- ²⁰K. Binder and A. Young, Rev. Mod. Phys. **58**, 4, 801.
- ²¹S. Chikazana, Y. Yaochanas, and Y. Miyalo, J. Phys. Soc. Jpn. **49**, 1260 (1980).
- ²²J. de Almedia and D. Thouless, J. Phys. A **11**, 983 (1978).
- ²³C. Paulsen, J. Nanida, S. Williamson, and H. Maletta, J. Appl. Phys. **55**, 1652 (1984).
- ²⁴W. Pan, Ph.D. dissertation, The Pennsylvania State University (1988).
- ²⁵S. Swartz and T. Shroud, Mater. Res. Bull. **17**, 1245 (1982).
- ²⁶D. Viehland, S. Jang, M. Wuttig, and L. Cross (unpublished).
- ²⁷J. Tholence, J. Appl. Phys. **50**, 7369 (1979).
- ²⁸S. Shtrikman and E. Wohlfarth, Phys. Lett. **85A**, 467 (1981).
- ²⁹L. Neel, C. R. Acad. Sci. **228**, 664 (1949).
- ³⁰R. Chantrel and E. Wohlfarth, J. Magn. Magn. Mater. **40**, 1 (1983).
- ³¹B. Vugemeister and M. Glinchuck, Sov. Phys. JETP **52**, 482 (1980).
- ³²S. Vakhrushev, B. Kvyatkovsky, A. Naberezhnor, N. Okuneva, and B. Topervers, Ferroelectrics **90**, 173 (1989).

APPENDIX 25

Accept. Ph.D. Mag.B

1

THE DIELECTRIC RELAXATION OF LEAD MAGNESIUM NIOBATE RELAXOR FERROELECTRICS

Dwight Viehland, S. Jang, L. Eric Cross

Materials Research Laboratory, The Pennsylvania State University
University Park, Pa. 16802

Manfred Wuttig

Department of Materials and Nuclear Engineering, University of Maryland
College Park, Md. 20742

The dielectric spectroscopy of lead magnesium niobate relaxor ferroelectrics has been investigated over the frequency range of 10^2 to 10^7 Hz. The imaginary component was found to become nearly frequency independent below a freezing temperature, and scaled to a phenomenological equation involving the Vogel-Fulcher relationship. The absorption and Cole-Cole plots were found to become very broad near this freezing temperature. The relaxation time distribution was subsequently calculated by analogy to spin and dipolar glasses. A strong broadening of the distribution was found in the vicinity of the freezing temperature. It is proposed that this deviation from Debye behavior is a result of the development of correlations between polar moments leading to the onset of nonergodicity near freezing.

I. INTRODUCTION

Lead magnesium niobate (PMN) is a relaxor ferroelectric. In the zero field cooled (ZFC) state relaxors are characterized by a relaxational process typical of a classic dielectric relaxator, and by the lack of macroscopic polarization and anisotropy. Burns (Burns and Dacol 1983) (Burns and Dacol 1986) has shown that a local polarization exists in the ZFC state to temperatures much higher than that at which a remanent polarization can be sustained. In the field cooled (FC) state relaxation is not observed (Viehland, Jang, Wuttig, and Cross 1990b), and the system is able to sustain a macroscopic polarization below a "critical" temperature which is significantly lower than the radio frequency permittivity maxima. Smolenskii (Smolenski and Agranovskya 1960) originally proposed that underlying the relaxor behavior is a chemical inhomogeneity on the B-site cation, leading to a spatially varying composition with local Curie temperatures. Randall (Randall and Bhalla 1990) and Chen (Chen, Chan, and Harmer 1989) have recently shown that in PMN there is a partitioning on the nanometer scale into chemically homogeneous clusters. It is currently believed that it is the scale of this process which underlies the relaxor behavior. Cross has suggested that local ferroelectric phase transitions may occur inside of these individual chemical regions (Cross 1987). The size of these moments is such that their orientations may be thermally agitated, analogous to superparamagnetism (Neel 1949).

Schmidt (Kersten, Rost, and Schmidt 1983) has shown that the dielectric relaxation is Debye-like at temperatures significantly above the temperature of the permittivity maximum (T_{\max}). Yushin (Yushin, Smirnova, Dorogortsev, Smirnov, Gylamov 1987) has recently found a broadening of the relaxation time distribution near T_{\max} , unlike a Debye process. Kirolov (Kirolov and Isupov 1973) has analyzed the frequency dispersion of T_{\max} with the Debye relationship; obtaining an activation energy and pre-exponential factor of 7 eV and 10^{40} sec^{-1} .

respectively. Cross has recently analyzed the frequency dispersion of T_{\max} with the Vogel-Fulcher relationship (Viehland, Jang, Wuttig and Cross 1990a), analogous to spin glasses (Tholence 1979) (Tholence 1980); obtaining an activation energy and pre-exponential factor of 0.04 eV and 10^{12} sec^{-1} , respectively. He found that the freezing temperature (T_f) coincided with the temperature at which a stable remanent polarization can be sustained. A dipole glass model for relaxors was subsequently proposed (Viehland, Jang, Li, Wuttig, and Cross), with local dipole fields between superparaelectric moments leading to the development of a frustration below the freezing temperature.

The magnetic and dielectric relaxations of spin and dipolar glasses are believed to undergo freezing, due to frustrated interactions (Kirkpatrick and Sherrington 1978) (Edwards and Anderson 1975) and random fields (Nozav, Sechovsky, Kambersky 1987) (Morgownik and Mydosh 1981). The magnetic absorption and Argrand plots are known to become broad near T_f (Huser, Wenger, vanDuyneveldt, and Mydosh 1983). It is believed that on cooling through T_f , the relaxation time distribution strongly broadens extending from microscopic to macroscopic time periods. The broadening is believed to be due to the onset of nonergodicity above the freezing temperature. It is the purpose of this work to investigate the dielectric dispersion of PMN around the freezing temperature, and compare the results to spin and dipolar glasses.

II. EXPERIMENTAL PROCEDURE

The samples used in the study were PMN single crystals. The crystals were grown by a flux method as described by Setter (Setter 1980). They were orientated along the (100) direction, were of dimensions 0.2cm x 0.1cm x 0.08cm, and were electroded with gold.

The dielectric constant was measured as a function of frequency (ω) between 450 and 150 °K at a cooling rate of 4°C/min. The frequencies used were 10^2 , 10^3 ,

10^4 , 10^5 , 10^6 , and 10^7 Hz. The measurements were made using HP4275A and 4274A LCR meters. The dielectric curve for each frequency was smoothed and interpolated to determine the temperature of the permittivity maximum (T_{max}) as accurately as possible. The remanent polarization was also measured for comparison using a standard pyroelectric technique.

III. RESULTS AND DISCUSSION

The complex susceptibility, $\chi = \chi' - i\chi''$, is shown in Figures 1(a) and (b) for various measurement frequencies. The real component (χ') had a maximum of approximately 22000 at 260°K for a measurement frequency of 100 Hz, and the imaginary part (χ'') had a maximum of approximately 1200 at 250°K. It should be noted that the inflection point of χ'' corresponds in temperature to the maximum χ' . The quantity χ'' was essentially frequency independent below 230°K, indicative of a freezing into a glassy state. The value of χ'' seemingly extrapolated to zero near 0°K, unlike the metallic spin glasses (Mulder, vanDunneveldt 1982) whose absorption extrapolates to approximately 60% of its maximum. At lower temperatures the dispersion of χ' was significantly less, but was observed at much lower temperatures than for χ'' .

The strong decrease in the frequency dispersion of χ'' below 230°K suggests that the data can be scaled by approximating $\chi''(T, \omega)$ as $h(T)R(u)$ following Courtens (Courtens 1984); where $h(T)$ and $R(u)$ describe the frozen and dynamic contributions respectively, and $u(\omega, T)$ is a scaling variable. The function $R(u)$ is given by equation 1;

$$R(u) = \frac{1}{2} (1 + \tanh(u)) \quad (1)$$

where, $u = d(E_C - E)$

where d is a constant in units of $^0\text{K}^{-1}$, and E_C is a cutoff energy in units of ^0K . The value of E can be approximated by the Vogel-Fulcher relationship $\tau = \tau_0 e^{E/(T-T_f)}$

(Vogel 1921) (Fulcher 1924), where $1/\tau_0$ is the Debye frequency and T_f a freezing temperature. At lower temperatures $R(u)$ is approximately 1, and $\chi''(T,\omega)=h(T)$. At higher temperatures $R(u)$ decreases approaching zero, consequently $\chi''(T,\omega)=0$. At intermediate temperatures, $R(u)$ varies as a function of frequency ($\omega=1/\tau$), as given by the Vogel-Fulcher relationship. The functional dependence of $h(T)$ was empirically determined from low temperatures ($T < 230^{\circ}\text{K}$) by an exponential fitting, $c_1 \exp(c_2 T)$. The modelling was done using a Levenberg-Marquardt fitting solving for d , E_C , and T_f . The values of c_1 and c_2 were held constant during the fitting, and τ_0 was assumed to be 1×10^{-12} sec as previously reported (Viehland, Jang, Wuttig, and Cross 1990a). Minimum variance (~2%) was obtained for d , E_C , and T_f equal to 5.08×10^{-3} , 886.2°K , and 220.33°K respectively. The phenomenological model is shown along side the experimental data in Figure 2(a). Reasonable agreement can be seen. The function $R(u)$ is shown in Figure 2(b) for various measurement frequencies. The data scales quite readily to $(E_C - E)$ over a wide range of frequencies.

The value of T_f was also estimated by modelling the dispersion of T_{\max} with the Vogel-Fulcher relationship for comparison. A minimum variance was obtained for $1/\tau_0$ equal to 10^{12} sec $^{-1}$ and T_f equal to 217.7°K , which is in close agreement with T_f as determined from the modelling of χ'' using equation 1. The fitting of the data is shown in Figure 3(a). Analysis with the Arrhenius relationship yielded an activation energy and a pre-exponential factor of 7 eV and 10^{40} sec $^{-1}$, respectively. Both of which are physically unreasonable for a thermally activated process. The remanent polarization (P_r) as a function of temperature is shown in Figure 3(b). The extrapolation of P_r to zero yielded a temperature between 215 and 220 $^{\circ}\text{K}$, which is close to T_f . This shows that on zero field heating from the field cooled state, the macroscopic polarization collapses near the Vogel-Fulcher freezing temperature. The implication is that the "thawing" temperature of the field cooled

state and freezing temperature of the zero field cooled state coincide, reflecting the kinetics of the polarization reversals. The static polarization of PMN-10PT has recently been determined from Sawyer-Tower measurements and shown to scale to hyperbolic functions involving a reduced temperature somewhat similar to equation 1 (Viehland, Jang, Li, Wuttig, and Cross 1990).

The Vogel-Fulcher scaling of χ'' has been interpreted to mean that freezing does not occur by cluster growth, but rather by the freezing of local modes (Courtens 1984). The scaling in RADP is believed to be due to a competition between antiferroelectric and ferroelectric exchanges on the atomic level (Courtens 1984) (Courtens, Rosenbaum, Nagler, and Horn 1984). This is further substantiated by the saturation of the correlation length at 12 \AA^0 near T_f (Courtens, Rosenbaum, Nagler, and Horn 1984). The Vogel-Fulcher scaling of χ'' in PMN may have its origins in the phase separated superparaelectric regions. Chemically homogeneous regions on the scale of approximately 50 \AA^0 have been observed by TEM (Randall and Bhalla 1990) (Chen, Chan, and Harmer 1989). The local polarization may be homogeneous within each region and of predetermined size. Dipole fields between superparaelectric moments may subsequently lead to a freezing of the polarization fluctuations into a glassy state at lower temperatures. This is further substantiated by the saturation of the correlation length in PMN crystals at 200 \AA^0 near the Vogel-Fulcher freezing temperature (Viehland, Jang, Li, Wuttig, and Cross 1990) (Vakhrushev, Kvyatkovsky, Naberezhev, Okuneva, Topervers 1989).

The absorption, χ'' , over a wide range of frequency at various temperatures around T_f is shown in Figure 4. The width of the χ'' curves exceeds that which can be attributed to a single relaxation time, and strongly suggest a wide distribution. The absorption width increases as the temperature decreases approaching T_f , and becomes essentially flat below T_f with all curves remaining parallel. The implication

is that dramatic changes occur in the relaxation time distribution on cooling through T_f . This change cannot be attributed to a normal Debye like relaxational process, because τ_{\max} does not shift steadily down in frequency. Kersten (Kersten, Rost, and Schmidt 1983) has previously analyzed the temperature dependence of τ_{\max} with the Debye relationship obtaining an activation energy and pre-exponential factor of approximately 0.5 eV and 10^{-16} sec, respectively. His modelling was done at temperatures significantly above the permittivity maximum, where the absorption has distinct peaks as shown in Figure 4. In this temperature range the local polarization fluctuates at relatively rapid frequencies, i.e. the superparaelectric moments are nearly decoupled. The shift of τ_{\max} can then be modelled by the Debye relationship over a limited temperature interval. But as strong correlations develop between neighboring moments on cooling, the relaxation deviates significantly from Debye behavior as reflected in a strong temperature dependance of the activation energy and pre-exponential factor (Kirolov and Isupov 1973). Cole-Cole plots are shown in Figure 5 around T_f , to further illustrate the broadness of the relaxation time distribution. Near T_f the plot is flat, on increasing temperature curvature can be seen, and near the temperature of the radio frequency permittivity maxima semicircles are observed. The flattening of the Cole-Cole curves near the Vogel-Fulcher freezing temperature suggests as well that the relaxation time distribution is becoming very broad with the tail of the distribution extending in the macroscopic time regime.

The dielectric and magnetic responses of dipolar and spin glasses can be represented by a summation over a distribution of relaxators (Courtens 1984) (Lundgren, Svelinich, and Beckman 1981), as given in equation 2;

$$\chi''(T, \tau) = \int_{\tau_0}^{\infty} G(\tau, T) \frac{\chi'_0(T)}{1-i\omega\tau} d\ln\tau \quad (2)$$

where $G(\tau, T)$ is the distribution of relaxation times, $\chi'_0(T)$ the low frequency limit of $\chi'(T, \omega)$, and $\omega = \tau^{-1}$. Assuming $G(\tau, T)$ is very broad in $\ln(\tau)$, χ'' can be approximated from equation 2 as given in equation 3.

$$\chi''(T, \tau) \approx \chi'_0(T) G(\tau, T) \quad (3)$$

Following such a procedure causality predicts that $\chi'' \sim -\delta\chi'/\delta\ln(\omega)$ (Lundgren, Svelinch, and Beckman 1981), which is illustrated in Figure 1(c). The agreement with the data in Figure 1(b) is quite good.

Isothermal cross sections of $G(\tau, T_0)$ as a function of τ for PMN are shown in Figure 6(a) at $T=T_f$, $T>T_f$, $T=T_{max}$, and $T>T_{max}$ respectively. The value of $\chi'_0(T)$ was assumed to be the 100 Hz $\chi'(T)$. Dashed lines are drawn in to represent what the distribution most probably looks like over the whole frequency range. The drawing of these lines was guided by the fact that $G(\tau, T_0)=0$ near τ_{Debye} , and that at higher temperatures the distribution will be Gaussian. Near T_f the distribution was found to be essentially flat between 10^{-2} and 10^{-7} sec, tailing to zero near 10^{-12} . With increasing temperature the distribution sharpened, developing a distinct τ_{max} near the temperature of the radio frequency permittivity maximum. At higher temperatures τ_{max} was found to shift to higher frequencies, analogous to a Debye type relaxation, but the width and shape of the distribution continued to change with increasing temperature. Isotemporal cross sections, $G(\tau_0, T)$, are shown in Figure 6(b) at various measurement frequencies. A sharp step in $G(\tau_0, T)$ was found near T_{max} and shifted to higher temperatures with increasing frequency. Below T_f , $G(\tau_0, T)$ decreased slowly with decreasing temperature. The magnitude of $G(\tau_0, T)$ also increased with frequency, over the

range investigated. The isothermal cross sections are essentially the dielectric loss factor. A previously proposed relaxation time distribution as a function of temperature is illustrated in Figure 7 (Viehland, Jang, Wuttig, and Cross 1990a). It can be seen that this model is supported by the experimental data. The isothermal width of the spectrum is shown to become very broad near T_f , approaching the macroscopic time regime. The shortest relaxation time (τ_{\min}) is shown to approach macroscopic times only at temperatures far below T_f . Above T_f the isothermal width of the relaxation time spectrum continuously sharpens as the temperature is increased with τ_{ave} and τ_{\min} approaching the microscopic time regime.

The dielectric spectroscopy results can be understood in terms of the interacting superparaelectric dipole glass model, discussed above. At high temperatures the moments are decoupled exhibiting typical Debye type behavior, but on cooling local dipole fields couple the polarization fluctuations and τ_{\max} varies in a nonlinear manner parameterizable by the Vogel-Fulcher relationship. It is proposed that as a consequence of increasing correlations, the relaxation time distribution broadens and flattens out with decreasing temperature reflecting the onset of nonergodicity. Near a critical temperature the distribution becomes extremely broad, as the polarization fluctuations undergo Vogel-Fulcher freezing into a dipole glass state. Consequently, the system can sustain a remanent polarization below this temperature. The relaxation time distribution remains relatively wide above T_f , in effect leading to a diffuse phase transformation. The diffuse nature of the transformation is thus not a reflection of compositional heterogeneity as originally proposed by Smolenski (Smolenski and Agranovskya 1960); but rather a consequence of a size dispersions of polar moments, and the development of correlations.

IV. CONCLUSIONS

The dielectric relaxation of PMN single crystals has been investigated, and shown to be similar to spin and dipole glasses. The absorption was found to be nearly frequency independent below a freezing temperature which correlated with the temperature at which a stable remanent polarization collapsed on heating from the field cooled state. The absorption spectra and Cole-Cole plots were found to become very broad near this freezing temperature. The relaxation time distribution has also been calculated and shown to strongly broaden near freezing, extending from the microscopic to macroscopic time regimes.

ACKNOWLEDGEMENTS

This work has been supported in full by contracts administered through the Office of Naval Research.

REFERENCES

- Burns, G., Dacol, F., Sol. State Com. **48**, 10, 853 (1983).
- Burns, G., Dacol, F., Sol. State Com. **58**, 9, 567 (1986).
- Chen, J., Chan, H., Harmer, M., J. Am. Cer. Soc. **79**, 593 (1989).
- Courtens, E., Phys. Rev. Lett. **52**, 69 (1984).
- Courtens, E., Rosenbaum, T., Nagler, S., Horn, P., Phys. Rev. B **29**, 1, 515 (1984).
- Cross, L.E., Ferroelectrics **76**, 241 (1987).
- Edwards, S., Anderson, P.W., J. Phys. F **5**, 765 (1975).
- Fulcher, G., J. Am. Cer. Soc. **8**, 339 (1925).
- Huser, D., Wenger, L., vanDuyneveldt, A., Mydosh, J., Phys. Rev. B **27**, 5, 3100 (1983).
- Kersten, O., Rost, A., Schmidt, G., Phys. Stat. Sol (a) **75**, 495 (1983).
- Kirkpatrick, S., Sherrington, D., Phys. Rev. B **17**, 4384 (1978).
- Kirollov, V. Isupov, V., Ferroelectrics **5**, 3 (1973).
- Lundgren, L., Svedlinch, P., Beckman, O., J. Magn. Magn. Mat. **25**, 33 (1981).
- Morgownik, A., Mydosh, J., Phys. Rev. B **24**, 5277 (1981).
- Mulder, C., vanDuneveldt, A., Physica (Utrecht) **113B**, 123 (1982).
- Neel, L., Compt. Rend. Acad. Sci. **228**, 664 (1949).
- Nozav, P., Sechovsky, V., Kambersky, V., J. Mag. and Magn. Mat. **69**, 71 (1987).
- Randall, C., Bhalla, A., J. Mat. Sci. **29**, 5 (1990).
- Setter, N., PhD Dissertation, The Pennsylvania State University (1980).
- Smolenski, G., Agranovskya, A., Sov. Phys. Sol. State **1**, 1429 (1960).
- Tholence, J., J. Appl. Phys. **50**, 7369 (1979).
- Tholence, J., Sol. State Com. **35**, 113 (1980).

- Vakhrushev, S., Kvyatkovsky, B., Naberezhov, A., Okuneva, N.,
Topervers, B., Ferroelectrics 90, 173 (1989).
- Viehland, D., Jang, S., Wuttig, M., Cross, L., J. Appl. Phys. 68, 2916 (1990a).
- Viehland, D., Jang, S., Wuttig, M., Cross, L.E., Accept. for Publ. in J. Appl.
Phys. (1990b)
- Viehland, D., Jang, S., Li, J., Wuttig, M., Cross, L., Accetp. for Publ. in Phys.
Rev. B. (1990)
- Vogel, H., Phys. Z 22, 695 (1921)
- Yushin, N., Smirnova, E., Dorogortsev, S. Smirnov, S., Gulyamov, G., Sov.
Phys. Sol. State 29, 10 1693 (1987).

LIST OF FIGURES

Figure 1. (a) The dielectric permittivity (χ') of PMN as a function of temperature for measurement frequencies of 10^2 , 10^3 , 10^4 , 10^5 , 10^6 , and 10^7 Hz. The top curve is the lowest frequency and the bottom the highest. (b) The imaginary part of the dielectric response (χ'') as a function of temperature for measurement frequencies of 10^2 , 10^3 , 10^4 , 10^5 , 10^6 , and 10^7 Hz. The bottom curve is the lowest frequency and the top the highest. (c) $\Delta\chi'/\Delta\log(\omega)$ as a function of temperature.

Figure 2. The points are the imaginary contribution of the dielectric response (χ'') as a function of temperature for measurement frequencies of 10^2 , 10^3 , 10^4 , 10^5 , 10^6 , and 10^7 Hz. The bottom curve is the lowest frequency and the top the highest, and where T_f is the freezing temperature. The solid line is a phenomenological fitting to equation 1. (b) The scaling parameter ($R(u)$) as a function of the scaling variable (u) for various measurement frequencies.

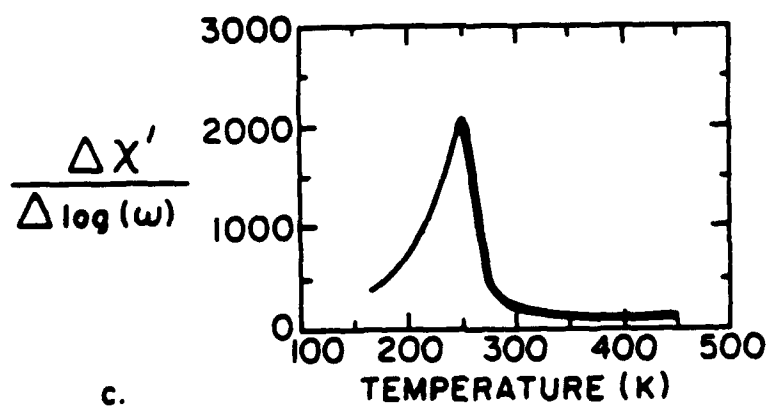
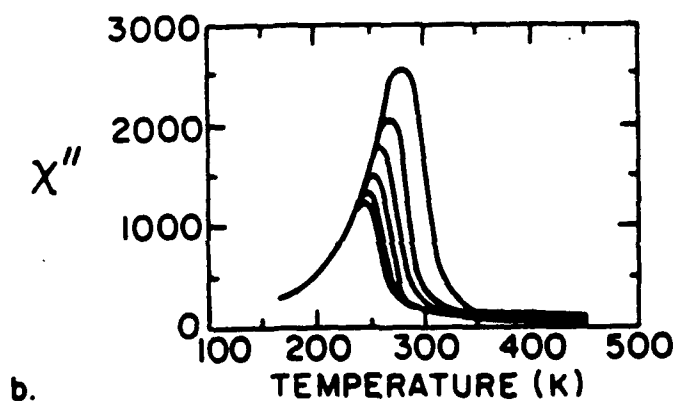
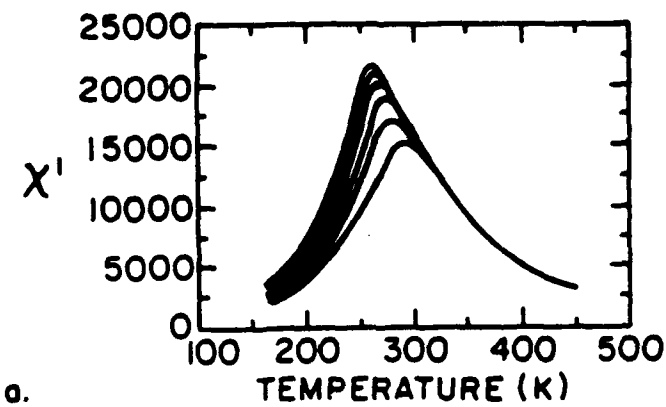
Figure 3. (a) The temperature of the permittivity maximum as a function of the measurement frequency. The dots are the data and the solid line is the fitting to the Vogel-Fulcher relationship. (b) The remanent polarization as a function of temperature.

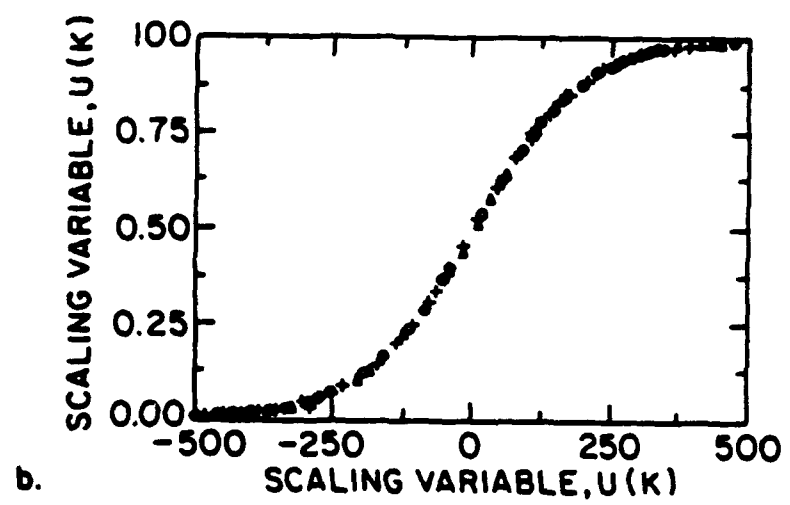
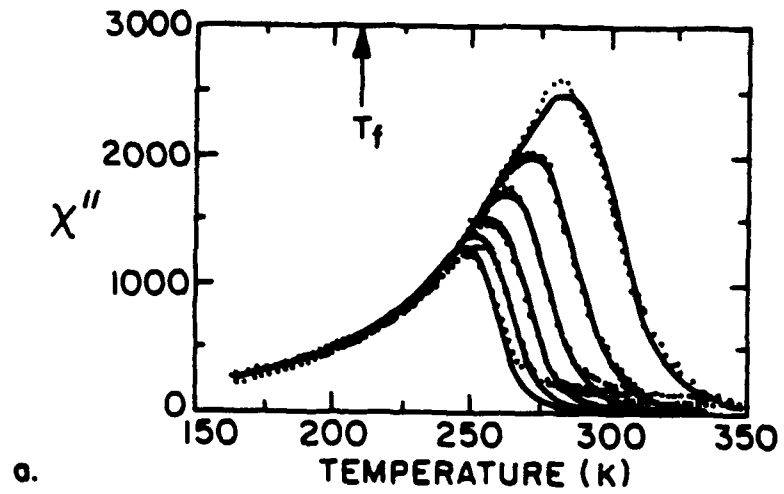
Figure 4. The dielectric absorption (χ'') as a function of frequency at various temperatures.

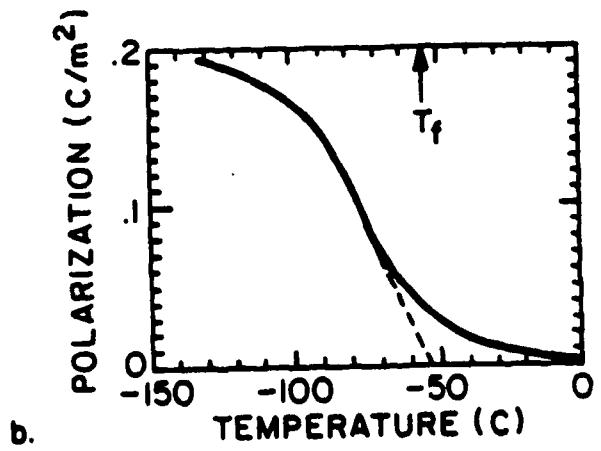
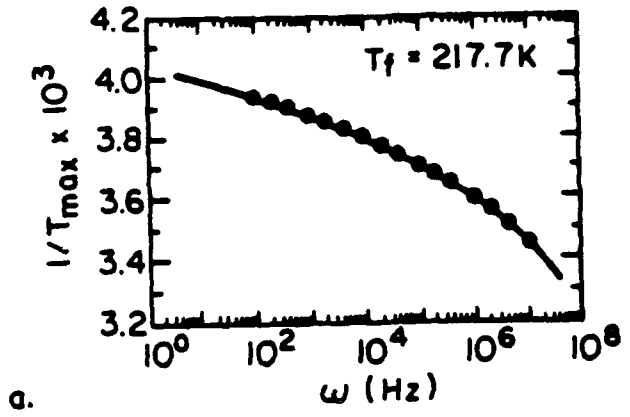
Figure 5. Cole-Cole plots at various temperatures around freezing.

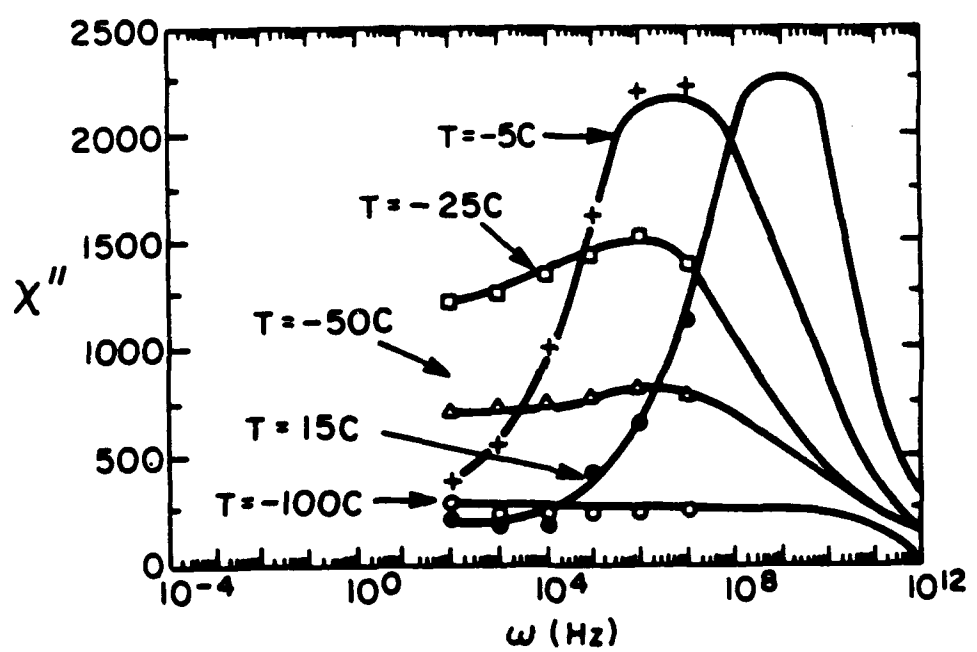
Figure 6. (a) The relaxation time distribution ($G(\tau, T_0)$) as a function of τ at various temperatures. (a) $T=T_f$, (b) $T>T_f$, (c) $T=T_{max}$, and (d) $T>T_{max}$. (b) The relaxation time distribution ($G(\tau_0, T)$) as a function of temperature at various measurement frequencies. The measurement frequencies shown are 10^2 , 10^3 , 10^4 , 10^5 , 10^6 , and 10^7 Hz. The bottom curve is the lowest frequency, and the top curve the highest.

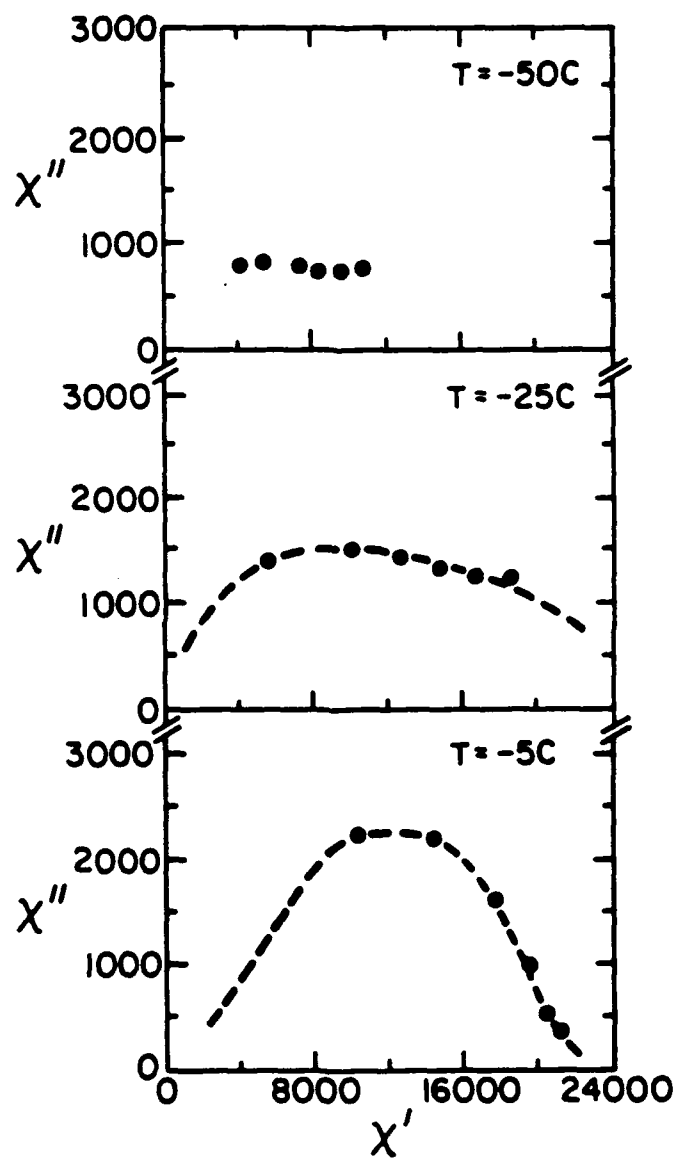
Figure 7. Diagram illustrated the proposed temperature dependent relaxation time spectrum. Where $G(\tau, T)$ is the number of polar regions having a relaxation time τ , T_f is the freezing temperature, and τ_D is the Debye frequency.

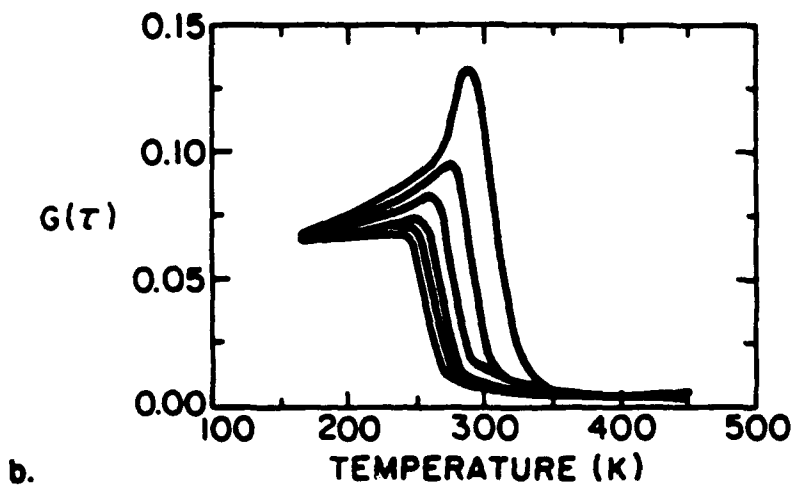
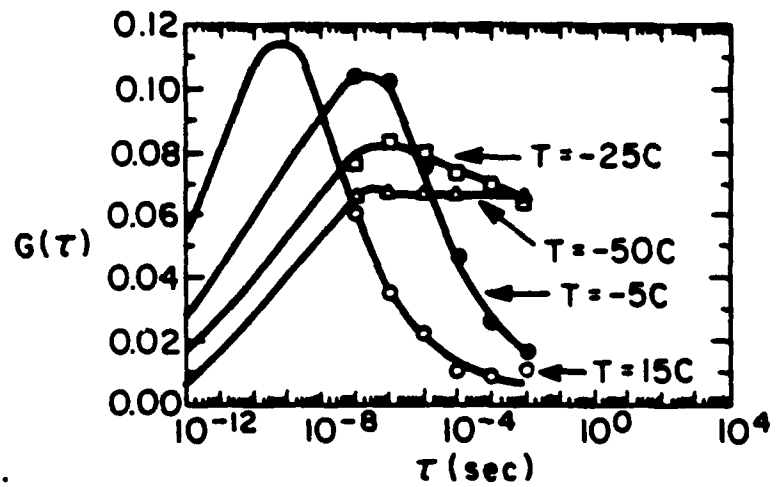


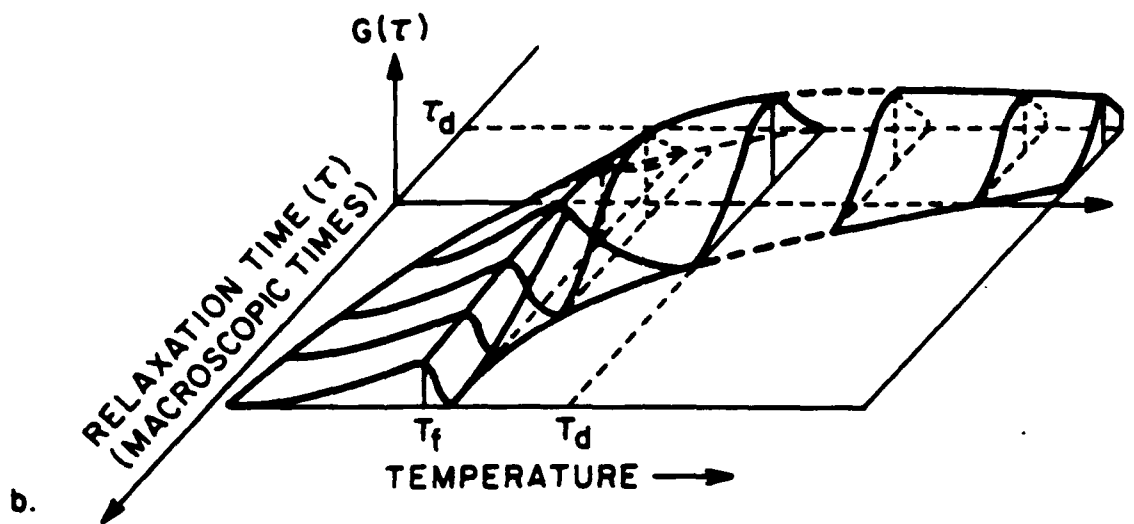












APPENDIX 26

THE GLASSY POLARIZATION BEHAVIOR OF RELAXOR FERROELECTRICS

Dwight Viehland, J.F. Li, S. Jang, and L.E. Cross

Materials Research Laboratory, The Pennsylvania State University
State College, Pa. 16802

Manfred Wuttig

Department of Nuclear and Materials Engineering, University of Maryland
College Park, Md. 20742

The polarization behavior of La-modified lead zirconate titanate relaxors has been investigated for various electrical and thermal histories. The field cooled and zero field cooled behaviors were both studied. The magnitude of both polarizations were found to be equal above a critical temperature. A macroscopic polarization developed under bias in the zero field cooled state, with the temperature of the maximum charging current decreasing with bias. This decrease was modelled using the deAlmeida Thouless relationship (deAlmedia and Thouless 1978), which predicted an average moment size freezing of approximately 3×10^{-27} C-m. A glassy polarization mechanism was subsequently proposed with correlations between superparaelectric moments leading to the development of effective nonergodicity in a frozen state. Arguments are presented that this freezing process is dispersive due to a distribution of correlation strengths. The time dependence of the polarization was also investigated.

I. INTRODUCTION

La-modified lead zirconate titanate with a Zr/Ti ratio of 65/35 (PLZT) and La contents between 4 and 14 atomic% are relaxor ferroelectrics. Relaxors have an inability to sustain a remanent polarization until temperatures significantly below the temperature of the permittivity maximum, but a local polarization is believed to exist to much higher temperatures (Burns and Dacol 1983). The implication is that the local symmetry is lower than the global. Randall has observed contrast on the nanometer level using transmission electron microscopy (TEM) (Randall 1987; Randall and Bhalla 1990). It is believed that the composition is locally homogeneous on a scale of approximately 50 \AA^0 , i.e. phase separated. This local chemistry is believed to prevent the establishment of normal long range polar ordering at a Curie temperature, instead the system establishes polar moments on the scale of the local chemistry. The size of these regions is such that the orientation of the polarization is believed to be thermally reversible (Cross 1987), analogous to superparamagnetism (Neel 1949). Cross has recently shown that the polarization fluctuations undergo a freezing (Viehland, Jang, Wuttig and Cross 1990a), analogous to spin and dipole glasses (Binder and Young 1986; Hochli, Kofel, and Maglione 1985). It was suggested that interactions between superparaelectric regions were responsible for this freezing. The freezing temperature (T_f) was also shown to correlate with the collapse in the remanent polarization.

The zero field cooled (ZFC) state of the relaxor appears cubic to x-rays down to liquid nitrogen temperatures, implying that the scale of the polar behavior is smaller than the coherence length of x-rays and is relatively temperature independent. The field cooled (FC) state appears rhombohedral even at room temperature. Xi (Xi, Zhili, and Cross 1983) has previously measured the polarization behavior of PLZT. He found no macroscopic polarization in the ZFC state, but upon application of a bias polarization developed. He interpreted his

results in terms of a micro to macrodomain transition. Somewhat similar differences between the ZFC and FC states have been found in spin and dipole glasses (Hochli, Kofel, and Maglione 1985). The re-orientating moments are believed to freeze devoid of long range order due to frustrated interactions. On application of a bias the moments tend to order, and properties characteristic of a normal ferroic state are observed. The differences between the ZFC and FC states in spin and dipolar glasses are usually attributed to a breakdown of ergodicity in the frozen state (Hochli, Kofel, and Maglione 1985).

II. EXPERIMENTAL PROCEDURE

The samples used in this study were PLZT ceramics with Zr/Ti ratios of 65/35 and La contents of 8 atomic%. They were donated by Honeywell Inc. of Bloomington, Minnesota. The samples were electroded with gold. The pyroelectric current was measured as a function of temperature on heating using a HP4140B pA meter. The polarization was then calculated by integration. Various measurement procedures were used reflecting different electrical histories. The sample was first cooled under zero bias and then heated under bias while measuring the pyroelectric current, designated as zero field cooled/ field heated (ZFC). The sample was subsequently cooled and heated, both under bias, while measuring the pyroelectric current, designated as field cooled/ field heated (FC). The remanent polarization was also measured by cooling under a bias, removing the bias and measuring the pyroelectric current on heating. The field levels used were 1, 3, 5, 7, 5, 8.5 and 10 kV/cm.

III. RESULTS AND DISCUSSION

The remanent polarization (P_r) as a function of temperature for PLZT-8 is shown in Figure 1. P_r collapsed near 60°C and seemingly tailed to zero at higher temperatures. This figure also shows other polarization curves. These curves were measured by heating the poled (field cooled) sample to temperatures below $T_f(0)$,

subsequently recooling the sample ($E=0$) and reheating measuring P_T . After this procedure P_T did not return to the previous low temperature value, but rather remained at the value of the highest temperature reached. This behavior is unlike a normal ferroelectric which would return to the low temperature value of P_T on recooling. The implication is that the scale of the polar ordering in relaxors is strongly dependent on the electrical and thermal histories. The field cooled (FC) state exhibits properties similar to a normal ferroelectric such as domains and anisotropy, whereas the zero field cooled (ZFC) state is devoid of long range order and is isotropic. These results are suggestive of a glassy polarization mechanism, similar to the dipole and spin glasses (Hochli, Kofel, and Maglione 1985). The differences between the ZFC and FC states in these glassy materials are well known.

The polarization of PLZT-8 is shown in Figure 2(a) and (b) for various electrical histories. The ZFC (zero field cooled, field heated) and FC (field cooled, field heated) polarizations are both shown in Figure 2(a) for a bias level of 3 kV/cm. The ZFC polarization exhibited a maximum of approximately 0.17 C/m^2 near 50°C . The FC polarization was approximately 0.3 C/m^2 at -100°C , and decreased with temperature approaching a value of 0.22 C/m^2 near 50°C . Near the temperature of the maximum ZFC polarization (T_{zfc}), the FC and ZFC polarizations were not equal. This difference is probably a reflection of a very broad relaxation time distribution, consequently the polar regions in the long time tail remain in their ZFC configuration until above T_{zfc} . But on field cooling from high temperatures these regions freeze into an ordered configuration, consequently the polarization is higher for the FC measurement than for the ZFC. Figure 2(b) shows similar data at a bias levels of 5 kV/cm. The difference between the ZFC and FC polarizations decreased with bias. With increasing bias the polar regions in the long

time tail of the distribution can probably be perturbed from their ZFC configuration, consequently the ZFC and FC polarizations are approximately equal near T_{zfc} .

Figure 3 shows plots of the time dependence of the polarization at various temperatures. The polarization was measured by applying 3 kV/cm, cooling down, removing the bias, and measuring the pyroelectric current as a function of time. The maximum polarization at each temperature, $P(t=0)$, was assumed to be that of the 3 kV/cm FC state (see Figure 2(a)). The polarization as a function of time was then calculated by subtracting the integral of the pyroelectric current. The decay of the polarization became slower with decreasing temperature. Above $T_f(0)$ the decay was rapid, slightly below T_{zfc} it was clearly exponential, and at lower temperatures it could not be detected. At a particular temperature, any configuration with an activation energy (E_a) less than kT will remain unchanged. Raising the temperature will allow the system to move across higher barriers, consequently the ZFC polarization approaches the FC values. On removal of the bias, the quasilogarithmic decay of the polarization may then occur as the thermal energy scrambles the FC state and the system searches configurational space finding the lowest local minima. The analogous magnetic viscosity has been modelled using many approaches (Binder and Young 1986; Ferre, Rajchenbach, and Maletta 1981), mostly involving a t^{-n} exponent. A similar relationship seemed to be observed for relaxors.

A small anomaly in the ZFC permittivity has been observed by Xi (Xi, Zhilli, and Cross 1983). This anomaly was shown to correlate in temperature with the maximum charging current, and decreased in temperature with bias. Figures 4(a) and (b) show plots of the ZFC pyroelectric current under 3 and 5 kV/cm, respectively. The temperature of the maximum charging current decreased with bias. The freezing temperature of the ZFC state, $T_f(0)$, has been shown to correlate with the extrapolation of the remanent polarization to zero (Viehland, Jang, Wuttig, and Cross 1990a). $T_f(0)$ is shown in Figure 1 to be approximately 60°C. Clearly a

characteristic temperature associated with the frozen state is decreasing with bias, and is suggestive of a breakdown of ergodicity below T_{zfc} .

If nonergodicity is occurring, then the decrease in this temperature with bias should follow the deAlmeida Thouless relationship (deAlmedia and Thouless 1978) given in equation 1;

$$E = A \left[\frac{T_f(0) - T_f(E)}{T_f(0)} \right]^{\frac{3}{2}} \quad (1)$$

where A is an adjustable parameter. The measurement field is plotted against $\{[T_f(0)-T_f(E)]/T_f(0)\}^{1.5}$ in Figure 5. The experimental behavior is compatible with equation 1, but is by no means a unique representation. A best parameter fit for A yielded a value of 30 kV/cm, and is shown as the solid line in the figure. A has been identified as $kT_f(0)/p$ (deAlmedia, and Thouless 1978; Chamberlin, Hardiman, Hardiman, Turkevich, and Orbach 1982) where p is the average magnitude of the polar moment freezing. A value of 3×10^{-27} C-m can then be deduced for p. This is close to the expected value of the superparaelectric moment in $Pb(Mg_{1/3}Nb_{2/3})O_3$ relaxors (Viehland, Jang, Wuttig, and Cross 1990b), which is approximately 5×10^{-27} C-m. With increasing La content, the scale of the polar behavior is believed to decrease. Consequently the field level necessary to decrease $T_f(E)$ by a unit amount would be expected to increase, i.e. $A=kT_f(0)/P_s V_{moment}$, which is experimentally observed (Xi, Zhili, and Cross 1983). These results give strong evidence that the individual moments undergoing freezing are superparaelectric, and that the glassy character is a reflection of correlations between these moments.

It is believed that the configurational energy of a spin glass possesses many quasidegenerate ground states (Edwards and Anderson 1975). The small energy

differences between these configurations may lead to the system being stabilized in one of them below $T_f(0)$, consequently breaking the ergodicity. This model has been substantiated by computer simulations (Walker and Walstedt 1980; Bantilan and Palmer 1981). A similar model may be extended to correlated superparaelectric moments. Local configurations of moment orientations are believed to exist on the scale of approximately 200 \AA^0 (Viehland, Jang, Wuttig, and Cross 1990b), effectively charge compensating the local polarization. There may be many minimas in configurational space associated with various combinations of moment orientations, all of nearly the same energy. But near $T_f(0)$ other configurations may become increasingly inaccessible as the relaxation time distribution approaches the macroscopic time scale, consequently effective nonergodicity may set in. Nonergodicity has previously been suggested to arise in $K_{1-x}Li_xTaO_3$ dipole glasses (Hochli, Kofel, and Maglione 1985) due to a freezing of superparaelectric moments. Analogy was made to the models of hierarchical spin glass dynamics (Nagai and Rajagopal 1984; Sibani and Hoffman 1989) in which some clusters must wait to relax until a number of neighboring clusters are in favorable positions, somewhat similar to the concepts presently suggested.

On application of a bias in the ZFC state, the quasi-degeneracy may be partially broken reflecting a preferred alignment. The system may then find the most favorable local configurations, and overtime adjust to the global equilibrium. The logarithmic time dependence (polarization viscosity) may then arise from readjustments in configurational space between local minima. Under higher biases the splitting of the degeneracy increases, consequently a global equilibrium can be established from the ZFC state at lower temperatures. The implication is that at a fixed temperature the polarization fluctuations may be nonergodic at zero bias but ergodic at finite biases. Any point below the maximum ZFC polarization (Figure 2) would then correspond to metastable local minima since sufficient time has not been

allowed for equilibrium, near T_{zfc} the system may start to approach a global equilibrium. The difference between the ZFC and FC polarizations near T_{zfc} indicate that the freezing is dispersive, such a difference was not observed in dipole glasses (Hochli, Kofel, and Maglione 1985). Between the temperature of the onset of local polarization (T_{Burns}) and $T_f(0)$, the susceptibility is nonlinear (Viehland, Jang, Wuttig, and Cross 1990b) and strong deviations from Curie-Weiss behavior develop (Kersten, Rost, and Schmidt 1983; Kirsh, Schmitt, and Muser 1986). The implication is that between T_{Burns} and $T_f(0)$ the energy surface is not featureless, but rather local minima which are correlated in configurational space exist. It can be anticipated that a significant dispersion of correlation strengths exist as a reflection of the cluster size dispersion observed by TEM (Randall and Bhalla 1990; J. chen, H. Chan, and M. Harmer 1989). The implication is that the smaller polar regions may remain ergodic to lower temperatures, and that the larger clusters may remain nonergodic to higher temperatures (as also suggested by the tailing of P_r , shown in Figure 1).

The FC state has a domain structure on the scale of 1-10 μm , whereas the scale of the polar behavior in the ZFC state is smaller than the coherence length of x-rays. The implication is that the scale of the polar behavior is field dependent, and in fact the correlation length has recently been found to increase with bias (Vakhrushev, Kvyattovsky, Naberezhnor, Okunera, and Toperres 1989). This does not reflect a simple dipole alignment but rather the establishment of a normal ferroelectric state, i.e. a micro to macrodomain transition. The bias must act to override the chemical inhomogeneity which normally prevents the establishment of long range polar ordering. A possible mechanism is the growth of the polar regions across the antiphase boundaries which are known to separate them (Randall 1987; Randall and Bhalla 1990). Similar generic behavior is observed in spin glasses. The ZFC state is isotropic with no evidence of long range magnetic ordering.

Where as the FC state has remanence, hysteresis, and irreversibility analogous to a normal ferromagnet. A switching from local configurations in the ZFC state to a macro-state (global equilibrium) under bias is seemingly observed in most glassy materials.

IV. CONCLUSION

The polarization behavior of the FC and ZFC states of relaxor ferroelectrics have been compared, and shown to be similar to spin and dipole glasses. The field dependence of a characteristic temperature has also been shown to follow the deAlmeida-Thouless relationship. A glassy polarization mechanism was subsequently proposed in which correlations between superparaelectric moments lead to the development of nonergodicity near a glass transition temperature.

ACKNOWLEDGEMENTS

**This work has been supported in full by contracts administered through the
Office of Naval Research.**

REFERENCES

- Bantilan, F., and Palmer, R., *J. Phys. F.* **261** (1981).
- Burns, G., and Dacol, F., *Sol. State Commun.* **48**, 853 (1983).
- Binder, K., and Young, A., *Rev. Mod. Phys.* **58**, 801 (1986).
- Chamberlin, R., Hardiman, M., Turkevich, L., and Orbach, R., *Phys. Rev. B* **25**, 6720 (1982).
- Chen, J., Chan, H., and Harmer, M., *J. Am. Cer. Soc.* **72**, 593 (1989).
- Cross, L.E., *Ferroelectrics* **76**, 241 (1987).
- deAlmeida, J., and Thouless, D., *J. Phys. A* **11**, 983 (1978).
- Edwards, S., and Anderson, P.W., *J. Phys. F* **5**, 965 (1975).
- Ferre, J., Rajchenbach, J., and Maletta, H., *J. Appl. Phys.* **52**, 1697 (1981).
- Hochli, U., Kofel, P., and Maglione, M., *Phys. Rev. B* **32**, 4546 (1985).
- Kersten, O., Rost, A., and Schmidt, G., *Phys. Stat. Sol. (a)* **75**, 495 (1983).
- Kirsh, B., Schmitt, H., and Muser, H., *Ferroelectrics* **68**, 275 (1986).
- Nagai, K., and Rajagopal, A., *Phys. Rev. Lett.* **53**, 1024 (1984).
- Neel, L., *Compt. Rend. Acad. Sci.* **228**, 664 (1949).
- Randall, C., PhD Dissertation, University of Essex (1987).
- Randall, C., and Bhalla, A., *J. Mat. Sci.* **29**, 5 (1990).
- Sibani, P., and Hoffman, K., *Phys. Rev. Lett.* **63**, 2853 (1989).
- Vakhrushev, S., Kvyatkovsky, B., Naberezhnor, A., Okunera, N., and Toperres, B., *Ferroelectrics* **90**, 173 (1989).
- Viehland, D., Jang, S., Wuttig, M., and Cross, L.E., *J. Appl. Phys.* **68**, 2916 (1990a).
- Viehland, D., Jang, S., Wuttig, M., and Cross, L.E., Accepted for publication in *J. Appl. Phys.* (1990b).
- Walker, L., and Walstedt, R., *Phys. Rev. B* **22**, 3816 (1980).
- Xi, Y., Zhili, C., and Cross, L.E., *J. Appl. Phys.* **54**, 3399 (1983).

LIST OF FIGURES

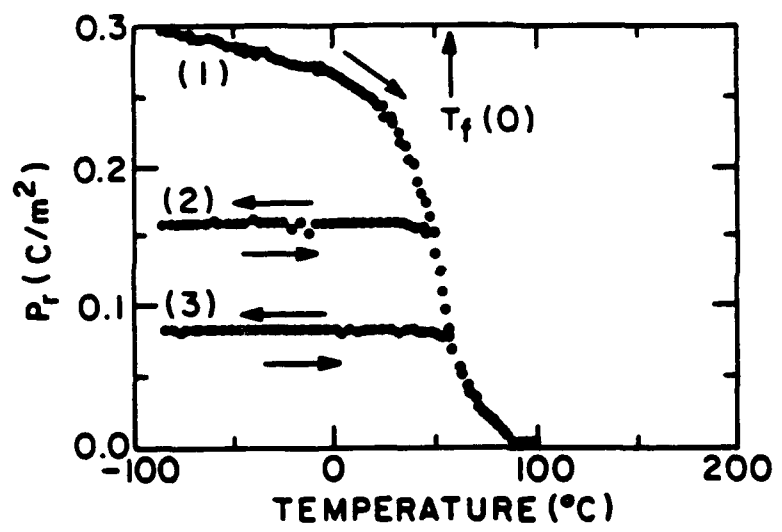
Figure 1. Remanent polarization (P_r) as a function of temperature, where $T_f(0)$ is a freezing temperature. The top curve, (1), was measured by heating to temperatures above $T_f(0)$. The bottom curves, (2) and (3), were measured by heating to temperatures below $T_f(0)$, subsequently recooling and measuring P_r .

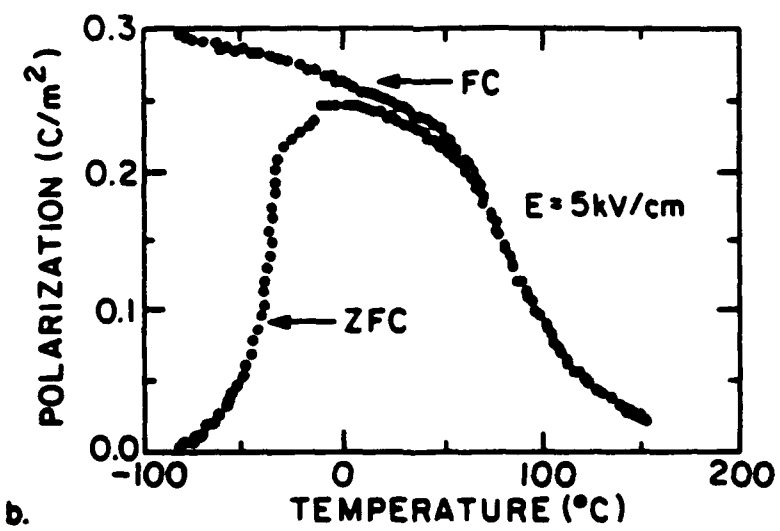
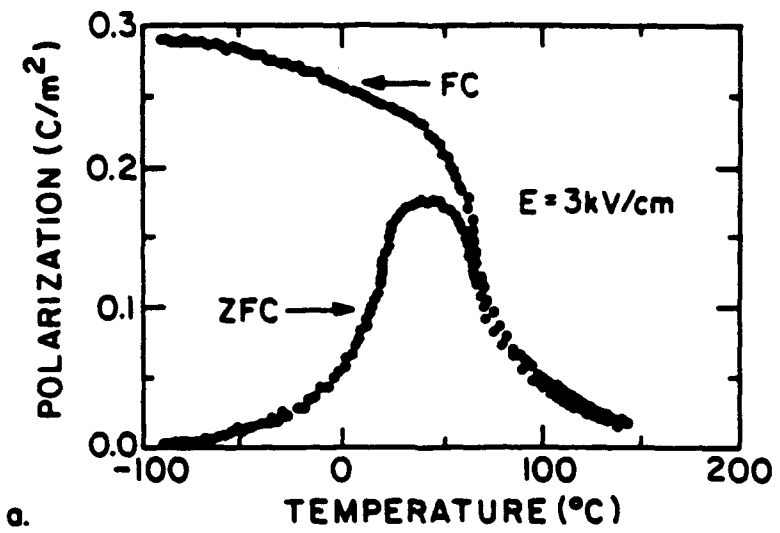
Figure 2. Polarization as a function of temperature for various electrical histories and bias levels, where FC means field cooled/ field heated and ZFC means zero field cooled/ field heated. (a) Bias level of 3 kV/cm, and (b) Bias level of 5 kV/cm.

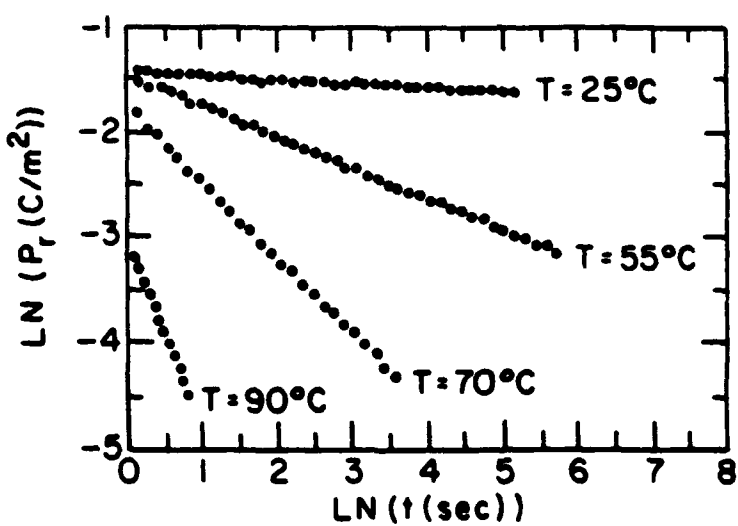
Figure 3. Remanent polarization as a function of time at various temperatures.

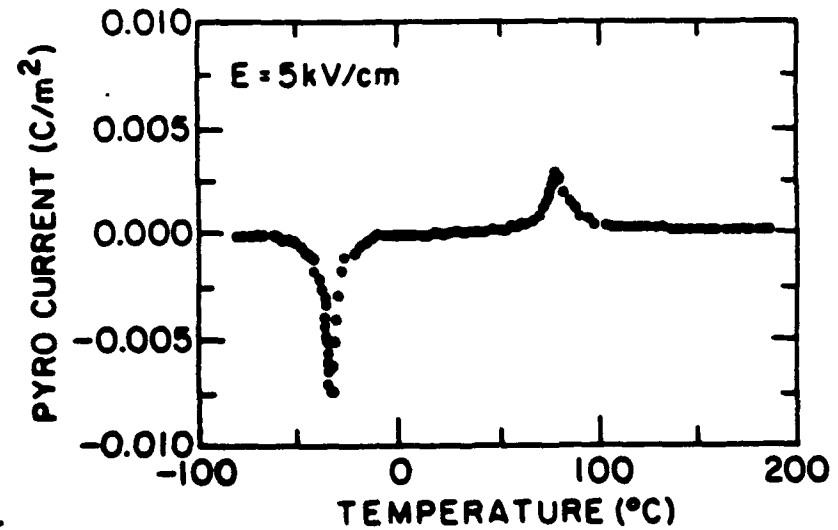
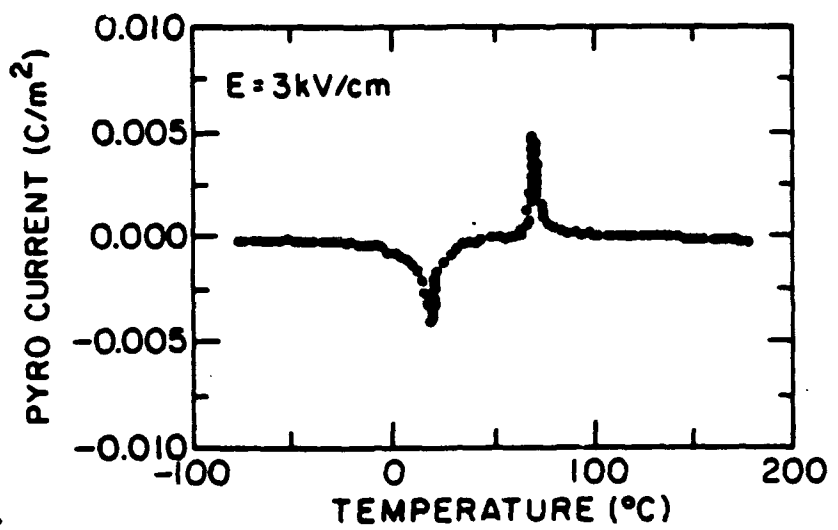
Figure 4. Pyroelectric current as a function of temperature at various bias levels. (a) Bias level of 3 kV/cm, and (b) Bias level of 5 kV/cm.

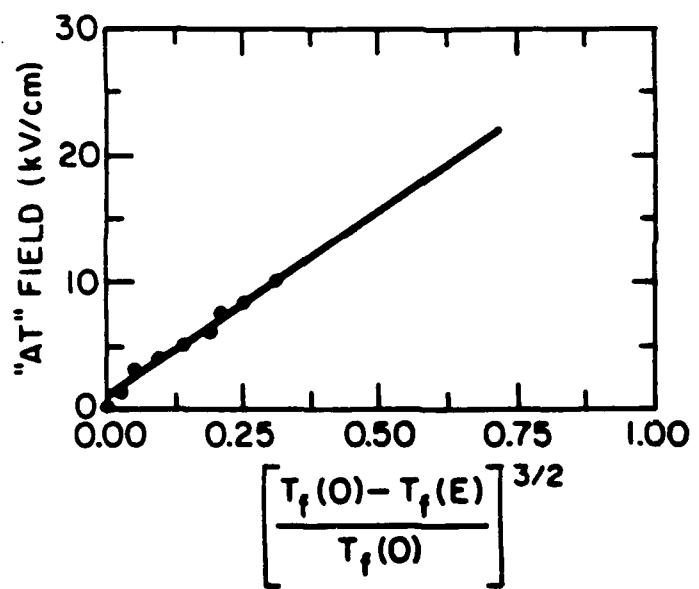
Figure 5. Plot of the applied bias ("AT" field) as a function of the temperature of maximum charging current, where $T_f(0)$ is the freezing temperature of the ZFC state and the solid line is the curve fitting to the deAlmedia Thouless relationship given in equation 1.











END